



HAL
open science

Synthesis, redox chemistry, and electronic structure investigation of lanthanide complexes with aromatic ligands of various sizes and bulkiness

Nolwenn Mahieu

► **To cite this version:**

Nolwenn Mahieu. Synthesis, redox chemistry, and electronic structure investigation of lanthanide complexes with aromatic ligands of various sizes and bulkiness. Chemical Sciences. Institut Polytechnique de Paris, 2023. English. NNT : 2023IPPAX128 . tel-04572995

HAL Id: tel-04572995

<https://theses.hal.science/tel-04572995>

Submitted on 13 May 2024

HAL is a multi-disciplinary open access archive for the deposit and dissemination of scientific research documents, whether they are published or not. The documents may come from teaching and research institutions in France or abroad, or from public or private research centers.

L'archive ouverte pluridisciplinaire **HAL**, est destinée au dépôt et à la diffusion de documents scientifiques de niveau recherche, publiés ou non, émanant des établissements d'enseignement et de recherche français ou étrangers, des laboratoires publics ou privés.

Synthesis, redox chemistry, and electronic structure investigation of lanthanide complexes with aromatic ligands of various sizes and bulkiness

Thèse de doctorat de l'Institut Polytechnique de Paris
préparée à École Polytechnique

École doctorale n°626 Ecole Doctorale de l'Institut Polytechnique de
Paris (ED IP Paris)
Spécialité de doctorat: Chimie

Thèse présentée et soutenue à Palaiseau, le 1 décembre, par

Nolwenn Mahieu

Composition du Jury :

Olivier Maury Directeur de Recherche, ENS Lyon	Président
Lucie Norel Professeure des Universités, Université de Rennes	Rapportrice
Michael Neidig Professeur des Universités, Université d'Oxford	Rapporteur
Nicolas Mézailles Directeur de Recherche, Université de Toulouse	Examineur
Grégory Nocton Directeur de Recherche, École Polytechnique	Directeur de thèse
Thomas Simler Chargé de Recherche, École Polytechnique	Invité



Synthesis, redox chemistry, and electronic structure investigation of lanthanide complexes with aromatic ligands of various sizes and bulkiness



Nolwenn Mahieu

Chemistry

LCM, CNRS, Ecole Polytechnique, Institut Polytechnique de Paris



A thesis submitted for the degree of Doctor of Philosophy

1st December 2023

A Padou,
J'aurais tellement aimé parcourir ce manuscrit avec toi,

A PhD cannot be undertaken alone and I am very grateful for all the people I have interacted with during those years.

First, I would like to thank the jury, Pr. Lucie Norel, Pr. Michael Neidig, Dr. Oliver Maury, Dr. Nicolas Mézailles, for accepting this role. Thank you for your comments on the manuscript and the presentation, I really appreciated our discussion during the defense.

Then, I would like to thank Greg for trusting me with these challenging subjects and encouraging me to investigate always further. Since my first year of master, you have always helped to develop my curiosity for the science and to strengthen my motivation to pursue a career in the academic world, for that I am very grateful.

I would like to thank Thomas for his support in the lab day after day as a postdoc and then as a researcher. I hope you know how much your knowledge of the lab and your patience helped all the PhD students of the lab 1. I am also very happy for you and your family and I wish you all the best!

Then, I would like to thank Bibi for his unwavering kindness and optimism. We probably would not have interacted particularly were it not for the (in)famous Gecom but I am so glad we did. Thank you for all those discussions and taking the time to hear me.

I would also like to acknowledge the collaborations I was involved in. Particularly Dr Boris Le Guennic, Prof Olivier Cador, Léo La Droitte and Dr. Maxime Grasset for the magnetism and computational studies. It has been a particularly challenging subject to reconcile experiments and computations and I am sure there is still more to surprise us with these compounds.

I would also like to thank Dr. Stefan Minasian for welcoming me to its lab and Dr. Olivia Gunther for her help in the lab and accepting to be my hands for a couple of weeks.

Coming into a new lab has always been a powerful experience for me. But in order for it to be a success, I feel that you need to understand more than what science is done, you need to understand how it is done. And for this perfect introduction to the 'lab1' and all that entails I will be forever grateful to Maxime. Thank you for showing me all the tricks and ropes in the lab as well as the best beers in the bars! I hope we will continue to cross path in the science world because it needs more people like you!

To all the members of the Lab 1 and especially the newcomers Adrien and Lucie, thank you for your uplifting spirit in the lab and outside. I wish you two good luck for the rest of your PhD and I am sure they are going to be great! I do not forget the even newer-comers Angus, Linda and Luca, I hope you have a great experience in the lab! I also need to thank the one who quickly became the best officemate, Claire. Thank you so much for all your advice and all our discussions, it really means a lot to me.

Of course, to all the students I have crossed path with in the LCM, thank you for your kindness of every day. A special mention to the lunch team, Pauline, Cate, Laureen, Marie-Sophie and Ingrid, thank you for making those breaks always interesting.

And in addition to the students, it is of course the whole LCM lab that I need to thank deeply for all those years. With a particular mention to Cédric, Véronique and Anne-Florence for their generous help and to Christophe for welcoming me and my glovebox upstairs while the lab was under renovation.

I also would like to thank all the students who came to the lab as interns and participated in my research. First with the modal William, Agathe, Kevin, Annaëlle and Gabriel, thank you for your curiosity and your engagement. Then Clara and Camille who both had very successful internships with profound impacts on my projects. Thank you very much for your enthusiasm and your contagious motivation. I wish you the very best for your next projects!

And because this passion for chemistry did not ignite by itself, I would like to acknowledge all the teachers that contributed to it over the years with a particular mention to Mme Ouvrard, Mr Beynier, Mr Le Roux and Mme Masson.

I would like to thank all the friends that I have made along the way and who have contributed in their own way to this long journey: Louise, Thierry, Nada&Simon, Apolline&Thibaut, Coco&Lucina, Maxime&Marie, Thibal, Noémie&Nicolas, Mathilde, Auriane, Mika, Alice, Corentin D., Nina, Fanny, Cécile, Camille, Juliette, Lucie&Louis, MH, Léo, Clémentine.

I would like to address particularly my thanks to Dr. Nicolas Casaretto who had the patience to analyse my small crystals an unfathomable number of times, to teach me the basis of crystal structure resolution and accompany me until I was more or less autonomous on the machines. Not only that, but you were also present for me when I had a rough time in the lab or outside always with the best/lengthiest recommendation of content and bringing us into your own worlds. This obviously extends to Amanda and the two clawed monsters; this journey would have been way less entertaining without you all!

A Benoît, je n'aurai pu imaginer de meilleur compagnon de route pour ces quelques années. Merci du fond du cœur pour tous et j'ai tellement hâte de passer les prochaines années qui s'annonce avec toi. To the Moon and Back !

A ma famille, Papa, Maman, Erell, merci infiniment pour votre aide et votre présence de tous les instants. Merci de m'avoir toujours encouragé à suivre mon instinct que ce soit à l'école ou dans toutes les activités que vous m'avez permise de faire. Sans vous je n'en serais pas arrivée là, alors merci milles fois. Je tiens également à remercier Padou et Madou pour leur extrême gentillesse et pour m'avoir tant de fois accueillie sur Paris quand je ne pouvais pas rentrer à la maison.

Table of Contents

List of abbreviations	11
List of synthesized complexes	13
Introduction	17
I. General presentation	19
1. Definition and discovery	19
2. Geopolitical implications of Rare-earth materials	20
3. Particularity of the <i>f</i> -orbitals and trending properties	20
II. Oxidation states and chemistry	22
1. Trivalent oxidation state	23
2. Tetravalent oxidation state	24
3. Divalent oxidation state	26
4. Intermediate-valence state	29
III. Physical Properties	31
1. Description of the electronic structure	31
2. Luminescence and optical properties	32
3. Magnetic properties	33
IV. Presentation of the work	41
References	43
Chapter 1: Reactive Thulium Complexes for Small Molecule Activation	47
I. Preliminary study with $\text{Tm}(\text{Cp}^{\text{ttt}})_2$ and CO/CO_2	49
1. Early study of divalent thulium	49
2. Synthesis and characterization of the reactive species	51
3. Summary of reactivity	52
II. Coupled reactivity with CO_2 and pyridine derivatives	55
1. Development of the synthetic path on the pyridine case	55
2. Generalization to pyridinium derivatives	58
3. Toward a CO_2 captor?	65
III. Extension to other small molecules	68
1. Reactivity with small oxygenated molecules	68
2. Reactivity with small organic molecules	70
3. Mechanism discussion	71
IV. Conclusion	72
References	74

Chapter 2: LnI ₂ as strong reductant for the formation of complexes with the Cnt ligand	75
I. Non classical divalent lanthanides in the literature	77
1. Development of LnI ₂ with dysprosium and neodymium	77
2. Established reactivity	77
3. Extension to organometallic complexes	78
II. The cyclononatetraenyl ligand	78
1. Discovery and synthesis	78
2. Rationalization of the Isomerization reaction	80
3. The Cnt as a ligand	81
III. Synthesis of Dy ₂ Cnt ₄ (thf) ₂ (2.1_{thf}) and Dy ₂ Cnt ₄ (2.1)	84
1. Salt metathesis approach	84
2. Approach toward thf removal	87
3. The trivalent approach	92
4. Characterization of Dy ₂ Cnt ₄ (2.1)	96
IV. Synthesis and characterization of Dy ₂ Cnt ₃ (thf) ₂ (2.3)	101
1. Naïve synthesis	101
2. Perfected synthetic path	102
3. Structural characterization	103
4. Computational approach	106
5. Magnetism study	109
6. Discussion	115
V. Extension to other LnI ₂	117
1. Synthesis of Nd ₂ Cnt ₄ (thf) ₂	117
2. Synthesis of Nd ₄ Cnt ₄ I ₄ (2.4)	117
VI. Conclusion	121
References	122
Chapter 3: Trivalent approach to dimeric lanthanide complexes with bridged Cnt ligands	125
I. Heteroleptic approach from trivalent starting material	127
1. Rationalization for the new path	127
2. Development of the new synthetic path	129
3. Synthesis and characterizations of Dy ₂ Cnt ₂ Cp ^{ttt} ₂ (3.3)	135
II. Direct reduction before the formation of the Cnt—dysprosium species	141
1. Synthesis and characterization of Dy ₂ CntCp ^{ttt} ₂ I (3.4)	141
2. Synthesis and characterizations of <i>endo</i> -Dy ₂ Cnt ₂ Cp ^{ttt} ₂ (3.3-endo)	152
III. Extension to other lanthanides	154

1.	Synthesis of $\text{LnCp}^{ttt}\text{I}_2(\text{thf})_2$ (3.1_{Ln})	154
2.	Adaptation of the synthesis	156
3.	Structural study of $\text{Ln}_2\text{Cnt}_2\text{Cp}^{ttt}_2$ (3.3_{Ln})	157
4.	Study of $\text{Er}_2\text{CntCp}^{ttt}_2\text{I}$ (3.4_{Er})	158
IV.	Discussion and conclusion on the Cnt species in its reduced form	161
	References	164
Chapter 4: Systematic study of the Cnt ligand in the LnCotCnt series		165
I.	Synthesis and characterization of LnCotCnt compounds with heavy lanthanides	167
1.	Reminder on sandwich compounds of lanthanides	167
2.	Synthetic path	169
3.	Discussion on the XRD structure	171
4.	NMR analysis and anisotropy discussion	173
5.	Observed flexibility with related systems	177
II.	Synthesis and characterization	178
1.	Extension of the synthesis and XRD characterization	178
2.	Problem arising from characterization	180
3.	Rationalizing the isomerization trigger	182
4.	A new molecular lanthanide switch	184
5.	Adapted synthesis and full characterization	185
III.	Isomerization study	189
1.	Come back on the case of KCnt	189
2.	Spectroscopic study of the isomerization of 4.2 _{Ln}	192
3.	Rationalization over the series	197
IV.	Conclusion	198
	References	199
Conclusion		201
Experimental section		211
1.	Supplementary information for Chapter 1	213
2.	Supplementary information for Chapter 2	235
3.	Supplementary information for Chapter 3	253
4.	Supplementary information for Chapter 4	279
Appendices		325

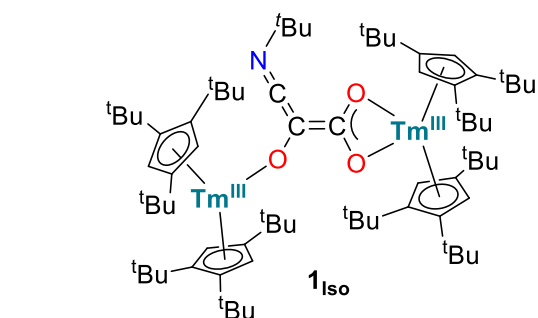
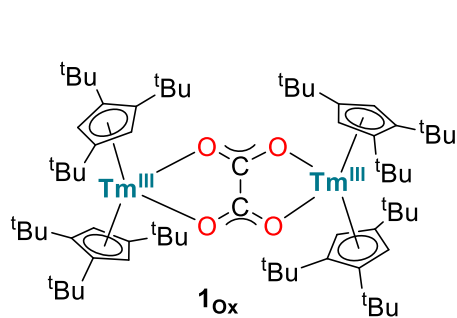
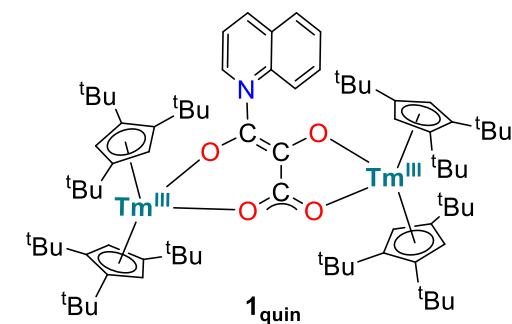
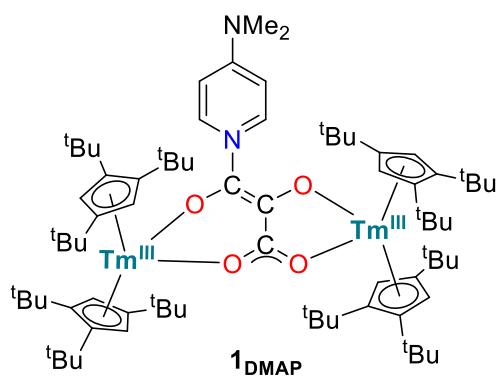
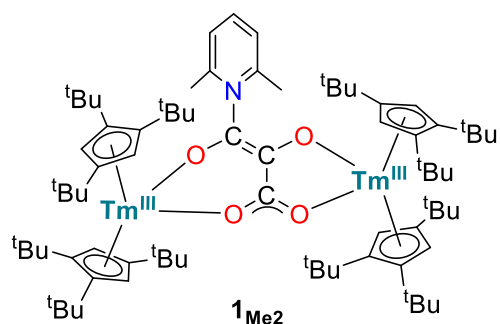
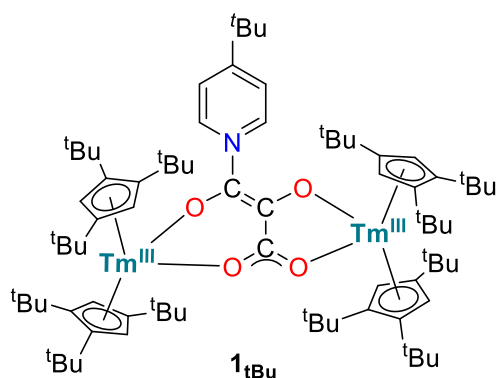
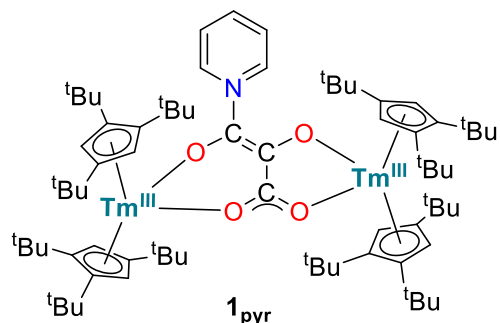
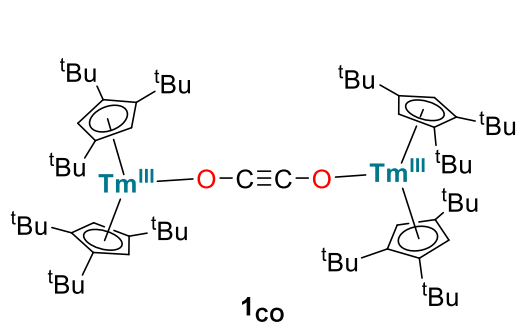
List of abbreviations

<i>ab initio</i>	Latin term = from the beginning
ADF	Amsterdam Density Functional
a.u.	Arbitrary unit
BVS	Bond valence sum
CASSCF	Complete Active Space Self Consistent Field
CASPT2	Second order Complete Active Space Perturbation Theory
Cnt	Cyclononatetraenyl
Cot	Cyclooctatetraenyl
Cp	Cyclopentadienyl
Cp ^{ttt}	1,2,4-tri(<i>tert</i> -butyl)cyclopentadienyl
Cp*	Pentamethylcyclopentadienyl
Cent	Centroids
d	Doublet
DFT	Density Functional Theory
DME	Dimethoxyethane
EPR	Electron Paramagnetic Resonance
equiv.	Equivalent
Et ₂ O	Diethyl Ether
<i>et al.</i>	et alia (= and others)
GGA	Generalized Gradient Approximation
<i>in-situ</i>	Latin term = on site
Ind	Indenyl
IR	Infra-Red
KHMDS	Potassium Hexamethyldisilazane
LMCT	Ligand to Metal Charge Transfer
Ln	Lanthanide
m	Multiplet
Me	Methyl
MeCN	Acetonitrile
NMR	Nuclear Magnetic Resonance
ORTEP	Oak Ridge Thermal Ellipsoid Plot
Ph	Phenyl
ppm	Parts per million

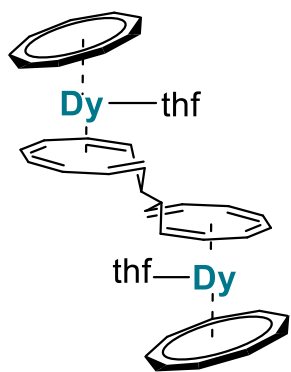
pyr	Pyridine/ pyridyl
QTM	Quantum tunnelling of the magnetization
r.t.	Room temperature
(br) s	(broad) singlet
SIM	Single Ion Magnet
SMM	Single Molecule Magnet
SQUID	Superconducting Quantum Interference Device
T_B	Blocking temperature
t	Triplet
<i>t</i> Bu	<i>tert</i> -Butyl
THF	Tetrahydrofuran
tol	Toluene
UV	Ultra-violet
U_{eff}	Energy Barrier for a spin reversal
VT	Variable Temperature
(SC)-XRD	Single-Crystal X-ray Diffraction

List of synthesized complexes

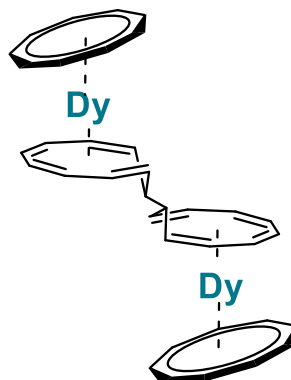
Chapter 1 :



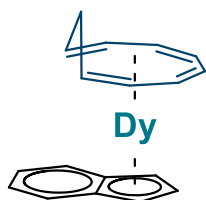
Chapter 2 :



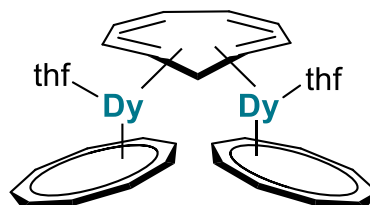
2.1_{thf}



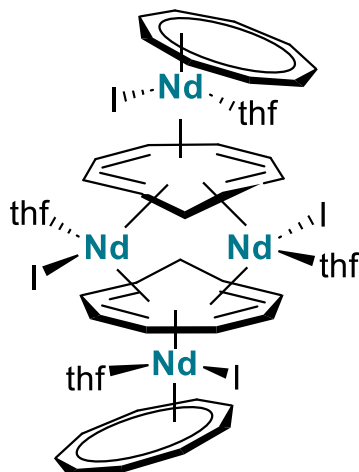
2.1



2.2

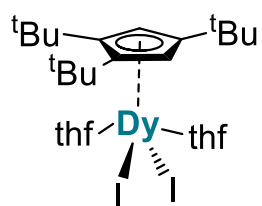


2.3

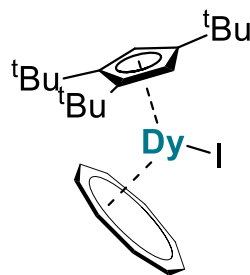


2.4

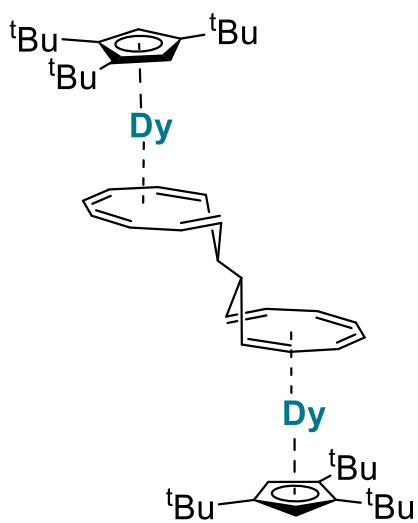
Chapter 3 :



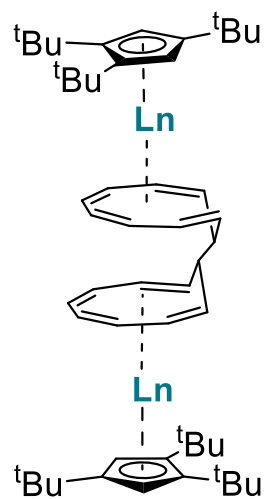
3.1



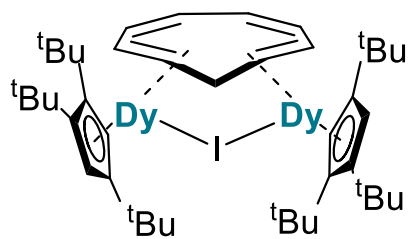
3.2



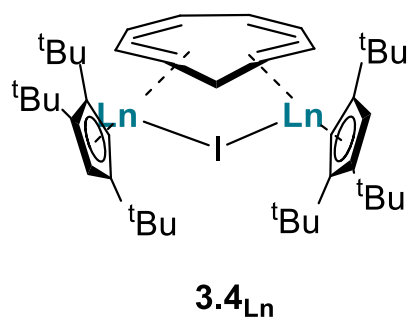
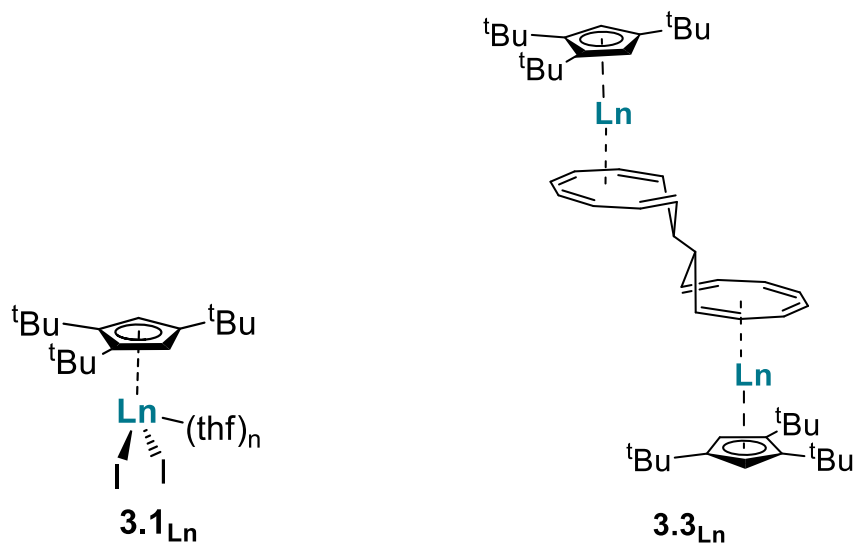
3.3



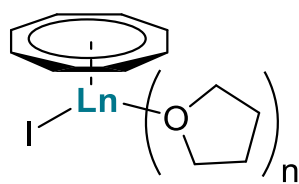
3.3-endo



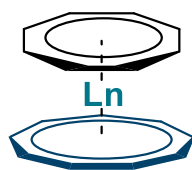
3.4



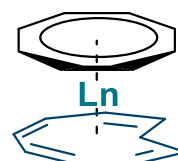
Chapter 4 :



(Ln = La-Nd, Sm, Gd-Tm
n = 2 or 3)



Ln = La-Nd, Sm, Gd-Tm, Lu



Ln = Ce-Nd, Sm, Gd-Ho

Introduction

I. General presentation	19
1. Definition and discovery	19
2. Geopolitical implications of Rare-earth materials	20
3. Particularity of the <i>f</i> -orbitals and trending properties	20
II. Oxidation states and chemistry	22
1. Trivalent oxidation state	23
2. Tetravalent oxidation state	24
3. Divalent oxidation state	26
4. Intermediate-valence state	29
III. Physical Properties	31
1. Description of the electronic structure	31
2. Luminescence and optical properties	32
3. Magnetic properties	33
IV. Presentation of the work	41
References	43

Introduction

1. General presentation

The placement of the f-block on the outside of the main periodic table is a striking illustration of its peculiar nature.

1. Definition and discovery

On the top row of the f-block reside the lanthanides. They are defined by having a partial filling of their 4f orbitals, from $n = 0$ for lanthanum to $n = 14$ for lutetium. They are often considered together with scandium and yttrium due to their similar behaviour. This entire group is referred to as the “rare earth”. However, they are not to be confused with the rare metals.

Indeed, they were mistakenly thought to be rare because of their late discovery. After careful investigation, although they are found as mixtures in ores, several rare earth such as cerium are quite abundant (see **Figure 1**).¹ The lengthy process of separations of each lanthanide from its counterpart contributes to this common misconception. Numerous claims of separation of a new element were invalidated as the new ones were found to be a mixture. It is only through the very demanding process of successive crystallisations that all of the rare earth metals were finally separated from each other.² Even if the tools at the disposition of chemists have changed tremendously in the past century, lanthanide separation remains a critical research direction to this day.^{2,3}

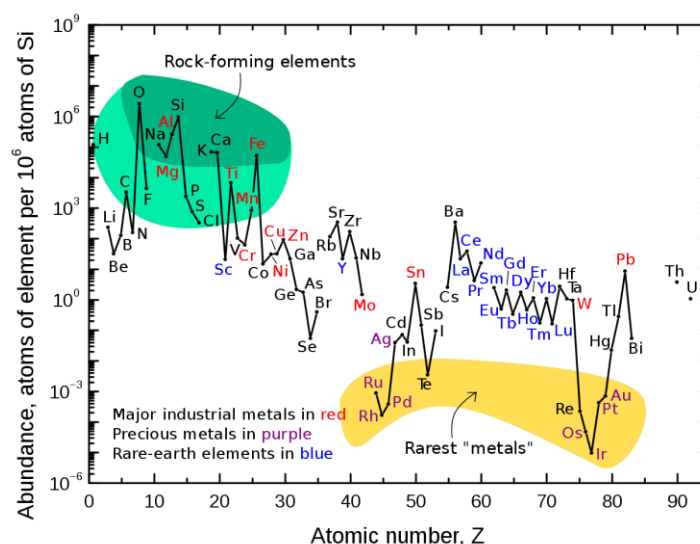


Figure 1 Graphical representation of the natural abundance of elements as a function of their atomic numbers. (Reproduced from ¹) Rare earth elements are shown in blue.

2. Geopolitical implications of Rare-earth materials

Indeed, one of the features of the rare-earth supply is its unequal repartition on the planet as well as its localized process plants. According to the International Energy Agency (IEA), 60% of all rare-earths are extracted in China, where more than 85% of the world production of these materials is processed.⁴ This drastic repartition of the activities was placed under the spotlight in 2010-2011 when China placed an embargo on its exportation.⁵ This motivated countries, which had stopped their production, to restart their mines, particularly the United States or Sweden where one of the largest-known deposits in Europe was found.^{3,6}

These types of conflicts are expected to become more prevalent as rare-earth metal are key in the development of new technologies and their use is expected to continue growing.^{7,8} Indeed, they are at the forefront of electronic, magnetic and luminescent technologies, thanks to all of the different properties presented in the following manuscript.

Another important aspect to consider is the difficulty to separate and recycle them.² These additional steps needed to obtain pure materials can put pressure on the environment and will require additional development to be viable alternatives in the energetic transitions.⁷

3. Particularity of the *f*-orbitals and trending properties

The criticality of the rare-earth elements can be easily explained by their unequal repartition in the world and intrinsically challenging separation process. However, their increasing demand due to their high performance in a plethora of domains such as magnetism and luminescence is also at play. All of these particularities can often be linked to the unique properties of their *f*-orbitals.

1. Presentation of *f*-orbitals and electronic configurations

The lanthanide series sees their *f*-orbital gradually filling. They are known to be spatially constricted and, as such, to have minimal interaction with the environment. This is opposite to their *d*-orbitals counterpart which are essential to understand the behaviour of transition metal complexes. Most notably, the visual representation of the *d*-orbitals is used to construct basic orbital diagram for simple complexes. This helps comprehend the directionality of the *d*-orbitals. This factor is not at play for *4f*-metals, explaining why they are seldom represented in textbooks. If no direct bonding can be expected with the core-like *f*-electrons, the symmetry of the orbitals is however, still at play in the determination of orbital overlap. Thus, a general knowledge of their representation can be beneficial. They can be depicted as two sets, the cubic set as seen in **Figure 2** and the general set.⁹

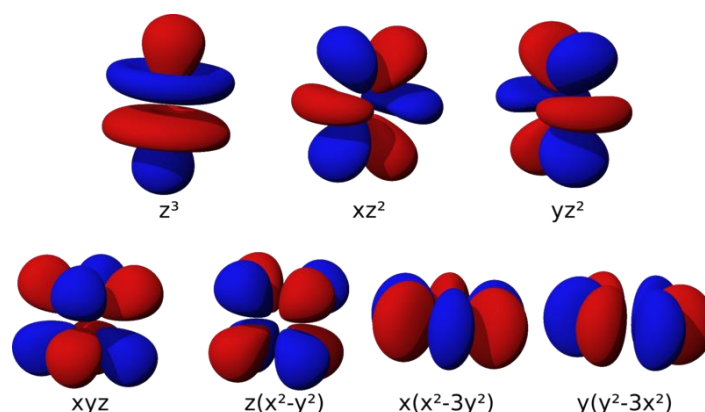


Figure 2 Schematic representation of the cubic set of f-orbitals (Reproduced from ⁹)

The orbital filling is also complexified by the presence of the empty 5d orbitals lying very close in energy. This explains why in **Table 1**, the electronic configurations for La, Ce and Gd features one electron in the 5d orbitals.⁹ This has limited impact in this work as long as trivalent species are used. However, for reduced species, particularly dysprosium and neodymium, these *d*-orbitals bear the additional electron. This is notably important for magnetic applications and will be discussed further in **Chapters 2 & 3**. The electronic configurations for Ln³⁺ is described in **Table 1**.

	Atom	Ln ³⁺
La	[Xe] 5d ¹ 6s ²	[Xe]
Ce	[Xe] 4f ¹ 5d ¹ 6s ²	[Xe] 4f ¹
Pr	[Xe] 4f ³ 6s ²	[Xe] 4f ²
Nd	[Xe] 4f ⁴ 6s ²	[Xe] 4f ³
Pm	[Xe] 4f ⁵ 6s ²	[Xe] 4f ⁴
Sm	[Xe] 4f ⁶ 6s ²	[Xe] 4f ⁵
Eu	[Xe] 4f ⁷ 6s ²	[Xe] 4f ⁶
Gd	[Xe] 4f ⁷ 5d ¹ 6s ²	[Xe] 4f ⁷
Tb	[Xe] 4f ⁹ 6s ²	[Xe] 4f ⁸
Dy	[Xe] 4f ¹⁰ 6s ²	[Xe] 4f ⁹
Ho	[Xe] 4f ¹¹ 6s ²	[Xe] 4f ¹⁰
Er	[Xe] 4f ¹² 6s ²	[Xe] 4f ¹¹
Tm	[Xe] 4f ¹³ 6s ²	[Xe] 4f ¹²
Yb	[Xe] 4f ¹⁴ 6s ²	[Xe] 4f ¹³
Lu	[Xe] 4f ¹⁴ 5d ¹ 6s ²	[Xe] 4f ¹⁴

Table 1 Electronic configuration for the metal and the ionic lanthanide in their trivalent state

2. Ionic radius

The lanthanide ions show a steady decrease in ionic radius with increase of the atomic number, dubbed the lanthanide contraction. This phenomenon is seen across the periodic table when moving from left to right with the increase of atomic number. However, the lanthanide series is the longest series of elements alongside which it can be observed. Additionally, with all members of the series having similar chemical properties, the size difference is one of the leverages that can be used to differentiate or separate them.^{10,11}

3. Lewis acidity

Rare earth compounds are also known to be hard Lewis acids. Particularly, this Lewis acidity is expected to increase along the series, which once again can give an insight to their separations.¹²

II. Oxidation states and chemistry

The notion of oxidation states discussed further will refer to molecular compounds unless noted otherwise. The solid-state chemistry of lanthanide is an extremely rich subject exploring very similar question of stability and electronic structure to the molecular chemistry. However, the techniques and criteria used are markedly different between the two which impedes a proper comparison. For the sake of clarity, the rest of this manuscript will mainly address the problem from the molecular point of view. As an interesting note, the different oxidation states known for lanthanides compounds are reported in **Table 2**.

	Ln^{+1}	Ln^{2+}	Ln^{3+}	Ln^{4+}	Ln^{5+}
La	s	s,m	s,m	--	--
Ce	--	s,m	s,m	s,m,g	--
Pr	--	s,m	s,m	s,m	g
Nd	--	s,m	s,m	s,g	--
Pm	--	--	<i>undefined</i>	--	--
Sm	--	s,m	s,m	--	--
Eu	--	s,m	s,m	--	--
Gd	--	s,m	s,m	--	--
Tb	--	s,m	s,m	s,m,g	--
Dy	--	s,m	s,m	s,g	--
Ho	--	s,m	s,m	--	--
Er	--	s,m	s,m	--	--
Tm	--	s,m	s,m	--	--
Yb	--	s,m	s,m	--	--
Lu	--	s,m	s,m	--	--

Table 2 representing the known oxidation states of the lanthanides depending on the phase of identification (*s*, *m* and *g* denoting extended solids, molecular compounds and gas-phase respectively) (adapted from ¹³)

1. Trivalent oxidation state

1. Generalities

Trivalent chemistry largely dominates the field as it is the most stable state for most lanthanide ions. They mostly act as positively charged ions with electrostatic interactions. As such, they are often thought to be limited to their role of Lewis acid. Consequently, they can be used as Lewis acid catalyst in a variety of application.^{14,15}

2. Ligands development

To target coordination compounds with trivalent lanthanide, the ideal ligand set features charged ligands or hard Lewis bases. Consequently, the chemistry of oxygen and nitrogen-based ligands has been extensively studied over the years.¹⁶ The chemistry starts to be slightly more difficult with the introduction of carbon-based compounds. Indeed, in that case, an anionic ligand is often required as f-orbitals cannot engage in π -interaction. Thus, the monoanionic cyclopentadienyl ligand (Cp), used extensively with transition metal, is potentially a good fit.^{17,18} The reaction of lanthanide halide salts and Cp⁻ salts formed LnCp₃ as stable compounds. The speciation is entirely dictated by the steric arrangement around the metal, highlighting the importance of the electrostatic interaction in lanthanide complexes. This steric demand was further tuned by smart ligand engineering targeting concomitantly bulkier and larger ligand as illustrated on **Figure 3**.^{19,20} For the rest of the manuscript, the common notation where ' denotes substitution with a trimethyl-silyl group and ^t with a tert-butyl group will be adopted.

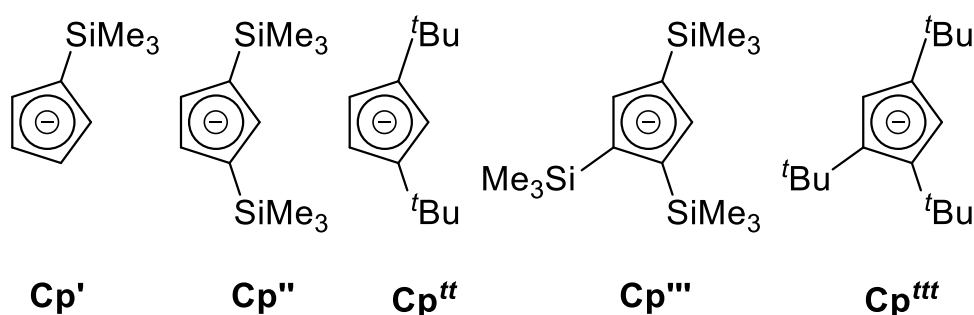


Figure 3 Schematic representation of different Cp type ligand from least to most encumbered.

Even if today, a precise control can be applied to the coordination sphere of different lanthanide ions, another strategy developed by chemists consists in targeting different oxidation states in the hope of tuning the reactivity.

2. Tetravalent oxidation state

The tetravalent state of the lanthanide ion is well known in solid-state chemistry but its translation to molecular system has been challenging.²¹⁻²³ Until very recently, it was only known for cerium complexes.

1. The cerium exception

Cerium was seen for a long time as an exception in the periodic table. Thanks to its peculiar electronic structure $[\text{Xe}]6d^25d^14f^1$, it is easy to see that an oxidation state of +IV yielding a noble gas' electronic structure is favorable.

Although this configuration can be stabilized, the resulting compounds are often powerful oxidants. These Ce(IV) salts are typically used in organic chemistry.^{24,25} Molecular chemistry tools have then been used to create more soluble compounds with a large range of redox potentials.²⁶

If strongly coordinating ligands makes it possible to isolate molecular compounds of Ce(IV), carbon-based ligands represent a challenge. For instance, one could assume that similarly to LnCp_3 , a tetravalent Ce ion should be able to form CeCp_4 . However, this was not found to be the case, and larger dianionic ligands are required to form a neutral arrangement with Ce, such as the cyclooctatetraene or the pentafulvalene derivatives presented in **Figure 4**.²⁷⁻²⁹

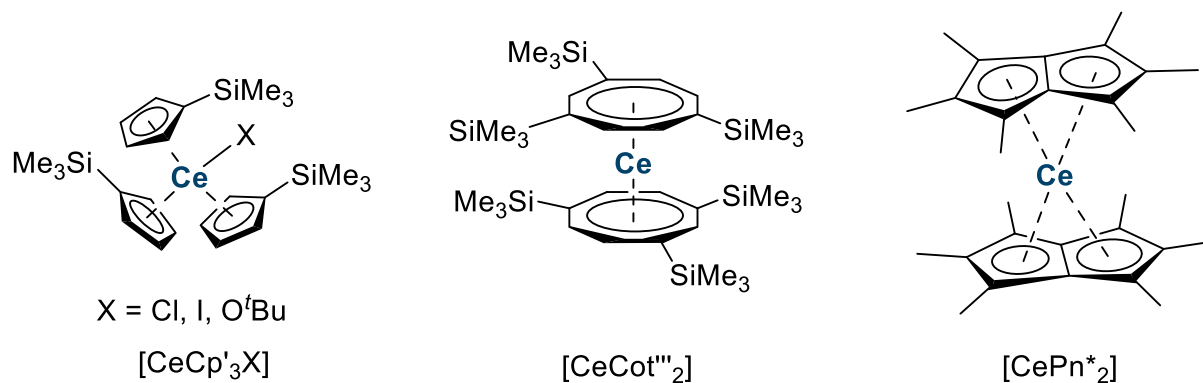


Figure 4 Structure of organometallic Ce(IV) complexes (from left to right: CeCp^*_3X , CeCot''_2 , $\text{Ce}(\text{permethylated-fulvalene})_2$)

Interestingly, these organometallic complexes of Ce(IV) are often thought to not be formally comprised of Ce^{4+} cation and two L^{2-} (with L an organic ligand) but rather a superposition of Ce^{3+} and Ce^{4+} . This puzzling phenomenon, referred to as intermediate-valence, will be described later in II.4.²⁹

An interesting topic when working with tetravalent cerium is the possibility to compare it with its actinide counterparts.^{30,31} Indeed, the tetravalent state is more common for those bigger ions such as thorium, uranium, neptunium and plutonium, which can all access it. The study of cerium (IV) can then be used as a proxy to study radioactive materials. Although the strict

comparison should be made cautiously because the actinides are often thought to be more covalent, it is still a useful tool on the radiochemist belt.^{32,33}

2. Ligand tuning and state of the art example

When looking to expand the chemistry of tetravalent cerium, one needs to consider the similar electronic configurations of other lanthanides. Namely, terbium, which possess an f^8 structure in its +III oxidation state, which presents a good candidate for further oxidation to yield a half-filled f subshell. Similarly, praseodymium presents another candidate for oxidation, being close to an empty f -subshell in its +IV oxidation state.

Despite this *a priori* favourable electronic structure, these species remained elusive in their molecular form until 2019, when two concomitant reports from the groups of Mazzanti and La Pierre reported the formation of tetravalent terbium complexes.^{34–36} The two chosen ligand sets presented in **Figure 5**, are different but rely on a similar strategy. In both cases, the structures possess strongly donating ligand. La Pierre *et al.* chose an imidophosphorane ligand set, consisting of 4 moieties occupying the coordination sphere. The Mazzanti group used a siloxide ligand that did not saturate the coordination sphere.

The Mazzanti group then extended this chemistry to the praseodymium analogue as illustrated in **Figure 5**, which was expected due to the very close oxidation potential.³⁷

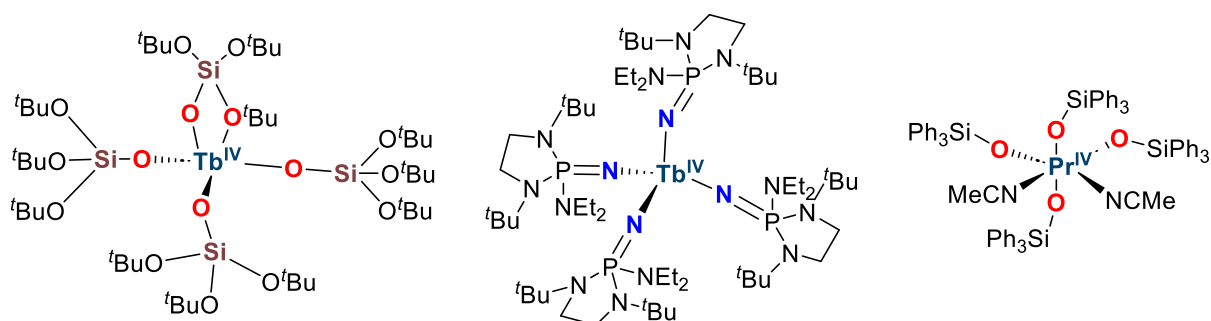


Figure 5 From left to right, first Tb(IV) compound by the Mazzanti group based on siloxide ligand,³⁴ LaPierre group's Tb(IV) with imidophosphorane ligands,³⁶ and the first Pr(IV) complex by the Mazzanti group with siloxide ligands.³⁷

As of now, this chemistry is limited to these ions and these specific ligand sets. It is predicted that neodymium and dysprosium could be the next target as they have been observed in the solid-state in tetravalent environments.^{13,38}

3. Divalent oxidation state

If removing an electron from a lanthanide ion creates strongly oxidizing species, it follows that adding an excess of electrons might lead to reducing species.

1. Diverging strategies in solid state and molecular chemistry

The chemistry of molecular divalent lanthanides is intrinsically linked to solid state chemistry and has always been slightly behind. A large number of the LnX_2 type salts (with X a halide), which are now common starting material for molecular chemistry, have already been researched in the early 60's by solid-state chemists.^{21,22} They were made through comproportionation of the trihalide salts and the corresponding metal. A complex apparatus made of a sealed quartz tube inside a sealed tantalum tube and several days of heating complicated the use of this protocol in other field of chemistry.

From a molecular point of view, the only readily accessible elements were those possessing stable configuration such as europium, ytterbium and samarium, adopting configurations of $4f^7$, $4f^{14}$, $4f^6$ respectively. The first attempt at utilising them in reactions was linked to the possibility of having soluble compounds. As such, the first attempt took place in liquid ammonia which dissolves europium and ytterbium.³⁹ However, this is not convenient and the chemistry of divalent lanthanide really started to gain traction with the straightforward synthesis of SmI_2 with diiodoethane in THF reported by Kagan along its associated reactivity.⁴⁰

2. SET type reaction

One feature of their divalent state is the possibility to perform single electron reductions. This has most notably been studied by the group of Kagan who investigated the reactivity of SmI_2 .⁴¹ It has been particularly noted that its functional selectivity makes it a great candidate for reduction of polyfunctional compounds, for example in natural product synthesis.⁴²

This type of reactivity has also been studied with stronger lanthanide reductants such as thulium, dysprosium and neodymium in their divalent states.⁴³ This will be described further in **Chapter 1 and 2**.

3. Organometallic control

However, if simple lanthanide salts were explored for organic reactivity purposes, a better tuning of the reactivity was investigated through ligand development. Given the already important applications of reduced lanthanide complexes, exploration of this chemistry was a central target for lanthanide chemists at the end of the 20th century.

a. Ligand set developments

By analogy with the LnCp_3 compounds, the coordination sphere of LnCp_2 should be driven by electrostatic interactions. However, it was found by several characterisation techniques that the rings do not adopt the expected linear arrangements, but rather a tilted version. This was attributed to a possible compromise between repulsive and attractive interaction.^{44–46} Furthermore, the solid-state structure of LnCp_2 is polymeric and these material are insoluble in non-polar solvents.^{47,48}

Interestingly, further substitution of the Cp ring by methyl groups to form the Cp* ligand (pentamethylcyclopentadienyl or C_5Me_5) did not allow alignment to form linear complexes. However, it yielded fairly soluble starting material to study the reactivity of divalent lanthanides. Multiple substitutions were necessary to ensure a higher linearity, for instance $\text{Eu}(\text{Cp}^{\text{iPr}_5})_2$ or $\text{Yb}(\text{Cp}^{\text{Ph}_5})_2$.^{49,50}

b. Larger aromatic ligand

This search for linearity, however, has encountered more success with larger aromatic ligand such as the cyclooctatetraene ligand (Cot, C_8H_8) or the cyclononatetraenyl ligand (Cnt, C_9H_9), both presented in **Figure 6**.

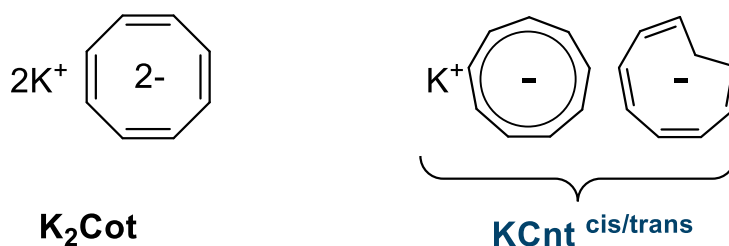


Figure 6 Schematic representation of two large aromatic ligands, K_2Cot on the left and KCnt on the right

These two molecules are Hückel aromatic molecules with 10 π -electrons, however the Cot ligand is dianionic while the Cnt ligand is monoanionic. This means that divalent lanthanides are likely to form linear but charged complexes with Cot ligand, and neutral ones with Cnt ligand as shown in **Figure 7**.^{51,52} An additional particularity of the Cnt ligand is its presence as a *cis/trans* isomer pair due to its large ring size as illustrated in **Figure 6**.^{53,54} This impacts the overall symmetry expected for linear homoleptic complexes. This ligand was central in the work presented in this manuscript and as such will be further discussed in **Chapter 2**.

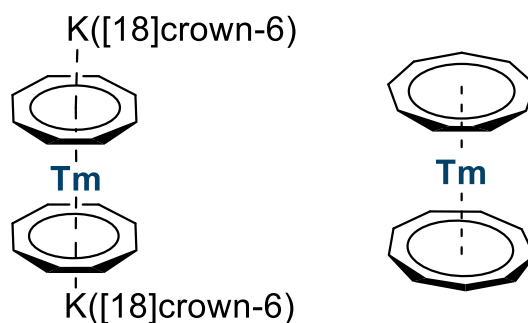


Figure 7 Molecular structure of linear sandwich type compound with two large aromatic ligands, $[TmCot_2][K([18]crown-6)]_2$ on the left⁵¹ and $[TmCnt_2]$ on the right.⁵²

c. The chemistry of $LnCp^*$

As mentioned previously, Cp ligands have been used extensively and particularly the permethylated version. The first report of crystallographically identified complexes of $LnCp^*_2$ as thf-adduct ($Ln = Sm$ and Yb) dates back to the beginning of the 80's.^{55,56} It is noted in those reports that the use of alkylated Cp ligand will help with the solubility of the material.

As expected from the redox potential, the ytterbium complex is less reactive than the samarium adduct. Nevertheless, a large body of work by the Andersen group shed light on the reduction of nitrogen-containing ligand bonded to the $YbCp^*_2$ fragment.⁵⁷⁻⁶⁰ This particularly leads to radical coupling reaction controlled by the ligand. Notably, in addition to the reactivity, careful examination of the electronic properties showed several incoherences, which were later described as intermediate valence character (*vide infra*).

The samarocene adduct was later characterised in its solvent free form as shown in **Figure 8**.⁶¹ Further study of this reactive species allowed for the isolation of a CO oligomerisation reaction forming a ketenecarboxylate type adduct.⁶² Further reactivity studies demonstrated the reaction with N_2 to form a side-on adduct.⁶³ This two adducts are illustrated in **Figure 8**.

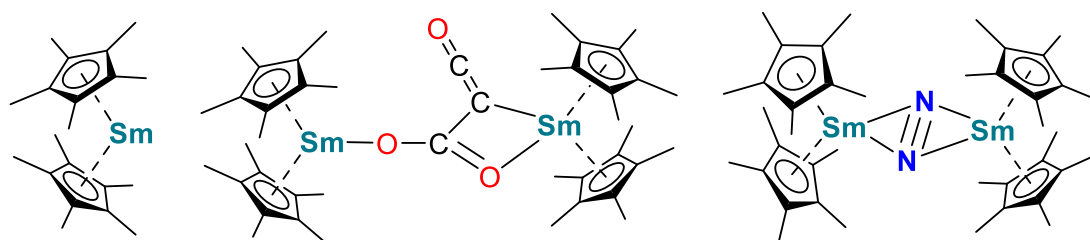


Figure 8 Molecular structure of samarocene (left) and its product with CO (middle) and N_2 (right)⁶¹⁻⁶³

These few examples demonstrate the rich reductive chemistry performed by divalent lanthanide complexes with adequately tuned ligands.

4. Intermediate-valence state

In-depth characterization of the complex lanthanide electronic structure has helped develop an additional concept to correctly describe their oxidation state: the intermediate valence. This concept started to develop at the end of the 20th century to bridge non-accurate theoretical prediction with new experimental observation and spectroscopic characterization.

1. Manifestation of the phenomenon

Spectroscopic methods are ubiquitous for characterization of inorganic complexes. They give powerful insight on various properties such as magnetic behaviors or electronic structures. However, sometimes, the information conflicts with established models. For instance, YbCp₃ complexes have always had recorded magnetic moment weaker than what were expected.^{18,64} Once the measurements had been reproduced enough to not fall under the category of experimental error, the validity of the predictive model came into question.

Indeed, by using numerous types of spectroscopy and high-level computations, it was postulated that, to account for the lower magnetic moment of YbCp₃ for instance, a certain divalent character had to be considered.^{65,66}

This is not to be confused with mixed valence character in metallic dimers.⁶⁷ It is not a question of which atom is divalent and which is trivalent but rather a quantic superposition of two possible electronic configurations.²⁹

This field brought up a consequent amount of debate and emulation as computational chemists and spectroscopists worked together to disentangle this phenomenon, contributing concomitantly to a deeper understanding of lanthanide chemistry.

2. Origin of this phenomenon

To understand this particularity, a careful analysis of the electronic structure is needed. Indeed, two criteria drives the interaction between two orbitals. As mentioned previously, the core nature of the f-orbitals prevents significant orbital overlap. However, if the energy difference is small, the electron has the possibility to find itself in both orbitals. This gives rise to two singlet configurations, one closed-shell configuration with the electron in the f-orbitals and one open-shell configurations where the electron is transferred into one of the empty π orbitals of the ligand, as illustrated in **Figure 9**.⁵⁷⁻⁶⁰

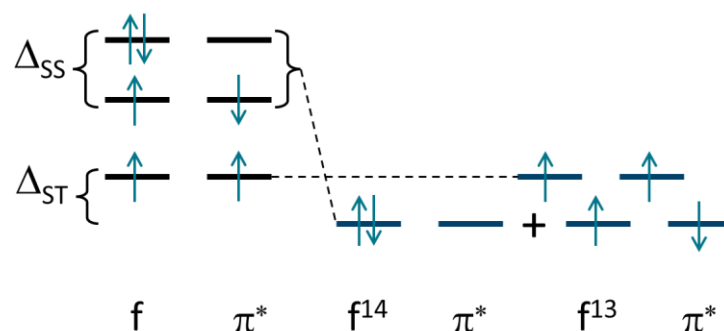
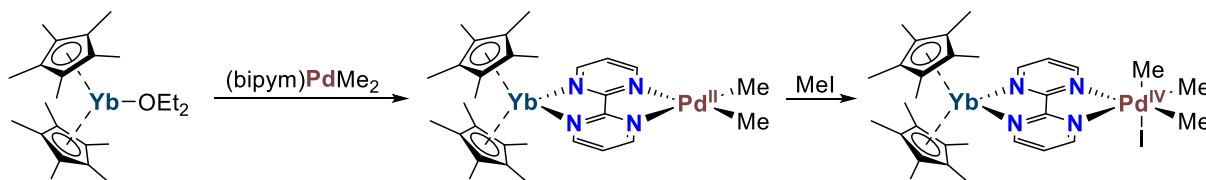


Figure 9 Qualitative energy level scheme highlighting the origin of intermediate valence state properties in ytterbium (Δ_{SS} denotes the energy difference between the two singlet states and Δ_{ST} corresponds to the stabilization brought by the mixing of the singlet states compared to the triplet states.)

3. Practical cases in chemistry

This particularity is not only a topic for theoretical and physical chemists, as it can have an impact on the chemistry performed by some of those species.

For instance, the reaction between neutral YbCp^*_2 with a bipyrimidine-palladium complex gives rise to an intermediate valence state for the ytterbium ion.^{29,68} The adequate symmetry of the stabilized π orbitals of the ligand is then involved in the stabilisation of the palladium center as illustrated in **Scheme 1**. Indeed, upon addition of MeI to this heterometallic complex, the observed stability for the oxidised palladium(IV) species is greatly improved.



Scheme 1 Synthesis of the heterometallic Pd(IV) species stabilized through the bipyrimidine (bipym) ligand.

This overview of the different oxidation state involved in the chemistry of lanthanide metal shows the variety of their electronic features. This in turn brings forward a wide scope of chemical reactivity.^{13,43,69} But also, associated with the electronic structure comes distinctive physical properties for which lanthanide metals have been particularly studied.⁷⁰⁻⁷²

III. Physical Properties

1. Description of the electronic structure

The electronic structures of *f*-metal-containing complexes differ quite significantly from those of transition metals. Indeed, their high number of electrons added to the restricted nature of their *f*-orbitals produce different patterns. Where the classical Hamiltonian is composed of the nuclear and electronic contribution first, completed by the crystal field and finally perturbed by the spin-orbit coupling; lanthanides will typically require consideration of the spin-orbit first and then the crystal field as a perturbation, as illustrated in **Figure 10**.^{9,73,74} It means that the correct quantum number dictating the electronic structure in that case is *J* and applying the crystal field breaks the degeneracy in *m_J* states. This can be further disturbed through the magnetic field inducing Zeeman splitting with each *m_J* separated in +*m_J* and -*m_J*.

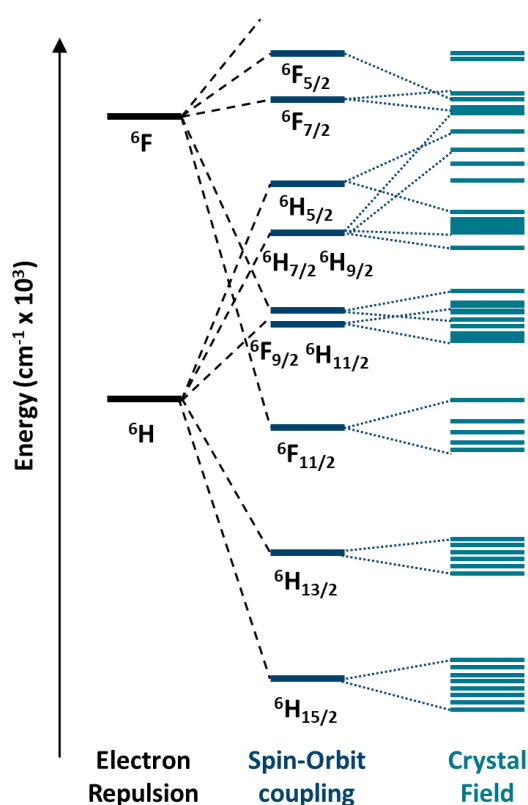


Figure 10 Schematic representation of the splitting of the energy level for a dysprosium (III) ion (reproduced from ^{73,74})

Adding the crystal field, only as a modification of the spin-orbit coupling, could translate the weak influence of this term, and it is often the approximation made for luminescence studies to justify fairly stable properties depending mostly on the nature of the ion rather than its environment.⁷⁵ This contrasts with d-block compounds. Indeed, transition metal-based luminescent complexes are known for the versatility in absorption and emission behaviour depending on the symmetry, the donating character of the ligand and even the solvent.^{76,77} However, if the effects are markedly smaller for lanthanides-based compounds, they are

nonetheless appreciable in highly-resolved spectra at low temperature.⁹ Furthermore, the impact of the crystal field is the key feature, which allows for the synthesis of lanthanide-based single molecule magnets (see III.3.3)

This particular way to split the energy levels, mixed with the particularity of f-orbitals, gives the lanthanide prime importance in spectroscopic research.

2. Luminescence and optical properties

1. Origin of the luminescence

Lanthanide-based luminescence often involves f-f transitions forbidden by symmetry rules. As such, the intensities of the absorption are fairly small in most cases. Another particularity, coming from the f-orbitals, is the sharpness of the spectroscopic bands due to the minimal overlap with the environment. This translates to a spectrum with fairly distinctive patterns for each ion independently from its ligand sets.⁷⁵

Most of the lanthanide ions can display luminescence. However, only the atoms with a large energy gap between their emissive exciting state and their ground multiplets show discernable signal, as small energy gap can easily give rise to non-radiative de-activation. Consequently, interesting ions for luminescence lie in between samarium and dysprosium, with an increased interest in europium, gadolinium and terbium as illustrated in **Figure 11**. Furthermore, smaller energy gaps can also give rise to NIR emissions such as in the case of neodymium and ytterbium.

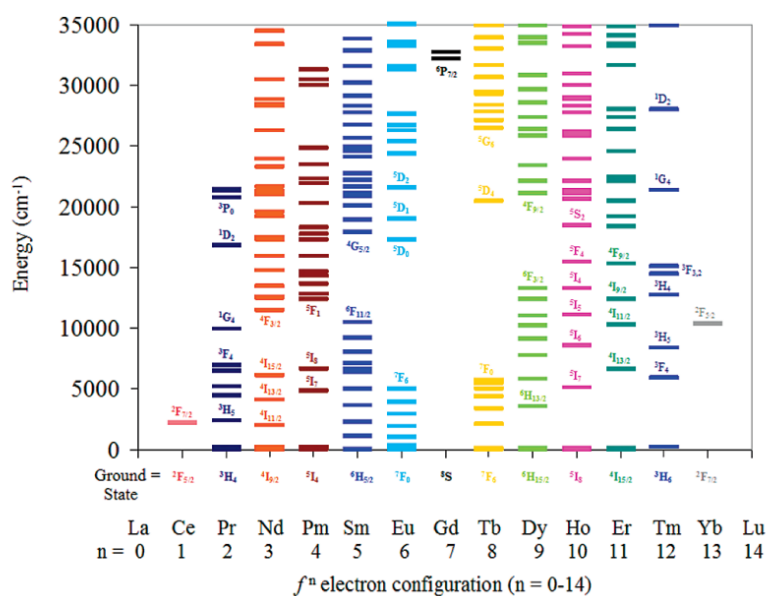


Figure 11 Representation of the electronic structures of the Ln^{3+} ions from ⁷⁸

2. Antenna effect

To circumvent the low efficiency of energy transfer to the lanthanide, the so-called antenna effect has been used. A very absorbent organic molecule is placed in close proximity to a lanthanide ion and is used to transfer the energy directly in its excited state giving rise to lanthanide-based luminescence.⁷⁹

3. Current development

The particularity of long-lived excited states can be particularly useful for biological applications. As such, decorated with stabilizing ligands, a lot of lanthanide-containing probes have been developed.⁸⁰

Among the current strategies to develop their usage, the up-conversion phenomenon is very promising. Indeed, it allows absorption of two low energy photon and emission of fluorescence at a lower wavelength. This is particularly useful in biological application as the tissues are more transparent to NIR light.⁸¹ Particularly, the possibility of having cooperative up-conversion mechanism allows a variety of energy ladder to be created with f-f arrangement or even small *d-f* assemblies.^{82,83}

Another interesting development is circularly polarized luminescence, which allows direct emission of polarized light. This could find application in biological assays as well as the telecommunication industry thanks to the added dimension for a signal.^{84,85}

3. Magnetic properties

Thanks to their high number of unpaired electrons, lanthanide ions usually display magnetic properties harnessed in bulk magnets as well as single-molecule magnets.

1. General magnetic properties

Due to the prevalence of the trivalent state, most of the magnetic applications have been developed on Ln^{3+} type ions. In this configuration, with the exception of lanthanum and lutetium, all lanthanide ions possess at least one unpaired electron making them paramagnetic ions.

The contracted nature of the *f*-orbitals, to a large extent, diminishes the interaction between the unpaired electron and the environment. This means that the expected magnetic moment for a free ion, Ln^{3+} , is close to the measured value for a lanthanide in a ligand field.⁹ It also means that creating long range magnetic interaction (akin to iron) to create bulk magnets is significantly more challenging. Intermediary transition metals are often involved to help create the magnetic communications.^{64,86}

2. Bulk magnets

Typical permanent magnets derive their properties from three-dimensional arrangements of atoms. Rare earth elements do not form magnets on their own but when mixed with other elements, they can form some of the strongest commercially available magnets.³

One ubiquitous type are the neodymium magnets made of neodymium iron and boron.⁸⁷ They possess very high remanent magnetization which can go above 1 T and their coercivity is also quite high. One drawback is their low Curie temperatures, around 400 °C, problematic in particular applications. Another type of rare earth magnet developed for the industry are samarium-cobalt magnets.^{88,89} They possess intrinsic magnetic properties that are less impressive than neodymium magnet, but their Curie temperature can go to 800 °C.

3. SMM

Another very different type of research, referred to as single-molecule magnets (SMMs), favours not the three-dimensional building blocks but directly the spin anisotropy that can be created by a small number of spin species. Ideally, the goal is to create magnets at the molecular scale. To do that, the challenges are multiple.

a. Historical debut

The field of SMMs did not start with f-block metals. The first complex possessing slow magnetic relaxation was a manganese-oxo cluster in 1993.⁹⁰ This mixed valence cluster possessed a spin = 10 and showed hysteresis behaviour at very low temperature below 3 K. Shortly after this discovery, it was determined that the activation barrier would be proportional to the term S^2D with S the spin and D the anisotropy term. This prompted chemists to focus on the S term of the equation and, during this period, clusters of different transition metals have been designed. The spin term of this arrangements was increased up to a record 51/2, nevertheless the improvement of the magnetic properties did not scale at all with the increase of S.⁹¹

Unfortunately, as some researchers started to demonstrate, S and D were not unrelated and an increase of S tended to diminish D significantly.⁹²⁻⁹⁴

In 2003, Ishikawa published the first lanthanide based SMM.^{95,96} He studied the family of $[\text{Ln}(\text{Pc})_2]^-$ with Pc representing the phthalocyanine ligand depicted in **Figure 12 left**, and found that the terbium and dysprosium complexes showed slow relaxation of the magnetisation. This was linked to the determined electronic levels, showing an important stabilisation of the electronic levels of high m_j . Furthermore, the terbium compound featured better magnetic properties thanks to a large energetic gap in between the ground state and the first excited

state as illustrated in **Figure 12 right**. Overall, this example had an important impact in the community. It convinced researchers that the exploration of lanthanide-based complexes was worthwhile and helped coin the term single-ion magnet (SIM) for mononuclear SMM.

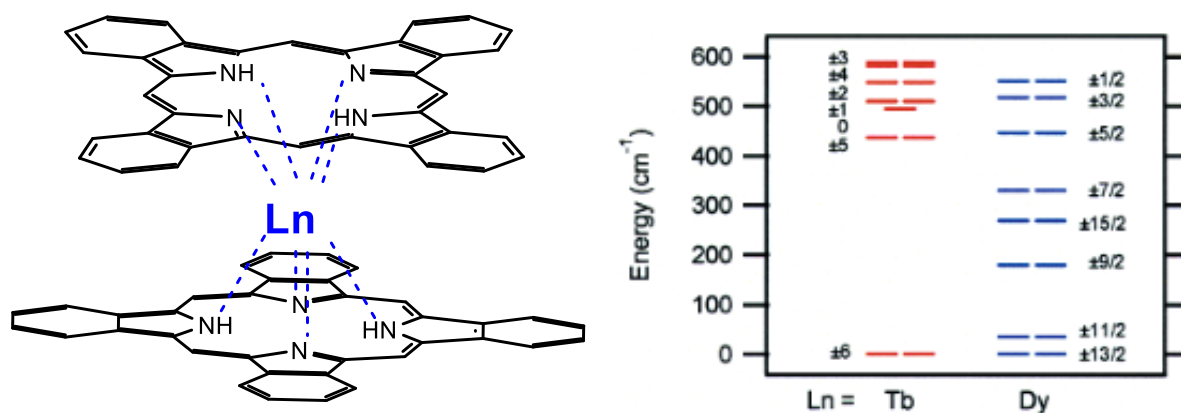


Figure 12 Molecular structure of the first lanthanide-based SMM on the left and the associated low lying energy levels for Ln = Tb and Dy on the right. (Reproduced from ^{95,96})

b. Specificity of the lanthanides

Contrarily to transition metal clusters, there is no simple expression of the energetic barrier to reversal for *f* metal-based SMMs. For a few years, this led to the exploration of different possibilities thanks to significant efforts in coordination chemistry.

In 2011, a foundational review by Rinehart and Long started to rationalize the design of the ligand field.⁷³ Particularly, the *f*-electronic density could be modeled as two different shapes, diverging from the isotropic sphere, depending on the filling of the *f*-orbitals. The first one is a flattened sphere along the *xy* plane and is called oblate. The second model resembles a sphere elongated along the *z* axis, and is called prolate. These shapes represented in **Figure 13** can be used to tune the ideal ligand field that should be used.

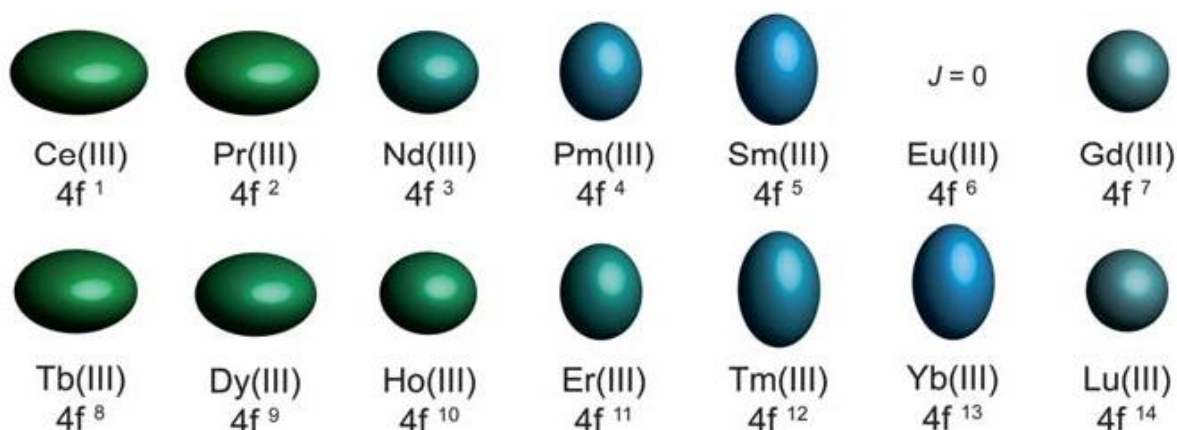


Figure 13 Schematic representation of the electronic disposition for standard Ln³⁺ (reproduced from ⁷³)

This modeling is only the first step in the process as it is incomplete. Indeed, as discussed in **III.1**, a better picture needs to take into account the ligand field on top of the spin-orbit

coupling. Thus, to this preliminary vision, the authors apply a quadrupolar ligand field in order to obtain the removal of degeneracy of the m_j levels (see **Figure 14**). This modeling then informs the overall shape of each m_j state. It is then possible to rationalize the ligand interaction responsible for stabilizing/de-stabilizing certain m_j states. To obtain the best properties, one should stabilize the highest m_j and destabilize the lowest m_j . This creates an energy ladder used to rationalize the evolution from a magnetized state to a non-magnetic state.

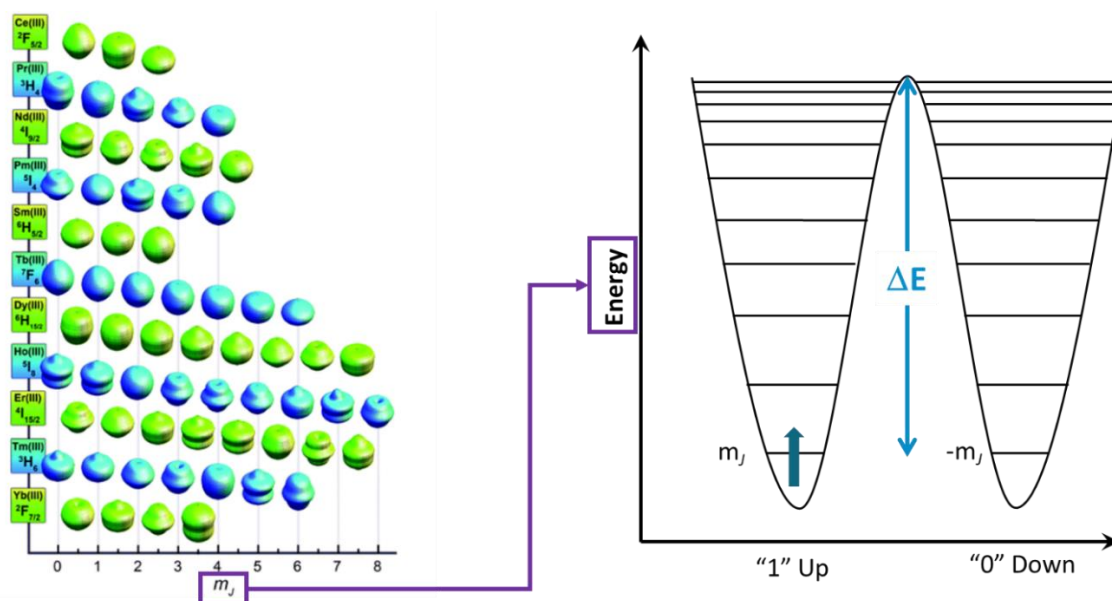


Figure 14 On the left is represented the shape of every m_j sublevels for each lanthanide (reproduced from ⁷³). This informs, on the right, the shape of the classical double well of energy representing the blocking of the magnetization.

The energy difference noted ΔE in **Figure 14** is akin to the energy barrier discussed previously. As such, this can be used as a simple design tool to try and enhance the magnetic properties.

c. Principal directions

Through application of these simple considerations, three main situations for the different shape of electronic densities emerge.

Spheric lanthanide ions

To begin with, for lanthanide ions with half-filled f -subshells such as Gd(III), Eu(II) or filled f -subshells such as Yb(II), the resulting electronic density will be isotropic. In this case there is no preferential orientation of the magnetic axes and these ions cannot retain magnetic orientation in the absence of an external field.

Oblate lanthanide ions

In this consideration, in order to stabilize the highest m_j , the electronic density should be situated along the main axis with as little densities on the periphery as possible, as illustrated in **Figure 15**. As the lanthanides primarily engage in electrostatic interaction, the best ligand

should be a small charged entity. Large efforts have been put in the development of adequate ligand field.

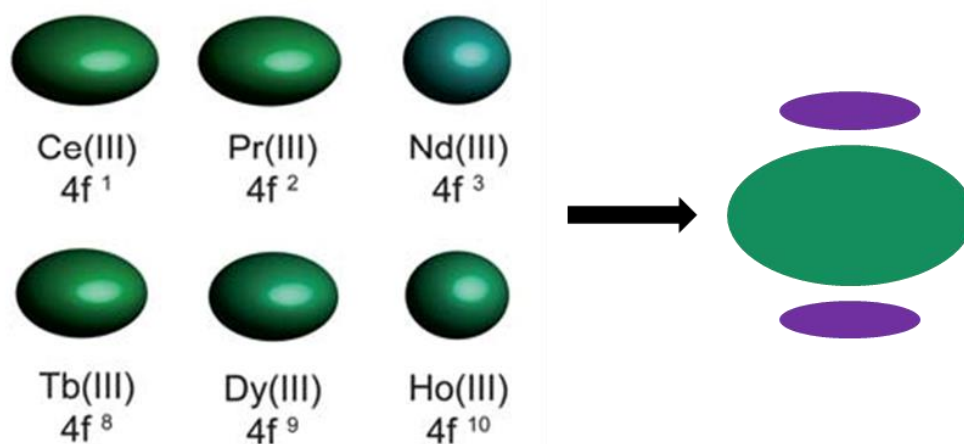


Figure 15 Schematic representation of the ideal ligand set represented in purple) for oblate ions (represented in green).

For instance, theoretical chemists have investigated and proposed a large number of possible choices.⁹⁷ However, lanthanide ions tend to saturate their coordination sphere with donating ligand which brings electronic densities in the plane. As such, ligands have to be carefully designed to saturate the coordination sphere without disturbing too much the electronic density of the metal.^{98,99} One of the most successful strategies to date has been the use of substituted Cp ligands. Indeed, as mentioned previously, they constitute good ligand for lanthanides due to their charge, and their ease of substitution makes them easy to tune. Particularly the development of Cp ligands such as Cp^{ttt} allowed for the stabilization of fairly linear Cp-Ln-Cp motifs.¹⁰⁰ In the study of formally divalent Dy species with Cp^{ttt} ligand, Nief *et al.* showed that even upon reduction, it was difficult to separate the third equatorial ligand from the metallic centers.^{101,102} This was solved in 2016 by two groups concomitantly thanks to the use of a strong halogene-abstraction compound, namely [H(SiEt₃)₂][B(C₆F₅)₄]. The resulting cationic fragment [DyCp^{ttt}₂]⁺ is presented on **Figure 16**.^{103,104} These studies significantly raised the temperature at which magnetic properties can be observed, and they were followed several years later, by a similar compound with different substituents, breaking the frontier of liquid nitrogen temperature.¹⁰⁵

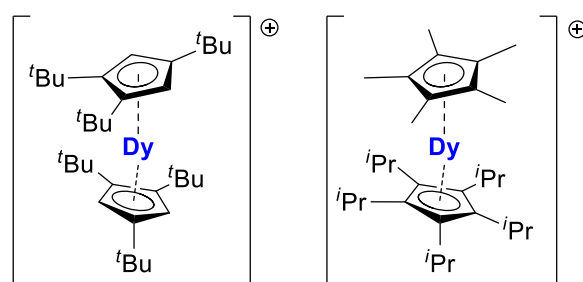


Figure 16 Molecular structure of two dysprosium-based SIM utilizing Cp type ligands

Prolate lanthanides ions

On the opposite side, the prolate anion are better accommodated by an equatorial electronic density as represented in **Figure 17**. In-plane coordination is greatly favorable, however, similarly to the challenges faced for oblate ions, it is difficult to keep axial positions entirely free.

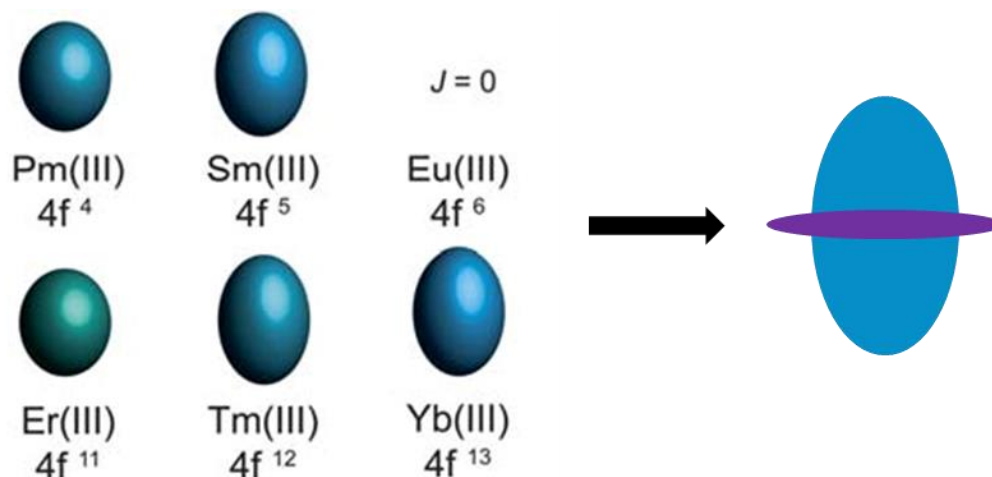


Figure 17 Schematic representation of the ideal ligand set represented in purple for prolate ions (represented in blue).

To solve that, a large ligand with diffuse electronic densities can be used such as iodine.^{106,107} Although it was successful in creating SMM species, it is difficult to put in place due to the low steric encumberment. Thus, an intermediate method has been developed using larger aromatic ligand such as the cyclooctatetraenyl ligand (Cot²⁻). This ligand has similar features to the Cp ligand by its charge and its relative electronic tunability. However, its large size can allow preferential stabilization along the equatorial plane rather than axial contribution, as illustrated in **Figure 18**.

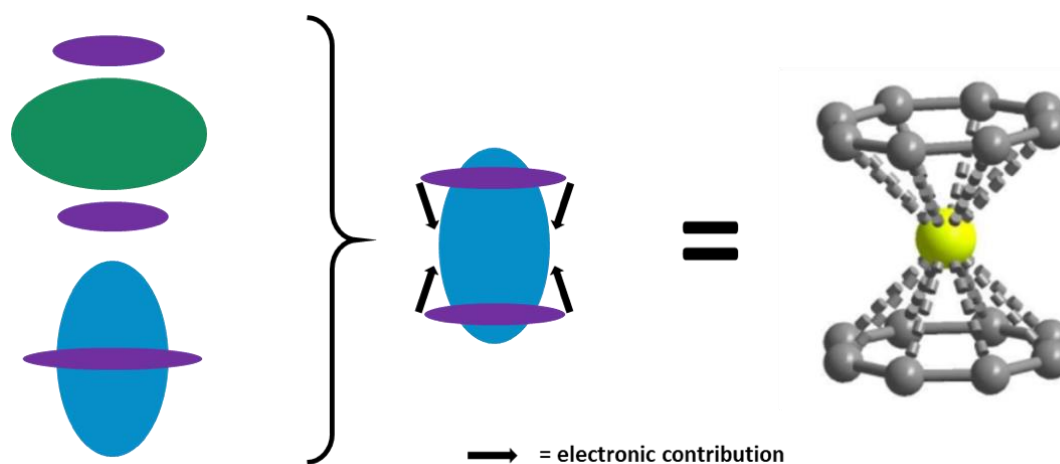


Figure 18 Schematic representation of the electronic contribution from large aromatic ligand to the metallic centers and the molecular structure of ErCot_2 , the counter ions have been omitted for clarity.

This particular strategy has been used for erbium.¹⁰⁸ It led to fundamental study on the anisotropy axis resulting from the Er-Cot fragment.^{109–111}

The family of large aromatic ligands was also extended to the cyclic nine-membered ring cyclononatetraenyl ligand.¹¹²

d. Radical ligands for enhanced magnetic communication

Borrowing from the strategies of forming transition metal clusters, some ligands have been used not only for their crystal fields splitting, but also for their capacity to bridge two lanthanide ions. As mentioned previously, the retracted nature of the f-orbitals leads to weak exchange with potential neighbours. However, adequate choices of a radical bridging ligand have been shown to promote the coupling between the metallic centers resulting in blocking temperatures four-times higher than the previous systems.^{113,114} Pioneered by Long and Rinehart, these systems, later extended by Long and Demir, have allowed a better understanding of metal-metal magnetic exchange and particularly helped to underline the necessity of keeping an overall axial ligand field.^{19,115–118}

e. Current research

The development of new ligand sets to apply the ideal ligand field is still undergoing. Particularly, introduction of non-carbon atoms has renewed the interest of the community in ligand development, leading to original bonding and symmetry.^{119,120}

In 2022, the report of a lanthanide dimer featuring Ln-Ln interaction, thanks to a metal-based radical character, demonstrated the importance of maximizing magnetic exchange.¹²¹ The key component in this system residing in the *d*-character of the radical as illustrated in **Figure 19**, which allows strong ferromagnetic coupling of the two metallic centers.

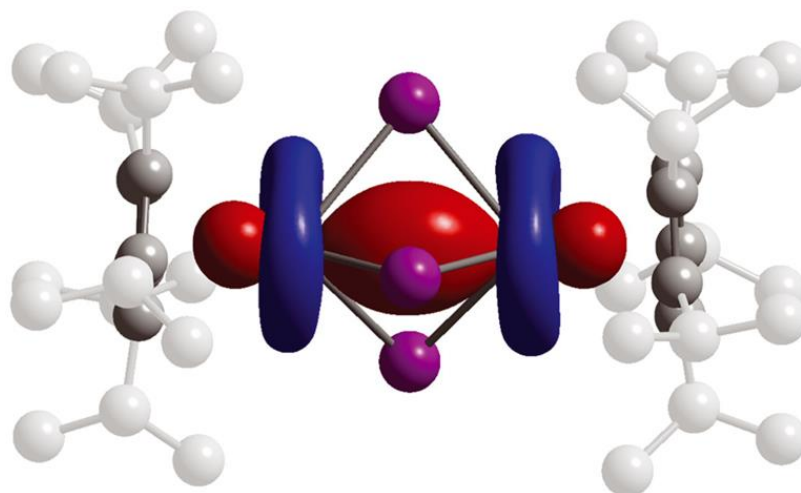


Figure 19 Molecular structure of $\text{Ln}_2\text{I}_3\text{Cp}^{\text{Pr}5}_2$ with the super-imposed representation of the calculated SOMO responsible for the metal coupling. (Reproduced from ¹²¹)

As noted above, this molecule displays the two criteria highlighted in the study of radical bridge ligands. First, the communication is direct as the radical is delocalized in between the two metallic centres. The two ions are very close to each other favoring a very high magnetic exchange. Long *et al.* goes as far as calling it a lanthanide-lanthanide bond. Additionally, the $\text{Ln-Cp}^{\text{Pr}5}$ fragment is also aligned with the so-called Ln-Ln bond.

Consequently, this system is ideally built to promote a high-spin ground state and a slow relaxation of the magnetization. In addition to this, it was found that this compound has a very high coercive field superior to 14 T at 60 K rivalling that of commercial magnets.¹²¹

The continuing discoveries made for the lanthanide SMM systems contribute, each time, to a better understanding of these phenomenon. Thus, working to create new edifices and bonding schemes is a desirable goal.

IV. Presentation of the work

The following manuscript focuses on different aspects of the organometallic chemistry of lanthanide in relation to small molecule activation, magnetic properties and electronic structure particularities.

First, following previous work by the group, the use of small and bulky aromatic ligands known to stabilize divalent lanthanide ions and promote their reactivity was applied to the activation of small molecules. Particularly, divalent thulium complexes with the tris tert-butyl cyclopentadienyl ligand (Cp^{tbt}) were known to dimerize CO molecules to form linear adducts while retaining some reactivity.¹²² As such, we proceeded to combined additions of CO_2 and pyridine-type molecules on this linear adduct to probe its capacity to undergo a nucleophilic attack while reacting with CO_2 . The synthesized complexes were exhibiting strong coloration in solution. Consequently, a combined spectroscopic study using UV-visible absorption and single-crystal X-Ray diffraction was carried out. These data showed a correlation between the angle of the pyridine-type motif and the rest of the organic backbone with the profile of the absorption spectrum. For small angles, the corresponding molar extinction coefficient was relatively higher. The angles closer to 90° showed much weaker absorption. Similarly, there appears to be correlation between the donor character of the pyridine adduct and the wavelength of the maximum of absorption. Considering the apparent high rate of the reaction with CO_2 , further studies were carried out to gauge the potential of the linear compound as a CO_2 detector. However, it was observed that it reacts with O_2 to form an oxalate adduct. Additional small molecule activation reactions were performed to understand the mechanism of addition in these systems.

Then, this knowledge of divalent lanthanide reactivity was applied in a second study where the chemistry of another aromatic ligand, the cyclononatetraenyl ligand or C_9H_9 (Cnt), was explored. Preliminary studies showed that it allowed access to neutral and linear sandwich compounds with the classical divalent lanthanide Sm, Eu, Tm and Yb.⁵² However, upon reaction with dysprosium diiodide, a reductive coupling of two units of the ligand was observed. This formed a Cnt_2 -type moiety which was characterized through XRD-diffraction. Overall, the dimer had a consistent spectroscopic signature for two trivalent dysprosium centers and a Cnt_2^{-4} unit. Tuning of the reaction conditions and adoption of low temperatures (-35°C) allowed for the isolation of another type of dysprosium dimer where the Cnt ligand acts as a bridging unit for the two ions. The analysis of the molecular structure obtained by XRD showed an overall symmetrical role of the metallic ions. This was supported by the computation, which predicted a delocalized mixed-valent state equivalent to a 2.5 oxidation state for each dysprosium. However, the acquired magnetic data did not validate this

hypothesis, indicating a weak antiferromagnetic interaction between the two metal centers. Other characterizations were performed to investigate further but a clear-cut conclusion remained difficult to draw due to the extreme sensitivity of the dimeric complex.

Thus, the synthetic path was modified to start from easier to handle, trivalent starting materials. Additionally, a bulky ligand, the Cp^{ttt} was chosen to obtain complexes with better-defined coordination motifs. This strategy allowed for the obtention of similar dimers. The reduction of the heteroleptic species containing both a Cp^{ttt} ligand and a Cnt unit led to their reductive coupling forming the Cnt₂⁻⁴ motifs. The spectroscopic signatures were coherent with two trivalent dysprosium centers and a -4 Cnt₂ unit. Interestingly, the direct reduction of the starting material with the Cp^{ttt} coordinated in presence of KCnt resulted in the formation of a new bridging Cnt dimer. Strikingly, XRD diffraction analysis showed that the molecular structure was non-symmetrical. This could be rationalized as a difference in oxidation state for the two metal centers. This possibility was also supported by the presence of a relatively intense but broad absorption band in the visible which is typical of this type of electronic configuration. Combining the information from those two studies allowed us to reduce the number of hypotheses for the electronic configuration of the bridged-type dimers. Particularly, the possibility of having a mono-reduced Cnt ligand as a bridging unit, pointed toward a potential divalent character for the dysprosium center of the full Cnt dimer. Importantly, these two studies showcased the particularities of the Cnt ligand, its redox-active behavior, its flexibility as well as its presence as two isomers.

Thus, to develop a better understanding of the ligand, older studies of its isomerization were investigated and expended upon. Particularly, irradiation with low wavelength (370 nm – 450 nm) was found to be the main trigger for the isomerization from its *cis-cis,cis,trans* (*trans*) form to its *cis-cis,cis,cis* (*cis*) form. During those studies the retro-isomerisation was not observed. Then a similar investigation was carried out on the Cnt unit in heteroleptic complexes with trivalent lanthanide and a dianionic cyclooctatetraenyl ligand. Contrary to the ligand salt, in this framework, the *trans/cis* ratio can be controlled depending on the identity of the lanthanide as well as the wavelength of irradiation. These observations gave us insight into the isomerization behavior of the Cnt unit depending on its coordination and will be extended to investigate possible changes in reactivity.

To conclude, this work extended our knowledge of the reactivity of organometallic lanthanide complexes with various organic ligands as well as contributed to a deeper understanding of the behavior of the Cnt ligand.

References

- (1) Haxel, G. B.; Boore, S.; Mayfield, S. *Rare Earth Elements—Critical Resources for High Technology*. <https://pubs.usgs.gov/fs/2002/fs087-02/> (accessed 2023-08-09).
- (2) Cheisson, T.; Schelter, E. J. *Science* **2019**, *363* (6426), 489–493.
- (3) Department of Energy, U. S. *Critical Materials Strategy*; 2011; pp 1–196.
- (4) International Energy Agency. *The Role of Critical Minerals in Clean Energy Transitions*; International Energy Agency, 2022.
- (5) Hetzel, M. P.; Bataille, D. *Les Enjeux Stratégiques des Terres Rares et des Matières Premières Stratégiques et Critiques*; 617; 2016; pp 39–42.
- (6) Northam, J. *It's a journey to the center of the rare earths discovered in Sweden*. NPR. <https://www.npr.org/2023/07/18/1187075988/europe-rare-earth-sweden> (accessed 2023-09-08).
- (7) Fujita, Y.; McCall, S. K.; Ginosar, D. *MRS Bull.* **2022**, *47* (3), 283–288.
- (8) Guillaume Pitron. *La guerre des métaux rares: La face cachée de la transition énergétique et numérique*, Les Liens qui Libèrent.; 2018.
- (9) Cotton, S. *Lanthanide and Actinide Chemistry*, John Wiley&Sons.; 2006.
- (10) Bogart, J. A.; Lippincott, C. A.; Carroll, P. J.; Schelter, E. J. *Angew. Chem. Int. Ed.* **2015**, *54* (28), 8222–8225.
- (11) Mattocks, J. A.; Jung, J. J.; Lin, C.-Y.; Dong, Z.; Yennawar, N. H.; Featherston, E. R.; Kang-Yun, C. S.; Hamilton, T. A.; Park, D. M.; Boal, A. K.; Cotruvo, J. A. *Nature* **2023**, *618* (7963), 87–93.
- (12) Spedding, F. H.; Fulmer, E. I.; Butler, T. A.; Gladrow, E. M.; Gobush, M.; Porter, P. E.; Powell, J. E.; Wright, J. M. *J. Am. Chem. Soc.* **1947**, *69* (11), 2812–2818.
- (13) Gompa, T. P.; Ramanathan, A.; Rice, N. T.; La Pierre, H. S. *Dalton Trans.* **2020**, *49* (45), 15945–15987.
- (14) Kobylarski, M.; Berthet, J.-C.; Cantat, T. *Chem. Commun.* **2022**, *58* (17), 2830–2833.
- (15) Kobayashi, S.; Manabe, K. *Pure Appl. Chem.* **2000**, *72* (7), 1373–1380.
- (16) Ortu, F. *Chem. Rev.* **2022**, *122* (6), 6040–6116.
- (17) Wilkinson, G.; Birmingham, J. M. *J. Am. Chem. Soc.* **1954**, *76* (23), 6210–6210.
- (18) Birmingham, J. M.; Wilkinson, G. *J. Am. Chem. Soc.* **1956**, *78* (1), 42–44.
- (19) Mahieu, N.; Piątkowski, J.; Simler, T.; Nocton, G. *Chem. Sci.* **2023**, *14* (3), 443–457.
- (20) Nief, F. *Dalton Trans.* **2010**, *39* (29), 6589.
- (21) Corbett, J. D. REDUCED HALIDES OF THE RARE EARTH ELEMENTS. *Rev Chim Min.* **1973**, *10* (1–2), pp 239-257.
- (22) Corbett, J. D. Comproportionation Routes to Reduced Lanthanide Halides. In *Synthesis of Lanthanide and Actinide Compounds*; Springer Science, 1991; pp 159–174.
- (23) Martin, J. *J. Am. Chem. Soc.* **1927**, *49* (9), 2133–2136.
- (24) Kagan, H. B.; Namy, J. L. Tetrahedron Report Number 213. *Tetrahedron* **1986**, *42* (24), 6573–6614.
- (25) Sridharan, V.; Menéndez, J. C. *Chem. Rev.* **2010**, *110* (6), 3805–3849.
- (26) Piro, N. A.; Robinson, J. R.; Walsh, P. J.; Schelter, E. J. *Coord. Chem. Rev.* **2014**, *260*, 21–36.
- (27) Greco, A.; Cesca, S.; Bertolini, W. *J. Organomet. Chem.* **1976**, *113* (4), 321–330.
- (28) Anwander, R.; Dolg, M.; Edelman, F. T. *Chem. Soc. Rev.* **2017**, *46* (22), 6697–6709.
- (29) Tricoire, M.; Mahieu, N.; Simler, T.; Nocton, G. *Chem. – Eur. J.* **2021**, *27* (23), 6860–6879.
- (30) Cheisson, T.; Kersey, K. D.; Mahieu, N.; McSkimming, A.; Gau, M. R.; Carroll, P. J.; Schelter, E. J. *J. Am. Chem. Soc.* **2019**, *141* (23), 9185–9190.
- (31) Klamm, B. E.; Windorff, C. J.; Marsh, M. L.; Meeker, D. S.; Albrecht-Schmitt, T. E. *Chem. Commun.* **2018**, *54* (62), 8634–8636.
- (32) Pace, K. A.; Klepov, V. V.; Berseneva, A. A.; Zur Loye, H. *Chem. – Eur. J.* **2021**, *27* (19), 5835–5841.
- (33) Su, J.; Batista, E. R.; Boland, K. S.; Bone, S. E.; Bradley, J. A.; Cary, S. K.; Clark, D. L.; Conradson, S. D.; Ditter, A. S.; Kaltsoyannis, N.; Keith, J. M.; Kerridge, A.; Kozimor, S. A.; Löble, M. W.; Martin, R. L.; Minasian, S. G.; Mocko, V.; La Pierre, H. S.; Seidler, G. T.; Shuh, D. K.; Wilkerson, M. P.; Wolfsberg, L. E.; Yang, P. *J. Am. Chem. Soc.* **2018**, *140* (51), 17977–17984.

- (34) Palumbo, C. T.; Zivkovic, I.; Scopelliti, R.; Mazzanti, M. *J. Am. Chem. Soc.* **2019**, *141* (25), 9827–9831.
- (35) Willauer, A. R.; Palumbo, C. T.; Scopelliti, R.; Zivkovic, I.; Douair, I.; Maron, L.; Mazzanti, M. *Angew. Chem.* **2020**, *132* (9), 3577–3581.
- (36) Rice, N. T.; Popov, I. A.; Russo, D. R.; Bacsa, J.; Batista, E. R.; Yang, P.; Telser, J.; La Pierre, H. S. *J. Am. Chem. Soc.* **2019**, *141* (33), 13222–13233.
- (37) Willauer, A. R.; Palumbo, C. T.; Fadaei-Tirani, F.; Zivkovic, I.; Douair, I.; Maron, L.; Mazzanti, M. *J. Am. Chem. Soc.* **2020**, *142* (12), 5538–5542.
- (38) Hu, Z.; Kaindl, G.; Vandr e, D.; Hoppe, R.; Wortmann, G. *J. Alloys Compd.* **1994**, *205* (1–2), 263–269.
- (39) Fischer, E. O.; Fischer, H. *Angew. Chem. Int. Ed. Engl.* **1964**, *3* (2), 132–133.
- (40) Namy, J. L.; Girard, P.; Kagan, H. B. *Nouv. J. Chim.* **1977**, *1* (1), 5–7.
- (41) Kagan, H. B. *Tetrahedron* **2003**, *59* (52), 10351–10372.
- (42) Heravi, Majid. M.; Nazari, A. *RSC Adv.* **2022**, *12* (16), 9944–9994.
- (43) Szostak, M.; Procter, D. J. *Angew. Chem. Int. Ed.* **2012**, *51* (37), 9238–9256.
- (44) Andersen, R. A.; Boncella, J. M.; Burns, C. J.; Green, J. C.; Hohl, D.; R sch, N. *J. Chem. Soc. Chem. Commun.* **1986**, No. 5, 405–407.
- (45) Perrin, L.; Maron, L.; Eisenstein, O.; Schwartz, D. J.; Burns, C. J.; Andersen, R. A. *Organometallics* **2003**, *22* (26), 5447–5453.
- (46) Andersen, R. A.; Boncella, J. M.; Burns, C. J.; Blom, R.; Haaland, A.; Volden, H. V. *J. Organomet. Chem.* **1986**, *312* (3), C49–C52.
- (47) Apostolidis, C.; Deacon, G. B.; Dornberger, E.; Edelmann, F. T.; Kanellakopoulos, B.; MacKinnon, P.; Stalke, D. *Chem. Commun.* **1997**, No. 11, 1047–1048.
- (48) Schultz, M.; Burns, C. J.; Schwartz, D. J.; Andersen, R. A. *Organometallics* **2000**, *19* (5), 781–789.
- (49) Sitzmann, H.; Dezember, T.; Schmitt, O.; Weber, F.; Wolmersh user, G.; Ruck, M. *Z. F r Anorg. Allg. Chem.* **2000**, *626* (11), 2241–2244.
- (50) Deacon, G. B.; Forsyth, C. M.; Jaroschik, F.; Junk, P. C.; Kay, D. L.; Maschmeyer, T.; Masters, A. F.; Wang, J.; Field, L. D. *Organometallics* **2008**, *27* (18), 4772–4778.
- (51) Moutet, J.; Schleinitz, J.; La Droitte, L.; Tricoire, M.; Pointillart, F.; Gendron, F.; Simler, T.; Clavagu era, C.; Le Guennic, B.; Cador, O.; Nocton, G. *Angew. Chem. Int. Ed.* **2021**, *60* (11), 6042–6046.
- (52) X mard, M.; Zimmer, S.; Cordier, M.; Goudy, V.; Ricard, L.; Clavagu era, C.; Nocton, G. *J. Am. Chem. Soc.* **2018**, *140* (43), 14433–14439.
- (53) Boche, G.; Martens, D.; Danzer, W. *Angew. Chem. Int. Ed. Engl.* **1969**, *8* (12), 984–984.
- (54) Boche, G.; Bieberbach, A. *Chem. Ber.* **1978**, *111* (8), 2850–2858.
- (55) Tilley, T. D.; Andersen, R. A.; Spencer, B.; Ruben, H.; Zalkin, A.; Templeton, D. H. *Inorg. Chem.* **1980**, *19* (10), 2999–3003.
- (56) Evans, W. J.; Bloom, I.; Hunter, W. E.; Atwood, J. L. *J. Am. Chem. Soc.* **1981**, *103* (21), 6507–6508.
- (57) Nocton, G.; Booth, C. H.; Maron, L.; Andersen, R. A. *Organometallics* **2013**, *32* (5), 1150–1158.
- (58) Nocton, G.; Booth, C. H.; Maron, L.; Andersen, R. A. *Organometallics* **2013**, *32* (19), 5305–5312.
- (59) Nocton, G.; Booth, C. H.; Maron, L.; Ricard, L.; Andersen, R. A. *Organometallics* **2014**, *33* (23), 6819–6829.
- (60) Walter, M. D.; Berg, D. J.; Andersen, R. A. *Organometallics* **2007**, *26* (9), 2296–2307.
- (61) Evans, W. J.; Hughes, L. A.; Hanusa, T. P. *J. Am. Chem. Soc.* **1984**, *106* (15), 4270–4272.
- (62) Evans, W. J.; Grate, J. W.; Hughes, L. A.; Zhang, H.; Atwood, J. L. *J. Am. Chem. Soc.* **1985**, *107* (12), 3728–3730.
- (63) Evans, W. J.; Ulibarri, T. A.; Ziller, J. W. *J. Am. Chem. Soc.* **1988**, *110* (20), 6877–6879.
- (64) Benelli, C.; Gatteschi, D. In *Introduction to Molecular Magnetism: From Transition Metals to Lanthanides*; 2015; p 71.
- (65) Coreno, M.; de Simone, M.; Coates, R.; Denning, M. S.; Denning, R. G.; Green, J. C.; Hunston, C.; Kaltsoyannis, N.; Sella, A. *Organometallics* **2010**, *29* (21), 4752–4755.
- (66) Denning, R. G.; Harmer, J.; Green, J. C.; Irwin, M. *J. Am. Chem. Soc.* **2011**, *133* (50), 20644–20660.

- (67) Launay, J. *Eur. J. Inorg. Chem.* **2020**, 2020 (4), 329–341.
- (68) Goudy, V.; Jaoul, A.; Cordier, M.; Clavaguéra, C.; Nocton, G. *J. Am. Chem. Soc.* **2017**, 139 (31), 10633–10636.
- (69) Dicken, R. D.; Motta, A.; Marks, T. J. *ACS Catal.* **2021**, 11 (5), 2715–2734.
- (70) Qiao, Y.; Schelter, E. J. *Acc. Chem. Res.* **2018**, 51 (11), 2926–2936.
- (71) Woodruff, D. N.; Winpenny, R. E. P.; Layfield, R. A. *Chem. Rev.* **2013**, 113 (7), 5110–5148.
- (72) McAdams, S. G.; Ariciu, A.-M.; Kostopoulos, A. K.; Walsh, J. P. S.; Tuna, F. *Coord. Chem. Rev.* **2017**, 346, 216–239.
- (73) Rinehart, J. D.; Long, J. R. *Chem. Sci.* **2011**, 2 (11), 2078.
- (74) Jank, S.; Reddmann, H.; Amberger, H.-D. *Inorganica Chim. Acta* **2008**, 361 (7), 2154–2158.
- (75) Bünzli, J.-C. G.; Piguet, C. *Chem. Soc. Rev.* **2005**, 34 (12), 1048.
- (76) Chou, P.-T.; Chi, Y.; Chung, M.-W.; Lin, C.-C. *Coord. Chem. Rev.* **2011**, 255 (21–22), 2653–2665.
- (77) Kinzhalov, M. A.; Grachova, E. V.; Luzyanin, K. V. *Inorg. Chem. Front.* **2022**, 9 (3), 417–439.
- (78) Moore, E. G.; Samuel, A. P. S.; Raymond, K. N. *Acc. Chem. Res.* **2009**, 42 (4), 542–552.
- (79) Atwood, D. A. *The Rare Earth Elements: Fundamentals and Applications*; Wiley, 2013; pp 1–654.
- (80) Bünzli, J.-C. G. *Chem. Lett.* **2009**, 38 (2), 104–109.
- (81) Picot, A.; D’Aléo, A.; Baldeck, P. L.; Grichine, A.; Duperray, A.; Andraud, C.; Maury, O. *J. Am. Chem. Soc.* **2008**, 130 (5), 1532–1533.
- (82) Knighton, R. C.; Soro, L. K.; Francés-Soriano, L.; Rodríguez-Rodríguez, A.; Pilet, G.; Lenertz, M.; Platas-Iglesias, C.; Hildebrandt, N.; Charbonnière, L. J. *Angew. Chem. Int. Ed.* **2022**, 61 (4), e202113114.
- (83) Knighton, R. C.; Soro, L. K.; Thor, W.; Strub, J.-M.; Cianférani, S.; Mély, Y.; Lenertz, M.; Wong, K.-L.; Platas-Iglesias, C.; Przybilla, F.; Charbonnière, L. J. *J. Am. Chem. Soc.* **2022**, 144 (29), 13356–13365.
- (84) Willis, O. G.; Zinna, F.; Di Bari, L. *Angew. Chem. Int. Ed.* **2023**, 62 (25), e202302358.
- (85) Mukhtar, N. F. M.; Schley, N. D.; Ung, G. *J. Am. Chem. Soc.* **2022**, 144 (14), 6148–6153.
- (86) Rosado Piquer, L.; Sañudo, E. C. *Dalton Trans.* **2015**, 44 (19), 8771–8780.
- (87) Sagawa, M.; Fujimura, S.; Togawa, N.; Yamamoto, H.; Matsuura, Y. *N J. Appl. Phys.* **1984**, 55 (6), 2083–2087.
- (88) Strnat, K.; Hoffer, G.; Olson, J.; Ostertag, W.; Becker, J. J. *J. Appl. Phys.* **1967**, 38 (3), 1001–1002.
- (89) Ojima, T.; Tomizawa, S.; Yoneyama, T.; Hori, T. *IEEE Trans. Magn.* **1977**, 13 (5), 1317–1319.
- (90) Sessoli, R.; Gatteschi, D.; Caneschi, A.; Novak, M. A. *Nature* **1993**, 365 (6442), 141–143.
- (91) Murugesu, M.; Habrych, M.; Wernsdorfer, W.; Abboud, K. A.; Christou, G. *J. Am. Chem. Soc.* **2004**, 126 (15), 4766–4767.
- (92) Ruiz, E.; Cirera, J.; Cano, J.; Alvarez, S.; Loose, C.; Kortus, J. *Chem Commun* **2008**, No. 1, 52–54.
- (93) Neese, F.; Pantazis, D. A. *Faraday Discuss* **2011**, 148, 229–238.
- (94) Waldmann, O. *Inorg. Chem.* **2007**, 46 (24), 10035–10037.
- (95) Ishikawa, N.; Sugita, M.; Ishikawa, T.; Koshihara, S.; Kaizu, Y. *J. Am. Chem. Soc.* **2003**, 125 (29), 8694–8695.
- (96) Ishikawa, N.; Sugita, M.; Okubo, T.; Tanaka, N.; Iino, T.; Kaizu, Y. D. *Inorg. Chem.* **2003**, 42 (7), 2440–2446.
- (97) Reta, D.; Kragoskow, J. G. C.; Chilton, N. F. *J. Am. Chem. Soc.* **2021**, 143 (15), 5943–5950.
- (98) Liu, J.; Chen, Y.-C.; Liu, J.-L.; Vieru, V.; Ungur, L.; Jia, J.-H.; Chibotaru, L. F.; Lan, Y.; Wernsdorfer, W.; Gao, S.; Chen, X.-M.; Tong, M.-L. *J. Am. Chem. Soc.* **2016**, 138 (16), 5441–5450.
- (99) El Beyrouiti, N.; Houard, F.; Cordier, M.; Trzop, E.; Rigaut, S.; Le Guennic, B.; Bernot, K.; Norel, L. *Chem. Commun.* **2023**, 59 (35), 5265–5268.
- (100) Jaroschik, F.; Nief, F.; Ricard, L. *Chem Commun* **2006**, No. 4, 426–428.
- (101) Jaroschik, F.; Momin, A.; Nief, F.; Le Goff, X.-F.; Deacon, G. B.; Junk, P. C. *Angew. Chem.* **2009**, 121 (6), 1137–1141.
- (102) Jaroschik, F.; Nief, F.; Le Goff, X.-F.; Ricard, L. *Organometallics* **2007**, 26 (5), 1123–1125.
- (103) Goodwin, C. A. P.; Ortu, F.; Reta, D.; Chilton, N. F.; Mills, D. P. *Nature* **2017**, 548 (7668), 439–442.

- (104) Guo, F.-S.; Day, B. M.; Chen, Y.-C.; Tong, M.-L.; Mansikkamäki, A.; Layfield, R. A. *Angew. Chem. Int. Ed.* **2017**, *56* (38), 11445–11449.
- (105) Guo, F.-S.; Day, B. M.; Chen, Y.-C.; Tong, M.-L.; Mansikkamäki, A.; Layfield, R. A. *Science* **2018**, *362* (6421), 1400–1403.
- (106) Xémard, M.; Cordier, M.; Molton, F.; Duboc, C.; Le Guennic, B.; Maury, O.; Cador, O.; Nocton, G. *Inorg. Chem.* **2019**, *58* (4), 2872–2880.
- (107) Maxwell, L.; Amoza, M.; Ruiz, E. *Inorg. Chem.* **2018**, *57* (21), 13225–13234.
- (108) Le Roy, J. J.; Korobkov, I.; Murugesu, M. *Chem Commun* **2014**, *50* (13), 1602–1604.
- (109) Hilgar, J. D.; Flores, B. S.; Rinehart, J. D. *Chem. Commun.* **2017**, *53* (53), 7322–7324.
- (110) Hilgar, J. D.; Bernbeck, M. G.; Flores, B. S.; Rinehart, J. D. *Chem. Sci.* **2018**, *9* (36), 7204–7209.
- (111) Hilgar, J. D.; Bernbeck, M. G.; Rinehart, J. D. *J. Am. Chem. Soc.* **2019**, *141* (5), 1913–1917.
- (112) Tricoire, M.; Münzfeld, L.; Moutet, J.; Mahieu, N.; La Droitte, L.; Moreno-Pineda, E.; Gendron, F.; Hilgar, J. D.; Rinehart, J. D.; Ruben, M.; Le Guennic, B.; Cador, O.; Roesky, P. W.; Nocton, G. *Chem. – Eur. J.* **2021**, *27* (54), 13558–13567.
- (113) Rinehart, J. D.; Fang, M.; Evans, W. J.; Long, J. R. *Nat. Chem.* **2011**, *3* (7), 538–542.
- (114) Rinehart, J. D.; Fang, M.; Evans, W. J.; Long, J. R. *J. Am. Chem. Soc.* **2011**, *133* (36), 14236–14239.
- (115) Demir, S.; Zadrozny, J. M.; Nippe, M.; Long, J. R. *J. Am. Chem. Soc.* **2012**, *134* (45), 18546–18549.
- (116) Demir, S.; Gonzalez, M. I.; Darago, L. E.; Evans, W. J.; Long, J. R. *Nat. Commun.* **2017**, *8* (1), 2144.
- (117) Gould, C. A.; Mu, E.; Vieru, V.; Darago, L. E.; Chakarawet, K.; Gonzalez, M. I.; Demir, S.; Long, J. R. *J. Am. Chem. Soc.* **2020**, *142* (50), 21197–21209.
- (118) Demir, S.; Nippe, M.; Gonzalez, M. I.; Long, J. R. *Chem Sci* **2014**, *5* (12), 4701–4711.
- (119) Zhang, P.; Benner, F.; Chilton, N. F.; Demir, S. *Chem* **2022**, *8* (3), 717–730.
- (120) Vanjak, J. C.; Wilkins, B. O.; Vieru, V.; Bhuvanesh, N. S.; Reibenspies, J. H.; Martin, C. D.; Chibotaru, L. F.; Nippe, M. *J. Am. Chem. Soc.* **2022**, *144* (39), 17743–17747.
- (121) Gould, C. A.; McClain, K. R.; Reta, D.; Kragoskow, J. G. C.; Marchiori, D. A.; Lachman, E.; Choi, E.-S.; Analytis, J. G.; Britt, R. D.; Chilton, N. F.; Harvey, B. G.; Long, J. R. *Science* **2022**, *375* (6577), 198–202.
- (122) Simler, T.; McCabe, K. N.; Maron, L.; Nocton, G. *Chem. Sci.* **2022**, *13* (25), 7449–7461.

Chapter 1: Reactive Thulium Complexes for Small Molecule Activation

I. Preliminary study with $\text{Tm}(\text{Cp}^{\text{tnt}})_2$ and CO/CO_2	49
1. Early study of divalent thulium	49
2. Synthesis and characterization of the reactive species	51
3. Summary of reactivity	52
II. Coupled reactivity with CO_2 and pyridine derivatives	55
1. Development of the synthetic path on the pyridine case	55
2. Generalization to pyridinium derivatives	58
3. Toward a CO_2 captor?	65
III. Extension to other small molecules	68
1. Reactivity with small oxygenated molecules	68
2. Reactivity with small organic molecules	70
3. Mechanism discussion	71
IV. Conclusion	72
References	74

Chapter 1: Reactive Thulium Complexes for Small Molecule Activation

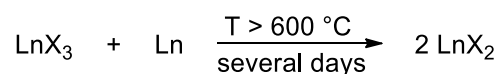
I. Preliminary study with $Tm(Cp^{ttt})_2$ and CO/CO₂

1. Early study of divalent thulium

1. Finding an adequate starting material

As often, in synthetic chemistry, the first question is about the starting material. Particularly, in coordination chemistry, finding a suitable metallic precursor can be challenging for several reasons such as solubility and side reactions. In order to develop the chemistry for a new oxidation state, new metallic precursors were needed. In lanthanide chemistry, one ubiquitous type, is the corresponding binary halides. Particularly, iodide and chloride salts have been extensively used for coordination chemistry.^{1,2}

Some obvious choices to access divalent lanthanide complexes were materials possessing an overall composition of (Ln: I in a 1: 2 ratio). These compounds had been described since the early 60's and examples with almost all the rare earth elements had been synthesized with the exception of terbium, holmium, erbium and lutecium materials.^{3,4} They were made by comproportionation of LnI₃ and the corresponding metallic lanthanide metals following the procedure described in **Scheme 1. 1**. However, this type of chemistry requires specific equipment because the mixture is sealed inside a tantalum reactor closed on both ends, itself included inside a sealed quartz tube. This apparatus then needs to be heated at 600 °C for several days. The difficulty of the synthesis probably explains why this chemistry had not been used by molecular chemists.

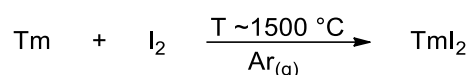


Scheme 1. 1 Comproportionation of LnX₃ and Ln to give the desired divalent lanthanide compound (with X, a halide atom).

Molecular chemists also value the solubility of the starting material and consequently primarily looked for soluble starting materials. For example, in 1964, Fischer described the synthesis of EuCp₂ in liquid ammonia, possible thanks to the solubility of europium in this solvent.⁵ Since ytterbium is the only other lanthanide soluble under those conditions, this method cannot be a general procedure for the synthesis of LnI₂ compounds. In the end of the 70's, the group of Kagan took interest in the chemistry of divalent lanthanides for their single electron reduction properties. In their seminal paper, they described the synthesis of SmI₂ by reaction of metallic samarium with diiodoethane in THF.⁶ This preparation was then extended to the other most stable divalent lanthanides as presented in the **Introduction**, ytterbium and

europium.^{7,8} Although only those three metals could be synthesized in this way, the chemistry of SmI_2 continued to develop rapidly thanks to its powerful but targeted reduction.^{9,10}

The first breakthrough for less classical divalent lanthanides came from a joint discovery from the Evans' and Bochkarev's groups.¹¹ A solvated form of TmI_2 is accessible through reduction of TmI_3 with metallic thulium in refluxing DME. This gave the first crystallographically characterized complex with a divalent lanthanide other than Sm, Eu or Yb. The solubility of this compound and its high reactivity placed this species at the potential start of a new chemistry. Further work by the two groups showed that another viable synthetic path for very reducing LnI_2 was heating a solid mixture of the metallic lanthanides with iodine up to 1500 °C in a quartz crucible using a gas burner, as illustrated in **Scheme 1. 2**.^{12,13} This method presents the interest of not needing specialized equipment such as a tantalum vessel. Furthermore, the reaction happens readily when the adequate temperature is reached. Given the rapidity of the reaction and the important iodine sublimation, an open vessel under inert atmosphere is recommended. This method has been followed for the synthesis of TmI_2 during this work.



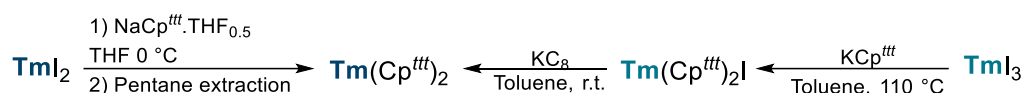
Scheme 1. 2 Synthesis of TmI_2 starting from metallic thulium using a gas burner.

2. Investigation in ligand design

Early reactivity studies on TmI_2 , particularly compared to SmI_2 , showed its very high reducing character and the necessity to find an adequate set of ligands to gain control over the reaction.¹⁴ This was further demonstrated by the first attempt at salt metathesis reaction by the group of Bochkarev. Most notably, contrary to the samarium chemistry, the pentamethylated version of the cyclopentadienyl ligand or Cp^* was not suitable to stabilize the corresponding Tm(II) complex. Indeed, the reaction of TmI_2 and KCp^* in THF led to the formation of a trivalent complex featuring two Cp^* and an iodine.¹⁵ Further studies showed that in diethyl ether, the solvent is cleaved by the reactive complex that is formed.¹⁶ Interestingly, this work also showed the facile nitrogen reduction performed by Tm(II) species and the need to work under argon atmosphere in order to prevent potential divalent species to further react. However, by using a different substitution group on the Cp backbone such as TMS group and switching for THF as a solvent, the Evans' group was able to isolate the first divalent organo-thulium complex.¹⁷ This study marked the beginning of ligand development to stabilize specifically the divalent state. The most successful candidates were presented in **Figure 3** in the **Introduction**.^{2,18}

3. Base-free adduct with the Cp^{ttt} ligand

Presented with the very high reactivity of Tm(II) species, finding an adequate ligand was of utmost importance. One type of substituent particularly interested the group of Nief, the bulky *tert*-butyl (^tBu) group. After a first moderately successful attempt with a disubstituted Cp ligand which was still fairly reactive, they introduced the trisubstituted Cp^{ttt} ligand.¹⁹ They showed in their study that in addition to stabilizing the divalent complex, this ligand also allowed the possibility to proceed through trivalent thulium species and reduce it at the end as described in **Scheme 1. 3**.²⁰



Scheme 1. 3 Proposed synthesis by the group of Nief to access the TmCp^{ttt}₂ complex.

As of note, more recent studies have shown the success of an even more substituted Cp backbone with ⁱPr groups. The Cp^{iPr5}, with five substituents, has been shown to stabilize the full lanthanide series (except promethium) in their divalent states as linear sandwiches.^{21,22}

2. Synthesis and characterization of the reactive species

1. Adopted synthesis for TmI₂

The synthesis of TmI₂ is done according to the reported synthesis for DyI₂ and NdI₂.^{12,16} A special but simple apparatus is used according to **Figure 1. 1**. The bottom part is made of quartz to prevent melting and deformation from the high temperature as well as pressure differences. These reactions are usually run under argon atmosphere. This allows easier manipulation due to the high density of the gas.

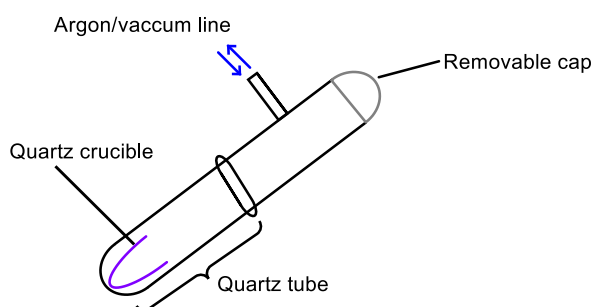


Figure 1. 1 Schematic representation of the apparatus used for TmI₂ synthesis.

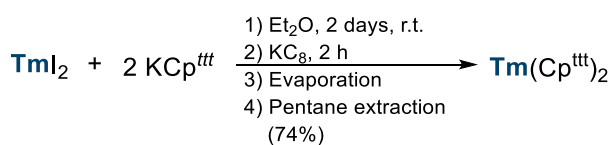
In the quartz crucible, a solid mixture of thulium powder and iodine in a slight excess were placed. These manipulations were done inside a glovebox to ensure proper storage of the metallic powder. The crucible was then quickly placed in the apparatus under inert

atmosphere. A gas burner was used to ensure the very high temperature reaches the reagent. At this moment, the cap of the apparatus was removed to avoid any over pressure. After a few instants, a purple cloud formed at the bottom from the iodine sublimation. Then, when the temperature was high enough, the thulium started to react and a bright spark could be seen moving from the bottom of the crucible to the top. When the gaz mixture was settled, the burner was turned off and the cap was placed back. The apparatus was then placed under *vacuum* to remove the excess of iodine. Once this process is complete, the crucible was entered in a glovebox for further treatment. A white powder was usually present on the wall of the crucible, believed to be TmI_3 coming from over-reaction. This powder could be removed by pentane washing. The remaining material was composed of a pellet of TmI_2 and some solidified drops of metallic thulium. These two products could be separated quite well after grinding the pellet to form the corresponding powder. This dark powder was obtained in a decent yield, typically 40%, allowing further synthesis. Moreover, the stability of TmI_2 in THF allowed for further extraction of the thulium drops still containing some product. This in turn yielded the adduct $\text{TmI}_2(\text{thf})_3$. It can be used in reaction which do not necessitates base free thulium starting material.

2. Synthesis path to $\text{Tm}(\text{Cp}^{\text{ttt}})_2$

As demonstrated by the group of Nief, the title compound can be made *via* two different routes: either formation of the trivalent species $\text{Tm}(\text{Cp}^{\text{ttt}})_2\text{I}$ and reduction, or direct salt metathesis from TmI_2 using a sodium salt of the ligand.¹⁸

During this work, the title compound was made according to the published procedure and as described on **Scheme 1. 4**.²³



Scheme 1. 4 Synthetic path to $\text{Tm}(\text{Cp}^{\text{ttt}})_2$.

3. Summary of reactivity

1. Discussion on the notion of stability Vs. reactivity

One goal of molecular organometallic chemistry is to develop a ligand set able to stabilize extremely reactive species so that they can be isolated and properly characterized. Indeed, the control of the ligand brings the possibility to impose a relative kinetic stability by a strong encumberment. However, if the characterization and fundamental understanding of different

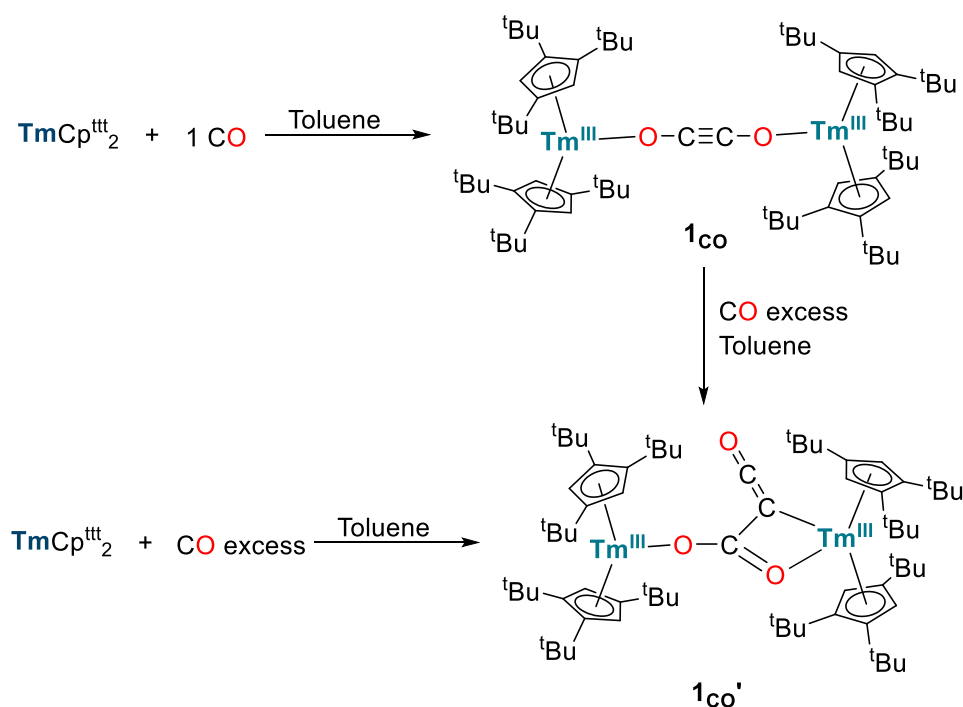
chemical entities is a worthwhile endeavor, the next logical step is to be able to harness the remaining reactivity. Indeed, sterically protecting a metallic center for instance, also means diminishing its reactivity. As shown in **1.1.2**, without proper steric and electronic properties, divalent thulium species will react with the first molecule they encounter, which in solution chemistry, is often the solvent. Now, with properly designed ligands, those species have been found to be stable enough to be handled. However, the question remains of their potential reactivity. The high steric hindrance from the Cp^{ttt} ligand participates in the stabilization of the metallic center, but it could also prevent other molecules to benefit from the reactivity at the metallic center.

In this particular case, previous studies showed that THF is able to coordinate the thulium center. Furthermore, studies on the same ligand with different metals showed that the coordination is indeed possible with isocyanide and N-heterocycles.^{24,25} Interestingly, for the samarium complex with Cp^{ttt}, the coordination of pyridine was not accompanied by an electron transfer from the metal to the ligand. This contrasts with results obtained by Evans with the permethylated Cp* ligand in which a coupling of two radical pyridine is observed.^{25,26} It comes to show the criticality of the ligand choice on the subsequent reactivity.

As such, our group decided to study the reactivity of the base free TmCp^{ttt}₂ which is more reactive than the THF adduct and more soluble in low-polarity hydrocarbon solvents such as pentane or toluene. Particularly, given the high oxophilicity known for lanthanides and our society's interest for the valorization of small carbonated molecules, the first investigations were carried with CO and CO₂.

2. Reactivity toward CO and multiple addition

The reactions with CO were performed after degassing of the solution and replacement of the atmosphere with gaseous CO. Interestingly, the reaction was found to be influenced by the stoichiometry. Indeed, upon addition of one equivalent of CO gas into a partially solvated TmCp^{ttt}₂ mixture, formation of a linear intermediate **1_{CO}** was observed. This complex was characterized through several methods and features an ethynediolate moiety in between two thulium centers. In contrast, when two equivalents of CO are added onto the divalent thulium, a trimerization of CO occurs, forming **1_{CO}'** a ketenecarboxylate still complexed by two TmCp^{ttt}₂ units. This reactivity is summarized in **Scheme 1. 5**. Interestingly, the reaction probably happens stepwise as addition of a second equivalent of CO onto the linear intermediate forms the expected ketenecarboxylate moiety.

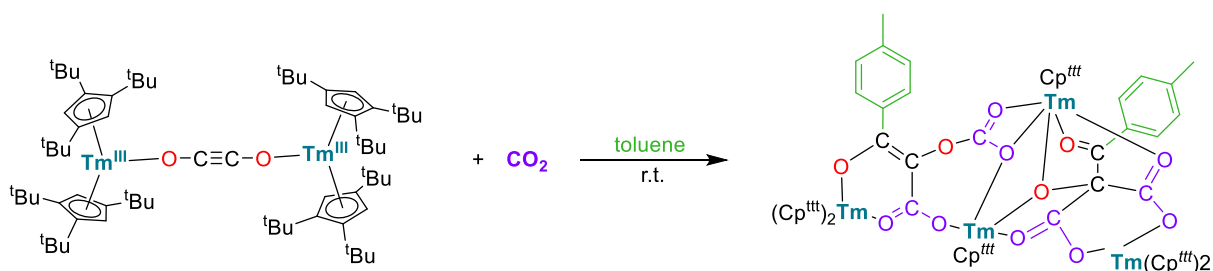


Scheme 1. 5 CO oligomerisation reactions depending on the stoichiometry.

3. Reactivity of the linear complex toward CO₂ and Friedel-craft type reactivity

Earlier investigation in the group focused on the reactivity toward electrophiles such as CO₂. Direct reaction of TmCp^{ttt}₂ with CO₂, is expected to yield either the carbonate or the oxalate. This is a well-known reactivity for divalent lanthanides.²⁷ As was obtained for the samarium analogue, the reaction yields in this case the carbonate adducts.²⁸

Another reactivity which can be further investigated comes from the linear intermediate. Indeed, as shown above, this compound can react with CO, leading to a trimerization of the small molecule. As such, its reactivity with CO₂ was explored. Quite surprisingly, the product of this reaction in aromatic solvents shows introduction of two solvent molecules into the organic fragment. More precisely, the toluene moieties undergo C—H activation and functionalization in the *para* position as described on **Scheme 1. 6**. Four molecules of CO₂ also seem to have participated in the reaction.



Scheme 1. 6 Reaction of CO₂ onto the linear intermediate 1_{CO}.

II. Coupled reactivity with CO₂ and pyridine derivatives

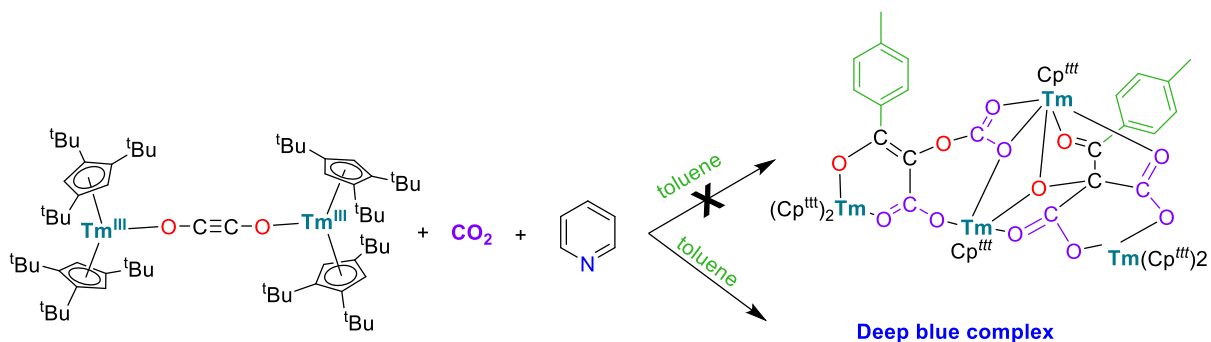
1. Development of the synthetic path on the pyridine case

1. Establishing the adequate solvent

Discovering the diverse reactivities of the linear complex, we were interested in building more complex organic platforms. Most notably, considering the high activity upon addition of CO₂, we decided to investigate the corresponding reactivity in the presence of external nucleophiles. Pyridine derivatives were used as first candidates.

Because of the relatively fast reaction observed upon addition of CO₂ in standard aromatic solvent, the decision was taken to perform this reaction directly with the nucleophile as a solvent. The reaction was performed in a J. Young NMR tube adapted on a glass Schlenk line. The suspension of **1_{Co}** in pyridine was degassed three times and about one atmosphere of CO₂ was added. This led to an extremely fast change of colors from yellow to dark blue along with a complete dissolution of the thulium complex. This tube was then brought inside a glove box and several crystallizations were attempted to identify the nature of the blue compound formed. However, the very high solubility of this complex in pyridine solvent precluded the obtention of crystals suitable for SC-XRD. Other attempts were made with different pyridine derivatives to see if the solubility would be affected, however no structural information could be gathered due to the formation of oily products.

Confronted with this problematic and considering the exceedingly fast reaction, I tried to run a similar reaction directly in pentane. Although the starting complex **1_{Co}** is sparingly soluble in pentane, it readily dissolves upon addition of CO₂, indicating reaction. In the presence of one equivalent of pyridine, the reaction in pentane proceeded in a similar fashion than those with pyridine as solvent giving quickly a deep blue solution. This showed that the activation of the solvent seemed kinetically slower than the reaction with the pyridine. Similarly, attempts in toluene showed that the Friedel-Crafts-type reactivity was not observed but rather the reaction with the pyridine, as illustrated in **Scheme 1. 7**.



*Scheme 1. 7 Addition of CO₂ to **1_{Co}** in the presence of pyridine.*

This change in solvent however, proved critical in the obtention of structural characterizations. Indeed, upon slight concentration of the pentane supernatant, large dark blue crystalline blocks suitable for XRD analysis appeared in the vessel.

2. Structural considerations

The resulting crystals were analyzed by XRD diffraction and confirmed the addition of CO₂ and the pyridine moiety onto the organic backbone as showed on **Figure 1. 2**. The product crystallizes in the monoclinic space group C2/c and features only half of the molecule with one thulium centers per asymmetric unit. The crystallographic symmetry imposed by the space group leads to a central fragment disordered over two positions in between the two thulium centers.

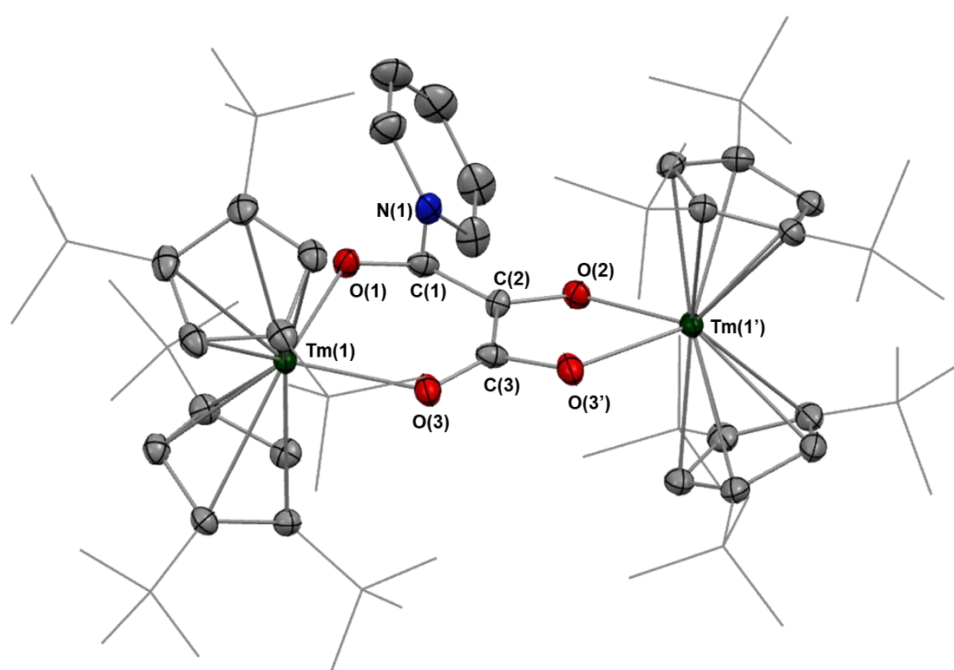


Figure 1. 2 Molecular structure of the product of the addition of CO₂ and pyridine on the linear intermediate in the solid state with thermal ellipsoid at the 50% probability level (except for the ^tBu groups depicted in wireframe). Thulium atoms are depicted in dark green, carbon atoms in grey, oxygen and nitrogen atoms in red and blue respectively. The disorder on the central part of the molecule has been omitted. H atoms and one disordered solvent molecule have been omitted for clarity.

The main distances are reported in the experimental section at the end of the chapter. It is interesting to note that the distance Tm – Cp^{ttt}(ctr) is slightly larger than in the linear complex probably due to the high steric pressure added. Analysis of the structure also shows that the fragment O(2)-C(2)-C(3)-O(3) is fairly planar with a torsion angle of 8.70 °, similarly the fragment O(1)-C(1)-C(2)-O(2), which in all likelihood arises from the linear OCCO fragment in the linear complex, is still fairly planar with a torsion angle of 6.62 °. However, the fragment now strongly deviates from linearity with O(1)-C(1)-C(2) at 130.49 ° and O(2)-C(2)-C(1) at 125.93 °. The two C–O bonds that were already present in the molecule compare with the

linear complex while the C—O from CO₂ have been slightly elongated from typical 1.16 Å to 1.26 Å. Regarding the pyridine ring, all the internal bonds are measured at 1.39 Å, quite close to the bond length in the free pyridine.²⁹ It is important to note that because of the disorder present on the organic molecules, reasonable restraints have been used to allow the analysis of the structure. Typically, a similar restraint on the bond distances were used on the pyridine ring to obtain a regular hexagon. As such the comparison of the bond distances should not be overanalyzed.

3. Discussion

This reaction features a few interesting points.

First, the reaction happens immediately upon dissolution of CO₂ in the solvent showing that it is kinetically favorable. Then, the formation of this non-trivial organic backbone starting only from gases and simple pyridine could be inspiring to create and detach even more complicated molecules. Finally, an interesting phenomenon is the stark change in color upon reaction. Indeed, the metrics of the structure show that in all likelihood, the thulium centers did not change their oxidation state. It would be fairly unusual for a trivalent lanthanide to possess such a deep color in the blue translating to a strong absorption in the orange.³⁰

The absorption could then be due to the organic part. It does indeed display an aromatic cycle with the pyridine and a carbonated chain with what appear to be single and double bonds. Nevertheless, the angle between the medium plan of the pyridine ring and the carbonated fragment of 42.68 ° seems to indicate that there is no full conjugation in between the two systems.

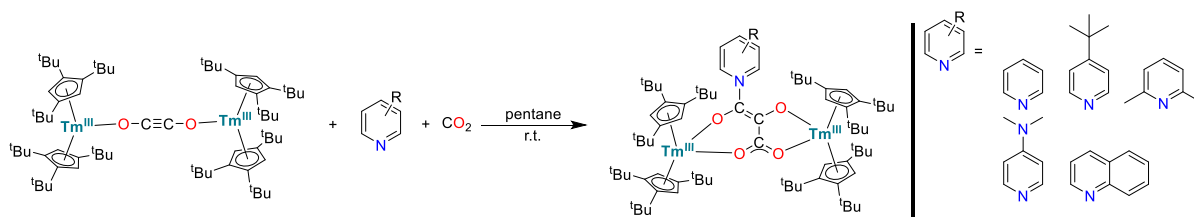
Additionally, the organic fragments seem to contain formally separated charges with a cationic site on the pyridinium moiety and an anionic site on the carboxylate group. As such, this large absorption coefficient could come from intramolecular charge transfer. Although, those information are not sufficient to prove the origin of the bright coloration.

For all those reasons, we decided to carry on the study with different pyridine derivatives to obtain more structural data, as well as determine the influence those changes could have on the spectroscopic properties. Furthermore, this was an opportunity to investigate the type of organic platform that can be created from the linear intermediate and could be of interest.

2. Generalization to pyridinium derivatives

1. General synthetic procedure

The general procedure described above in II.1.1, was adapted for different pyridine derivatives as pictured on **Scheme 1. 8**. Those reactions yielded the expected product in decent crystalline yield and will be noted as **1_{Pyr}**, **1_{tBu}**, **1_{Me2}**, **1_{DMAP}** and **1_{quin}** respectively for the reaction with pyridine, 4-*t*-Butylpyridine, 2,5-dimethylpyridine, 4-dimethylaminopyridine and quinoline.



Scheme 1. 8 General procedure for the reaction of the linear intermediate with CO₂ and a pyridine derivative.

The reaction with 2,5-dimethylpyridine differs from the other as the desired product precipitates very quickly out of the solution as extremely thin needles. As such, crystals suitable for X-ray diffraction were obtained from the reaction in toluene solvent. Paramagnetic ¹H NMR analysis of both solids proved that the product of the reaction in the two solvents is the same. The fact that the reaction also happens in toluene instead of giving the activation of solvents gave us the opportunity to perform *in situ* NMR monitoring of the reaction mixture, showing that the product is rapidly consumed to form the final product. All the products were then characterized by SC-XRD (Single-Crystal X-Ray Diffraction), NMR analysis, infra-red and UV spectroscopy to gain insight on the reactivity as well as the spectroscopic properties.

An interesting point, which will be explored further, is the singular color of the different product. If **1_{Pyr}** and **1_{tBu}** both feature similar deep blue color, **1_{Me2}** is purple, **1_{DMAP}** is bright red and **1_{quin}** is green.

2. Structural study

The compounds obtained were analyzed by SC-XRD. The five structures are quite close to **1_{Pyr}**, however **1_{DMAP}** and **1_{tBu}** do not crystallize in the same manner.

As mentioned previously in II.1.2, for **1_{Pyr}**, only half of the molecule is present in the asymmetric unit, namely one thulium center with its two Cp^{ttt} ligands and one organic motif containing the added pyridine ring and the CO₂ as depicted in **Figure 1. 3 left**. This organic motif is populated at half the population of the thulium ion as it will be constructed a second time by the symmetry operations of the space group (**Figure 1. 3 right**).

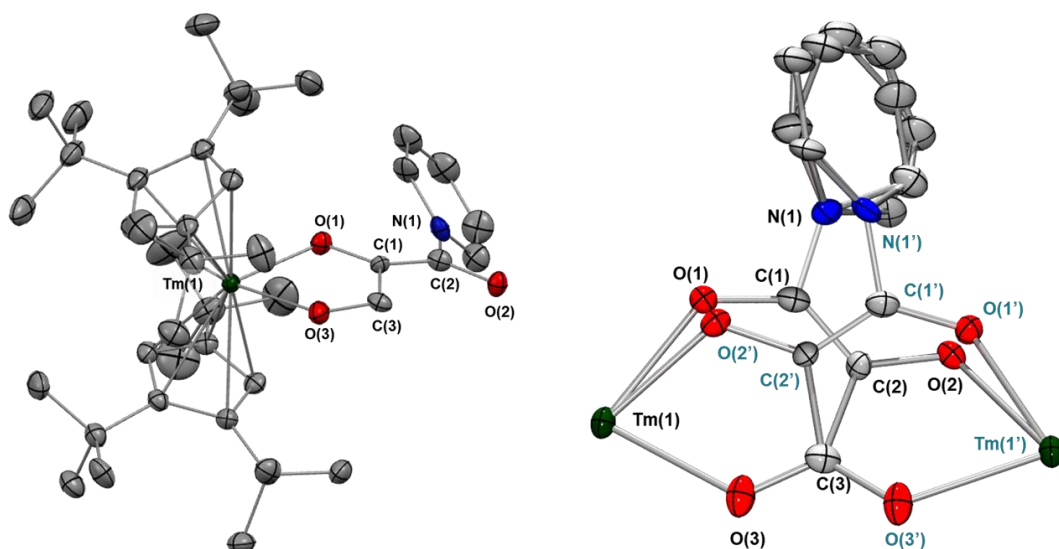


Figure 1. 3 On the left, molecular structure of **1_{Pyr}**, depicting only the asymmetric unit. Thulium atoms are depicted in dark green, carbon atoms in grey, oxygen and nitrogen atoms in red and blue respectively. H atoms and one disordered solvent molecule have been omitted for clarity. And, on the right, structural representation of the disorder created by application of the symmetry operations on the organic moiety and the two thulium atoms (Cp^{*tt} , H atoms and disordered solvents have been omitted)

This symmetrical disorder is also present for **1_{Me2}** and **1_{quin}**. In contrast, **1_{DMAP}**, which crystallizes in the same space group, but presents one molecule per asymmetric unit. This time a non-crystallographically imposed positional disorder is present as the two orientations of the organic fragment are possible.

3. Spectroscopic insight

In order to gather information on their electronic structures, those complexes (**1_{Pyr}**, **1_{tBu}**, **1_{Me2}**, **1_{DMAP}**) were studied through different spectroscopic means.

First, the presence of two thulium (III) centers makes all of those complexes strongly paramagnetic. However, their ^1H NMR spectrum were recorded and several broad resonances could be observed in the range $\delta = -250$ to 250 ppm. The corresponding spectra are presented in the experimental section at the end of the chapter. The low-symmetry of the structures and the paramagnetic nature of the compounds render difficult any precise assignments. The main resonances can nonetheless be attributed to the $t\text{Bu}$ groups for which the rotation is most likely partially restricted. The comparison between the different products in **Figure 1. 4** shows similar patterns which is coherent with the overall similarities of the molecular structures. Further insights on the overall symmetry and the rotation of the Cp^{*tt} ligand could likely be pursued through ^1H VT-NMR but it is hampered by the very large resonances of Tm(III) complexes and the difficult assignment of the signals.

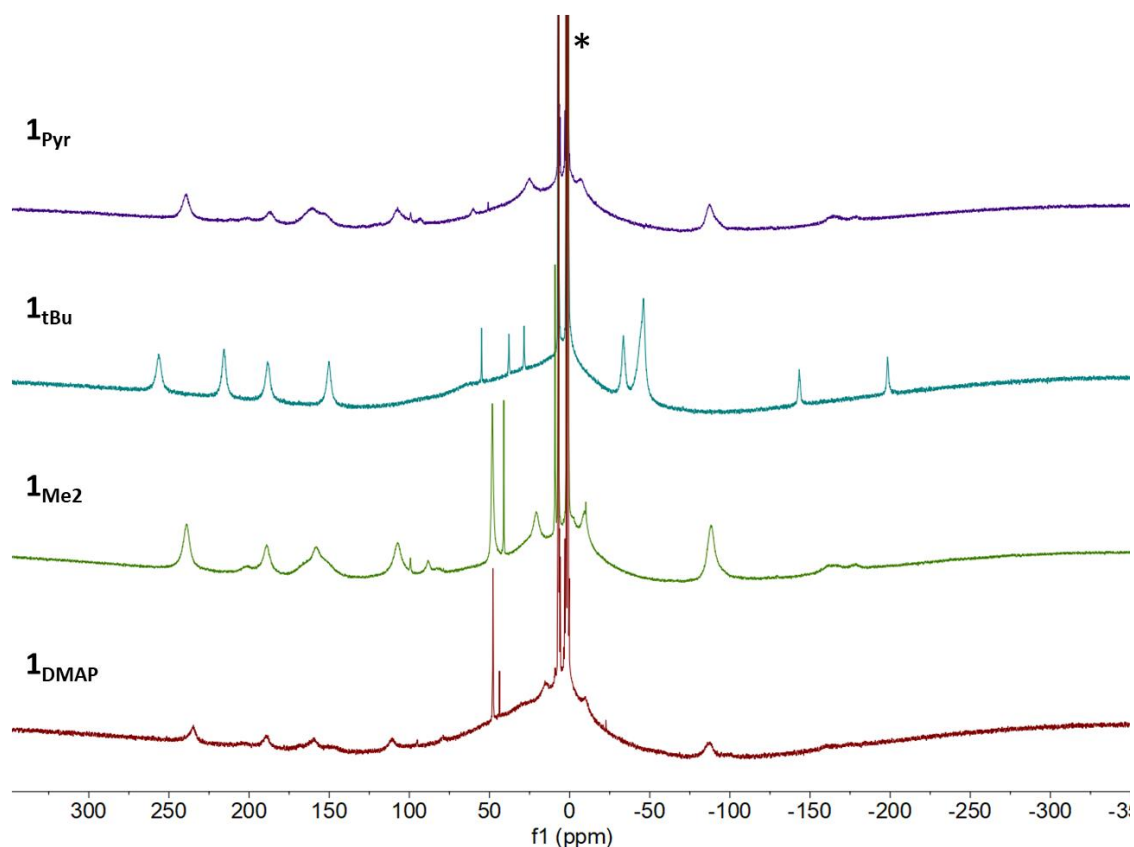


Figure 1. 4 Comparison of the NMR spectra recorded at 298 K in $\text{tol-}d_8$ for the different pyridine product. (* Denotes residual protio peaks from the solvent).

The same complexes were characterized by IR spectroscopy. No distinctive features are observed on those spectra. Similarly to what had been reported by Simler *et al.*, one complex medium absorption band is observed around 2900 cm^{-1} , most likely corresponding to the C—H bonds of the ligand. The spectra are reported in the experimental section at the end of this chapter.

Then, one particular feature of interest is their intense color which we investigated through UV-visible spectroscopy.

4. UV-visible study

a. Experimental considerations

All the organometallic complexes handled during this study were expected to be water and oxygen sensitive. As such, all sample preparations were performed inside a nitrogen atmosphere glove box with appropriately prepared solvents. The cuvettes used are adapted with a J. Young valve to ensure hermeticity and allow removal of the atmosphere when needed.

The solvent used for most of the crystallization was pentane. However, due to its high volatility, working on precise concentration with this solvent inside a glovebox is difficult. To

counter that, a solvent with a higher boiling point such as toluene is needed. One important drawback of this solvent is a small transparency window in the UV with a cutoff around 285 nm. Although, the main feature of interest in this study being located in the visible region, we decided to use toluene solutions.

It is important to note that due to the very strong color, relatively low concentrations were used [1×10^{-4} – 1×10^{-5} mol.L⁻¹]. This situation is quite typical in UV-visible spectroscopy; however, the sensitivity of these reactive complexes renders this task quite challenging. Even in specifically prepared solvents which have been dried on sodium and degassed multiple times, degradations were observed at concentrations lower than 1×10^{-4} mol.L⁻¹. This made the full characterization and determination of absorption coefficients difficult.

As such, a compromise between saturation of the detector and stability of the species had to be found.

b. Experimental setup with pyridine

The J. Young valve adapted cuvettes used for air-sensitive compounds have the advantage to allow for removal/addition of atmosphere. A stock solution of **1co** concentrated at 1×10^{-3} mol.L⁻¹ was used and directly added to two equivalents of pyridine. The reaction was then degassed and CO₂ was added to form the deep blue solution of the pyridine adduct directly into the cuvettes.

To characterize at best the product, two spectra were recorded, before and after the addition of CO₂. Unfortunately, due to the high absorbance of this complex, the detector showed sign of saturation below 400 nm and in the main feature in the visible around 600 nm. As such, further dilution was performed to bring the solution down to 1×10^{-4} mol.L⁻¹. The resulting graph represented in molar absorbance coefficient is presented in **Figure 1. 5**. To be able to compare, the approximation was made that the reaction is complete and the concentration of the reagent is equal to the concentration of the product.

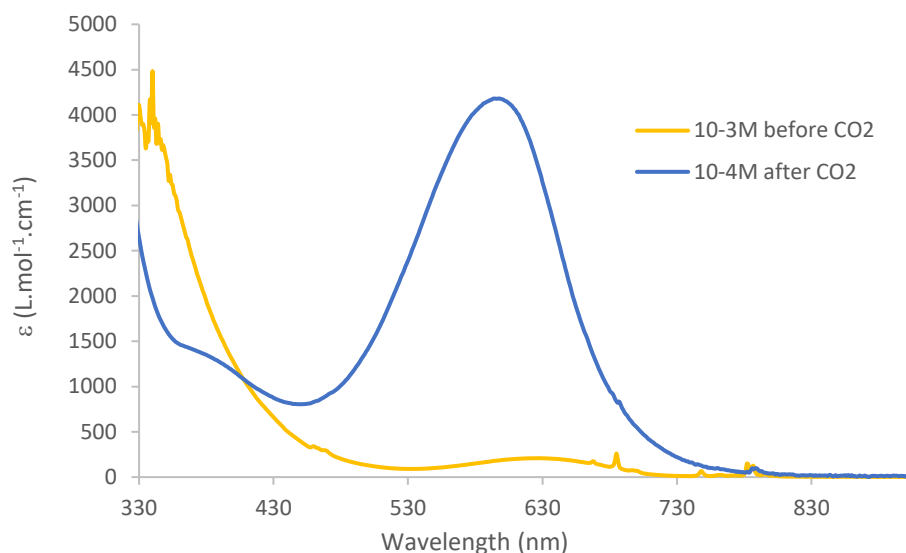


Figure 1. 5 Absorption spectra of a solution of the linear adduct and pyridine before and after addition of CO_2 .

As expected for a deep blue compound, the absorption spectrum features a large absorption band in the visible with a maximum around 594 nm. At higher concentration, another feature appears closer to the UV region around 380 nm but with a smaller absorption coefficient. Considering a cuvette which width is 1 cm and a solution at approximately $1 \times 10^{-4} \text{ mol.L}^{-1}$ in concentration leads to an estimation of the absorption coefficient for the visible band of about $4000 \text{ L.mol}^{-1}.\text{cm}^{-1}$.

This value could be due to charge transfer involving the thulium centers and the organic platforms. In order to determine more precisely the origin of this transition, a spectrum could be simulated through TD-DFT. In contrast to standard DFT, this method allows to consider the electronic transition at the origin of the absorption band and as such, can be an efficient tool for spectral assignment.

Another peculiar feature on the UV spectra appearing at the higher wavelength, are the $f-f$ transition as shown in **Figure 1. 6**. Those transitions are Laporte forbidden, as they do not change symmetry, which explains their low absorption coefficient. However, due to the shielded nature of the f orbitals and their relatively weak interaction with the environment, they are quite sharp. The reaction seems to slightly affect the $f-f$ transition even though the main features remain.

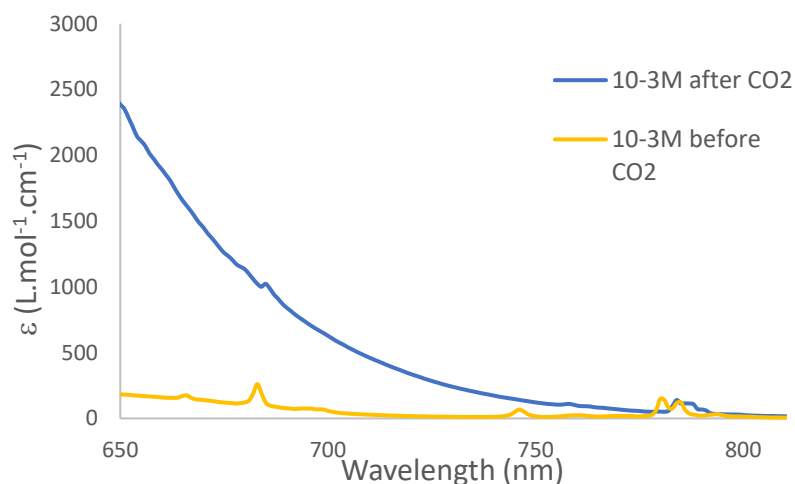


Figure 1. 6 Zoom in on the absorption spectra of the high concentration at higher wavelength.

If the $f-f$ transitions are easy to identify with their distinctive features, the main transition in the visible has less hints about its nature. We then decided to pursue UV-visible characterization of the different pyridine derivatives to gather insight on the electronic features.

c. Trends with other pyridine derivatives

A similar process was repeated with the different pyridine rings in order to assess the influence of the electronic of the ligand on the overall electronic structure.

In order to compare the behavior of the different product, a concatenated spectrum of the absorption spectra at about $1 \times 10^{-4} \text{ mol.L}^{-1}$ for each product is presented in **Figure 1. 7**.

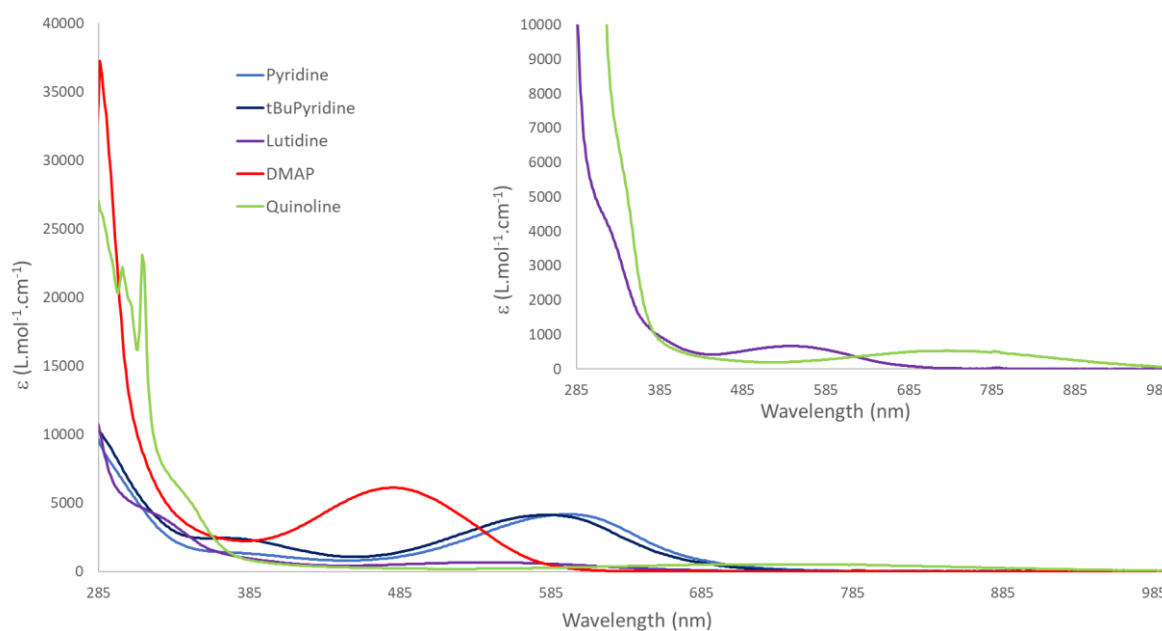


Figure 1. 7 UV-visible absorption spectra of the different compounds normalized by their concentration. An insert with only the lutidine and quinoline derivatives is shown to highlight their features.

The main metrics for each feature in the visible, namely λ_{\max} , the absorption maximum and the corresponding absorption coefficient are regrouped in **Table 1. 1**. If the overall behavior is quite similar for every complex with absorption in the visible and strong bands in the near UV, there appear to be two groups in those complexes.

The first group akin to the pyridine complex is comprised of **1_{Pyr}**, **1_{tBu}** and **1_{DMAP}**. They show a large band with absorption coefficient around 4000-6000 L.mol⁻¹.cm⁻¹. The maxima of absorption are fairly close for **1_{Pyr}** and **1_{tBu}** with $\lambda_{\max} = 594$ nm and $\lambda_{\max} = 585$ nm respectively. The maximum for **1_{DMAP}** is strongly blue shifted and stands at 480 nm which is coherent with its distinctive shade of red.

The second group, comprised of **1_{Me2}** and **1_{quin}**, seems to be quite different from the other compounds as it doesn't display strong absorption in the visible. A very large feature is nonetheless visible around $\lambda_{\max} = 542$ nm and $\lambda_{\max} = 733$ nm for **1_{Me2}** and **1_{quin}** respectively. In these cases, the absorption coefficient is closer to 500 L.mol⁻¹.cm⁻¹.

Compound	λ_{\max} (nm)	A_{\max} (au)	$\epsilon_{\lambda_{\max}}$ (L.mol ⁻¹ .cm ⁻¹)
1_{pyr}	594	0.418	4181
1_{tBu}	585	0.413	4129
1_{Me2}	542	0.067	667
1_{DMAP}	480	0.611	6113
1_{Quin}	733	0.053	531

Table 1. 1 Table summarizing the values extracted from the UV-visible spectra recorded for the different complexes.

Overall, two main conclusions can be drawn.

First, the donating character of the substituting group is to be accompanied by a blue shift (or hypsochromic shift) in the absorption maxima. The effects are quite small for weak hyperconjugation donor such as the alkyl substituent. The effect of the ^tBu group is even lower probably due to its *para* position as the hyperconjugation effect is often significant at very short distances, typically one or two bonds.³¹ The amine substituent in the DMAP however has a strong influence, probably because it involves mesomeric effect of the delocalization of the π -electrons. This indicates that the electronic structure of the pyridine derivatives appears to be of significance in the electronic transition associated with the visible band.

Then, to reconcile the two different values of absorption coefficient, one hint could come from the solid structure. Indeed, as discussed previously, the steric encumbrance of the pyridine moiety has a strong impact on the angle between the mean plan of this derivatives and the rest of the skeleton. For the simple pyridine ring **1_{Pyr}** or in the case of substituent at the *para*

position **1**_{tBu} and **1**_{DMAP}, the angle is around 40 ° whereas **1**_{Me2} and **1**_{quin} the angles are 86 ° and 63 ° respectively. This angle could render difficult the electronic communication in between the aromatic ring and the carbonated part. As such, an electronic transition involving both those parts would have a lower probability of occurring or in other word, feature a weak absorption coefficient. If this explanation seems quite coherent for **1**_{Me2} where the angle is almost 90 ° showing an orthogonality of the two fragments it is harder to reconcile **1**_{quin}. In that case the angle, while being larger than for **1**_{Pyr}, is still far from orthogonality but the observed absorption coefficient comparable to **1**_{Me2}.

To conclude, it is likely that the transition does involve a certain form of communication in between the two organic fragments, rendered more difficult by large geometric angles in between them. However, the complexity of the object probably leads to intricate transitions which, to be explained more in-depth, would require TD-DFT calculations.

3. Toward a CO₂ captor?

As mentioned previously, while working with fairly dilute solutions of **1**_{CO} and pyridine, we observed degradation. Most notably, in several cases the originally yellow solution of **1**_{CO} in toluene would take a blueish - green color. We hypothesized that it could be selectively reacting with very low amount of CO₂ present in the glovebox, creating a mix of yellow and blue colors. Considering this potential selectivity, we then wondered if we could construct a CO₂ detector based on this type of complexes.

1. Attempt at dry air CO₂ reactivity

In order to detect CO₂ in the atmosphere, we needed to remove humidity traces as all those complexes are organometallic species with basic ligands. Unfortunately, we did not possess a dry air bottle. As such, we tried several air-drying methods. Most notably, we used a Schlenk-type vessel with molecular sieves and placed regular atmosphere inside. The vessel was then closed and the tip with the molecular sieves was placed at low temperature in a dry ice bath. This should have had the effect of condensing the water and blocking it inside the sieves. Another method used, was the creation of drying guard using tissues and CaH₂ as a drying agent. This guard was placed inside a J-Y valve adaptor to be placed on either NMR tubes or UV-visible cuvettes. Those two methods are illustrated in **Figure 1. 8**.

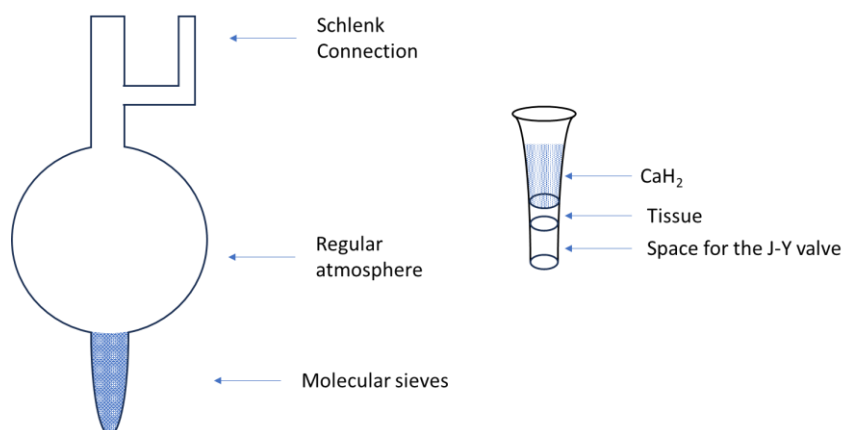


Figure 1. 8 On the left, representation of the Schlenk-type apparatus with molecular sieve represented as a textured zone, on the right the drying guard with CaH₂ represented in textured zone.

2. Troubleshooting the reactivity with O₂

The first trials were performed with the Schlenk-like apparatus. It was connected to a glass Schlenk line next to a degassed NMR tube containing a mixture of **1_{CO}**. Opening the two vessels prompted a slight change of color in the NMR tubes. Although this color was closer to a pale green than the expected deep blue coloration of **1_{Pyr}**, it could be the consequence of a sub-stoichiometric reaction due to the low amount of CO₂ in the atmosphere (~400 ppm). However, it could also be due to a parasitic reaction.

Different attempts were performed with the drying guard allowing continuous reaction with the exterior atmosphere, possibly leading full conversion. To ascertain the nature of this reaction, a UV-visible follow-up reaction was run with the drying guard adapted onto a cuvette. The resulting UV-visible spectra are reported in **Figure 1. 9**.

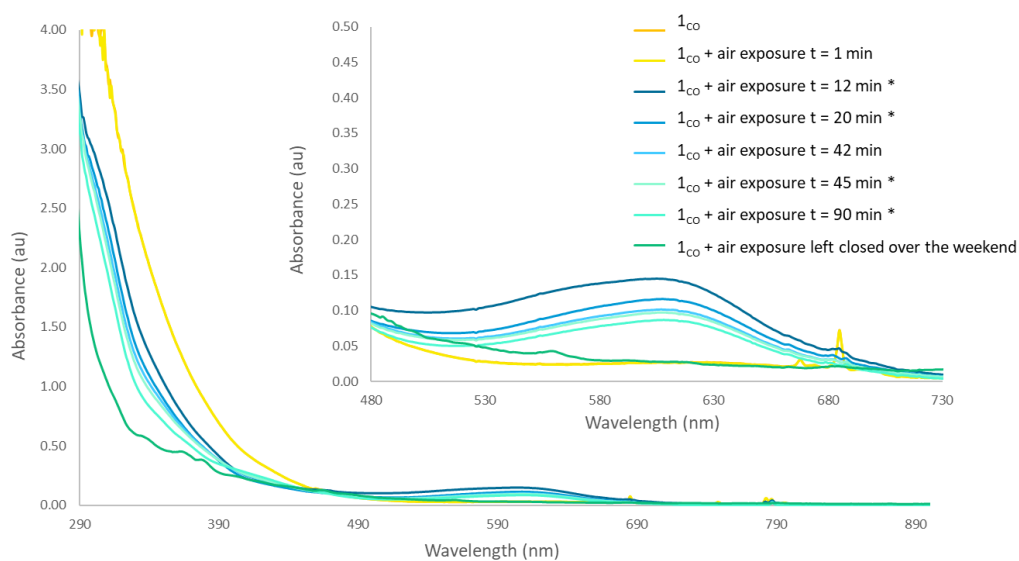


Figure 1. 9 Evolution of the UV-visible absorption spectra of **1_{CO}** upon air exposure and. An insert focused on the visible part of the spectrum is presented. The * denote manual homogenization of the solution inside the cuvette.

This experiment shows that upon exposure to air, a small feature in the UV-visible spectra can be seen growing however it quickly starts to diminish. After two days with a normal atmosphere in the cuvette, no significant absorption in the visible can be seen. The feature around 600 nm can be compared with the previously characterized 1_{Pyr} as illustrated on **Figure 1. 10**. To allow comparison, all spectra are represented in molar coefficient using the concentration of the starting material. This introduces a bias but should not influence the conclusion here as we are not quantitatively comparing the signals. Despite a difference of more than a factor ten, the feature that is identified on the spectra on **Figure 1. 9** could be coherent with the formation of a small amount of 1_{Pyr} .

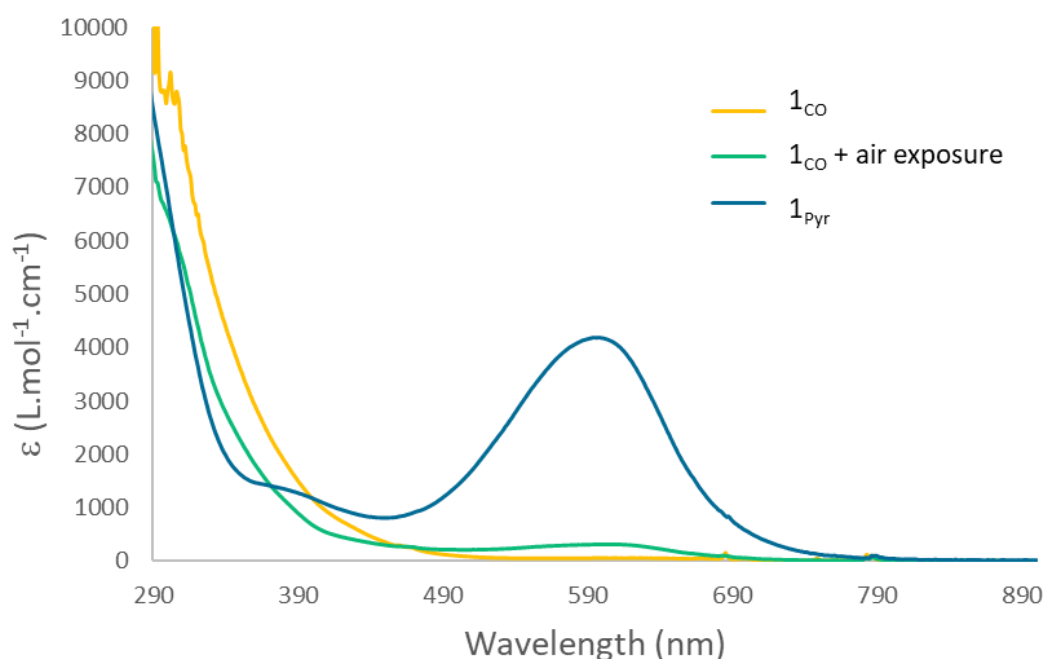


Figure 1. 10 Comparison of the UV-visible spectra of 1_{CO} , 1_{CO} after 12 min of air exposure and homogenization of the solution and 1_{Pyr} formed in situ.

However, the feature quickly disappears as presented in **Figure 1. 10**. Several similar experiments were attempted in J. Young tubes to be monitored by ^1H NMR spectroscopy and help identifying more precisely 1_{Pyr} as well as a potential side-product. However, the guard volume present in the NMR tube rendered the diffusion of the atmosphere more difficult. Confronted with this side-reactivity, we decided to investigate a potential reaction with the dioxygen from the atmosphere.

III. Extension to other small molecules

As such we were interested in the reactivity of our system with small oxygenated molecule to better understand the reactivity with the atmosphere.

1. Reactivity with small oxygenated molecules

The first trials were performed with O₂.

1. Reactivity with dioxygen

A bottle of oxygen for gaz burner was used an O₂ source. Similarly to previous gas reaction, a mixture of **1_{co}** in an NMR tube was degassed and dioxygen was added. A change of color similar to what had been observed both in the glovebox and with atmosphere addition was observed. However, only clear crystals were observed growing in the tube. XRD diffraction analysis revealed the presence of an oxalate group in between the two thulium centers as presented on **Figure 1. 11**. This molecule, referred to as **1_{ox}**, crystallizes in the P-1 space group and a small disorder with a carbonate type adduct can be modelled at 0.15 occupation.

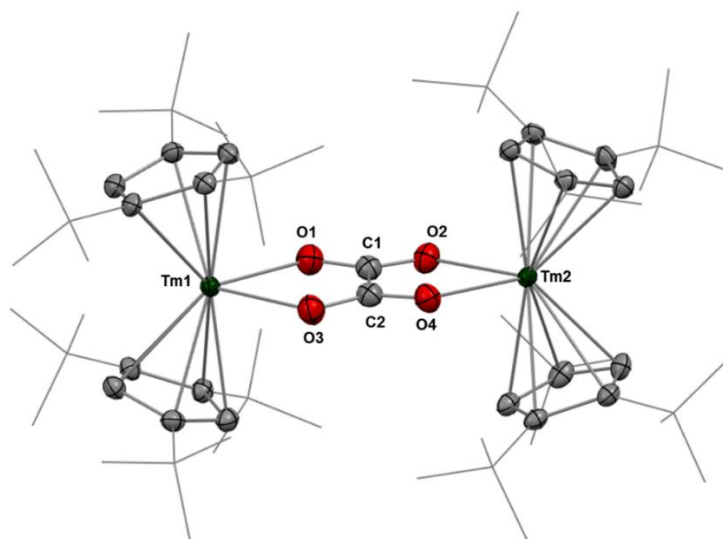


Figure 1. 11 Molecular structure of the product of the addition of O₂ on the linear intermediate in the solid state with thermal ellipsoid at the 50% probability level (except for the ^tBu groups depicted in wireframe). Thulium atoms are depicted in dark green, carbon atoms in grey, and oxygen atoms in red. The disorder on the central part of the carbonate adduct has been omitted. H atoms have been omitted for clarity.

The obtention of such a stoichiometry tends to indicate the two oxygen atoms from O₂ were transferred to the linear adduct to form C₂O₄ from C₂O₂.

Interestingly, the pyridine moiety seems spectator in this reaction and reproducing the reaction in its absence shows the same NMR signature.

While this reactivity invalidates the possibility to use this system as a CO₂ captor, it interrogated us about the possibility of tuning the number of oxygen atoms given to the

complex and create different arrangements. We thought about ozone reaction however, we did not find a set up that could allow this addition in the required air-free system. As such, we decided to target N_2O addition, to simulate a one-oxygen atom transfer.

2. Reactivity with dinitrogen oxide

Upon addition of gaseous N_2O to a tube of $\mathbf{1}_{\text{Co}}$, an immediate reaction is observed. NMR analysis of the mixture revealed a more complicated symmetry than the oxalate. Unfortunately, due to the high paramagnetism of thulium ions, it is difficult to deduce more information from the NMR spectrum. After a couple days, orange crystals were seen forming in the tube. XRD analysis revealed a highly disordered molecule crystallizing in the $\text{Pca}2_1$ space group. Different modelling strategies were tried to see which one would better fit the data. One repartition of the atom was found to be the more coherent with the information in our possession and is presented in **Figure 1. 12**. This proposition features two disordered molecules forming a cross with four carbon atoms possessing a 0.5 occupation each as well as 4 oxygen atoms with 0.75 repartition. Overall, this gives a formula of C_2O_3 for the central organic moiety. Interestingly this does not correspond to usual reaction forming either carbonate or oxalate but it does correspond to the formal addition of one oxygen to the OCCO linear motif. Additionally, to respect the neutrality of the complex, this fragment is expected to bear a -2 charge.

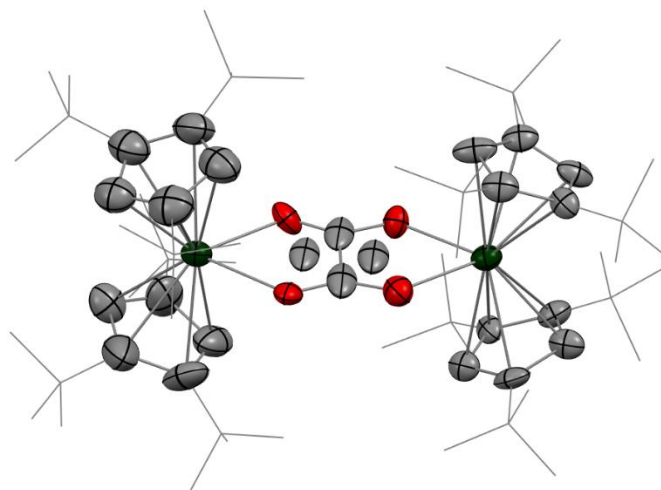


Figure 1. 12 Putative molecular structure of the product of the addition of N_2O on the linear intermediate in the solid state with thermal ellipsoid at the 50% probability level (except for the $t\text{-Bu}$ groups depicted in wireframe). Thulium atoms are depicted in dark green, carbon atoms in grey, and oxygen atoms in red. The disorder on the central part is depicted, each carbon atom has an occupancy of 0.5 and each oxygen has an occupancy of 0.75. H atoms have been omitted for clarity.

To investigate further the make-up of this organic fragment, elemental analysis was run on this compound. The results tend to indicate that nitrogen is present in the complex and as such, the previous hypothesis may not stand. The N_2O did not act as an oxygen transfer reagent but nitrogen atoms were involved in the transformation.

The only experiment that we have access to in order to solve the exact nature of this adduct, is the XRD. Unfortunately, carbon, nitrogen and oxygen atoms differ by a couple of electrons which make them particularly difficult to differentiate with this technique. This is even further complicated by the disorder fractioning the atoms. To conclude, we are not yet capable of identifying this product. Perhaps neutron diffraction on larger crystals could help magnify the electronic differences in between each atom.

Intrigued by the plurality of reactivity demonstrated by this compound, we decided to explore further the reactivity with small molecule.

2. Reactivity with small organic molecules

Particularly, the reactivity with CO₂ presented in **1.1.3** was quite intriguing with the activation of solvents. We looked for equivalent small molecules that could undergo similar reactions. Some attempts with carbodiimide molecules featuring a N=C=N fragment showed no reaction. I proposed to study the mixed unit N=C=O with an isocyanate molecule (more precisely we used the tBu-isocyanate). The small molecule was added directly to **1_{CO}** in solution in toluene. The reaction mixture immediately turned bright orange. The solution was concentrated and small orange crystals were formed at low temperature. The product **1_{ISO}**, crystallizes in the P2₁/n space group and is presented on **Figure 1. 13**.

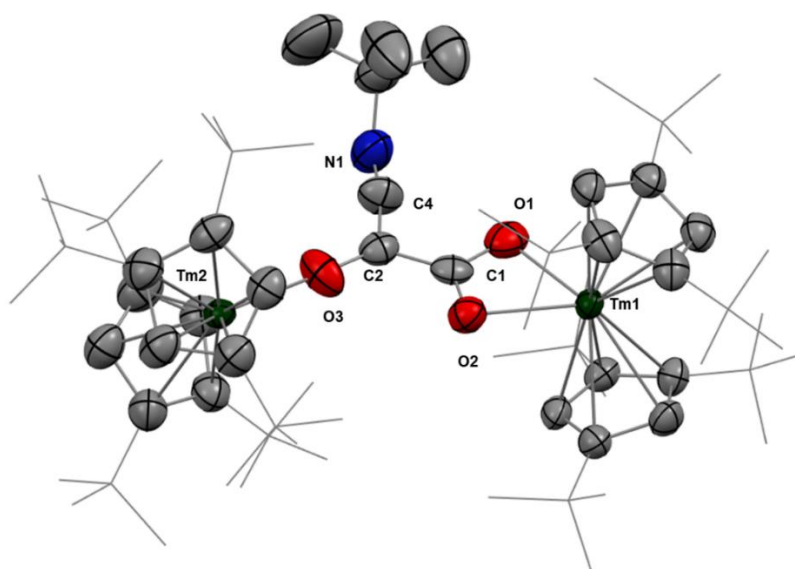


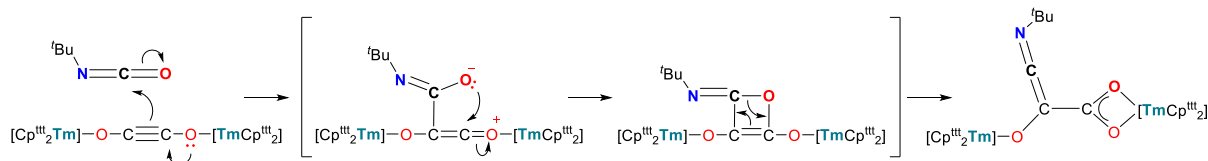
Figure 1. 13 Molecular structure of the product of the addition of ^tBuNCO on the linear intermediate in the solid state with thermal ellipsoid at the 50% probability level (except for the ^tBu groups depicted in wireframe). Thulium atoms are depicted in dark green, carbon atoms in grey, oxygen and nitrogen atoms in red and blue respectively. H atoms have been omitted for clarity.

It appears that the C=O bond was broken and the ^tBuN=C adduct added onto the linear fragment. Considering the wide range of reactions that were observed on **1_{CO}**, we were

interested in the mechanism at play for the addition of small molecules. Exemplified in the reactivity with isocyanate moiety, one possible mechanism for the creation of such product would be a [2 + 2] addition.

3. Mechanism discussion

The reactivity of the stable di-*t*-butoxyethyne was investigated through computational means by Serratosa *et al.* as the formed cyclic oxo-carbons represent useful synthons. They found that the mechanism most likely involved a highly non-synchronous pathway. Furthermore, this type of reactivity has been observed by Walensky *et al.* in their study of a uranium dimer linked by an ethynediolate motif.³² Indeed, upon addition of a ketene moiety or a SO₂ containing compound, they observe [2 + 2] addition reactions. Interestingly, with the ketene only the initial addition was observed with the C—C—O motif left unbroken, while for the SO₂ addition, one sulfur-oxygen double bond is severed in the process. This particular reaction is supported by calculation. A similar scenario could be proposed for the formation of **1_{iso}** and a corresponding scheme is presented in **Scheme 1. 9**.



Scheme 1. 9 Proposed mechanism for the formation of **1_{iso}**

The mechanism of this transformation is currently under investigation by DFT calculation and seem to involve a concerted but highly asynchronous pathway. The reactivity with additional unsaturated substrates is also currently examined to investigate the generality of this transformation.

The question of the mechanism for the reactions presented in this manuscript for O₂ and N₂O addition is also under investigation. The formation of the oxalate motif could be the product of a [2 + 2] addition followed by a rearrangement. Indeed, the addition of dioxygen to unsaturated molecules is known.³³ However, it is interesting to note that it only happens if dioxygen is placed in its singlet state, for example using light and a sensitizer.³⁴ The unusual structure of **1_{co}** could be at the origin of a low-lying singlet state enabling the observed reactivity. In the literature, examples of Cp-containing lanthanide complexes containing oxalate moieties usually do not involve O₂ addition but reductive coupling of CO₂ moiety.^{35–37} However, the ability of rare earth metals species to cleave O₂ molecules has already been observed, but it usually leads to the formation of oxo-species rather than the addition on a preexisting substrate.³⁸ This report also showed that, similarly, addition of N₂O to low-valent

lanthanide salts would lead to the same oxo-bridged species through a formal oxygen-atom transfer reaction. This reactivity is also contrasted with the result of N_2O addition onto alkyl or allyl lanthanide complexes where the small molecule inserts in the reactive $\text{Ln}-\text{C}$ bond.^{39,40} None of these reactivities appears to be at play in the addition of N_2O on $\mathbf{1}_{\text{CO}}$. Indeed, XRD analysis of the obtained product seems to point toward a symmetrical – although highly-disordered – moiety while the elemental analysis revealed the presence of nitrogen in the final product. Drawing possible products resulting from a [2 + 2] addition of N_2O , similarly to the mechanism proposed for the formation of $\mathbf{1}_{\text{ISO}}$, gives relatively unsymmetrical products, as illustrated in **Figure 1. 14**. One possible pathway to lead to a simpler organic moiety could involve a rearrangement but the exact nature of the obtained product remained elusive to date.

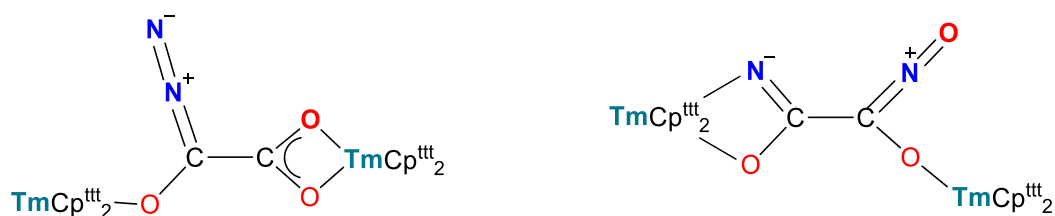


Figure 1. 14 Proposed product after a [2 + 2] addition of N_2O on $\mathbf{1}_{\text{CO}}$.

IV. Conclusion

To conclude this first chapter, the utilization of a small and highly substituted ligand allowing the stabilization of divalent thulium centers has allowed the activation of small molecules and the creation of unusual organic platform.

This system had previously been reported in the literature as a stable yet reactive divalent thulium complex able to activate CO and CO_2 .^{20,23} This new work then focused on the extension of the reactivity study. Particularly the combination of CO_2 and a nucleophile, in this case a pyridine, unlocked the formation of complex organic platforms. Furthermore, this reaction can be performed with several pyridine derivatives to obtain a family of similar compounds. We think that the charge separation created in this motif by the presence of a pyridinium moiety and a carboxylate group is at the origin of the strong coloration of these edifices. This hypothesis could be challenged by TD-DFT calculations which could help attribute the features of the UV-visible spectrum. Moreover, a combined structural and spectroscopic study showed correlation between the angle of the pyridine motif with the carbonated skeleton and the profile of the absorption behavior. This could be studied further with a larger variety of pyridine derivatives. To extend this work, other nucleophiles could be

placed in reaction to assess their impact on the reactivity. This could also be a way to access a wider variety of organic molecules.

Then other types of reactivity have been studied, notably with oxygen-containing gases such as O₂ and N₂O. This allowed to illustrate the transfer of two oxygen atoms in the first case and a more complicated reaction in the second one.

Furthermore, other small unsaturated molecules have been used to demonstrate the wide range of reactivity displayed by this simple platform and postulate a [2 + 2] addition in the case of isocyanate derivative.

Finally, the creation of unusual organic motif could be a very interesting tool if it was shown that the organic part could be removed from the metallic centers. This could be an interesting but challenging project due to the high oxophilicity of the lanthanide. Some preliminary results have shown that acidification of the media using TMS-Cl and deuterated methanol could break down the complex while preserving an organic moiety. We are currently working on a thorough characterization of the formed molecule by NMR to show the viability of the process. However, it could be even more valuable to find a strategy keeping intact the [Cp^{ttt}₂Tm] fragment. Indeed, if possible, this would be the first step toward a catalytic reaction to form complex molecules from simple CO and CO₂ bricks. The question of the reduction of the thulium would also be quite challenging but recent development in the use of electrochemically generated divalent samarium species could inspire some strategies to be applied to thulium compounds.^{41,42}

Understanding the critical aspect of stabilization brought by the adequate organic ligand during this study prompted the exploration of a new platform. Indeed, if small and substituted ligand have shown much success, some larger rings such as the cyclooctatetraenyl ligand have also been used to stabilize divalent lanthanides.⁴³ One disadvantage of this ligand is that it is dianionic in its aromatic form. Meaning that it is not the best strategy to create neutral arrangements with Ln²⁺ ions. As such, the next chapters will be focused on the development of the chemistry of the next Hückel aromatic ring, the C₉H₉ or cyclononatetraenyl ligand, indeed monoanionic.^{44,45} Particularly, the next chapter will discuss the difference of reactivity depending on the nature of the lanthanide and its redox potential.

References

- (1) Ortu, F. *Chem. Rev.* **2022**, *122* (6), 6040–6116.
- (2) Nief, F. *Dalton Trans.* **2010**, *39* (29), 6589.
- (3) Corbett, J. D. *Rev Chim Min.* **1973**, *10* (1–2), pp 239–257.
- (4) Corbett, J. D. In *Synthesis of Lanthanide and Actinide Compounds*; Springer Science, 1991; pp 159–174.
- (5) Fischer, E. O.; Fischer, H. *Angew. Chem. Int. Ed. Engl.* **1964**, *3* (2), 132–133.
- (6) Namy, J. L.; Girard, P.; Kagan, H. B. *Nouv. J. Chim.* **1977**, *1* (1), 5–7.
- (7) Cotton, S. *Lanthanide and Actinide Chemistry*; 2013.
- (8) Watson, P. L.; Tulip, T. H.; Williams, I. *Organometallics* **1990**, *9* (7), 1999–2009
- (9) Girard, P.; Namy, J. L.; Kagan, H. B. *J. Am. Chem. Soc.* **1980**, *102* (8), 2693–2698.
- (10) Kagan, H. B. *Tetrahedron* **2003**, *59* (52), 10351–10372.
- (11) Bochkarev, M. N.; Fedushkin, I. L.; Fagin, A. A.; Petrovskaya, T. V.; Ziller, J. W.; Broomhall-Dillard, R. N. R.; Evans, W. J. *Angew. Chem. Int. Ed. Engl.* **1997**, *36* (12), 133–135.
- (12) Anatolii A. Fagin, M. N. Bochkarev. *Chem. Eur. J.* **1999**, *5* (10), 2990–2992.
- (13) Evans, W. J.; Allen, N. T.; Workman, P. S.; Meyer, J. C. *Inorg. Chem.* **2003**, *42* (9), 3097–3099.
- (14) Evans, W. J.; Broomhall-Dillard, R. N. R.; Ziller, J. W. *Polyhedron* **1998**, *17* (19), 3361–3370.
- (15) Fedushkin, I. L.; Girgsdies, F.; Schumann, H.; Bochkarev, M. N. *Eur. J. Inorg. Chem.* **2001**, *2001* (9), 2405–2410.
- (16) Evans, W. J.; Allen, N. T.; Ziller, J. W. *J. Am. Chem. Soc.* **2001**, *123* (32), 7927–7928.
- (17) Evans, William. J.; Allen, N. T.; Ziller, J. W. *Angew. Chem. Int. Ed.* **2002**, *41* (2), 359–361.
- (18) Jaroschik, F.; Nief, F.; Le Goff, X.-F.; Ricard, L. *Organometallics* **2007**, *26* (14), 3552–3558.
- (19) Nief, F.; De Borms, B. T.; Ricard, L.; Carmichael, D. *Eur. J. Inorg. Chem.* **2005**, *2005* (4), 637–643.
- (20) Jaroschik, F.; Nief, F.; Ricard, L. *Chem Commun* **2006**, No. 4, 426–428.
- (21) Gould, C. A.; McClain, K. R.; Yu, J. M.; Groshens, T. J.; Furche, F.; Harvey, B. G.; Long, J. R. *J. Am. Chem. Soc.* **2019**, *141* (33), 12967–12973.
- (22) McClain, K. R.; Gould, C. A.; Marchiori, D. A.; Kwon, H.; Nguyen, T. T.; Rosenkoetter, K. E.; Kuzmina, D.; Tuna, F.; Britt, R. D.; Long, J. R.; Harvey, B. G. *J. Am. Chem. Soc.* **2022**, *144* (48), 22193–22201.
- (23) Simler, T.; McCabe, K. N.; Maron, L.; Nocton, G. *Chem. Sci.* **2022**, *13* (25), 7449–7461.
- (24) Weber, F.; Sitzmann, H.; Schultz, M.; Sofield, C. D.; Andersen, R. A. *Organometallics* **2002**, *21* (15), 3139–3146.
- (25) Nocton, G.; Ricard, L. *Dalton Trans* **2014**, *43* (11), 4380–4387.
- (26) Labouille, S.; Nief, F.; Le Goff, X.-F.; Maron, L.; Kindra, D. R.; Houghton, H. L.; Ziller, J. W.; Evans, W. J. *Organometallics* **2012**, *31* (14), 5196–5203.
- (27) Bayer, U.; Anwander, R. *Dalton Trans.* **2020**, *49* (48), 17472–17493.
- (28) Xémard, M.; Goudy, V.; Braun, A.; Tricoire, M.; Cordier, M.; Ricard, L.; Castro, L.; Louyriac, E.; Kefalidis, C. E.; Clavaguéra, C.; Maron, L.; Nocton, G. *Organometallics* **2017**, *36* (23), 4660–4668.
- (29) Mootz, D.; Wussow, H.-G. *J. Chem. Phys.* **1981**, *75* (3), 1517–1522.
- (30) Cotton, S.; Harrowfield, J. M. In *The Rare Earth Elements, Fundamentals and Applications*; 2012; p p 56.
- (31) Alabugin, I. V.; Dos Passos Gomes, G.; Abdo, M. A. *Comput. Mol. Sci.* **2019**, *9* (2), e1389.
- (32) Ward, R. J.; Rosal, I. D.; Kelley, S. P.; Maron, L.; Walensky, J. R. *Chem. Sci.* **2023**, *14* (8), 2024–2032.
- (33) Mazur, S.; Foote, C. S. *J. Am. Chem. Soc.* **1970**, *92* (10), 3225–3226.
- (34) Foote, C. S. *Pure Appl. Chem.* **1971**, *27* (4), 635–646.
- (35) Evans, W. J.; Seibel, C. A.; Ziller, J. W. *Inorg. Chem.* **1998**, *37* (4), 770–776.
- (36) Evans, W. J.; Perotti, J. M.; Brady, J. C.; Ziller, J. W. *J. Am. Chem. Soc.* **2003**, *125* (17), 5204–5212.
- (37) Evans, W. J.; Lorenz, S. E.; Ziller, J. W. *Inorg. Chem.* **2009**, *48* (5), 2001–2009.
- (38) Xémard, M.; Cordier, M.; Louyriac, E.; Maron, L.; Clavaguéra, C.; Nocton, G. *Dalton Trans.* **2018**, *47* (28), 9226–9230.
- (39) Demir, S.; Montalvo, E.; Ziller, J. W.; Meyer, G.; Evans, W. J. *Organometallics* **2010**, *29* (23), 6608–6611.
- (40) Labahn, T.; Mandel, A.; Magull, J. Z. *Für Anorg. Allg. Chem.* **1999**, *625* (8), 1273–1277.
- (41) Sun, L.; Mellah, M. *Organometallics* **2014**, *33* (18), 4625–4628.
- (42) Bazzi, S.; Hu, L.; Schulz, E.; Mellah, M. *Organometallics* **2023**, *42* (12), 1425–1431.
- (43) Moutet, J.; Schleinitz, J.; La Droitte, L.; Tricoire, M.; Pointillart, F.; Gendron, F.; Simler, T.; Clavaguéra, C.; Le Guennic, B.; Cador, O.; Nocton, G. *Angew. Chem. Int. Ed.* **2021**, *60* (11), 6042–6046.
- (44) Katz, T. J.; Garratt, P. J. *J. Am. Chem. Soc.* **1963**, *85* (18), 2852–2853.
- (45) Lalancette, E. A.; Benson, R. E. *J. Am. Chem. Soc.* **1963**, *85* (18), 2853–2853.

Chapter 2: LnI₂ as strong reductant for the formation of new complexes with the Cnt ligand

I.	Non classical divalent lanthanides in the literature	77
1.	Development of LnI ₂ with dysprosium and neodymium	77
2.	Established reactivity	77
3.	Extension to organometallic complexes	78
II.	The cyclononatetraenyl ligand	78
1.	Discovery and synthesis	78
2.	Rationalization of the Isomerization reaction	80
3.	The Cnt as a ligand	81
III.	Synthesis of Dy ₂ Cnt ₄ (thf) ₂ (2.1_{thf}) and Dy ₂ Cnt ₄ (2.1)	84
1.	Salt metathesis approach	84
2.	Approach toward thf removal	87
3.	The trivalent approach	92
4.	Characterization of Dy ₂ Cnt ₄ (2.1)	96
IV.	Synthesis and characterization of Dy ₂ Cnt ₃ (thf) ₂ (2.3)	101
1.	Naïve synthesis	101
2.	Perfected synthetic path	102
3.	Structural characterization	103
4.	Computational approach	106
5.	Magnetism study	109
6.	Discussion	115
V.	Extension to other LnI ₂	117
1.	Synthesis of Nd ₂ Cnt ₄ (thf) ₂	117
2.	Synthesis of Nd ₄ Cnt ₄ I ₄ (2.4)	117
VI.	Conclusion	121
	References	122

Chapter 2: LnI_2 as strong reductant for the formation of new complexes with the *Cnt* ligand

Using sterically tuned ligand with reducing divalent thulium centers has allowed for the identification of several small molecule activation pathways. Going toward even more reactive metallic centers could be an interesting foray into new types of reactivities.

1. Non classical divalent lanthanides in the literature

1. Development of LnI_2 with dysprosium and neodymium

Parallel to the development of the divalent thulium chemistry, other reducing salts LnX_2 , such as, dysprosium and neodymium iodides, were also studied.¹⁻³ Indeed, similarly to their thulium analogue, they present the particularity to be relatively stable as monomeric LnI_2 . However, their very strong reducing potential and their temperature sensitivity while in solution rendered their synthesis more difficult. It was finally in 1999, that the group of Bochkarev proposed a new version of the solid-state synthesis requiring only a quartz vessel.⁴ The protocol was further investigated by the group of Evans and they created a new quartz apparatus allowing to tune the respective quantities of metal and iodine during the synthesis.⁵ As discussed in **Chapter 1**, this apparatus is not necessary but it allows access to large quantities of the starting material. Despite their high reactivity, dissolving powders of LnI_2 ($\text{Ln} = \text{Dy}, \text{Nd}$) in either THF or DME has allowed for the crystallization of different complexes.^{6,7} However, for a long time, the complexes were limited to solvent adduct. Some attempts by the group of Bochkarev highlighted the reactivity of those species with amine type ligands for example, only managing to stabilize them in isopropylamine.⁸

Their intrinsic reactivity impeded the development of their molecular chemistry, particularly compared to the trajectory thulium compounds undertook. However, they found some usage directly as halide salts.

2. Established reactivity

In a similar fashion to samarium and later thulium, dysprosium and neodymium also found their application as single electron reductant.^{9,10} Although, their use was limited by their higher cost and reactivity to the environment.¹¹

Another interesting aspect is their application as polymerization agent. It is rather common to use trivalent lanthanide salts and particularly neodymium-based ones.¹² But they are also active in their divalent oxidation state.^{13,14}

3. Extension to organometallic complexes

Due to their high reactivity, the isolation of organometallic species of divalent dysprosium and neodymium is challenging. Similarly to the discussion in **Chapter 1**, the synthesis of divalent lanthanide requires either: divalent starting materials such as the halide salts presented before or the use of trivalent starting material and subsequent reduction. The latter strategy was more successful with those species and will be discussed more extensively in **Chapter 3**.

Although there is not a lot of examples, several attempts have been made to react DyI_2 with organic ligands. For instance, Evans *et al.* published in 2002 the N_2 activation by in situ $DyCp''_2$ type species under nitrogen atmosphere. This study highlights the intrinsic reactivity of organometallic divalent dysprosium compounds. It also highlights the difference in reactivity between thulium and dysprosium complexes. Indeed, after witnessing the activation of nitrogen, they conducted similar salt metathesis reaction under argon atmosphere. They reported the formation of $TmCp''_2(thf)$ while dysprosium was too much active to be stabilized in this oxidation state.¹⁵

According to these preliminary studies, dysprosium ions are difficult to stabilize in their divalent state with organic type ligands. This was also the conclusion of the reaction of DyI_2 with naphthalene, which yields a trivalent dysprosium and a reduced naphthalene.⁶ Other organic ligands such as different cyclopentadienyl (Cp) or cyclooctatetraenyl (Cot) have in all likelihood been tried to stabilize dysprosium ions in their divalent state. Recently, the Mills group reported the synthesis of bis amidinate of dysprosium.¹⁶ We propose that a larger aromatic monoanionic ligand could be an ideal substrate to test divalent dysprosium stability and reactivity.

II. The cyclononatetraenyl ligand

1. Discovery and synthesis

In the early 60's, following the recent theory of aromaticity and the developments of methods such as the Hückel method, organic chemists started to be fascinated by large aromatic ligand. Several questions were intriguing to them. Is there a limit to the number of atoms in an aromatic cycle and what is the influence on the delocalisation? What is their stability and topology?¹⁷

Following the $4n+2 \pi e^-$ rule allowed for a straightforward method. Indeed, if benzene is the starting point, there are now two different directions: one can either try to decrease or increase the size of the ring, each time matching the desired number of π -electrons as illustrated in **Figure 2. 1**.

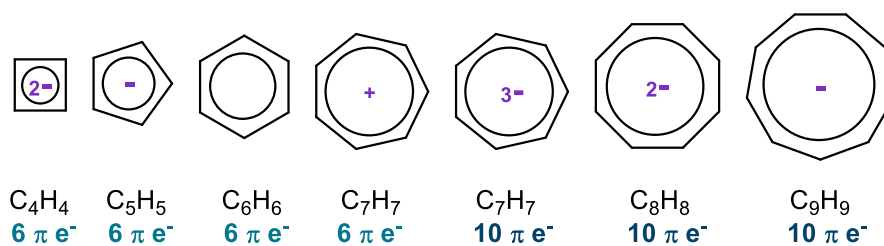
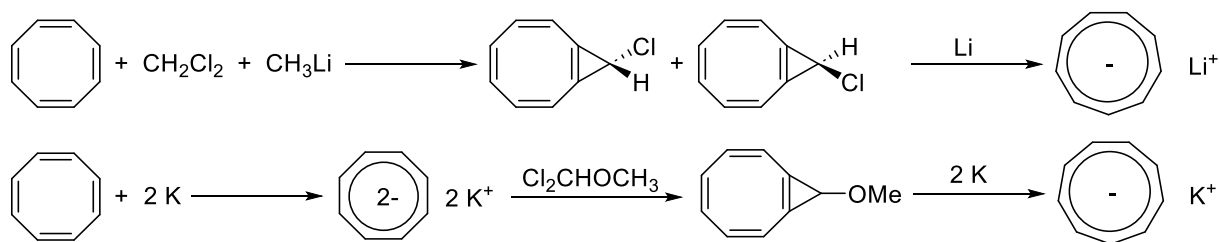


Figure 2. 1 Schematic representation of the possible aromatic rings with C_nH_n ($n \in [4:9]$)

The cyclopentadienyl ligands have been extensively studied with most of the metallic centers of the periodic table.^{18–20} The smaller cyclobutadienyl ligand had a slower start due to its high instability in its neutral form.²¹ However, coordination chemists have found the way to stabilize it as a dianionic ligand. Recently, this chemistry has gained some traction with f-block metals most notably for its impact on the magnetic properties.^{22,23}

The first step toward larger rings is the peculiar case of cycloheptatrienyl, C_7H_7 or Cht. It can be aromatic as a $6 \pi e^-$ in its $C_7H_7^+$ form (also called the tropylium cation) or $10 \pi e^-$ in its $C_7H_7^{3-}$ form. Due to this specificity, the Cht possesses a unique chemistry as a ligand and has not been studied in this work.^{24,25} The next step is the cyclooctatetraene molecule, C_8H_8 . This compound might appear quite similar to benzene. However, due to its anti-aromatic character (only 8 electrons in the π -system) it differs greatly. It is not planar and the simple/double bond alternance confers it a tub-like structure. However, to make it aromatic, two more electrons are needed, which can be delivered easily by potassium metal to form K_2Cot .²⁶ This dianion is now aromatic and planar, it can be used in organometallic chemistry. Its larger size and higher charge make it an interesting ligand for large ions such as the f-block. Indeed, as mentioned earlier, the development of this type of chemistry started in the beginning of the 60's with transition metals but was quickly adapted to lanthanide and actinides.²⁷ In 1968, the synthesis of uranocene was described and was further adapted to all the lanthanides in an anionic fashion $[LnCot_2]^-$.²⁸ Looking for other possible 10π -electronic systems, organic chemists targeted the next accessible ring, C_9H_9 . Contrarily to its predecessor, this molecule is not stable in its neutral state and rearranges readily to form indenyl or dihydroindene type molecules.^{29,30} This probably explains why the synthesis was not published before 1963.^{30–33} Two groups actually reached similar product at the same time. The strategies had some differences as illustrated in **Scheme 2. 1**.



Scheme 2. 1 Synthetic scheme developed simultaneously to access the cyclononatetraenyl ion, top scheme from ³² and bottom scheme from ³¹

In both cases, the main idea was to go through cyclopropanation of the K_2Cot molecule and then use an excess of reductant to simultaneously open the cycle and charge the compound giving an alkali salt of the desired motif.

2. Rationalization of the Isomerization reaction

By characterizing the cyclopropane intermediate through NMR spectroscopy, one can access the ratio of isomers that are created. Indeed, because of the non-planarity of the molecules, a *cis* and *trans* isomer can be found. Katz and Garratt found that this phenomenon was dependent on the chlorinated compound used for the addition on the aromatic Cot ligand.³⁰ Later, Boche and his group postulated that the presence of intermediate could have an influence on the ring-opening.^{34,35} Indeed, according to the Woodward Hoffman rules on the opening of small cycles, it can happen in a *syn*-rotatory or *con*-rotatory fashion. As such, Boche *et al.* hypothesized that when opening the intermediate with the -OMe substituent, the formed double bond should be in a “*trans*” isomeric state. To probe this possibility, they performed the synthesis at low temperature and proceeded to characterize the intermediate through NMR spectroscopy. In doing so, they observed a signal compatible with the full *cis* Cnt anion but also other complex signals in the aromatic region. Perhaps the most diagnostic proton that they identified was giving a triple signal at $\delta = -3.5$ ppm.^{35,36} This can be explained very easily by the presence of a proton inside a ring of current and, as such, rather shielded. These two isomers can be represented as follows on **Figure 2. 2**.

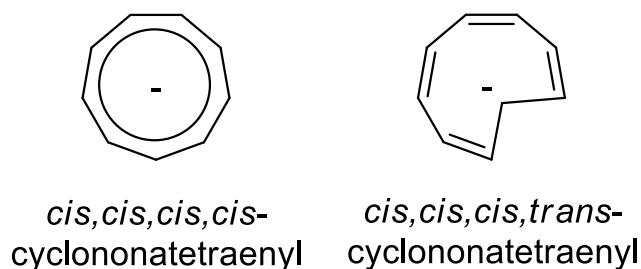


Figure 2. 2 Schematic representation of the two isomers of the Cnt anion

After this study, they started to heat up the product and found that the compound would readily isomerize to the allegedly more stable full *cis* compound.

The existence of this *trans* intermediate asked a lot of questions regarding its stability. First the possibility to assign the different signals of the *trans* isomer through NMR spectroscopy showed that the topomerization process, if present, was slow compared to the time frame of this method. Subsequent deuteration experiments of one of the positions showed that this process was indeed happening. After the opening of the cycle, the shielded signal was made up of a triplet and a doublet. The triplet came as explained before from the coupling of the proton inside the ring with its two neighbors. The doublet however, translated the presence of the deuterium just next to the inside position. The shielded proton could couple with only one other giving the observed doublet. The interesting feature was the doublet/triplet ratio of 1:3 showing that the deuterium atom was likely to be present at each position of the ring and that topomerization reaction was happening. They concluded that the isomerization process is much less likely to occur at this temperature.³⁵ They proposed that this is due to the repartition of the charge needed for this process.

Having studied the topomerization process, Boche and its group targeted the isomerization reaction.³⁷ They identified several key parameters to study their influence on the isomerization process. These studies will be further discussed in **Chapter 4**.

3. The Cnt as a ligand

Despite being synthesized in the early 60's, the Cnt⁻ fragment has not been crystallographically identified before 2009.³⁸

1. Early attempt with transition metals

In 1975, an attempt was made by reacting an organometallic complex of titanium with LiCnt. If both the mass-spectra and elemental analysis pointed toward a heteroleptic complex TiCpCnt, the NMR spectra was more difficult to interpret. Indeed, two protons seemed to possess a signal at higher field while the other proton integrating for seven are found in the aromatic region.³⁹ The authors concluded that only seven carbon atoms were involved in complexation forming a sandwich compound with a slipped Cnt ligand, although the lack of discussion regarding the oxidation state of titanium in this putative complex rendered the final attribution difficult. Similarly, two years later, De Liefde Mejer, who investigated the titanium compound, published with Westerhof a new study on niobium complexes.⁴⁰ This time, the putative NbCp₂Cnt complex was formed by salt metathesis involving NbCp₂Cl₂. The elemental analysis confirmed the NbC₁₉H₁₉ ratio in the complex. The NMR featured three singlets

integrating accordingly for each ligand. However, upon cooling of the system, the peak corresponding to the Cnt coalesced at -40°C and new peaks have been identified at -95°C . This would be explained by a partial coordination of the Cnt ligand with a fluxional character at room temperature. Upon cooling the movement of the Cnt ligand could be partially restricted giving rise to several signals. The authors postulated an η^3 coordination mode.⁴⁰ In both of these cases, no XRD analysis could be run to investigate the solid-state structure and hopefully shed light on the coordination of the Cnt motif.

Interestingly, in 2013, Sitzman *et al.*, showed that upon coordination to zirconium, the Cnt molecule would collapse into an indenyl type structure while losing two hydrogens.²⁹ This was discovered by NMR analysis as only 7 resonances could be found. Unfortunately, no suitable crystals could be grown to confirm this hypothesis.

2. Accommodation of its large sized

As evidenced by the previous studies, synthesis and characterization of Cnt containing motifs can be challenging. Its fluxional character, culminating in its potential collapse, complicates its coordination with “small” ions. To better accommodate its large size, two strategies have been used.

First, the group of Murahashi used the Cnt ligand in cooperation with Cot ligand to create metal sheet sandwich complex. In this strategy, four palladium centers accommodate the full Cnt. XRD suitable crystals were analyzed and revealed a planar ring as shown on **Figure 2. 3** demonstrating the need of large electronic densities to fully saturate this compound.³⁸

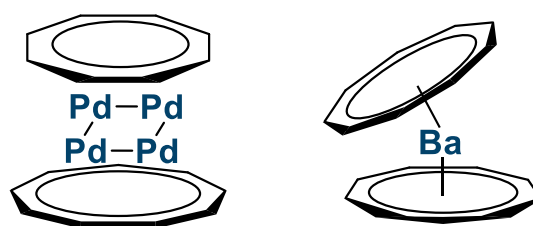


Figure 2. 3 Schematic representation of two Cnt-containing complexes with crystallographic evidence, on the left the characterized tetra-palladium complex stabilized by a Cot and a Cnt ligand.³⁸ On the right, the BaCnt₂ complex reported by Walter in his thesis work where only the connectivity can be solved.⁴¹

Another possibility is to target larger metallic ions. For example, in 2005, the group of Sitzman studied the coordination of the Cnt ligand onto barium cations.⁴¹ They found that BaI₂ readily undergoes salt metathesis reaction with KCnt in THF at room temperature. ¹H NMR analysis showed one signal illustrating the symmetry of the complex in solution. Unfortunately, no XRD-suitable crystals were obtained at that point. The thesis work by Walter in 2005, reported that very weakly diffracting crystals were obtained and showed diffraction pattern in accordance with the formulated BaCnt₂.⁴² However, the very low resolution does not allow

more analysis than that of a general connectivity pattern. Interestingly, the complex appeared bent, similarly to the divalent lanthanide metallocenes as illustrated in **Figure 2. 3**.

This work paved the way for further study with large cationic metals.

3. Lanthanide Cnt compounds

The ubiquitous trivalent state for lanthanide renders their synthesis as neutral sandwich compound rather difficult. As such, the divalent states have been easier to tackle first for the classical lanthanides: Sm, Eu and Yb. Their complexation has been studied extensively with Cp type ligands as reported in the Introduction and shown in **Figure 2. 4**.¹⁸ Their chemistry with the Cot ligand is known, however it does not yield neutral complexes.⁴³

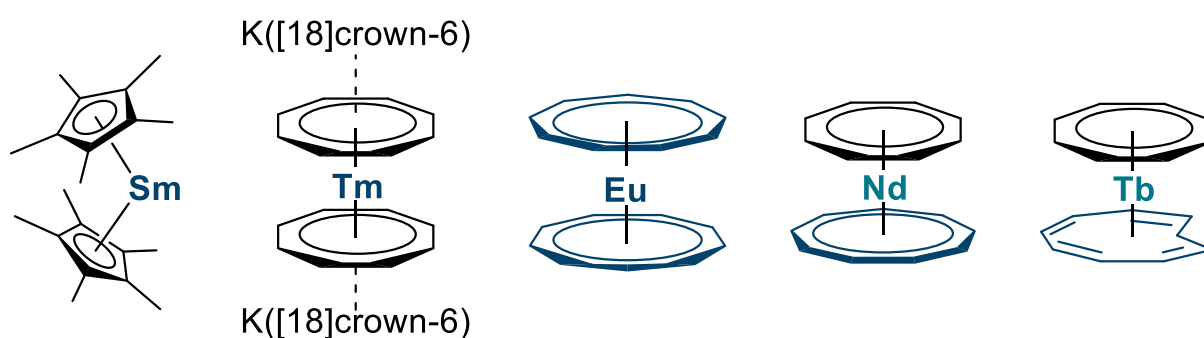


Figure 2. 4 Molecular structure of SmCp^*_2 ,⁴⁴ $[\text{Tm}(\text{Cot})_2][\text{K}([\text{16}]\text{crown-6})]$,⁴³ EuCnt_2 ,⁴⁵ NdCotCnt ,⁴⁶ TbCotCnt-trans .⁴⁷

In 2017, the group of Nakajima reported the first rare earth neutral sandwich compound containing two Cnt units.⁴⁵ XRD analysis showed that europium lied on a special symmetry position and that the two rings were symmetric with regard to the metallic center. This yielded two planar aromatic rings as well as a perfect linearity of the centroid of the ligands and the metal ($\text{Cnt}^9\text{-Eu-Cnt}^9 = 180^\circ$). Contrary to the barium, no bent structure was observed. This linearity was further observed by our group, when the synthesis and structure the bis-Cnt complexes of samarium, ytterbium and thulium were published.⁴⁸ As expected considering the similarity of these ions, they are isostructural to the europium complex. This method allowed for the isolation of neutral sandwich compounds; however, it only targeted classical divalent compounds.

As such, to access all the lanthanide ions in this framework, an alternative strategy needs to be employed. To correctly accommodate trivalent lanthanides an heteroleptic approach can be used with a dianionic and a monoanionic ligand. Interestingly, this was already postulated in 1971 by the group of Streitwieser.⁴⁹ However, no heteroleptic compounds were identified but a di-cerium complex bridged by chlorine ions was. The first successful synthesis of neutral LnCotCnt compounds was reported by Roesky *et al.* in 2019 for $\text{Ln} = \text{Nd, Sm, Dy and Er}$.⁴⁶ It was followed by a collaborative work between our group and theirs and extended the synthesis to Tb, Ho, Tm and Lu.⁴⁷ This study allowed us to showcase the Cnt peculiarity on

several levels. First, it tends to slip away from the coordination sphere as the cation size diminishes. For instance, it features an η^9 coordination pattern for the terbium complex but only an η^6 for the lutecium analogue. Furthermore, the terbium compound appears under two different isomers with crystallographic evidence of both *cis* and *trans* coordinated Cnt. The possibility of coordinating a *trans* isomer onto a rare earth metal had already been reported in the study of the divalent lanthanide. However, in this report, the *trans* analogue seems to be formed *in situ* from a *cis* isomer.⁴⁷ The origin of this odd and, at first glance, contra-thermodynamic process, was left unexplained in the report but will be discussed further in **Chapter 4**.

4. Extension of the divalent chemistry with Cnt

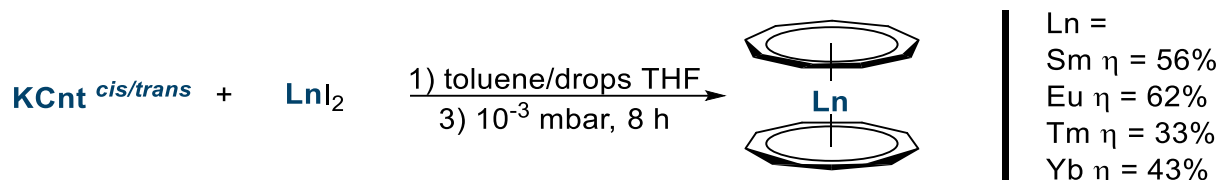
As mentioned earlier in **I.3**, dysprosium ions are difficult to stabilize in their divalent state. Several attempts with organic ligands have yielded unplanned reactivity either with the atmosphere or directly the ligand.^{6,15} Considering the possibility to synthesize LnCnt_2 from LnI_2 with Sm, Eu, Yb but also thulium, which is known to be much more reducing, begs the question of the outcome of the reaction with DyI_2 as a starting material. As such, this question will be explored in the following parts.

III. Synthesis of $\text{Dy}_2\text{Cnt}_4(\text{thf})_2$ (2.1_{thf}) and Dy_2Cnt_4 (2.1)

1. Salt metathesis approach

1. Conventional Synthetic Path

In the first report of the lanthanidocene, the synthesis was described as a salt metathesis between LnI_2 and KCnt with one particularity in the solvents used.⁴⁸ The halide salts are known to not be readily soluble in aromatic or aliphatic solvents and only slightly in ethereal solvents such as THF. KCnt is itself soluble in polar solvent but almost insoluble in aromatic solvent. Unfortunately, it was found that the presence of coordinating solvent tends to displace the weakly coordinating Cnt ligand. As such, a mixture of toluene and THF is used for the salt metathesis but, rather than directly isolate the product of the reaction, several evaporations are performed before final crystallization according to **Scheme 2. 2**. This ensures removal of the THF and obtention of the fully coordinated Cnt ligand.



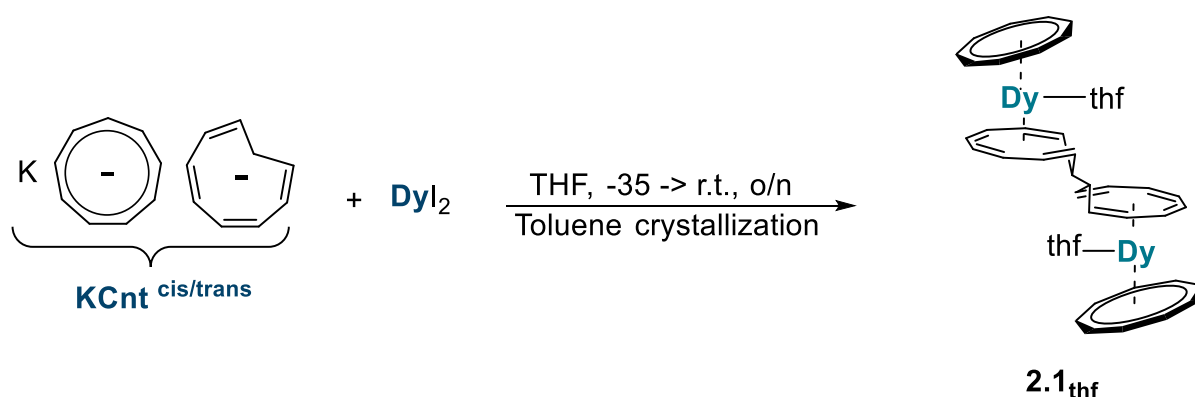
Scheme 2.2 Synthetic scheme for the synthesis of LnCnt_2 complexes with $\text{Ln} = \text{Sm, Eu, Tm}$ and Yb ⁴⁸

Another particularity is the use of KCnt as a mixture of both isomers. This was decided as the *trans* isomer features an increased solubility to help the salt metathesis reaction.

2. Extension to DyI_2

The same protocol was extended to DyI_2 , however no reliable results were obtained through this route. Two potential sources of challenge were identified in this reaction.

First, as previously mentioned, the relative thermal sensitivity of divalent dysprosium species in solution could precipitate the destruction of the reductive species before undergoing the salt metathesis reaction. Then, if the formed complex is somewhat sensitive, several rounds of evaporation could deteriorate it. To tackle this, modifications were made to the protocol according to **Scheme 2.3**. The two solids are suspended directly into cold THF as to promote its stability. The reaction mixture rapidly forms a red-brown suspension. The reaction was left overnight under stirring to slowly warm up and continue to react. Rather than proceed with several evaporations, the reaction mixture was brought to dryness and extracted with toluene. The resulting brown solution was filtered and placed at cold temperature to crystallize. This method allowed to reliably obtain crystals of the species $\text{Dy}_2\text{Cnt}_4(\text{thf})_2$ noted **2.1_{thf}** as presented on **Scheme 2.3**.



*Scheme 2.3 Synthesis of **2.1_{thf}** through the new protocol*

3. Rationalization of the reaction

The structure was analyzed by SC-XRD diffraction and is presented in **Figure 2.5**. The compound crystallizes in the $\text{P2}_1/\text{c}$ space group and the asymmetric unit contains half of the dimer. It features a point symmetry on the center of the newly formed C—C bond. The dimeric

[Cnt₂] shows two strongly distorted Cnt motifs. A thf molecule is coordinated onto the metal. The uncoupled Cnt is not coordinated in an η⁹-fashion but rather a lower hapticity, as it was observed previously for such solvent adduct.^{47,50}

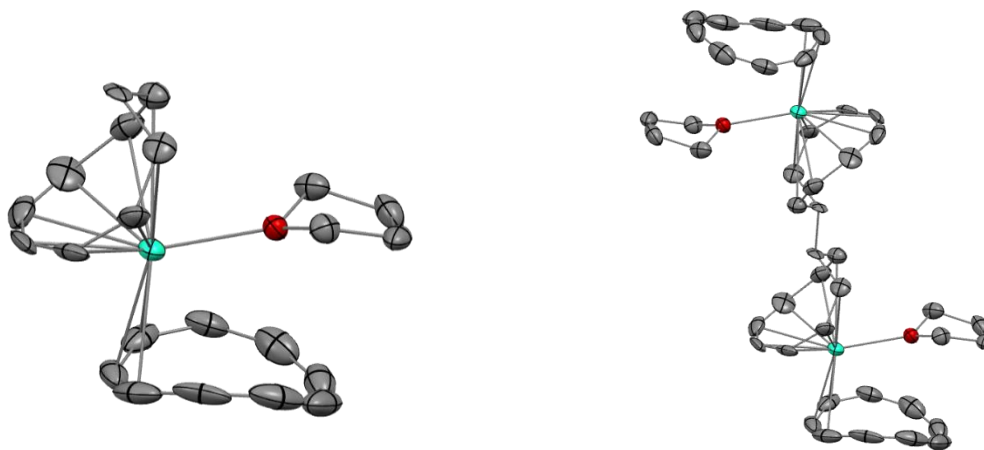


Figure 2. 5. Molecular structure of **2.1_{thf}** in the solid state with thermal ellipsoid at the 50% probability level. The asymmetric unit is presented on the left and the full molecule on the right. Dysprosium atoms are depicted in light green, carbon atoms in grey and oxygen atoms in red. H atoms and two solvent molecules have been omitted for clarity.

The overall assembly is neutral. The thermal stability of the molecule would point toward trivalent dysprosium centers. To obtain charge compensation, the [Cnt₂] central motif should then bear a – 4 charge. This can be rationalized by a transfer from the reductive dysprosium(II) center to the Cnt^{•-} moiety to yield Cnt²⁻. This radical couples with one of itself leading to the [Cnt₂]⁴⁻ motif. The resulting molecule no longer possesses a radical character; however, its formal charge is – 4 as illustrated in **Figure 2. 6**.

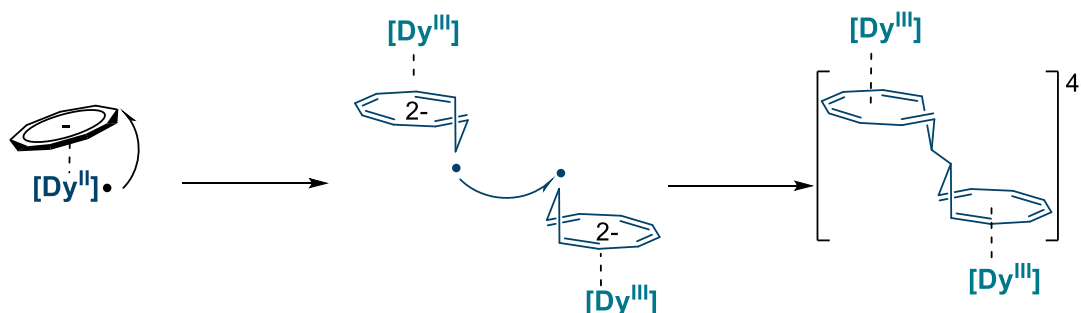


Figure 2. 6 Schematic representation of the hypothetical reduction of Cnt^{•-} by divalent dysprosium.

A discussion of the main distances of **2.1_{THF}** will be held later in the manuscript (I.1.3).

This intriguing reactivity of the Cnt ligand shows its capacity to act as an electron acceptor. This type of behavior has not been seen with smaller aromatic rings. Yet, this coupled [Cnt₂]⁴⁻ motif had previously been proposed by Neuenschwander.⁵¹ Although, at that time, no structural proofs had been identified. To the best of our knowledge this is the first time such a motif has been structurally identified with a Cnt unit.

2. Approach toward thf removal

As observed in the crystal structure, one THF molecule is present in the complex and prompts the lowering of the hapticity for the Cnt ring. As our initial goal was to study sandwich compounds, we were interested in the adduct free version.

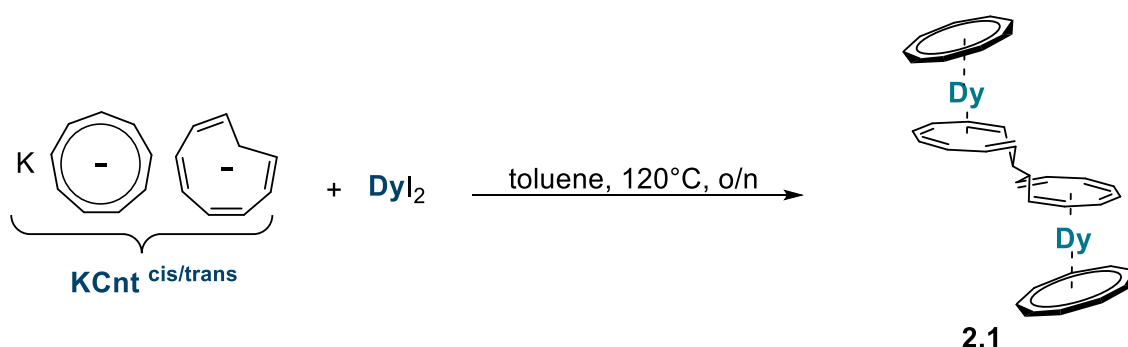
1. THF removal through physical means

As mentioned earlier, several rounds of evaporation of the reaction mixture led to decomposition of the desired molecule. Another possibility is to directly expose the crystals of **2.1**_{thf} under reduced pressure. However, considering the small quantities of **2.1**_{thf} obtained and its relative insolubility in toluene, we chose to pursue other synthetic routes.

2. Development of THF-free synthesis

The very low solubility of the starting material is a general challenge in the chemistry involving KCnt. Indeed, it is soluble in polar solvents, however any trace of these solvents tends to displace the ligand. To promote the solubility of the ligand but also the metallic precursor we thought to increase the temperature of the reaction. It seems counterintuitive to use high temperatures for divalent lanthanide which are known to be thermally sensitive. Nevertheless, the obtention of **2.1**_{thf} already shows an instability of the putative divalent intermediate. As such, a similar electron transfer could happen at higher temperature. Furthermore, the formed product features trivalent dysprosium center, and should not be overly sensitive to the temperature.

This reaction was performed according to **Scheme 2.4** and allowed for the isolation of thf free Dy₂Cnt₄ complex noted **2.1**. X-ray suitable crystals were obtained and the structure confirmed the absence of coordinated THF molecules.



*Scheme 2.4 Synthetic scheme for the formation **2.1** from DyI₂ and KCnt at high temperatures.*

3. Structural analysis (comparison with 2.1_{thf})

As illustrated in **Figure 2. 1**, similarly to 2.1_{thf}, the asymmetric unit contains half of the dimer and the second half constructed thanks to a point symmetry on the newly created C—C bond. Overall, the structures are very similar.

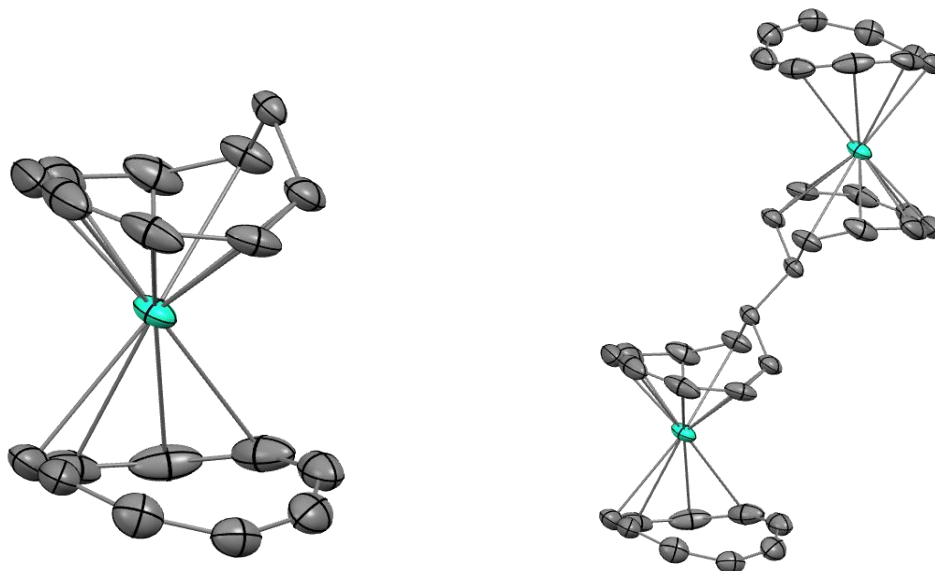


Figure 2. 7 Molecular structure of 2.1 in the solid state with thermal ellipsoid at the 50% probability level. The asymmetric unit is presented on the left and the full molecule on the right. Dysprosium atoms are depicted in light green and carbon atoms in grey. H atoms and two solvent molecules have been omitted for clarity.

a. Comparison of the Cnt-ligand

Interestingly, removing the THF did not allow for full coordination of the exterior Cnt-ligands. Nevertheless, side by side comparisons shows several differences, mainly that the hapticity slip does not happen in the same direction. For 2.1_{thf}, the lower hapticity accommodates the THF molecules and as such it is parallel to the distortion of the Cnt-ligand. In the absence of THF, the hapticity slip is perpendicular to the distortion as illustrated in **Figure 2. 8**. Considering the non-directionality of the *f*-orbitals it is difficult to explain such a behavior but it may come from the release of steric pressure.

This particular coordination of the ligand prompts very different Dy—C distance as reported in **Table 2. 1**. Interestingly, it appears that the shortest Dy—C distance remains essentially the same, however the longest distance is significantly increased in the presence of THF. This points toward the capacity of the Cnt ligand to modulate its hapticity to better fit the coordination sphere.

Distances in Å	2.1_{thf}	2.1
Shortest Dy(1) —C (Cnt)	2.648(14)	2.641(9)
Largest Dy(1) —C (Cnt)	4.41(2)	3.86(1)
Avg Dy(1) —C (Cnt)	3.41(2)	3.09(2)

Table 2. 1 Selected Dy—C bond distances for the compound **2.1_{THF}** and **2.1**.

This particular behavior has been studied by our group previously.⁴⁷ To have a reproducible characterization of the coordination of the flexible Cnt unit, we built an approach allowing the determination of formal coordination number. To do so, different centroids are constructed taking into account different numbers of the carbon atoms of the Cnt motif. This reproduces different hapticity the Cnt ligand could adopt. Then, the distance between the metal center and the different centroids informs on the effective hapticity giving a formal coordination number. This approach is not a definitive answer on the number of coordinated carbon atoms but rather a tool to help compare several complexes with different coordination of the Cnt unit.

Thus, a similar strategy is used for this comparison and three centroids are constructed; as illustrated on **Figure 2. 8**. In each case, one centroid is constructed for the entire ring and two others correspond to lower hapticities of 4 and 6.

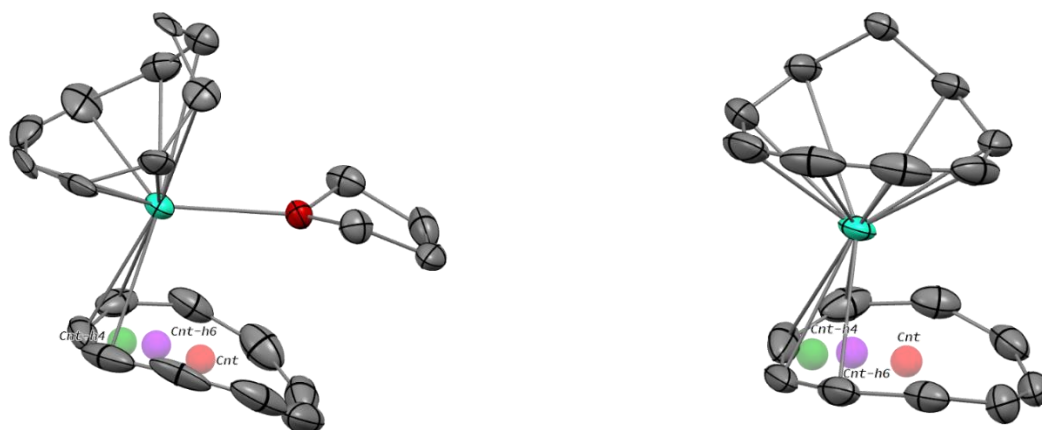


Figure 2. 8 Representation of the different constructed centroids for the Cnt-ligands in **2.1_{THF}** and **2.1**, dysprosium atoms are in light green, carbon atoms in grey, oxygen in red and hydrogen atoms have been omitted for clarity. The red, purple and green spots represent Cnt η^9 , Cnt η^6 and Cnt η^4 respectively.

At first glance, the centroid for the full ring seems out of alignment similarly to the reported LuCotCnt.⁴⁷ However, the non-symmetrical [Cnt₂] ligand preclude the use of the angle to determine the most fitting scenarii. For **2.1_{thf}**, looking at the distances reported in **Table 2. 2**, the shortest ones are reported for the hapticity η^4 and η^6 with very similar values. As such, attribution of a formal hapticity is difficult and the situation is considered intermediate between these two numbers. For **2.1**, the shortest distance is reported for η^6 .

Distances in Å	2.1_{thf}	2.1
Dy—Cent (Cnt- η^9)	2.84	2.39
Dy—Cent (Cnt- η^6)	2.42	2.13
Dy—Cent (Cnt- η^4)	2.40	2.27

Table 2. 2 Comparison of the dysprosium centroid distances for the three constructed centroids.

Overall, it is evident that the Cnt ligand is closer to the dysprosium center in the absence of coordinated THF. This can notably be important for SMM application as it will be further discussed later.

Nevertheless, if the distances are shortened, the de-coordination of the THF molecule did not have a stark impact on the hapticity of the exterior Cnt ligand. This is a very different situation than what has been reported for the sandwich complexes DyCotCnt which switches from η^6 hapticity when an acetonitrile molecule is coordinated to η^8 when it is removed.^{47,50}

b. Comparison with the [Cnt₂] motif

A similar approach can be used for the [Cnt₂] motif. This time the most suitable hapticity seem higher than in the previous case. Indeed, only one of the carbon atoms of the ring appear strongly out of the plane. As such, three centroids are created for the full ring, η^8 and η^6 as illustrated in **Figure 2. 9**.

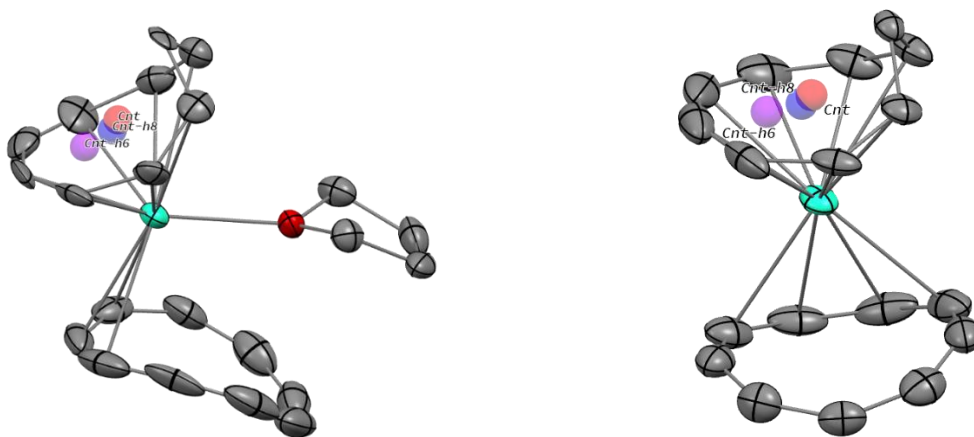


Figure 2. 9. Representation of the different constructed centroids for the [Cnt₂] motif. The red, blue and purple spots represent Cnt η^9 , Cnt η^8 and Cnt η^6 respectively.

The full hapticity centroid and the η^8 centroid are rather close to each other as reported in **Table 2. 3**, the main difference being the distance with the metallic center. Even though these are not strictly speaking sandwich compounds, in both cases the η^6 centroids is out of alignment. In case of THF coordination, the hapticity cannot be really determined as the η^8 and η^6 are very close. Similarly for **2.1**, the η^8 and η^9 are fairly close. Interestingly, the loss of THF seems to have a bigger impact on the coordination of the [Cnt₂] motif.

Distances in Å	2.1_{thf}	2.1
Dy—Cent (Cnt- η^9)	1.88	1.68
Dy—Cent (Cnt- η^8)	1.73	1.65
Dy—Cent (Cnt- η^6)	1.74	1.77
C(1)—C(1')	1.58(2)	1.532(15)

Table 2. 3 Comparison of the dysprosium centroid distances for the three constructed centroids

c. Comparison between the two types of Cnt ligand

Another comparison can be made, not between the two molecules, but between the two types of Cnt ligands on one dysprosium centers. Indeed, even though we referred to the coupled Cnt product as [Cnt₂] motif, its real nature is in question. As mentioned earlier, this coupled Cnt ligand is likely to possess a – 4 charge.

Particularly, as reported in **Table 2. 3**, the coupled carbons appear to be sp³ carbons with a single C—C between the two Cnt units. This means that there is no electronic communication through the single C—C bond and each ring is likely to be di-anionic. Considering the lower hapticity of the Cnt motif, this is reminiscent of the Cot dianion. As such the distances involved in similar systems will be compared in the next paragraph.

d. Comparison with other assemblies

DyCotCnt

In a report in 2021, the group studied the series of heteroleptic sandwich compounds LnCotCnt with the late lanthanide.⁴⁷ Particularly, the complex DyCotCnt was reported and characterized through XRD analysis. As illustrated in **Table 2. 4**, it is interesting to note that the metrics are similar. Indeed, the distance between the dysprosium center and the Cot centroid is 1.77 Å which is close to what is observed for the η^8 centroid in both cases here. For the Cnt ligand, it was reported that the hapticity in the DyCotCnt compound was closer to η^8 . This contrasts with the value of η^6 and η^4 that would be more adapted for **2.1** and **2.1_{thf}**.

DyCotCnt.MeCN

Another relevant comparison is with a complex featuring an acetonitrile adduct, reported in the same study.⁴⁷ In that case, even though the solvent is different, the metrics for the Cnt ligand are similar to 0.1 Å, as reported in **Table 2. 4**. Similarly, the centroid of the Cot is at the same distance than with the η^8 centroid for **2.1_{thf}**.⁴⁷

DyCotCp^{ttt}

Additionally other trivalent complexes such as DyCotCp^{ttt} can also be used as comparisons. Once again, the comparison with both the monoanionic and dianionic ligand shows very similar distances as illustrated in **Table 2. 4**.⁵²

Distances Dy –X in Å	2.1 ^{thf}	2.1	DyCotCnt	DyCotCnt.MeCN	DyCotCp ^{ttt}
Centroid of monoanionic ligand full hapticity	2.84	2.39	2.02	2.75	2.34
Centroid of monoanionic ligand formal hapticity	2.42	2.13	2.00	2.33	2.33
Centroid of dianionic ligand full hapticity	1.88	1.68	1.77	1.80	1.76
Centroid of dianionic ligand formal hapticity	1.73	1.65	1.77	1.80	1.76

Table 2. 4 Comparison of the main distances for different dysprosium complexes.

Although, X-Ray suitable crystals were obtained through this route and allowed for in depth structure analysis, the overall crystallization yields were extremely low. This prevented any further characterization such as magnetism study. As such a new synthetic route was developed.

3. The trivalent approach

Considering the difficulty to handle divalent species and the very low yield that were associated with those reactions, a new starting material was sought after. Ideally, the reaction could be mimicked from the trivalent state. Indeed, presumably, a trivalent dysprosium coordinated to a Cnt ligand and under reducing condition could transfer one electron in a similar fashion.

The chemistry of the Cnt ligand with trivalent metals is mainly driven by electrostatics. Thus, similarly to the Cp type ligand, salt metathesis between lanthanide halide and alkali salt of the Cnt ligand leads to the formation of LnCnt₃ compounds.⁵³ Notably, attempts to form the heteroleptic species Ln₂Cnt and LnCnt₂ by playing on the stoichiometry of the reaction were unsuccessful. Consequently, the main DyCnt_x type starting material readily accessible was DyCnt₃ and several reduction attempts were performed.

As an additional note, during the redaction of this manuscript, Roesky *et al.* published a report of mono-Cnt compounds using Ln(BH₄)₃ as a starting material.⁵⁴ Interestingly, they report that the attempt to synthesize DyCnt(BH₄)₂ was unsuccessful.

1. Potassium graphite reduction

Potassium graphite is a very strong reducing agent intensively used in reductive lanthanide chemistry. It is an heterogenous reductant and as such is typically used in large excess and in polar solvents with higher conductivity. It has, however, been used successfully in aromatic solvent such as toluene.

Several attempts were performed for the reduction of DyCnt₃ with KC₈, however no reliable results were obtained. The reaction mixture typically turns from bright orange to translucent over the course of 12 hours with concomitant formation of a black powder. This powder is insoluble in most common solvents and could not be analyzed. However, it likely comes from formation of graphite from the reductant as well as degradation product from unknown dysprosium species.

To reproduce more closely the condition of the successful synthesis of **2.1**, several one-pot attempts were made according to **Scheme 2. 5**. Once again, the color change in the reaction mixture indicated a potential reactivity but no reliable results have been obtained.



Scheme 2. 5 General synthetic scheme for the one-pot reduction of KCnt and dysprosium species.

However, one of the trials yielded a small quantity of crystals which were analyzed through XRD. The unusual structure **2.2**, presented in **Figure 2. 10**, features an indenyl type ligand as well as a strongly distorted Cnt unit.

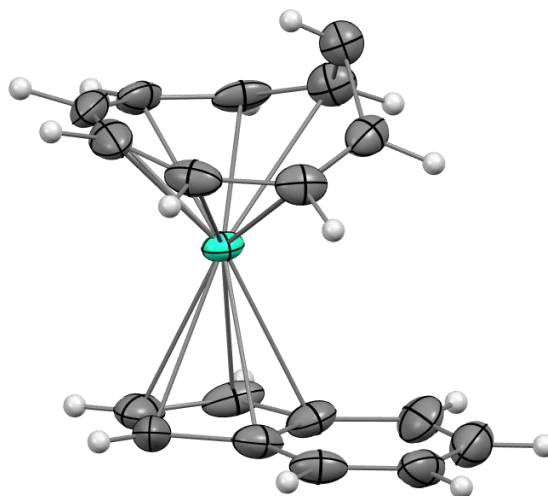


*Figure 2. 10 Molecular structure of **2.2** in the solid-state with thermal ellipsoid at the 50% probability level. Dysprosium atoms are depicted in light green and carbon atoms in grey.*

This structure is quite puzzling and difficult to rationalize in regard to the previous reaction observed with KCnt.

First, the presence of an indenyl, if not surprising in view of the literature of KCnt, had not been observed previously with lanthanide ions.²⁹ The loss of two hydrogen atoms to form the aromatic compound is clear from the crystal structure. Electronically, this agrees better with a monoanionic ligand.

Then, the second ligand is likely to possess a C₉H₉ structure. Yet, it is strongly distorted and appears closer to the half ligand of the coupled Cnt₂⁴⁻. The question of the charge is also very important. Indeed, these crystals were orange which is usually a color more associated with the trivalent state of dysprosium. Additionally, no particular precautions were needed to analyze the crystals, which makes it unlikely for them to feature a divalent dysprosium. **2.2** does not figure a counter-ion meaning that the assembly is neutral. As such, this distorted Cnt unit likely bears two negative charges. This is reminiscent of the formation of **2.1** where one Cnt ligand is reduced by one electron. Although, in this case, the created radical is reactive and readily couples. The situation for **2.2** seems more complicated. Analysis of the electronic density on the crystal structure shows remaining traces on the out of plane carbon. With this information, it is difficult to judge the nature of this density. It could either be the electronic cloud of the radical or a hydrogen atom which was abstracted during the reaction. This would mean that the ligand is no longer a C₉H₉ but rather a C₉H₁₀. However, contrary to the neutral C₉H₁₀ which evolves into the dihydro-indenyl, this ligand possesses a doubly negative charge. Taking into account the structure of the ligand, one could propose an C₈-center with 10 π -electron and two negative charges and an out of plane carbon with two hydrogen which is not involved in the delocalization. This phenomenon called homoaromaticity has been developed in the organic literature.⁵⁵⁻⁵⁷

Analysis of the distances and comparison with **2.1** are reported in **Table 2. 5**. Once again, each attribution of charge, either monoanionic or dianionic, is coherent with the distances recorded for similar compounds.

Distances Dy –X in Å	2.1_{thf}	2.1	2.2
Centroid of monoanionic ligand full hapticity	2.84	2.39	2.34
Centroid of monoanionic ligand formal hapticity	2.42	2.13	2.34
Centroid of dianionic ligand full hapticity	1.88	1.68	1.74
Centroid of dianionic ligand formal hapticity	1.73	1.65	1.62

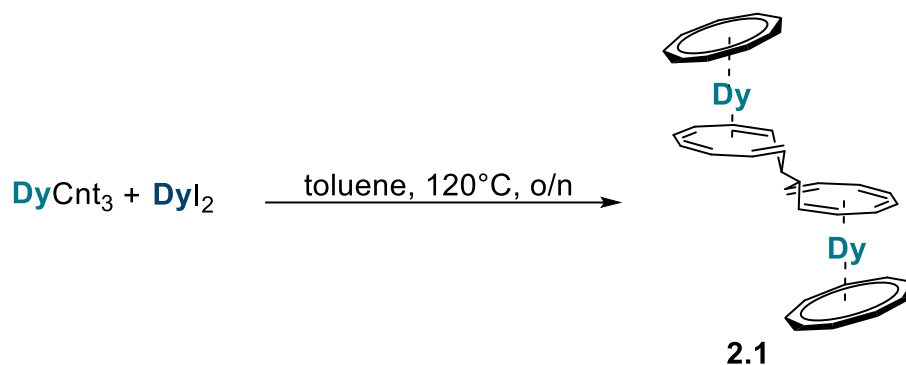
Table 2. 5 Comparison of the distances Dy–X with X various centroids for 2.1_{THF}, 2.1 and 2.2.

Unfortunately, all attempts to reproduce the reaction were unsuccessful and no further analysis were possible. Particularly, EPR spectroscopy could help investigate the radical character of the compound. Additionally, if it was possible to crystallize this product in large enough edifices, a neutron diffraction could also be a useful tool to determine the presence and position of the hydrogen atoms.

In order to replicate the result, a sequential approach might be preferable to the one-pot reduction. More particularly, initial complexation with an indenyl ligand would be preferable. This could be followed by Cnt complexation and then further reaction. Regrettably, this work could not be pursued during the timeframe of the PhD.

2. Dyl₂ as an external reductant

In view of the non-reproducible reactions with KC₈, another strong reductant was considered, Dyl₂. As previously mentioned, it is a challenging reagent to work with, due to its high reactivity. We thought that by using it as a reductant and not directly the source of dysprosium we could increase the yield of the reaction. The reduction was adapted from the previous synthesis of 2.1 as illustrated in **Scheme 2. 6**.

Scheme 2. 6 New synthetic pathway to **2.1**

This allowed us to access **2.1** in a slightly higher yield and gather enough materials for magnetism study.

4. Characterization of Dy₂Cnt₄ (**2.1**)

In addition to the structural analysis, we were interested in the electronic structure of **2.1**. Indeed, it features a ligand that has not been studied before and allows formation of a dysprosium dimer. Even if the two metal centers are far away in the structure, it could be interesting to study their magnetic interaction. Furthermore, each metal ion is placed in a pseudo-linear arrangement reminiscent of the ideal ligand field to create SMMs. We investigated this compound through theoretical calculations and SQUID-spectroscopy. This work was performed in collaboration with the team of Dr. Le Guennic and Prof. Cador.

1. Computation analysis: brief description

The electronic structure of **2.1** was analyzed using theoretical calculation tools. To begin with, the structure used as a starting point is the one obtained by SC-XRD. To retain a structure coherent with the solid-state conformation, the position of the atoms, except hydrogen atoms, are kept. Indeed, due to their single electron, little information is known about the position of the hydrogen atoms in XRD. In standard structure refinement, they are placed according to the hybridization of the associated carbon (bond length and angle). Consequently, only the position of the hydrogens was then optimized by Density Functional Theory (DFT).

Once this optimized structure is obtained, the method is switched from DFT to CASSCF (Complete Active Space Self-Consistent Field). Indeed, DFT methods are limited to the study of a single Slater determinant. Yet, to study magnetism phenomenon, excited states need to be taken into account. For this reason, *ab initio* methods such as CASSCF are commonly used to study the energy ladder that gives rise to SMM properties.

This method breaks down the orbitals of a molecule into three categories: inactive orbitals, active orbitals and virtual orbitals. This allows more in-depth computation for a small number of orbitals while keeping the computation cost as low as possible. Particularly, for f-block compounds, the active space is often comprised of the f-orbitals and sometimes, a couple orbitals of the ligand. Within this active space, a full configuration interaction is computed, allowing to describe, in most cases, the energy sublevel with a good accuracy. A few additional measures are needed when working with lanthanide, such as spin-orbit coupling and relativistic effect.

Another specificity of **2.1** is the presence of two dysprosium centers. This doubles the number of orbitals and electrons considered and exponentially increases the computation time. Fortunately, in most cases a workaround is possible. Indeed, the computation can be broken in two halves, one for each metallic center. The other ion is replaced with a diamagnetic equivalent such as yttrium or lutecium. In that case, they do not influence the active space which brings down the computation time to only twice the study of one center. A program such as POLY_ANISO can then be used to compute the information relating to the interaction between the magnetic centers.

2. Computation analysis: results

a. Anisotropy axes

From these computations, the main direction of the anisotropy can be extracted. As mentioned in the introduction, for high-performing SMM based on dysprosium, the ideal anisotropy axis is along the axial symmetry. However, we already showed that with large ligand such as Cot or Cnt, this axis is often skewed from the main axial direction.⁴⁷ As illustrated in **Figure 2. 11** this trend is also observed for **2.1**. The two dysprosium centers have co-linear alignment of the anisotropy in a diagonal fashion.

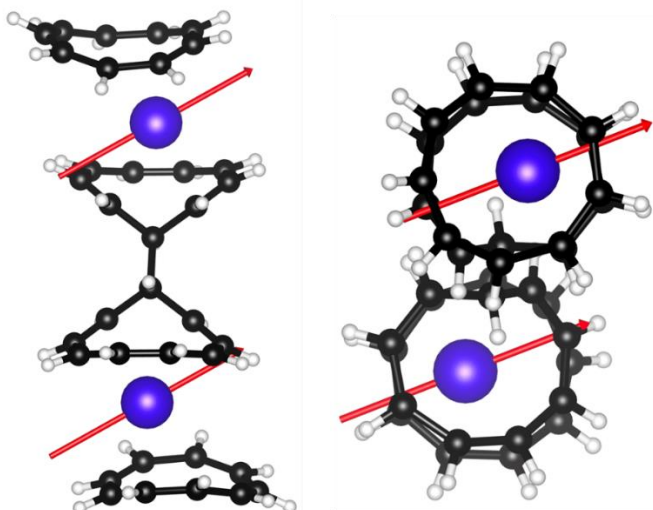


Figure 2.11 Molecular representation of **2.1** with superimposed preferential direction of the magnetic anisotropy from the side on the left and from the top on the right. The dysprosium centers are in purple, the carbon are in black and the hydrogen in white.

b. Energy levels

From the computations, the energy repartition of the sublevels can be extracted. As mentioned in the **Introduction**, the proper stabilization of the m_J sublevels drives the magnetic properties. By stabilizing the highest m_J and destabilizing the other, one can ensure a large energy gap from the ground state and consequently a high energy barrier to magnetic relaxation. As these sublevels stem from lifting of the degeneracy by application of the crystal field, they can be tuned by the ligand set.

Small ligands are usually preferred for dysprosium centers, yet this scaffold seems to be effective in stabilization of the highest m_J as indicated by the energy diagram presented in **Figure 2.12**. Unfortunately, there is no significant energy gap between the ground state and the excited states meaning that very low temperature will yield mixing of the states and drives the loss of magnetic information.

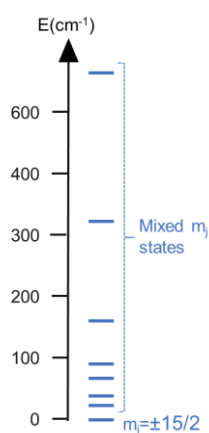


Figure 2.12 Schematic representation of the energy diagram of the m_J sublevel of **2.1**

c. Simulated magnetic curves

Using this electronic structure, it is possible to simulate the magnetic response of the sample. As presented in **Figure 2. 13**, two main figures can be studied.

First, the magnetic susceptibility, which represents the ease with which a material will become magnetized. It is defined as the ratio of the magnetization by the applied field. It is often represented as a product with the temperature as paramagnets follow the Curie law at high temperature. The Curie law states that the product χT is a constant. And indeed, on **Figure 2. 13**, it can be observed that approaching room temperature, a plateau is reached. The value of $28 \text{ cm}^3 \cdot \text{K} \cdot \text{mol}^{-1}$ is what is expected for two mostly non-interacting trivalent dysprosium. Interestingly, the computation with POLY_ANISO predicts a slight antiferromagnetic contribution between the two centers of $J_{\text{dipolar}} = -0.013 \text{ cm}^{-1}$. This can explain why the value of χT diminishes slightly while decreasing the temperature. Additionally, this feature could also be caused by the crystal field.⁵⁸

Then, the magnetization which represents the density of magnetic moment. It is expressed in Bohr magneton and linked to the number of unpaired electrons. For instance, in **Figure 2. 13 right**, the value of magnetization at room temperature is around $10 \mu_B$ which accounts for the 10 unpaired electrons of a system comprised of two trivalent dysprosium.

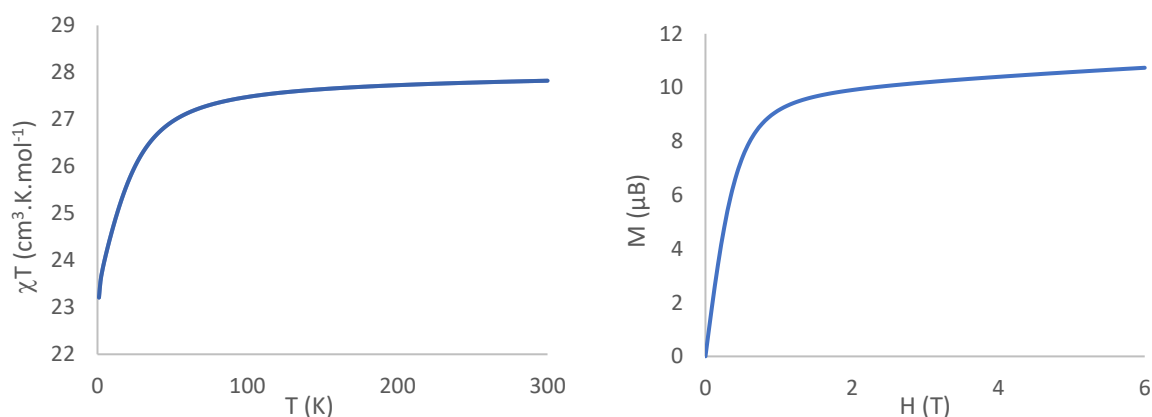


Figure 2. 13 Graphical representation of the computed χT vs the temperature (on the left) and of the magnetization vs the field (on the right)

Overall, this theoretical prediction is in agreement with the vision of a dimer of trivalent dysprosium centers barely interacting with each other.

3. Magnetism study

Even though theoretical computations allow very accurate predictions, it is still very interesting to compare with experimental data, particularly in the case of dimers as some parameters can be tuned regarding the interaction of the two metal centers.

a. DC measurements

As mentioned previously two primary data are measured, the magnetization and the susceptibility. They are shown on **Figure 2. 14** with the computed values.

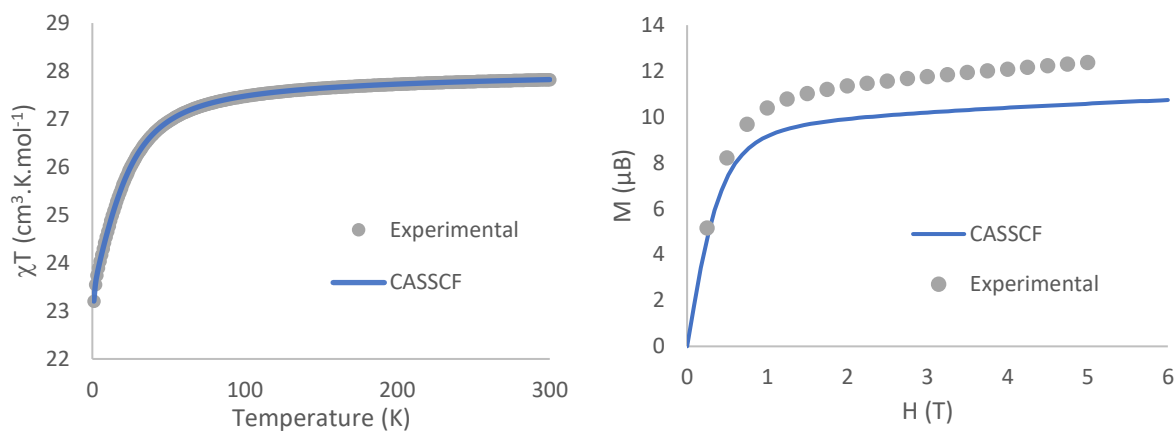


Figure 2. 14 Combined plot of the experimental and computed data for the product of the magnetic susceptibility and the temperature depending on the temperature (on the left) and of the magnetization depending on the field (on the right).

For the magnetization data, the computed values reproduce the behavior of the experimental measure. Yet, the value of the plateau is slightly higher in the experimental set. For the magnetic susceptibility, the value at high temperature is close and correspond to two dysprosium centers not interacting. It confirms that the two centers are probably too far away and not connected through the ligand set to have a sizable exchange correlation.

b. AC measurements

Then, the dynamic magnetic behavior was investigated. Measurements at zero applied field show no features in the in-phase and out-phase magnetic susceptibility. This means that no SMM behavior is observed. However, as illustrated in **Figure 2. 15**, application of a DC-field allows identification of a maxima in the χ_M'' plot.

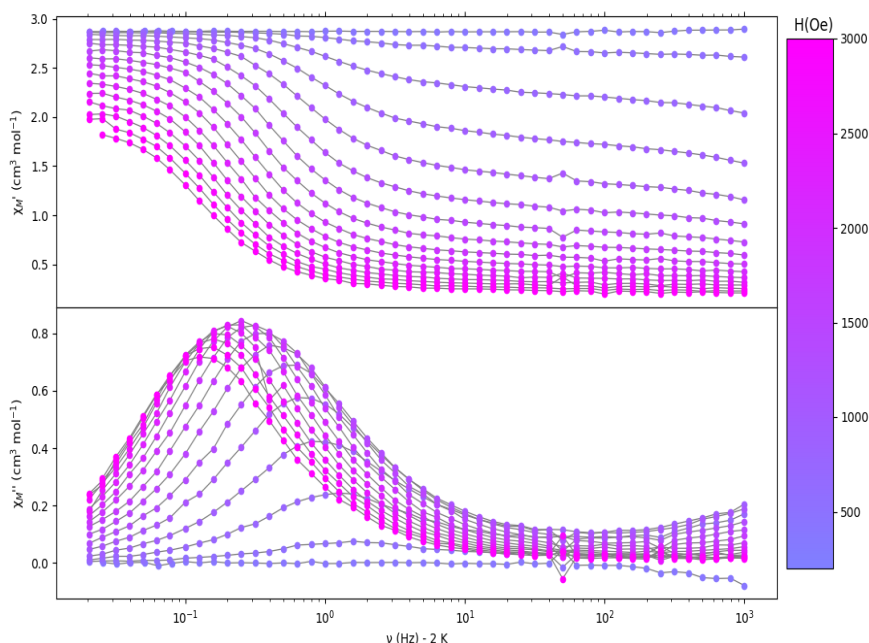


Figure 2. 15 Frequency dependences of both the in-phase, χ_M' and out-of-phase, χ_M'' , components of the ac susceptibility for **2.1** at various external dc field at 2 K.

The maximum is dependent on the applied field and reaches a maximum at around $\nu = 0.3$ Hz for $H = 2000$ Oe. As such, **2.1** can be considered as a field-induced SMM. This term can be used to describe compounds that need a field to show slow relaxation of the magnetization. It is often due to high quantum tunneling of the magnetization at low temperature. Applying an outside field allows degeneracy lifting of $+m_J$ and $-m_J$ which makes tunneling less likely. These compounds however, do not display magnetic hysteresis at zero field and are therefore poor magnets.

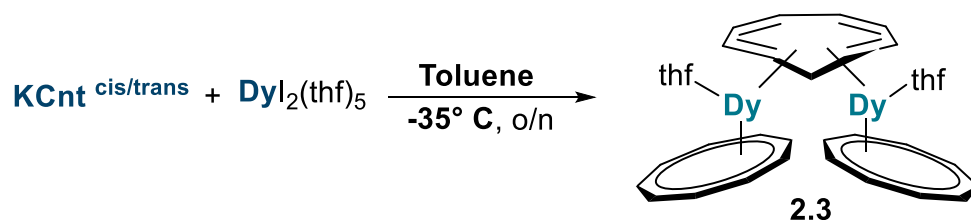
IV.Synthesis and characterization of $Dy_2Cnt_3(thf)_2$ (2.3)

While investigating the synthesis of **2.1_{thf}** and **2.1**, we found synthetic paths always requiring relatively high temperature for highly reactive species. We thought that finding a low-temperature path could enable us to isolate more reactive species.

1. Naive synthesis

As described in the literature, adding cold THF onto DyI_2 yields a very dark green solution of $DyI_2(thf)_5$.^{4,6} Often, resulting powders coming from unreacted dysprosium and DyI_3 are also present. In order to minimize the amount of THF in the reaction as well as potential impurities, we decided to isolate the THF-adduct intermediate as a deep green powder which could then

be reacted with a suspension of KCnt in toluene. Yet, as mentioned previously, the solvent adducts of DyI_2 are thermally sensitive. The lowering of the temperature due to the endothermic evaporation process was not sufficient to retain a low temperature in the mixture. Particularly, the product that would deposit on the side of the vial could be seen changing color from green to brown. These changes meant decomposition of the $DyI_2(thf)_5$ adduct. As such, to perform the evaporation, the mixture needs to be periodically cooled in the freezer. With periodical decrease of the temperature, the solvent was successfully removed while retaining a deep green solid. At this point, a cold suspension of KCnt was added and the reaction medium immediately turned brown-red. The reaction was allowed 12 hours to react and was then filtered with cold material. The remaining bright brown-red solution was placed to crystallize at cold. This allowed us to isolate **2.3** for the first time, see **Scheme 2.7**.

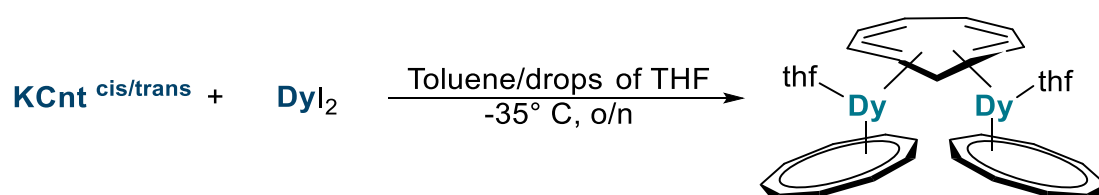


Scheme 2.7. Synthetic path used for the first obtention of 2.3

Although we managed to isolate a new compound and structurally characterize it, the difficulty of evaporating the dysprosium adduct while retaining temperature cold enough for it not to decompose made this route a non-viable path.

2. Perfected synthetic path

Consequently, I tuned the synthesis to mimick as close as possible the previous conditions. Contrarily to the first synthesis, the amount of THF added was lowered as much as possible to form the dysprosium adduct *in situ* as reported in **Scheme 2.8**. Typically, a few drops of THF were sufficient to color the solid in green. The cold suspension of KCnt in toluene was then added. A very similar color change was observed and similar treatment allowed the isolation of **2.3** as red-brown needles. Once again, the yield was extremely low but the reaction was very reproducible.



Scheme 2.8 Synthetic path to 2.3

The crystals obtained through this route were very small, but a structure could be extracted and is discussed below. The purity of the crystalline material was investigated through cell measurement of a statistical number of crystals. No deviation from the main product was found. Unfortunately, other bulk analyses were unsuccessful. No NMR signals could be detected in toluene solution. Several attempts to run powder-XRD analyses showed the high reactivity of this species as the powder would decolorate in a few minutes even in appropriate sample holder.

3. Structural characterization

1. General description

The obtained structure of the dimer is presented in **Figure 2. 16**, it crystallizes in the $P2_1/n$ space group. The molecule is fairly symmetrical. However, the two dysprosium centers are crystallographically different. One THF molecule is coordinated to each dysprosium center.

In total, three Cnt units can be identified, one bridged and two mono-coordinated. The question of the bridging motif actual atomic make-up was investigated. The nine carbon atoms were easily identified. The hydrogens atoms were also sought after in the residual electronic density and could all be identified. As such, the bridging unit, despite its strong distortion appear to be a formal C_9H_9 unit.

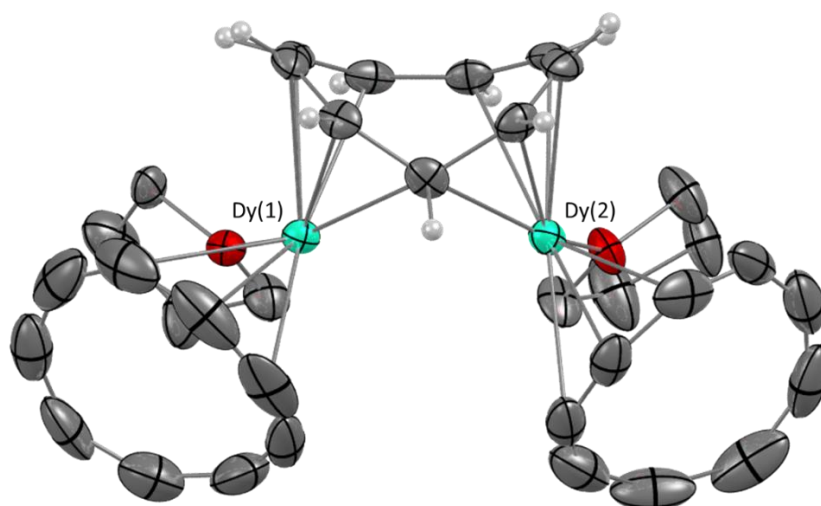


Figure 2. 16. Molecular structure of 2.3 in the solid state with thermal ellipsoid at the 50% probability level. Dysprosium atoms are depicted in light green, carbon atoms in grey and oxygen atoms in red. Hydrogen atoms on peripheral ligand, thf disorder and one solvent molecule have been omitted for clarity.

2. Bonding motifs with the external Cnt

The bonding of the mono-coordinated Cnt ligands can be compared to the previous **2.1_{thf}**. Similarly, centroids can be defined corresponding to different hapticity. For the sake of

comparison, the same hapticity are considered: η^9 , η^6 and η^4 . In **Table 2. 6** are compared the distances Dy—Centroid for each distinct dysprosium center of **2.3** and the dysprosium center of **2.1_{thf}**. These measured distances show that, the two dysprosium centers have very similar environments. Moreover, even though the coupled and bridging Cnt motifs are very different, the bonding scheme for the capping Cnt ligand is extremely close with **2.1_{thf}**. In both cases, the hapticity is closer to η^4 and η^6 .

Distances in Å	Dy(1)	Dy(2)	2.1 _{thf}
Dy(X)—Cent (Cnt- η^9)	2.82	2.83	2.84
Dy(X)—Cent (Cnt- η^6)	2.42	2.42	2.42
Dy(X)—Cent (Cnt- η^4)	2.40	2.40	2.40

Table 2. 6 Distances measured for the distances Dy—Centroid for the two centers of **2.3** and the center of **2.1_{thf}**.

3. Structural description of the bridging unit

For the central Cnt unit, the comparison is more difficult because there is no equivalent of a Cnt motif bridging two metallic centers. One point of comparison could be the [Cnt₂] unit described for **2.1**. Indeed, their distortion is similar in both motifs. The **Figure 2. 17** shows a side and face view of the Cnt from **2.1** and **2.3** without showing the metal centers.

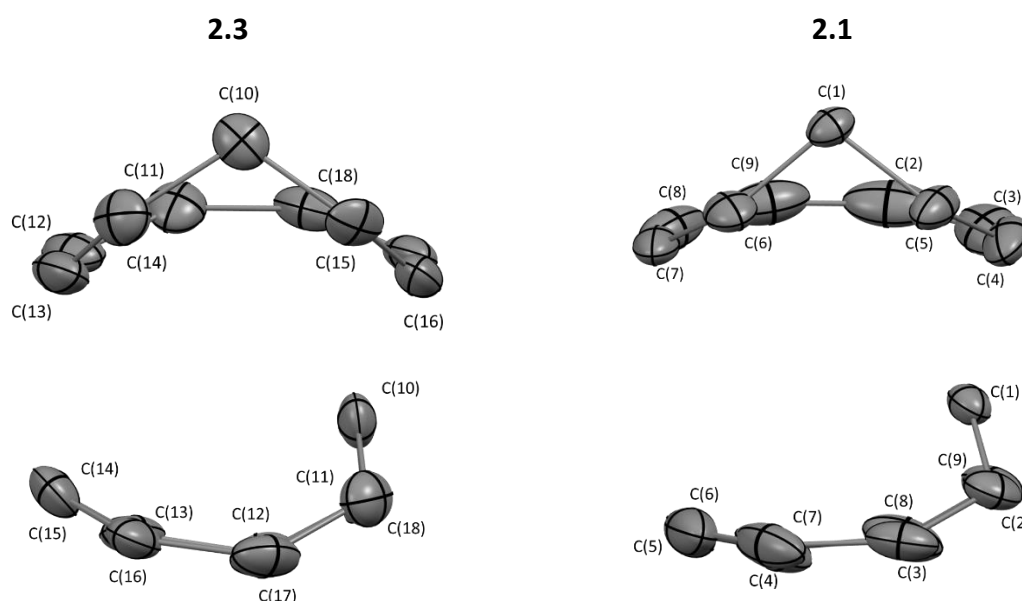


Figure 2. 17 Molecular representation of the distorted unit of **2.3** and **2.1** complexes from two different views.

In this representation, the metrics indicate a similar distortion. Yet, the Cnt of **2.3** appears slightly more constrained. This can be illustrated by constructing mean planes with [C(11)-C(14)] and [C(15)-C(18)] for **2.3** (as illustrated in **Figure 2. 18**) and similarly [C(6)-C(9)] and [C(2)-C(5)] for **2.1**. The angle between these planes for each molecule translates the departure

from planarity as a planar Cnt ligand would feature 180 ° angle. For **2.1** this angle is 141.2 ° and for **2.3** it figures at 118.8 ° showing a stronger distortion.

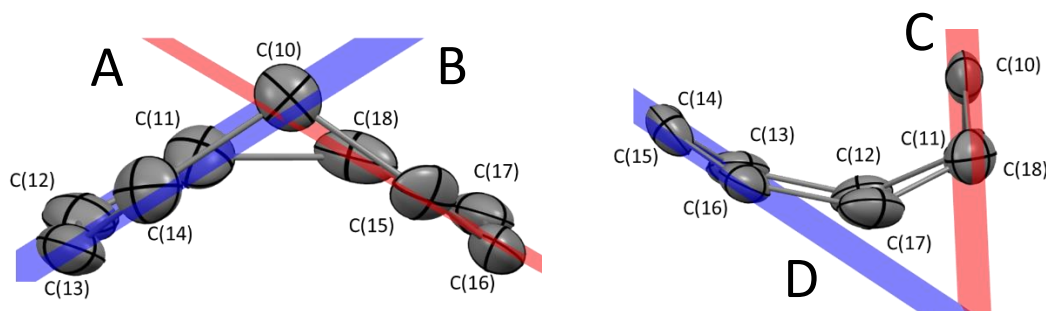


Figure 2. 18 Example of the planes constructed on the Cnt unit for 2.3 to explain the distortion.

Similarly, from the side view, several planes can be constructed to assess the distortion from planarity. From this molecules, two planes can be used from [C(13)-C(15)], [C(11), C(10), C(18)] and [C(4)-C(7),] [C(1), C(2), C(9)] for **2.3** (as illustrated in **Figure 2. 18**) and **2.1** respectively. In a planar case, the angle between these two planes should be 180 °, for this version they total 54.5 ° and 64.6 ° showing once again a more pronounced curvature for the Cnt ligand of **2.3** compared to **2.1**. These results are compiled in **Table 2. 7**.

Angles in °	2.3	2.1
A^B	118.8 °	141.2 °
C^D	54.5 °	64.6 °

Table 2. 7 Main geometric angles to asses the differences between 2.1 and 2.3.

4. Consequences for the electronic structure

This stronger distortion is difficult to rationalize in terms of electronic structure because of the markedly different coordination scheme. It could come from a different overall charge state of the Cnt ligand or rather arise from the coordination by two dysprosium centers.

The question of the charge repartition in this species is then central to the understanding of its electronic structure. The absence of counter-ion shows that **2.3** is neutral. Additionally, the odd number of electrons points to the presence of a radical which should be investigated.

The THF should not, influence the charge repartition. Considering the very similar structure and distances observed for the Cnt ligand, at first glance, it seems unlikely that they accessed a more reduced state. The question is then centered around the dysprosium atoms and the bridging Cnt ligand. This leaves 4 scenarii of charge repartition possible represented by the schematic drawing in **Figure 2. 19**.

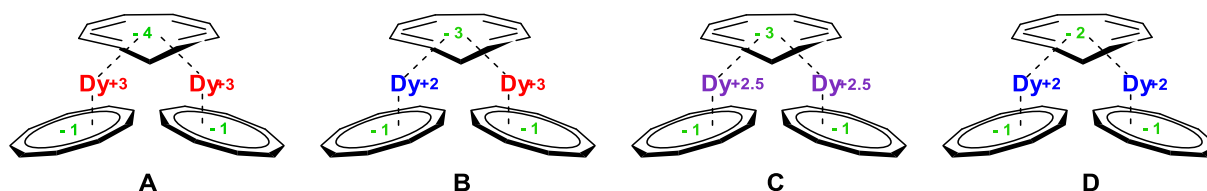


Figure 2. 19 Schematic representation of the different charge repartition scenarii for **2.3**

These simple drawings, where the coordinated solvents were removed for clarity, are separated in two different categories depending on the localization of the radical. For **A** and **D**, the charges localized on the Cnt motifs making them organic radicals. On the contrary, for **B** and **C**, the radical is metal-based in essence. The difference between **B** and **C** would be about the possibility to delocalize this radical in between the two centers in a type III mixed valence complex in the formalism of Robin-Day.^{59–61} As presented in **1.3** and as it will be developed in **Chapter 3**, the isolation of divalent dysprosium centers in organometallic complexes is very rare.^{16,62,63} Furthermore, divalent species are notoriously sensitive to the temperature.⁴ Considering the relative stability of the crystalline form of **2.3**, the case **D** was not considered at first. Similarly, the reduction of KCnt to its -4 state would require three additional reduction events. Thus, mixed valent scenarii were considered the best options.

In order to investigate this phenomenon, computation analysis as well as magnetism characterization were pursued.

4. Computational approach

Considering the low yield of the molecule, the magnetism sample took a long time to be prepared, as such, the theoretical analyses were the first data to be obtained.

To distinguish between the different *scenarii*, the structure was studied through theoretical computation methods. A similar pipeline than **2.1** was applied to **2.3**. This time several hydrogens had been placed according to residual electronic density directly. As such, these ones were not optimized by DFT. Only the hydrogen atoms, from the THF and the Cnt⁻ rings were optimized.

1. DFT approach

The first attempts at understanding the electronic structure of **2.3** were performed using DFT methods, namely the functional used were GGA-revPBE and the basis set of the type TZP in the ADF software. After optimization of the geometry, a single-point in energy as well as frequencies were computed. The frequencies were checked for negative values which would indicate that the geometry is not a minimum of energy. The single point allows access to the orbital diagram and plot the residual spin density as well as the singly occupied molecular

orbital (SOMO), these are presented in **Figure 2. 20**. A particularity of *f*-elements complexes is that they almost always possess unpaired electrons in their *f*-orbitals, except for La(III), Lu(III), Ce(IV) and Yb(II). In this case, in addition to the unpaired *f*-electrons, some electronic density is found in an orbital involving the dz^2 orbitals from the dysprosium centers.

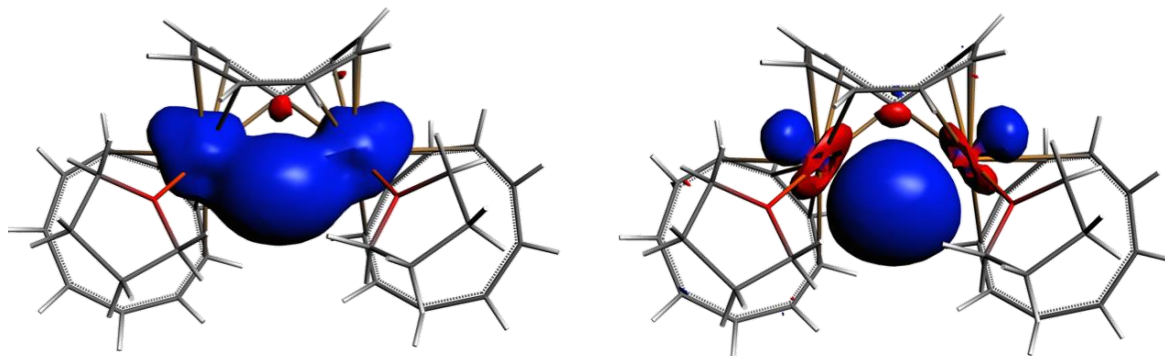


Figure 2. 20 Representation of the residual spin density (on the left) and the singly occupied molecular orbital (on the right)

The radical is then located mainly on the metallic centers and the density is delocalized on both metal centers. Particularly, the SOMO shows a symmetrical orbital which results from two dz^2 orbitals overlapping in the middle of the two dysprosium atoms. This is in agreement with the recent research on the nature of the new electron in the case of reduction of Dy(III) centers. Preliminary study shows that it is of *d* character with a mixing of *s* character.^{62,63}

2. CASSCF approach

As briefly mentioned in III.4.1, *ab initio*, and in particular CASSCF methods are ubiquitous in the study of electronic structure. Particularly, they allow the investigation of excited state phenomenon in the magnetic response.

Nevertheless, they are computationally heavy and several rounds of model refinements are needed. Particularly, as mentioned for lanthanide dimers, the first investigation is carried out with one center replaced by a diamagnetic ion. Then diverse methods can be used to model the entire system.

a. Mono-dysprosium computation

To run such a computation, one should determine the number of orbitals in the active space as well as the number of electrons involved. For a standard trivalent dysprosium, the seven *f*-orbitals are usually considered with their 9 electrons. For the radical, one more electron and one orbital are taken into account. This means a CAS(10,8) with the first term standing for the number of electrons and the second the number of orbitals in the active space.

The molecule being close to symmetrical, the computation replacing either Dy(1) or Dy(2) yielded very similar results. These two results were then run through the POLY_ANISO software allow modeling of the physical properties for the entire molecule.

The seven *f*-orbitals can be found in the active space as expected. Interestingly the 8th orbitals depicted in **Figure 2. 21** is also metal-centered of 5d parentage. This points toward a radical centered on the dysprosium ions.

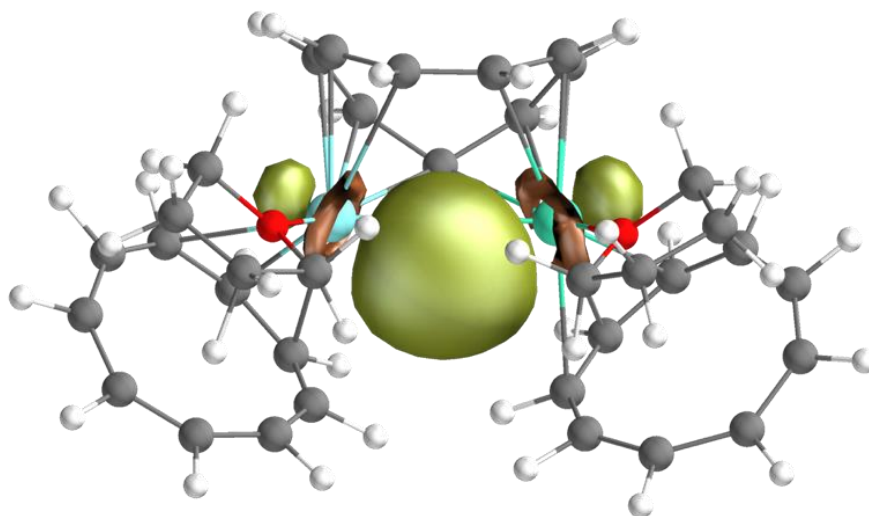


*Figure 2. 21. Representation of the non *f*-orbital present in the active space of the CAS(10,8) for 2.3.*

However, it felt insufficient to justify delocalization of the electron as the two lanthanides centers were not considered at the same time in computation. As a consequence, even though it is computationally heavy, a CAS investigation was started on the entire molecule.

b. Considering both dysprosium atoms

Following the same logic as for the half compound, a CAS(19,15) containing 19 electrons in 15 orbitals was studied.

Considering both dysprosium centers to be almost identical, this allows three types of systems depending on the coupling between the two centers and the radical. The resulting spin of the system are 11/2, 9/2 or 1/2. Computation of the energy for each of these conformations shows that the maximum spin system is energetically favored as the Hund rule would predict. The additional orbital in the active space is similar to the one obtain for the CAS(10,8). This time it seems justified to say that computationally this compound is predicted to be a type III mixed-valent complex with complete delocalization of an electron over the two dysprosium centers.⁶⁴

As such, this would translate into χT values higher at room temperature than the sum of the theoretical value for dysprosium, about 56 cm³.K/mol⁻¹ VS 28 cm³.K/mol⁻¹. This phenomenon was reported by Long and co-workers for a similar bridged Dy₂ dimer.⁶³ As such, the magnetic data should be able to confirm this behavior easily.

5. Magnetism study

1. DC measurements

Similarly than for **2.1**, the first investigation were performed under DC field. Both the magnetization and the magnetic susceptibility were recorded.

Due to the low yield, incertitude over the weight of the compound were corrected in the magnetization spectra. Indeed, as explained in the computational part, this molecule is expected to be 11/2 spin system. The rescaled spectrum in Presented in **Figure 2. 22**.

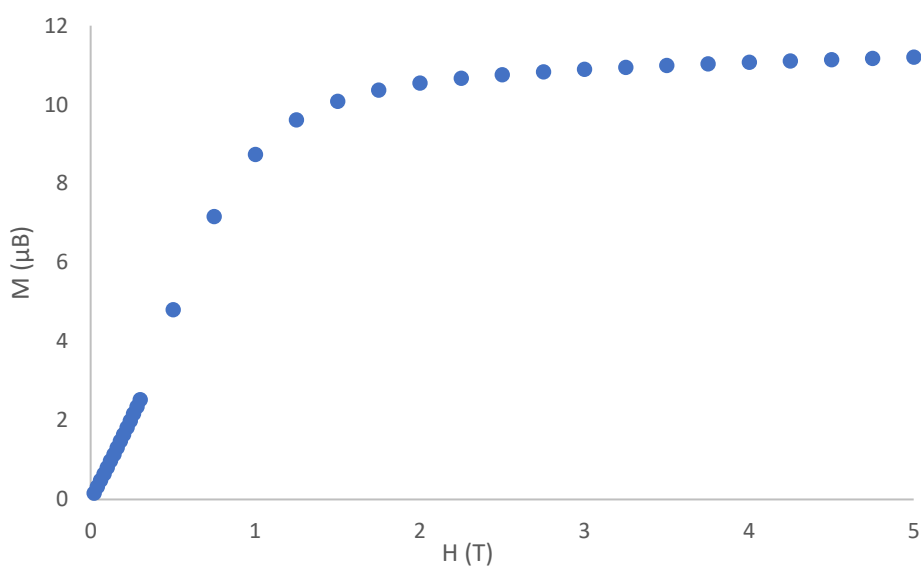


Figure 2. 22 Graphical representation of the magnetization vs the applied field H , recorded at 2 K.

The other interesting figure is the magnetic susceptibility which is represented in **Figure 2. 23**.

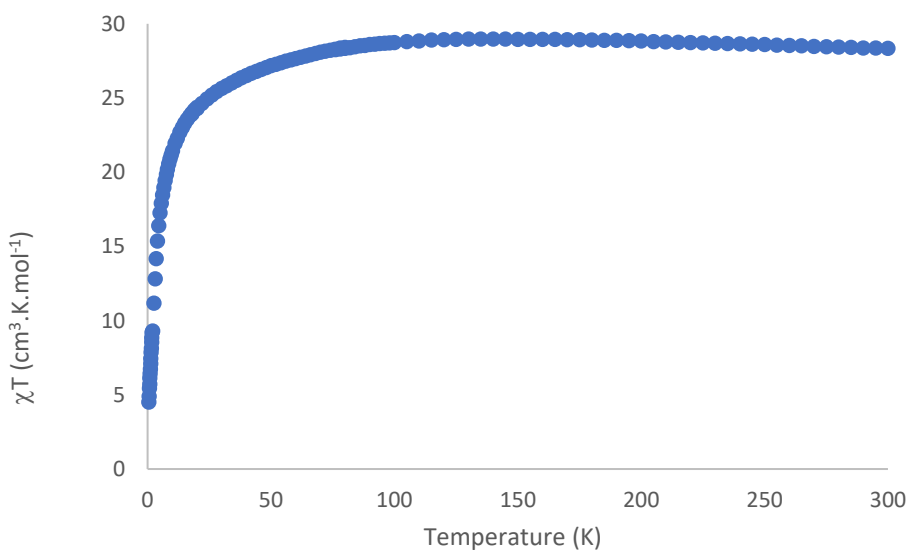


Figure 2. 23 Graphical representation of the product of magnetic susceptibility and the temperature vs the temperature.

Analysis of this behavior yields several information.

The first conclusion is that, contrary to the theoretical predictions, there is no delocalization of an electron between the two dysprosium centers. Indeed, even considering the applied weight correction, the value of χT at room temperature is significantly smaller than the $\chi T = 56 \text{ cm}^3 \cdot \text{K} \cdot \text{mol}^{-1}$ mark obtained by Long and coworkers.⁶³ As such, the most likely situation is either that both centers have the same oxidation state or that the mixed-valence is restricted to class II.

Then, it is difficult to further analyze the oxidation state make-up of this dimer. Indeed, as mentioned weight correction was applied. And it is known that the expected values of magnetic susceptibility at room temperature of divalent and trivalent dysprosium are fairly close as seen in **Table 2. 8**.⁶⁵ As such, this is not an appropriate method to assign the adequate electronic structure.

Coupling scheme	χT in $\text{cm}^3 \cdot \text{K} \cdot \text{mol}^{-1}$
Dy(III)	14.13
Dy(II) $4f^{n+1}$	14.07
Dy(II) $4f^n 5d^1$ coupled	17.01
Dy(II) $4f^n 5d^1$ uncoupled	14.51

Table 2. 8 Theoretical values of magnetic susceptibility expected for a dysprosium center in its +II and +III oxidation state and under different couplings as reported in ⁶⁵.

Additionally, the overall shape of the curve is slightly different than for a typical paramagnetic complex. Indeed, the usual plateau observed at higher temperature; because of the Curie behavior, is replaced here with a slight increase when the temperature decrease. This is usually the mark of a ferromagnetic interaction. However, they are also usually more pronounced. As such it is difficult to attribute this behavior. Then contrary to **2.1** showing a decrease of the magnetic susceptibility at low temperature to about $\chi T = 21 \text{ cm}^3 \cdot \text{K} \cdot \text{mol}^{-1}$, a stark decrease to about $\chi T = 5 \text{ cm}^3 \cdot \text{K} \cdot \text{mol}^{-1}$ is observed for **2.3** as illustrated in **Figure 2. 24**.

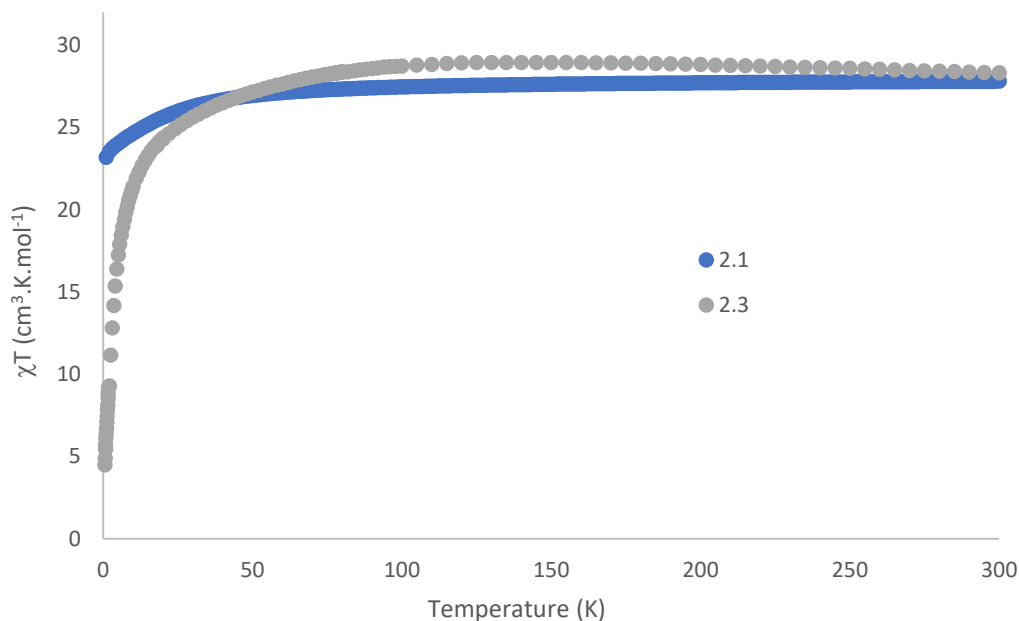


Figure 2. 24 Comparison of the χT vs T behavior for **2.1** and **2.3**.

This decrease could be due to either crystal field effect or antiferromagnetic coupling of the two centers. Overall, this behavior is difficult to explain with the element that we have. As such we tried a different modelling of the system which will be described in **I.1.3**.

2. AC measurements

Despite the possible antiferromagnetic coupling between the two dysprosium atoms, we decided to investigate further the AC behavior.

This time **2.3** was found to possess zero-field slow magnetic relaxation. However, it happens at very high frequency meaning that the relaxation rate is high. Indeed, when studying out-of-phase signal the objective is to observe a non-0 χ_M'' at the lowest frequency possible. This translates into a long retention of the magnetic information.

As such, the optimal field to show the slow magnetic relaxation behavior was scanned by looking at the in-phase and out-of-phase signal for different DC fields applied. The results are presented in the following spectra in **Figure 2. 25**.

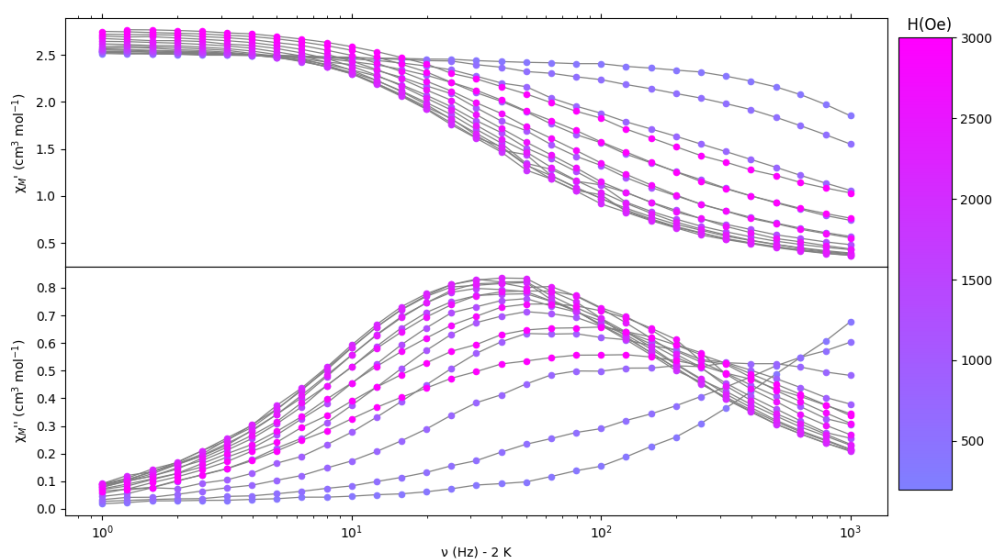


Figure 2.25 Frequency dependences of both the in-phase, $\chi M'$ and out-of-phase, $\chi M''$, components of the ac susceptibility for 2.3 at various external dc field at 2 K.

This yields that the behavior is observed best at 2.2 kOe. A sweep in temperature presented in **Figure 2.26** was then recorded to investigate its influence on the SMM behavior.

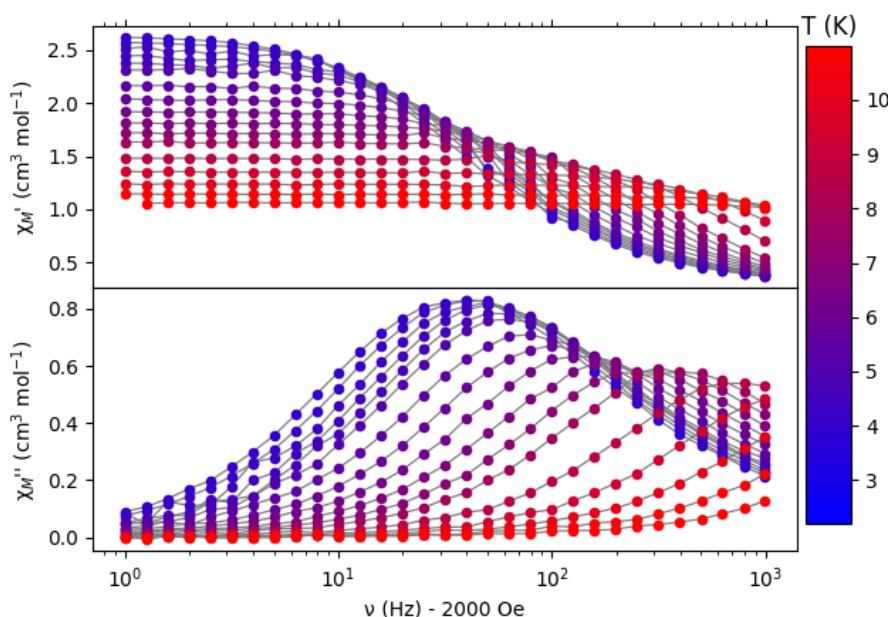


Figure 2.26 Frequency dependences of both the in-phase, $\chi M'$ and out-of-phase, $\chi M''$, components of the ac susceptibility for 2.3 at 2.2 kOe external dc field and at various temperatures.

On this graph the signal rapidly shifts outside of the window toward higher frequency at higher temperature. This means that the SMM behavior is observed only at low temperature. Another interesting point, is that the maxima of the out-of-phase signal diminishes in intensity while shifting frequency. This indicates that at low temperatures, the relaxation process is most likely not driven by quantum tunneling of the magnetization (QTM). This probably

explained why this molecule behaves as a SMM at very low temperature in the absence of field. However, to achieve a deeper understanding of the phenomenon at play, a study of the rate of relaxation as a function of the temperature would be needed.

3. Further investigation

Considering the difficulty to explain the electronic structure of **2.3** with the current magnetic data, additional characterizations were sought after. Particularly, the presence of a solitary electron was investigated both through magnetic behavior and computation. Acquisition of the magnetic curve at extremely low temperature $T = 0.5$ K using ^3He refrigeration allowed the observation of an inflexion point at low temperature as shown in **Figure 2. 27**. This feature shows that at very low temperature, there is a change in behavior from the system. We rationalize this as a bi-stability of the system induced through application of the magnetic field allowing ferromagnetic alignment of the radical which would otherwise be antiferromagnetically aligned with the dysprosium centers.

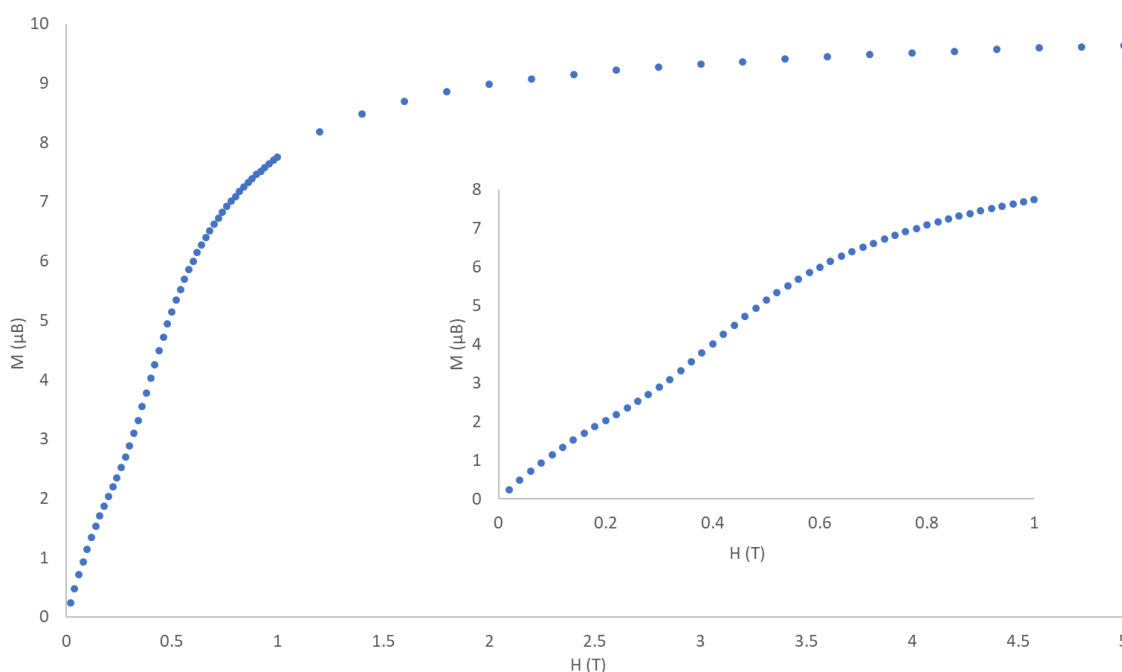


Figure 2. 27 Graphical representation of the magnetization vs the applied field H , recorded at 0.5 K.

Nevertheless, it could come from another source and as such, we tried to model this system through computational means. A similar process was followed by computing the Dy-Y dimers but this time only with the nine f -electrons of the trivalent dysprosium. This then allows to simulate the remainder radical directly in POLY_ANISO. It was chosen to place it at the barycenter of the supposed d orbital. The influence of the magnetic dipole on one another can be modelled as dipolar coupling, a through-space long-range interaction.^{66,67} The amount of coupling can then be tuned to see what type of interaction could be at play in this

compound. For instance, we were able to reproduce an inflexion point in the magnetization curve as shown in **Figure 2. 28**.

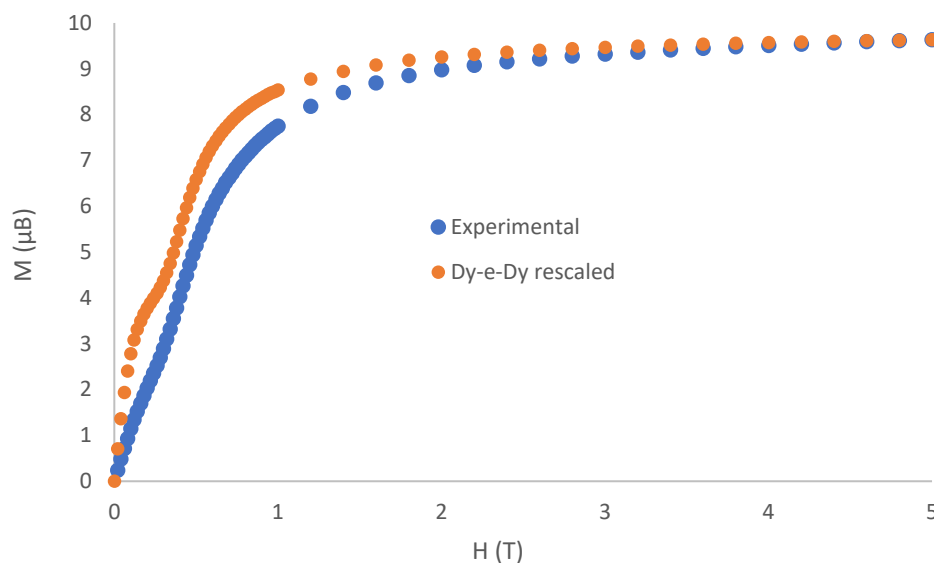


Figure 2. 28 Graphical representation of the magnetization vs the applied field H , recorded at 0.5 K and superimposed with the simulation of electron placed at the center of the supposed d -orbital with a $J_{Dip} = -2.14 \text{ cm}^{-1}$.

Similarly, in the magnetic susceptibility, considering a small J_{Dip} values allows to introduce the stark decrease of value at low temperature as illustrated in **Figure 2. 29**.

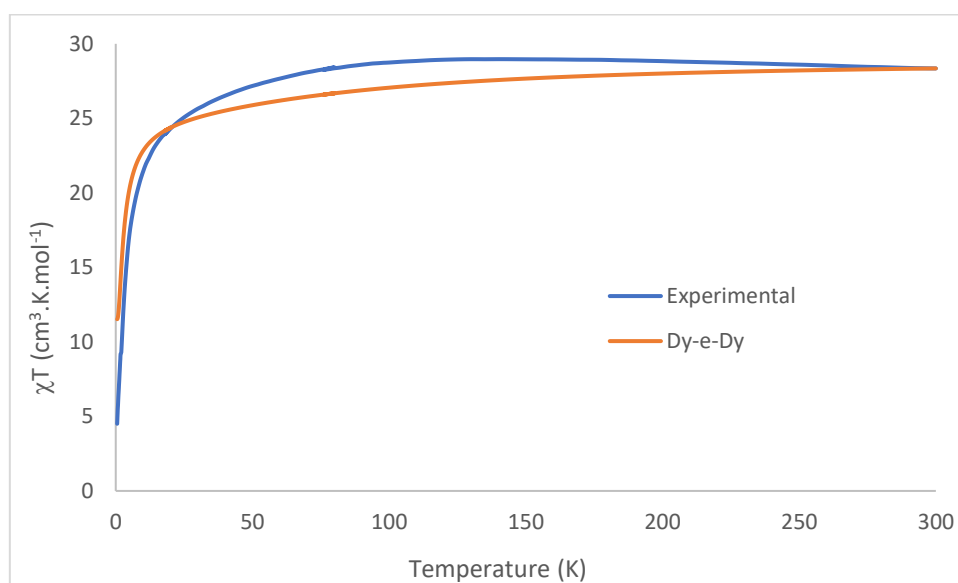


Figure 2. 29 Graphical representation of the product of magnetic susceptibility and the temperature vs the temperature for 2.3 and the simulated system.

Overall, this modelling allows to reproduce important features of both the magnetic susceptibility and the magnetization. Although this reproduction is closer to the real system than the initial vision, it does not allow reproduction of the slight increase of χT when the temperature decreases between [300 K – 80 K].

6. Discussion

To conclude this part, we can have a look back at the proposed scenario from **I.1.4** as illustrated on **Figure 2. 30**.

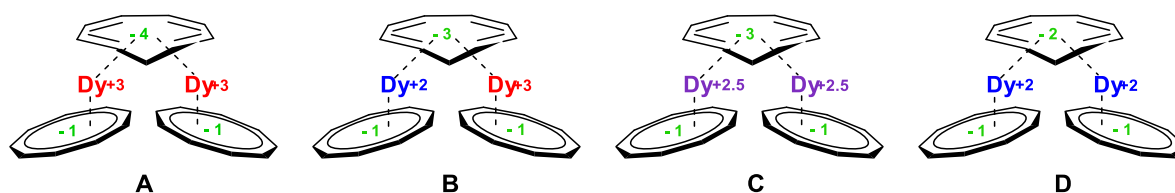


Figure 2. 30 Schematic representation of the possible electronic structure of **2.3**.

According to the magnetic susceptibility value at room temperature, it is highly unlikely that this compound features as class III mixed-valent compounds as depicted for *scenarii C*.

The situation **B** appears as a good candidate. It would be coherent with the value of χT at room temperature and of the magnetization. It could also be coherent with the final computation of an antiferromagnetic interaction between the dysprosium centers with a d^1 electron located on one of the centers rather than the barycenter of the dz^2 - dz^2 SOMO. Although several experimental evidences would be coherent with this picture, the fact that the CASSCF computation systematically forces the delocalization of the radical as well as predict antiferromagnetic behavior to be higher in energy, leads to doubt in the attribution. Furthermore, the structural proof of an overall symmetric molecule by SC-XRD makes it peculiar that the dysprosium would have different oxidation states.

One possible source of discrepancy was identified in the presence of THF molecules. Indeed, the THF molecules could be labile and as such be displaced upon preparation of the sample for experimental characterization. In this case, it would explain why the computation and the crystal structure are coherent and argue for situation **C**, while the experimental measures differs because they were run on a different compound with less coordinated THF. This could lead to a strong dissymmetry in the molecule which could explain the magnetism data. DFT-optimization of the structure shows a strong dissymmetrization as illustrated in **Figure 2. 31**.

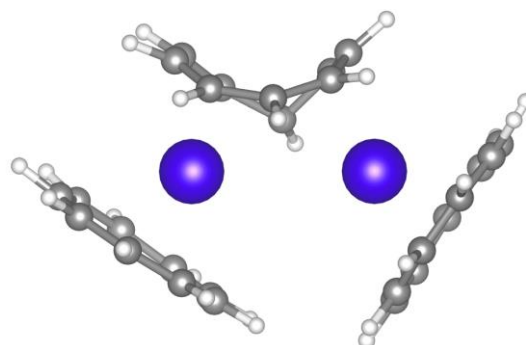


Figure 2. 31 Optimised structure of **2.3** without coordinated THF molecules. Dysprosium atoms are in purple, carbon in grey and hydrogens in white

Unfortunately, no differences were seen in the experimental characterization of carefully prepared sample. Furthermore, attempt at changing the solvent of the reaction for 2-MeTHF to force it out of the coordination sphere did not yield any product.⁶⁸

Additionally, more than the oxidation make-up of the compound the actual repartition of the spins needs to be taken into account, as illustrated in **Table 2. 9**. For instance, the mixed-valent scenarii only give rise to one total spin value if the f-electrons are excluded. However, if we consider a mono-reduced Cnt ligand, then there are ways to create either a $S = 3/2$ or $S = 1/2$. Similarly, if the Cnt ligand has been reduced, there are different ways to place the electrons. Unfortunately, EPR experiments did not allow us to obtain identifiable signals which could help in this investigation. As such, computations appear as the most potent tool to explore these different possibilities. From this chapter, we already concluded that in a mixed-valent scenario, the most stable conformation was ferromagnetic coupling of the dysprosium centers with delocalization of the radical onto the two dysprosium ions which is not supported by the magnetic data. We are then currently investigating the other scenario. Particularly, the comparison made in **I.1.3** showed that the molecular make-up of the Cnt was very similar in **2.1** and **2.3** which could be coherent with a mono-reduced Cnt bridging unit with two divalent dysprosium centers. As such we are exploring the magnetic response of the different multiplicities presented in **Table 2. 9**, while keeping one radical character in the Cnt ligand, to determine whether this could be coherent with our experimental magnetic data. If this study does not yield coherent study, then a closer look at the reduction of the Cnt unit will be needed to determine whether its triple reduction is a likely event.

Spin\Situations	A	B	C	D
$S = 3/2$				
$S = 1/2$				

Table 2. 9 Possible multiplicities obtained for the different scenarii of electron repartition. (The color of the metallic atoms denotes its assumed redox states, blue, purple and red meaning respectively, divalent, mixed-valent and trivalent.)

Confronted with the discrepancy issues and the technical difficulty, an attempt at expending this chemistry to neodymium was started. Given the high thermal sensitivity of NdI_2 it was unlikely to be a change for the better however, accessing similar species could show a trend in the behavior of the reduced Cnt.

V. Extension to other LnI₂

In addition to Sm, Eu, Dy, Yb and Tm, Nd also possesses a binary halide form as a diiodide. Considering the difficulties to solve the electronic structure of **2.3**, an investigation of its reactivity in similar conditions tested above was started.

1. Synthesis of Nd₂Cnt₄(thf)₂

To reproduce the Cnt-Cnt coupling, different methods have been tried. An analogue of the **2.1_{thf}** was obtained. Unfortunately, the synthetic routes have been found to be rather not reproducible.

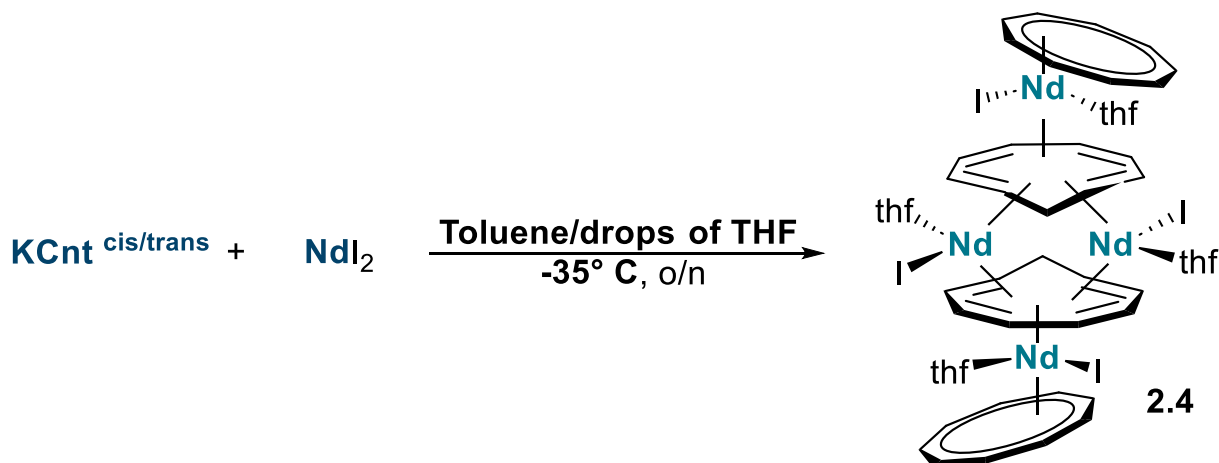
However, the THF-free version was not obtained. Indeed, the synthetic pathway with high temperature was not successful and the starting material NdCnt₃ has never been successfully made.

The reproducibility issues as well as the failure of the high temperature methods, could be due to the higher thermal sensitivity of NdI₂.^{4,7,9}

2. Synthesis of Nd₄Cnt₄I₄ (**2.4**)

1. Synthesis of a new multi-metallic complexes

A process similar to the synthesis of **2.3** was also applied. Small black needles of the product were obtained following **Scheme 2.9**.



Scheme 2.9 Synthesis of 2.4

Although this method is reproducible, similarly to **2.3**, only very little amount of material was obtained with each crystallization. Furthermore, the crystallization is even more challenging. Indeed, the product often precipitates rather than crystallize and only very small needles were obtained.

2. Qualitative XRD analysis

XRD analysis of **2.4** revealed the overall structure of the molecule presented in **Figure 2. 32**. However, the relatively low resolution of the data set does not allow quantitative analysis. The molecule crystallizes in R-3 space group and possesses a symmetry center. As such the asymmetric unit figures only two neodymium atoms.

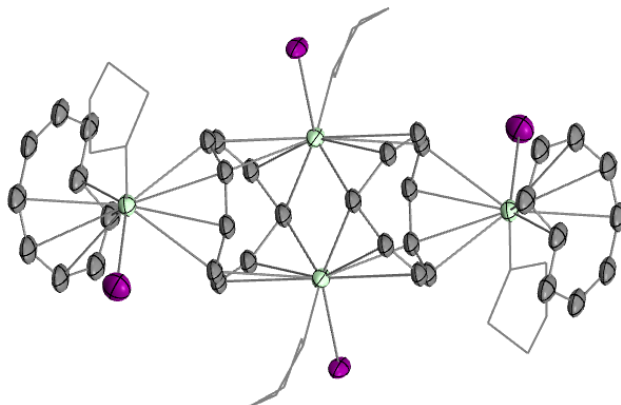


Figure 2. 32 Molecular representation of **2.4** in the solid-state with thermal ellipsoid at the 50% probability level. Neodymium atoms are depicted in light green, carbon atoms in grey and iodine in purple. H atoms were not placed due to the low resolution, thf molecules are represented in wireframe and one solvent molecule have been omitted for clarity.

As previously mentioned, attempts at quantitative analysis would not be justified due to the low resolution of the data. However, the connectivity and identity of the different atoms can be discussed.

a. Description of the central motif

The central part of this molecule is comprised of two strongly distorted Cnt unit, two neodymium ions as well as two iodine and thf molecules. Visually the Cnt moiety are close to the species studied previously, particularly **2.3**, as illustrated in **Figure 2. 33**.

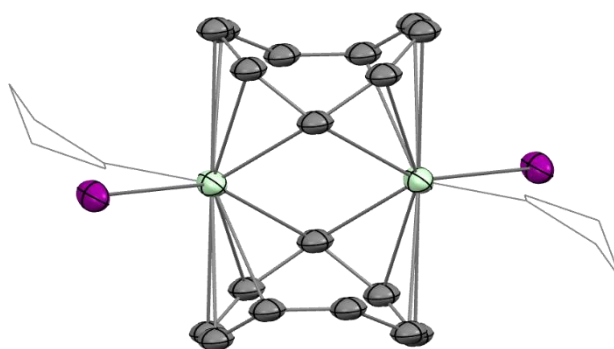


Figure 2. 33 Molecular representation of the central part of **2.4** in the solid state with thermal ellipsoid at the 50% probability level. Neodymium atoms are depicted in light green, carbon atoms in grey and iodine in purple. H atoms were not placed due to the low resolution, thf are represented in wireframe and one solvent molecule have been omitted for clarity.

The distance in this central unit between the neodymium is 3.663(2) Å which, even with low precision, scores relatively low for a lanthanide-lanthanide distance.⁶³ Of note, the coordination scheme of the two neodymium ions with one distorted Cnt ligand is very close to **2.3** although the coordination mode allows two of the units to interact to form a sandwich-like structure. Another difference to highlight is the presence of iodine in the coordination sphere. The distance Nd—I of 3.159(2) Å is *on par* with literature value for trivalent and divalent neodymium with bulky ligand (3.140 Å and 3.156 Å respectively).⁶⁹

b. Description of the exterior part of the coordination

Contrary to **2.3**, **2.4** features an interaction between the distorted Cnt ligand and another metal than the central dimer as illustrated in **Figure 2. 34**. Interestingly this additional metallic ion appears to interact with the back of the distorted Cnt ligand. Once again, quantitative analysis must be taken with caution, however the distances of the exterior neodymium ions are comparable for the two Cnt ligand, around 2.8 Å. This asks questions on the electronic structure of the KCnt. Even more so considering that this is the first time such an interaction has been observed.

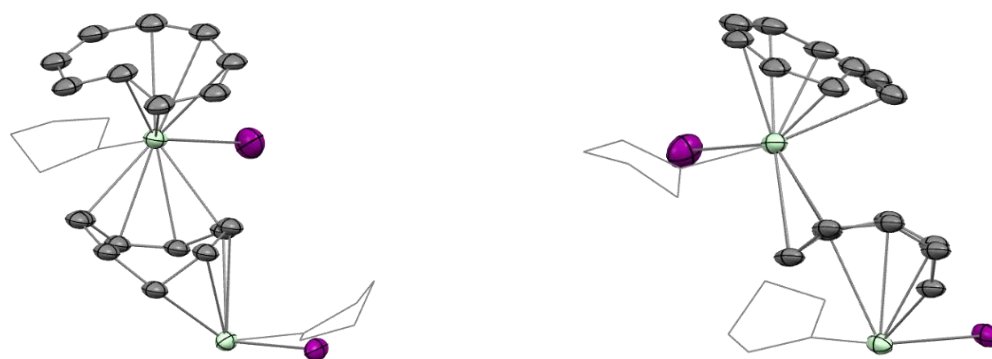


Figure 2. 34. Molecular representation of the asymmetric unit from two points of view (Nd, C, I: light green, grey, purple; thf are represented in wireframe)

Indeed, lanthanide ions are known to possess a mostly electrostatic interaction with the ligand favoring hard anionic atoms. This coordination asks the question of the localization of the charge on the distorted Cnt ligand.

Unfortunately, the low resolution does not allow study over the C—C bond length to detect a possible single-double bond character.

2. Electronic structure description

Unfortunately, the very low yield did not allow for the isolation of enough material for additional characterizations. As such, discussion over the electronic structure can only rely on the structure and the previous work on **2.1** and **2.3**. According to the crystal structure, **2.4** is overall neutral. Due to its symmetrical nature, it is granted that the structure does not possess

a radical character as a whole. Following similar logic than the discussion on **2.3**, several possibilities can be brought forward regarding the oxidation state of both the Cnt unit and the dysprosium ions. They are illustrated on **Figure 2.35**.

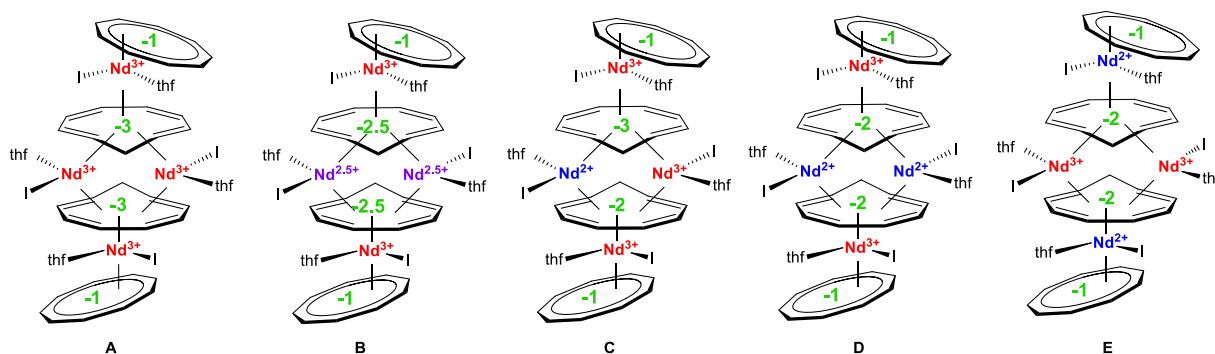


Figure 2.35 Schematic representation of the repartition of the charges in the 2.4 structure

Similarly, to reduce the number of possibilities, a few hypotheses are made. First, the attribution of a charge for the external Cnt is more challenging due to their *trans* isomerization. Whether the electronic structure influences the Cnt to remain in its *trans* form could be questioned. However, due to the lack of additional information, the $\text{Cnt}^{\text{trans}}$ ligand will be considered similarly to the ligand salt KCnt , monoanionic. The iodine ligands are also considered monoanionic.

For the Cnt ligand and the neodymium centers, several repartitions can be envisioned. One argument could be made due to the perfect symmetry of the structure that option **C** seems unlikely. This also probably applies to option **B** which would necessitates perfect delocalization of 2 electrons across two metal centers and two organic molecules. Overall, option **A**, **D** and **E** appear the most credible.

For a better understanding of the electronic structure several spectroscopic techniques could be applied. The situation being fairly similar to **2.3** in terms of thermal sensitivity and low yield, this would most likely bring few definitive results. Nevertheless, magnetism and EPR study could help probe the interaction between the two metallic centers and the potential organic radical. Once again, the presence of *f*-electrons, arguably less in the neodymium case, will complicate the EPR signal. Similarly, the expected magnetic susceptibility at room temperature for neodymium ions in their trivalent and divalent case are relatively close, meaning that an attribution would be very difficult.⁶⁵

VI. Conclusion

To conclude this chapter, KCnt can be reacted with divalent lanthanide salts to form different products. In this work, it was observed that there is a stark difference between the reactivities with Sm, Eu, Tm and Yb and the more reductive Dy and Nd. This translated in the obtention of several dimers.

The rationalization of the formation of **2.1_{thf}** and **2.1** is straightforward and the different data gathered were overall coherent. They support the formation of a radical Cnt unit from an electron transfer, in all likelihood from a divalent dysprosium center. This radical center can then couple with another to form the dimers. Different synthetic paths were explored, including from trivalent starting material. Unfortunately, the yields were low in all of them. Nonetheless, this allowed for computational and magnetic characterization.

The picture is more complicated with **2.3**. Discrepancies were observed in between the XRD structure and the computation for one part and the experimental spectra for the other part. Despite these hurdles, several scenarios of electronic repartitions were proposed. Unfortunately, the very low yield made the needed characterizations very challenging. One of the main ones being the lack of bulk study of this compound. Indeed, in the absence of NMR spectra, only SC-XRD allows identification of **2.3**. This means that it is impossible to verify that the product placed in a spectrometer, whether EPR or SQUID, indeed still contains unaltered **2.3**. As such, several possibilities were formulated to explain the lack of coherence. It is possible that preparation of the sample prompts degradation of the product either due to thermal sensitivity or loss of coordinated THF molecules. Furthermore, it could also be possible that several radicals could be present in this complex on both the Cnt and the dysprosium center creating unusual magnetic response.

Due to the absence of definitive answer, it was decided to change slightly the target compound for an heteroleptic complex featuring a bulky ligand. Indeed, preliminary results showed that reacting **2.3** with KCp^{ttt} was successful in changing the Cnt⁻ ligand for Cp^{ttt} ligand. A preliminary crystal structure showed that this was efficient at removing the THF from the coordination sphere. Consequently, this molecule was an interesting goal to study a similar electronic structure under easier conditions.

To tackle at the same time, the challenging synthesis with DyI₂, it was decided that another synthetic path was needed, particularly a route from the easier to handle and control trivalent dysprosium species.

This study will be described in the next chapter.

References

- (1) Corbett, D. *Rev Chim Min.* **1973**, *10* (1–2), pp 239–257.
- (2) Corbett, J. D. In *Synthesis of Lanthanide and Actinide Compounds*; Springer Science, 1991; pp 159–174.
- (3) Nief, F. *Dalton Trans.* **2010**, *39* (29), 6589.
- (4) Anatolii A. Fagin, M. N. B. **1999**, *5* (10), 2990–2992.
- (5) Evans, W. J.; Allen, N. T.; Workman, P. S.; Meyer, J. C. *Inorg. Chem.* **2003**, *42* (9), 3097–3099.
- (6) Evans, W. J.; Allen, N. T.; Ziller, J. W. *J. Am. Chem. Soc.* **2000**, *122* (47), 11749–11750.
- (7) Bochkarev, M. N.; Fedushkin, I. L.; Dechert, S.; Fagin, A. A.; Schumann, H. *Angew. Chem. Int. Ed.* **2001**, *40* (17), 3176–3178.
- (8) Bochkarev, M. N.; Khoroshen'kov, G. V.; Burin, M. E.; Kuzyaev, D. M.; Fagin, A. A.; Maleev, A. A.; Fukin, G. K.; Baranov, E. V. *Russ. Chem. Bull.* **2006**, *55* (3), 588–590.
- (9) Fagin, A. A.; Balashova, T. V.; Kusyaev, D. M.; Kulikova, T. I.; Glukhova, T. A.; Makarenko, N. P.; Kurskii, Y. A.; Evans, W. J.; Bochkarev, M. N. *Polyhedron* **2006**, *25* (5), 1105–1110.
- (10) Katkova, M. A.; Fukin, G. K.; Fagin, A. A.; Bochkarev, M. N. *J. Organomet. Chem.* **2003**, *682* (1–2), 218–223.
- (11) Kagan, H. B. *Tetrahedron* **2003**, *59* (52), 10351–10372.
- (12) Wang, H.; Cue, J. M. O.; Calubaquib, E. L.; Kularatne, R. N.; Taslimy, S.; Miller, J. T.; Stefan, M. C. *Polym. Chem.* **2021**, *12* (47), 6790–6823.
- (13) Evans, W. J.; Giarikos, D. G.; Allen, N. T. *Macromolecules* **2003**, *36* (12), 4256–4257.
- (14) Balashova, T. V.; Kuzyaev, D. M.; Semchikov, Yu. D.; Bochkarev, M. N. *Russ. Chem. Bull.* **2005**, *54* (11), 2506–2510.
- (15) Evans, W. J.; Allen, N. T.; Ziller, J. W. *Angew. Chem. Int. Ed.* **2002**, *41* (2), 359.
- (16) Jin, P.-B.; Luo, Q.-C.; Gransbury, G.; Vitorica-Yrezabal, I.; Hajdu, T.; McInnes, E. J. L.; Winpenny, R. E. P.; Chilton, N. F.; Mills, D. P.; Zheng, Y.-Z. ChemRxiv. 2023. <https://chemrxiv.org/engage/chemrxiv/article-details/64b69dff605c6803bee5c3e> (accessed 2023-10-02).
- (17) Mislow, K. J. *Chem. Phys.* **1952**, *20*, 1489.
- (18) Schäfer, S.; Kaufmann, S.; Rösch, E. S.; Roesky, P. W. *Chem. Soc. Rev.* **2023**, *52* (12), 4006–4045.
- (19) Coville, N. J.; Du Plooy, K. E.; Pickl, W. *Coord. Chem. Rev.* **1992**, *116*, 1–267.
- (20) Harder, S. *Coord. Chem. Rev.* **1998**, *176* (1), 17–66.
- (21) Maier, G. *Angew. Chem. Int. Ed. Engl.* **1974**, *13* (7), 425–438.
- (22) Day, B. M.; Guo, F.; Giblin, S. R.; Sekiguchi, A.; Mansikkamäki, A.; Layfield, R. *Chem. – Eur. J.* **2018**, *24* (63), 16779–16782.
- (23) Boronski, J. T.; Liddle, S. T. *Eur. J. Inorg. Chem.* **2020**, *2020* (30), 2851–2861.
- (24) Zahra, F. T.; Saeed, A.; Mumtaz, K.; Albericio, F. *Molecules* **2023**, *28* (10), 4095.
- (25) Harriman, K. L. M.; Le Roy, J. J.; Ungur, L.; Holmberg, R. J.; Korobkov, I.; Murugesu, M. *Chem. Sci.* **2017**, *8* (1), 231–240.
- (26) Katz, T. J. *J. Am. Chem. Soc.* **1960**, *82* (14), 3784–3785.
- (27) Mahieu, N.; Piątkowski, J.; Simler, T.; Nocton, G. *Chem. Sci.* **2023**, *14* (3), 443–457.
- (28) Streitwieser, Andrew.; Mueller-Westerhoff, Ulrich. *J. Am. Chem. Soc.* **1968**, *90* (26), 7364–7364.
- (29) Schäfer, S.; Bauer, H.; Becker, J.; Sun, Y.; Sitzmann, H. *Eur. J. Inorg. Chem.* **2013**, *2013* (33), 5694–5700.
- (30) Katz, T. J.; Garratt, P. J. *J. Am. Chem. Soc.* **1964**, *86* (23), 5194–5202.
- (31) Katz, T. J.; Garratt, P. J. *J. Am. Chem. Soc.* **1963**, *85* (18), 2852–2853.
- (32) Lalancette, E. A.; Benson, R. E. *J. Am. Chem. Soc.* **1963**, *85* (18), 2853–2853.
- (33) Lalancette, E. A.; Benson, R. E. *J. Am. Chem. Soc.* **1965**, *87* (9), 1941–1946.
- (34) Boche, G.; Martens, D.; Danzer, W. *Angew. Chem. Int. Ed. Engl.* **1969**, *8* (12), 984–984.
- (35) Boche, G.; Weber, H.; Bieberbach, A. *Topomerisierung* **1978**, *111* (8), 2833–2849.
- (36) Boche, G.; Bieberbach, A.; Weber, H. *Angew. Chem.* **1975**, *87* (15), 550–551.
- (37) Boche, G.; Bieberbach, A. *Chem. Ber.* **1978**, *111* (8), 2850–2858.

- (38) Murahashi, T.; Inoue, R.; Usui, K.; Ogoshi, S. *J. Am. Chem. Soc.* **2009**, *131* (29), 9888–9889.
- (39) Verkouw, H. T.; Veldman, M. E. E.; Groenenboom, C. J.; Van Oven, H. O.; De Leifde Meijer, H. J. *J. Organomet. Chem.* **1975**, *102* (1), 49–56.
- (40) Westerhof, A.; De Liefde Meijer, H. J. *J. Organomet. Chem.* **1978**, *149* (3), 321–325.
- (41) Walter, M. D.; Wolmershäuser, G.; Sitzmann, H. *J. Am. Chem. Soc.* **2005**, *127* (49), 17494–17503.
- (42) Walter, M. D. Structure and Bonding Studies of Paramagnetic Metallocenes and Their Adducts of the D- and f-Block Metals, PhD thesis, Technischen Universität Kaiserslautern, 2005.
- (43) Moutet, J.; Schleinitz, J.; La Droitte, L.; Tricoire, M.; Pointillart, F.; Gendron, F.; Simler, T.; Clavaguéra, C.; Le Guennic, B.; Cador, O.; Nocton, G. *Angew. Chem. Int. Ed.* **2021**, *60* (11), 6042–6046.
- (44) Evans, W. J.; Hughes, L. A.; Hanusa, T. P. *J. Am. Chem. Soc.* **1984**, *106* (15), 4270–4272.
- (45) Kawasaki, K.; Sugiyama, R.; Tsuji, T.; Iwasa, T.; Tsunoyama, H.; Mizuhata, Y.; Tokitoh, N.; Nakajima, A. *Chem. Commun.* **2017**, *53* (49), 6557–6560.
- (46) Münzfeld, L.; Schoo, C.; Bestgen, S.; Moreno-Pineda, E.; Köppe, R.; Ruben, M.; Roesky, P. W. *Nat. Commun.* **2019**, *10* (1), 3135.
- (47) Tricoire, M.; Münzfeld, L.; Moutet, J.; Mahieu, N.; La Droitte, L.; Moreno-Pineda, E.; Gendron, F.; Hilgar, J. D.; Rinehart, J. D.; Ruben, M.; Le Guennic, B.; Cador, O.; Roesky, P. W.; Nocton, G. *Chem. – Eur. J.* **2021**, *27* (54), 13558–13567.
- (48) Xémard, M.; Zimmer, S.; Cordier, M.; Goudy, V.; Ricard, L.; Clavaguéra, C.; Nocton, G. *J. Am. Chem. Soc.* **2018**, *140* (43), 14433–14439.
- (49) Mares, F.; Hodgson, K. O.; Streitwieser, A. *J. Organomet. Chem.* **1971**, *28* (2), C24–C26.
- (50) Münzfeld, L.; Dahlen, M.; Hauser, A.; Mahieu, N.; Kuppasamy, S. K.; Moutet, J.; Tricoire, M.; Köppe, R.; La Droitte, L.; Cador, O.; Le Guennic, B.; Nocton, G.; Moreno-Pineda, E.; Ruben, M.; Roesky, P. W. *Angew. Chem.* **2023**.
- (51) Escher, A.; Neuenschwander, M.; Engel, P. *Helv. Chim. Acta* **1987**, *70* (6), 1623–1637.
- (52) Korzyński, M. D.; Bernhardt, M.; Romankov, V.; Dreiser, J.; Matmon, G.; Pointillart, F.; Le Guennic, B.; Cador, O.; Copéret, C. *Chem. Sci.* **2022**, *13* (35), 10574–10580.
- (53) Stetsiuk, O.; La Droitte, L.; Goudy, V.; Le Guennic, B.; Cador, O.; Nocton, G. *Organometallics* **2022**, *41* (2), 133–140.
- (54) Münzfeld, L.; Hauser, A.; Gamer, M. T.; Roesky, P. W. *Chem. Commun.* **2023**, *59* (59), 9070–9073.
- (55) Katz, T. J.; Talcott, C. *J. Am. Chem. Soc.* **1966**, *88* (20), 4732–4733.
- (56) Brewer, D. A.; Schug, J. C.; Ogliaruso, M. A. *Tetrahedron* **1975**, *31* (1), 69–72.
- (57) Paquette, L. A. *Angew. Chem. Int. Ed. Engl.* **1978**, *17* (2), 106–117.
- (58) Cascales, C.; Sáez-Puche, R.; Porcher, P. *J. Solid State Chem.* **1995**, *114* (1), 52–56.
- (59) Parthey, M.; Kaupp, M. *Chem Soc Rev* **2014**, *43* (14), 5067–5088.
- (60) Brunschwig, B. S.; Creutz, C.; Sutin, N. *Chem. Soc. Rev.* **2002**, *31* (3), 168–184.
- (61) D’Alessandro, D. M.; Keene, F. R. *CChem. Soc. Rev.* **2006**, 10.1039.b514590m.
- (62) Gould, C. A.; McClain, K. R.; Yu, J. M.; Groshens, T. J.; Furche, F.; Harvey, B. G.; Long, J. R. *J. Am. Chem. Soc.* **2019**, *141* (33), 12967–12973.
- (63) Gould, C. A.; McClain, K. R.; Reta, D.; Kragoskow, J. G. C.; Marchiori, D. A.; Lachman, E.; Choi, E.-S.; Analytis, J. G.; Britt, R. D.; Chilton, N. F.; Harvey, B. G.; Long, J. R. *Science* **2022**, *375* (6577), 198–202.
- (64) Robin, M. B. MIXED VALENCE CHEMISTRY-A SURVEY AND CLASSIFICATION. 176.
- (65) Meihaus, K. R.; Fieser, M. E.; Corbey, J. F.; Evans, W. J.; Long, J. R. *J. Am. Chem. Soc.* **2015**, *137* (31), 9855–9860.
- (66) Kahn, O. *Molecular Magnetism*, 2nd ed.; Dover, 2022.
- (67) Molcas. *Molcas Manual: Poly_Aniso*.
<https://www.molcas.org/documentation/manual/node106.html> (accessed 2023-09-20).
- (68) Demir, S.; Gonzalez, M. I.; Darago, L. E.; Evans, W. J.; Long, J. R. *Nat. Commun.* **2017**, *8* (1), 2144.
- (69) Jaroschik, F.; Momin, A.; Nief, F.; Le Goff, X.-F.; Deacon, G. B.; Junk, P. C. *Angew. Chem.* **2009**, *121* (6), 1137–1141.

Chapter 3: A trivalent approach to access dimeric lanthanide complexes with bridged Cnt ligands

I.	Heteroleptic approach from trivalent starting material	127
1.	Rationalization for the new path	127
2.	Development of the new synthetic path	129
3.	Synthesis and characterizations of Dy ₂ Cnt ₂ Cp ^{ttt} ₂ (3.3)	135
II.	Direct reduction before the formation of the Cnt—dysprosium species	141
1.	Synthesis and characterization of Dy ₂ CntCp ^{ttt} ₂ I (3.4)	141
2.	Synthesis and characterizations of <i>endo</i> -Dy ₂ Cnt ₂ Cp ^{ttt} ₂ (3.3-endo)	152
III.	Extension to other lanthanides	154
1.	Synthesis of LnCp ^{ttt} ₂ (thf) ₂ (3.1_{Ln})	154
2.	Adaptation of the synthesis	156
3.	Structural study of Ln ₂ Cnt ₂ Cp ^{ttt} ₂ (3.3_{Ln})	157
4.	Study of Er ₂ CntCp ^{ttt} ₂ I (3.4_{Er})	158
IV.	Discussion and conclusion on the Cnt species in its reduced form	161
	References	164

Chapter 3: A trivalent approach to access dimeric lanthanide complexes with bridged Cnt ligands

I. Heteroleptic approach from trivalent starting material

1. Rationalization for the new path

As mentioned in the previous chapter, there are two paths for the obtention of reduced lanthanide complexes. Either, starting from a reduced starting material such as the LnI_2 which have been described previously, or, from the reduction of an oxidized species.

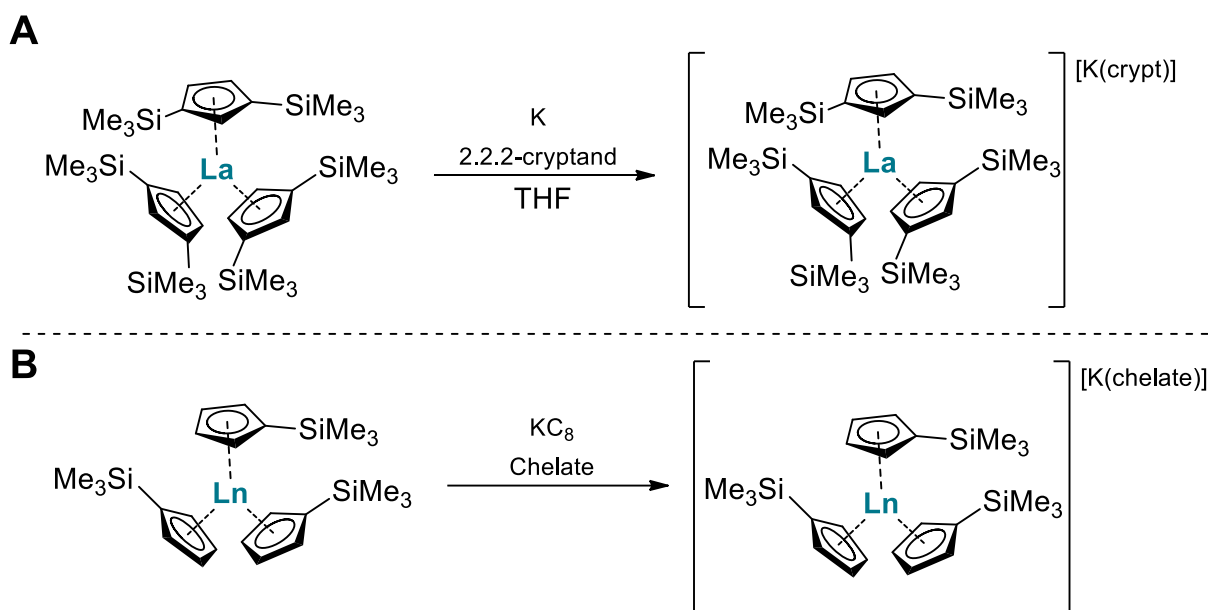
1. Departing from standard divalent starting material

Because of the challenge to work with non-classical divalent lanthanide the reduction path has become the preferred route in the literature.^{1,2} It has been developed in parallel with the development of the divalent chemistry of thulium, dysprosium and neodymium complexes.^{3,4} Indeed, the groups which greatly advanced the synthesis and use of LnI_2 ($\text{Ln} = \text{Nd}, \text{Dy}$ and Tm) such as Evans, Bochkarev and Nief, also realised that the reduction path could help isolating divalent lanthanide of otherwise inaccessible ions.⁵

To prevent unwanted reactivity with either the atmosphere or the solvent, the strategy was based on trivalent starting material, often with two stabilizing bulky Cp ligand and a halogen.^{4,6,7} Those complexes were then reduced using a standard heterogenic reductant for inorganic chemistry, KC_8 .⁸ One advantage of this method is that the reducing potassium metal will then stay in the scaffold and can be trapped by either a cryptand or crown ether molecule.^{9,10} This was particularly highlighted in the group of Nief which elegantly showed that even though the halogenated ligand is still in interaction with the lanthanide centre, the latter display typical divalent character.^{6,7}

2. Extension of these strategy for the full series

As an example, the work started by Lappert and later extended by Evans proposed a similar procedure illustrated in **Scheme 3. 1** for the tris Cp lanthanide complexes.¹¹ To increase the stability, they opted for Cp ligands substituted with trimethylsilyl groups. Both potassium and potassium graphite were used as reductants. Those very bulky and stabilized complexes allow to apply this method to the entire lanthanide series with the exception of radioactive promethium.¹²⁻¹⁴



Scheme 3.1 Synthesis of divalent lanthanide; **A** reports the original synthesis by Lappert and coworkers¹¹; **B** illustrates the scaffold chosen by Evans to extend this chemistry to most of the lanthanides (Ln = La, Ce, Pr, Nd, Sm, Gd, Tb, Dy, Ho, Er, Tm, Yb, Lu and chelate = 18-crown-6 or 2.2.2-cryptand).^{12–14}

This discovery constitutes a turning point in the lanthanide chemistry showing that under the right circumstances, all those metals could show divalent character.⁵ However, the particularity of Evans's compounds is their bulkiness which allows their reduction and stability, also preventing their reactivity. More recently, multiple works on divalent lanthanide have shown that the bis-Cp sandwich complexes could be made stable with multiple substituted ligand such as Cp^{ttt} and Cp^{iPr5} opening new doors of reactivity as well as spectroscopic and magnetic investigations.^{1,2,15}

3. Heteroleptic approach to tackle the reduction of Cnt ligand

The use of the Cnt ligand together with divalent lanthanide halide has been explored in the previous chapter. However, the challenging synthesis due to the high reactivity, thermal sensitivity and the very low yield rendered difficult a detailed and coherent characterisation of the species. For this reason, it was decided to change the strategy and investigate trivalent approaches to our synthetic issues.

In the previous chapter, it was mentioned that no adequate starting material of Ln—Cnt was found that could lead to similar molecules when reduced. As such, an heteroleptic approach seemed necessary to obtain equivalent dimers.

Moreover, the presence of THF molecules coordinated in **2.3** was presumed to be an issue in the characterisation of this species. It was then decided to target compounds, featuring a bulkier and strongly coordinated ligand. The Cp^{ttt} ligand has been extensively studied in the

laboratory particularly in association with divalent thulium and is known to be very sterically demanding.^{6,15,16}

We felt that this approach would tackle most of the challenging part of the previous synthesis as well as potentially allowing access to similar molecule which could help our understanding of the electronic structure of **2.3**.

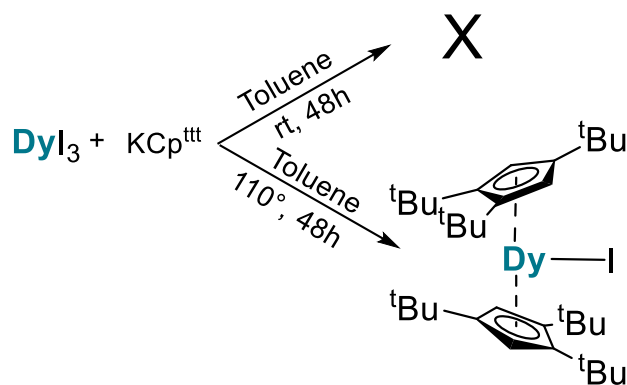
2. Development of the new synthetic path

The aim for this study is to synthesize an heteroleptic compound featuring one Cp^{ttt} ligand and one Cnt unit, which will then be reduced. Considering the weak coordination of Cnt ligand with lanthanide metals, it was decided to install it last. As such the first efforts were targeted toward the coordination of the Cp^{ttt} ligand. In a second step, the coordination of Cnt ligand was investigated. The condition for the reduction will be discussed last.

1. Formation of the Cp^{ttt}— dysprosium complex

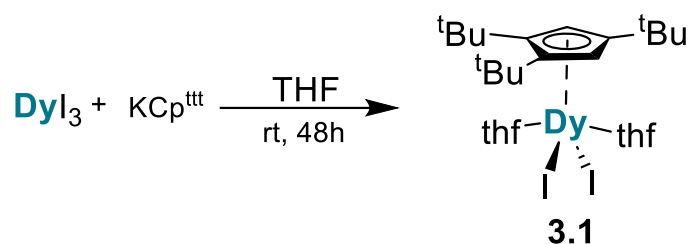
a. Salt metathesis conditions

Due to the nature of the starting material, a salt metathesis route was preferred. Two of the main starting material for lanthanide chemistry are the iodide and chloride salts.¹⁷ LnCl₃, was initially investigated because of its relatively lower cost, however, it showed the formation of multimetallic assemblies rather than the straightforward coordination of the Cp ligand to form monomeric complexes. The iodine salt was then selected as the starting material. Considering the observed difficulty to handle complexes of lanthanide with the Cnt ligand when THF molecules are present, several trials were run to optimize the reaction in toluene and prevent the formation of any THF adduct. However, the low solubility of the starting material in this solvent prevents the formation of the Cp^{ttt}DyI₂ at room temperature, while running the reaction at higher temperatures directly yields a double substitution to form DyCp^{ttt}₂I as illustrated in **Scheme 3. 2**.



Scheme 3. 2 Attempt at running salt metathesis reaction in toluene

As a consequence, the synthesis in THF was then adopted and ran as illustrated in **Scheme 3.3**. The product **3.1** was obtained as clear crystalline blocks. And additional crystallizations were carried out to increase the yield.



Scheme 3.3 Salt metathesis reaction in toluene to form **3.1** in 51 % yield.

b. Solid state characterization

The crystals were characterized through SC-XRD. The product crystallizes in the C2/c space group and the structure is presented in **Figure 3.1**. Two iodine atoms and one Cp^{tBu} ligand are shown coordinated around the lanthanide which is in agreement with the trivalent oxidation state. Additionally, two THF molecules are present in the first coordination sphere.

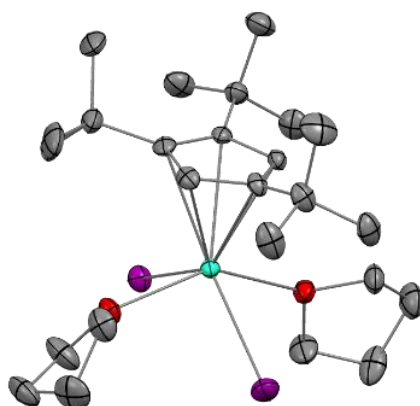


Figure 3.1 Molecular representation of **3.1** at 50% probability, dysprosium atoms are represented in light green, iodine in purple, oxygen in red and carbon in grey. Hydrogen atoms are omitted for clarity.

The overall distances are also in agreement with a trivalent dysprosium center. The Dy—I distances sit at 2.9713(3) Å and 3.0012(3) Å which is quite close to 2.9618(5) Å reported by Nief for DyI(Cp^{tBu})₂.¹⁸ Similarly, the Dy—C_{ent} (Cp^{tBu}) distances are close to what is reported with 2.37 Å compared to 2.38 Å and 2.39 Å.¹⁸

c. NMR spectroscopy

Contrary to **2.1** and **2.3**, this compound was characterized by ¹H NMR spectroscopy. **3.1** is paramagnetic as demonstrated by the chemical shifts observed in **Figure 3.2**. The signals from the Cp^{tBu} ligand can be observed and show a relative symmetry as one peak integrates for two of the ^tBu groups. A third smaller signal can be observed integrating for the two aromatic protons of the Cp^{tBu} unit.

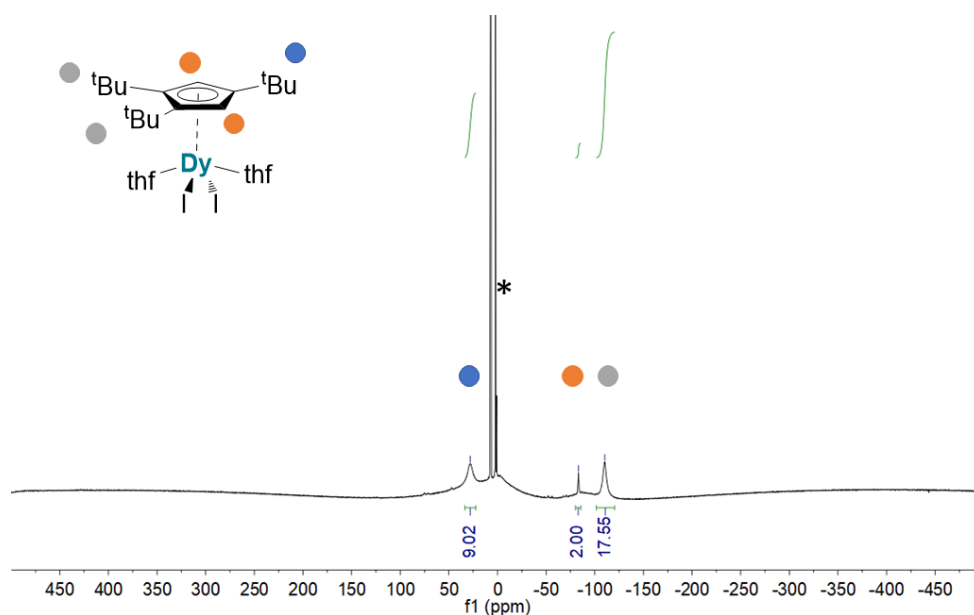


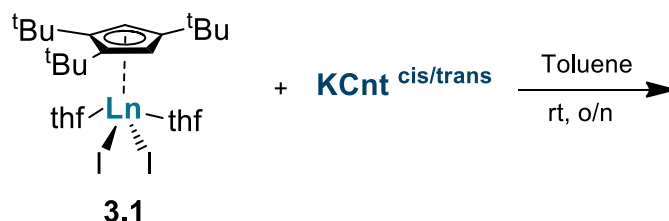
Figure 3.2 ^1H NMR of **3.1** in toluene- d_8 measured at 293 K (* residual protio signal of the solvent)

The next step in the sequence is to install a Cnt moiety in the coordination sphere.

2. Complexation of the Cnt

a. Straightforward approach

The first attempts were carried out by simple salt metathesis with **3.1** and KCnt in toluene to favour the coordination as shown in **Scheme 3.4**.



Scheme 3.4 Reaction conditions chosen to perform the salt metathesis with KCnt salt.

3.1 is rather soluble in this solvent. However, the KCnt salt is not. Nevertheless, after a few hours, the supernatant was observed to evolve from clear to yellow. In situ NMR following of the reaction showed a modification of the peaks indicating a new species. The supernatant was filtered and concentrated. The deep yellow solution was placed in the freezer to crystallize. The resulting yellow blocks were analysed through XRD. The complex crystallizes in $P2_1/c$ and only half of the molecule is contained in the asymmetric unit, the full structure is shown in **Figure 3.3**. It revealed that the Cnt motif was not coordinated to the metal center.

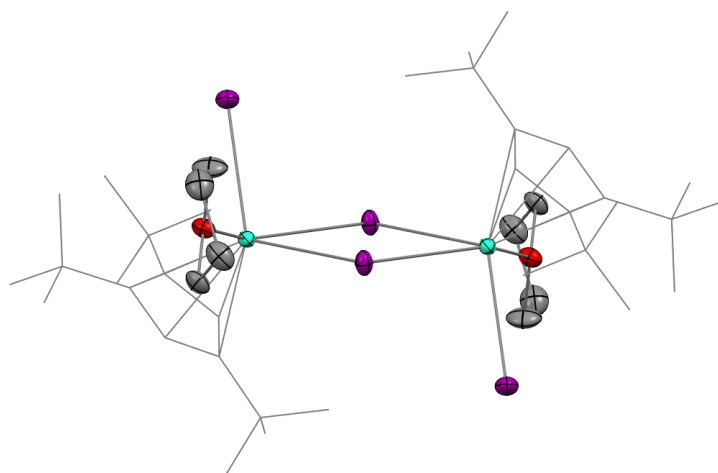
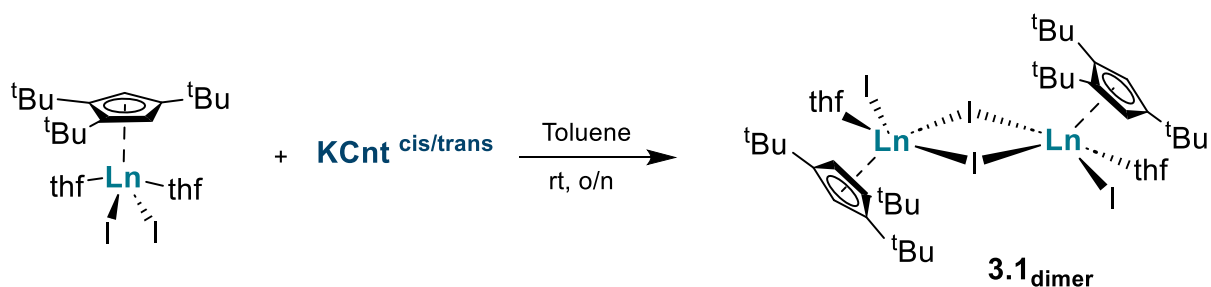


Figure 3. 3 Molecular representation of the dimer at 50% probability, dysprosium atoms are represented in light green, iodine in purple, oxygen in red and carbon in grey. Hydrogen atoms are omitted for clarity and Cp^{ttt} ligand are presented in wireframe.

Rather than promoting precipitation of potassium iodide, addition of one equivalent of KCnt seems to have prompted removal of one THF molecule. This in turn favoured a dimerization of the starting material to give **3.1_{dimer}** according to **Scheme 3. 5**.

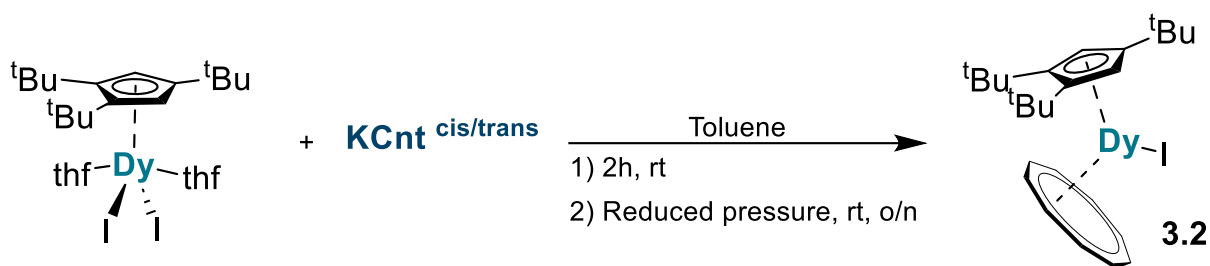


Scheme 3. 5 Dimerization of the starting material upon addition of KCnt.

This shows, once again, that the complexation of the Cnt motif in presence of coordinating solvent is not often the favoured reaction.

b. Modification of the conditions to remove THF molecules

To remediate that, the reaction was allowed to run for a couple hours and then placed under reduced pressure for the remainder of the time, see **Scheme 3. 6**. A similar method was used for the synthesis of TmCnt₂ starting from the thf adduct of TmI₂.¹⁹ The reaction mixture turned deep yellow over the course of 15 h. The supernatant was then treated by filtration and concentration.



Scheme 3. 6 Salt metathesis under reduced pressure to form 3.2

c. Solid-state characterization

Crystallization of this solution yielded yellow blocks, which were characterized through XRD. This compound crystallizes in $P2_1/n$ and two molecules are present by asymmetric units. One of these molecules is represented in **Figure 3.4** and shows coordination of one Cnt.

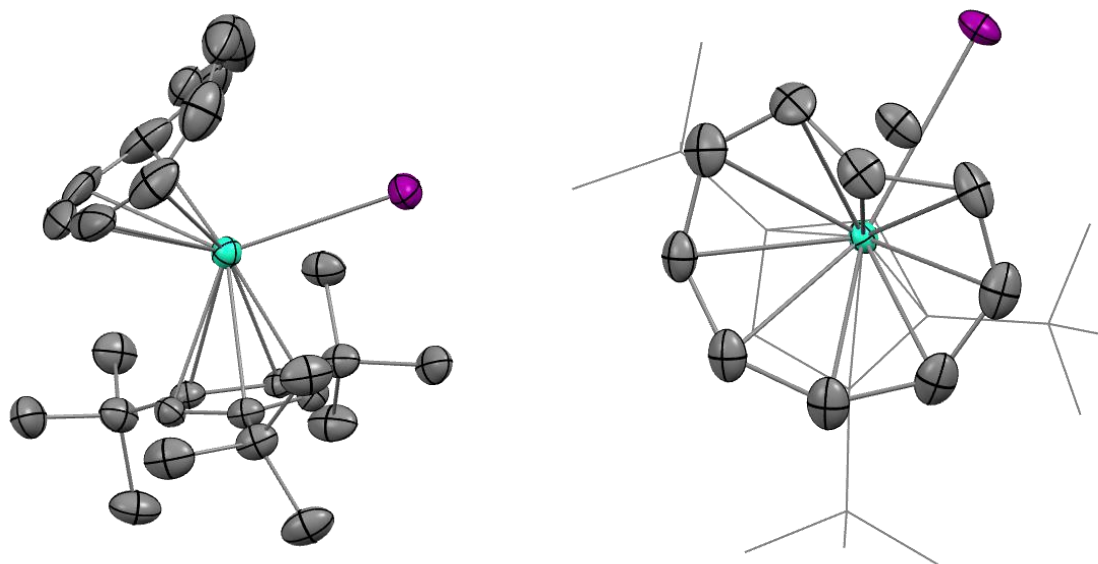


Figure 3. 4 Molecular structure of 3.2 represented at 50% probability, dysprosium atoms are in light green, iodine in purple and carbon atoms in grey. Hydrogen atoms were omitted for clarity. The left panel constitutes a side view of the molecule and on the right, a top view of the Cnt ligand is shown with the Cp^{tt} ligand represented in wireframe for clarity.

Interestingly, the structure shows the complete removal of the coordinated THF. One iodine is still coordinated in accordance with the trivalent state of the metallic center.

For the Cnt moiety, two of its distinctive features are displayed here. First, the modelling of the structure with a standard full *cis* Cnt moiety leaves a high-density peak on the inside of the ring as illustrated in **Figure 3. 5 left**. This peak can be attributed to a fraction of carbon atoms and allows modelling the isomerisation of the Cnt ligand in the solid-state as displayed in **Figure 3. 5 right**. The Cnt ligand shows a low hapticity mode as demonstrated in **Table 3. 1**. Indeed, by attributing centroids corresponding to several hapticity, it can be noticed that the

centroid for η^6 is notably closer to the metallic center than both of the η^9 centroids for the isomers *cis/trans*.

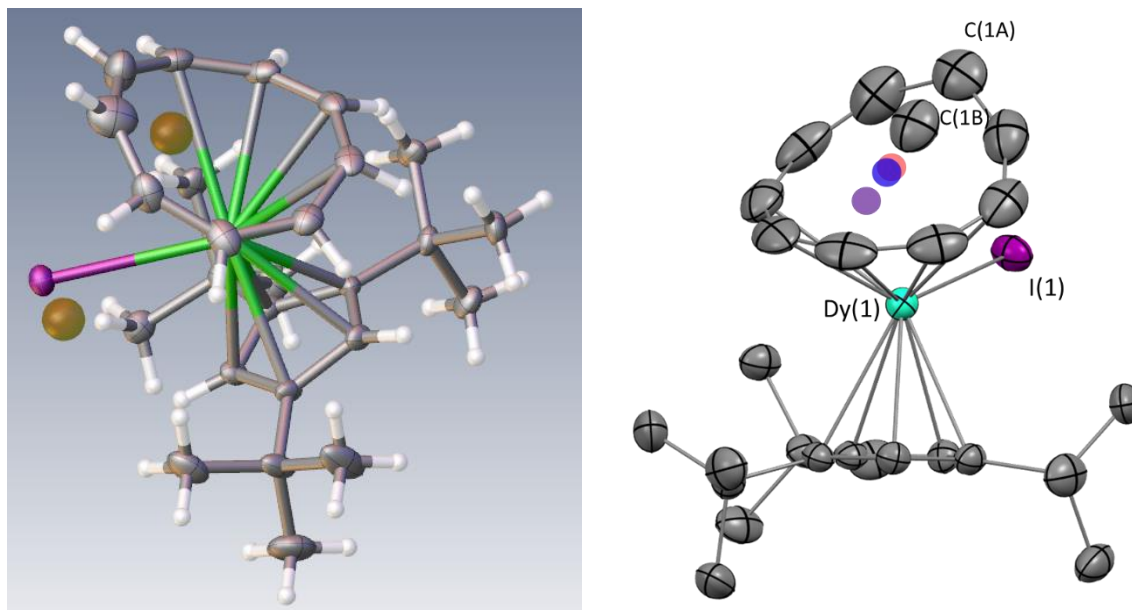


Figure 3. 5 Molecular representation of **3.2**, on the left a partially solved structure is shown with residual density peaks noted in brown and stemming from a certain degree of isomerization. On the right, thermal ellipsoids are depicted at 50% probability level. In both, dysprosium atoms are in light green, carbon in grey and iodine in purple. Hydrogen atoms are omitted for clarity on the right figure and the red, blue and purple spots represent the centroids for the *Cnt-cis*, the *Cnt-trans* and the *Cnt* in η^6 hapticity respectively.

Overall, as reported in **Table 3. 1**, the distances Dy—I are very similar to **3.1**. The slightly smaller Dy—C distances can probably be explained by the replacement of an iodine with a large electronic cloud by a flexible Cnt ligand.

Distances (in Å)	3.1	3.2
Dy(1)—I(1)	3.0012(3)	3.0117(4)
Dy(1)—I(2)	2.9713(3)	NA
Dy(1)—C (Cp ^{ttt})	2.629(3) – 2.709(3)	2.596(3) – 2.689(3)
Dy(1)—Cent (Cp ^{ttt})	2.38	2.35
Dy(1)—Cent (Cnt- η^6)	--	2.01
Dy(1)—Cent (Cnt- η^9 - <i>cis</i>)	--	2.16
Dy(1)—Cent (Cnt- η^9 - <i>trans</i>)	--	2.11

Table 3. 1 Main distances and comparison for **3.1** and **3.2** (-- denotes the non-availability of the measure).

d. NMR spectroscopy

This product was characterized through ^1H NMR spectroscopy and shows four main peaks. Due to the paramagnetism of the dysprosium ion and a more complicated structure, the peaks are difficult to attribute. One hypothesis is that, as observed in the solid-state structure,

two products are present depending on the isomerisation of the Cnt moiety. As it will be developed in **Chapter 4**, concomitant studies revealed the influence of light on the isomerization ratio of the Cnt-containing complexes. As such, the speciation of **3.2** was briefly investigated through irradiation at several wavelength. Preliminary result suggests that indeed, two species are present in this sample, and the corresponding peaks are represented in **Figure 3. 6** along a possible attribution of the isomers. The proposed attribution cis/trans is based upon the ratio obtained in the solid structure. Unfortunately, further attribution of the peaks is complicated as it appears that all the peaks are not visible. Additional experiments with larger spectral width as well as VT-NMR investigation could help identify all the signals.

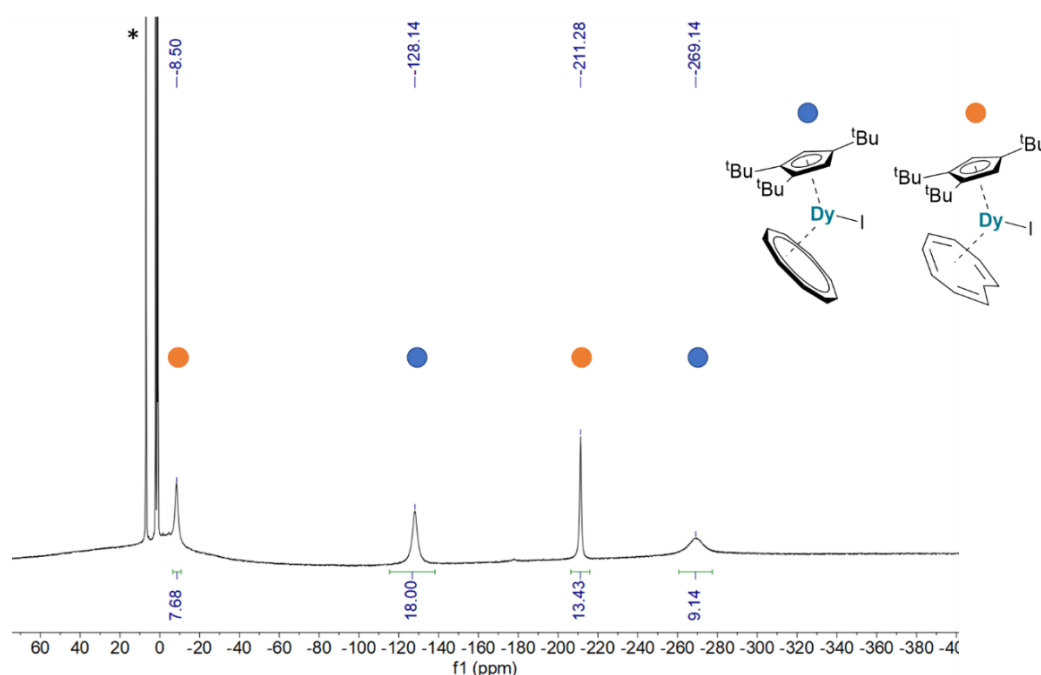


Figure 3. 6. ^1H NMR of **3.2** in toluene- d_8 measured at 293 K (* residual protio signal of the solvent) A proposed peak attribution is also given.

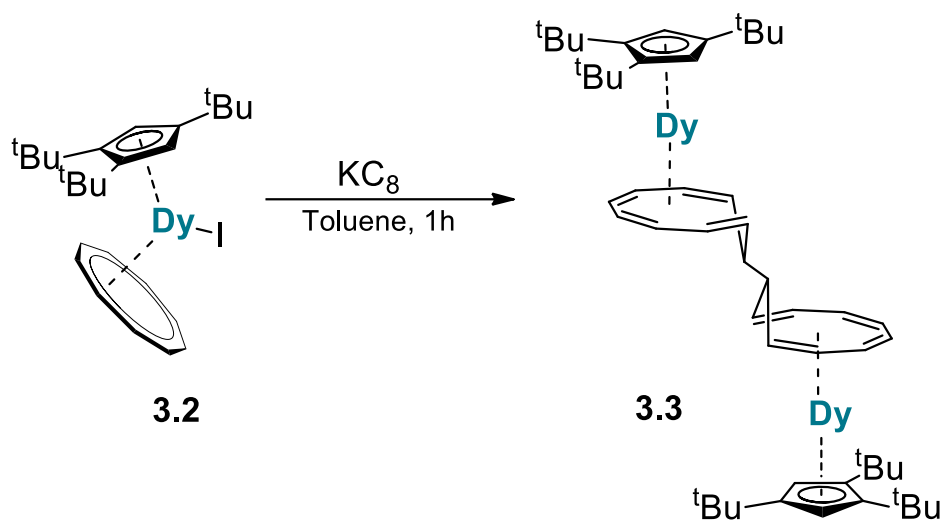
The reason of this non-isomerisation towards the *cis* form is unknown. It was not observed in the formation of **2.3**. However, it was seen for the formation of reduced neodymium containing species **2.4**. The question of isomerisation will be further discussed in **Chapter 4**.

3. Synthesis and characterizations of $\text{Dy}_2\text{Cnt}_2\text{Cp}^{\text{tnt}}_2$ (**3.3**)

Once the trivalent species containing both a Cp^{tnt} and a Cnt motif was obtained, only the matter of the reduction was left.

1. External reduction to form the coupled species

To proceed with the reduction, the ubiquitous reductant KC_8 was selected. The reaction was run according to the following **Scheme 3. 7**.



Scheme 3.7 Synthesis of **3.3** by reduction of **3.2** in the presence of KC₈.

The important solubility of **3.2** thanks to the Cp^{ttt} ligand render this reduction possible in non-polar solvent such as toluene. The reaction mixture quickly turns orange-red and the reaction is stopped after one hour. The supernatant is filtered and placed to crystallize at room temperature. Orange crystals of the desired compound readily appears in the medium. **3.3** is sparingly soluble in toluene and as such, any attempt at drying and resolubilizing this compound yielded very low concentration solutions. However, fully dried powder washed with pentane yielded pure microcrystalline product.

2. XRD analysis

a. Overall structure

Large orange block crystals were obtained from the supernatant placed at low temperature. They were analysed through SC-XRD and the corresponding solid-state structure is presented in **Figure 3.7**. This structure shows a clear resemblance with **2.1**. Only half of the molecule is present in the asymmetric unit and a similar crystallographic axis allows reconstruction of the dimer. The full complex bears a Cnt₂ type ligand with likely, an overall – 4 charge to create a neutral arrangement. Similarly, on each end of the structure, sits a mono-anionic ligand. Here the structural rigidity of Cp^{ttt} allows it to display the expected η^5 hapticity.

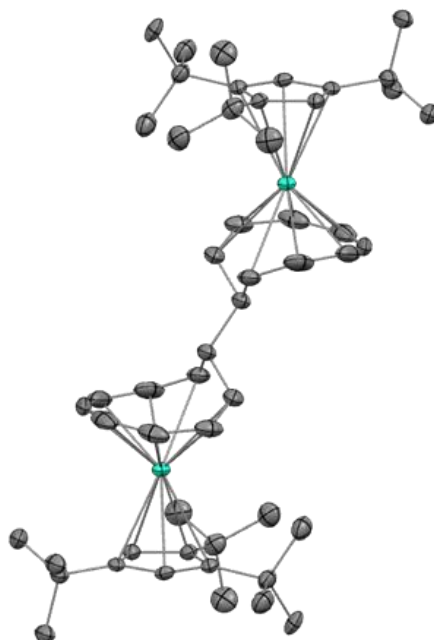


Figure 3. 7 Molecular structure of **3.3** represented at 50% probability, dysprosium atoms are in light green and carbon atoms are in grey. Hydrogen atoms are omitted for clarity.

b. Quantitative comparison

This structure can be quantitatively compared to the **2.1** structure by taking a few common references. For example, centroids can be constructed with an η^5 hapticity of the external ligand and η^8 aromaticity for the central Cnt as displayed in **Figure 3. 8**.

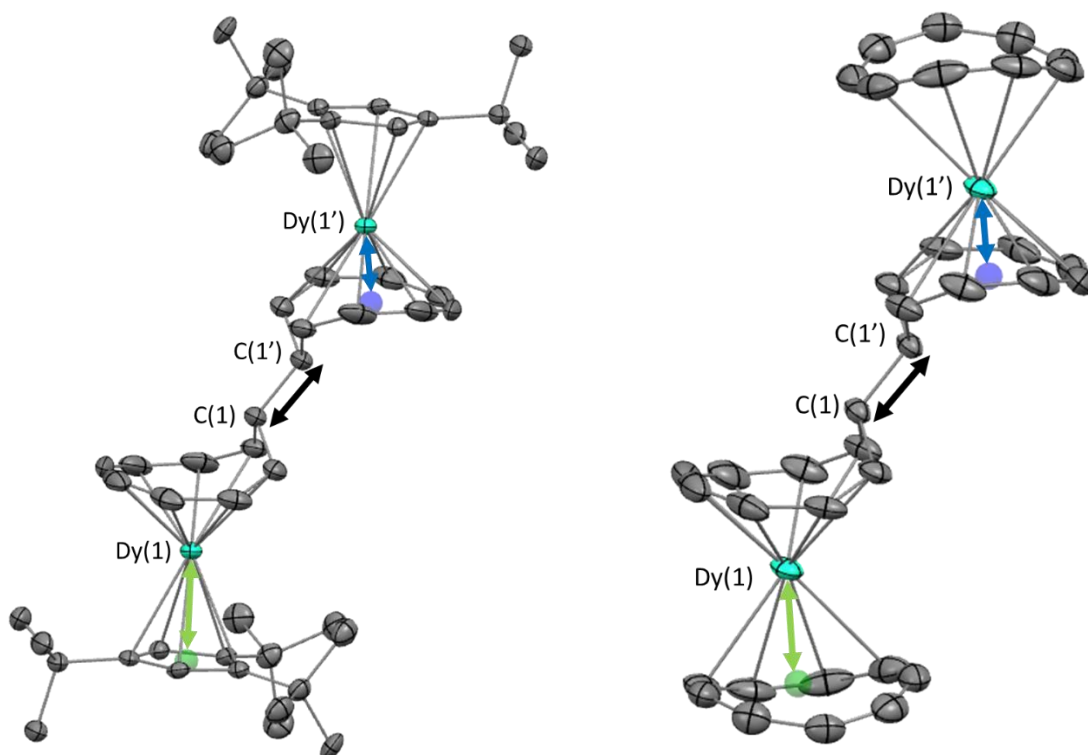


Figure 3. 8. Side by side comparison of the molecular structure of **3.3** (on the left) and **2.1** (on the right).

The relevant distances are gathered in the following **Table 3. 2**.

Distances (in Å)	3.3	2.1
Dy(1)—Dy(1')	7.771(1)	7.827(1)
Dy(1')—Cent η^8	1.65	1.65
C(1)—C(1')	1.538(5)	1.532(2)
Dy(1)—Cent η^5	2.35	2.19

Table 3. 2 Relevant distances to compare the structure of **2.1** and **3.3**

This comparison shows few differences. Overall, the metrics are fairly similar particularly the central unit around the reduced Cnt. The main difference is located on the Cnt⁻ of the molecule between the metal and the centroid of the capping ligand. The distance is similar for **3.3** compared to **3.2** and **3.1** with 2.35 Å, 2.35 Å and 2.38 Å respectively. Interestingly, the flexibility of the Cnt moiety seems to allow an hapticity switch which effectively brings the centroid closer to the dysprosium to 2.19 Å. This could seem counterintuitive as Cp^{ttt} ligands are known for their strong coordination behaviour. Nevertheless, it is also a bulky ligand which, in this case might explain why the highly flexible Cnt ligand is able to go closer.

3. Magnetism study

a. Magnetization curve

To further characterize this species, we investigated its magnetic behavior. The magnetization was recorded and is presented in **Figure 3. 9**.

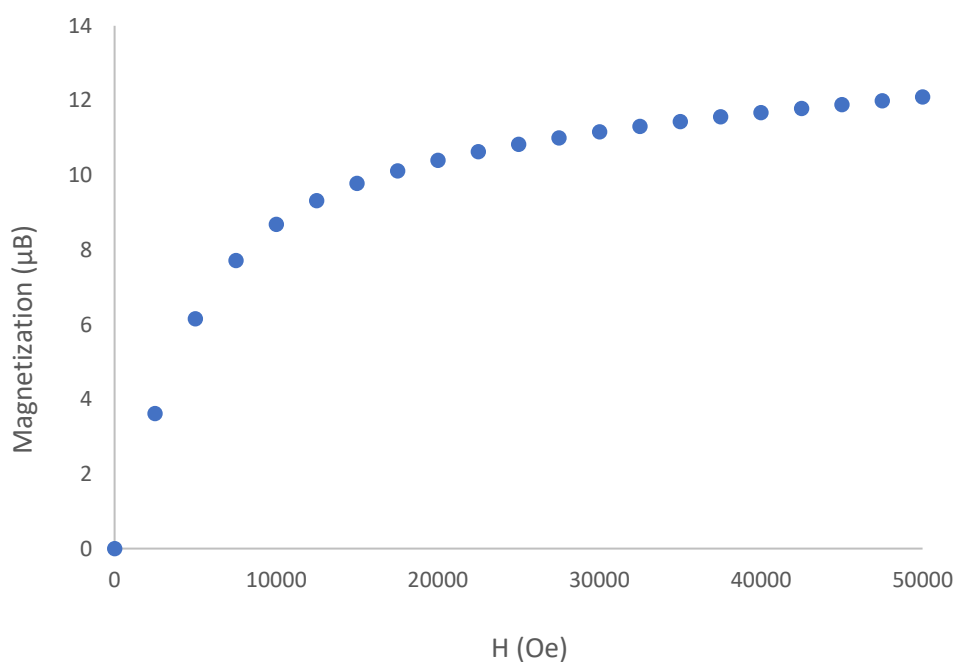


Figure 3. 9 Graphical representation of the magnetization of **3.2** at 2 K as a function of the external field.

The values of around 12 μB appear mostly coherent with a dysprosium dimer. The usual plateau reached at high field does not appear here, this could indicate the sample might have been oriented by the field of the spectrometer.

b. Magnetic susceptibility

The magnetic susceptibility was also recorded and is presented in **Figure 3. 10** as a product with the temperature.

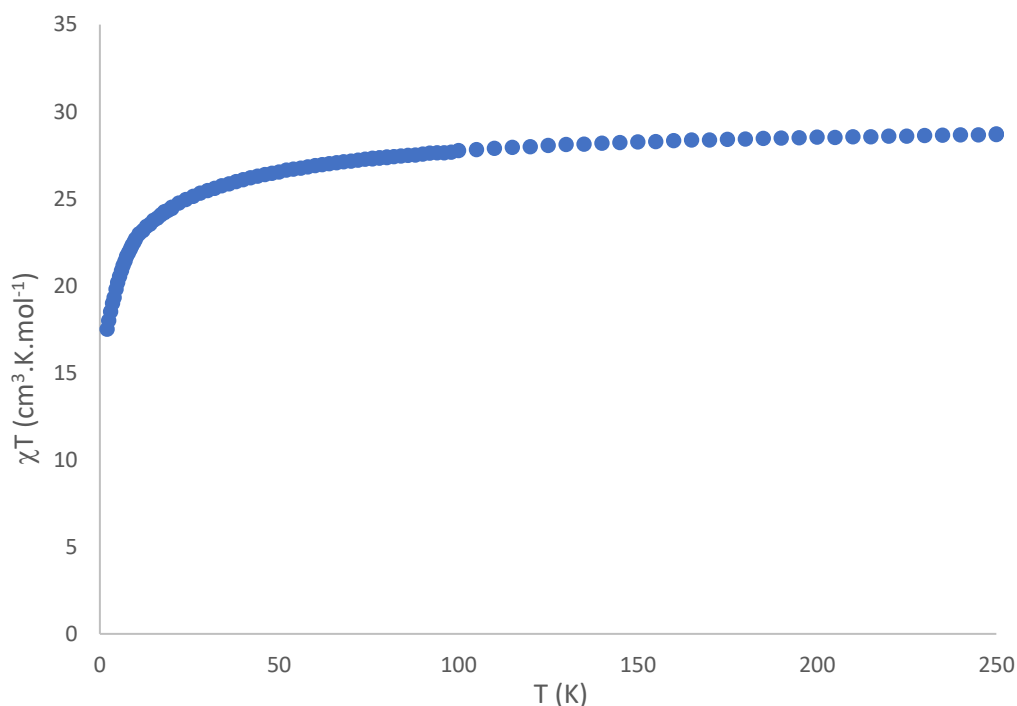


Figure 3. 10 Graphical representation of the product of the magnetic susceptibility by the temperature of **3.3** as a function of the temperature.

Here a plateau is reached at high temperature as expected for a paramagnet with Curie behavior. Furthermore, the value of the plateau is coherent with two trivalent dysprosium centers. As mentioned in this manuscript, the values for divalent and trivalent dysprosium centers are often close. However, the agreement between the structure and the rationalisation of the mechanism as well as the magnetism constitutes several indicators that **3.3** is indeed a dimer of trivalent dysprosium.

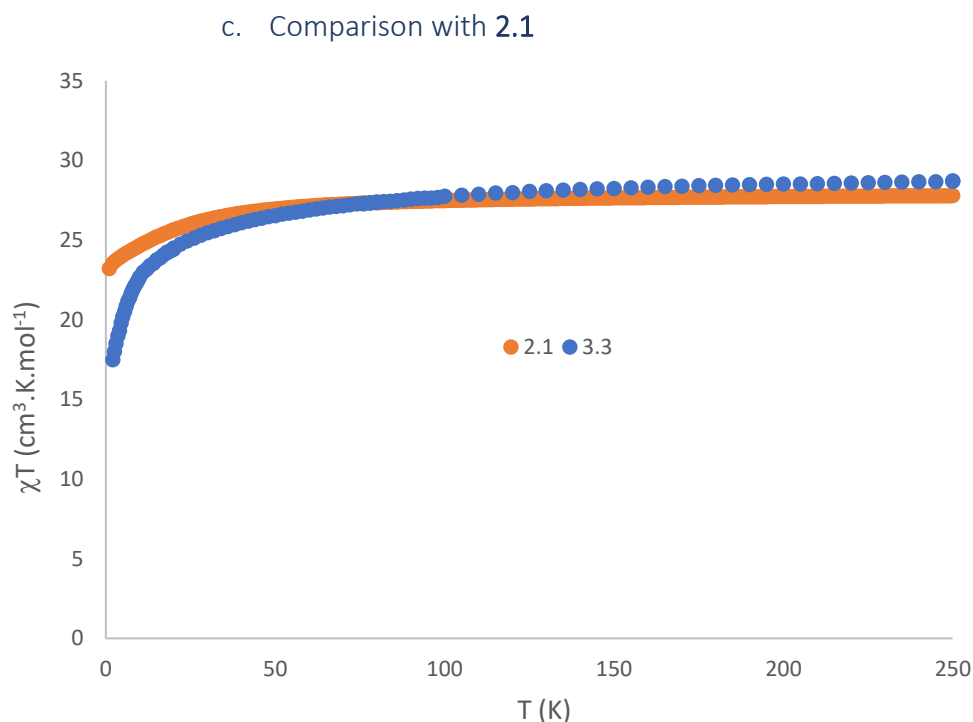


Figure 3. 11 Overlay of the graphical representations of the product of the magnetic susceptibility by the temperature of **3.3** and **2.1** as a function of the temperature.

The comparison with the Cnt-analogue **2.1** shows a slightly different behavior at low temperature. Indeed, a relatively important decrease is observed for **3.3**. This could be indicative of the population of the substate $m_j = 13/2$ even at low temperature and as such of the weak energy difference between the substate. Furthermore, no AC signal was detected for this compound in the absence of a field. Overall, these characterizations are coherent with the presence of ground state resulting from a mixing of the substate $m_j = 15/2$ and $m_j = 13/2$ at low temperature prompting fast magnetic relaxation. It could be interesting to investigate the behavior of **3.3** through computational means to determine if this is reproduced. Particularly, the capping Cnt ligand appears better suited to favor the substate $m_j = 15/2$. As seen in **I.1.2**, it is interesting to note that the centroid for the η^5 hapticity of the Cnt ligand sits closer to the dysprosium center than for the Cp^{ttt} ligand. This could help the Cnt to enforce a slightly stronger crystal field and prevent mixing of the substate.^{20,21}

II. Direct reduction before the formation of the Cnt–dysprosium species

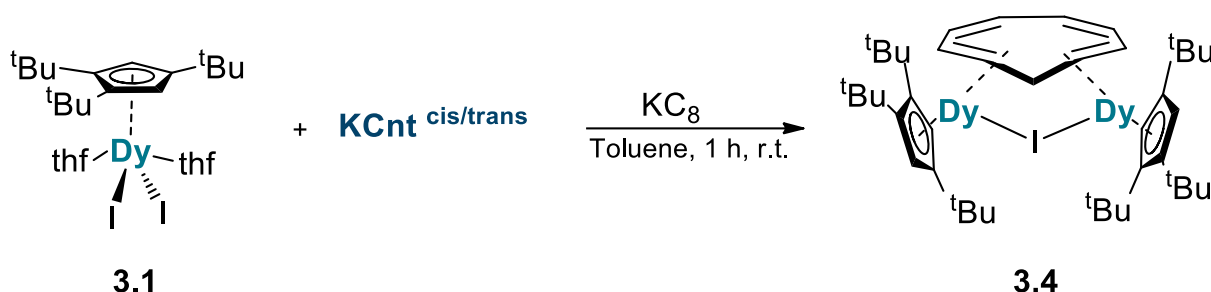
The previous study showed how to obtain a heteroleptic analogous complex of **2.1**. But the most problematic studies were those on **2.3**. As such, other reductions were attempted by changing the conditions.

1. Synthesis and characterization of Dy₂CntCp^{ttt}₂I (**3.4**)

Considering that the stepwise approach yielded the less reactive coupled species **3.3**, we decided to adopt a method similar to those with DyI₂ and try to perform the coordination of Cnt and the reduction concomitantly.

1. Synthesis

The reaction was run according to **Scheme 3. 8** where the starting complex **3.1** is reacted with KCnt and KC₈ *in situ*. To promote the coordination of Cnt ligand, the reaction was run in toluene. First attempts were tried at room temperature, as the reduced species should only appear transiently. The supernatant could be seen turning deep purple over the course of an hour. This supernatant was then filtered and evaporated to dryness. The residue was extracted with pentane to give a deep purple supernatant. Concentration at cold allowed the obtention of brown needles of the product.



Scheme 3. 8 Synthetic scheme for the formation of 3.4

2. Structural considerations

a. Overall structure

Even though the crystallinity of the previous brown needle was proven by the obtention of X-ray diffraction pattern, the data extracted were of poor quality. Despite several effort to mitigate the crystallization conditions, a better structure was not obtained through this route. However, an alternative synthetic method – reduction of a very concentrated solution of **3.2** – yielded suitable crystal that confirmed the structure and allowed for structural analysis. The complex crystallizes in the P2₁/c space group and the structure is shown in **Figure 3. 12**.

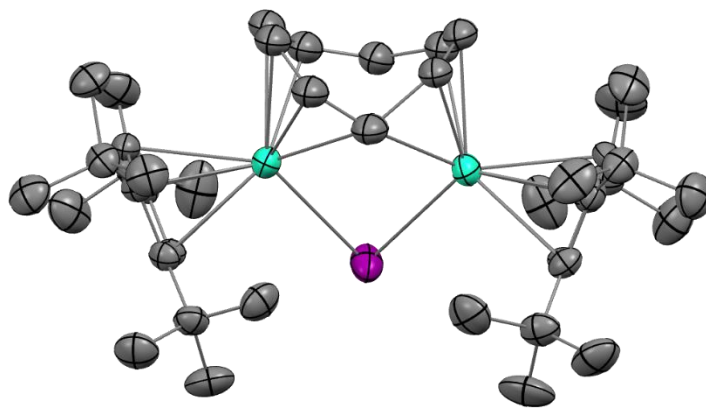


Figure 3. 12 Molecular structure of **3.4** represented at 50% probability, dysprosium atoms are in light green, iodine in purple and carbon atoms are in grey. Hydrogen atoms are omitted for clarity. A disordered Cnt ligand is omitted for clarity.

This structure is reminiscent of **2.3** with a bridging type Cnt unit. Interestingly the use of Cp^{ttt} ligand allows to avoid coordination of the THF molecules present in **3.1** from the first coordination sphere. Additionally, an iodine atom can still be seen in interaction with the two dysprosium centers deviating from the reactivity of divalent dysprosium. The reason for this remaining iodine interaction is unknown, particularly since the fragment [Dy-Cnt-Dy] appeared stable in **2.3**. A more detailed comparison of **2.3** and **3.4** will be discussed in the conclusion of this chapter.

Another important difference is the lack of symmetry in **3.4**.

b. Disordered Cnt

Indeed, the Cnt unit appears skewed toward one dysprosium ion. However, as mentioned in **Figure 3. 12**, one of the disordered Cnt ligand is omitted as such this needs to be investigated further. As illustrated in **Figure 3. 13**, the two Cnt units look like mirror image of each other.

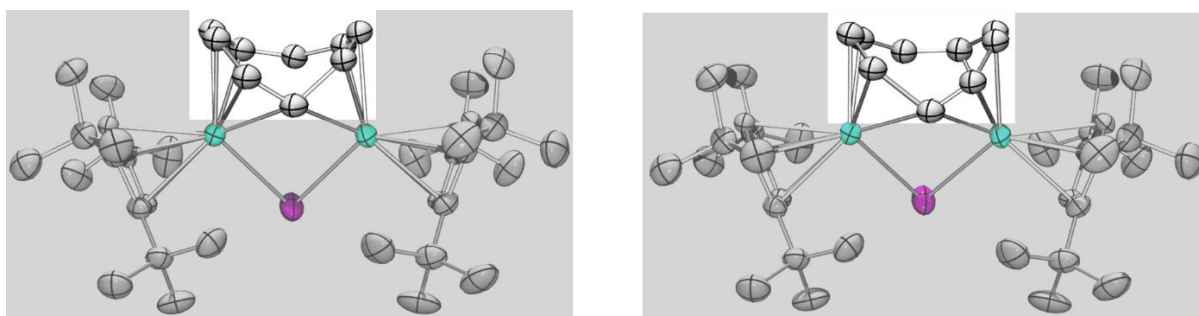


Figure 3. 13 Side by side comparison of the disordered Cnt unit in **3.4**. The disorder ratio is 70% for the left molecule.

However, analysis of the C—C bond distances disclose that they are different as shown in **Table 3. 3**. Particularly for the disordered Cnt, the extremes are more shifted compared to the other Cnt. This could translate to a different electronic structure however, the average C—C bond distances over each Cnt unit are extremely close. As such, it is difficult to conclude

whether this phenomenon comes from an artefact of the XRD model or an actual electronic difference from two singular Cnt species.

Distances (in Å)	3.3 Cnt 1	3.3 Cnt 2
List C—C distances	1.39(1)	1.28(3)
ordered by increasing	1.39(1)	1.40(3)
values	1.39(2)	1.40(4)
	1.40(2)	1.41(3)
	1.40(2)	1.41(3)
	1.40(2)	1.41(4)
	1.41(2)	1.42(4)
	1.42(1)	1.42(4)
	1.62(2)	1.75(3)
C—C bond averaged over the Cnt	1.42(8)	1.43(13)

Table 3. 3 List of the C—C bond distances and their average for each disordered Cnt.

Indeed, resolution of this structure is challenging. Attributing carbon atoms already necessitates to find 6 electrons in between two dysprosium centers accounting each for 66 electrons. As such, splitting carbon centers to correctly model the disorder probably has an impact on the obtained structure. For this reason, further structural analyses will be run with only on the main Cnt unit.

c. Overall dissymmetry

Another hint for the dissymmetry, is the comparison of the Dy—I distances showing a difference of 0.075(2) Å. To account for this difference, the distances Dy—C also needs to be taken into account and are presented in **Table 3. 4**. One way to gage the electronic differences between metals in an assembly is to use the Bond Valence Sum (BVS) analysis.²² This analysis allows the metrics of the system, typically Metal—O bonds, to be linked back to the oxidation state of the metal. Unfortunately, this method is based on empirical value gathered in the literature and the data for comprehensive Dy—C bond analysis do not exist (particularly in the divalent state). As a consequence, the distance here will be compared relatively to each other.

Distances (in Å)	Dy(1)	Dy(2)
Dy(X)—I(1)	3.1144 (6)	3.0293 (5)
Dy(X)—C(1)	2.532 (7)	2.471 (7)
Dy(X)—C(2)	2.508 (11)	3.816 (10)
Dy(X)—C(3)	2.609 (10)	4.537 (10)
Dy(X)—C(4)	2.559 (11)	4.610 (10)
Dy(X)—C(5)	2.596 (11)	3.997 (10)
Dy(X)—C(6)	3.263 (10)	3.125 (10)
Dy(X)—C(7)	4.051 (10)	2.520 (10)
Dy(X)—C(8)	4.376 (10)	2.570 (10)
Dy(X)—C(9)	3.899 (10)	2.440 (12)
Avg Dy(X)—C _{Cnt}	3.15(1)	3.34(1)
Avg short interactions	2.65(1)	2.61(1)

Table 3. 4 Main distances used to determine electronic interaction in 3.4

To investigate the electronic differences without the BVS analysis, two approaches can be used. First an average over the Dy—C_{Cnt} bonds can help gauge a difference of interaction. This value is reported in **Table 3. 4** and shows a slight difference of around 0.2 Å. Although in the case of this molecule, because of the strong distortion of the Cnt unit it might be more accurate to only consider the atom which are *coordinated* to the metal. However, to do that, a distance threshold of interaction needs to be set. For instance, in **Table 3. 4**, the distances between 2.471(7) Å and 2.609(10) Å seem clearly on the shorter range, but the distance Dy(2)—C(6) of 3.125(10) Å stands out as intermediate between those and the longer distances. Considering the large difference with the other short interactions and the fact that Dy(1)—C(6) and Dy(2)—C(6) are fairly close, this carbon atoms is not considered to be in close interaction with the metallic center. As such, Dy(1) is in closer interaction with five carbons while Dy(2) only seem to closely interact with four. The preferential interactions are illustrated in **Figure 3. 14**.

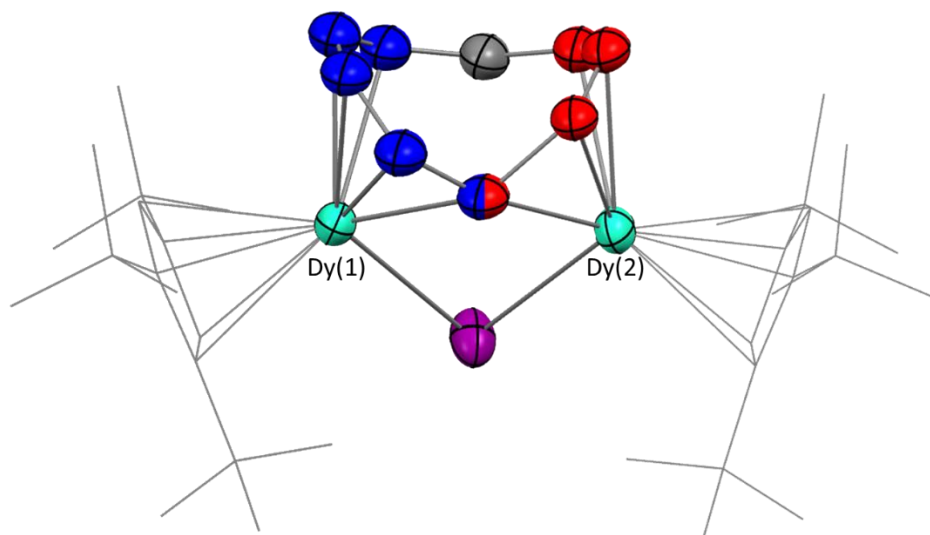


Figure 3. 14 Molecular representation of **3.4**, dysprosium atoms are in light green, iodine in purple and carbon atoms are represented according to the following: grey is not in particular interaction, blue is close interaction with Dy(1) and red is close interaction with Dy(2). Hydrogen atoms are omitted for clarity and two Cp^{ttt} ligand are represented in wireframe.

This attribution is more to be used as a visual guide to understand the structural dissymmetry than to show an actual electronic difference. Indeed, calculating the average Dy—C distances for those attributions yield fairly similar values as reported in **Table 3. 4**.

Furthermore, the distances between the dysprosium centers and the Cp^{ttt} ligand are similar with an average of 2.65(3) Å and 2.64(2) Å for Dy(1) and Dy(2) respectively.

To conclude, even though the dissymmetry seems visually striking, it does not seem to come from a stark difference in electronics. At this point it would be difficult to claim a particular electronic structure and additional characterization are needed.

Nevertheless, the presence of both the dissymmetry and the Cnt disorder which had not been observed before asks the question of a possible common cause. For instance, if the dissymmetry indeed comes from a difference in electronics between the dysprosium centers - such as a mixed-valence compound Dy^{II}/Dy^{III} - then it could be possible that the Cnt dissymmetry translates the existence of the Dy^{III}/Dy^{II} molecule dimer. This would be a class II dimer with a high enough barrier to observe both repartition of charges at the temperature of the acquisition (250 K). This could explain why the dissymmetry, if visible, is not electronically striking. It stems from a superposition of electronic structures. At this point, it only constitutes a working hypothesis and needs further investigation.

Particularly, the thermal sensitivity of **3.4** allows for more spectroscopic investigation. One useful tool for the determination of mixed-valence compounds is the UV-visible absorption. We then set up to analyze the behavior of **3.4**.

3. Uv-vis spectroscopy

a. Analysis of the spectra

Considering the deep color of the product, its solubility in most solvent and its thermal stability, it was characterized by UV-vis spectroscopy in toluene and is shown in **Figure 3. 15**. The absorption was normalized and represented by molar absorption coefficient ϵ .

The spectra show one large absorption band in the visible with $\lambda_{\text{max}} = 549$ nm. Other features can be identified at $\lambda = 400$ nm and $\lambda = 338$ nm. In these spectra, no $f-f$ transition can be identified.

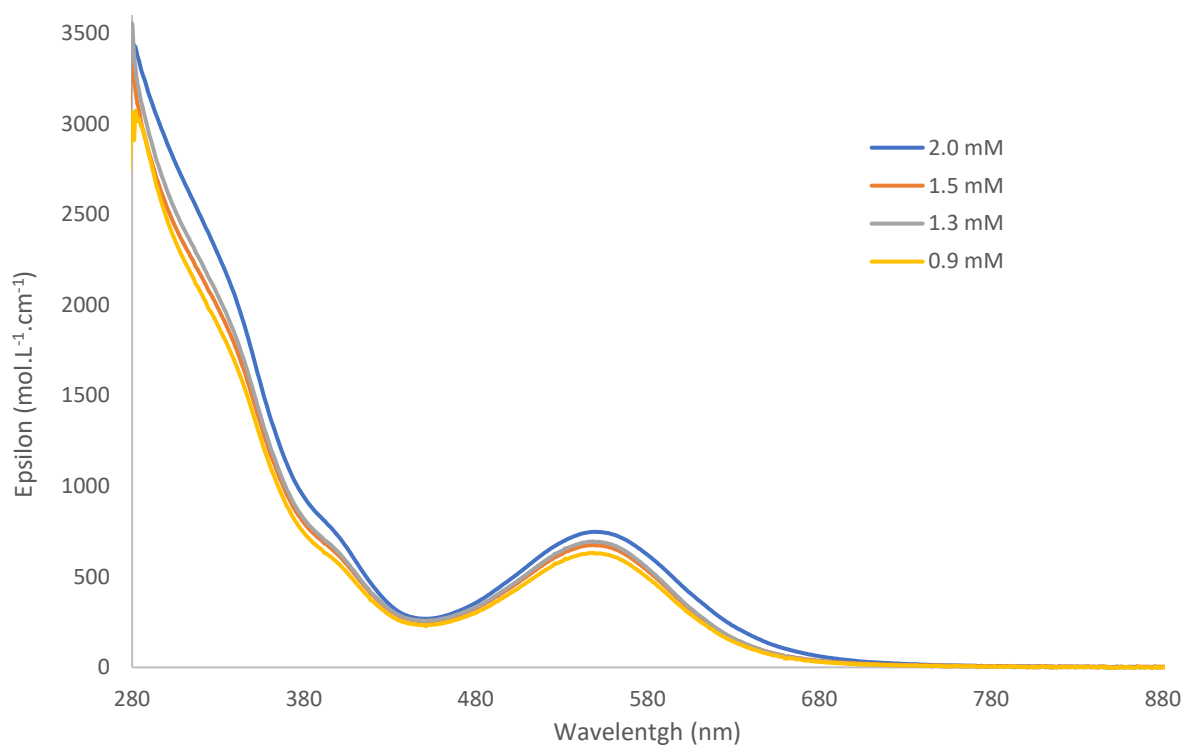


Figure 3. 15 Graphical representation of the molar absorption coefficient depending on the wavelength at several concentration of **3.4** in toluene.

The analysis at four different concentrations shows that the spectra is reproducible. Furthermore, it allows determination of $\epsilon_{\lambda_{\text{max}}}$ by linear regression as presented in **Figure 3. 16**.

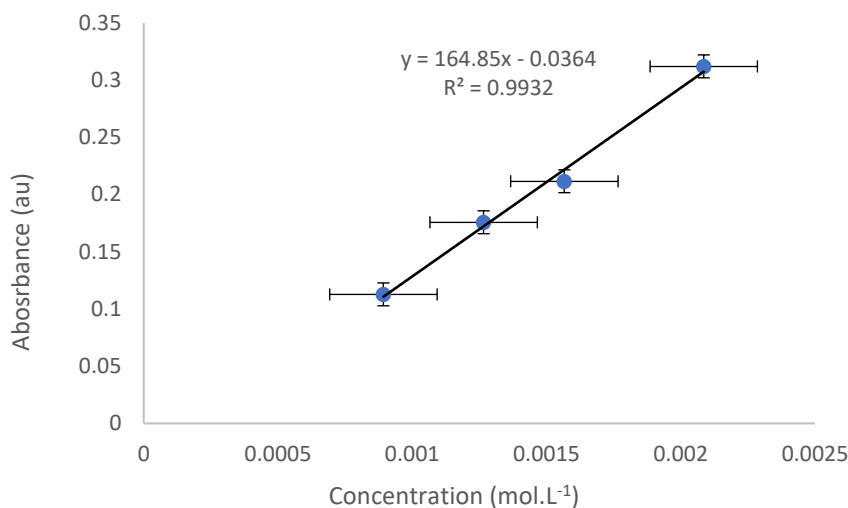


Figure 3. 16 Graphical representation of the absorbance as a function of the concentration and linear regression to access the molar absorption coefficient

According to the Beer-Lambert empirical law, the coefficient to this linear regression is the product of ϵ by the width of the cuvette (in this case 0.2 cm). This yields a value of $\epsilon = 824 \text{ mol.L}^{-1}.\text{cm}^{-1}$, slightly higher than the average epsilon value over the four spectra.

b. Analysis of the visible band

The large band at 549 nm is rather interesting and is reminiscent of Intermediate Valence Charge Transfer features which stem from mixed-valent character.

Definition

Mixed-valent complexes are metallic molecules bearing several metals possessing different oxidation states. This dissymmetry creates several repartitions of the oxidation states often referred to as Robin-Day class.^{23–27} To simplify the definition, the example of a dimer will be studied.

The class I denotes molecules in which the electron is fixed onto one of the metallic centers. The two ions act independently. *The class II* denotes an overall localization of the electron with a low barrier to reversal. The energy surface adopts a typical double well structure, where both minima denote localization on either of the metallic centers as illustrated on **Figure 3. 17**.^{23,27} In this case, spectroscopic method can be used to get access to the different values which describe the interaction between the metal. In the final *class III*, the double well gives place to a single minimum translating the complete delocalization of the electron in between the two centers, as represented in **Figure 3. 17**.

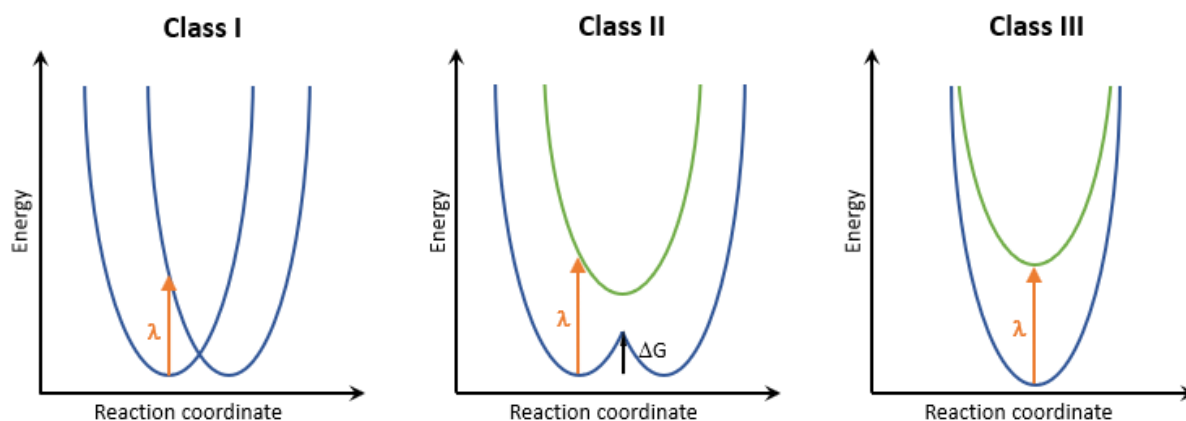


Figure 3. 17. Schematic representation of the energy surface for mixed-valent metallic dimer of Rabin-Day class I (on the left), class II (in the middle) and class III (on the right) adapted from ²³

One important feature to determine the type of mixed-valence observed in a complex is the aforementioned IVCT band. Indeed, a class I complex, as its two metallic ions act independently, will show no particular feature. But the (partial) delocalization of class (II) III will give rise to a relatively intense absorption band. Furthermore, the value of ϵ associated as well as the width of the band can hint toward a classification between class II or III.

Analysis of the molar absorption coefficient

First, due to the strong electronic communication the absorption for class III system show strong molar absorption coefficient usually $\epsilon > 5000 \text{ M}^{-1}\cdot\text{cm}^{-1}$.²⁷ Where less strongly interacting class II compound show $\epsilon < 5000 \text{ M}^{-1}\cdot\text{cm}^{-1}$. If the feature observed on the UV-visible band indeed correspond to an IVCT band, **3.4** seems more coherent with a class II compound with $\epsilon \sim 800 \text{ L}\cdot\text{mol}^{-1}\cdot\text{cm}^{-1}$.

Analysis of the width

Then, the value associated with the width of the band is referred to as full-width at half-max (FWHM expressed in cm^{-1}) and can be calculated by formula (1):

$$\Delta\nu_{\frac{1}{2}} = \frac{1}{\lambda_1} - \frac{1}{\lambda_2} \quad (1)$$

In this case λ_1 and λ_2 refer to the wavelength for which $A(\lambda_n) = 0.5 A_{\text{max}}$. For **3.4** the value amounts to 4310 cm^{-1} . The theoretical value can be obtained through formula (2) with λ in cm^{-1} , R the gaz constant in $\text{J}\cdot\text{K}^{-1}\cdot\text{mol}^{-1}$ and T the temperature in K:

$$\Delta\nu_{1/2}^\circ = 2\sqrt{4 \ln(2) \lambda RT} \quad (2)$$

Which at room temperature simplifies into equation (3):

$$\Delta\nu_{1/2}^\circ = \sqrt{2310\lambda} \quad (3)$$

Finally this theoretical value is calculated at $\Delta v_{(1/2)}^{\circ} = 6487 \text{ cm}^{-1}$, which is significantly wider than what is obtained. A useful metric Γ has been developed to sort compound in the class II or III. It can be accessed following the equation (4):

$$\Gamma = 1 - \frac{\Delta v_{\frac{1}{2}}}{\Delta v_{\frac{1}{2}}^{\circ}} \quad (4)$$

Applied for **3.4**, it gives $\Gamma = 0.34$ which is a value typically attributed with a class II system.

c. Discussion on the mixed-valent character

Overall, the analysis of this feature seems to be in agreement with an intermediate valence of Robin-Day class II with a partial localization of the charge on one of the dysprosium centers. This would agree with the disorder observed for the Cnt unit as it could stem from the two localization of the charge either on Dy(1) or Dy(2). Due to the low barrier between the two states, they could be observable at temperature close to room temperature. It is difficult to compare the energy involved in the different process as the charge transfer happens on time scale much smaller than any structural modifications associated with accommodation of the charge on a metal center.

Furthermore, all this study was run with the assumption that this absorption band denotes an IVCT, however, it could also come from other type of CT such as metal to ligand or ligand to metal. In order to investigate the origin of this transition, TD-DFT calculations are being tackled for **3.4**.

4. Magnetism analysis

Another, characterization which can inform about the electronic structure of **3.4** is its magnetic behavior. Particularly, in the case of the mixed-valent dimer, as explained in the previous chapter, a strong class III behavior will lead to extremely high magnetic susceptibility at room temperature. Unfortunately, it was also observed that attributing redox state to non-coupled system is difficult due to fairly close susceptibility for trivalent and divalent dysprosium ions.^{28,29}

To gather those information, both the magnetization and the magnetic susceptibility were recorded and the data are presented in **Figure 3. 18** and **Figure 3. 19**.

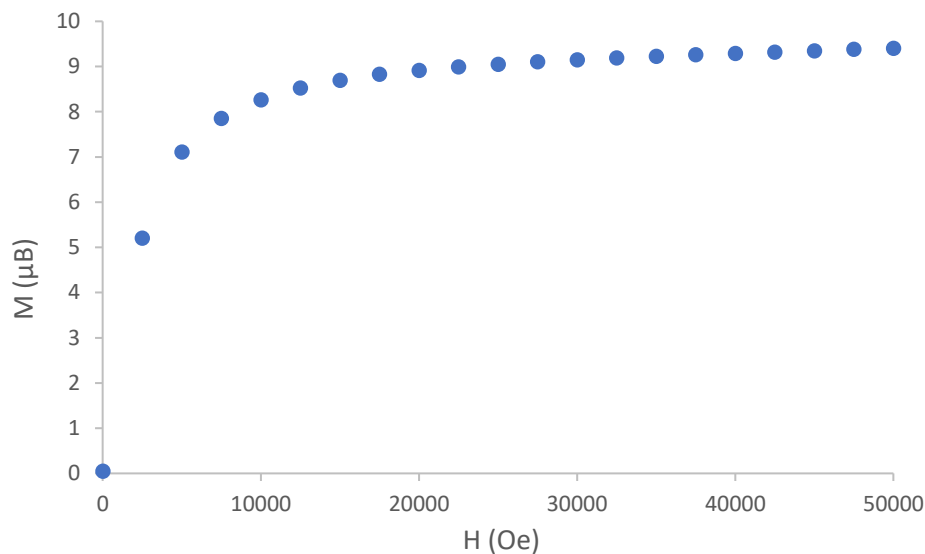


Figure 3. 18 Graphical representation of the magnetization of **3.4** as a function of the external field.

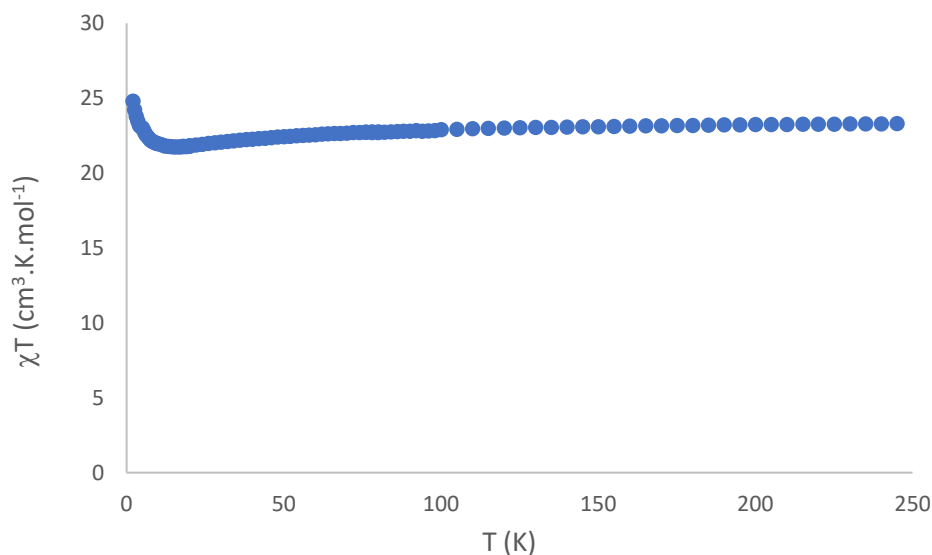


Figure 3. 19 Graphical representation of the product of the magnetic susceptibility by the temperature of **3.4** as a function of the temperature.

The first observation is similar to **2.3**, there does not appear to be delocalization of one electron over the two dysprosium centers as χT is limited to $23.3 \text{ cm}^3 \cdot \text{K} \cdot \text{mol}^{-1}$ at 250 K.

That being said, the overall behavior is quite different. There is no inflexion point in the magnetization curve. Furthermore, no increase of the susceptibility can be observed at intermediate temperature. Finally at low temperature the feature observed might be due alignment of the crystallites particle inside the field. As such there is no indication of radical behavior in the magnetic curves besides the f -electrons from the dysprosium centers.

Due the small impact of the crystal field, the value of χT at room temperature can be an adequate measurement of the oxidation state of a lanthanide ion. However, in the case of

dysprosium centers, the difference of expected value is not always significant.^{28,29} Indeed for a trivalent ion, the expected value at room temperature is about $\chi T = 14.1 \text{ cm}^3 \cdot \text{K} \cdot \text{mol}^{-1}$. However, for a divalent ion, several values can be expected depending on the coupling between the f -electrons and the additional electron ranging from $\chi T = 14.5 - 17.0 \text{ cm}^3 \cdot \text{K} \cdot \text{mol}^{-1}$.²⁹ As such, the values for trivalent and divalent ions are close and can fall into uncertainty of mass measurements for small samples.

It is important to note that the obtained value for **3.4** is only $\chi T = 23.3 \text{ cm}^3 \cdot \text{K} \cdot \text{mol}^{-1}$ and most likely requires a correction to the measured mass. Due to this experimental error, it is difficult to discuss attribution of the oxidation states.

As expected, the information regarding the oxidation state of the dysprosium cannot be decided using the magnetic behavior in the case of **3.4**.

5. Discussion

Overall, the simplification of the structure that we hoped to obtain by removing the THF ended up bringing a fair number of new challenges. However, if we try to apply a similar method to decide on the electronic structure, the same type of scenario can be drawn in **Figure 3. 20**.

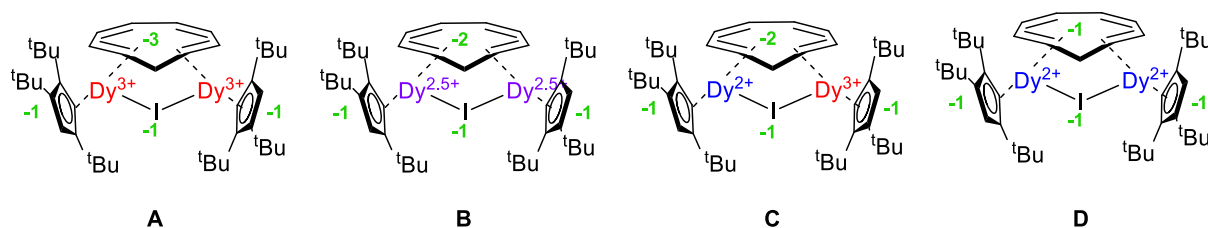


Figure 3. 20 Schematic representation of the possible electronic structure of 3.4

According to magnetic data, the scenario **B** can most likely be ruled out. Unfortunately, this is the only scenario on which magnetic data can weight in.

Considering the easy transfer of one electron from the dysprosium to the Cnt ligand in both **2.1** and **3.3**, it seems unlikely that a monoanionic Cnt ligand could be coordinated onto two divalent dysprosium such as proposed in **D**.

To conclude, both **A** and **C** could be coherent with the current data. The deciding factor would be the origin of the UV-visible.

In order to explain this behavior, computations were started on this species. Unfortunately, as of the moment of redaction they are still running. Two different strategies are employed. On the first hand a TD-DFT analysis could help identify the source of the absorption band present in the UV-visible spectra. On the other hand, CASSCF analysis on the full compound with the adequate multiplicity could allow energetic comparison of the different scenario.

2. Synthesis and characterizations of *endo*-Dy₂Cnt₂Cp^{ttt}₂ (**3.3-endo**)

1. Synthesis

During exploration of the reaction condition, another species **3.3-endo** was discovered serendipitously. It was observed several times as a byproduct of the reduction of **3.4** and **3.3**. Alternative reductants were tried such as potassium metal and K/KI in order to find a reproducible reaction path. Crystals of the product were identified in K/KI reduction although several species seemed to be present.

Despite my best effort, the synthesis of **3.3-endo** was not rationalized and, as such, only its solid-state structure was characterized. However, the following structure present interesting features that could improve our understanding of those reactions, which explain why it is presented in this manuscript.

2. Structural study

Red crystalline blocks were observed as a side product upon one isolation of **3.4** and were analyzed through SC-XRD. The compound crystalizes in the space group P2₁/c and the structure is presented below on **Figure 3. 21**.

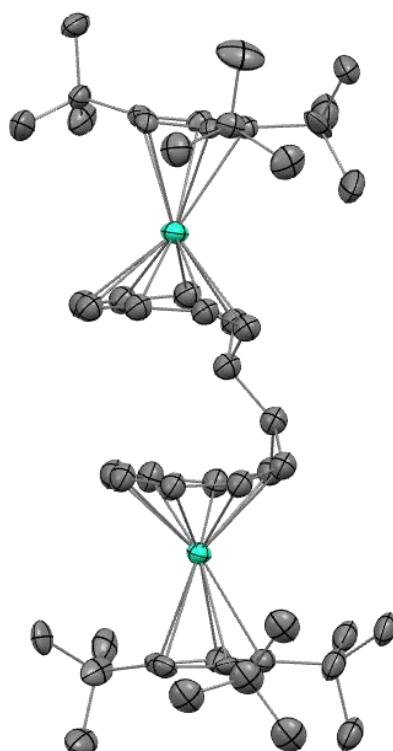


Figure 3. 21. Molecular structure of **3.3-endo** represented at 50% probability, dysprosium atoms are in light green, and carbon atoms are in grey. Hydrogen atoms are omitted for clarity. A disordered Cnt₂ ligand is omitted for clarity.

At first glance **3.3-endo** seems very similar to **3.3** with a rotation around the newly formed C—C bond. However, careful consideration of the bonding in the Cnt₂ units shows that this moiety cannot be obtained by simple rotation and requires bond breaking to superpose with **3.3**. This means that **3.3** and **3.3-endo** are isomers of one another. The obtention of either one results from the radical-radical coupling happening from one side or the other of a Cnt unit. A simplified illustration is proposed on **Figure 3. 22**.

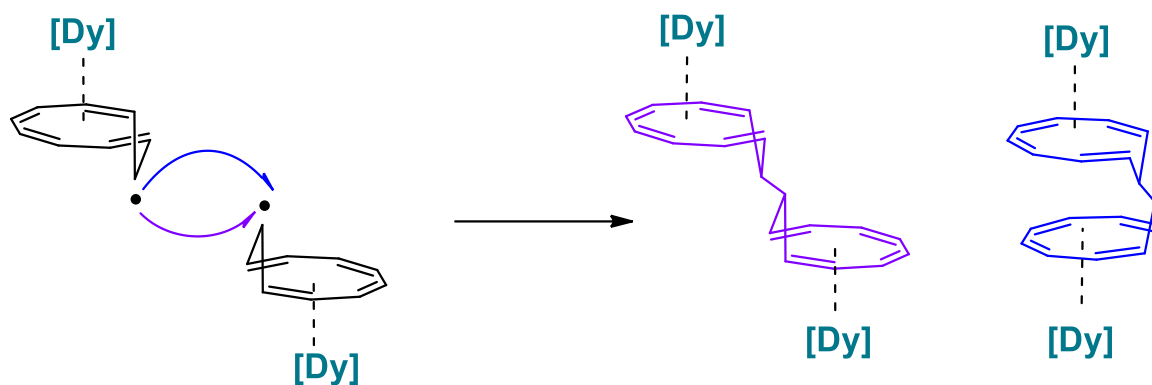


Figure 3. 22 Schematic explanation of the obtention of different isomers **3.3** and **3.3-endo**

3. Discussion

The obtention of this new compound asks a lot of questions about the mechanism of the radical-radical coupling. First it has been obtained both from direct reduction and reduction of **3.2**. This means that both **3.1** with added KCnt and **3.2** possess the possibility of showing this difference in coupling. Following this, one hypothesis could be that the obtention of the other isomer is dependent on the isomerization status of the KCnt. Particularly as this isomerization was observed in the solid-state structure of **3.2**. Several attempts at controlling the quantity of *trans* isomer in **3.2** were left unsuccessful. As a consequence, as of yet this hypothesis has not been proven nor disproven. The work carried out on the chapter four will be focused on the control of the isomerization of KCnt and could yield useful insight for the rationalization of this synthesis in the future.

Additionally, an important feature of **3.3-endo** is the apparent alignment of the metallic ions and the center of the four rings. This could be an efficient scaffold to harness the anisotropy of lanthanide ions and create a SMM. As often the Cnt rings might be large for prolate ions such as dysprosium, however erbium centers could be an interesting metal to study in this conformation as soon as the synthetic path is rationalized.

To conclude, characterization of **3.4** showed behavior reminiscent of mixed-valent behavior. Despite several methods used to investigate this electronic repartition, no definitive answers were reached. To try and explore this further, extending this chemistry over a series of lanthanide complexes could help observe trends and bring additional insight on the electronic structure.

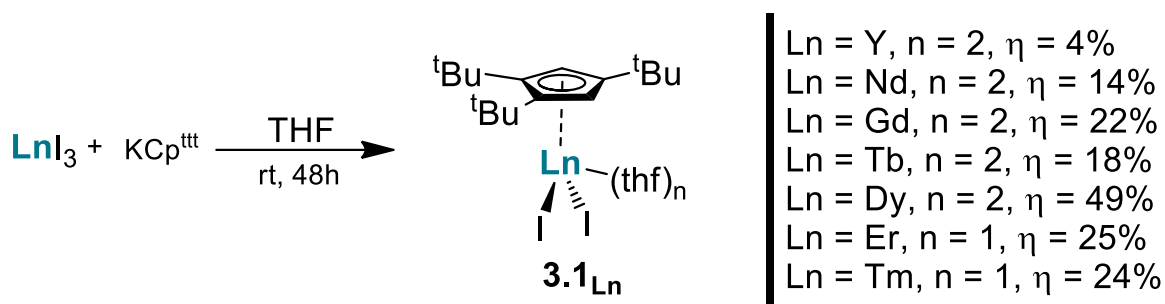
This highlights another crucial advantage of the heteroleptic route: it can be attempted with any lanthanide which possess a LnI_3 starting material. Thus, the next part will present the results obtained toward extending this chemistry to other lanthanides.

III. Extension to other lanthanides

As mentioned previously, the chemistry detailed in **1.2** and **1.1** of this chapter could, theoretically, be adapted for every lanthanide which can be found as LnI_3 salts. For lack of time, this was not investigated on the full series but with selected examples to help shed light on the electronic structure of **2.3** and **3.4**. For instance, this chemistry was tried with YI_3 and GdI_3 which both possess interesting magnetic properties. Yttrium is quite often used as a diamagnetic equivalent of lanthanide due to its similar size. It is particularly useful for EPR experiment to investigate the radical nature of the molecule without the involvement of f -electrons.² Then, gadolinium compounds show spin-only behavior in magnetism which can allow decoupling of the spin-orbit contribution and help the understanding of the magnetic behavior.² Additionally, other late rare-earth metal have been studied for their usually good magnetic properties. Most notably erbium and thulium can also have other interesting application. Erbium is known to be an interesting ion for upconversion mechanism and as such, obtention of a short-distance erbium dimer could be an interesting probe to study. Finally, thulium was used in the recent report by the Long group as the breaking point in the series of mixed-valent lanthanide dimer.² Indeed divalent thulium is known to be f^{13} and not $f^{12}d^1$ meaning that it cannot show delocalization along the d_{z^2} orbital. This could be a useful information to investigate the mixed-valent behavior in this particular scaffold.

1. Synthesis of $\text{LnCp}^{\text{ttr}}\text{I}_2(\text{thf})_2$ (**3.1_{Ln}**)

The previous synthesis by salt metathesis to form **3.1** was adapted for different LnI_3 as presented below in **Scheme 3.9**.



Scheme 3. 9 Synthetic path to access 3.1_{Ln} with n = 2 for Ln = Y, Nd, Gd, Tb, Dy, and n = 1 for Ln = Er, Tm

Unfortunately, with other metals than dysprosium the yields were very poor. Thulium also showed some traces of THF ring-opening reaction which seems odd for a simple salt-metathesis. Overall, only the late lanthanide showed high enough yield to be investigated further.

The products were obtained as pale crystalline blocks and were characterized by SC-XRD and are represented in **Figure 3. 23**. Despite their apparent resemblance, they crystallize in different space groups as detailed in the experimental part.

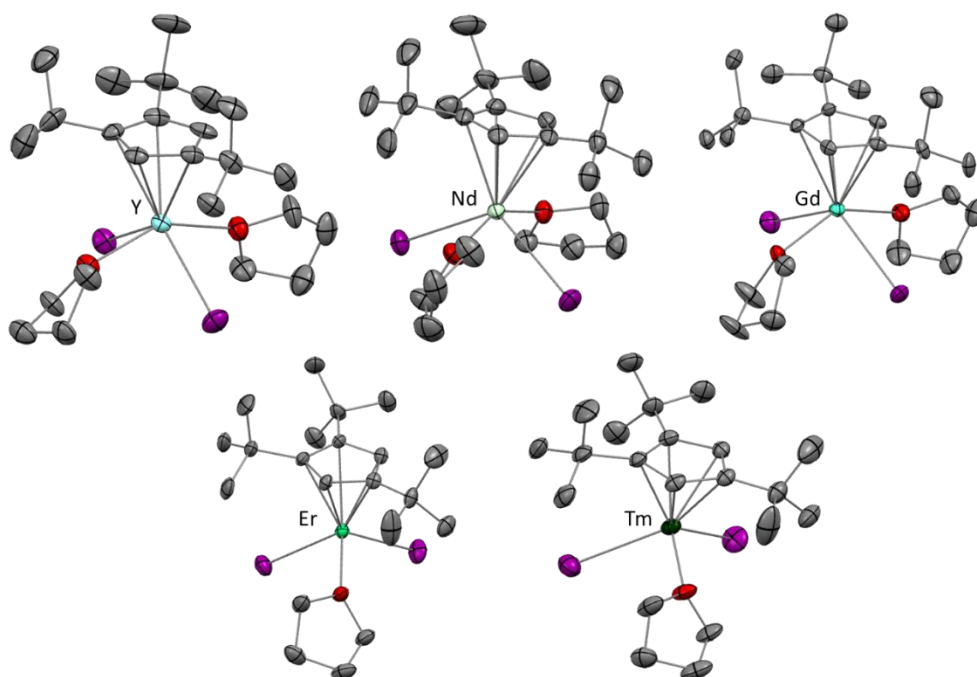


Figure 3. 23 Molecular structure of 3.1_{Ln} with Ln = Y, Nd, Gd, Er, Tm represented in light blue, light yellow, light green, green, dark green respectively. Additionally, carbon atoms are represented in grey, oxygen in red and iodine in purple.

The main structural differences which can be seen, is the presence of only one coordinated THF for the late erbium and thulium. This makes sense as the radii of lanthanide follow the lanthanide contraction. The main distances for those compounds are shown in **Table 3. 5** below.

Distances (in Å)	3.1_Y	3.1_{Nd}	3.1_{Gd}	3.1	3.1_{Er}	3.1_{Tm}
Ln(1)—I(1)	2.9735(10)	3.0603(3)	3.0008(4)	3.0012(3)	2.8900(4)	3.0883(3)
Ln(1)—I(2)	3.0112(11)	3.0831(3)	3.0194(5)	2.9713(3)	2.8793(5)	2.8393(2)
Dy—C (Cp^{ttt})	2.635(8) – 2.711(8)	2.705(2) – 2.778(2)	2.737(5) – 2.648(5)	2.629(3) – 2.709(3)	2.571(3) – 2.614(3)	2.416(3) – 2.600(3)
Dy—Cent (Cp^{ttt})	2.37	2.46	2.41	2.38	2.29	2.16

Table 3. 5 Main distances for the compound **3.1_{Ln}**

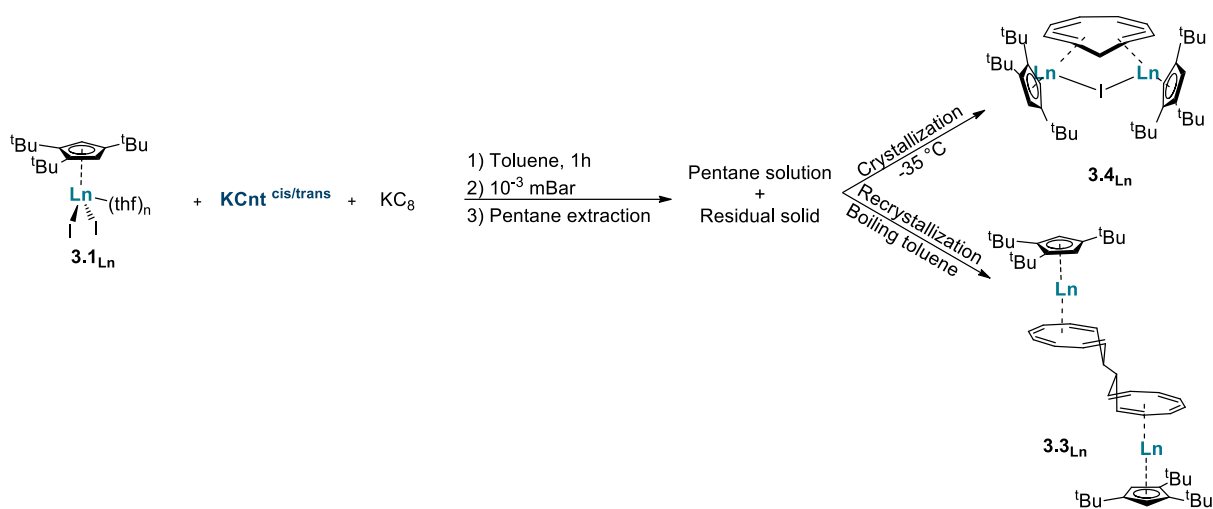
The distances Dy—C reported in table above clearly follow the lanthanide contraction as expected.

As mentioned previously, only the late lanthanide ions were showing decent yields for the synthesis of **3.1_{Ln}**. As a consequence, the following steps of the reaction were carried out mainly with Ln = Gd, Tb and Er. The first attempt at extending the synthesis of **3.2** to other lanthanides were unsuccessful. For this reason, it was decided to focus on the direct reduction of **3.1_{Ln}** with KC₈ in the presence of KCnt.

2. Adaptation of the synthesis

The first path reported for **3.3** was run with the question of the stability of the formed product. Indeed, **2.3** being thermally sensitive, it would be possible for **3.4** to be equally sensitive. Notably, it was observed that upon removal of the toluene, lighter solid would deposit on the side of the vial. This was thought to be product decomposition. For this reason, the filtering step was run after solubilization in pentane rather than before removal of the toluene. This allowed the product to stay in contact with the reducing agent and mitigate any decomposition or oxidation.

However, careful analysis of this presumed degradation product found it to be **3.3**. It appears that both products are formed simultaneously and can be separated by selective precipitation. Indeed, after removal of the toluene, if the residual solid is washed with pentane, **3.3** stays as a brightly colored powder while **3.4** is extracted in pentane. **3.4** can then be crystalized according to the previous synthesis, while **3.3** is obtained as a microcrystalline powder. This powder was then recrystallized in boiling toluene for **3.3_{Gd}** and **3.3_{Tb}**. As mentioned previously, extension of the procedure to access **3.2** was unsuccessful, as such it was decided that both **3.3_{Ln}** and **3.4_{Ln}** would be obtained from direct reduction of **3.1_{Ln}** according to the following Scheme 3. 10.



*Scheme 3. 10. Adopted synthetic path for the concomitant isolation of **3.3_{Ln}** and **3.4_{Ln}***

This synthetic path allowed us to structurally characterize **3.3_{Gd}**, **3.3_{Tb}**, **3.3_{Er}** and **3.4_{Er}**. Unfortunately, the pentane solution extracted in the case of the terbium and the gadolinium reaction did not yield any crystalline product.

3. Structural study of Ln₂Cnt₂Cp^{ttt}₂ (**3.3_{Ln}**)

The compounds **3.3_{Ln}** with Ln = Gd, Tb and Er are isostructural with **3.3**. They crystallize in the Pccn space group and only half of the molecule is contained in the asymmetric unit. The full structures are presented in **Figure 3. 24**. Twinning in the crystal of **3.3_{Er}** allowed for resolution of the overall structure but did not yield a structure up to publishing standard. Nevertheless, the general connectivity pattern as well as distances between heavy atoms can be determined and used with the appropriate estimated standard deviation.

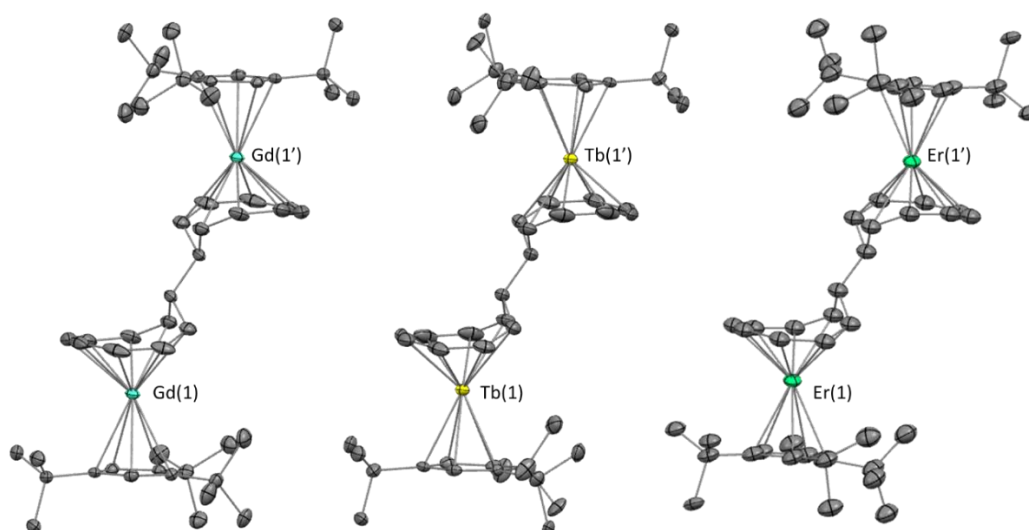


*Figure 3. 24. Molecular representation of **3.3_{Ln}** with Ln = Gd, Tb, Er; being represented in light green, yellow and green respectively. Carbon atoms are represented in grey and hydrogen are omitted for clarity*

Analysis of the main bond distances are reported in **Table 3. 6**.

Distances (in Å)	3.3_{Gd}	3.3_{Tb}	3.3	3.3_{Er}
Ln(1)—Ln(1)	7.8156(6)	7.7767(7)	7.771(1)	7.682(2)
Ln(1)—Cent η^8	1.69	1.67	1.65	1.60
C1—C1¹	1.523(3)	1.514(6)	1.538(5)	1.49(5)
Ln(1)—Cent η^5	2.39	2.37	2.35	2.32

*Table 3. 6 Main distances for the comparison of the series **3.3_{Ln}***

Once again, the distances seem to mostly follow the lanthanide contraction. The only distance which does not follow this trend is the C(1)—C(1)¹ bond. It could be linked to the overall electronic interaction between the metal and the Cnt₂ ligand. Unfortunately, with this limited number of examples it is difficult to establish a strong hypothesis.

4. Study of Er₂CntCp^{ttt}₂I (**3.4_{Er}**)

3.4_{Er} is the only analogous molecule to **3.4** obtained through the method described previously.

1. Structural analysis

It was characterized by SC-XRD, it crystallizes in the P2₁/n space group and the structure is presented in **Figure 3. 25**. Due to the small size of the crystals of **3.4_{Er}** the C—C bond precision is lower than **3.4**. Additionally, there is a substantial residual electronic density on the Er—Er axis. As a consequence, a disorder of the Cnt unit could not be modelled in the structure contrary to **3.4**. considering the precision of the data, it does not constitute a proof that there is none.

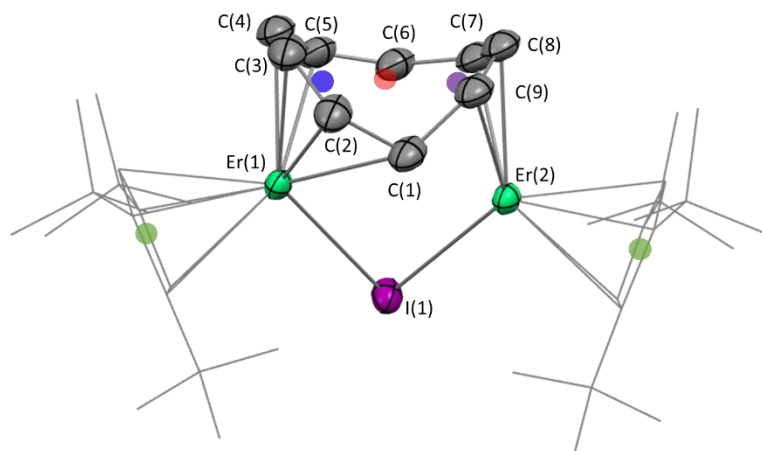


*Figure 3. 25 Molecular structure of **3.4_{Er}** represented at 50% probability, erbium atoms are in green, iodine in purple and carbon atoms are in grey. Hydrogen atoms are omitted for clarity. The red, blue, purple and green spots represent the full Cnt, the η^5 Cnt, the η^4 Cnt and the η^5 Cp^{ttt} respectively.*

The distance Er—Er is 3.7217(8) Å which is slightly shorter than in **3.4** which can be linked to the smaller radii for erbium ions. The main distances of **3.4_{Er}** are presented in **Table 3.7** and compared with their equivalent in **3.4**.

Distances (in Å)	3.4	3.4	3.4_{Er}	3.4_{Er}
	Dy(1)	Dy(2)	Er(1)	Er(2)
Ln(X)—I(1)	3.1144(6)	3.0293(5)	3.116(1)	2.963(1)
Ln(X)—Cent η^9	2.61	2.87	2.52	2.88
Ln(X)—Cent η^5	2.04	--	1.98	--
Ln(X)—Cent η^4	--	2.09	--	2.08
Ln(X)—Cent η^5 Cp ^{ttt}	2.36	2.35	2.31	2.32
Avg short interaction	2.65	2.61	2.60	2.61

Table 3.7 Main distances of **3.4_{Er}** and their equivalent in **3.4** for the main Cnt unit.

This comparison shows very similar behavior for the two lanthanides. The structure of **3.4_{Er}** appears dissymmetrical. However, similar analysis on the closest bonded atoms reveal an average of 2.60 Å for Er(1) and 2.61 Å for Er(2). Showing that, once again, if there is a difference in electronics between the two centers, it cannot be established solely by SC-XRD.

2. UV-visible spectroscopy

As this compound features a similar color to **3.4**, we were interested in the spectroscopic signature of the complex in UV-Visible absorption. The spectra presented in **Figure 3.26** were recorded in toluene. The absorption spectra of **3.4** is added for comparison.

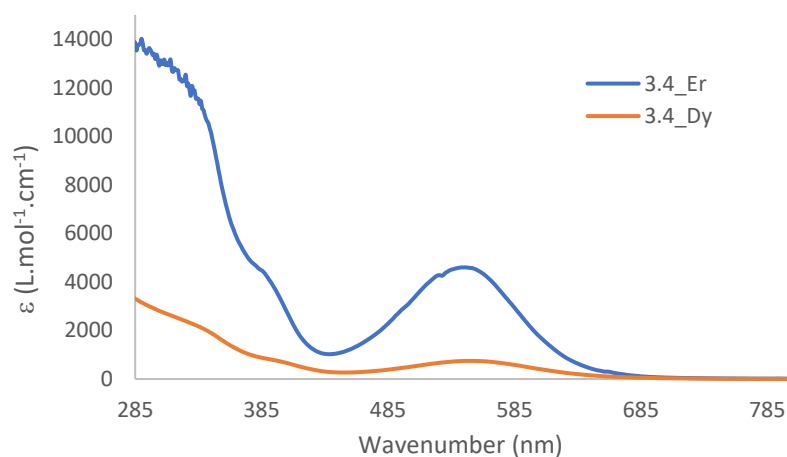


Figure 3.26 Graphical representation of the molar absorption coefficient in function of the wavelength of **3.4_{Er}** and **3.4** in toluene.

Comparison of the two spectra shows very similar behavior with one main feature in the visible region around 546 nm as well as two other band in the near UV. Overall, the absorption coefficients appear higher for **3.4_{Er}**. For the feature in the visible, the coefficient is reported to be $\epsilon = 4760 \text{ L.mol}^{-1}.\text{cm}^{-1}$ using a similar linear regression as for **3.4**.

A similar study was then carried out to determine the type of mixed-valence involved in this compound, if this band stems from IVCT. They are reported in **Table 3. 8** and compared with the value for **3.4**.

	3.4	3.4_{Er}
λ_{\max} (nm)	549	546
A_{\max}	0.312	1.23
ε (L.mol ⁻¹ .cm ⁻¹)	748	4600
λ_1 (nm)	610	485
λ_2 (nm)	483	595
FWHM (cm ⁻¹)	4310	3811
$\Delta\nu_{1/2}$ (cm ⁻¹)	6487	6504
Γ	0.34	0.41

Table 3. 8. Main values for the determination of the mixed-valence character of the complex

As shown in **Table 3. 8**, the bandwidth for the erbium complex is slightly lower, which translate into a higher Γ coefficient. However, this value is still lower than 0.5 and as such, if this band is indeed indicative of IVCT, **3.4_{Er}** probably also qualifies as mixed-valent class II.^{26,27}

3. Discussion

Overall, the two compounds are very similar in both their structural parameters and their behavior in UV-Visible absorption. In order to investigate further the difference in electronic structure, computations could be run. First TD-DFT computations could be used to study the origin of the absorption band in the visible. Then CASSCF computations could be used to study the orbitals in the active space. Most often with *f*-block elements, they are comprised of *f*-orbitals however, in **2.3** we found an orbital of *d*-heritage which could be interested to probe. Furthermore, simulation of the magnetic properties could be interesting as erbium ions are magnetically active. In parallel, deeper spectroscopic insight such as magnetism and EPR could yield crucial information to better understand the electronic features of the dimer.

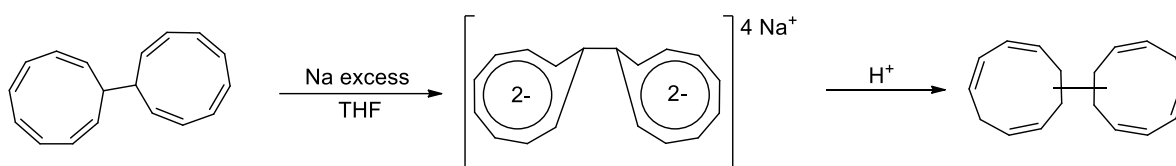
Finally, extending the chemistry developed for dysprosium to other lanthanides has not allowed us to completely solve their electronic structures. However, the isolation of several reduced Cnt units in different settings could be interesting to compare. Thus, in the last part of the chapter, a summary of what we know about reduced Cnt species and a discussion on the possible electronic structure will be presented.

IV. Discussion and conclusion on the Cnt species in its reduced form

As mentioned previously, the study of reduced Cnt species has brought a lot of question. The lack of final conclusion does not preclude summarizing all that has been learnt.

First, the study of **Chapter 2 & 3** proved that the Cnt ligand could be reduced and as such features redox non-innocent character which was unknown. According to the different reactivity with TmI_2 and DyI_2 it would seem logical that the reduction potential would be in this range. Preliminary electrochemical study has not yielded conclusive result but could be an interesting tool to probe the reduction chemistry of KCnt. Particularly, it could help investigate the potentiality of single and double reduction to the Cnt^{2-} and Cnt^{3-} species respectively alleged as bridging species in **2.3** and **3.4**.

Then, we showed that single reduction of a Cnt unit can lead to the formation of a dimer by C—C bond formation. This unit most likely bears a -4 charge to create a neutral arrangement in both **2.1** and **3.3**. Interestingly, this type of Cnt dimers had been postulated by Neuenschwander in 1987.³⁰ Although they were not obtained by direct overreduction of a Cnt salt but rather by reduction of the Cnt_2 unit as illustrated by **Scheme 3. 11**.



Scheme 3. 11 Reproduction of the synthetic path proposed by Neuenschwander to explain the formation of the protonated bis-Cnt dimer upon addition of acid.³⁰

Any attempt to reproduce this type of coupling with standard reductant such as KC_8 , potassium metal, lithium metal did not allow isolation this tetra-anionic ligand.

For the bridging type of reduced Cnt ligand, the picture is less clear. As demonstrated previously, the study of the electronic of those compounds is challenging on several aspects. Switching the Cnt^- ligand allowed us to access similar heteroleptic compounds however, strong distortion of the bridging unit complicates the direct comparison of this unit. One metric that can be used is the C—C bond distance average over the cycle. This was already used to compare the two disordered Cnt for **3.4** but can be extended to **2.3** as well. The average C—C bond distances calculated for **2.3** and **3.4_{Cnt1}** are exactly the same up to the standard deviation precision. This could be an indication that the overall electronic structure of the Cnt moiety is the same. This would then mean that two principal hypotheses can be considered as illustrated in **Figure 3. 27**.

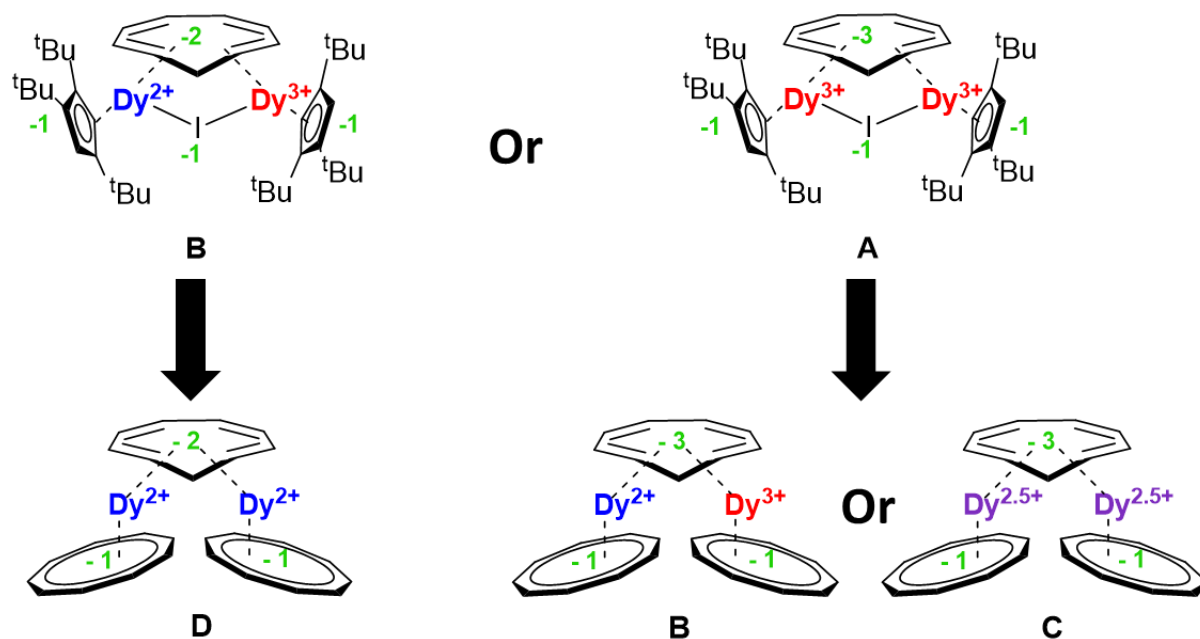


Figure 3. 27 Selected hypothesis if the two bridged Cnt unit have similar electronic identity.

The first hypothesis which assumes **3.4** does display mixed-valent behavior, then proposes a doubly divalent dysprosium dimer. This could explain the difficulties that were experienced in trying to characterize its behavior. The extreme thermal sensitivity probably associated with such a species most likely led us to characterize a degradation product rather than **2.3**.

The second hypothesis assumes that **3.4** features two trivalent dysprosium center and the feature in the UV-visible is imputable to another phenomenon such as ligand to metal charge transfer. In that case, the mixed-valence would have to be present in **2.3**, bringing again two possibilities. Either **2.3** indeed shows a class III mixed-valence but is degraded when prepared for magnetism study. Or the compound features a class II mixed-valence. In that case the computations are not able to predict accurately this electronic structure for unknown reasons.

Overall, the computation data that are currently being worked on by the collaborators will be crucial in determining the electronic structure of **3.4**. Additionally, if the hypothesis that the bridging Cnt ligand in **2.3** and **3.4** have the same electronic identity is true, it could help attribute the redox state of the dysprosium centers in **2.3**.

Interestingly, the analysis of the average C—C distances can be expanded to different Cnt containing compounds. These values are summarized in **Table 3. 9**.

Compound	Cnt type/hapticity	Avg C—C distances in Å
KCnt - <i>cis</i>	Cnt ⁻ / η ⁹	1.393 (5)
KCnt - <i>trans</i>	Cnt ⁻ / η ⁹	1.393 (6)
DyCotCnt	Cnt ⁻ / η ⁸	1.34 (3)
3.2 <i>cis</i>	Cnt ⁻ / η ⁶	1.400 (6)
3.2 <i>trans</i>	Cnt ⁻ / η ⁶	1.390 (6)
2.1	Cnt ⁻ / η ^{4/6}	1.39(2)
2.3	Cnt ⁻ / η ⁶	1.37 (3)
2.1	Reduced and coupled	1.42(2)
3.3	Reduced and coupled	1.42(2)
2.3	Reduced and bridged	1.42(1)
3.4	Reduced and bridged	1.42(2)
3.4_{Er}	Reduced and bridged	1.42(3)

Table 3. 9 Summary of the average C—C bond distances over a Cnt ring for different complex.

Overall, there seems to be a trend of values under 1.40 Å for non-reduced Cnt unit. While the reduced Cnt tend to score around 1.42 Å. Unfortunately, the difference is fairly small compared to the ESD. As such it is difficult to estimate the pertinence of such an analysis.

Even though few definitive answers have been gathered in **Chapter 2 & 3**, a lot of question have been asked and, overall, our knowledge of the KCnt ligand has been greatly extended. Most particularly its redox reactivity. As mentioned several times along those study, another key aspect of the KCnt was not investigated in detail, its isomerization. Even though the starting material of all salt metathesis uses KCnt in a *cis/trans* mixture and it can be observed in several crystal structure, its impact has not been evaluated. One key aspect is that reproduction of the synthesis of **2.3** with a full *cis* mixture of Cnt does not yield the expected product. As such, understanding its *cis/trans* isomerization will be key in building a more extensive knowledge of the Cnt ligand. The preliminary part of this study will be presented in **Chapter 4**.

References

- (1) McClain, K. R.; Gould, C. A.; Marchiori, D. A.; Kwon, H.; Nguyen, T. T.; Rosenkoetter, K. E.; Kuzmina, D.; Tuna, F.; Britt, R. D.; Long, J. R.; Harvey, B. G. *J. Am. Chem. Soc.* **2022**, *144* (48), 22193–22201.
- (2) Gould, C. A.; McClain, K. R.; Reta, D.; Kragoskow, J. G. C.; Marchiori, D. A.; Lachman, E.; Choi, E.-S.; Analytis, J. G.; Britt, R. D.; Chilton, N. F.; Harvey, B. G.; Long, J. R. *Science* **2022**, *375* (6577), 198–202.
- (3) Nief, F. *Dalton Trans.* **2010**, *39* (29), 6589.
- (4) Jaroschik, F.; Nief, F.; Ricard, L. *Chem Commun* **2006**, No. 4, 426–428.
- (5) Wedal, J. C.; Evans, W. J. *J. Am. Chem. Soc.* **2021**, *143* (44), 18354–18367.
- (6) Jaroschik, F.; Nief, F.; Le Goff, X.-F.; Ricard, L. *Organometallics* **2007**, *26* (14), 3552–3558.
- (7) Jaroschik, F.; Momin, A.; Nief, F.; Le Goff, X.-F.; Deacon, G. B.; Junk, P. C. *Angew. Chem.* **2009**, *121* (6), 1137–1141.
- (8) Lalancette, J.-M.; Rollin, G.; Dumas, P. *Can. J. Chem.* **1972**, *50* (18), 3058–3062.
- (9) Pedersen, C. J. *Science* **1988**, *241* (4865), 536–540.
- (10) Steed, J. W. *Coord. Chem. Rev.* **2001**, *215* (1), 171–221.
- (11) Hitchcock, P. B.; Lappert, M. F.; Maron, L.; Protchenko, A. V. *Angew. Chem. Int. Ed.* **2008**, *47* (8), 1488–1491.
- (12) MacDonald, M. R.; Ziller, J. W.; Evans, W. J. *J. Am. Chem. Soc.* **2011**, *133* (40), 15914–15917.
- (13) MacDonald, M. R.; Bates, J. E.; Fieser, M. E.; Ziller, J. W.; Furche, F.; Evans, W. J. *J. Am. Chem. Soc.* **2012**, *134* (20), 8420–8423.
- (14) MacDonald, M. R.; Bates, J. E.; Ziller, J. W.; Furche, F.; Evans, W. J. *J. Am. Chem. Soc.* **2013**, *135* (26), 9857–9868.
- (15) Simler, T.; McCabe, K. N.; Maron, L.; Nocton, G. *Chem. Sci.* **2022**, *13* (25), 7449–7461.
- (16) Nocton, G.; Ricard, L. *Dalton Trans* **2014**, *43* (11), 4380–4387.
- (17) Ortu, F. *Chem. Rev.* **2022**, *122* (6), 6040–6116.
- (18) Jaroschik, F.; Nief, F.; Le Goff, X.-F.; Ricard, L. *Organometallics* **2007**, *26* (5), 1123–1125.
- (19) Xémard, M.; Zimmer, S.; Cordier, M.; Goudy, V.; Ricard, L.; Clavaguéra, C.; Nocton, G. *J. Am. Chem. Soc.* **2018**, *140* (43), 14433–14439.
- (20) Reta, D.; Kragoskow, J. G. C.; Chilton, N. F. *J. Am. Chem. Soc.* **2021**, *143* (15), 5943–5950.
- (21) Rinehart, J. D.; Long, J. R. *Chem. Sci.* **2011**, *2* (11), 2078.
- (22) Brown, I. D. *Chem. Rev.* **2009**, *109* (12), 6858–6919.
- (23) Parthey, M.; Kaupp, M. *Chem Soc Rev* **2014**, *43* (14), 5067–5088.
- (24) Allen, G. C.; Hush, N. S. Intervalence-Transfer Absorption. Part 1. Qualitative Evidence for Intervalence-Transfer Absorption in Inorganic Systems in Solution and in the Solid State. In *Progress in Inorganic Chemistry*; Cotton, F. A., Ed.; Wiley, **1967**; Vol. 8, pp 357–389.
- (25) Hush, N. S. Intervalence-Transfer Absorption. Part 2. Theoretical Considerations and Spectroscopic Data. In *Progress in Inorganic Chemistry*; Cotton, F. A., Ed.; Wiley, **1967**; Vol. 8, pp 391–444.
- (26) Brunschwig, B. S.; Creutz, C.; Sutin, N. *Chem. Soc. Rev.* **2002**, *31* (3), 168–184.
- (27) D’Alessandro, D. M.; Keene, F. R. *Chem. Soc. Rev.* **2006**, 10.1039.b514590m.
- (28) Gould, C. A.; McClain, K. R.; Yu, J. M.; Groshens, T. J.; Furche, F.; Harvey, B. G.; Long, J. R. *J. Am. Chem. Soc.* **2019**, *141* (33), 12967–12973.
- (29) Meihaus, K. R.; Fieser, M. E.; Corbey, J. F.; Evans, W. J.; Long, J. R. *Am. Chem. Soc.* **2015**, *137* (31), 9855–9860.
- (30) Escher, A.; Neuenschwander, M.; Engel, P. *Helv. Chim. Acta* **1987**, *70* (6), 1623–1637.

Chapter 4: Systematic study of the Cnt ligand in the LnCotCnt series

I. Synthesis and characterization of LnCotCnt compounds with heavy lanthanides	167
1. Reminder on sandwich compounds of lanthanides	167
2. Synthetic path	169
3. Discussion on the XRD structure	171
4. NMR analysis and anisotropy discussion	173
5. Observed flexibility with related systems	177
II. Synthesis and characterization	178
1. Extension of the synthesis and XRD characterization	178
2. Problem arising from characterization	180
3. Rationalizing the isomerization trigger	182
4. A new molecular lanthanide switch	184
5. Adapted synthesis and full characterization	185
III. Isomerization study	189
1. Come back on the case of KCnt	189
2. Spectroscopic study of the isomerization of 4.2 _{Ln}	194
3. Rationalization over the series	197
IV. Conclusion	198
References	199

Chapter 4: Systematic study of the Cnt ligand in the LnCotCnt series

I. Synthesis and characterization of LnCotCnt compounds with heavy lanthanides

1. Reminder on sandwich compounds of lanthanides

Since the discovery of ferrocene, the obtention of sandwich compounds has been a central investigation in organometallic chemistry as illustrate in **Figure 4. 1**.¹ More than structurally fascinating, they also have a variety of usage.²⁻⁵

1. First attempts

Only a few years after the initial discovery of such structures, their synthesis was extended to lanthanide compounds. However, due to their mainly electrostatic interaction, they predominantly formed LnCp₃ compounds.^{6,7} The few compounds that were able to form LnCp₂ complexes showed a polymeric structure due to the non-saturated coordination sphere of the large lanthanide ions as displayed in **Figure 4. 1**.⁸⁻¹⁰ As discussed previously, this interaction can be broken by solvation. However, even base-free, the presented structures feature a bending angle due to a mix of interaction and van der Waals forces.^{11,12}

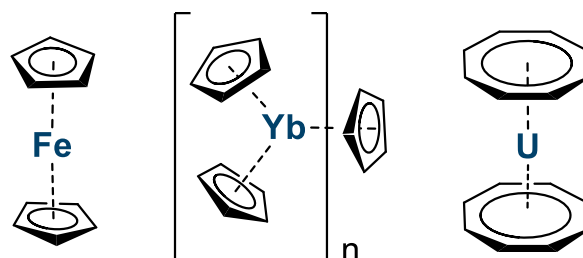


Figure 4. 1 Schematic representation from left to right of ferrocene¹, polymeric YbCp₂¹⁰ and uranocene.¹³

As a consequence, the use of a larger ligand was warranted to ensure saturation of the coordination sphere. In 1968, the publication, by the group of Streitwieser, of the uranocene structure, using two cyclooctatetraene (Cot) ligand showed in **Figure 4. 1**, constitutes a nice example of a better size-match between the ligand and the metal.¹³ One disadvantage of the Cot ligand is its dianionic charge, making it difficult to create neutral complexes with lanthanide ions. To this day, most of the anionic LnCot₂⁻ have been reported and only cerium was able to form the neutral CeCot₂.¹⁴⁻¹⁶

2. Fine tuning the physical properties

Both strategies were then fine-tuned to access different properties.¹⁷ For the small Cp ligand, substitution has been the main subject of work. The aims were two-fold, first increasing the solubility of the complex and then using large enough substituents to saturate the coordination sphere.¹⁸ On the other side, the Cot ligand has been substituted to tune its electronics, and some work has also been done on the counter-ion.¹⁹

One striking example of application of this type of research has been the single molecule magnet field. Indeed, it has been shown since 2003, that the sandwich type arrangement was highly favorable to show interesting magnetic properties with lanthanide ions.^{20,21} As such, the drive to find the perfect ligand to fit these metals in an almost linear scaffold has led to a lot of various studies on ligand development. For example, the use of ^tBu and ⁱPr groups on the Cp scaffold has unlocked the synthesis of high blocking temperature SMM for the dysprosocenium type complexes.^{22,23} Furthermore, the Cot ligand has been used both in its non-substituted and substituted form in combination with erbium ion to form decent SMMs.^{24–26}

3. The Cnt ligand, a new player

If those studies were quite successful in developing new properties, our group was interested in the possibility of finding a ligand that was both an adequate size match and monoanionic more fitted for lanthanide ions. In the series of Hückel aromatic molecule, the next compound after the Cot ligand is the cyclononatetraenyl ligand or Cnt, a monoanion in its aromatic form. It was then decided to investigate its coordinating behavior with divalent lanthanide. During this study, the group of Nakajima published a luminescence study of EuCnt₂. Interestingly, this proved that it was indeed possible to form neutral linear complexes with the Cnt ligand and divalent lanthanide ion. However, they report an overall very low yield of 4 %.²⁷

By tuning the synthesis of the ligand, the group managed to obtain a mixture of the two isomers Cnt^{cis} and Cnt^{trans} as presented in **Figure 4. 2**.²⁸ It was observed that the presence of the Cnt^{trans} isomer would increase the overall solubility of the ligand. This was particularly harnessed in the development of the salt metathesis route used to extend the synthesis of LnCnt₂ to Ln = Sm, Yb and Tm. As presented in **Figure 4. 2**, by using a more soluble mixture of the ligand with a small amount of coordinating solvent, the group was able to promote the salt metathesis reaction. Additional step of solvents removal allowed for the isolation of the desired neutral sandwich compound in reasonable yields (33% - 62%).²⁸ This study also reports the weak coordination of the Cnt ligand with the metallic center, showing that it is easily displaced by coordinating solvent such as THF. The low solubility in its *cis* form added with its

high lability probably explains why the initial studies on the coordination of Cnt discussed in **Chapter 2** had difficulties crystallizing the Cnt-bonded compounds.^{29,30}

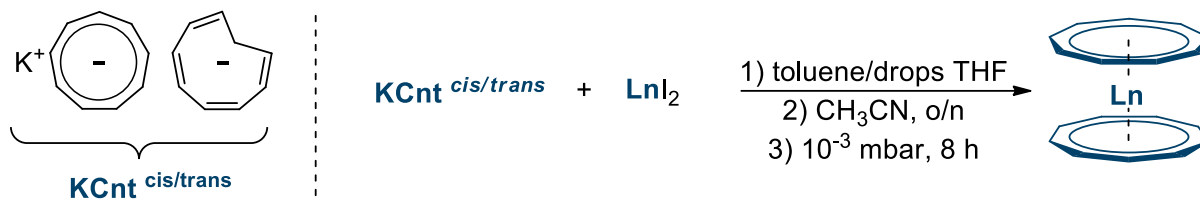


Figure 4. 2 On the left, representation of the KCnt salt as its two isomers Cnt^{cis} and Cnt^{trans} , on the right, synthetic path to $LnCnt_2$ complexes with $Ln = Sm, Eu, Yb, Tm$.

Once the Cnt ligand had allowed the synthesis of neutral sandwich compounds of lanthanide ions, we decided to extend this chemistry to the most common oxidation state of this family, the trivalent state. To continue toward the obtention of neutral compound, we decided to target an heteroleptic scaffold with a dianionic ligand. As mentioned previously, a better match for lanthanide ions is the Cot ligand. Hence, we looked into the synthesis of the $LnCotCnt$ family.

During this study, a communication by the Roesky group reported the formation of $LnCotCnt$ complexes with $Ln = Nd, Sm, Dy, Er$.³¹ Identifying some discrepancies in the XRD resolution, we decided to continue our study and to extend the synthesis to all of the lanthanides. The following work will be divided in two studies focusing each on one particularity of the Cnt ligand. First, investigation of the Cnt ligand's flexibility revealed that it undergoes a hapticity switch to adapt to the decrease of the ionic radius of the late lanthanides.³² Then, following an intriguing pattern of isomerization of the terbium compound and the extension to the early lanthanide, we discovered the possibility of a retro-isomerization of the ligand coordinated to the metal. This isomerization study will be the subject of the last part of this chapter.

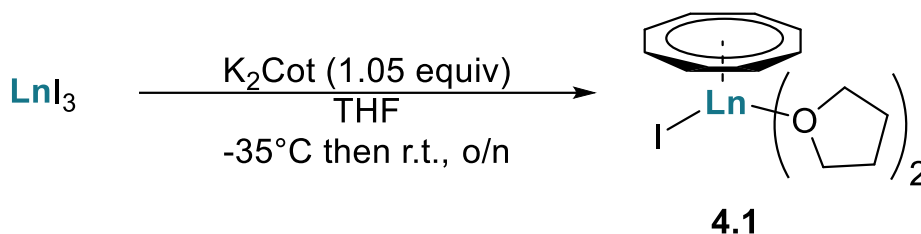
2. Synthetic path

To begin with, we were interested in the synthesis of the $LnCotCnt$ compound with the late lanthanide. Particularly, this study will be focused on $Ln = Tb, Dy, Ho, Er$ and Tm . The synthesis of both the ytterbium and lutecium analogues were not possible under those conditions. While the lutecium case was covered in our report, we did not manage to extend the synthesis to the ytterbium complex.³²

1. Synthesis of the starting material

Considering the weak coordination of the Cnt compound, it was decided to first prepare $[LnCot]$ compounds as a starting material.

To do so, adapted from literature procedure, a salt metathesis reaction was performed with LnI_3 and K_2Cot according to **Scheme 4. 1**.³³ The formed byproduct, KI , was then precipitated and filtered off. The product was crystallized in THF at low temperature. Several round of crystallization could be set up to increase the yields.

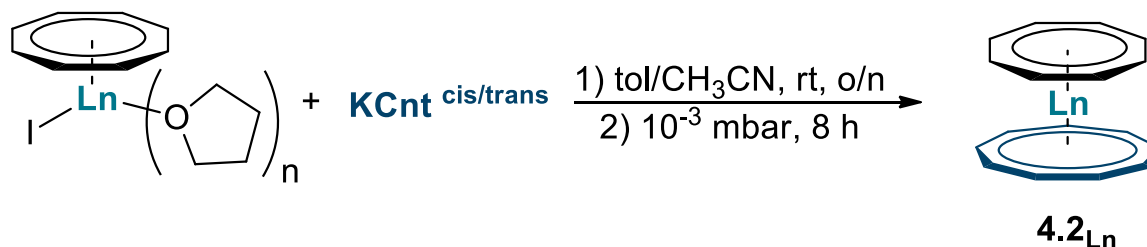


Scheme 4. 1 Salt metathesis reaction forming the Cot containing starting compound, Ln = Tb, Dy, Ho, Er, Tm.

Most of those compounds had already been described in the literature except for **4.1_{Tb}** and **4.1_{Ho}** which were analysed by SC-XRD. Despite a fairly larger metallic ion than the end of the series, they both show coordination of two THF molecules.

2. Reaction with KCnt

In a second time, another salt metathesis reaction was performed with the Cnt ligand salt according to **Scheme 4. 2** to form the linear sandwich compounds noted **4.2_{Ln}**. A mixture of solvent was used to promote the solubility without displacing too much the Cnt ligand, in a similar fashion to the previous report on LnCnt_2 .²⁸ To ensure that the crystalized compound was base free, the mixture was evaporated twice and taken up in toluene.



Scheme 4. 2 Salt metathesis reaction with the Cnt salt to form the sandwich compound 4.2_{Ln}, Ln = Tb, Dy, Ho, Er, Tm.

Crystalline material could be obtained for each reaction by concentration at cold of the saturated toluene solution of **4.2_{Ln}**. Their structural analysis will be discussed in the next part. However, due to the weak solubility of those compounds, the crystalline yields were very low. As such, it was decided to isolate them as pure microcrystalline powder by removal of the solvent after filtration for other analysis and characterisation.³²

3. Discussion on the XRD structure

1. Different approach

In their 2019 communication, the Roesky group presented the structure of the four LnCotCnt compound with Nd, Sm, Dy and Er.³¹ They reported the difference in behavior between the early lanthanides (neodymium and samarium) and the late lanthanides (dysprosium and erbium). Notably, they crystallize in the same space group $P2_1/n$ but for the early lanthanides, the metallic ion is located on a special symmetry position. For the late lanthanide, the ion is shifted and both of the ligands are delocalized on the same side. This allows reconstruction of the full molecule by application of the symmetry operation of the group. However, in that case, particularly for the erbium compounds, if the ring is restrained to be flat as it would be expected, the ellipsoids feature a large agitation factor. This indicated that there was potentially another model possible to describe those compounds.

2. Step by step resolution

For the resolution of 4.2_{Ln} , a comparable strategy was used. Notably, the compounds were found to crystallize in the $P2_1/n$ space group in a similar fashion (**Figure 4. 3 a**). Then, reconstructing the sandwich arrangements by application of the symmetry operation leads to the scenario where each element is doubled (**Figure 4. 3 b**). To remediate this, one of each ligand is removed (**Figure 4. 3 c**). However, as the metallic ion is not on the special position, there are two non-equivalent dispositions of the metal. This creates two different options both crystallographically valid (**Figure 4. 3 d** and **e**). In both cases, we noticed that one of the rings had a lower hapticity than expected. This behavior had already been observed for the Cnt ligand but never on the Cot ligand to the best of our knowledge. Considering the distances to the ion on top of this observation made us select the scenario where the Cnt is not fully coordinated as displayed in **Figure 4. 3 d** as the most likely.

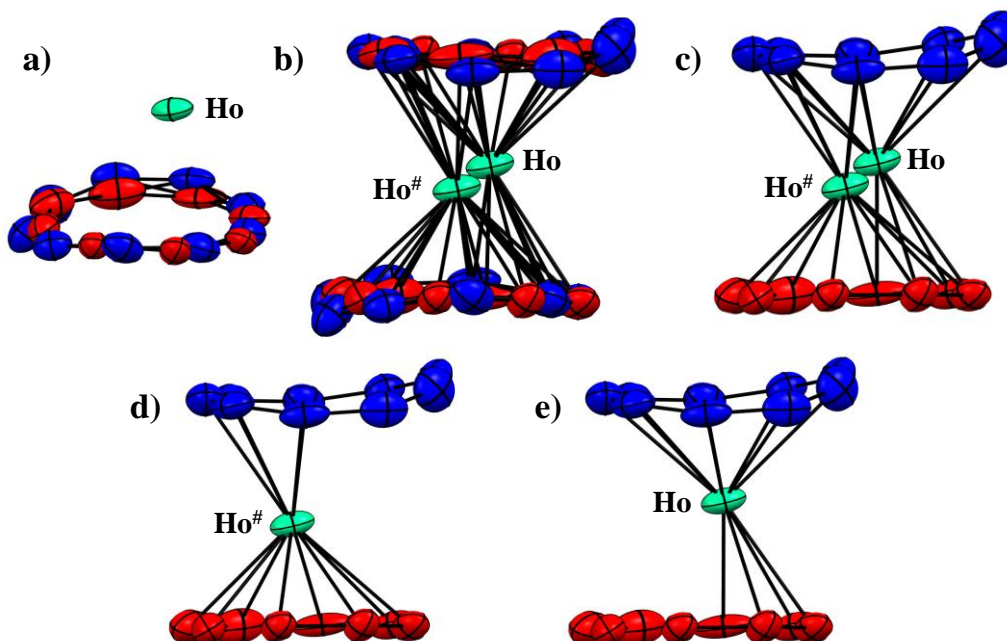


Figure 4.3 Step by step resolution of the structure of 4.2_{Ho} complex with symmetrical considerations (reproduced from ³²).

Replication of this approach on 4.2_{Dy} , 4.2_{Er} and 4.2_{Tm} showed similar behavior. An interesting trend noted was that the smaller the lanthanide ion, the more displaced the Cnt ligand. This was further illustrated by the synthesis of the lutecium compound through another route.³² Trying to rationalize this behavior led to the study of the attribution of formal hapticity numbers as illustrated on **Figure 4.4**. Those numbers were determined based on a structural analysis on several constructed centroids on the Cnt rings, where we tried to minimize both the deviation from linearity and the centroid—Ln distances.³²

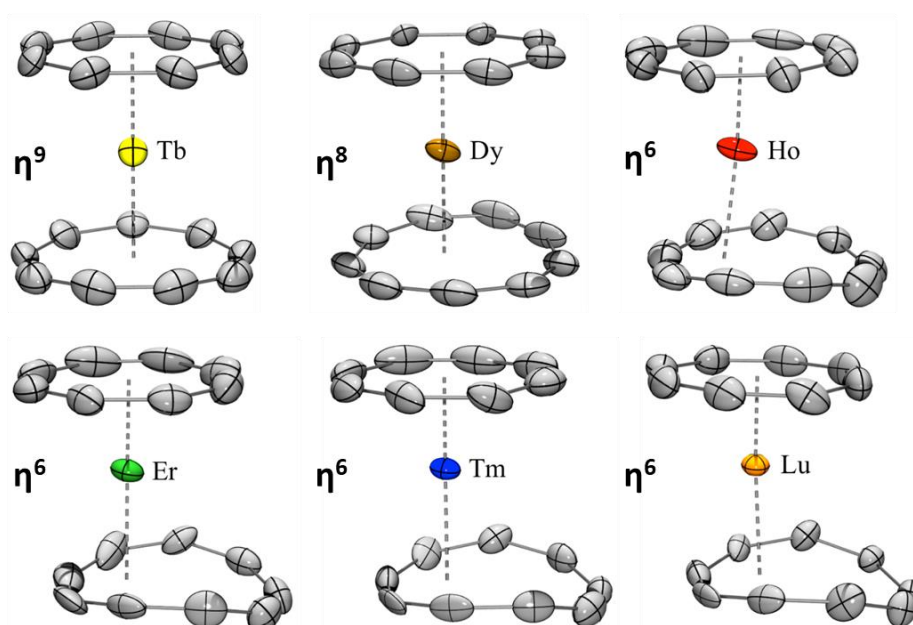


Figure 4.4 ORTEP representation of 4.2_{Ln} with $\text{Ln} = \text{Tb}, \text{Dy}, \text{Ho}, \text{Er}, \text{Tm}, \text{Lu}$ and the associated hapticity number (reproduced from ³²).

3. The case of the Terbium

On the previous **Figure 4. 4**, terbium is represented although it does not crystallize in the same fashion. We found that the shift in behavior observed in the previous study was present for early lanthanide ions and up until terbium.^{31,32} Contrary to their approach however, we decided to model these structures in the Pnma space group. This yields a structure where the Cnt ligand is fully coordinated to the metallic center, representing an η^9 hapticity, as illustrated in **Figure 4. 5**.

Furthermore, this was not the only difference of **4.2_{Tb}**. It was observed multiple times that another product would crystallize alongside the characterized terbium containing compound. XRD analysis revealed that the Cnt could crystallize in its *trans* conformation to form **4.2_{Tb}^{trans}** as illustrated on **Figure 4. 5**. This peculiar behavior had not been observed for any of the other **4.2_{Ln}** synthesized.

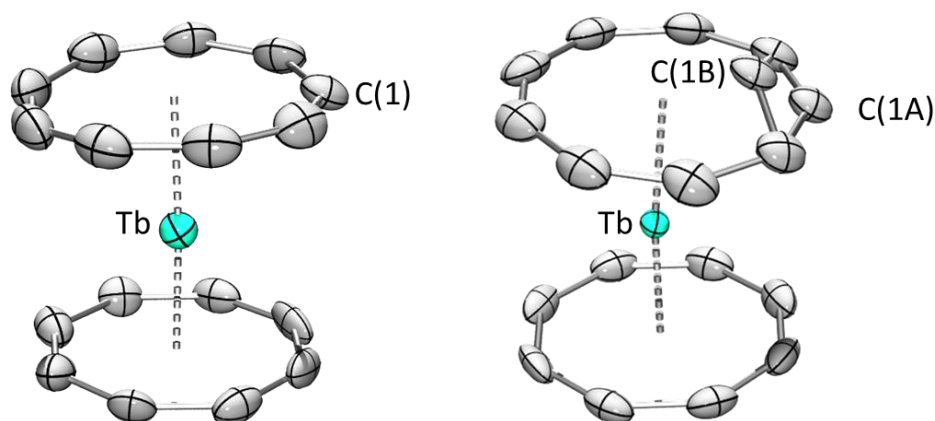


Figure 4. 5 Comparison of the ORTEP representation of **4.2_{Tb}^{cis}** on the left and a mixture of **4.2_{Tb}^{cis}** and **4.2_{Tb}^{trans}** on the right ellipsoids are represented at 50% probability, carbon atoms are in grey and terbium in light green, C(1A) and C(1B) denote the disordered carbon position corresponding respectively to the Cnt^{cis} and the Cnt^{trans}.

At that time, we did not understand the reason of the formation of **4.2_{Tb}^{trans}** and decided to focus on the hapticity switch behavior. With the structural information in the solid form at hand, we set to study a possible impact in solution by ¹H NMR spectroscopy.

4. NMR analysis and anisotropy discussion

1. Paramagnetic NMR

The compounds were characterized by solution ¹H NMR spectroscopy and their combined spectra are presented in **Figure 4. 6**.

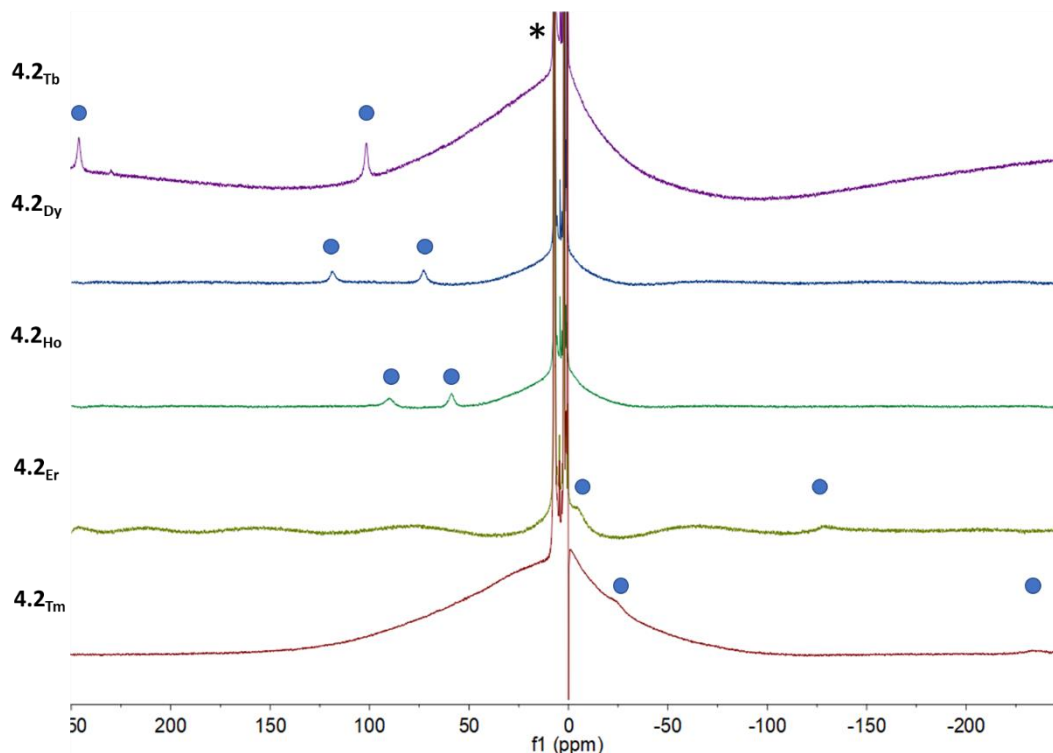


Figure 4. 6. NMR spectra recorded for the 4.2_{Ln} compounds in toluene- d_8 at 300 K. The ligands peaks are denoted by blue circles and * corresponds to the residual protio signal of the solvent.

Interestingly, their strong paramagnetism translates in the high value of chemical shifts but does not preclude analysis of their spectra. Particularly, the high symmetry of the complex can be seen in the obtention of two signals, one for each ring. Although, for 4.2_{Er} and 4.2_{Tm} , the resonances can be detected, their broadness do not allow attribution of the signals.

2. Discussion on the symmetry

As mentioned above, only two signals can be seen on the spectra. For the erbium spectra, the high paramagnetic character required a strong phase correction inducing deformation of the baseline. However, two signals could be discerned. This is coherent with the vision of sandwich compounds; however, it does not illustrate the hapticity switch, observed in the solid-state structure. One explanation could be that this feature comes from packing forces. It constrains the Cnt ligand to shift toward the outside of the coordination sphere in the solid form, while in solution, it is free to be placed in symmetrical fashion. It could also translate the fact that, at room temperature, the Cnt ligand has a rotatory movement homogenizing its chemical environment, and the different peaks coalesce into one single feature. This possibility of assigning the chemical shift of a non-symmetrical Cnt coordination was already discussed in **Chapter 2** while mentioning a previous study about an alleged Nb—Cnt compound.²⁹ As such, we investigated the temperature-dependent-behavior of the complexes and the variable temperature analysis of 4.2_{Dy} is presented in **Figure 4. 7**.

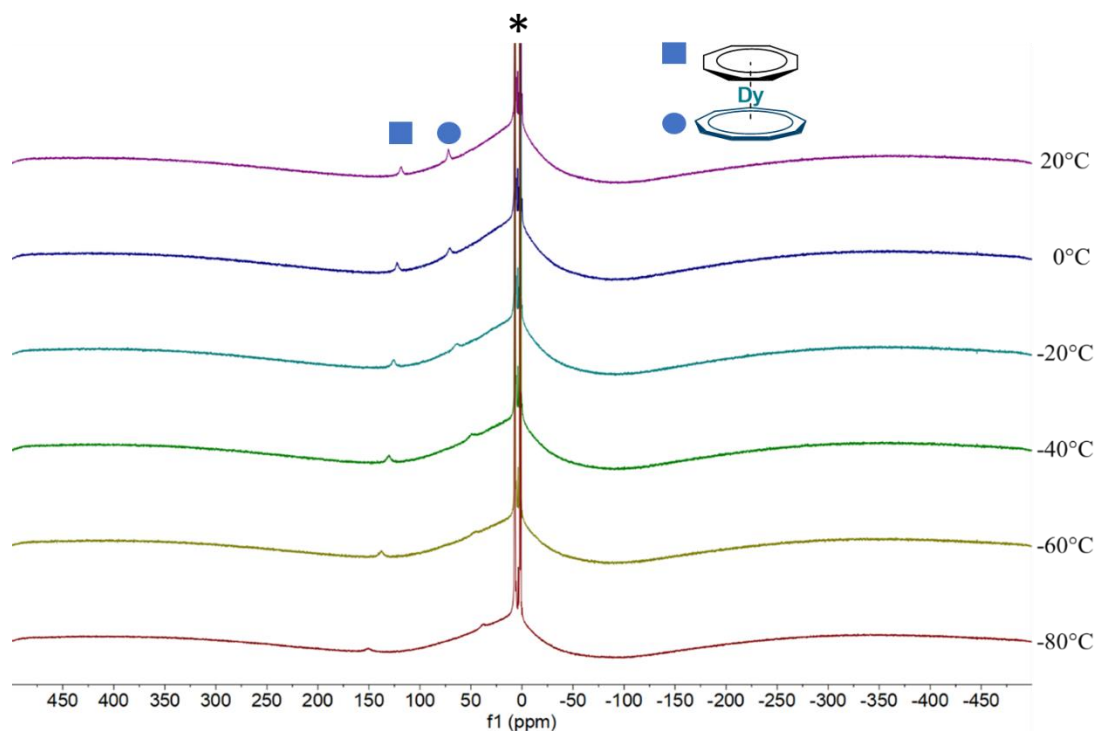


Figure 4. 7. VT-NMR analysis of **4.2_{Dy}** across the range [20 °C ; -80 °C], the blue dot and square denote the Cnt and the Cot resonances respectively.

Unfortunately, these studies did not allow to identify a change of behavior and a coalescence of the Cnt ligand resonances. This was also performed for **4.2_{Lu}**, a diamagnetic molecule presenting sharper peaks easier to analyse, but it was once again unsuccessful. As of note, the coalescence visible in the paper about the niobium compound was seen at -95 °C. It is then possible that we did not reach the coalescence temperature. Therefore, it is difficult to conclude on the structure in solution.

3. Discussion of the anisotropy

If the ^1H NMR analysis appears to be insufficient to properly characterize the Cnt behavior, a characteristic of the lanthanide ion can be identified. Indeed, the change of sign in the chemical shifts in between **4.2_{Ho}** and **4.2_{Er}** is reminiscent of the break of preferential anisotropy in the late lanthanide series.

The preferential anisotropies for Ln^{3+} ions were previously discussed in the **Introduction** to present the different strategy of synthesis for SMM complexes and are reminded in **Figure 4. 8.**

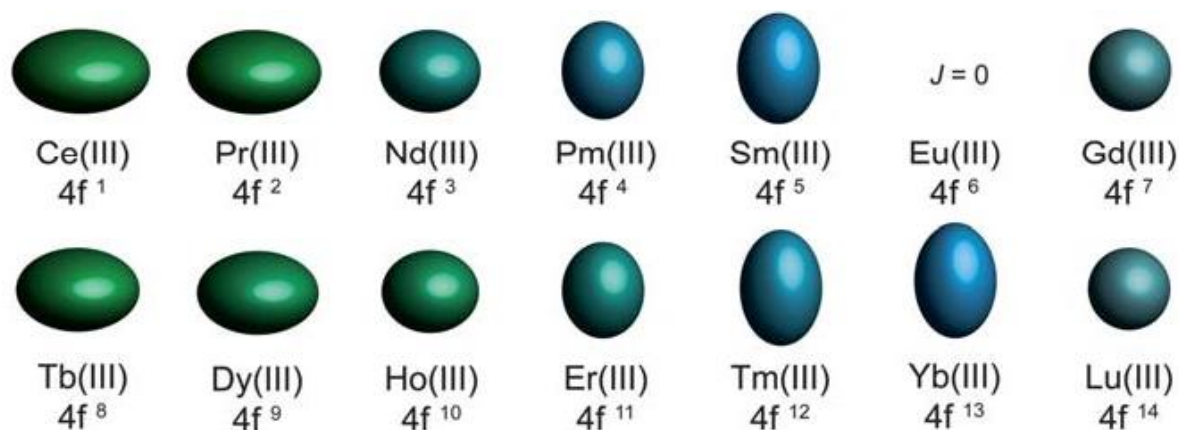


Figure 4. 8 Schematic representation of the electronic disposition for standard Ln^{3+} (reproduced from ref²¹)

It is interesting to see that the transition from oblate to prolate electronic density translates in the NMR spectra as a change of sign, as illustrated in **Figure 4. 9**. Additionally, this was also observed later in the study with computational analysis at the SA-CASSCF/RASSI-SO level.³² Representation of the anisotropy axis shows a diagonal placement for **4.2_{Dy}** and **4.2_{Ho}**. However, for **4.2_{Er}** and **4.2_{Tm}** the axis is significantly more aligned with the centroids of the ligands.

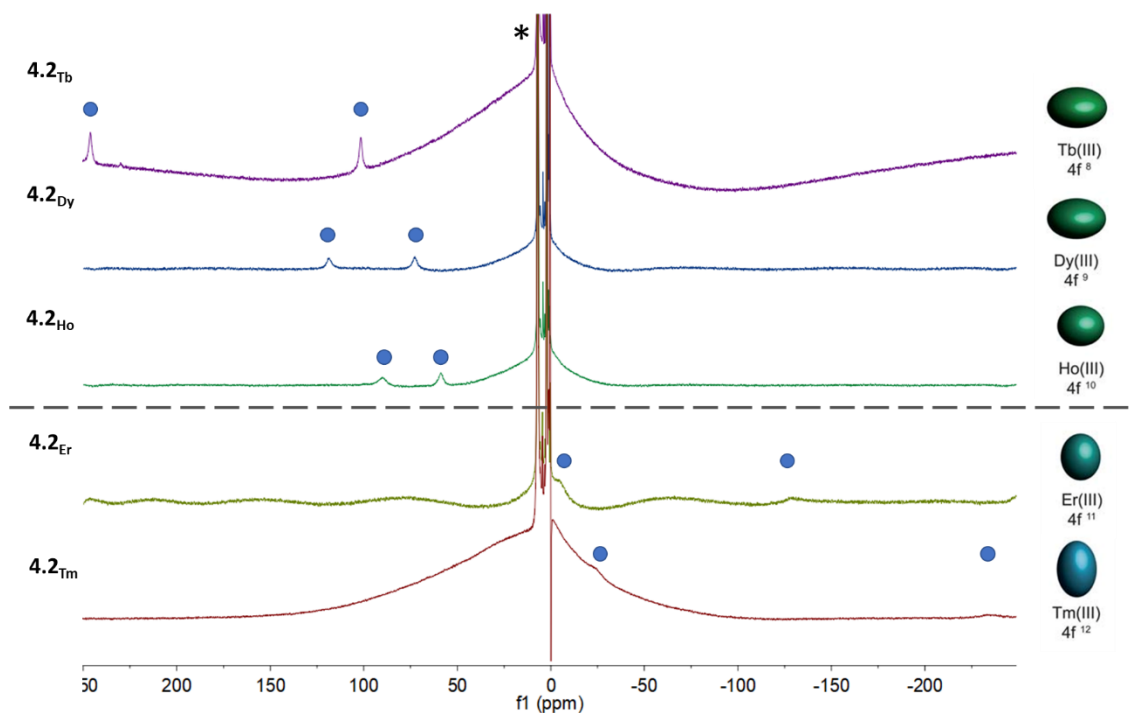


Figure 4. 9 NMR spectra recorded for the **4.2_{Ln}** compounds in toluene- d_8 at 300 K. The ligand peaks are denoted by blue circles and * corresponds to the residual protio signal of the solvent. The grey line marks the change of preferential anisotropy and on the right of the spectra are represented the electronic shape for the Ln^{3+} ions as reported by Long and Rinehart.²¹

This comes to show that NMR analysis on paramagnetic compound can be a really useful tool, even when they do not allow precise attribution of the resonances.

5. Observed flexibility with related systems

The flexibility demonstrated by this ligand diminishing its hapticity with smaller ion can also be induced by introducing coordinating molecule in the complex. In the seminal report of the LnCnt_2 , it was mentioned that improperly dried compounds often displayed coordinated solvent molecules such as THF or acetonitrile. Particularly, two behaviors were observed, either partial decoordination with lowering of the hapticity, or complete removal of the Cnt motif from the coordination sphere.

1. Solvent induced hapticity

This was found to be the case for the trivalent compound 4.2_{Ln} . As an example, we identified the compound $4.2_{\text{Dy}}\cdot\text{MeCN}$ and $4.2_{\text{La}}\cdot\text{MeCN}_2$, where molecules of solvent are still present as illustrated in **Figure 4. 10**.

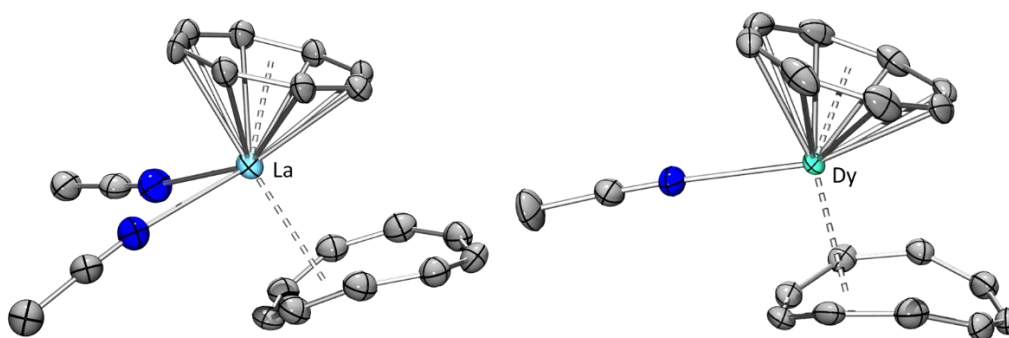


Figure 4. 10 ORTEP representation of $4.2_{\text{La}}\cdot\text{MeCN}_2$ and $4.2_{\text{Dy}}\cdot\text{MeCN}$, carbon atoms are in grey, nitrogen in blue, lanthanum and dysprosium in light blue and green respectively. Hydrogen atoms were omitted for clarity.

Our initial study was mostly targeted toward the obtention of the sandwich compounds and the double removal of the volatile was efficient in making disappear these solvent-adducts.

2. Harnessing the properties of the two molecules

For a joint study with the Roesky group, we got interested in the changes in properties between the solvated and unsolvated forms. Indeed, they noticed that this solvent-induced structural changes had a stark effect on the physical properties. As expected for SMM, change in the symmetry and coordination by solvent molecules turns off the slow magnetic relaxation. This is illustrated for the erbium compound in **Figure 4. 11**.^{31,34} For the luminescent properties, the opposite is observed, the formation of the sandwich arrangement turns off the emission, as shown for the cerium analogue.

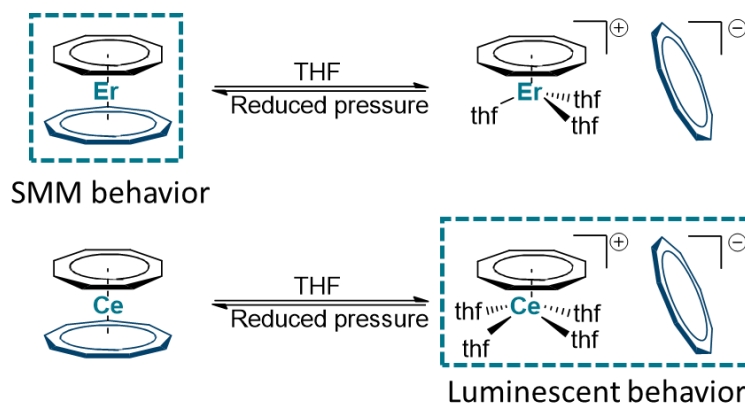


Figure 4. 11 Schematic representation of the property switch (on the top the magnetism and on the bottom the luminescence) provoked by the (de)coordination of the Cnt ligand.

With this study, we continued the original goal of completing the series of the LnCotCnt compound, particularly to try and rationalize the difference in behavior in the solid form between **4.2_{Tb}** and **4.2_{Dy}**. This could also help gather information of the peculiar isomerization observed with **4.2_{Tb}**.

II. Synthesis and characterization

This first study allowed us to investigate in depth the late lanthanides and we decided to carry on with the beginning of the series.

1. Extension of the synthesis and XRD characterization

1. Salt metathesis and toluene extraction

A similar reaction was performed with formation of the Cot compound as illustrated in **Figure 4. 12**. Interestingly, these compounds are also accessible through iodine-promoted oxidation of the lanthanide metal by cyclooctatetraene as reported by Mashima.³⁵ Due to the convenience of the first synthesis however, most of the **4.1_{Ln}** were synthesized through the salt metathesis route.

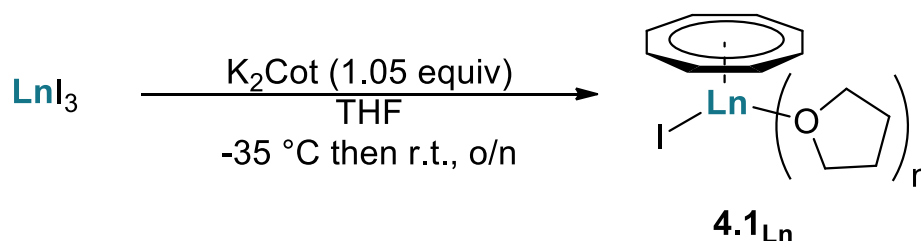


Figure 4. 12 Salt metathesis reaction forming the Cot containing starting compound ($n = 3$ for Ln = La, Ce, Pr, Nd, and Sm, $n = 2$ for Ln = Gd, Tb, Dy, Ho, Er, Tm).

Then, a similar reaction was performed to obtain coordination of the Cnt motif, as reported in **Figure 4. 13**.

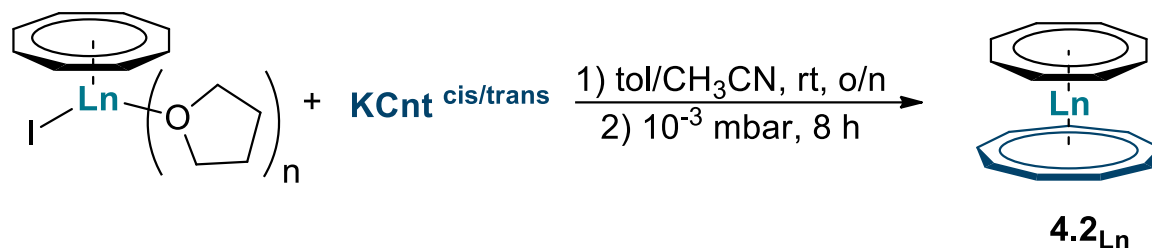


Figure 4. 13 Salt metathesis reaction with the Cnt salt to form the sandwich compound **4.2**, Ln = La, Ce, Pr, Nd, Sm, Gd, Tb, Dy, Ho, Er, Tm.

All the classical trivalent lanthanides react similarly in those conditions to give brightly coloured product. Once again, the very low crystalline yield prompted us to isolate those compounds as microcrystalline powders by removal of the toluene.

As of note, the compound of europium and ytterbium were not obtained despite our effort. First, due to their easily attainable divalent state, they do not form **4.1** analogue but instead create one-dimensional chain of (Ln—Cot) motif. Any attempt at creating adequate trivalent starting material and placing it in reaction led to reduction of the lanthanide centers to create LnCnt₂ complex.

2. XRD study

One main difference was identified in the behavior of the crystalline material. The crystalline needles obtained for the early lanthanides were systematically very small despite tuning of the condition of crystallization. Overall, this is probably linked to a lower solubility of those compounds in toluene. This problem also occurred during ¹H NMR analysis where it was particularly difficult to obtain concentrated solution of the desired compounds.

Similarly to **4.2_{Tb}**, the compounds crystallized in the orthorhombic Pnma space group. As for the terbium analogue, severe disorder of the two rings was observed and modelled for most of the ions. The final structures are presented below in **Figure 4. 14**.

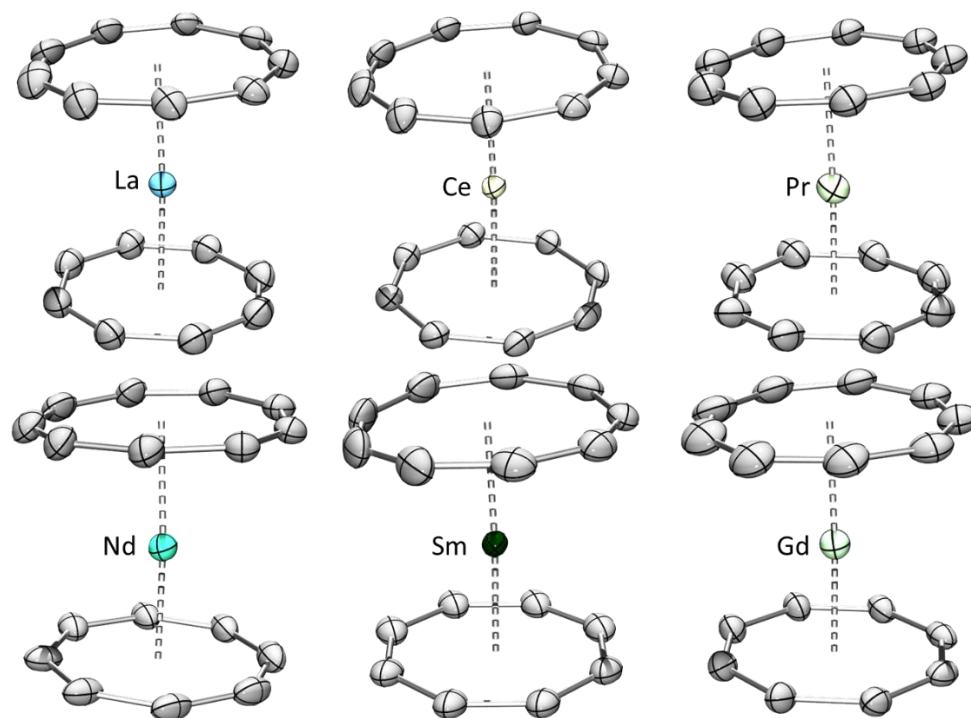


Figure 4. 14 ORTEP representation 4.2_{Ln} represented with ellipsoid at 50% and carbon atom in grey, Ln = La (light blue), Ce (light yellow), Pr (light green), Nd (light blue), Sm (dark green) and Gd (light green), hydrogen atoms and ring disorders are omitted for clarity.

2. Problem arising from characterization

However, if we managed to isolate and characterize each 4.2_{Ln} , several problems were identified during the course of this work.

1. Presence of *trans* isomer in XRD

It was observed several times, at the beginning of the project, that resolution of the different structures would necessitate modelling some amount of *trans* Cnt compound to correctly represent the data. At first, we estimated that it could come from a reaction time not long enough to allow isomerization of the KCnt salt present in 90% *trans* ratio. As such, the reaction times were elongated to 36 h to ensure full conversion of the starting material. This seemed to allowed reproducible synthesis of fully isomerized Cnt ligand. However, it did not manage to solve the other characterization issues.

2. Presence of the isomer in NMR

Similarly, characterization by solution ^1H NMR would sometimes reveal more than one signal for each ring. Having identified the problem for 4.2_{Tb} and using the molecular structure obtained, we hypothesized that we were observing the presence of the *trans* analogue

through NMR as well. At that time, it was unclear whether the former was present from the beginning or if it was forming *in situ*.

The first part of the answer came from the analysis of a solution of 4.2_{Tb} . Indeed, it was observed that this compound would spontaneously evolve from the 4.2_{Tb}^{cis} compound to a mixture of $4.2_{Tb}^{trans/cis}$ while in the NMR tube. The superposition of the NMR spectra is presented on **Figure 4. 15**.

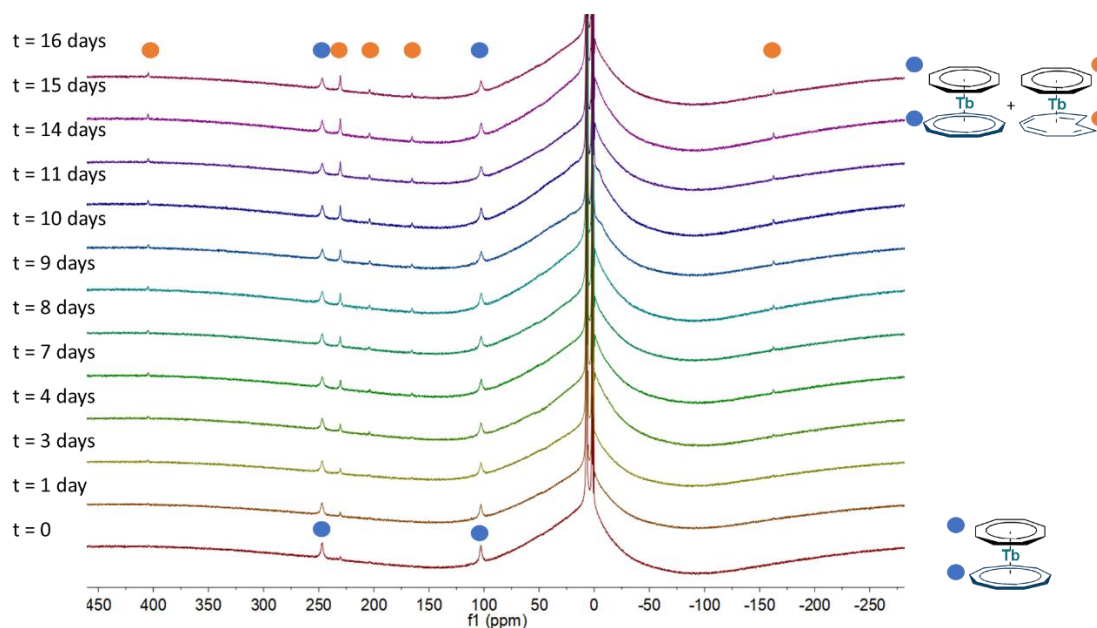


Figure 4. 15. NMR spectra superposition of the evolution of 4.2_{Tb}^{cis} into $4.2_{Tb}^{trans/cis}$ a mixture of the two isomers, blue dots denotes the signals coming from the full cis compound while the orange dots show the signals from the trans compound.

It shows that the isomerization was not complete, explaining the presence of some amount of isomerized compound in the XRD structure as explained above. It also demonstrates that the problem was not the time of reaction. Further work showed that 8 hours were enough to fully isomerize the KCnt salt to form the full *cis* compound. There is rather a subsequent phenomenon, which prompts the retro-isomerization of the ligand.

Quantitative analysis of the evolution is possible even though the strong paramagnetic character of the 4.2_{Tb} increases these uncertainties. The integration of the signal corresponding to the Cot of 4.2_{Tb}^{cis} is normalized at 8 and the other integrations are reported relative to this one. It is then possible to represent graphically the increase of the 4.2_{Tb}^{trans} across time. Looking at the integration of the Cnt compounds which should not vary, we estimate an uncertainty of 1 for the integration. This gives the following graph represented in **Figure 4. 16**, where the integration of the *trans* compound increases to be almost equivalent to the *cis* compound.

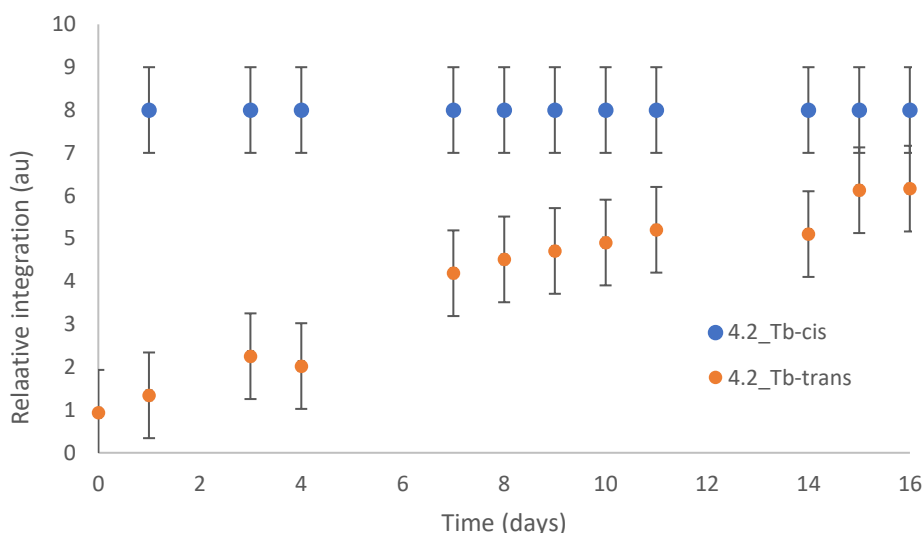


Figure 4. 16. Graphical representation of the evolution of the integration of the Cot moiety for 4.2_{Tb}^{cis} in blue and 4.2_{Tb}^{trans} in orange.

This phenomenon was quite puzzling as it is expected for the Cnt ligand to be more stable in its full *cis* form. *A priori* this reaction seemed contra-thermodynamic so we decided to probe this further.

3. Rationalizing the isomerization trigger

It was observed that this phenomenon was predominantly happening in solution as it was mostly identifiable in NMR spectra.

1. Influence of the solvent

To investigate further different stimuli that could cause isomerization, an NMR follow-up was set, starting from a mixture of $4.2_{Tb}^{trans/cis}$ with a majority of *trans* compound. A small amount of deuterated acetonitrile was added in the absence of light. Over the course of the few hours, the signal evolved to show only two peaks as reported in **Figure 4. 17**. It should be highlighted that they do not correspond to the reported signals for 4.2_{Tb}^{cis} . This is probably due to the formation of an adduct with the acetonitrile as we reported for 4.2_{Dy} . Indeed, upon evaporation and dissolution in toluene, the two peaks expected for 4.2_{Tb}^{cis} appear at much closer shifts to the reported compound as illustrated in **Figure 4. 17**. Of note, they are still slightly off compared to the reported value. It could come from a small amount of acetonitrile still in solution and in exchange with the complex. An additional experiment with a harsher drying could ensure that this is indeed due to the acetonitrile and not another source.

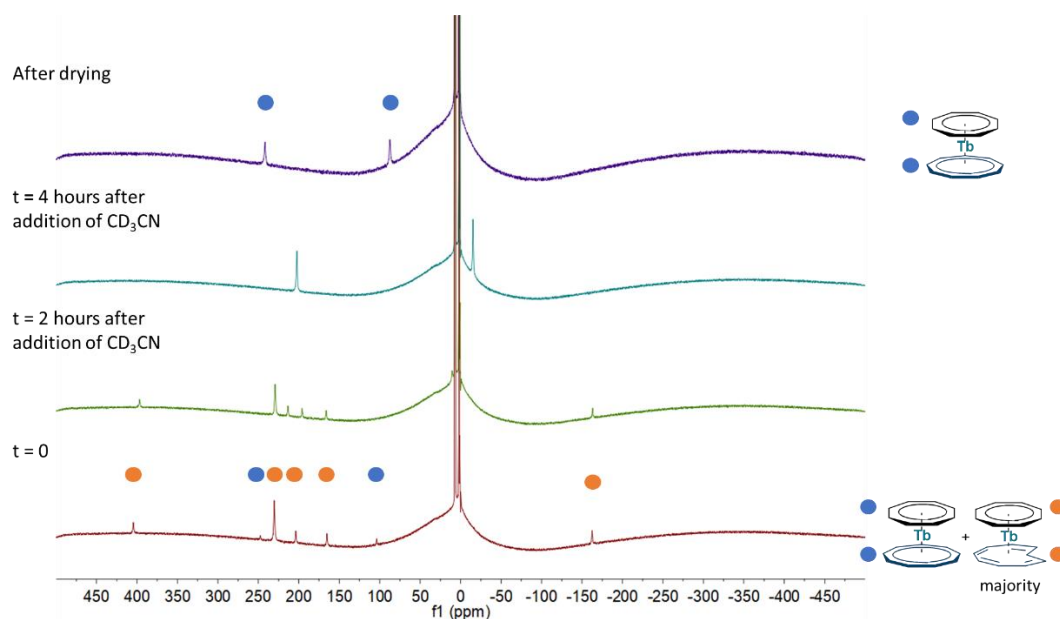


Figure 4. 17. NMR experiment in toluene- d_8 following the evolution of the mixture $4.2_{Tb}^{trans/cis}$ with addition of CD_3CN and after drying.

2. Influence of the light

We then decided after insightful conversations to examine the possibility of it being a light induced phenomenon. We kept the NMR tube of fully isomerized 4.2_{Tb}^{cis} under tin foil for several days and watched the evolution of the NMR spectra. As shown on **Figure 4. 18**, no significant evolution was observed during this time. Afterward, the tin foil was removed and the tube was placed under ambient light. We quickly saw a change in the spectrum and the characteristic peaks of 4.2_{Tb}^{trans} could be identified growing as illustrated in **Figure 4. 18**.

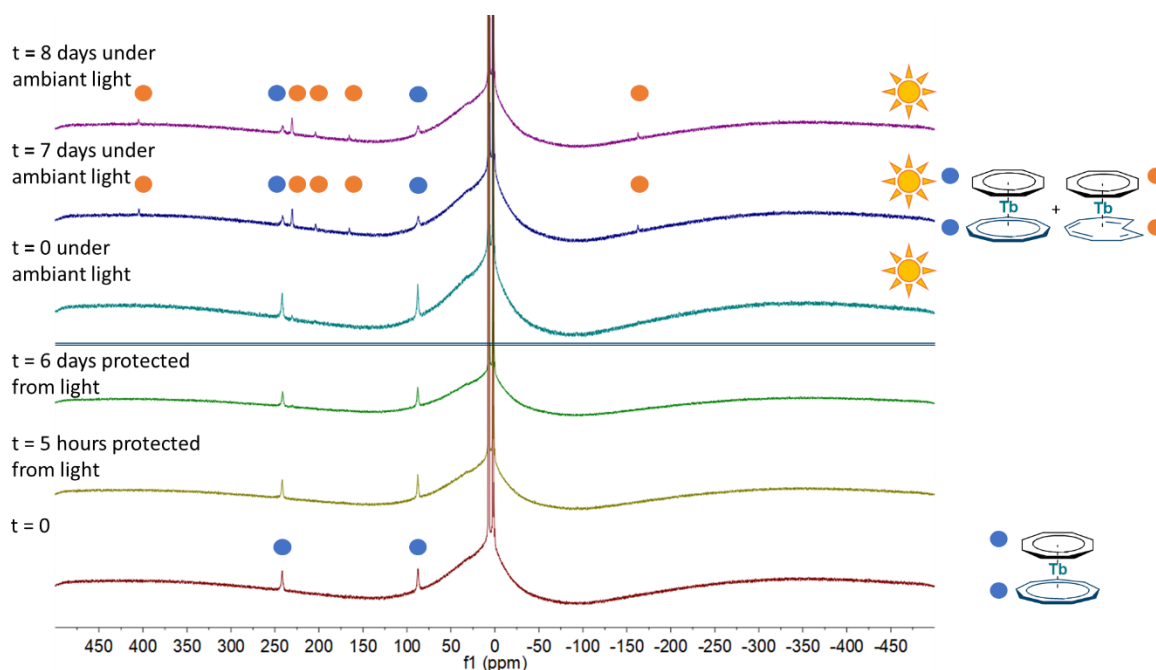


Figure 4. 18. NMR experiment in toluene- d_8 following the evolution of 4.2_{Tb}^{cis} in the absence of light and after irradiation under ambient light (the sun drawing denotes an irradiation under ambient light).

This experiment then reveals that there are at least two triggers for the isomerization of the **4.2_{Tb}^{trans/cis}** species. First, as in the usual sense as described since the first paper from the *trans* to the *cis* form, it can be triggered by the presence of acetonitrile.^{28,32} Then, the new behavior is the *retro*-isomerization from the *cis* form to the *trans* form, appearing to be light-induced. Of note, the term retro-isomerization is used to denote the reversal of what was expected to be a non-reversible phenomenon.

The discovery of the impact of the ambient light on the isomerization of the compound prompted us to explore the impact of the wavelength on the ratio. Preliminary results were obtained after irradiation with a blue light with a broad emission band. As observed in **Figure 4. 19**, the direct irradiation with blue light seems to push the system toward **4.2_{Tb}^{trans}**. Moreover, upon new exposure to ambient light, the system appears to return to its previous state. This further shows that this isomerization process seems reversible and reaches different photo-stationary state (PSS) depending on the wavelength of irradiation. This phenomenon will be explored in the last part of this chapter.

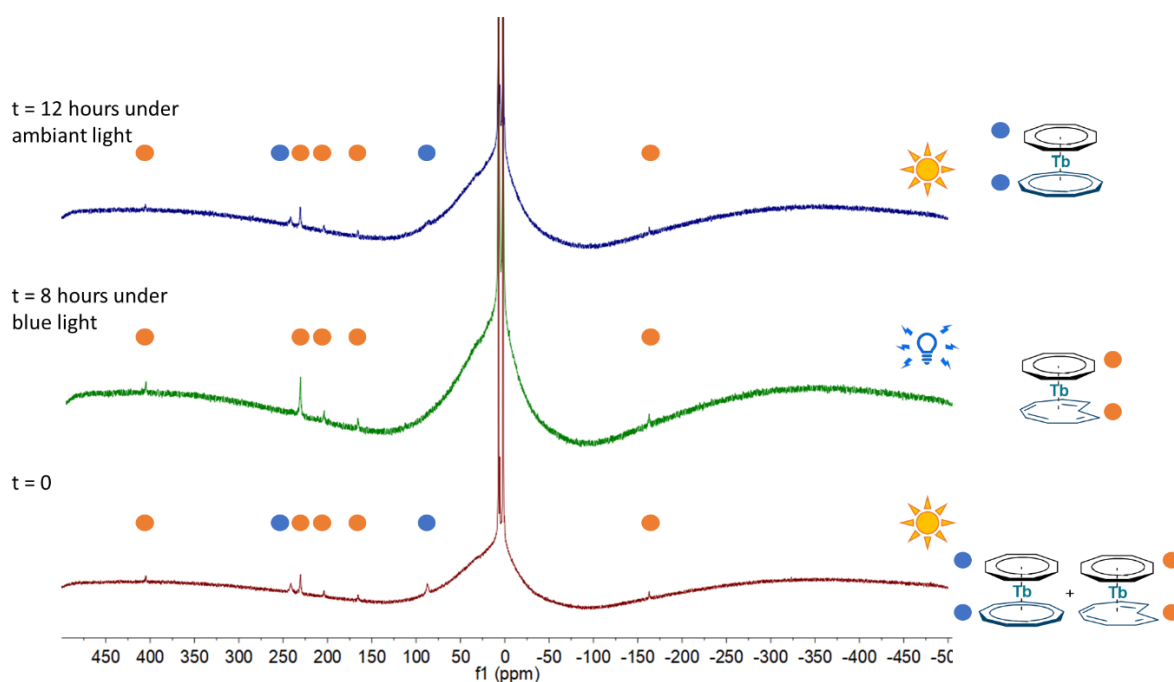
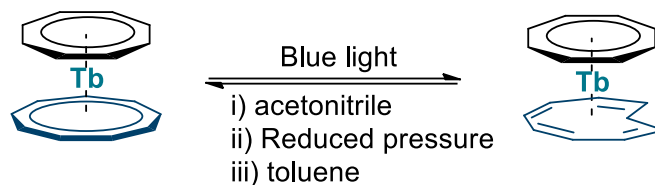


Figure 4. 19 NMR experiment in toluene-*d*₈ following the evolution of **4.2_{Tb}^{cis}** under different irradiation (the sun drawing denotes irradiation under ambient light while the blue lamp denotes irradiation under blue light).

4. A new molecular lanthanide switch

Interestingly, these two processes form what could be considered a switchable reaction similar to what was described for the solvent induced property changes by the Roesky group.³⁴ As illustrated in **Scheme 4. 3**, we are able to access two different forms of **4.2_{Tb}^{trans/cis}** and from the preliminary result, this could be reversible. Furthermore, using the adequate light, it

appears that both of those reactions could be total. This idealized system is represented in **Scheme 4. 3**.



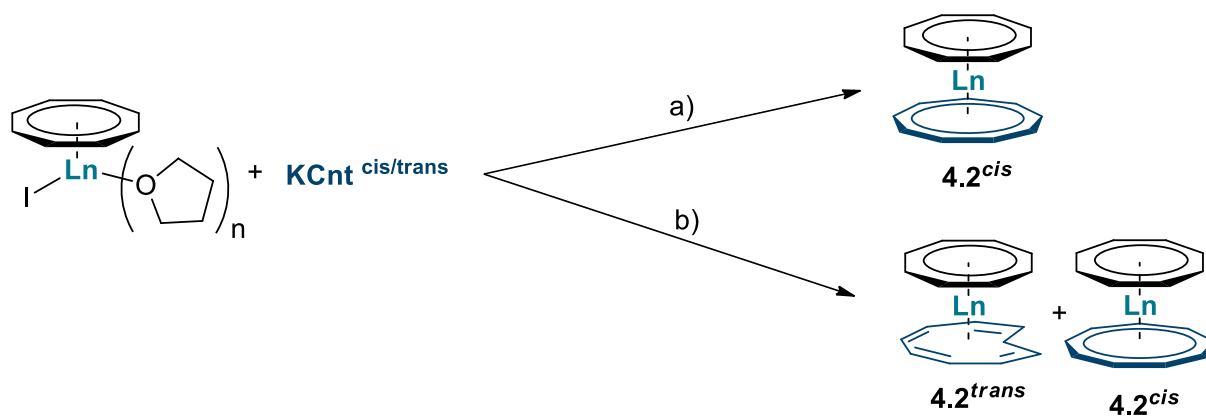
Scheme 4. 3 Idealized switch between 4.2_{Tb}^{cis} and 4.2_{Tb}^{trans}

Even though this system could be called a switch, the necessity of having an open system to place back the solvent after drying makes it not very practicable. Comparably to the work with the Roesky group, investigation of the possibility to observe this change under solid form could be interesting to limit the use of solvent. Furthermore, if different PSS can be found depending on the wavelength of irradiation, thorough UV-visible analysis could inform the choice of wavelength to obtain the fully isomerized compound not only in its *trans* form but also in its *cis* form, creating a fully light-induced switch. This will be the subject of the last part of this chapter. Finally, to make a useful switch, the properties of each species should differ in some ways. One possibility considering the rich redox active reactions described in **Chapter 2 and 3** could be to trigger reactivity thanks to the light-induced isomerization toward 4.2_{Tb}^{trans}. Preliminary studies have started to explore the reactivity of this compound but no results are reported yet.

5. Adapted synthesis and full characterization

1. Rationalized synthesis of the isomers

This elucidation of this unexpected retro-isomerization of the 4.2_{Ln} complexes meant that, not only is it possible to ensure they remain under their *cis* form, but that we could also access mostly *trans* mixtures of compounds. As such, the already reported method to obtain the sandwich form, was adapted to prevent any light irradiation during the evaporations phases as well as the storing of the compound, see **pathway a)** from **Scheme 4. 4**. Then, by using only toluene as a solvent and preventing light irradiation from the beginning of the reaction, a new process favored the obtention of the 4.2_{Tb}^{trans} compound, see **pathway b)** from **Scheme 4. 4**.



Scheme 4.4. Rationalized synthesis of both the *cis* and *trans* compound of 4.2, a) Toluene/MeCN mixture, o/n r.t. then 10^{-3} mbar, 12 h while protected from light, crystallization at low temperature in toluene protected from light, b) Toluene, protected from light, 14 h, r.t. then filtration and crystallization at low temperature in toluene while protected from light.

It is important to note that under the **pathway b)**, the product compound was always obtained as mixture of both isomers with very various *trans* ratio. This ratio will be discussed further in the characterization of the isomerization process.

Of note, 4.2_{La}^{trans} was observed in ^1H NMR (see I.1.3), however no suitable crystals were found for SC-XRD analysis.

2. XRD characterization

Crystallization of those mixtures allowed for the XRD analysis of the isomer mixture. The model used for the resolution of the structure had to be tuned to accurately portray the compounds.

Indeed, theoretically, two disorders need to be considered in this case: the *cis* and *trans* isomers, and the rotation of the ligand. One surprising feature is that the electronic density representing the isomerized carbon on the inside of the cycle seems to be localized at one main position. This is not quite coherent with the possibility of two disordered rings due to rotation, however it has been observed in every case. In some structures, there seemed to be a small amount of delocalised density for the shifted carbon, but not enough to be actually modelled.

This restriction of the localisation of the isomerized atom reduces the number of rings to be modelled to three. This is the method used in the first report of the terbium compound.³² However, this implies complex restraints to ensure the occupation of each carbon to be one. The development of this new synthetic pathways also led to the crystallization of majorly *trans* mixture, potentially limiting the severity of the disorder. Thus, for this next study, two more straightforward methods are used. In some cases, we found that the disorder was not important enough to warrant modelling. And the only drawback to the structure was the presence of fairly large ellipsoids. In some cases where the disorder was important and

needed to be modelled, we found that the modelling of two eclipsed rings with one being *trans* and one *cis* led to acceptable resolutions. This potentially induces a bias in the modelling, as the *cis* ring can most likely undergo rotation, which is not accounted for here. However, due to the complexity of the disorder and the coherence of the obtained molecule, it was chosen as the best option.

It was previously observed that the series was separated in crystallization behavior in between **4.2_{Tb}** and **4.2_{Dy}** (see **1.3.2**). Interestingly, when crystallized as a mixture of isomers, it was observed, for **4.2_{Ln}^{trans/cis}** with Ln = Dy and Ho, that they crystallized in the Pnma space group as well. For **4.2_{Er}** and **4.2_{Tm}** however, the behavior was unchanged. The severity of the disorder for the last two atoms have precluded their structure to be correctly solved.

The compounds crystallizing in the Pnma space group are represented in **Figure 4. 20**. Of note, the *cis/trans* disorder are omitted and the $\rho = r^{\text{trans/cis}}$ is indicated for each compound.

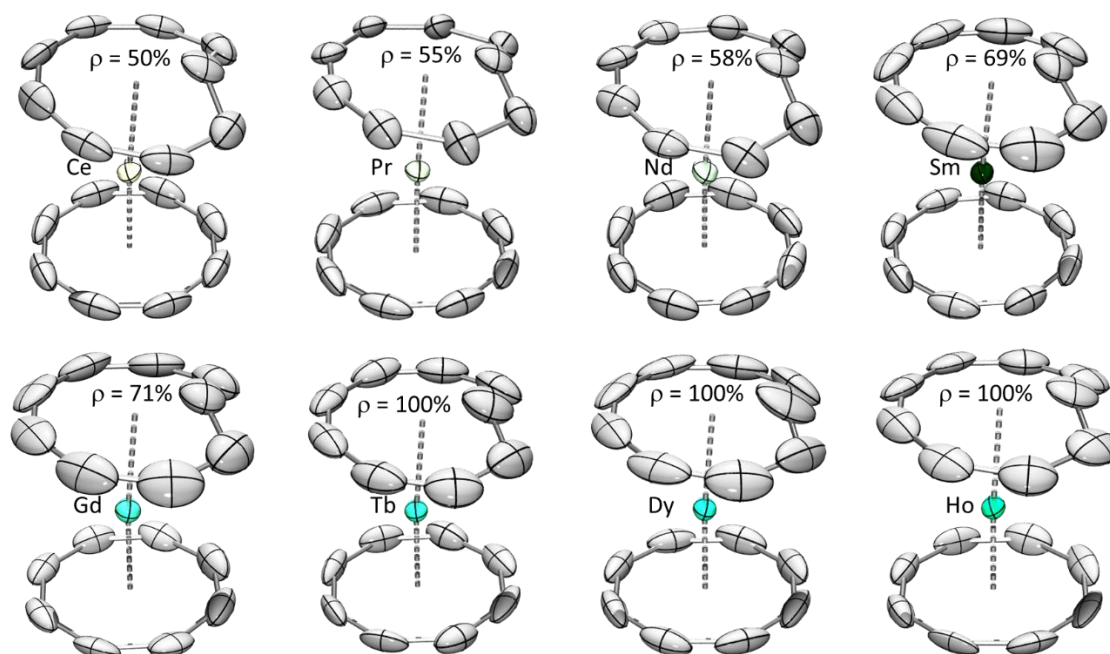


Figure 4. 20 ORTEP representation of the molecular structure of **4.2_{Ln}** at 50% probability, carbon atoms are in grey and the corresponding lanthanide ion are specified for each structure (hydrogen atoms are omitted for clarity)

It is important to note that this characterization only represents a picture of the average molecule in the crystal. First, as all models, the process of representing the molecule introduces some uncertainties. Indeed, attributing an electronic density to discrete atoms will lead to some amount of bias. Particularly carbon atoms only feature six electrons, and as such, modelling parts of atoms can be difficult. This for example, lead to $r^{\text{trans/cis}} = 100\%$ for some metals which, in all likelihood, is not the case to this precision. Then, another source of bias could come from the solubility of the species handled. The **KCn^t** is used due to its increased solubility and as such most likely undergoes salt metathesis faster. Furthermore, there could

be a difference in crystallization behavior dependent on the ratio of the compound. For instance, if the *trans* isomer of the complex is more soluble, then the crystals are probably show a lower $r^{trans/cis}$ than the solution.

To look further into this phenomenon, the compounds were characterized as their mixture by ^1H NMR spectroscopy.

3. NMR characterization

As previously, the compounds were solubilized to probe their behavior in solution. Their solubilities in deuterated toluene were found to be qualitatively higher than the 4.2_{Ln}^{cis} compounds. Additionally, they were also soluble in deuterated dichloromethane (CD_2Cl_2). However, further study showed that they were less stable in this solvent. Consequently, their characterization was performed in CD_2Cl_2 , but the longer analysis studied in the next part will be performed in toluene.

For the most part the spectra were close to what was expected. Most compounds show a superposition of the spectra of the two isomers. Of note, only four signals can be identified for the Cnt motif of 4.2_{Ln}^{trans} most of the time.

One noteworthy observation can be made on 4.2_{La}^{trans} . Indeed, as illustrated on **Figure 4. 21**, the pattern of peaks for the Cnt ligand in its *trans* form features a shielded peak akin to the free Cnt⁻ ligand.

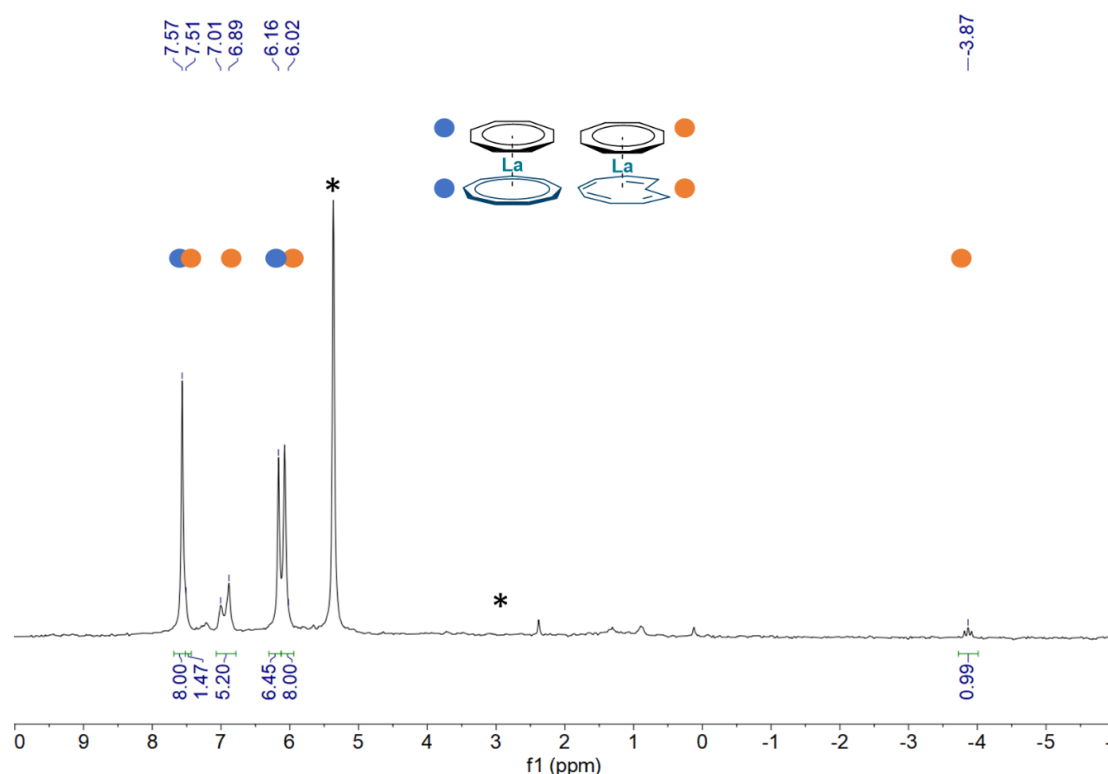


Figure 4. 21 ^1H NMR of $4.2_{\text{La}}^{trans/cis}$ in CD_2Cl_2 measured at 293 K (* residual protio signal of solvent and small impurities).

Having characterized the 4.2_{Ln}^{cis} and $4.2_{Ln}^{trans/cis}$ mixture, we set out to investigate the behavior shown under different light irradiation. Notably, we were interested in the reversibility of the phenomenon as well as the extent of ratio differences we could impose only with light stimuli.

Before studying the behavior of the complexes, we decided to come back on the case of the KCnt. Indeed, in light of what had been understood for the complex, a number of hypotheses could be explored for the ligand alone.

III. Isomerization study

1. Come back on the case of KCnt

Although the group of Boche had previously studied the isomerization of KCnt, to the extent of our knowledge, there have been no study on the light-induced isomerization.

1. Previous studies in the literature

As discussed in **Chapter 2**, the Cnt ligand has been synthesized in the 60's³⁶⁻³⁹ and has been the object of a few studies particularly on its properties of topomerization and isomerization.⁴⁰⁻⁴³ If the topomerization has been found to happen at room temperature allowing the scrambling of a deuterated Cnt moiety, the isomerization was reported by Boche to have a higher barrier to activation. Their group studied different stimuli which were responsible for faster isomerisation.

First, they noted that introduction of protons acidic enough to allow proton exchange would promote the formation of the *cis* moiety.⁴² Then, they found that the heavier alkali metal, potassium and cesium, used would also decrease the half-life of the *trans* Cnt monoanion. Interestingly, on this subject they hypothesized that this could be due to a reversible electron transfer from the alkali metal to the *trans* molecule. Particularly, as it works better for stronger reductant, they theorized that a certain potential need to be reached to allow this transformation. This is also supported by the experiments by Bauld who tried to reduce the *cis* isomer of the Cnt anion without success due to a higher reduction potential.⁴⁴

Finally, they noticed that irradiation at 275 nm allows a quicker isomerization toward the *cis* compound.⁴²

2. Solvent induced isomerization?

As it was observed for the complexes **4.2_{Ln}**, it was thought that the isomerization of KCnt was induced by coordinating solvent molecules. However, ¹H NMR follow-up of KCnt^{trans/cis} samples in deuterated THF presented in **Figure 4. 22** showed that no evolution was observed. A similar behavior was noted for deuterated acetonitrile. This contradicts what has been observed for **4.2_{Ln}**.

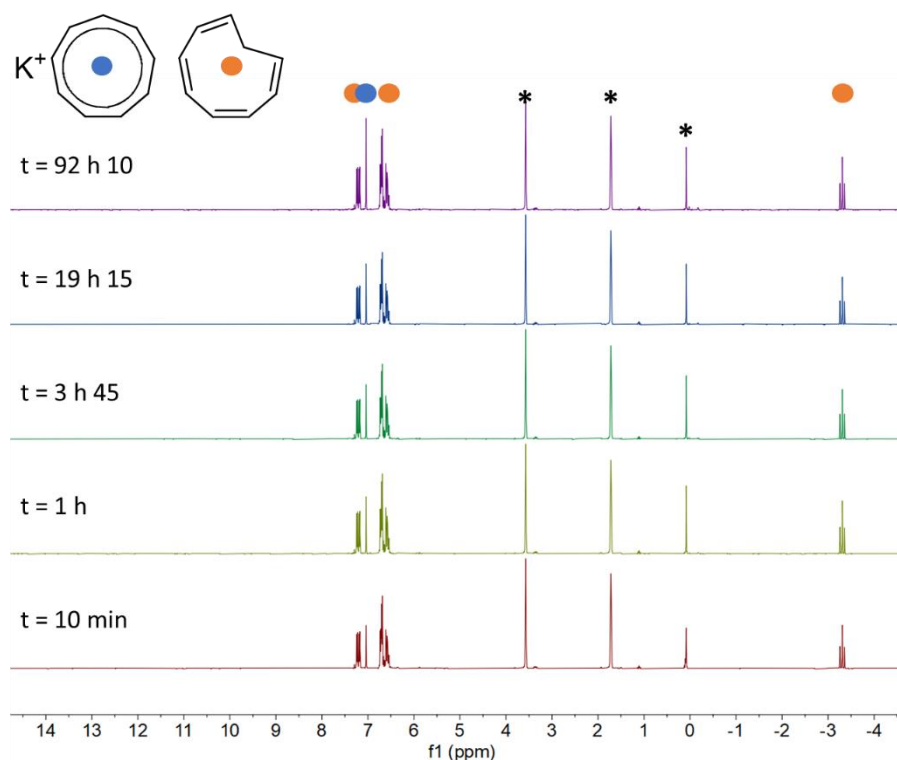


Figure 4. 22. NMR follow-up in THF-*d*₈ of KCnt^{trans/cis} protected from light (* denotes residual protio solvent peak)

This control experiment showed that the reactivity of the Cnt moiety is different between the potassium salt and the lanthanide complex. Then, if the observed isomerization from the *cis* form to the *trans* form of the Cnt unit is not due to the solvent, we needed to investigate the potential light-induced process.

3. Light induced isomerization

Thus, we decided to explore the light-induced phenomenon. We observed that shining blue light upon the Cnt ligand solution showed evolution of the signal to only one peak characteristic of the Cnt^{cis} ligand.

a. Kinetics of the reaction by NMR spectroscopy

To evaluate the rate of the reaction, a sample of KCnt^{trans/cis} was prepared inside an NMR tube and irradiated at 427 nm. Of note, the lamp used for this part have a broad emission band centered around one wavelength, they will be referred to as the central wavelength and the

corresponding emission spectra.⁴⁵ ¹H NMR spectra were recorded at different time interval during the irradiation process and are presented in **Figure 4. 23**. Additionally, the associated ratio of $KCn^{trans/cis}$ are added to their corresponding spectra.

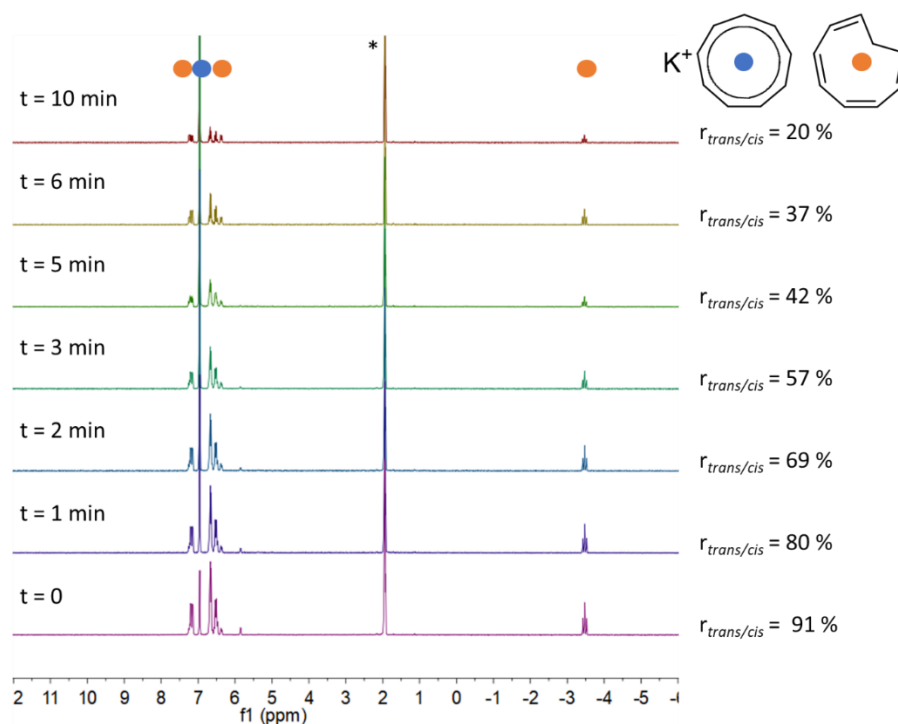


Figure 4. 23 NMR follow-up of the isomerization reaction with the associated $r^{trans/cis}$.

The modelling of the data shows the obtention of a linear relationship between the time of irradiation and the logarithm of the ratio as demonstrated in **Figure 4. 24** in a pseudo first-order fashion.

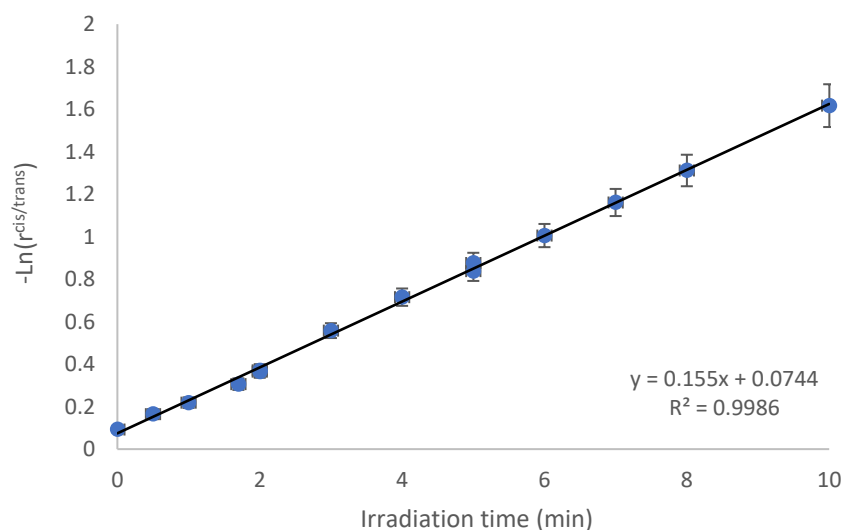


Figure 4. 24 Graphical representation of the logarithm of the cis/trans ratio as a function of the time of irradiation with a fitted linear modelisation

This first study was performed in acetonitrile. To ensure that the isomerization was not influenced by the solvent, several points were acquired twice after waiting time in the dark. This showed minimal influence on the ratio and as such, we could conclude that the isomerization was caused primarily by the irradiation, particularly on this timeframe.

Similar studies were performed in THF and at different wavelengths to ensure that this behavior can be generalized. Due to the wide emission of the lamp, it was not possible to compare the rates. However, one way to rationalize them is to perform UV-analysis of the mixture of $\text{KCnt}^{\text{trans/cis}}$.

b. Kinetics of the reaction through UV-visible spectroscopy

A similar reaction was run this time inside a JY. cuvette and followed by UV-visible absorption. Analysis of the increase and decrease of the bands allows to match signals to its isomer on **Figure 4. 25**.

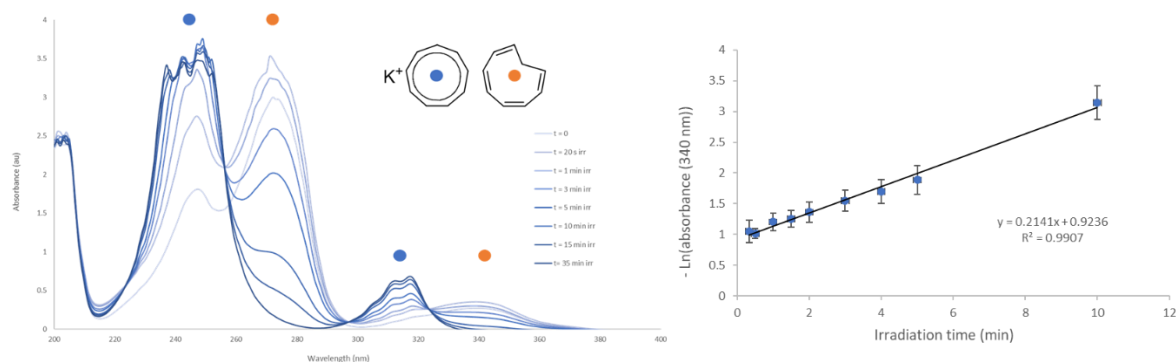


Figure 4. 25. On the left, UV-visible follow-up of the isomerisation of Kcnt under a 427 nm lamp, on the right, graphical representation of the logarithm of the absorbance at 340 nm and the fitted linear relationship.

Similarly to the NMR study, the reaction follows a first order rate law. The reaction rate of $k_{\text{UV}}^{\text{thf}} = 0.21 \text{ min}^{-1}$ is different from the NMR study in THF which gave $k_{\text{NMR}}^{\text{thf}} = 0.12 \text{ min}^{-1}$. This can be expected due to the differences in the shape of the vessels and the quantity of absorbed photons.

c. Rationalization of the behavior and extension to other wavelengths

As mentioned previously, these studies of isomerization have been performed with different lamps. While the kinetics cannot be compared, it is possible to observe which wavelength allows the transformation. For instance, isomerization reaction happened for the lamp centered around 370, 390 and 427 nm while for 467 and 525 nm, very slow to no reaction were detected.

This can be easily understood by superimposing the absorption signatures of the KCnt isomers with the lamp emission bands as pictured in **Figure 4. 26**.⁴⁵

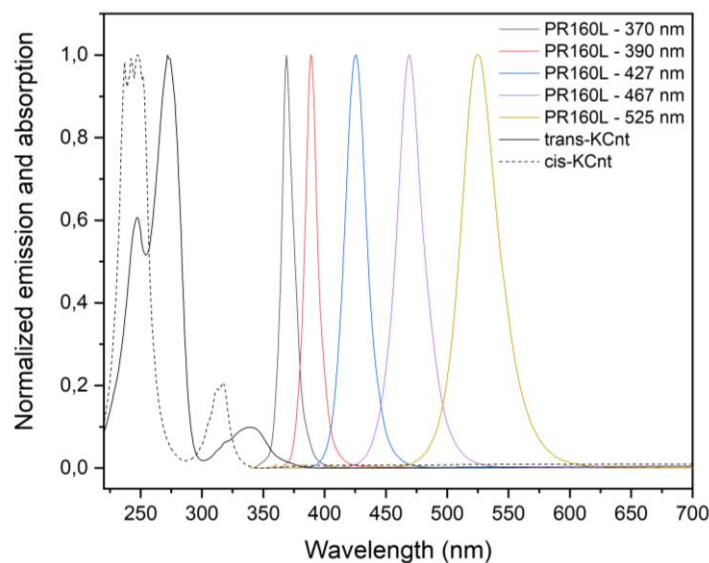


Figure 4. 26. Graphical representation of the normalized absorption and emission of the KCnt^{cis} and $\text{KCnt}^{\text{trans/cis}}$ with a majority of *trans* and the lamp used as irradiation sources.⁴⁵

Interestingly, the only isomerization behavior that has been observed is from the *cis* form to the *trans* form. Contrarily to the **4.2_{Ln}** complexes, the retro-isomerization do not appear to be possible. This could be due to a non-reversible reaction. However, it could also be due to a low cross section between the signal of the KCnt^{cis} compound and the emission band if the lamps. To test this theory, deep UV lamp would be needed. It is interesting to note that experiments by Boche already showing light-induced isomerization were performed at 275 nm, corresponding to a feature of the *trans* Cnt and as such do not help answering this question.⁴² This information could clarify the dynamic of the complexes. As of now, it is unclear whether the lanthanide ions allow the isomerization from the *cis* form to the *trans* form, or simply shifts the absorption band into the visible range, making it possible to displace the equilibrium.

An additional detail of note when studying the absorption spectra of the mostly *cis* and *trans* compounds is that the latter has a red shifted signature compared to the other. However, it is often assumed that aromaticity or delocalization of π -electrons tends to provoke such a bathochromic shift. This is then counter-intuitive compared to our representation of $\text{KCnt}^{\text{trans}}$. Indeed, it can be assumed that the non-planarity of the molecule will negatively impact the delocalization of the electron and thus its aromatic behavior. These UV-visible spectra could suggest that there is more to this. The notion of aromaticity is a complicated subject and has been central in the development of organic chemistry.^{46–48} If it is not the subject of this manuscript, probing the aromatic character of both isomer of the Cnt ligand could expand our comprehension. Not only could it be compelling from a fundamental standpoint, it could help understand several behaviors described within, notably for the reduction chemistry.

4. Study of the temperature influence

Previous studies by our group had brought up the possibility of this reaction to be contra-thermodynamic, meaning that it was slower at higher temperature.^{28,49} We performed a test at 60 °C with foil-covered NMR tubes, revealing almost no evolution of the corresponding spectra.

In hindsight, one possible explanation for the slower isomerization observed for KCnt at higher temperature could be the partial obscuration of the sample in the thermostatic bath. As such, it was not the increase of temperature influencing the process but a diminution of the light received by the system.

2. Spectroscopic study of the isomerization of 4.2_{Ln}

Having a better characterization of the isomerisation behavior of KCnt, we investigated more precisely the reaction of 4.2_{Ln} with light. The case of 4.2_{Tb} will be described first as it was the first complex observed displaying light-induced isomerization, and the generalization over the series will then be discussed.

1. In-depth study of Terbium

a. NMR study

Having already shown that the process was happening for 4.2_{Tb}, we were interested in exploring the reversibility of the process as well as the extent of ratio we were able to obtain. An NMR experiment where the sample was irradiated subsequently at different wavelength is shown below in **Figure 4. 27**.

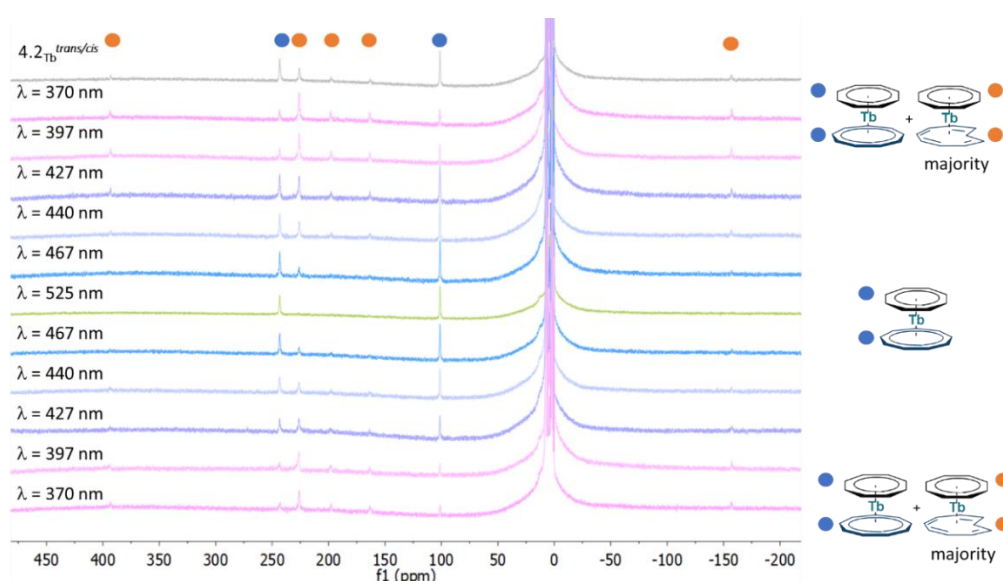


Figure 4. 27. NMR experiment following the signal for a sample of 4.2_{Tb} under subsequent light irradiation at different wavelength. The color used for each spectrum represent the wavelength at which it was irradiated.

Calculating the $r^{trans/cis}$ allows to plot its evolution upon irradiation. Particularly, we irradiated from 370 nm to 525 nm back down to 370 nm to see the reversibility of the phenomenon. At each step, it was ensured that the PSS was reached. The reaction seems to be reversible and is able to go from $r^{trans/cis} = 85\%$ to 0%. As illustrated in **Figure 4. 28**, a wide range of ratio can be reached with different wavelength of irradiation.

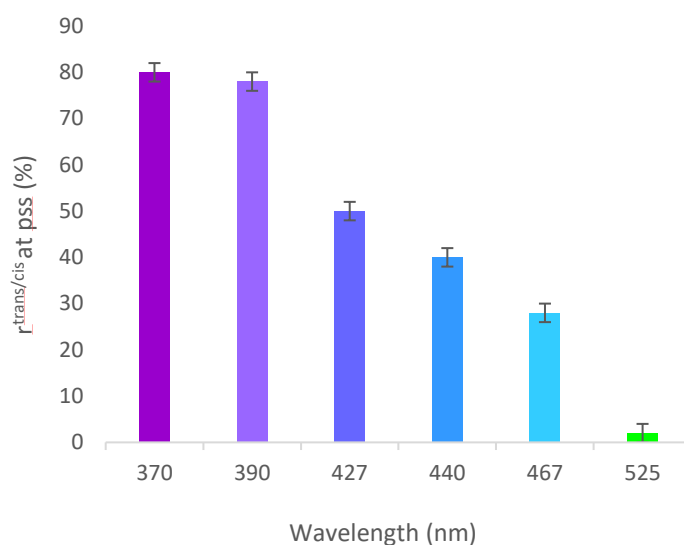


Figure 4. 28. Representation of $r^{trans/cis}$ as a function of the wavelength of irradiation.

Of note, these experiments were done without an internal standard, by directly comparing the integration of the signal for each isomer. Comparison of the integration with the solvent peaks ensure that there is no large loss of product. However, an internal standard would ensure a better knowledge of the yield of the reaction. Particularly, if we wanted to assess to durability of this phenomenon, it would be necessary to use an internal reference.

b. UV-visible study

This behavior can easily be rationalized through the absorption behavior of the complex. Indeed, the UV-visible spectra of **4.2_{Tb}** presented on **Figure 4. 29** shows that, at higher wavelength, only a band from the *trans* compound has a cross section with the emission of the lamp. At higher energy however, the lamps are able to irradiate in the features of the *cis* compounds favoring the formation of the *trans* isomer.

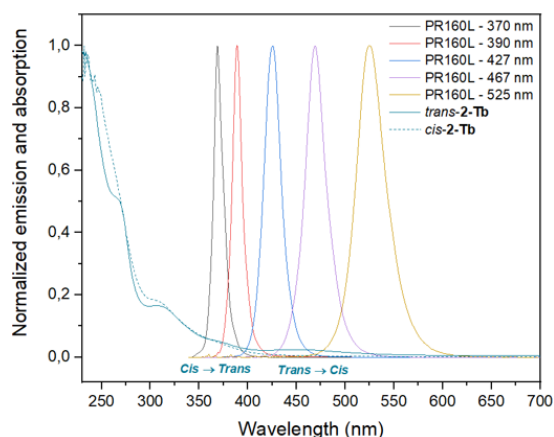


Figure 4. 29 Superposition of the normalized UV visible spectra of the **4.2_{Tb}** under its predominant *cis* and *trans* form and the emission spectra of the lamp used in the study.⁴⁵

2. Rationalization of the isomerization behavior over the series

a. UV-visible characterization

The previous focus on the terbium compound showed that this light induced phenomenon can be well interpreted using the absorbance behavior. As such, we decided to investigate the mostly *trans* mixture of **4.2_{Ln}** by UV-visible spectroscopy. The combined spectra are presented in **Figure 4. 30**.

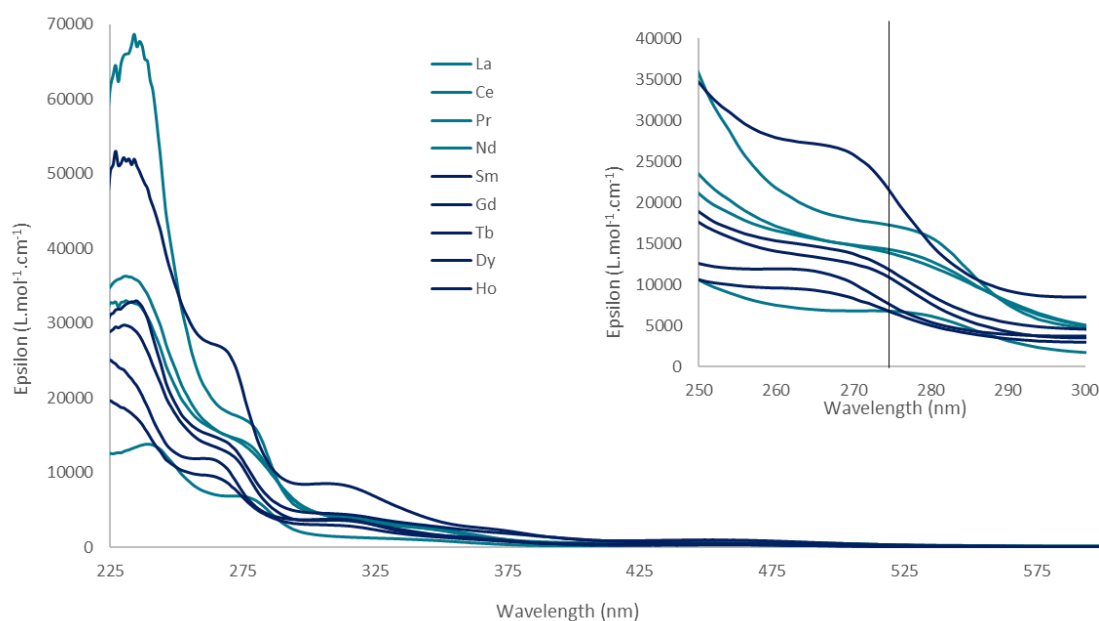


Figure 4. 30 Combined spectra of **4.2_{Ln}**, the early lanthanides are represented in blue while the late lanthanide are represented in green. Additionally, **4.2_{Sm}** is represented in green. The zoomed window shows the difference in the feature around 275 nm separating the two behaviors.

As illustrated in **Figure 4. 30**, there appear to be two main behaviors. First **4.2_{Ln}** with Ln = La, Ce, Pr and Nd show three main bands around 230 nm, 280 nm and a large shoulder from 300 to 375 nm. While **4.2_{Ln}** with Ln = Sm, Gd, Tb, Dy and Ho show four bands around 230 nm, 270 nm, 315 nm and a large shoulder from 340 nm to 400 nm.

Of note, due to the difficulty of attributing the $r^{trans/cis}$ for the erbium and thulium compounds, they are not represented here. Interestingly, the separation of behavior appears to take place between neodymium and samarium.

b. NMR analysis

We thus decided to analyze the behavior of those compounds through solution NMR spectroscopy while irradiated by different wavelengths. As predicted by the absorption spectra, there is a change of behavior in between neodymium and samarium.

For the late part of this series, similar changes of $r^{trans/cis}$ can be observed. At high energy, the system tends to its *trans* form, while at lower energy, the system is almost composed only of *cis* compound. As mentioned previously for Gd, Er, and Tm, any quantitative analysis is rendered impossible by the strong paramagnetism of the ion. The combined NMR for each element is presented in the experimental part.

The analysis for the early lanthanides is more complex. First, the very low solubility makes the small amounts of residual solvent or weak impurities difficult to identify compared to the compounds. Additionally, the weaker paramagnetism does not separate the peaks as much as for the late lanthanide. Overall quantitative analyses do not appear to be trustworthy. Qualitatively, light irradiation appears to have minimal influence over the ratio of isomers in the mixture.

3. Rationalization over the series

Overall, as expected, the absorption behavior appears intimately linked with the make-up of the *trans/cis* mixture under different irradiation. While the beginning of the series does show bi-stability of the compound under preferentially *trans* or *cis* isomer, the control with the light is not properly assessed by NMR spectroscopy due to solubility issues. It is possible that a UV-visible study could help as it is a sensitive method, which only shows absorbing molecules. Any quantitative ratio would however be difficult to compute as both compounds have very large absorption features difficult to deconvolute.

For the late part of the series, a quantitative analysis is easier in the case of terbium and dysprosium. Unfortunately, for gadolinium, holmium, erbium and thulium, it is difficult to properly analyze the NMR spectra. Similarly to earlier lanthanides, more insight could be gathered from a follow-up of the isomerization reaction by UV-visible spectroscopy. Additionally, it could be highlighted that samarium, while being an early lanthanide, shows a behavior quite close to the end of the series as showed in the experimental part.

IV. Conclusion

To conclude this chapter, we were able to synthesize and characterize by NMR and XRD the series of heteroleptic complexes LnCotCnt with Ln = La, Ce, Pr, Nd, Sm, Tb, Dy, Er, Ho, Tm.

While isolating these compounds, we identified an unexpected retro-isomerization of the Cnt ligand from the *cis* isomer to the *trans* isomer while coordinated to the lanthanide ion. This was first noticed with terbium. Careful analysis of its evolution revealed that this reaction was light induced. Further investigation revealed a possible switching of isomers through two stimuli. Addition of acetonitrile would promote the isomerization from the *trans* to the *cis* compound while irradiation under blue light reversed this reaction.

Rationalization of the light induced character of this reaction allowed us to develop a synthetic protocol to obtain **4.2_{Ln}^{trans/cis}** mixture with a majority of *trans* compound as demonstrated by the characterization through single crystal XRD. Additionally, mixtures of compounds were obtained, with solution NMR showing the presence of the *trans* compounds.

We then investigated the possibility of performing back and forth isomerization reaction using light. It was shown possible for **4.2_{Tb}^{trans/cis}** which reaches $r^{trans/cis} = 85\%$ for irradiation around 390 nm and $r^{trans/cis} = 0\%$ around 525 nm. We then decided to explore this behavior in the series of compound that we had previously synthesized. Similar behaviors were identified for Ln = Sm, Dy and Ho. For the beginning of the series, the analysis was more challenging. If the *trans* isomers were identified in XRD and NMR analysis, the quantitative analyses of the NMR spectra were less fruitful. Further analysis of those compounds through UV-visible spectroscopy could unlock the understanding of their behavior.

Additionally, one drawback of this work is the use of lamp with large emission band. This means that they are more likely to overlap with several absorption band of the mixture of isomers rendering more difficult the rationalization of the behavior. As such, the use of a filter to allow only small bandwidth to go through could help the analysis. Similarly, the use of laser could allow very powerful and precise irradiation of the compounds. It could also target deeper UV wavelength where the compounds have larger absorption coefficient to see if those transitions also trigger isomerization. This could also be used to probe the possibility of retro-isomerizing the KCnt salt.

Finally, one of the future extensions of this work will target the difference of reactivity between those two forms. Indeed **Chapter 2 & 3** have used the *trans* isomer of KCnt in majority to take advantage of the solubility, but we also think that it facilitates the reduction of the compounds. Consequently, one application could be the control of the reduction potential of the species through light.

References

- (1) Kealy, T. J.; Pauson, P. L. *Nature* **1951**, *168* (4285), 1039–1040.
- (2) Laszlo, P.; Hoffmann, R. *Angew. Chem. Int. Ed.* **2000**, *39* (1), 123–124.
- (3) Werner, H. *Angew. Chem. Int. Ed.* **2012**, *51* (25), 6052–6058.
- (4) Okuda, J. *Eur. J. Inorg. Chem.* **2017**, *2017* (2), 217–219.
- (5) Štěpnička, P. *Dalton Trans.* **2022**, *51* (21), 8085–8102.
- (6) Wilkinson, G.; Birmingham, J. M. *J. Am. Chem. Soc.* **1954**, *76* (23), 6210–6210.
- (7) Birmingham, J. M.; Wilkinson, G. *J. Am. Chem. Soc.* **1956**, *78* (1), 42–44.
- (8) Fischer, E. O.; Fischer, H. *Angew. Chem. Int. Ed. Engl.* **1964**, *3* (2), 132–133.
- (9) Fischer, E. O.; Fischer, H. *J. Organomet. Chem.* **1965**, *3* (3), 181–187.
- (10) Apostolidis, C.; Deacon, G. B.; Dornberger, E.; Edelmann, F. T.; Kanellakopoulos, B.; MacKinnon, P.; Stalke, *Chem. Commun.* **1997**, No. 11, 1047–1048.
- (11) Andersen, R. A.; Boncella, J. M.; Burns, C. J.; Green, J. C.; Hohl, D.; Rösch, N. *J Chem Soc Chem Commun* **1986**, No. 5, 405–407.
- (12) Perrin, L.; Maron, L.; Eisenstein, O.; Schwartz, D. J.; Burns, C. J.; Andersen, R. A. *Organometallics* **2003**, *22* (26), 5447–5453.
- (13) Streitwieser, Andrew.; Mueller-Westerhoff, Ulrich. *J. Am. Chem. Soc.* **1968**, *90* (26), 7364–7364.
- (14) Mares, F.; Hodgson, K.; Streitwieser, A. *J. Organomet. Chem.* **1970**, *24* (3), C68–C70.
- (15) Hodgson, K. O.; Mares, F.; Starks, D. F.; Streitwieser, A. *J. Am. Chem. Soc.* **1973**, *95* (26), 8650–8658.
- (16) Greco, A.; Cesca, S.; Bertolini, W. *J. Organomet. Chem.* **1976**, *113* (4), 321–330.
- (17) Mahieu, N.; Piątkowski, J.; Simler, T.; Nocton, G. *Chem. Sci.* **2023**, *14* (3), 443–457.
- (18) Nief, F. *Dalton Trans.* **2010**, *39* (29), 6589.
- (19) Rausch, J.; Apostolidis, C.; Walter, O.; Lorenz, V.; Hrib, C. G.; Hilfert, L.; Kühling, M.; Busse, S.; Edelmann, F. T. *New J. Chem.* **2015**, *39* (10), 7656–7666.
- (20) Ishikawa, N.; Sugita, M.; Okubo, T.; Tanaka, N.; Iino, T.; Kaizu, Y. *Inorg. Chem.* **2003**, *42* (7), 2440–2446.
- (21) Rinehart, J. D.; Long, J. R. *Chem. Sci.* **2011**, *2* (11), 2078.
- (22) Goodwin, C. A. P.; Ortu, F.; Reta, D.; Chilton, N. F.; Mills, D. P. *Nature* **2017**, *548* (7668), 439–442.
- (23) Guo, F.-S.; Day, B. M.; Chen, Y.-C.; Tong, M.-L.; Mansikkamäki, A.; Layfield, R. A. *Science* **2018**, *362* (6421), 1400–1403.
- (24) Meihaus, K. R.; Long, J. R. *J. Am. Chem. Soc.* **2013**, *135* (47), 17952–17957.
- (25) Ungur, L.; Le Roy, J. J.; Korobkov, I.; Murugesu, M.; Chibotaru, L. F. *Angew. Chem. Int. Ed.* **2014**, *53* (17), 4413–4417.
- (26) Le Roy, J. J.; Korobkov, I.; Kim, J. E.; Schelter, E. J.; Murugesu, M. *Dalton Trans* **2014**, *43* (7), 2737–2740.
- (27) Kawasaki, K.; Sugiyama, R.; Tsuji, T.; Iwasa, T.; Tsunoyama, H.; Mizuhata, Y.; Tokitoh, N.; Nakajima, A. *Chem. Commun.* **2017**, *53* (49), 6557–6560.
- (28) Xémard, M.; Zimmer, S.; Cordier, M.; Goudy, V.; Ricard, L.; Clavaguéra, C.; Nocton, G. *J. Am. Chem. Soc.* **2018**, *140* (43), 14433–14439.
- (29) Westerhof, A.; De Liefde Meijer, H. J. *J. Organomet. Chem.* **1978**, *149* (3), 321–325.
- (30) Walter, M. D.; Wolmershäuser, G.; Sitzmann, H. *J. Am. Chem. Soc.* **2005**, *127* (49), 17494–17503.
- (31) Münzfeld, L.; Schoo, C.; Bestgen, S.; Moreno-Pineda, E.; Köppe, R.; Ruben, M.; Roesky, P. W. *Nat. Commun.* **2019**, *10* (1), 3135.
- (32) Tricoire, M.; Münzfeld, L.; Moutet, J.; Mahieu, N.; La Droite, L.; Moreno-Pineda, E.; Gendron, F.; Hilgar, J. D.; Rinehart, J. D.; Ruben, M.; Le Guennic, B.; Cador, O.; Roesky, P. W.; Nocton, G. *Chem. – Eur. J.* **2021**.
- (33) Hilgar, J. D.; Bernbeck, M. G.; Flores, B. S.; Rinehart, J. D. *Chem. Sci.* **2018**, *9* (36), 7204–7209.

- (34) Münzfeld, L.; Dahlen, M.; Hauser, A.; Mahieu, N.; Kuppasamy, S. K.; Moutet, J.; Tricoire, M.; Köppe, R.; La Droitte, L.; Cador, O.; Le Guennic, B.; Nocton, G.; Moreno-Pineda, E.; Ruben, M.; Roesky, P. W. *Angew. Chem.* **2023**.
- (35) Mashima, K.; Takaya, H. *Tetrahedron Lett.* **1989**, *30* (28), 3697–3700.
- (36) Katz, T. J.; Garratt, P. J. *J. Am. Chem. Soc.* **1963**, *85* (18), 2852–2853.
- (37) Katz, T. J.; Garratt, P. J. *J. Am. Chem. Soc.* **1964**, *86* (23), 5194–5202.
- (38) Lalancette, E. A.; Benson, R. E. *J. Am. Chem. Soc.* **1963**, *85* (18), 2853–2853.
- (39) Lalancette, E. A.; Benson, R. E. *J. Am. Chem. Soc.* **1965**, *87* (9), 1941–1946.
- (40) Boche, G.; Martens, D.; Danzer, W. T. *Angew. Chem. Int. Ed. Engl.* **1969**, *8* (12), 984–984.
- (41) Boche, G.; Bieberbach, A.; Weber, H. *Angew. Chem.* **1975**, *87* (15), 550–551.
- (42) Boche, G.; Bieberbach, A. *Chem. Ber.* **1978**, *111* (8), 2850–2858.
- (43) Boche, G.; Weber, H.; Bieberbach, A. *Chem. Ber.* **1978**, *111* (8), 2833–2849.
- (44) Bauld, N. L.; Zoeller, J. H. *Tetrahedron Lett.* **1967**, *8* (10), 885–889.
- (45) Company, K. . https://kessil.com/products/science_PR160L.php (accessed 2023-09-08).
- (46) Schleyer, P. V. R. *Chem. Rev.* **2001**, *101* (5), 1115–1118.
- (47) Merino, G.; Solà, M.; Fernández, I.; Foroutan-Nejad, C.; Lazzeretti, P.; Frenking, G.; Anderson, H. L.; Sundholm, D.; Cossío, F. P.; Petrukhina, M. A.; Wu, J.; Wu, J. I.; Restrepo, A. Aromaticity: Quo Vadis. *Chem. Sci.* **2023**
- (48) Mercero, J. M.; Boldyrev, A. I.; Merino, G.; Ugalde, J. M. *Chem. Soc. Rev.* **2015**, *44* (18), 6519–6534.
- (49) Xémard, M. Synthèses d’assemblages Multimétalliques de Lanthanides: Des Propriétés Électroniques Des Précurseurs Divalents Au Contrôle de Leur Réactivité. Thèse de doctorat, Université Paris-Saclay, 2018.

Conclusion

This work has investigated various organolanthanide complexes to better understand their electronic structure and their reactivities.

In the first study, the well-known tris ^tBu-cyclopentadienyl (Cp^{ttt}) ligand was used to stabilize a divalent thulium complex which allowed the formation of a reactive ethynediolate adduct. This compound was shown to undergo reaction with CO₂ promoting C-H activation of the hydrogen in *para*-position of the solvent when using toluene and benzene. In order to better control this addition, we investigated the possibility to use pyridine-type moiety as nucleophile. At first, the pyridine was used as solvent to reproduce at best the previous conditions. In this case, very deeply colored solutions were obtained. Unfortunately, crystallization of a product from this reaction was unsuccessful. Thus, I decided to use the pyridine moiety as stoichiometric reagent in pentane as solvent. This method allowed for crystallization of the product and study of the solid-state structure. This showed that, under these conditions, the thulium complex could react with the pyridine and the CO₂ without showing any sign of solvent activation. Several pyridine-type moieties showed identical reactions with addition of the nucleophile prompting the reaction with the electrophilic carbon of CO₂ as illustrated on **Figure C. 1**.

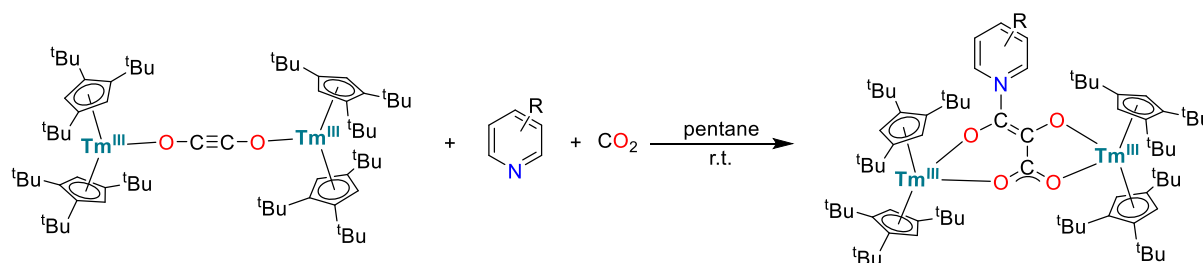


Figure C. 1 General procedure for the reaction of the linear intermediate with CO₂ and a pyridine derivative.

Interestingly, although the structures are fairly similar, the resulting colors were found to vary from purple to green. Analysis of the UV-visible signatures showed one main absorption feature in the visible region corresponding to the observed color for each compound. These features are likely to arise due to intramolecular charge transfer between the positively charged pyridine moiety and the carboxylate unit. First the intensity of the signal was shown to correlate with the angle formed by the pyridine fragment and the central carbonated backbone: the closer to 90°, the lower the absorption coefficient associated. Furthermore, the wavelength corresponding to the maximum of absorption seemed to be linked with the electronic donation of the substituent on the pyridine ring. For instance, donating alkyl group

tend to move the absorption to lower wavelength but the accepting mesomere effect of the second ring of quinoline brings the absorption to a higher wavelength.

One common feature over these reactions is the immediacy of the color change observed upon CO₂ addition. This led us to consider that this molecule could be used as a CO₂ indicator. To investigate this idea, I employed several air-drying methods to obtain water-free gas. Observation of a color change from yellow to pale blue-green upon reaction with air informed us that the desired reaction was in all likelihood not the only one happening. Further experiments showed that the ethynediolate compound was reacting with oxygen to form an oxalate compound. Consequently, this molecule cannot be used as a CO₂ captor but this discovery motivated a broader investigation into the displayed reactivities as reported in **Figure C. 2**. Notably, a reaction with an isocyanate derivative features what appears as a typical [2 + 2] addition to a triple bond. This type of mechanism followed by a rearrangement could also explain the formation of the oxalate compound from O₂. Although this type of reactivity is usually not accessible as O₂ is in a triplet state. As such, the thulium compound might feature a low-lying triplet. Computations are currently being carried out in order to investigate the plausibility of such a mechanism.

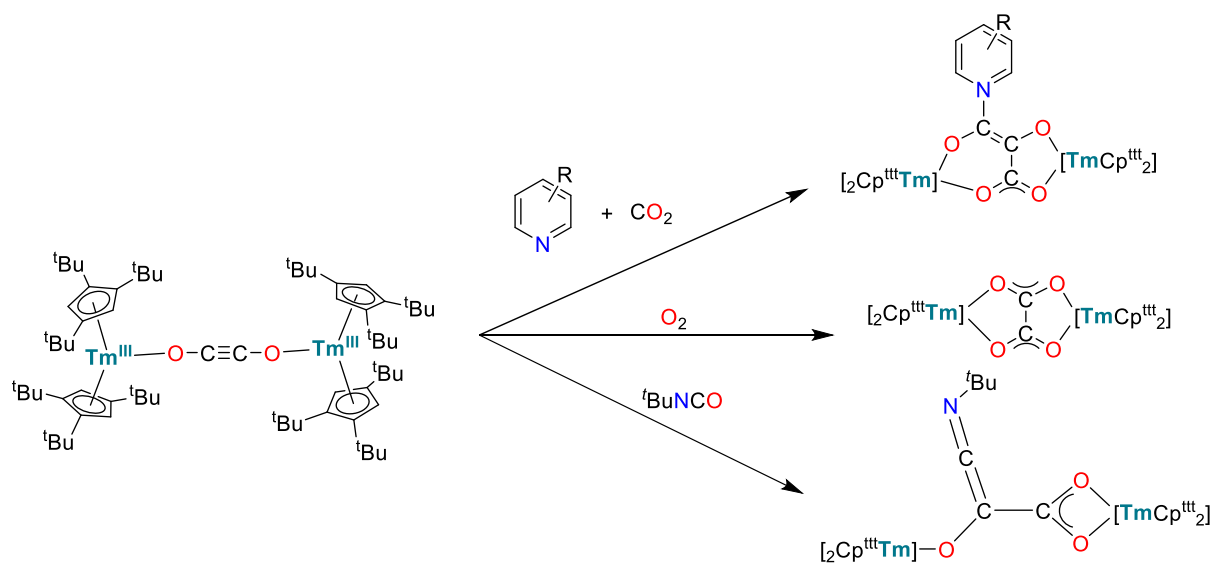


Figure C. 2 Summary of the product isolated and characterized during this work

To expand on this work, other unsaturated small molecules have been used to investigate the scope of the carbonated skeleton that can be formed between the thulium centers. One of the future goals of this work is to explore de-metallation methods. This could allow access to different organic fragments. Furthermore, there have been development of catalytic approaches to samarium reduction synthesis. Granted that the reduction potential for Tm(II)/Tm(III) species is more negative, it could nonetheless be interesting to investigate

reaction conditions which could facilitate the reduction step. Working on those two steps could allow the system to run catalytically.

Studying divalent thulium has shown the importance of ligands in lanthanide chemistry. As the crystal field is often weak, the ligands are usually chosen for their steric profile. For instance, the Cp^{tnt} ligand is used in divalent lanthanide chemistry, in part for its bulkiness. However, it was found that, coordinated around a trivalent dysprosium ion, it also creates a crystal field which allows retention of the magnetic information at relatively high temperature. This demonstrates the importance of both the encumbrment and the electronic features. Furthermore, during these studies, it was demonstrated that the obtention of linear sandwich compound was a desirable goal for magnetic applications. As such, we decided to investigate the coordination chemistry of a rarely used aromatic ligand, the cyclononatetraenyl ligand. This molecule has the particularity of being a large monoanionic ligand, which appears well suited for the obtention of neutral divalent lanthanide complexes. Before this work, it had been used for the formation of neutral sandwich type compound with the so-called "classical" divalent lanthanide Sm, Eu and Yb. Interestingly, divalent thulium, despite its more negative reduction potential, also formed the desired neutral complex. This prompted the study of the next more reducing lanthanide, dysprosium. Although similar starting material were used, no product could be isolated. As such, the conditions of the reaction were optimized, and this allowed the characterization of a new dysprosium dimer product as reported in **Figure C. 3**.

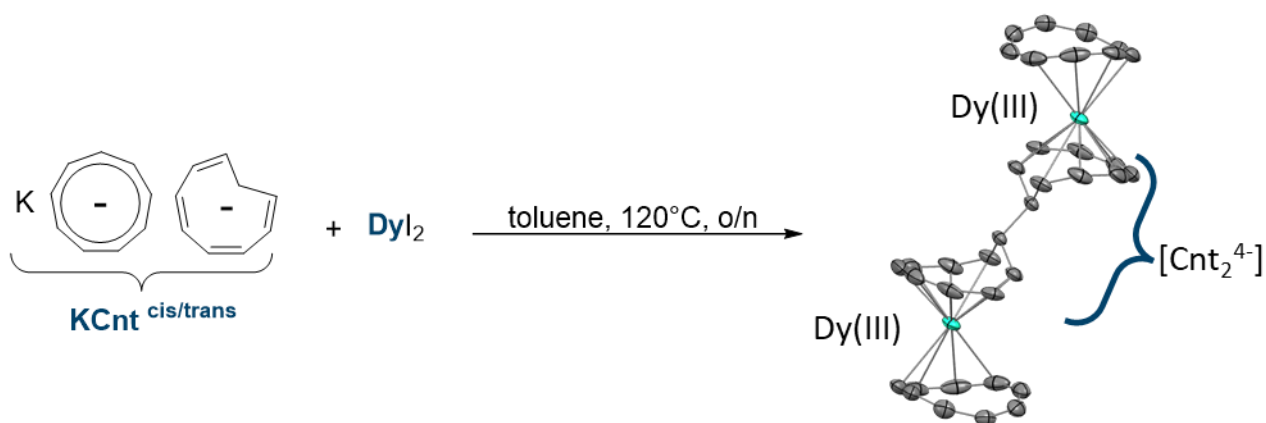


Figure C. 3 Synthetic scheme for the formation of the coupled dysprosium dimer. The product is presented as its solid-state structure with ellipsoids at 50% probability, dysprosium ions are in light green, carbons in grey and hydrogens have been omitted for clarity.

Several synthetic paths were explored to increase the yields of this reaction, however they remained low. Nonetheless, magnetic characterization and computational analysis were carried out. This species showed slow relaxation of the magnetization under an applied-field. Overall, rationalization of these data suggests that one electron from the dysprosium center

might be transferred onto the Cnt⁻ ring, creating a doubly charged radical species and two trivalent metallic centers. This radical moiety could then react with another radical, forming this bridging [Cnt₂⁴⁻] unit creating the neutral complex.

One feature in the explored synthetic path was the need to elevate the reaction to room temperature or higher. Given the known thermal sensitivity of solvated divalent dysprosium species, a new protocol was developed using limited amount of coordinating solvent to promote the solubility without precluding the Cnt ligand to interact with the metal. This led to the characterization of a new type of dimer with a bridging Cnt unit presented in **Figure C. 4**.

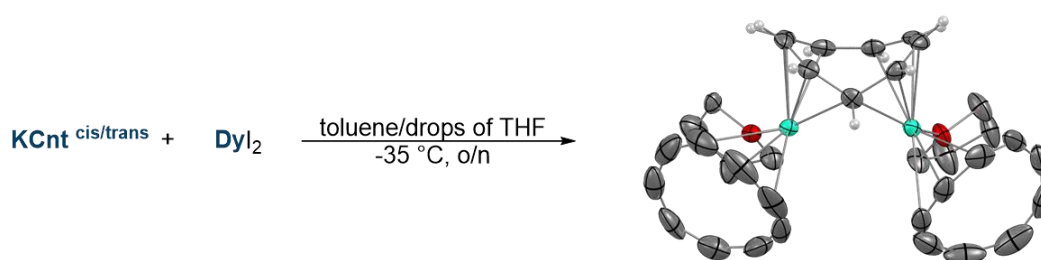


Figure C. 4 Synthetic scheme for the formation of the bridged dysprosium dimer. The product is presented as its solid-state structure with ellipsoids at 50% probability, dysprosium ions are in light green, carbons in grey, oxygens in red and hydrogens have been omitted for clarity except for the central Cnt motif.

The symmetry observed in the solid-state structure points towards a similar electronic structure for both metallic ions. Particularly, counting the electrons in this structure revealed the presence of a radical, likely to be either on the central ligand or delocalized on the dysprosium center. Computations at both DFT and CASSCF level suggest that the electron is delocalized in a d_z^2 -type orbital between the two lanthanides centers. However, analysis of the magnetic susceptibility does not support this conclusion. Additional investigations did not yield conclusive results and as of now, the oxidation state and charges repartition in this structure remain uncertain.

To try and understand better these species, we looked for similar starting material for another reducing lanthanide. However, only neodymium forms the required starting material. Application of similar reaction condition allowed for the isolation of a tetramer of neodymium presented in **Figure C. 5**. It is interesting to note that this complex features two bridging type Cnt units. However, due to the extreme thermal sensitivity and the high reactivity of the complex, no further data could be collected to understand the electronics at play in those species.

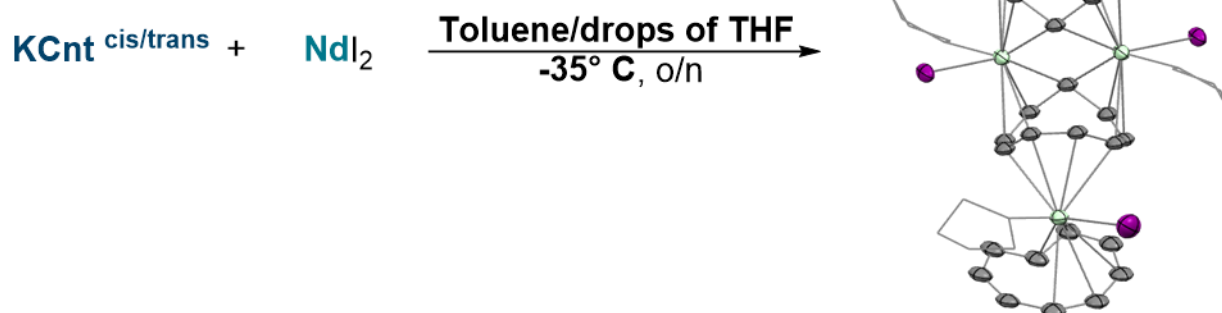


Figure C. 5 Synthetic path toward the neodymium tetramer, the product is represented by its solid-state structure with ellipsoids at 50% probability, neodymium ions are in light green, carbons in grey, iodines in purple, hydrogens atoms are not represented and THF molecules are represented in wireframe.

Given the difficulties of synthesizing other species to gather information about the reduced Cnt units, I decided to change the synthetic path involved and start from trivalent starting materials, easier to handle. Furthermore, we targeted heteroleptic complexes in order to have bulkier ligands that could keep THF molecules from entering the coordination sphere and displacing the Cnt ligand. The Cp^{tBu} compound was chosen as the additional ligand. This allowed the formation of heteroleptic complexes of dysprosium which upon reduction formed a similar coupled dysprosium dimer illustrated in **Figure C. 6**. Comparison of the metric with the previous coupled dimer suggests that similarly, the Cnt ligand has been reduced to its radical form and then coupled to form the $[\text{Cnt}_2^{4-}]$ ligand.

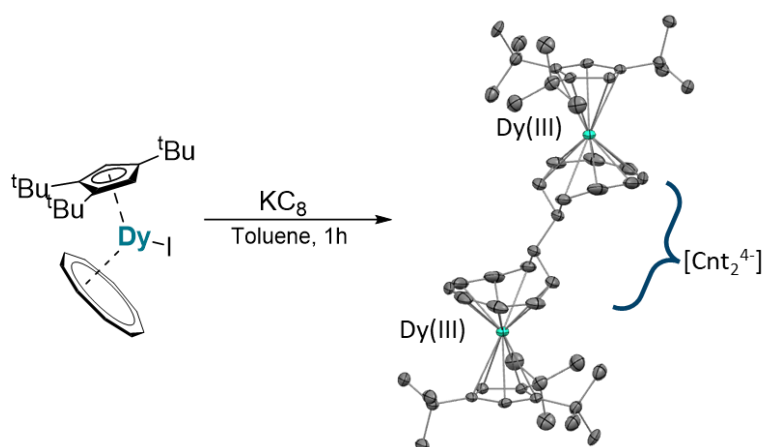


Figure C. 6 Synthetic scheme for the formation of the coupled heteroleptic dysprosium dimer. The product is presented as its solid-state structure with ellipsoids at 50% probability, dysprosium ions are in light green, carbon in grey and hydrogens have been omitted for clarity.

As the bridging dimer was the more elusive to rationalize, I optimized the condition of the reaction to form the equivalent heteroleptic complex. This was done by one-pot complexation and reduction of Cnt moiety as reported in **Figure C. 7**. The obtained compound showed a disorder of the central Cnt unit, creating two slightly distorted coordination patterns compared to the full Cnt analogue.

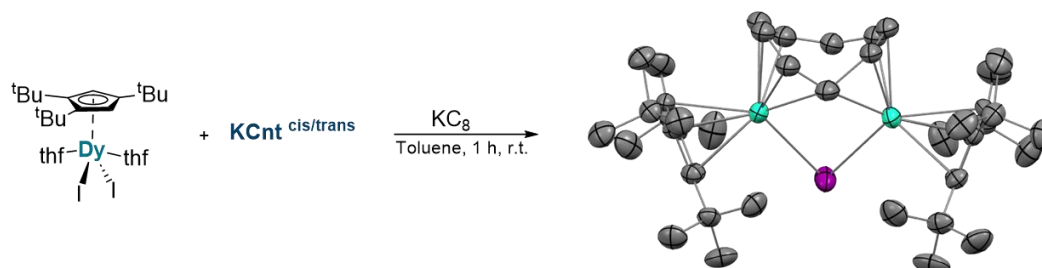


Figure C. 7 Synthetic scheme to the formation of the bridged heteroleptic dysprosium dimer. The product is presented as its solid-state structure with ellipsoids at 50% probability, dysprosium ions are in light green, carbons in grey, iodines in purple and hydrogens have been omitted for clarity.

Investigation of the magnetic behavior showed that there is no ferromagnetic coupling between the two metallic centers. Further spectroscopic study through UV-visible absorption spectroscopy revealed a feature which could be attributed to a mixed-valent character coherent with the non-symmetrical solid-state structure. Computational analyses are currently underway to investigate the origin of this transition and test this hypothesis. If it is revealed to be the case, then the bridging Cnt unit will be identified as mono-reduced. This could mean that there is a possibility that the bridging Cnt in the full-Cnt compound is also mono-reduced. This would imply that both dysprosium centers are divalent. Despite not providing a clear and definitive answer, the investigation of the heteroleptic compounds has provided us with new possible scenario of charge repartition. A summarized version of the different scenario is presented in **Figure C. 8**.

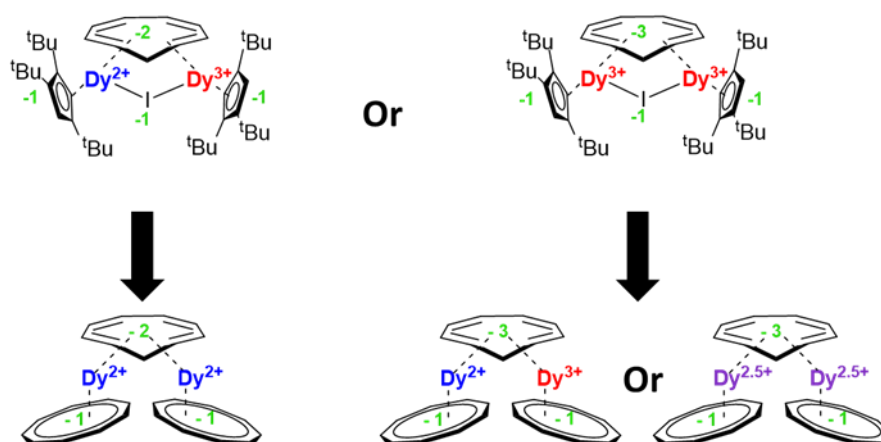


Figure C. 8 Schematic representation of the scenarios currently investigated.

To gather more information about these species, and thanks to the change of starting material, I decided to investigate the formation of similar dimers with other lanthanides. Unfortunately, the bridging species has only been obtained with erbium as of now. It shows similar dissymmetry in the solid-state structure as well as a feature in the UV-visible absorption spectrum. To extend this work, particular efforts will be targeted toward the obtention of the gadolinium and yttrium analogue for their spin-only and diamagnetic behavior respectively.

The ability displayed by the Cnt ligand to bring metallic centers together could be of interest in several fields. In this manuscript, we focused on single molecule magnet behavior, however this type of symmetry could also yield interesting molecular qubits. Particularly, extension of this chemistry towards actinide ions possessing adequate nuclear spin could be a desirable goal. As a proof of concept, a first complex featuring both a $[\text{Cnt}_2^{4-}]$ unit and uranium ions has been recently obtained and the preliminary structure is presented in **Figure C. 9**.

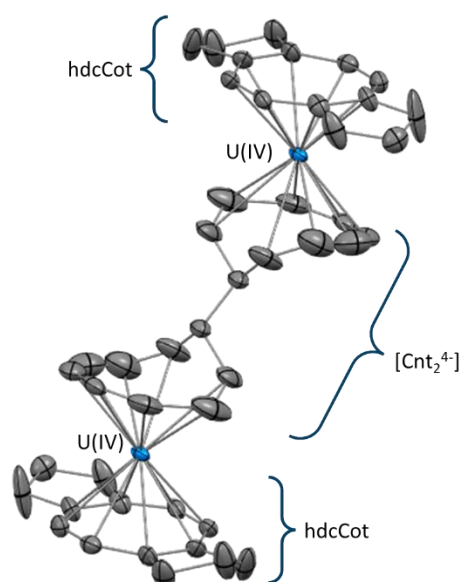


Figure C. 9 Molecular structure of the uranium-Cnt complex with ellipsoid at 50% probability, uranium ions are in blue and carbons in grey. Hydrogen atoms and one toluene molecule have been removed for clarity. hdcCot stands for dicyclopentane-cyclooctatetraenyl ligand.

The obtention of this structure with tetravalent uranium opens up the possibility to extend this chemistry toward thorium and neptunium which both adopt stable +IV oxidation states.

These different projects have shown that the Cnt ligand possesses a redox-active behavior. One additional feature of the Cnt ligand, that has not been elucidated as of yet, is its isomerization from the *cis-cis,cis,trans* (*trans*) form to its *cis-cis,cis,cis* (*cis*) form presented in **Figure C. 10**.

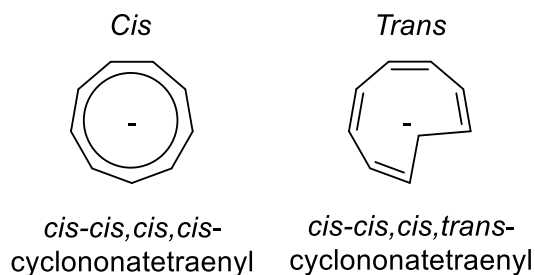


Figure C. 10 Schematic representation of the *cis* and *trans* form of the Cnt ligand.

Previous work had questioned the influence of solvent on this reaction. During this project, we showed that it is rather light-induced. Shining blue light on the ligand salt will yield full *cis* compound.

We decided to extend this investigation to coordinated Cnt ligand. Particularly, we observed that, for LnCotCnt compound, traces of *trans* Cnt ligand could be identified on solid-state structures. Study of the impact of light by ^1H solution NMR spectroscopy found that exposure to light has a reverse effect. Similar blue lights, which promote isomerisation from the *trans* form to the *cis* form of the Cnt ring, favor the obtention of LnCotCnt^{trans} from LnCotCnt^{cis}. As such, we developed a dual method to obtain the complexes with either as a majority of *cis* or *trans* ligands coordinated as illustrated in **Figure C. 11**.

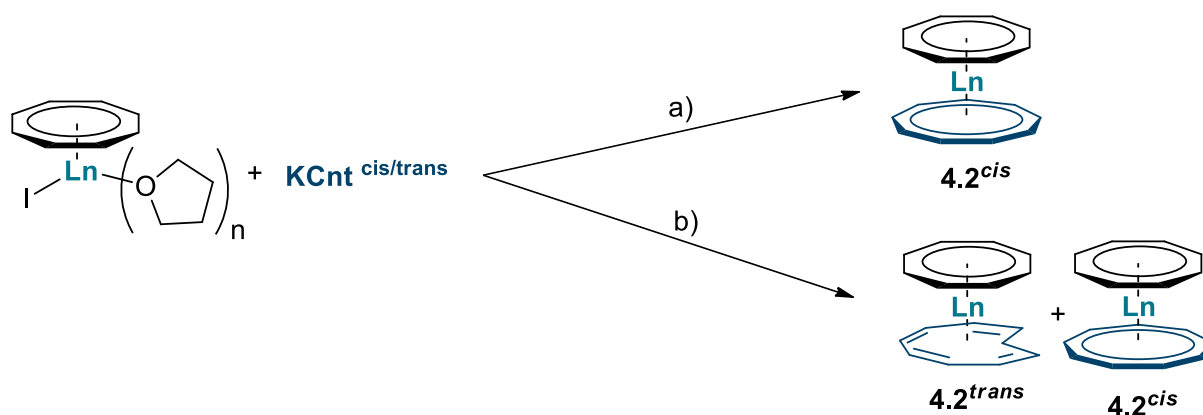


Figure C. 11 Rationalized synthesis of both the *cis* and *trans* compound of 4.2, a) Toluene/MeCN mixture, o/n r.t. then 10^{-3} mbar, 12h while protected from light, crystallization at low temperature in toluene protected from light, b) Toluene, protected from light, 14h, r.t. then filtration and crystallization at low temperature in toluene while protected from light.

Further studies showed that the wavelength of irradiation influenced the ratio of isomers for the mixture. This was particularly the case for late lanthanides. For TbCotCnt for instance, using light with $\lambda = 370$ nm, the mixture is close to $r^{\text{trans/cis}} = 85$ % whereas for higher wavelength $\lambda = 525$ nm, the ratio drops to almost $r^{\text{trans/cis}} = 0$ %. Furthermore, we showed that this isomerization was reversible, making those compounds light induced switches as illustrated in **Figure C. 12**.

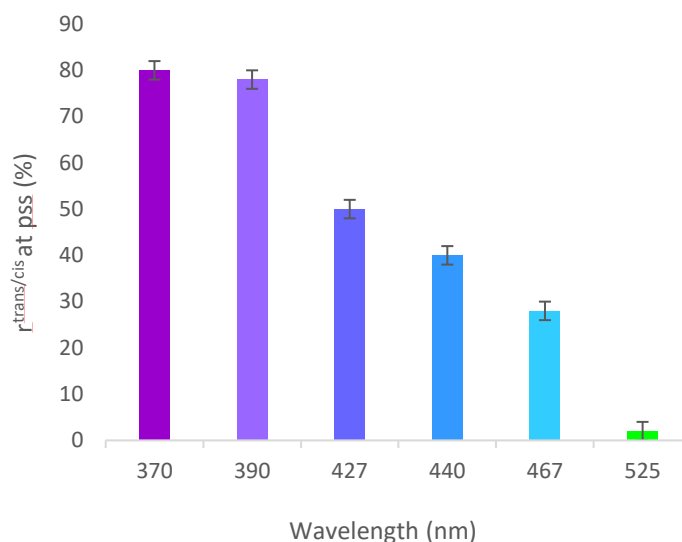


Figure C. 12 Representation of $r^{\text{trans/cis}}$ as a function of the wavelength of irradiation.

To continue this work, it could be interesting to investigate the influence of light on the redox-active behavior. Indeed, it is possible that both forms of the Cnt ligand have a different redox potential. Notably, the reactions involving divalent lanthanides were run with a *cis/trans* mixture of KCnt and it could be interesting to explore the difference of reactivity with various ratio of isomer mixture. Initial studies using KCnt^{cis} with Dyl₂ showed that the usual product was not obtained. If the light can influence the ratio of isomers, then it could help control the potential and as such, the outcome of the reaction.

To conclude, this work has allowed a better understanding of the reactivities associated with divalent and trivalent organothulium complexes. This knowledge of divalent lanthanide behaviors was further applied to study the reduction of the Cnt ligand. Different reaction conditions allowed the synthesis of four dysprosium dimers in both homoleptic and heteroleptic fashion. Several methods of characterization have been used to investigate the oxidation states of the dysprosium centers. The complexity of these electronic structures has precluded the obtention of a definitive answer. However, the different hypotheses have been reduced to a small number of possible scenarios. Exploring the reduction behavior of the Cnt ligand prompted us to study its isomerization reaction to gather a complete understanding of this molecule. The light-induced isomerization was then investigated in both the ligand form and the LnCotCnt series of complexes. In the latter, the control of the ratio of isomers through a change in wavelength of irradiation revealed a possible handle on the reactivity associated with Cnt containing complexes, which will be further explored.

Experimental Section

Supplementary information for Chapter 1 :	213
I. General information	213
II. Synthetic details	214
III. NMR characterization	217
IV. IR spectra	220
V. UV-visible characterisation	223
VI. XRD characterization	225
References	234
Supplementary information for Chapter 2:	235
I. General information	235
II. Synthetic details	235
III. Hydride investigation through NMR characterization	237
IV. XRD characterization	238
V. Magnetic studies	246
VI. Computation studies	251
References	252
Supplementary information for Chapter 3 :	253
I. General information	253
II. Synthetic details	254
III. NMR characterization	257
IV. XRD characterization	258
V. Magnetic studies	272
VI. UV-visible spectroscopy	275
VII. Computation studies	277
References	278

Supplementary information for Chapter 4:	279
I. General information	279
II. Synthetic details	280
III. NMR characterization	284
IV. XRD characterization	292
V. UV-visible spectroscopy	315
VI. Isomerization reactions	320
References	324

Supplementary information for Chapter 1:

I. General information	213
II. Synthetic details	214
III. NMR characterization	217
IV. IR spectra	220
V. UV-visible characterisation	223
VI. XRD characterization	225
References	234

I. General information

All air- and moisture-sensitive reactions were performed using standard Schlenk-line techniques under dry N₂ or Ar atmosphere or in argon or nitrogen-filled gloveboxes (MBraun). All glassware was dried at 140 °C for at least 12 h prior to use. All solvents (Et₂O, toluene, benzene, pentane, C₆D₆, tol-d₈, THF-d₈) were dried over sodium, degassed, and transferred under reduced pressure in a cold flask. TmI₂ was prepared from Tm metal and I₂ following the literature procedure for DyI₂.^{1,2} Commercial KN(SiMe₃)₂ (Sigma–Aldrich, 95%) was purified by recrystallization from toluene. KCp^{ttt} was prepared by deprotonation of HCp^{ttt} with KN(SiMe₃)₂ in Et₂O. HCp^{ttt},³ Tm(Cp^{ttt})₂⁴ and KC₈^{5,6} were prepared following the published procedures. All other chemicals were obtained from commercial sources and used without further purification. High purity CO gas (CO-N47, CO ≥ 99,997 %, < 1 ppm CO₂, < 3 ppm O₂, < 3 ppm H₂O) was purchased from Air Liquide. The control of the stoichiometry in the gas addition reactions was achieved by the use of standard 5 mm NMR tubes of known volumes equipped with J. Young valves. Upon addition of a precise volume of solvent, the headspace volume is pressurized accordingly following the ideal gas law. ¹H NMR spectra were recorded on a Bruker Avance III-300 MHz spectrometer and ¹H chemical shifts are given relative to internal solvent references in ppm. Infrared (IR) spectra were recorded at room temperature under argon atmosphere on a Thermo Scientific Nicolet iS5 FTIR spectrometer equipped with an iD7 ATR-Diamond unit. UV-visible absorption spectra were recorded on a Cary60 spectrometer in quartz cuvettes adapted with a J. Young valve. Elemental analyses were obtained from Mikroanalytisches Labor Pascher (Remagen, Germany).

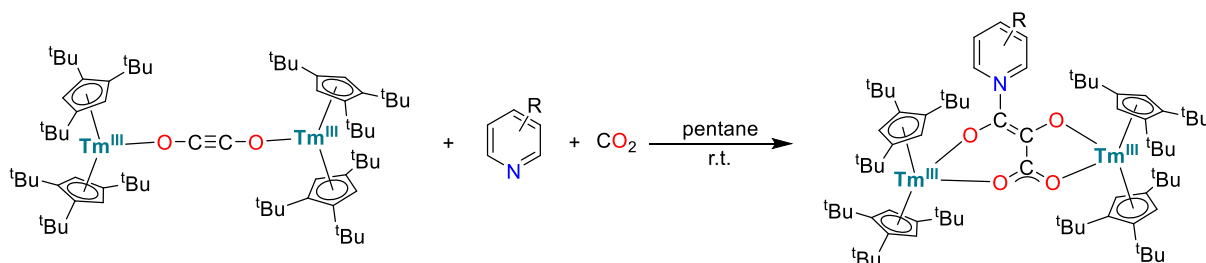
II. Synthetic details

Synthesis of **1_{CO}**⁷

In a J. Young NMR tube, **TmCp^{ttt}₂** (82 mg, 0.13 mmol) was dissolved in toluene (0.5 mL). The resulting solution was degassed three times by freeze-pump-thaw cycles. CO was added in the tube (approximately 1 equiv.) leading to a slow change in color from deep purple to brownish yellow. Lightly colored crystals suitable for X-ray diffraction studies typically formed over a period of two days at room temperature. The crystals were isolated by decantation, washed with small amount of pentane and dried under reduced pressure. Yield of the crystals: 46 mg, 35 μ mol, 53 % (based on the metal)

¹H NMR (300 MHz, tol-d₈, 353 K): only broad resonances are observed

General scheme for the formation of the pyridine type adducts



Synthesis of **1_{Pyr}**

In a J. Young NMR tube, **1_{CO}** (40 mg, 30 μ mol) was suspended in pentane (0.5 mL) and pyridine was added (4.9 μ L, 60 μ mol, 2 equiv.). The resulting solution was degassed three times by freeze-pump-thaw cycles. CO₂ was added in the tube (approximately 1 equiv.) leading to a sudden color change from yellow to deep blue and complete dissolution of solids. Deeply colored crystals suitable for X-ray diffraction studies formed over a period of two days at room temperature. The crystals were isolated by decantation, washed with small amount of pentane and dried under reduced pressure.

¹H NMR (300 MHz, tol-d₈, 353 K): δ (ppm): 239.3 (br s), 186.5 (br s), 160.1 (br s), 151.8 (br s), 107.3 (br s), 25.2 (br s), -7.0 (br s), -87.6 (br s), -163.4 (br s). Only the most intense resonances are reported.

IR (ATR): (cm⁻¹) = 2955 (m), 2900 (m), 2850 (m), 1594 (w), 1525 (m), 1459 (m), 1377 (w), 1358 (m), 1242 (s), 1167 (m), 1111 (w), 1002 (w), 809 (m), 780 (w), 723 (w), 685 (w), 671 (m)

Synthesis of **1_{tBu}**

In a J. Young NMR tube, **1_{CO}** (25 mg, 0.02 mmol) was suspended in pentane (0.5 mL) and 4-tert-Butylpyridine was added (6.1 μ L, 0.04 mmol, 2 equiv.). The resulting solution was degassed three times by freeze-pump-thaw cycles. CO₂ was added in the tube (approximately

1 equiv.) leading to a sudden color change from yellow to deep blue and complete dissolution of solids. Deeply colored crystals formed over a period of two days at room temperature. The crystals were isolated by decantation, washed with small amount of pentane and dried under reduced pressure.

^1H NMR (300 MHz, $\text{tol-}d_8$, 353 K): δ (ppm): 239.0 (br s), 189.1 (br s), 157.6, 107.3 (br s), 48.2 (s), 41.1 (s), 20.7 (br s), -12.4, -88.3 (br, s).

IR (ATR): (cm^{-1}) = 2954 (m), 2900 (m), 2850 (m), 1588 (m), 1526 (m), 1458 (w), 1357 (m), 1240 (s), 1201 (w), 1167 (w), 812 (m)

Synthesis of 1_{Me_2}

In a J. Young NMR tube, 1_{Co} (25 mg, 0.02 mmol) was suspended in pentane (0.5 mL) and 2,6-di-methylpyridine was added (4.6 μL , 0.04 mmol, 2 equiv.). The resulting solution was degassed three times by freeze-pump-thaw cycles. CO_2 was added in the tube (approximately 1 equiv.) leading to a sudden color change from yellow to blue and complete dissolution of solids. Homogenization of the tube led to precipitation of the product as purple solid. Deeply colored crystals suitable for X-ray diffraction studies were formed by slow diffusion of the CO_2 in the tube. Alternatively, the reaction was performed in toluene and concentration at cold, $-40\text{ }^\circ\text{C}$ of the solution yielded to the crystallization of the same complex. The crystals were isolated by decantation, washed with small amount of pentane and dried under reduced pressure. Yield: 15.1 mg (0.01 mmol), 50 %

^1H NMR (300 MHz, $\text{tol-}d_8$, 353 K): δ (ppm): 256.4 (br s), 215.6 (br s), 188.3 (br s), 150.2 (br s), 54.9 (s), 37.9 (s), 28.4 (s), -33.6 (br s), -46.0 (br), -143.3 (s), -198.4 (s)

IR (ATR): (cm^{-1}) = 2953 (m), 2900 (m), 2867 (m), 1627 (m), 1506 (m), 1458 (w), 1358 (m), 1168 (w), 1138 (w), 1002 (w), 823 (m), 808 (m), 757 (w), 698 (w), 671 (m)

Synthesis of 1_{DMAP}

In a J. Young NMR tube, 1_{Co} (38 mg, 0.03 mmol) was suspended in pentane (0.5 mL) and 4-dimethyl-aminopyridine was added (6.5 mg, 0.06 mmol, 2 equiv.). The resulting solution was degassed three times by freeze-pump-thaw cycles. CO_2 was added in the tube (approximately 1 equiv.) leading to a sudden color change from yellow to deep red and complete dissolution of solids. Deeply colored crystals suitable for X-ray diffraction studies formed over a period of two days at room temperature. The crystals were isolated by decantation, washed with small amount of pentane and dried under reduced pressure.

^1H NMR (300 MHz, $\text{tol-}d_8$, 353 K): δ (ppm): 234.8 (br s), 189.7 (br s), 160.1 (br s), 110.5 (br s), 47.8 (s), 43.8 (s), 15.0 (br s), -9.8 (br s), -87.3 (br s). Only the most intense resonances are reported.

IR (ATR): (cm⁻¹) = 2953 (m), 2900 (m), 2866 (m), 1645 (m), 1613 (m), 1517 (m), 1457 (w), 1359 (m), 1230 (s), 1209 (m), 1168 (w), 1121 (w), 1004 (w), 810 (m)

Synthesis of **1_{quin}**

In a J. Young NMR tube, **1_{co}** (25 mg, 0.02 mmol) was suspended in pentane (0.5 mL) and quinoline was added (4.3 μ L, 0.04 mmol, 2 equiv.). The resulting solution was degassed three times by freeze-pump-thaw cycles. CO₂ was added in the tube (approximately 1 equiv.) leading to a sudden color change from yellow to green and complete dissolution of solids. Deeply colored crystals suitable for X-ray diffraction studies were formed over a period of two days. The crystals were isolated, washed with small amount of pentane and dried under reduced pressure.

Synthesis of **1_{ox}**

In a J. Young NMR tube, **1_{co}** was suspended in pentane (0.5 mL). The mixture was degassed three times by freeze-pump-thaw cycles. O₂ was added in the tube leading to a color change from dark yellow to pale green and complete dissolution of solids. Colorless crystals suitable for X-ray diffraction studies were formed over a period of two days.

¹H NMR (300 MHz, tol-*d*₈, 353 K): δ (ppm): 226.6 (br s), 52.5 (br s)

Synthesis of **1_{iso}**

In a J. Young NMR tube, **1_{co}** (40 mg, 0.03 mmol) was suspended in toluene (0.5 mL) and tBu-isocyanate was added (3.4 μ L, 0.03 mmol, 2 equiv.), leading to a color change from yellow to deep orange and complete dissolution of solids. The resulting mixture was filtered and concentrated. Small crystals were grown at low temperature over the course of a month.

¹H NMR (300 MHz, tol-*d*₈, 353 K): δ (ppm): 325.4, 262.4, 211.3, 164.9, 113.6, 107.3, 83.3, 47.5, 40.2, 36.9, 24.1, -10.6, -17.5, -26.6, -39.9, -60.9, -72.1, -78.2, -80.9, -89.6.

III. NMR characterization

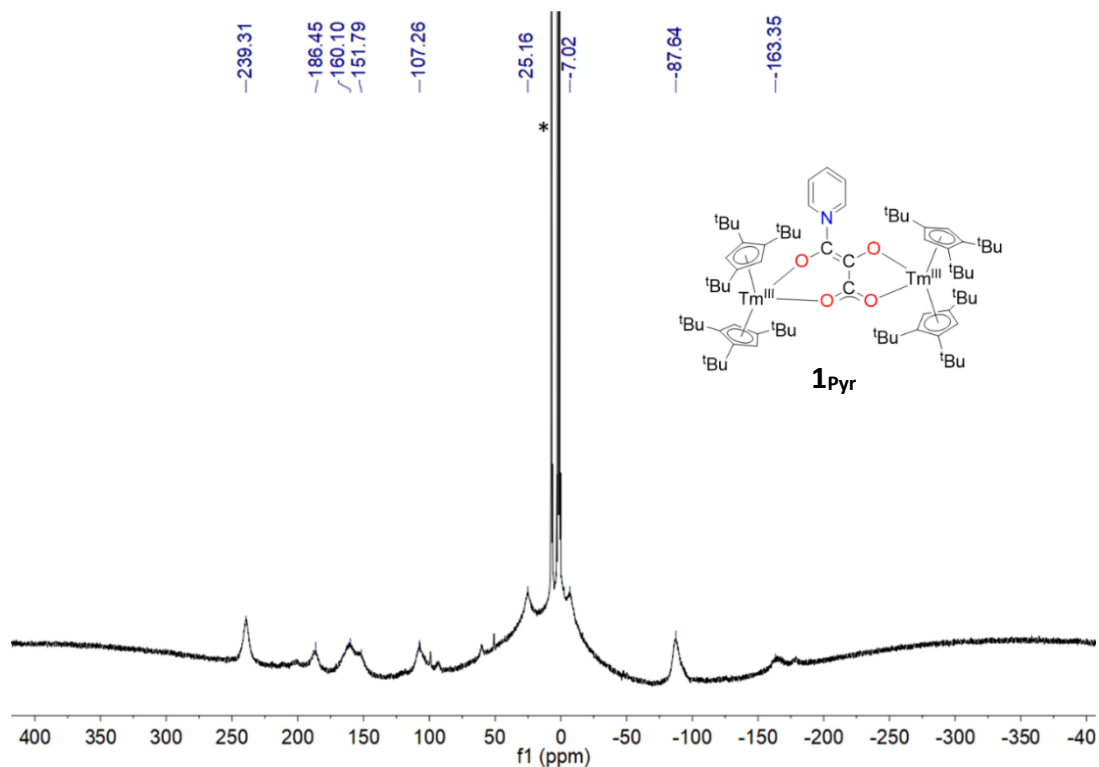
 ^1H NMR of 1_{Pyr} 

Figure S1. 1 ^1H NMR (300 MHz, tol-d_8 , 293 K) spectrum of 1_{Pyr} (residual protio solvent signal signified as *).

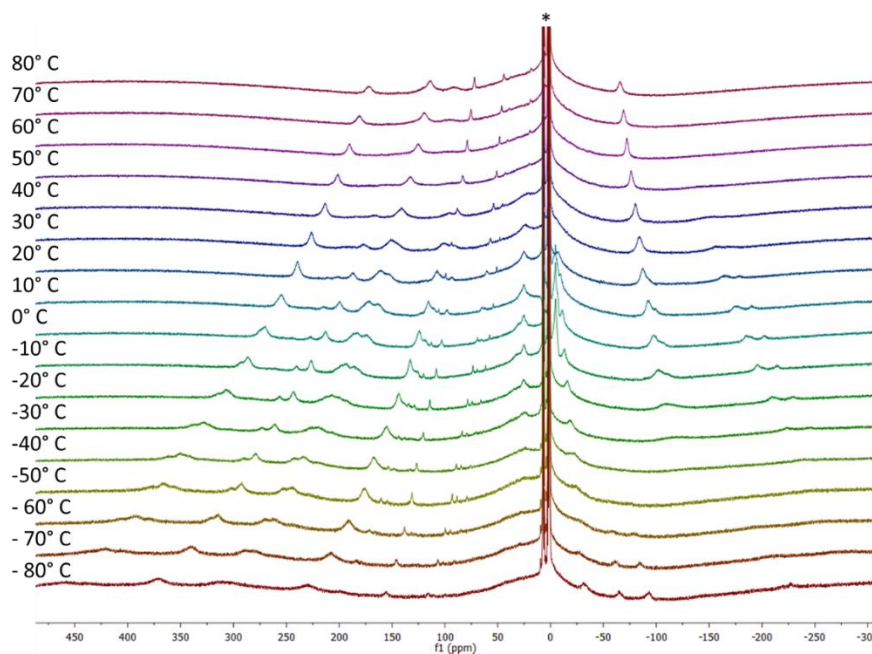
VT-NMR analysis of 1_{Pyr} 

Figure S1. 2 ^1H NMR (300 MHz, tol-d_8 , 293 K) spectra of 1_{Pyr} at variable temperatures (residual protio solvent signal signified as *).

^1H NMR of **1_{tBu}**

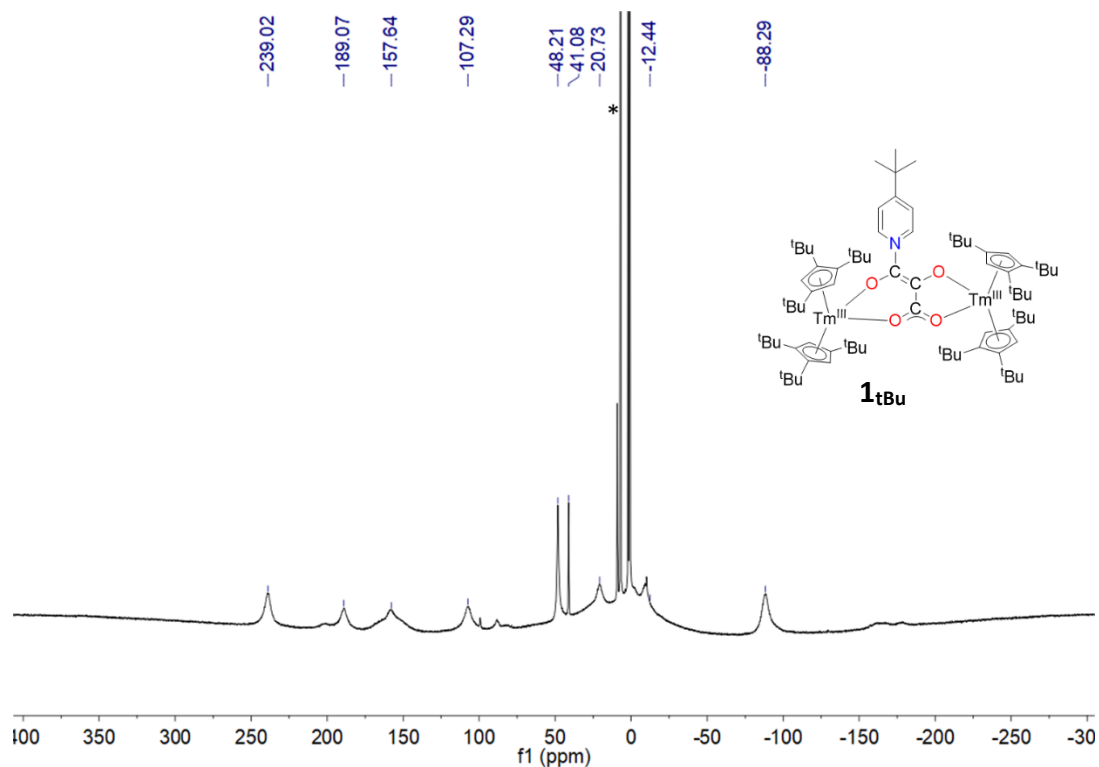


Figure S1. 3 ^1H NMR (300 MHz, *tol-d*₈, 293 K) spectrum of **1_{tBu}** (residual protio solvent signal signified as *).

^1H NMR of **1_{Me2}**

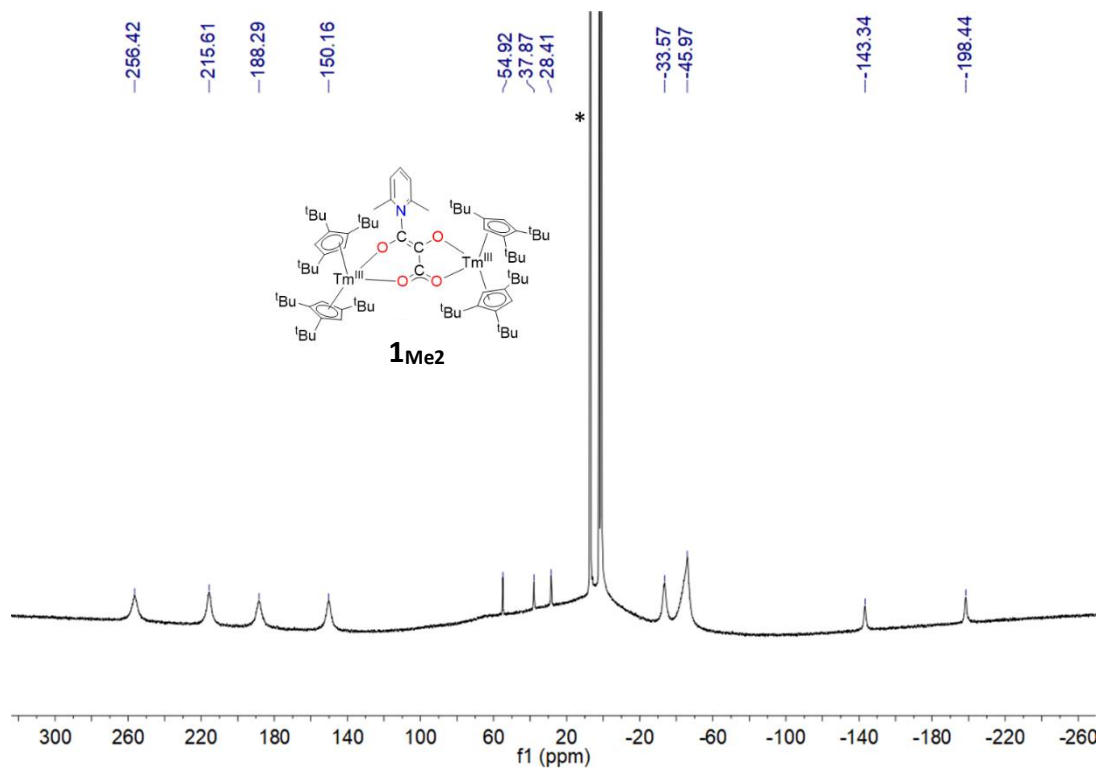


Figure S1. 4 ^1H NMR (300 MHz, *tol-d*₈, 293 K) spectrum of **1_{Me2}** (residual protio solvent signal signified as *).

^1H NMR of **1**_{DMAP}

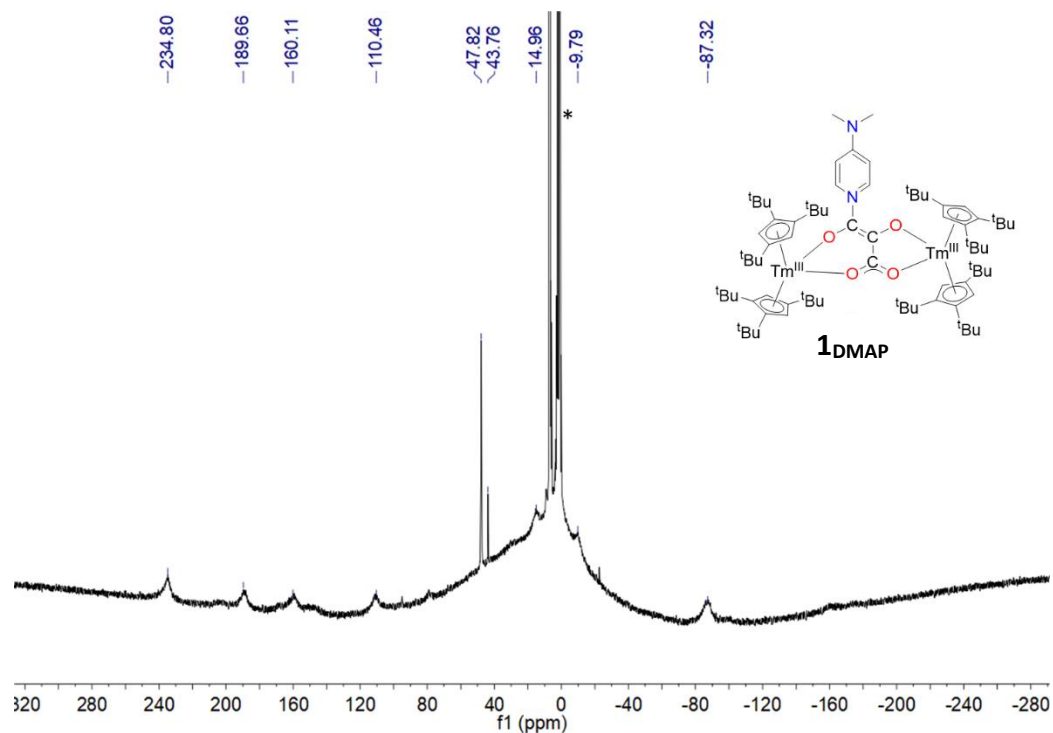


Figure S1. 5 ^1H NMR (300 MHz, *tol-d*₈, 293 K) spectrum of **1**_{DMAP} (residual protio solvent signal signified as *).

^1H NMR of **1**_{ox}

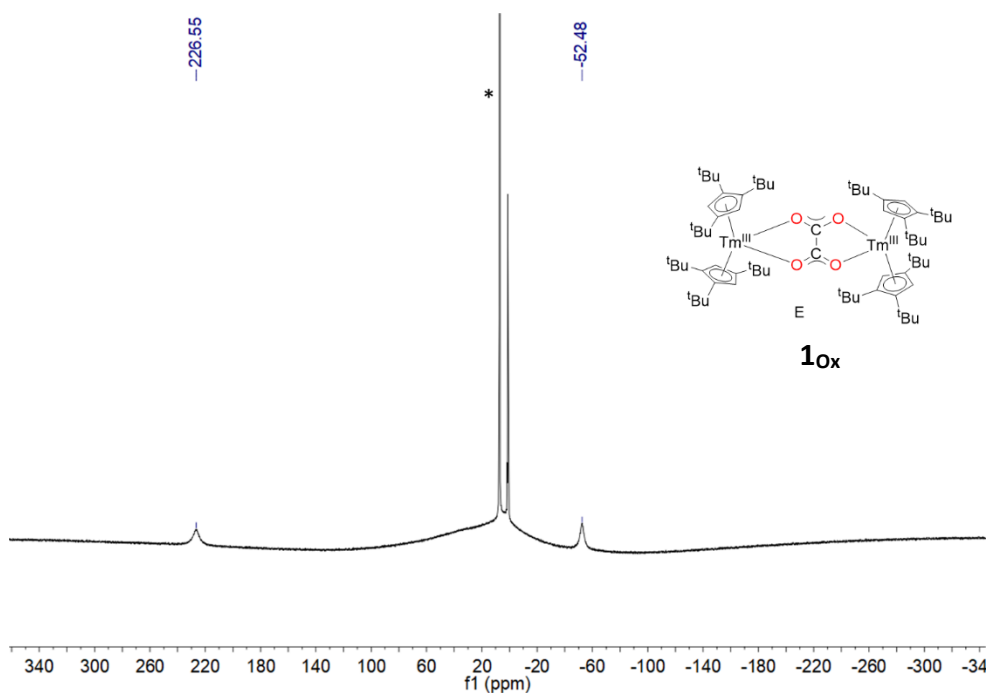


Figure S1. 6 ^1H NMR (300 MHz, *tol-d*₈, 293 K) spectrum of **1**_{ox} (residual protio solvent signal signified as *).

^1H NMR of **1_{Iso}**

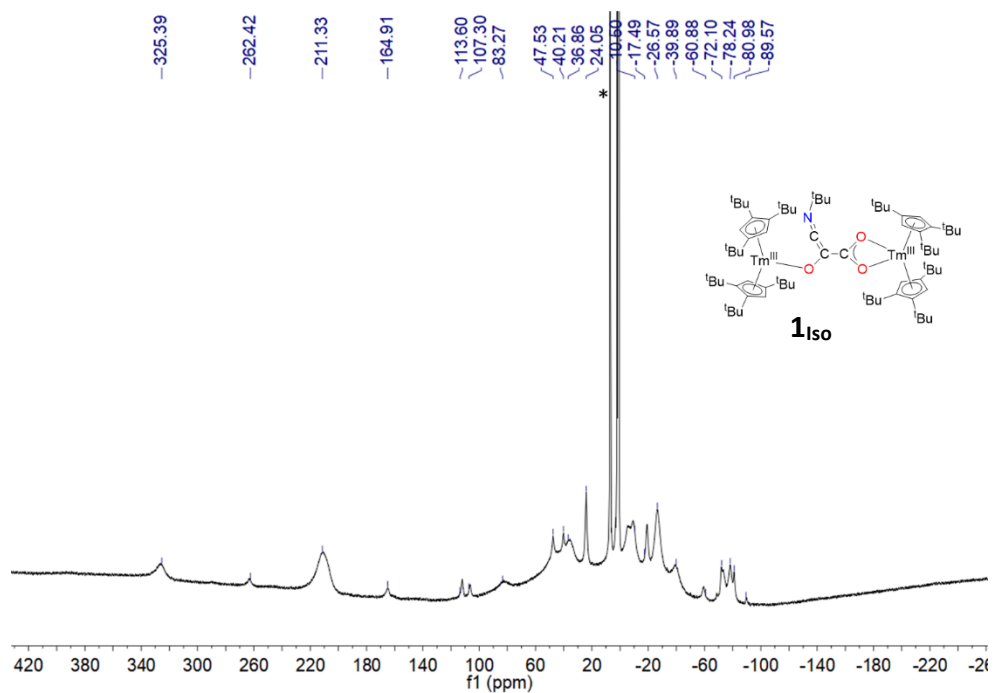


Figure S1. ^1H NMR (300 MHz, *tol-d*₈, 293 K) spectrum of **1_{Iso}** (residual protio solvent signal signified as *).

IV. IR spectra

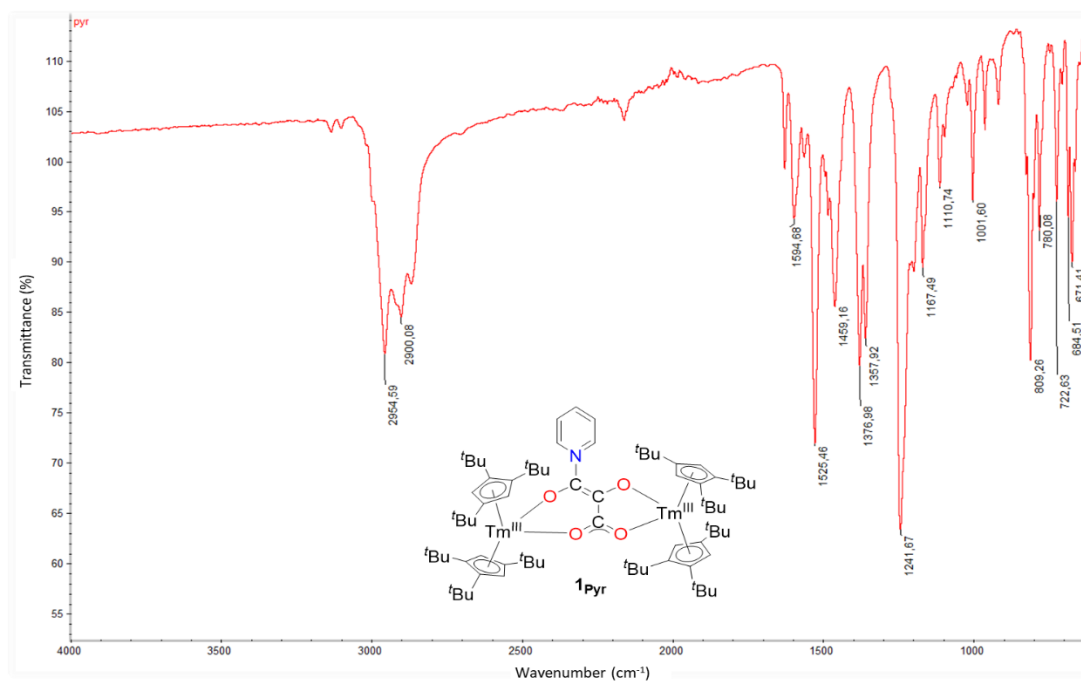


Figure S1. 8 IR spectrum of **1_{Pyr}**.

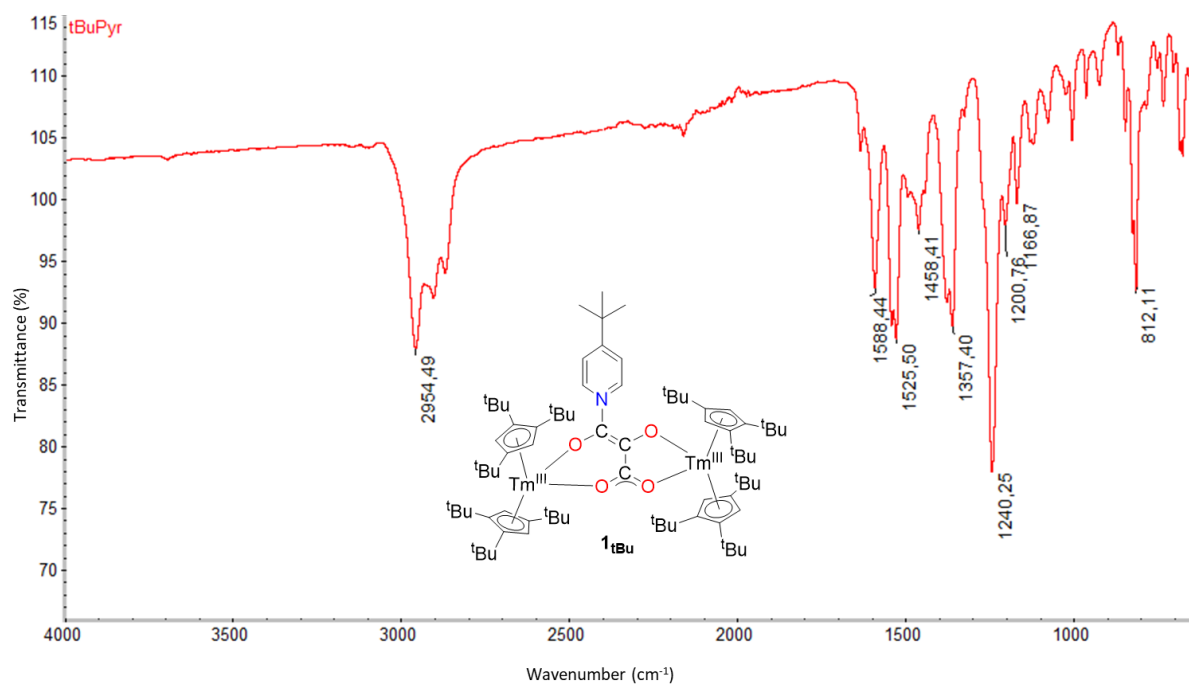


Figure S1. 9 IR spectrum of **1tBu**.

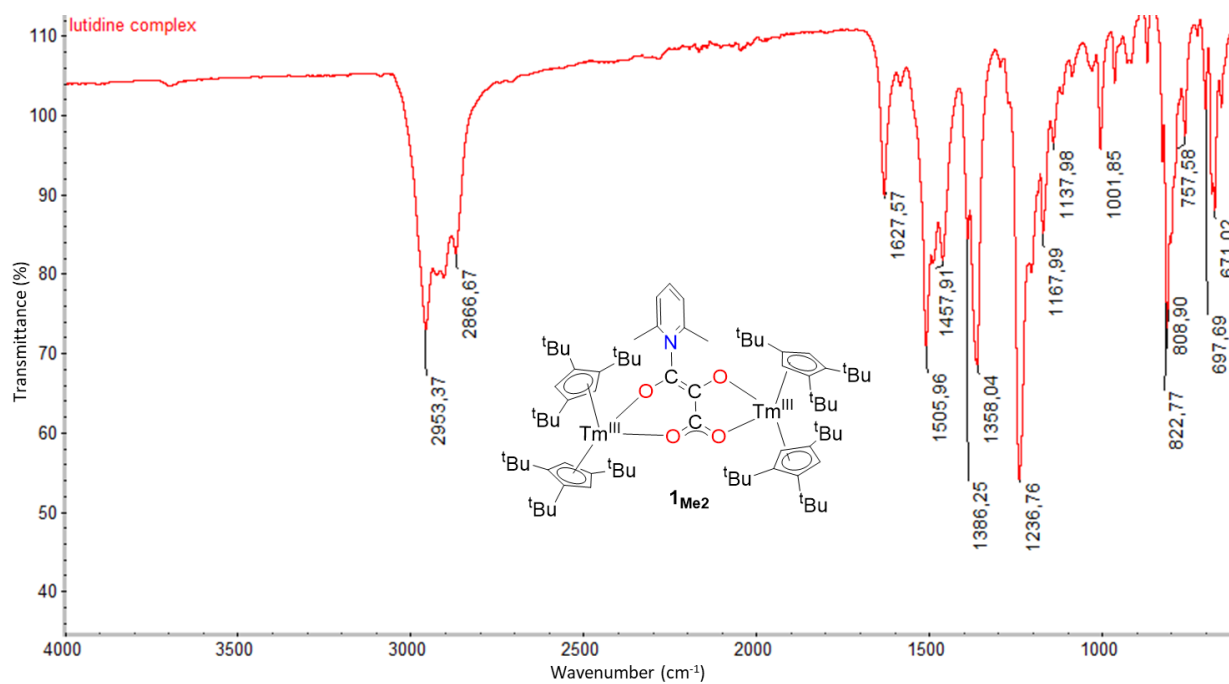


Figure S1. 10 IR spectrum of **1Me2**.

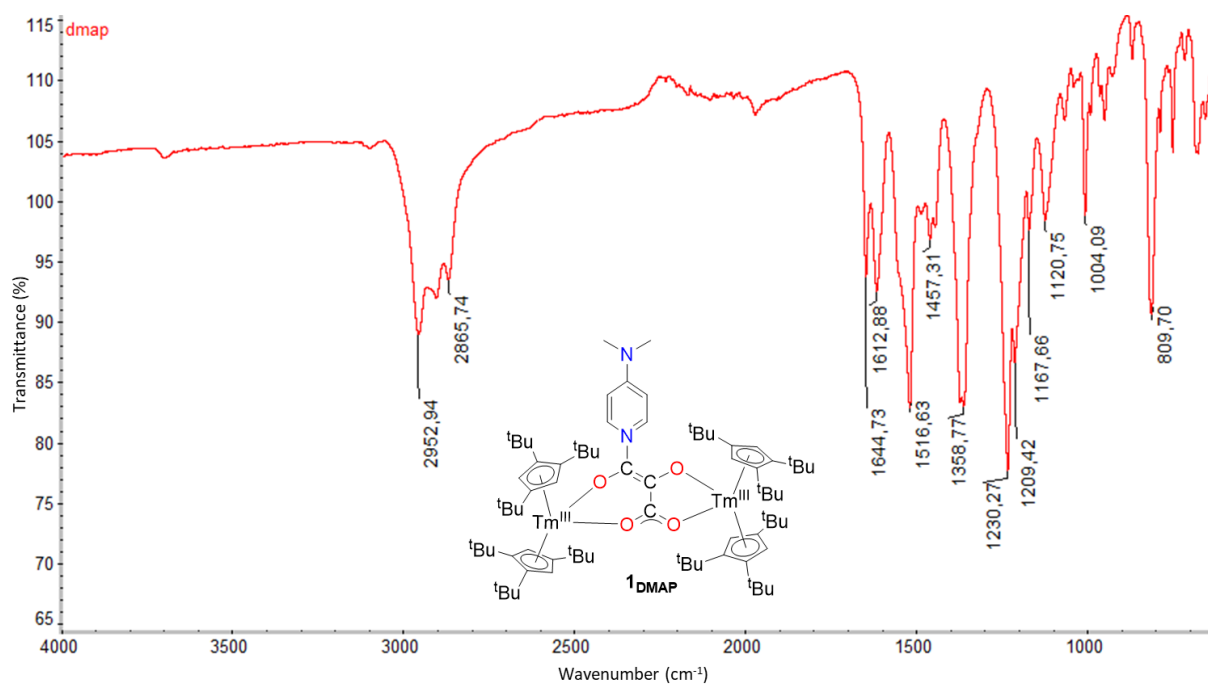


Figure S1. 11 IR spectrum of **1_{DMAP}**.

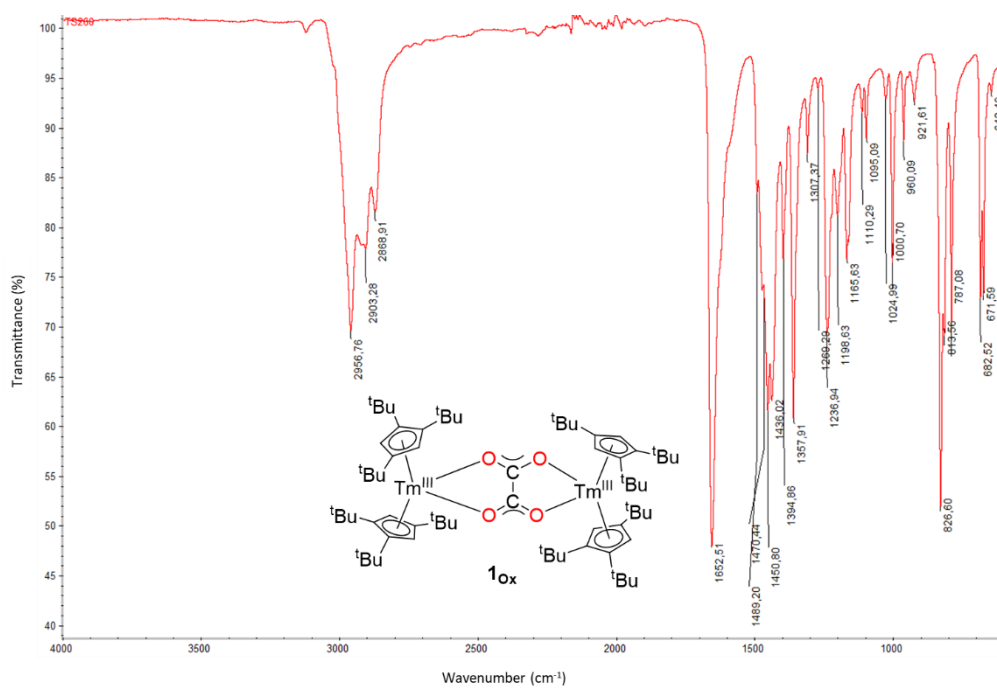


Figure S1. 12 IR spectrum of **1_{ox}**.

V. UV-visible characterisation

In situ study for **1_{tBu}**

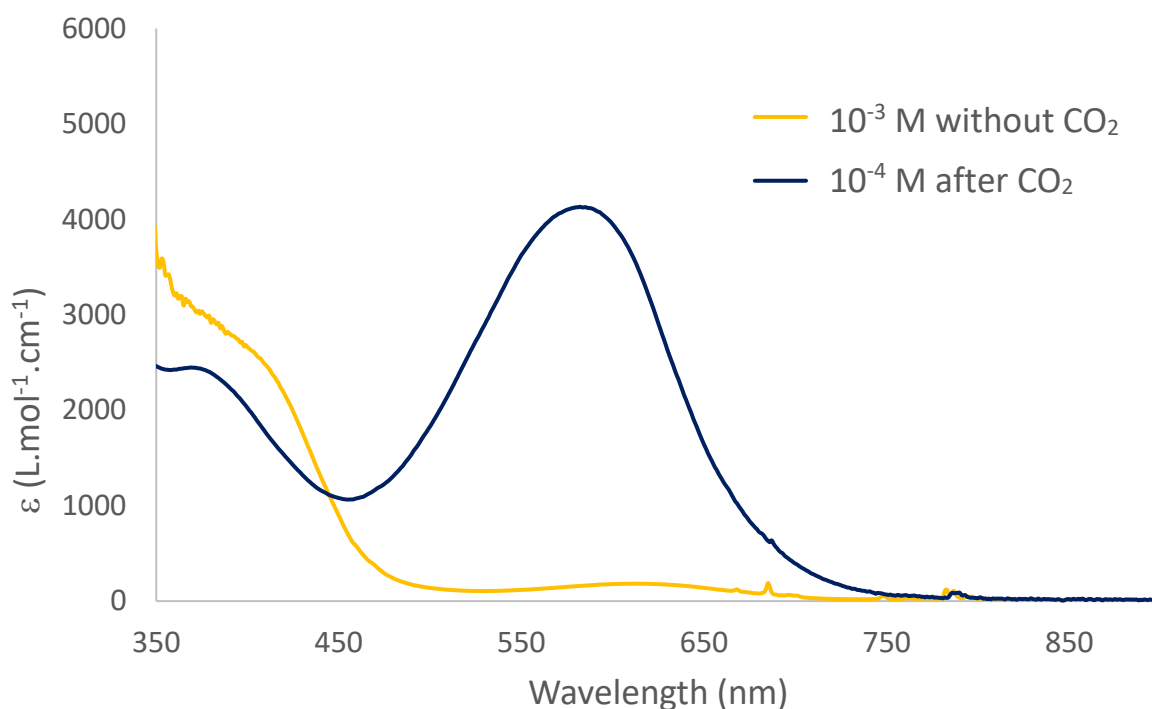


Figure S1. 13 In-situ evolution of the absorbance spectrum after the addition of CO_2 on a mixture of **1_{co}** and tBu-pyridine.

In situ study for **1_{Me2}**

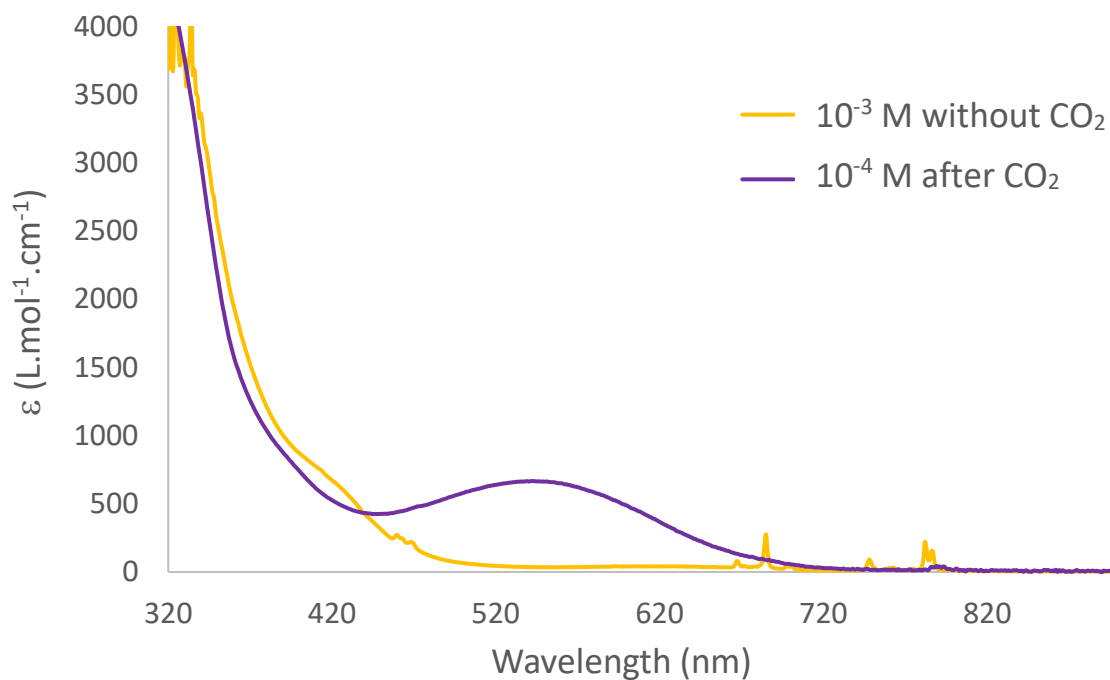


Figure S1. 14 In-situ evolution of the absorbance spectrum after the addition of CO_2 on a mixture of **1_{co}** and di-methylpyridine.

In situ study for **1_{DMAP}**

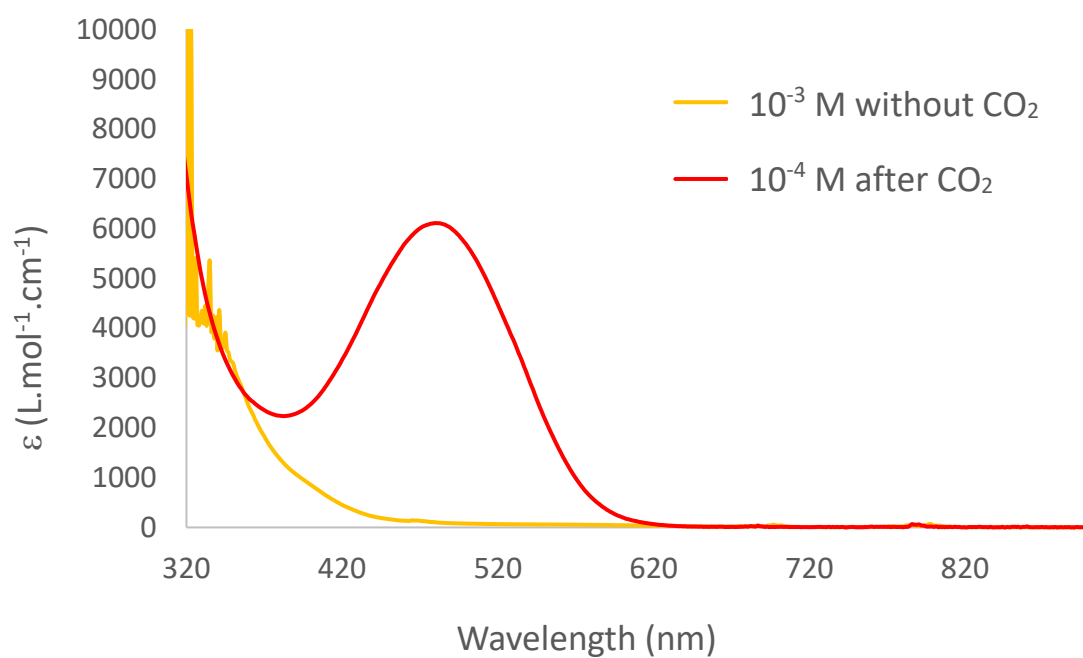


Figure S1. 15 In-situ evolution of the absorbance spectrum after the addition of CO_2 on a mixture of **1_{CO}** and DMAP

In situ study for **1_{quin}**

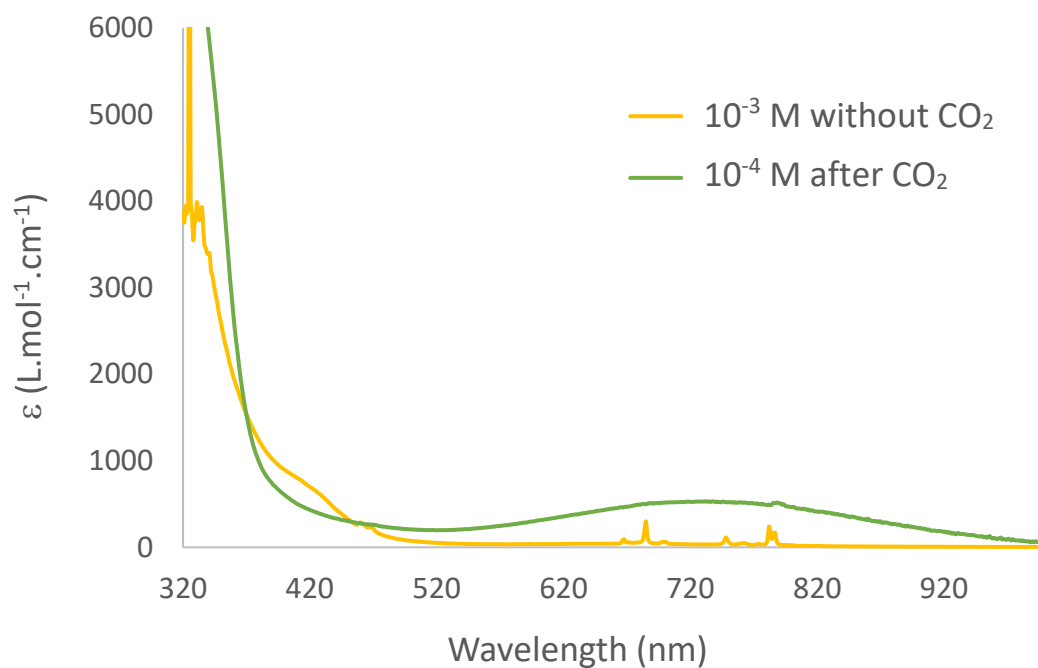


Figure S1. 16 In-situ evolution of the absorbance spectrum after the addition of CO_2 on a mixture of **1_{CO}** and quinoline.

VI. XRD characterization

1. General methods

Single crystals of the complexes suitable for X-ray analysis were mounted on a Kapton loop using a Paratone N oil. Two diffractometers were used during this for the data acquisition, either a Bruker diffractometer equipped with an APEX II CCD detector and a graphite Mo-K α monochromator or a Stoe stadivari diffractometer with a Eiger2 detector and a Mo-K α microsource. All measurements were done at 150 K and a refinement method was used for solving the structure. The resolution of the solid-state structure was accomplished using the SHELXS-97 or SHELXT programs.^{8,9} The refinement was performed with the SHELXL program using the Olex2 software.^{9,10} All atoms – except hydrogens – were refined anisotropically.

2. Summary of crystal data

Compound	1_{Pyr}	1_{Me2}	1_{DMAP}
Formula	C _{78.5} H ₁₂₇ NO ₄ Tm ₂	C ₉₂ H _{158.6} NO ₄ Tm ₂	C _{81.5} H _{134.4} N ₂ O ₄ Tm ₂
Crystal size (mm ³)	0.48 x 0.40 x 0.28	0.32 x 0.12 x 0.08	0.1 x 0.08 x 0.02
Crystal system	Monoclinic	Monoclinic	Monoclinic
Space group	C2/c	C2/c	C2/c
Volume (Å ³)	7721.3(10)	8015.4(11)	15822.4(6)
a (Å)	18.6605(14)	32.751(3)	22.1072(5)
b (Å)	18.0375(14)	10.9661(8)	27.1659(7)
c (Å)	23.6407(18)	22.4887(17)	26.8322(5)
α (deg)	90	90	90
β (deg)	103.986(3)	97.076(3)	100.923(2)
γ (deg)	90	90	90
Z	4	4	8
Formula weight (g/mol)	1486.66	1680.65	1544.16
Density (calcd) (g/cm ³)	1.279	1.393	1.296
Absorption coefficient (mm ⁻¹)	2.328	2.251	2.275
F(000)	3100.0	3550.0	6459.0
Temp (K)	150.00	150.01	150
Diffractometer	Kappa APEX II CCD	Kappa APEX II CCD	Stoe Stadivari
Radiation	MoKα (λ = 0.71073)	MoKα (λ = 0.71073)	MoKα (λ = 0.71073)
2θ range for data collection (deg)	3.55 to 61.036	5.25 to 52.986	4.308 to 60.068
Absorption correction	Multi-scan	Multi-scan	Multi-scan
Total no. reflections	108105	80291	67456
Unique reflections [R _{int}]	11787 [R _{int} = 0.0556]	8248 [R _{int} = 0.0574]	19281 [R _{int} = 0.0393]
Final R indices [I > 2σ(I)]	R ₁ = 0.0249, wR ₂ = 0.0581	R ₁ = 0.0239, wR ₂ = 0.0594	R ₁ = 0.0500, wR ₂ = 0.1180
R indices (all data)	R ₁ = 0.0467, wR ₂ = 0.0680	R ₁ = 0.0305, wR ₂ = 0.0619	R ₁ = 0.1167, wR ₂ = 0.1438
Largest diff. peak and hole (e.Å ⁻³)	0.66/-0.77	0.43/-0.39	1.72/-1.20
GooF	1.066	1.054	1.077

Compound	1_{quin}	1_{ox}	1_{iso}
Formula	C ₈₆ H _{137.4} NO ₄ Tm ₂	C ₇₀ H ₁₁₆ O _{4.3} Tm ₂	C ₇₅ H ₁₂₅ NO ₃ Tm ₂
Crystal size (mm ³)	0.15 × 0.12 × 0.1	0.26 × 0.24 × 0.22	0.24 × 0.1 × 0.04
Crystal system	Monoclinic	Triclinic	Monoclinic
Space group	C2/c	P-1	P2 ₁ /n
Volume (Å ³)	8358.9(5)	3356.3(7)	7214.7(2)
a (Å)	20.0268(8)	10.5413(14)	10.9204(2)
b (Å)	19.2471(4)	11.7857(16)	20.4648(3)
c (Å)	22.3399(7)	28.834(3)	32.2831(7)
α (deg)	90	89.968(3)	90
β (deg)	103.902(3)	84.864(3)	90.180(2)
γ (deg)	90	70.252(3)	90
Z	4	2	4
Formula weight (g/mol)	1587.22	1364.36	1426.61
Density (calcd) (g/cm ³)	1.261	1.350	1.313
Absorption coefficient (mm ⁻¹)	2.155	2.671	2.487
F(000)	3322.0	1417.0	2976.0
Temp (K)	150	150	150
Diffractionmeter	Stoe Stadivari	Stoe stadivari	Stoe stadivari
Radiation	MoKα (λ = 0.71073)	MoKα (λ = 0.71073)	MoKα (λ = 0.71073)
2θ range for data collection (deg)	4.63 to 54.996	3.674 to 67.788	4.228 to 58.968
Absorption correction	Multi-scan	Multi-scan	Multi-scan
Total no. Reflections	51250	113330	65348
Unique reflections [R _{int}]	9587 [R _{int} = 0.0706]	27080 [R _{int} = 0.0601]	18477 [R _{int} = 0.0307]
Final R indices [I>2σ(I)]	R ₁ = 0.1017, wR ₂ = 0.2282	R ₁ = 0.0335, wR ₂ = 0.0705	R ₁ = 0.0485, wR ₂ = 0.1283
R indices (all data)	R ₁ = 0.1130, wR ₂ = 0.2352	R ₁ = 0.0492, wR ₂ = 0.0766	R ₁ = 0.0860, wR ₂ = 0.1392
Largest diff. peak and hole (e.Å ⁻³)	2.36/-2.73	1.36/-0.88	1.88/-1.02
Goof	1.239	1.052	1.009

3. Crystal structures and main distances

Structure of **1_{Pyr}**

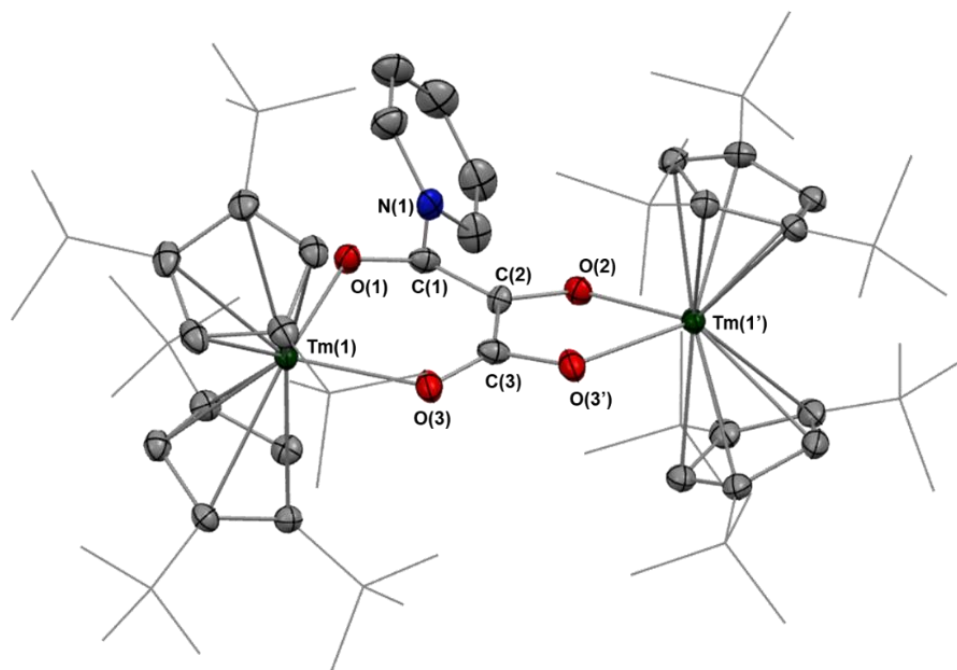


Figure S1. 17 Molecular structure of **1_{Pyr}** in the solid state with thermal ellipsoids at the 50% probability level. Thulium atoms are represented in dark green, carbon atoms in grey, nitrogen and oxygen are in blue and red respectively. H atoms have been omitted for clarity and ^tBu groups are represented in wireframe.

	Main distances in Å
Tm(1) – O(1)	2.256 (10)
Tm(1') – O(2)	2.135 (10)
Tm(1) – O(3)	2.2553 (17)
O(1) – C(1)	1.301(11)
C(1) – C(2)	1.354 (6)
C(2) – C(3)	1.516 (5)
C(2) – O(2)	1.351 (10)
C(3) – O(3)	1.262 (2)
C(1) – N(1)	1.462 (5)
Tm(1) – C(Cp ^{ttt})	2.638(2) – 2.822(2)
	2.622 (2) – 2.795(2)
Tm(1) – Cent (Cp ^{ttt})	2.426 / 2.433
(Cp ^{ttt}) Cent – Tm(1) – Cent (Cp ^{ttt})	138.5 °
Mean Cp ^{ttt} –Cp angle	38.45 °
O(1)C(1)C(2) plane ^pyr plane	42.68 °

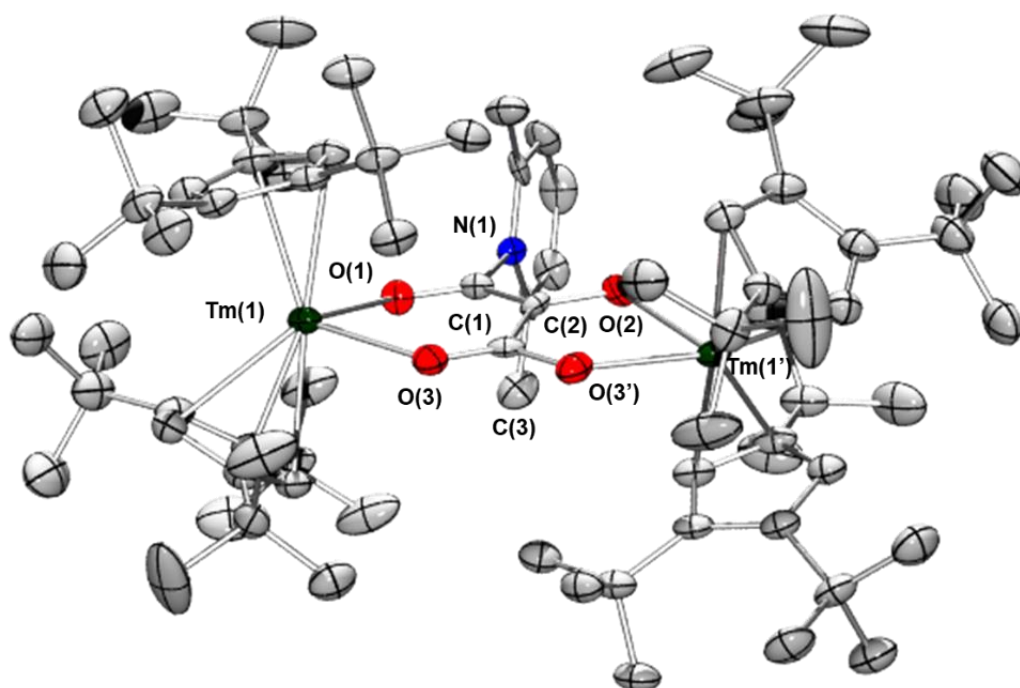
Structure of 1_{Me_2} 

Figure S1. 18 Molecular structure of 1_{Me_2} in the solid state with thermal ellipsoids at the 50% probability level. Thulium atoms are represented in dark green, carbon atoms in grey, nitrogen and oxygen are in blue and red respectively, H atoms have been omitted for clarity.

Main distances in Å	
Tm(1) – O(1)	2.211(11)
Tm(1') – O(2)	2.172(12)
Tm(1) – O(3)	2.298(2)
O(1) – C(1)	1.278(13)
C(1) – C(2)	1.350(7)
C(2) – C(3)	1.503(6)
C(2) – O(2)	1.361(9)
C(3) – O(3)	1.262(2)
C(1) – N(1)	1.495(6)
Tm(1) – C(Cp ^{ttt})	2.631(3) – 2.841(3)
	2.631(3) – 2.845(3)
Tm(1) – Cent (Cp ^{ttt})	2.45 / 2.44
(Cp ^{ttt}) Cent – Tm(1) – Cent (Cp ^{ttt})	133.2 °
Mean Cp ^{ttt} angle	43.1 °
O(1)C(1)C(2) plane ^pyr plane	88.1 °

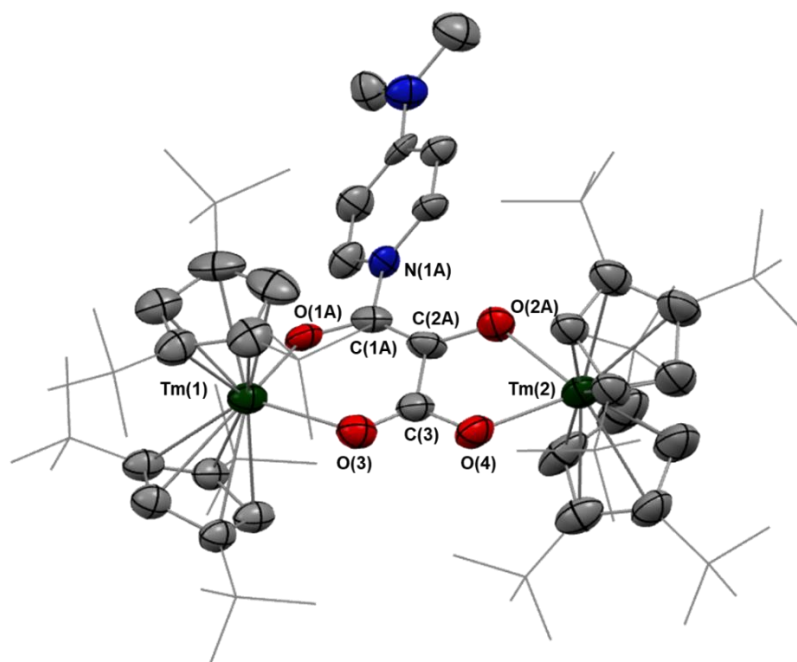
Structure of **1_{DMAP}**

Figure S1. 19 Molecular structure of **1_{DMAP}** in the solid state with thermal ellipsoids at the 50% probability level. Thulium atoms are represented in dark green, carbon atoms in grey, nitrogen and oxygen are in blue and red respectively. H atoms have been omitted for clarity and ^tBu groups are represented in wireframe.

Main distances in Å	
Tm(1) – O(1A)	2.130(15)
Tm(2) – O(2A)	2.17(2)
Tm(1) – O(3)	2.224(4)
Tm(2) – O(4)	2.232(4)
O(1A) – C(1A)	1.320(19)
C(1A) – C(2A)	1.351(19)
C(2A) – C(3)	1.470(12)
C(2A) – O(2A)	1.36(2)
C(3) – O(3)	1.274(7)
C(3) – O(4)	1.278(6)
C(1A) – N(1A)	1.470(14)
Tm(1) – C(Cp ^{tnt})	2.646(7) – 2.819(5)
Tm(2) – C(Cp ^{tnt})	2.649(7) – 2.813(6)
Tm(1) – Cent (Cp ^{tnt})	2.42 / 2.44
Tm(2) – Cent (Cp ^{tnt})	2.43 / 2.43
(Cp ^{tnt}) Cent – Tm(1) – Cent (Cp ^{tnt})	139.8 °
Cent (Cp ^{tnt}) – Tm(2) – Cent (Cp ^{tnt})	140.0 °
Mean Cp ^{tnt} angle	36.9° / 37.0°
O(1A)C(1A)C(2A) plane ^pyr plane	38.2 °

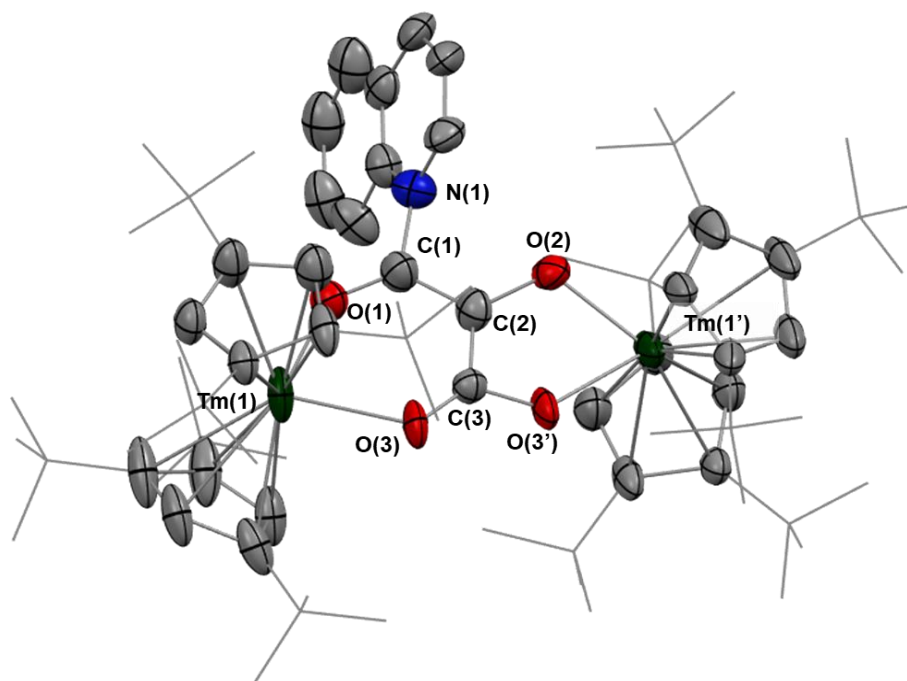
Structure of **1_{quin}**

Figure S1. 20 Molecular structure of **1_{quin}** in the solid state with thermal ellipsoids at the 50% probability level. Thulium atoms are represented in dark green, carbon atoms in grey, nitrogen and oxygen are in blue and red respectively. H atoms have been omitted for clarity and ^tBu groups are represented in wireframe.

Main distances in Å	
Tm(1) – O(1)	2.350(18)
Tm(1') – O(2)	2.071(18)
Tm(1) – O(3)	2.254(6)
O(1) – C(1)	1.25(3)
C(1) – C(2)	1.41(3)
C(2) – C(3)	1.45(3)
C(2) – O(2)	1.44(3)
C(3) – O(3)	1.286(10)
C(1) – N(1)	1.51(3)
Tm(1) – C(Cp ^{ttt})	2.62(1) – 2.81(1)
	2.66(1) – 2.82(1)
Tm(1) – Cent (Cp ^{ttt})	2.43 / 2.44
Cent (Cp ^{ttt}) – Tm(1) – Cent (Cp ^{ttt})	137.8 °
Mean Cp ^{ttt} angle	40.7 °
O(1)C(1)C(2) plane ^ pyr plane	62.4 °

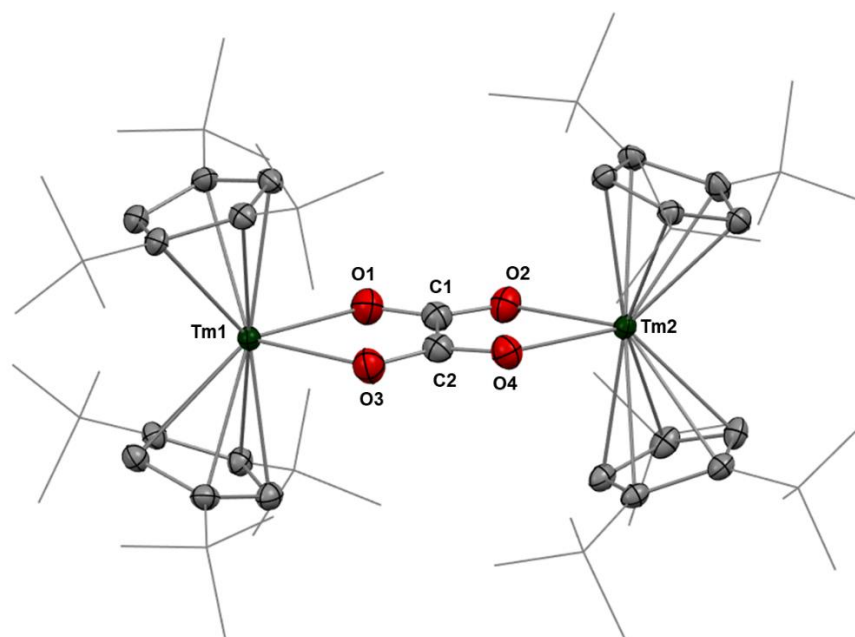
Structure of **1_{ox}**

Figure S1. 21 Molecular structure of **1_{ox}** in the solid state with thermal ellipsoids at the 50% probability level. Thulium atoms are represented in dark green, carbon atoms in grey, and oxygen are in red. H atoms have been omitted for clarity and ^tBu groups are represented in wireframe.

	Main distances in Å
Tm(1) – O(1)	2.303(2)
Tm(2) – O(2)	2.2973(18)
Tm(1) – O(3)	2.2888(19)
Tm(2) – O(4)	2.2898(18)
C(1) – O(1)	1.223(3)
C(1) – O(2)	1.222(3)
C(1) – C(2)	1.525(5)
C(2) – O(3)	1.234(3)
C(2) – O(4)	1.219(4)
Tm(1) – C(Cp ^{ttt})	2.617(2) – 2.718(2)
Tm(2) – C(Cp ^{ttt})	2.621(2) – 2.723(2)
Tm(1) – Cent (Cp ^{ttt})	2.38 / 2.38
Tm(2) – Cent (Cp ^{ttt})	2.38 / 2.38
Cent (Cp ^{ttt}) – Tm(1) – Cent (Cp ^{ttt})	142.7 °
Cent (Cp ^{ttt}) – Tm(2) – Cent (Cp ^{ttt})	143.0 °
Mean Cp ^{ttt} –Cp ^{ttt} angle	36.1 ° / 35.9 °
O(1)C(1)O(2) plane ^ O(3)C(2)O(4) plane	5.3 °

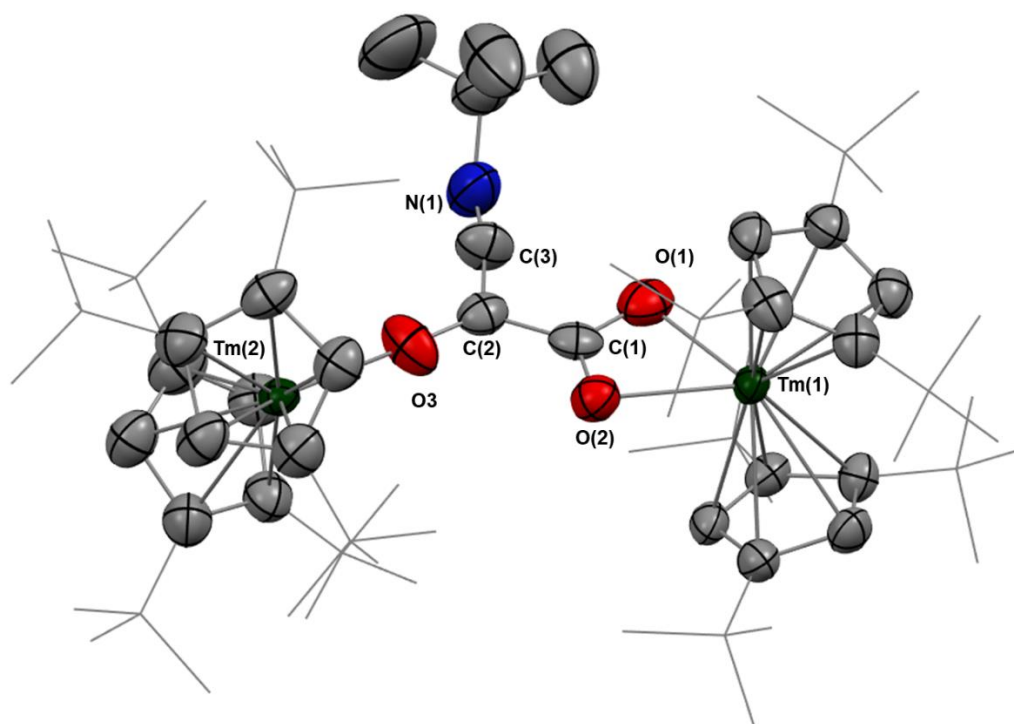
Structure of **1_{iso}**

Figure S1. 22 Molecular structure of **1_{iso}** in the solid state with thermal ellipsoids at the 50% probability level. Thulium atoms are represented in dark green, carbon atoms in grey, nitrogen and oxygen are in blue and red respectively. H atoms have been omitted for clarity and ^tBu groups are represented in wireframe.

Main distances in Å	
Tm(1) – O(1)	2.265(4)
Tm(1) – O(2)	2.331(4)
Tm(2) – O(3)	2.097(4)
C(1) – O(1)	1.381(7)
C(1) – O(2)	1.254(6)
C(1) – C(2)	1.446(8)
C(2) – O(3)	1.284(7)
C(2) – C(3)	1.404(8)
C(3) – N(1)	1.213(8)
Tm(1) – C(Cp ^{ttt})	2.606(6) – 2.781(6)
Tm(2) – C(Cp ^{ttt})	2.596(6) – 2.748(6)
Tm(1) – Cp ^{ttt} (ctr)	2.40 / 2.40
Tm(2) – Cp ^{ttt} (ctr)	2.36/2.39
Cp ^{ttt} (ctr) – Tm(1) – Cp ^{ttt} (ctr)	141.9 °
Cp ^{ttt} (ctr) – Tm(2) – Cp ^{ttt} (ctr)	143.4 °
Mean Cp ^{ttt} angle	36.3° / 43.6°
O(1)C(1)O(2) plane ^ O(3)C(2)C(4) plane	2.8 °

References

- (1) Anatolii A. Fagin, M. N. B. **1999**, *5* (10), 2990–2992.
- (2) Evans, W. J.; Allen, N. T.; Ziller, J. W. *J. Am. Chem. Soc.* **2000**, *122* (47), 11749–11750.
- (3) Reiners, M.; Ehrlich, N.; D. Walter, M. *Inorganic Synthesis*; 2018; Vol. 18, pp 199–204.
- (4) Jaroschik, F.; Nief, F.; Ricard, L. *Chem Commun* **2006**, No. 4, 426–428.
- (5) Lalancette, J.-M.; Rollin, G.; Dumas, P. *Can. J. Chem.* **1972**, *50* (18), 3058–3062.
- (6) Bergbreiter, D. E.; Killough, J. M. *J. Am. Chem. Soc.* **1978**, *100* (7), 2126–2134.
- (7) Simler, T.; McCabe, K. N.; Maron, L.; Nocton, G. *Chem. Sci.* **2022**, *13* (25), 7449–7461.
- (8) Sheldrick, G. M. *Acta Crystallogr. A* **2008**, *64* (1), 112–122.
- (9) Sheldrick, G. M. *Acta Crystallogr. Sect. Found. Adv.* **2015**, *71* (1), 3–8.
- (10) Dolomanov, O. V.; Bourhis, L. J.; Gildea, R. J.; Howard, J. A. K.; Puschmann, H. *OLEX2 : A J. Appl. Crystallogr.* **2009**, *42* (2), 339–341.

Supplementary information for Chapter 2:

I. General information	235
II. Synthetic details	235
III. Hydride investigation through NMR characterization	237
IV. XRD characterization	238
V. Magnetic studies	246
VI. Computation studies	251
References	252

I. General information

All air- and moisture-sensitive reactions were performed using standard Schlenk-line techniques under dry N₂ or Ar atmosphere or in argon-filled gloveboxes (MBraun). All glassware was dried at 140 °C for at least 12 h prior to use. All solvents (Et₂O, toluene, benzene, pentane, C₆D₆, tol-d₈, THF-d₈) were dried over sodium, degassed, and transferred under reduced pressure in a cold flask. Acetonitrile and deuterated acetonitrile were dried over CaH₂, degassed, and transferred under reduced pressure in a cold flask. DyI₂ was prepared from Dy metal and I₂ following the literature procedure.^{1,2} KCnt was prepared according to literature procedure.³ KC₈^{4,5} was prepared following the published procedures. All other chemicals were obtained from commercial sources and used without further purification. ¹H NMR spectra were recorded in 5 mm tubes adapted with a J. Young valve on a Bruker Avance III-300 MHz spectrometer and chemical shifts are expressed relative to internal solvent references in ppm.

II. Synthetic details

Synthesis of 2.1_{thf}

DyI₂ (2 equiv.) and KCnt were weighted into a cold vial. Cold THF was added to the solids and the reaction turned brown quickly. The reaction mixture was allowed to warm up to room temperature overnight while stirring. The volatiles were then removed and toluene was added to the vial. The resulting suspension is filtered and placed at -35 °C. A small amount of XRD suitable crystals were grown over a couple days.

Synthesis of 2.1

Dyl₂ (52.6 mg, 0.12 mmol, 2 equiv.) was added to DyCnt₃ (32.5, 0.06 mmol, 1 equiv.). The reaction was placed at 112 °C and stirred overnight. The resulting mixture was subsequently filtered and concentrated at room temperature and yielded the desired product as brown crystalline needles (1.3 mg, 0.01 mmol, 3 %) suitable for SC-XRD.

Anal. Calcd for C₄₃H₄₄Dy₂ (676.07): C, 58.3, H, 5.01. Found: C, 57.67, H, 4.85. (one toluene molecule present in the crystallographic cell is considered for the calculated values)

Synthesis of 2.3

The synthesis requires material (vials, pipettes, filters) to be cooled at least 15 min at -40 °C before use.

5 drops of cold (-40 °C) THF were added to 100 mg of solid Dyl₂ in a cold vial which was placed back in the freezer immediately. A suspension of KCnt (1 equiv.) in toluene was placed in the freezer. After 15 minutes, the cooled suspension of KCnt was added to the cold green Dyl₂-thf adduct. The supernatant immediately turned brown. The reaction mixture was placed back in the freezer overnight. After about 12 h, the supernatant turned to red-brown and was filtered through a cold micropore filter into another cold vial and let stand at -40 °C. XRD suitable crystals are typically obtained after a several days at -40 °C. Only a few crystals were obtained for each crystallization. Multiple crystals were chosen and investigated through SC-XRD to make sure only one product was present.

The compound remained silent in NMR. Because of the thermal sensitivity of the crystals, no elemental analysis was performed.

Synthesis of 2.4

5 drops of cold (-40 °C) THF were added to 100 mg of solid NdI₂ in a cold vial which was placed back in the freezer immediately. A suspension of KCnt (1 equiv.) in toluene was placed in the freezer. After 15 minutes, the cooled suspension of KCnt was added to the cold purple NdI₂-thf adduct. The supernatant immediately turned black. The reaction mixture was placed back in the freezer overnight. After about 12 h, the black supernatant was filtered through a cold micropore filter into another cold vial and let stand at -40 °C. Small black needles are typically obtained after a several days at -40 °C. Only a few crystals were obtained for each crystallization, none of them allowed for high resolution structural information. No other characterizations were performed.

III. Hydride investigation through NMR characterization

Addition of CCl_4 in a toluene suspension of **2.3**

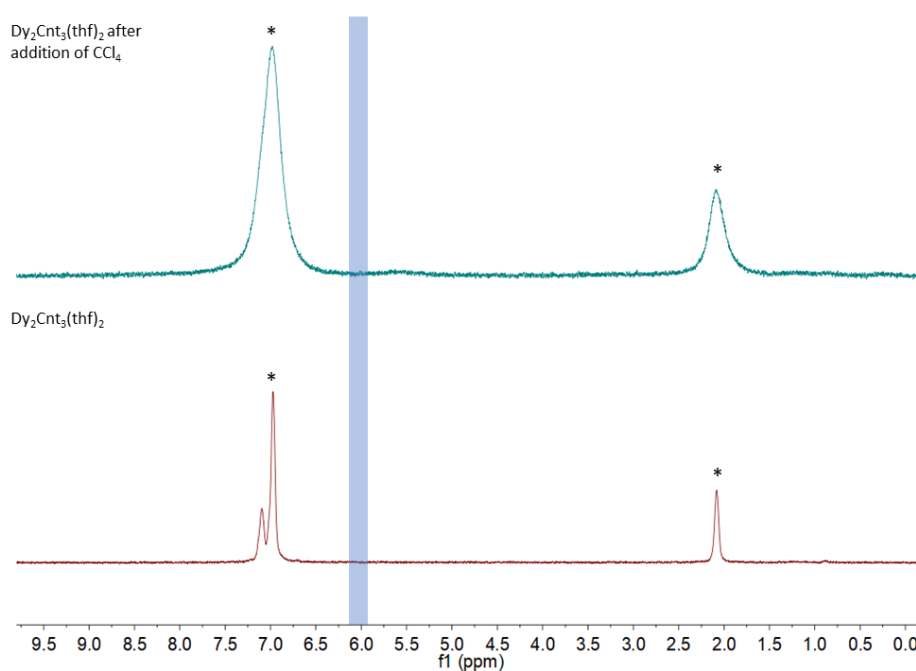


Figure S2. 1 ^1H NMR of **2.3** in toluene- d_8 measured at 293 K (* residual protio signal of the solvent). Only the diamagnetic part of the spectra is shown. Potential CHCl_3 formation would result in a signal in the transparent blue square.

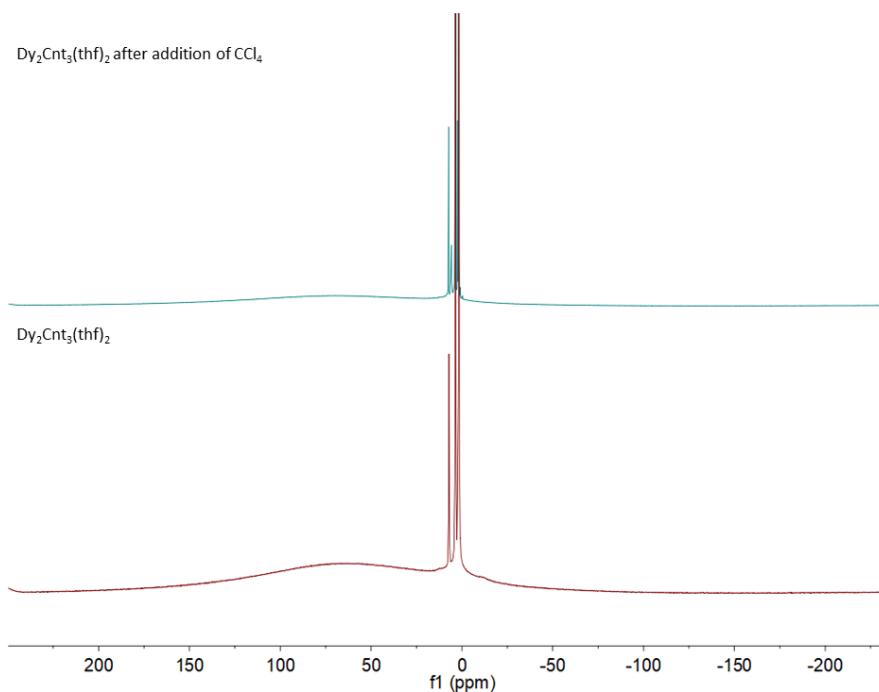


Figure S2. 2 ^1H NMR of **2.3** in toluene- d_8 measured at 293 K. No paramagnetic signals have been identified in either of those spectra.

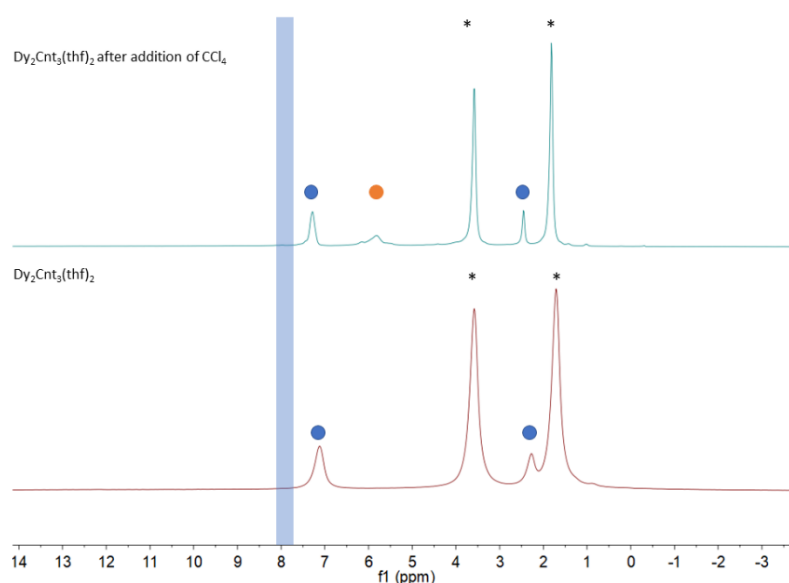
Addition of CCl_4 in a thf suspension of 2.3

Figure S2.3 ^1H NMR of 2.3 in thf-d_8 measured at 293 K (* residual protio signal of the solvent). Blue dots show the presence of residual toluene from the reaction, and orange dot indicate the formation of degradation product upon addition of CCl_4 . Potential CHCl_3 formation would result in a signal in the transparent blue square.

IV. XRD characterization

1. General methods

Single crystals of the complexes suitable for X-ray analysis were mounted on a Kapton loop using a Paratone N oil. Two diffractometers were used during this work for the data acquisition, either a Bruker diffractometer equipped with an APEX II CCD detector and a graphite $\text{Mo-K}\alpha$ monochromator or a Stoe stadivari diffractometer with a Eiger2 detector and a $\text{Mo-K}\alpha$ microsource. All measurements were done at 150 K and a refinement method was used for solving the structure. The resolution of the solid-state structure was accomplished using the SHELXS-97 or SHELXT programs.^{6,7} The refinement was performed with the SHELXL program using the Olex2 software.^{7,8} All atoms – except hydrogens – were refined anisotropically.

Specific treatment for 2.3

Residual electronic density corresponding to a toluene molecule was observed, however its modelling was complicated by severe disorder. As such a solvent mask has been applied on the toluene molecule which had an occupation of one. Additionally, the hydrogen present on the bridging Cnt unit were found in the residual density map directly.

2. Summary of crystals data

Compound	2.1 _{THF}	2.1	2.2
Formula	C ₆₅ H ₇₆ Dy ₂ O ₂	C ₄₃ H ₄₄ Dy ₂	C ₁₈ H ₁₆ Dy
Crystal size (mm ³)	0.2 × 0.12 × 0.06	0.12 × 0.08 × 0.06	0.9 × 0.8 × 0.2
Crystal system	Monoclinic	Monoclinic	Monoclinic
Space group	P2 ₁ /c	P2 ₁ /n	P2 ₁ /c
Volume (Å ³)	2742.6(10)	1704.8(2)	1371.1(3)
a (Å)	13.693(3)	7.1726(6)	9.7500(11)
b (Å)	14.587(3)	9.2440(8)	11.2350(14)
c (Å)	13.977(3)	25.715(2)	12.9651(17)
α (deg)	90	90	90
β (deg)	100.767(6)	90.907(3)	105.113(4)
γ (deg)	90	90	90
Z	2	2	4
Formula weight (g/mol)	1214.25	885.78	394.81
Density (calcd) (g/cm ³)	1.470	1.726	1.913
Absorption coefficient (mm ⁻¹)	2.746	4.379	5.431
F(000)	1228.0	868.0	760.0
Temp (K)	150.15	150	150.0
Diffractometer	Bruker APEX II CCD	Bruker APEX II CCD	Bruker APEX II CCD
Radiation	MoKα (λ = 0.71073)	MoKα (λ = 0.71073)	MoKα (λ = 0.71073)
2θ range for data collection (deg)	4.074 to 51.358	5.872 to 55.048	4.328 to 60.178
Absorption correction	Multi-scan	Multi-scan	Multi-scan
Total no. reflections	63029	28364	56028
Unique reflections [R _{int}]	5202 [R _{int} = 0.1387]	3892 [R _{int} = 0.0649]	4025 [R _{int} = 0.1173]
Final R indices [I > 2σ(I)]	R1 = 0.0796, wR2 = 0.2056	R1 = 0.0558, wR2 = 0.1369	R1 = 0.0364, wR2 = 0.0792
R indices (all data)	R1 = 0.1253, wR2 = 0.2486	R1 = 0.0640, wR2 = 0.1403	R1 = 0.0641, wR2 = 0.0901
Largest diff. peak and hole (e.Å ⁻³)	3.3°/-2.68	2.13/-2.65	1.61/-1.29
Goof	1.201	1.177	1.029

Compound	2.3	2.4
Formula	C _{38.5} H ₄₈ Dy ₂ O ₂	C ₃₃ I ₂ Nd ₂ O ₂
Crystal size (mm ³)	0.26 × 0.02 × 0.01	0.21 × 0.02 × 0.02
Crystal system	Monoclinic	Trigonal
Space group	P2 ₁ /n	R-3
Volume (Å ³)	3365.1(11)	19469(16)
a (Å)	8.4865(17)	47.337(18)
b (Å)	13.092(3)	47.337(18)
c (Å)	30.381(6)	10.032(4)
α (deg)	90	90
β (deg)	94.523(5)	90
γ (deg)	90	120
Z	4	18
Formula weight (g/mol)	867.77	970.61
Density (calcd) (g/cm ³)	1.713	1.490
Absorption coefficient (mm ⁻¹)	4.438	3.819
F(000)	1708.0	7920.0
Temp (K)	150	150.0
Diffractometer	Bruker APEX II CCD	Bruker APEX II CCD
Radiation	MoKα (λ = 0.71073)	MoKα (λ = 0.71073)
2θ range for data collection (deg)	5.1 to 50.054	4.52 to 46.51
Absorption correction	Multi-scan	Multi-scan
Total no. reflections	36338	89158
Unique reflections [R _{int}]	5935 [R _{int} = 0.1215]	6173 [R _{int} = 0.2485]
Final R indices [I > 2σ(I)]	R ₁ = 0.0471, wR ₂ = 0.1023	R1 = 0.0625, wR2 = 0.1294
R indices (all data)	R ₁ = 0.0779, wR ₂ = 0.1146	R1 = 0.1102, wR2 = 0.1446
Largest diff. peak and hole (e.Å ⁻³)	0.81/-1.20	1.02/-0.96
Goof	1.007	1.032

3. Crystal structures

Structure of **2.1_{THF}**

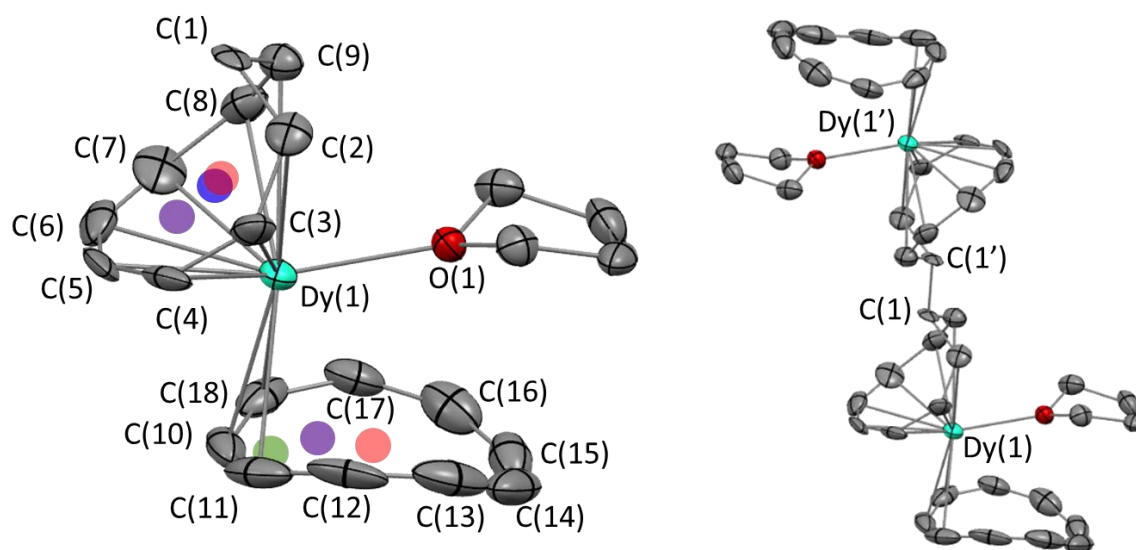


Figure S2. 4 Molecular structure of **2.1_{THF}**, ellipsoid are represented at 50% probability level. On the left is represented the asymmetric unit and, on the right, the entire complex by application of the space group's symmetry. In both, dysprosium atoms are in light green, carbon atoms in grey and oxygen in red. H atoms have been removed for clarity and as well as two disordered solvent molecules. additionally, centroids were constructed: red, blue, purple and green corresponds respectively to η^9 , η^8 , η^6 , and η^4 hapticity for the Cnt ligand or similar Cnt_2^{4-} moiety.

Main distances in Å	
Dy(1)—C(1)	3.30(1)
Dy(1)—C(2)	2.851(13)
Dy(1)—C(3)	2.508(15)
Dy(1)—C(4)	2.486(18)
Dy(1)—C(5)	2.559(15)
Dy(1)—C(6)	2.566(14)
Dy(1)—C(7)	2.486(18)
Dy(1)—C(8)	2.584(13)
Dy(1)—C(9)	2.873(13)
Dy(1)—Cent (Cnt- η^6)	1.74
Dy(1)—Cent (Cnt- η^8)	1.73
Dy(1)—Cent (Cnt- η^9)	1.88
Dy(1)—C(10)	2.648(14)
Dy(1)—C(11)	2.693(15)
Dy(1)—C(12)	2.99(2)
Dy(1)—C(13)	3.65(2)
Dy(1)—C(14)	4.32(2)
Dy(1)—C(15)	4.41(2)

Dy(1)—C(16)	3.99(2)
Dy(1)—C(17)	3.27(2)
Dy(1)—C(18)	2.763(14)
Dy(1)—Cent (Cnt- η^4)	2.40
Dy(1)—Cent (Cnt- η^6)	2.42
Dy(1)—Cent (Cnt- η^9)	2.84
Dy(1)—O(1)	2.354(8)
C(1)—C(1')	1.58(2)

Structure of 2.1

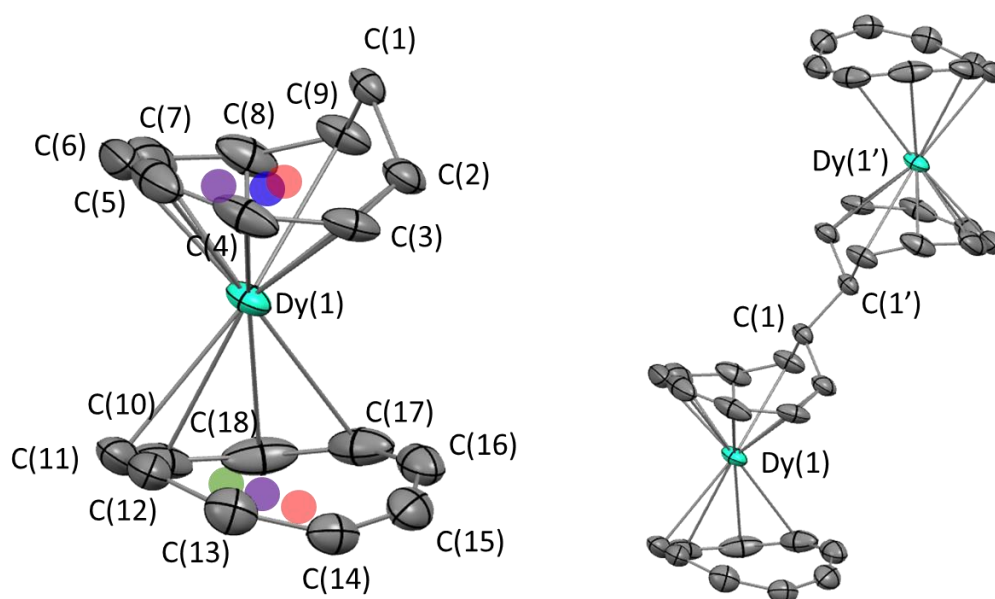


Figure S2. 5 Molecular structure of **2.1**, ellipsoids are represented at 50% probability level. On the left is represented the asymmetric unit and, on the right, the entire complex by application of the space group's symmetry. In both, dysprosium atoms are in light green and carbon atoms in grey. H atoms have been removed for clarity and as well as a disordered solvent molecule. Additionally, centroids were constructed: red, blue, purple and green corresponds respectively to η^9 , η^8 , η^6 , and η^4 hapticity for the Cnt ligand or similar Cnt_2^{4-} moiety.

Main distances in Å	
Dy(1)—C(1)	3.168(8)
Dy(1)—C(2)	2.734(8)
Dy(1)—C(3)	2.524(9)
Dy(1)—C(4)	2.493(10)
Dy(1)—C(5)	2.510(10)
Dy(1)—C(6)	2.496(12)
Dy(1)—C(7)	2.453(12)
Dy(1)—C(8)	2.526(10)
Dy(1)—C(9)	2.752(8)

Dy(1)—Cent (Cnt- η^6)	1.78
Dy(1)—Cent (Cnt- η^8)	1.65
Dy(1)—Cent (Cnt- η^9)	1.68
Dy(1)—C(10)	2.641(9)
Dy(1)—C(11)	2.662(9)
Dy(1)—C(12)	2.99(1)
Dy(1)—C(13)	3.56(1)
Dy(1)—C(14)	3.86(1)
Dy(1)—C(15)	3.66(1)
Dy(1)—C(16)	3.12(1)
Dy(1)—C(17)	2.718(10)
Dy(1)—C(18)	2.654(10)
Dy(1)—Cent (Cnt- η^4)	2.27
Dy(1)—Cent (Cnt- η^6)	2.13
Dy(1)—Cent (Cnt- η^9)	2.39
C(1)—C(1')	1.532(15)

Structure of 2.2

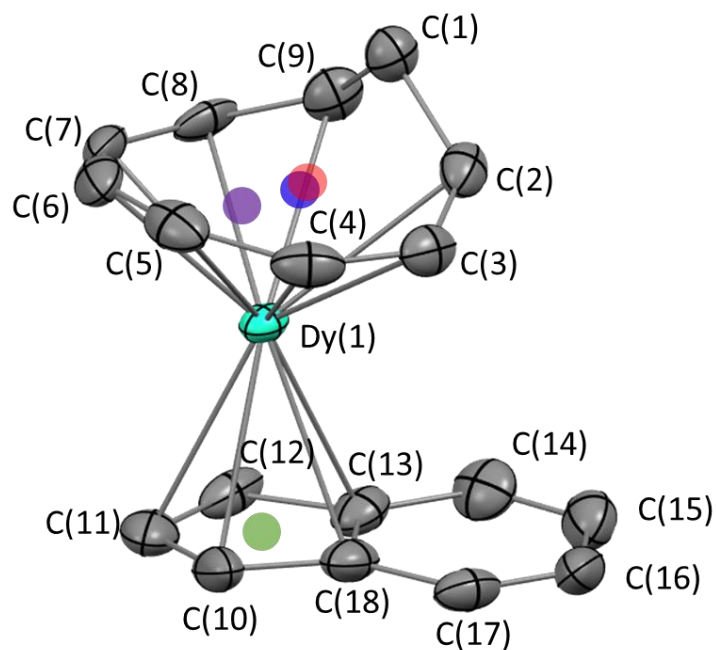


Figure S2. 6 Molecular structure of **2.2**, ellipsoids are represented at 50% probability level. Dysprosium atoms are in light green and carbon atoms in grey. H atoms have been removed for clarity. Additionally, centroids were constructed: red, blue, purple and green corresponds respectively to η^9 , η^8 , η^6 , and η^4 hapticity for the Cnt ligand or indenyl moiety.

Main distances in Å	
Dy(1)—C(1)	3.111(6)
Dy(1)—C(2)	2.707(5)
Dy(1)—C(3)	2.530(5)
Dy(1)—C(4)	2.496(6)
Dy(1)—C(5)	2.511(5)
Dy(1)—C(6)	2.505(5)
Dy(1)—C(7)	2.489(5)
Dy(1)—C(8)	2.529(5)
Dy(1)—C(9)	2.702(5)
Dy(1)—Cent (Cnt- η^6)	1.67
Dy(1)—Cent (Cnt- η^8)	1.62
Dy(1)—Cent (Cnt- η^9)	1.74
Dy(1)—C(10)	2.622(5)
Dy(1)—C(11)	2.639(6)
Dy(1)—C(12)	2.633(5)
Dy(1)—C(13)	2.634(5)
Dy(1)—C(18)	2.631(5)
Dy(1)—Cent (Ind- η^5)	2.34

Structure of 2.3

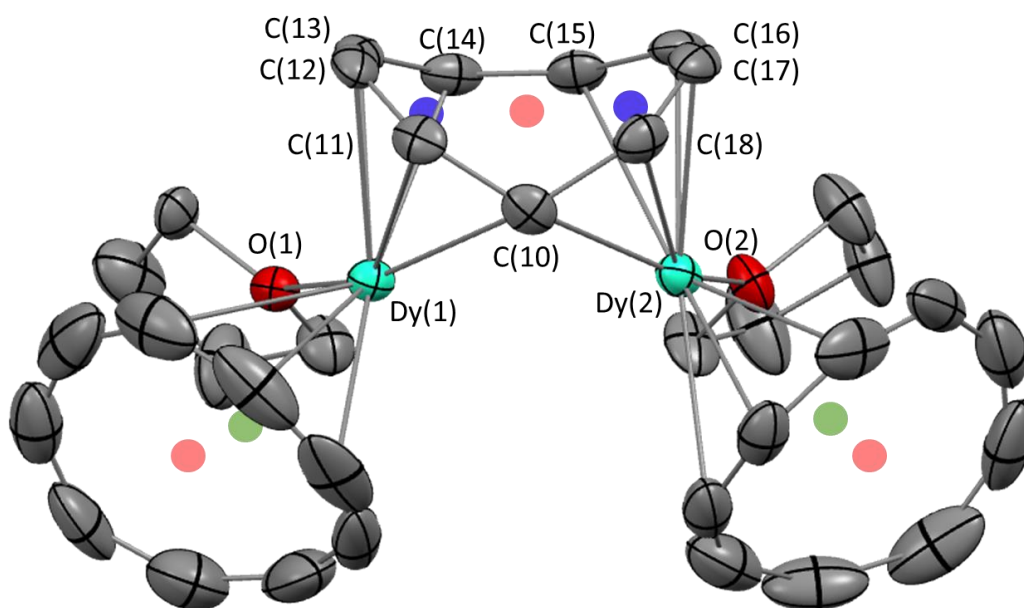


Figure S2. 7 Molecular structure of 2.3, ellipsoids are represented at 50% probability level. Dysprosium atoms are in light green, carbon atoms in grey and oxygen in red. H atoms have been removed for clarity and as well as one disordered solvent molecule. Additionally, centroids were constructed: red, blue and green corresponds respectively to η^9 , η^8 and η^6 hapticity for the Cnt ligand.

Main distances in Å	Dy(1)	Dy(2)
Dy(X)—C(10)	2.456(9)	2.498(10)
Dy(X)—C(11)	2.501(8)	3.842(9)
Dy(X)—C(12)	2.587(9)	4.45(1)
Dy(X)—C(13)	2.545(8)	4.34(1)
Dy(X)—C(14)	2.797(9)	3.56(1)
Dy(X)—C(15)	3.544(9)	2.806(9)
Dy(X)—C(16)	4.31(1)	2.553(8)
Dy(X)—C(17)	4.42(1)	2.583(9)
Dy(X)—C(18)	3.184(9)	2.490(10)
Dy(X)—Cent (Cnt- η^5)	2.06	2.07
Dy(X)—Cent (Cnt- η^9) bridge	2.68	2.70
Dy(X)—Cent (Cnt- η^9) ext	2.82	2.83
Dy(X)—Cent (Cnt- η^4)	2.40	2.40

Structure of 2.4

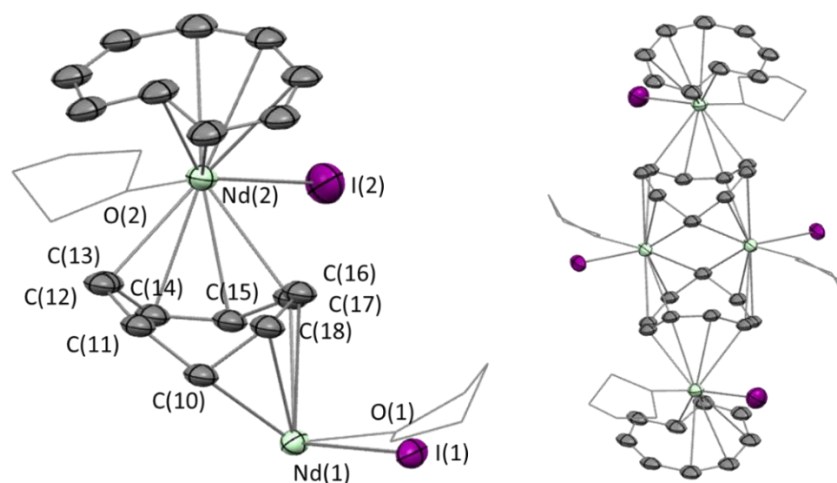


Figure S2. 8 Molecular structure of 2.4, ellipsoids are represented at 50% probability level. on the left is represented the asymmetric unit and, on the right, the entire complex by application of the space group's symmetry. In both, neodymium atoms are in light green, carbon atoms in grey and iodine in purple. H atoms have been removed for clarity and as well as one disordered solvent molecule. THF molecules are represented in wireframe. Additionally, one solvent molecule was modelled through the use of a solvent mask.

Due to the low quality of the data, only the main distances between the heavy atom are reported.

Main distances in Å	
Nd(1)—Nd(1')	3.6628(18)
Nd(1)—I(1)	3.1591(15)
Nd(2)—I(2)	3.256(2)

V. Magnetic studies

1. General considerations

Magnetic measurements were obtained in a Quantum Design MPMS-XL SQUID magnetometer. An applied magnetic field of 2 kOe is used in the temperature range 2-20 K, and 10 kOe for temperatures above 20 K, for the $\chi_M T$ vs. T curves. To avoid reorientation and sample degradation the microcrystals are trapped and slightly pressed between quartz wool and sealed in quartz tubes.

The samples were prepared at LCM laboratory and the magnetic data acquisitions were performed in collaboration with Léo La droite and Dr. Olivier Cador. Initial treatment of the data was performed by the other team. Representation of the corrected data set was performed at LCM.

2. Magnetic susceptibility

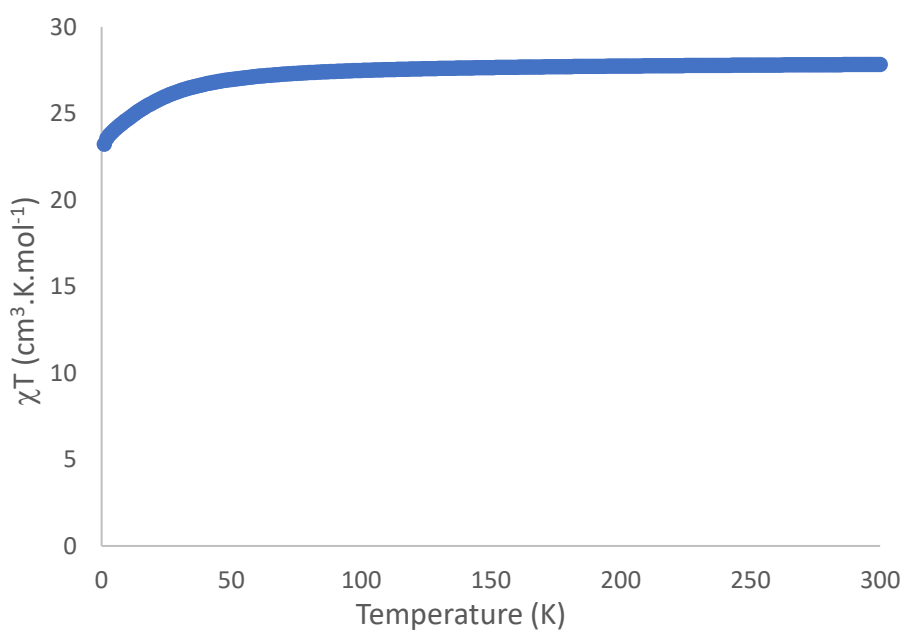


Figure S2. 9 Static χT curves of 2.1

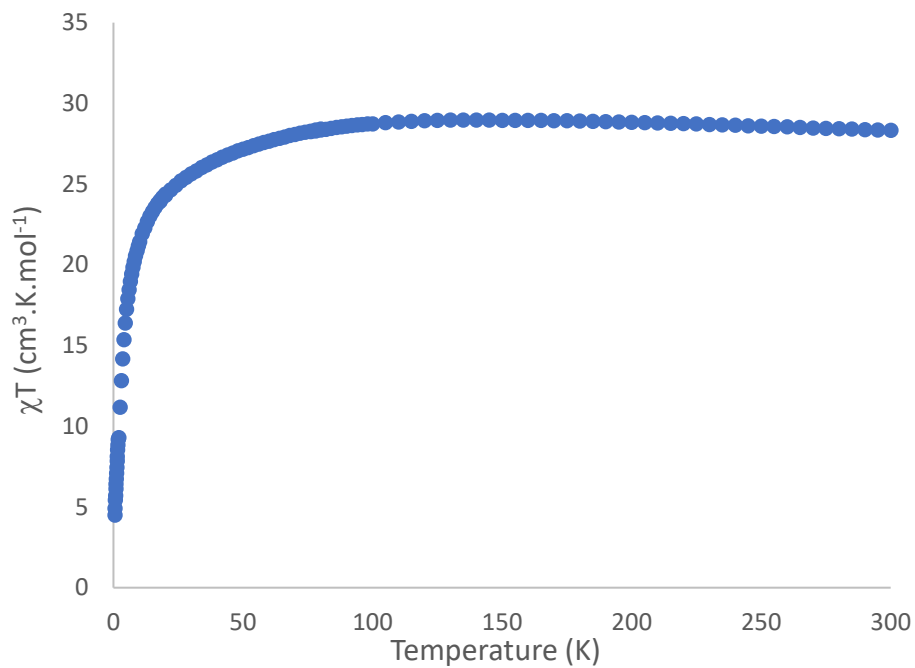


Figure S2.10 Static χT curves of 2.3

3. Magnetization experiments

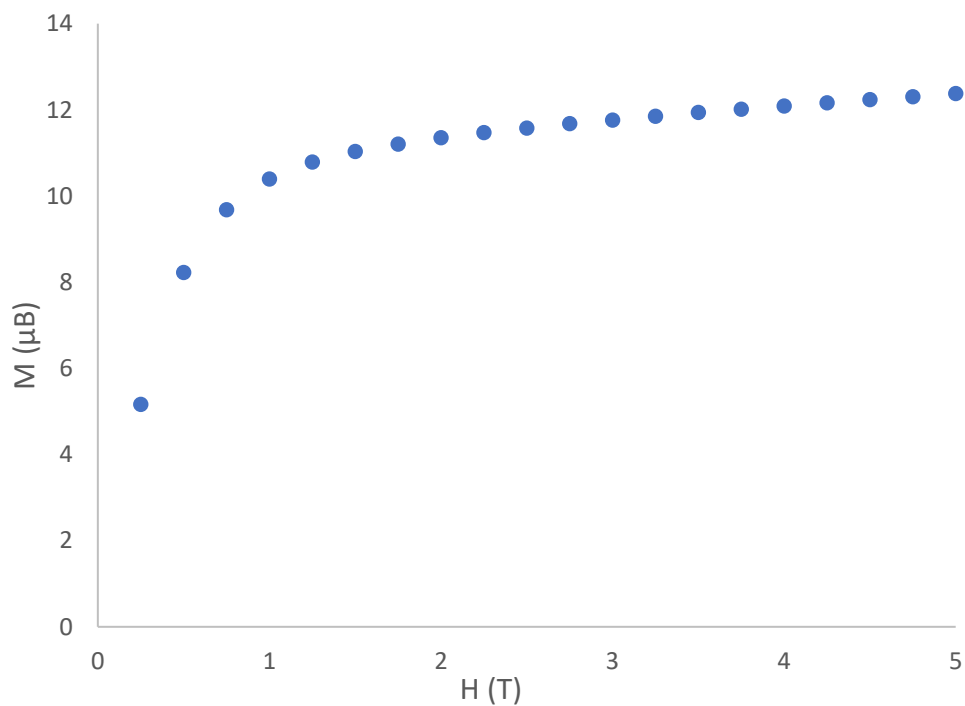


Figure S2.11 Magnetization curve of 2.1 at 2 K

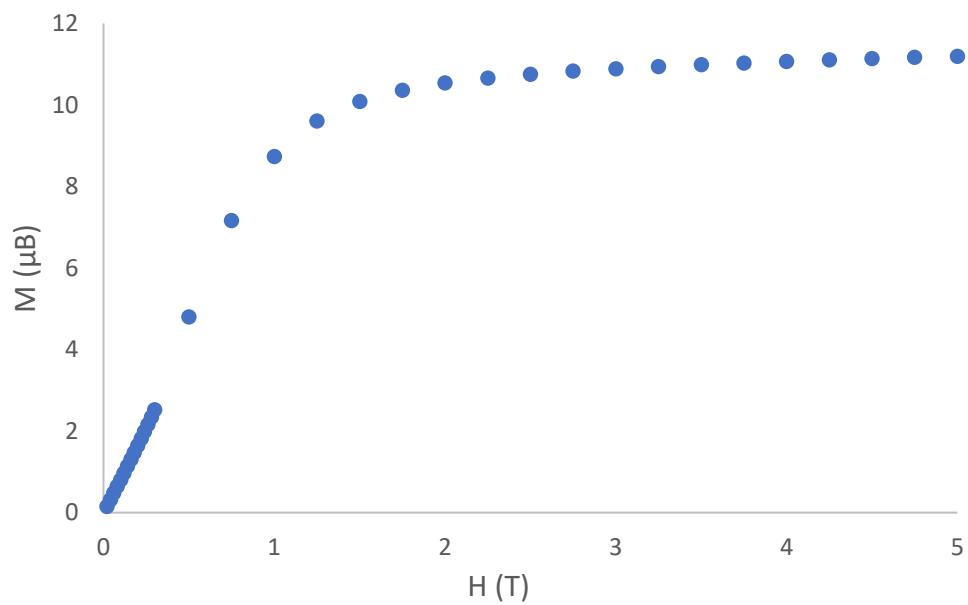


Figure S2. 12 Magnetization curve of 2.3 at 2 K.

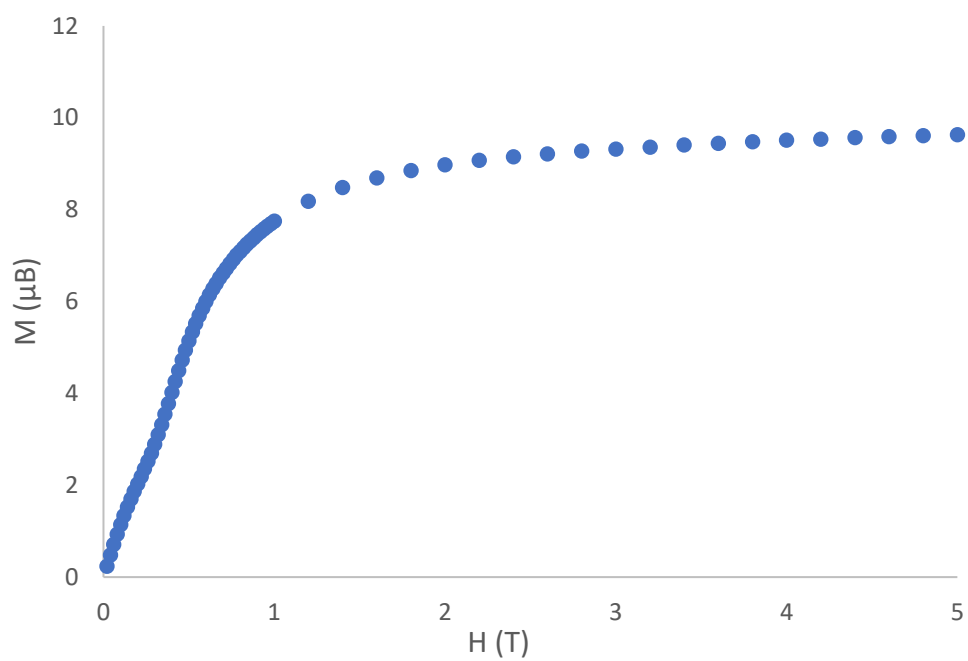


Figure S2. 13 Magnetization curve of 2.3 at 0.5 K.

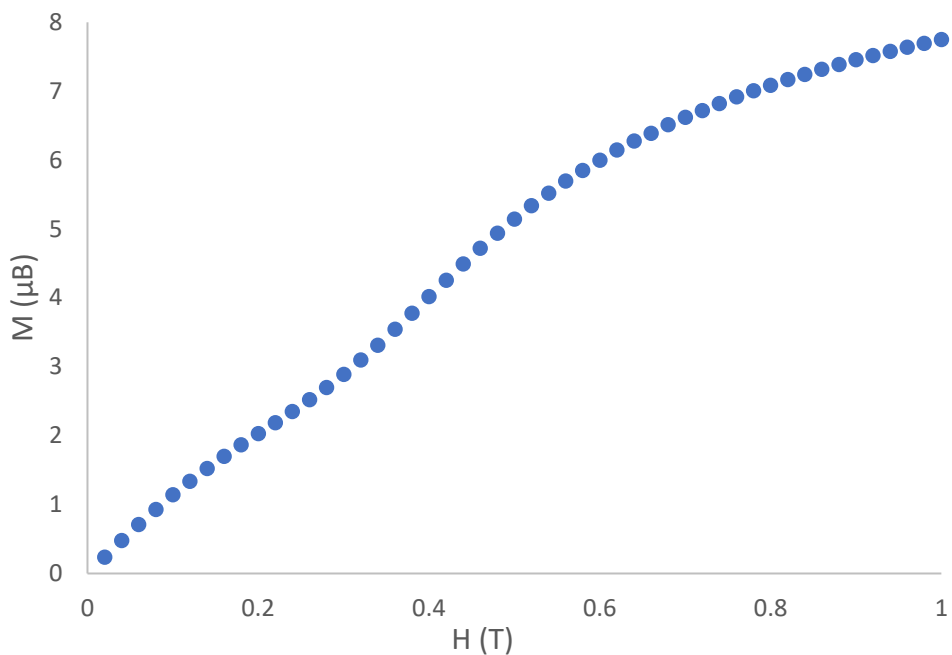


Figure S2. 14 Magnetization curve of 2.3 at 0.5 K, zoomed in to highlight the inflexion of the curve.

4. AC measurements

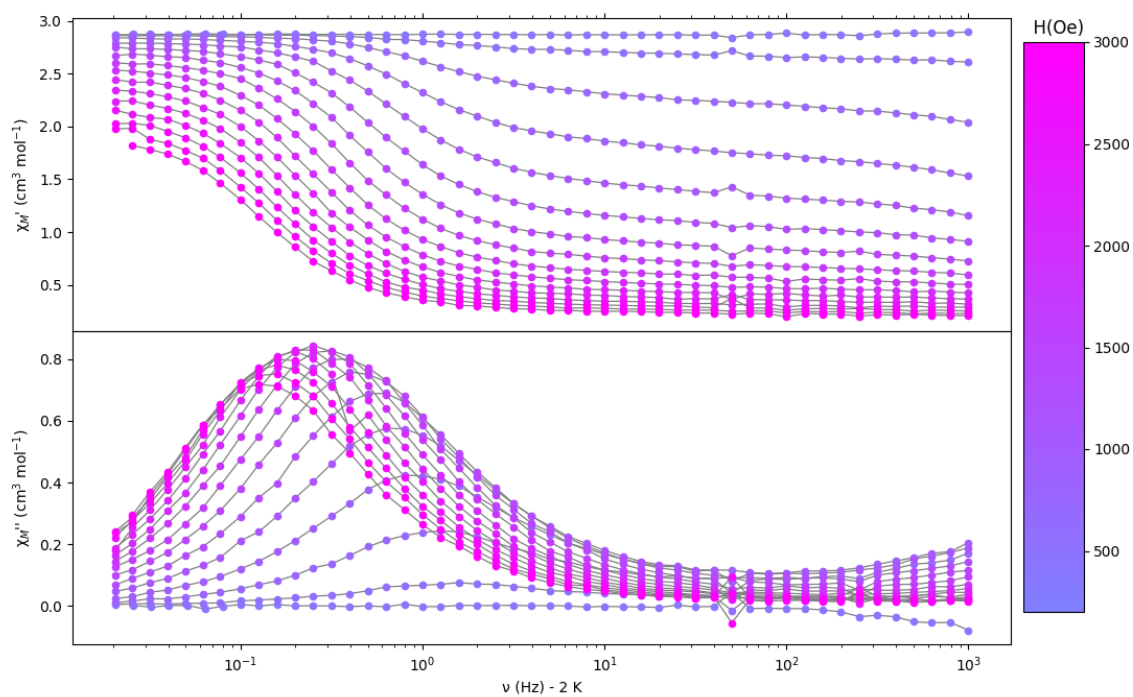


Figure S2. 15 Frequency dependences of both the in-phase, χ_M' and out-of-phase, χ_M'' components of the ac susceptibility of 2.1 at various external dc field at 2 K.

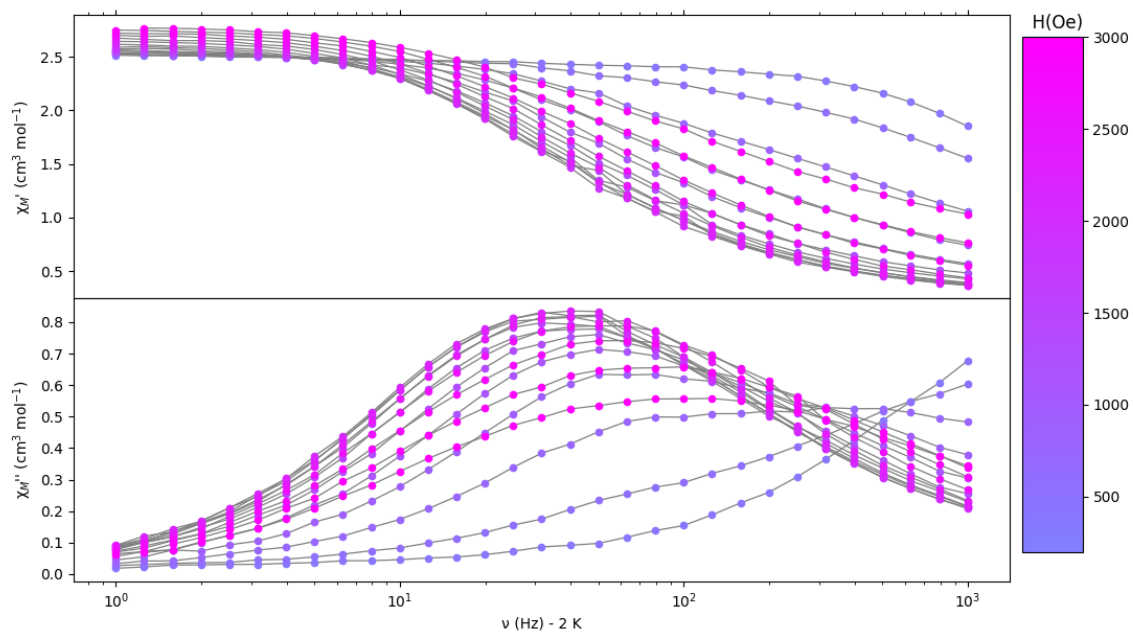


Figure S2. 16 Frequency dependences of both the in-phase, χ_M' and out-of-phase, χ_M'' components of the ac susceptibility of 2.3 at various external dc field at 2 K.

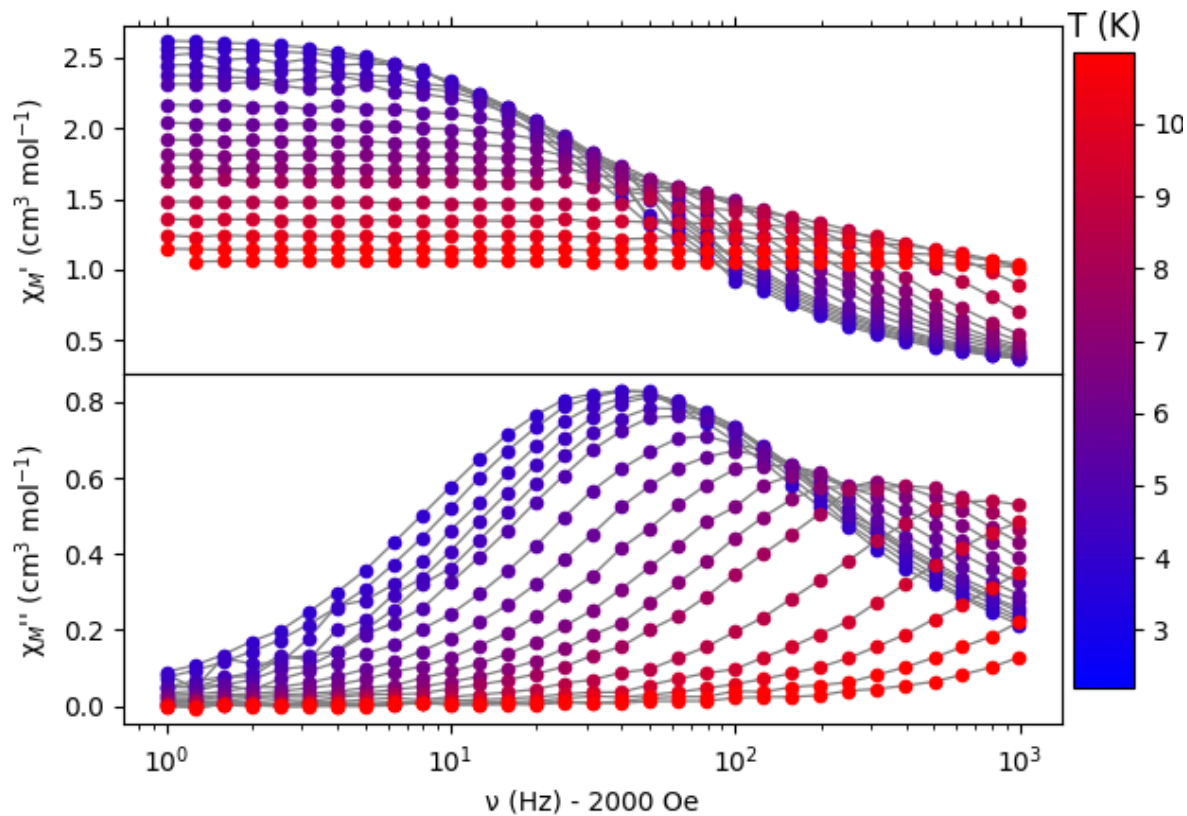


Figure S2. 17 Frequency dependences of both the in-phase, χ_M' and out-of-phase, χ_M'' components of the ac susceptibility of 2.3 at various temperature at 2000 Oe.

5. Hysteresis recording

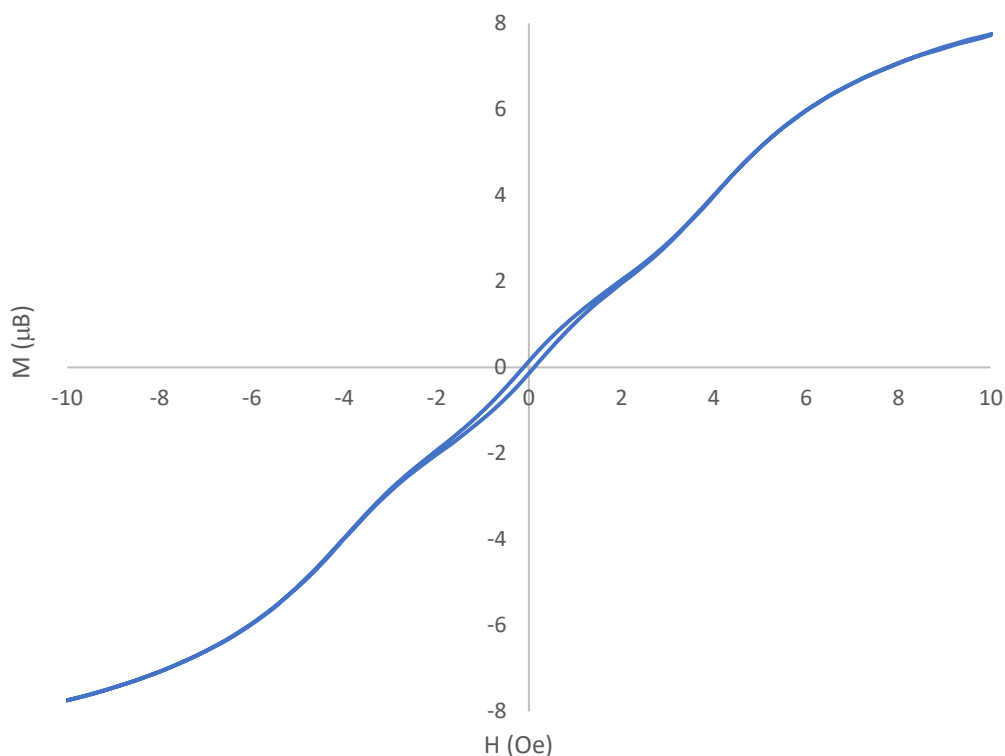


Figure S2. 18 Hysteresis curve for 2.3 at 0.5 K.

VI. Computation studies

Computations were performed in collaboration with Léo La Droitte et Dr. Boris Le Guennic, the necessary information were presented in the manuscript. The general details of the computations are presented below.

The atomic positions were extracted from the X-ray diffraction crystal structures. Structure optimizations were performed using density functional theory (DFT) as implemented in the 2017 release of the Amsterdam Density Functional (ADF) package.^{9–11} The exchange-correlation was treated within the generalized gradient approximation (GGA) using the revPBE functional.^{12–14} The scalar relativistic (SR) effects were treated within the zeroth-order regular approximation (ZORA). All atoms were described using triple- ζ polarized all-electron Slater type basis (TZP). During the geometry optimization, only H positions are allowed to relax while all other positions are kept frozen

All wave function-based calculations were performed using the State-Averaged Complete Active Space Self-Consistent Field approach with Restricted-Active-Space-State-Interaction method (SA-CASSCF/RASSI-SO), as implemented in the OpenMolcas quantum-chemistry package.¹⁵ In this approach, the relativistic effects are treated in two steps on the basis of the

Douglas–Kroll Hamiltonian.¹⁶ The scalar terms are included in the basis-set generation and are used to determine the CASSCF wave functions and energies.¹⁷ Spin-orbit coupling is then added within the RASSI-SO method, which mixes the calculated CASSCF wave functions.^{18,19} Spin-orbit (SO) integrals are calculated using the AMFI (atomic mean-field integrals) approximation.²⁰ The resulting spin-orbit wave functions and energies are used to compute the magnetic properties and g-tensors of the ground state multiplet following the pseudospin $S = 1/2$ formalism, as implemented in the SINGLE_ANISO routine.²¹ Cholesky decomposition of the bielectronic integrals was employed to save disk space and to speed up the calculations.²²

References

- (1) Anatolii A. Fagin, M. N. B. **1999**, *5* (10), 2990–2992.
- (2) Evans, W. J.; Allen, N. T.; Ziller, J. W. *J. Am. Chem. Soc.* **2000**, *122* (47), 11749–11750.
- (3) Xémard, M.; Zimmer, S.; Cordier, M.; Goudy, V.; Ricard, L.; Clavaguéra, C.; Nocton, G. *J. Am. Chem. Soc.* **2018**, *140* (43), 14433–14439.
- (4) Lalancette, J.-M.; Rollin, G.; Dumas, P. *Can. J. Chem.* **1972**, *50* (18), 3058–3062.
- (5) Bergbreiter, D. E.; Killough, J. M. *J. Am. Chem. Soc.* **1978**, *100* (7), 2126–2134.
- (6) Sheldrick, G. M. *Acta Crystallogr. A* **2008**, *64* (1), 112–122.
- (7) Sheldrick, G. M. *Acta Crystallogr. Sect. Found. Adv.* **2015**, *71* (1), 3–8.
- (8) Dolomanov, O. V.; Bourhis, L. J.; Gildea, R. J.; Howard, J. A. K.; Puschmann, H. *OLEX2 : A J. Appl. Crystallogr.* **2009**, *42* (2), 339–341.
- (9) Te Velde, G.; Bickelhaupt, F. M.; Baerends, E. J.; Fonseca Guerra, C.; Van Gisbergen, S. J. A.; Snijders, J. G.; Ziegler, T. *J. Comput. Chem.* **2001**, *22* (9), 931–967.
- (10) Fonseca Guerra, C.; Snijders, J. G.; Te Velde, G.; Baerends, E. J. *Theor. Chim. Acta* **1998**, *99* (6), 391–403.
- (11) SCM, A. Theoretical Chemistry, 2017. <http://www.scm.com>.
- (12) Perdew, J. P.; Burke, K.; Ernzerhof, M. *Phys. Rev. Lett.* **1996**, *77* (18), 3865–3868.
- (13) Ernzerhof, M.; Scuseria, G. E. *J. Chem. Phys.* **1999**, *110*, 5029.
- (14) Lenthe, E. V.; Baerends, E. J. *J. Chem. Phys.* **1993**, *99*, 4597.
- (15) Fdez. Galván, I.; Vacher, M.; Alavi, A.; Angeli, C.; Aquilante, F.; Autschbach, J.; Bao, J. J.; Bokarev, S. I.; Bogdanov, N. A.; Carlson, R. K.; Chibotaru, L. F.; Creutzberg, J.; Dattani, N.; Delcey, M. G.; Dong, S. S.; Dreuw, A.; Freitag, L.; Frutos, L. M.; Gagliardi, L.; Gendron, F.; Giussani, A.; González, L.; Grell, G.; Guo, M.; Hoyer, C. E.; Johansson, M.; Keller, S.; Knecht, S.; Kovačević, G.; Källman, E.; Li Manni, G.; Lundberg, M.; Ma, Y.; Mai, S.; Malhado, J. P.; Malmqvist, P. Å.; Marquetand, P.; Mewes, S. A.; Norell, J.; Olivucci, M.; Oppel, M.; Phung, Q. M.; Pierloot, K.; Plasser, F.; Reiher, M.; Sand, A. M.; Schapiro, I.; Sharma, P.; Stein, C. J.; Sørensen, L. K.; Truhlar, D. G.; Ugandi, M.; Ungur, L.; Valentini, A.; Vancoillie, S.; Veryazov, V.; Weser, O.; Wesolowski, T. A.; Widmark, P.-O.; Wouters, S.; Zech, A.; Zobel, J. P.; Lindh, R. OpenMolcas: From Source Code to Insight. *J. Chem. Theory Comput.* **2019**, *15* (11), 5925–5964.
- (16) Hess, B. *Phys. Rev. A* **1986**, *33* (6), 3742–3748.
- (17) Roos, B. O.; Taylor, P. R.; Sigbahn, P. E. M. *AChem. Phys.* **1980**, *48* (2), 157–173.
- (18) Malmqvist, P. Å.; Roos, B. O.; Schimmelpfennig, B. *Chem. Phys. Lett.* **2002**, *357* (3–4), 230–240.
- (19) Malmqvist, P.-Å.; Roos, B. O. *Chem. Phys. Lett.* **1989**, *155* (2), 189–194.
- (20) Heß, B. A.; Marian, C. M.; Wahlgren, U.; Gropen, O. *Chem. Phys. Lett.* **1996**, *251* (5–6), 365–371.
- (21) Chibotaru, L. F.; Ungur, L. *J. Chem. Phys.* **2012**, *137* (6), 064112.
- (22) Ungur, L.; Van Den Heuvel, W.; Chibotaru, L. F. *New J. Chem.* **2009**, *33* (6), 1224.

Supplementary information for Chapter 3 :

I. General information	253
II. Synthetic details	254
III. NMR characterization	257
IV. XRD characterization	258
V. Magnetic studies	272
VI. UV-visible spectroscopy	275
VII. Computation studies	277
References	278

I. General information

All air- and moisture-sensitive reactions were performed using standard Schlenk-line techniques under dry N₂ or Ar atmosphere or in argon-filled gloveboxes (MBraun). All glassware was dried at 140 °C for at least 12 h prior to use. All solvents (Et₂O, toluene, benzene, pentane, C₆D₆, tol-d₈, THF-d₈) were dried over sodium, degassed, and transferred under reduced pressure in a cold flask. Acetonitrile and deuterated acetonitrile were dried over CaH₂, degassed, and transferred under reduced pressure in a cold flask. DyI₂ was prepared from Dy metal and I₂ following the literature procedure.^{1,2} KCp^{ttt} was prepared by deprotonation of HCp^{ttt} with KN(SiMe₃)₂ in Et₂O. HCp^{ttt}, KCnt and KC₈ were prepared according to literature procedures.³⁻⁵ All other chemicals were obtained from commercial sources and used without further purification. ¹H NMR spectra were recorded in 5 mm tubes adapted with a J. Young valve on a Bruker Avance III-300 MHz spectrometer and chemical shifts are expressed relative to internal solvent references in ppm. UV-visible absorption spectra were recorded on a Cary60 spectrometer in quartz cuvettes adapted with a J. Young valve. Elemental analyses were obtained from Mikroanalytisches Labor Pascher (Remagen, Germany).

II. Synthetic details

Synthesis of **3.1**

5 mL of THF were added to a mixture of Dyl₃ (102.2 mg, 0.19 mmol, 1 equiv.) and KCp^{ttt} (51 mg, 0.19 mmol, 1.0 equiv) at room temperature. The resulting white suspension was stirred for 3 days at room temperature. The suspension was decanted and the slightly yellow supernatant was filtered and evaporated under reduced pressure. The resulting sticky solid was dissolved in pentane and filtered to remove additional KI. Concentration of this pale-yellow solution at room temperature yielded the desired product (72.6 mg, 0.09 mmol, 51% yield) as white crystals, which were characterized by SC-XRD.

Anal. Calcd for C₂₅H₄₅Dyl₂O₂ (793.942): C, 37.82, H, 5.71. Found: C, 38.65; H, 5.96.

¹H NMR (300 MHz, toluene-d₈, 293 K): δ (ppm), -110.3 (s, 18H, 2 ^tBu of Cp^{ttt}), -83.3 (s, 2H, Aromatic proton of Cp^{ttt}), 27.97 (s, 9H, ^tBu of Cp^{ttt}).

Synthesis of **3.2**

1 equivalent of KCnt (13.8 mg) was added to a solution of 70 mg of **3.1** in toluene. The solution turned yellow in less than 10 minutes. After two hours, the reaction mixture was placed under reduced pressure for 5 minutes to remove the traces of THF. The yellow reaction mixture was allowed to stir overnight in a depressurized vessel. The yellow mixture was subsequently evaporated to dryness and the resulting yellow powder was extracted with pentane. Concentration at cold (-40 °C) of the pentane yellow solution yielded the desired product as yellow blocks (13.8 mg, 24% yield) suitable for SC-XRD.

Anal. Calcd for C_{28.5}H₄₄Dyl (676.07): C, 50.63, H, 6.56. Found: C, 51.73, H, 6.46

¹H NMR (300 MHz, toluene-d₈, 293 K): δ (ppm), -269.1, -211.3, -128.1, -8.5

Synthesis of **3.3**

2 equivalents of KC₈ (10.6 mg, 0.07 mmol, 1.2 equiv.) were added to a solution of **3.2** (42.2 mg, 0.06, 1 equiv.) in toluene at room temperature. The reaction mixture was stirred for 1 h turning gradually from yellow to red-orange with a dark precipitate. The colored supernatant was filtered and the solvent was removed. The residual orange solid was washed with pentane and dried to give **3.3** (8.5 mg, 25%) as a microcrystalline product. Alternatively, XRD suitable crystals can be grown from the toluene solution at cold (-40 °C).

Anal. Calcd for C₂₆H₃₈Dyl (676.07): C, 60.86, H, 7.47. Found: C, 57.27, H, 6.81. Although the values are outside the range viewed as establishing analytical purity, these results are provided to illustrate the best values obtained to date.

^1H NMR (300 MHz, toluene- d_8 , 293 K): δ (ppm), 512.6 (Cnt), 483.9, (Cnt), 152.1 (Cnt), -24.8 ((s, 9H, ^tBu of Cp^{ttt})) -31.5 (s, 18H, 2 ^tBu of Cp^{ttt}), -38.4 (Cnt), -172.0 (Cnt).

Synthesis of 3.4

5 mL of toluene were added to a mixture of **3.1** (142.1 mg, 0.18 mmol, 1 equiv.), KCnt (14.1 mg, 0.09 mmol, 10.5 equiv.) and KC_8 (48.4 mg, 0.36 mmol, 2 equiv.). The resulting light-yellow suspension was stirred for 3 h at room temperature. During this time, the supernatant gradually colored from light yellow to deep purple. The reaction medium was then evaporated to dryness. The resulting solid was extracted in pentane and the resulting purple solution was filtered. The concentration of this solution at $-40\text{ }^\circ\text{C}$ yields the desired compounds as deep orange-brown crystals which were characterized by SC-XRD (15.6 mg, 17 %)

General synthesis for 3.1_{Ln}

5 mL of THF were added to a mixture of LnI_3 (1 equiv.) and KCp^{ttt} (1 equiv.) at room temperature. The resulting suspension was stirred for 3 days at room temperature. The suspension was decanted and the supernatant was filtered and evaporated under reduced pressure. The resulting sticky solid was dissolved in pentane and filtered to remove additional KI. Concentration of this pale solution at room temperature yielded the desired product as white crystals, which were characterized by SC-XRD.

Synthesis 3.1_Y

Prepared according to the general procedure with YI_3 (150.1 mg, 0.32 mmol, 1.0 equiv.) and KCp^{ttt} (87.2 mg, 0.32 mmol, 1.0 equiv.).

Yield of crystals (31.5 mg, 14 %)

Synthesis of 3.1_{Nd}

Prepared according to the general procedure with NdI_3 (149.3 mg, 0.28 mmol, 1.0 equiv.) and KCp^{ttt} (77.4 mg, 0.28 mmol, 1.0 equiv.).

Yield of crystals (13 mg, 6 %)

Synthesis of 3.1_{Gd}

Prepared according to the general procedure with GdI_3 (152.8 mg, 0.28 mmol, 1.0 equiv.) and KCp^{ttt} (78.2 mg, 0.28 mmol, 1.0 equiv.).

Yield of crystals (49.3 mg, 22 %)

Synthesis of 3.1_{Tb}

Prepared according to the general procedure with TbI_3 (149.9 mg, 0.28 mmol, 1.0 equiv.) and KCp^{ttt} (76.1 mg, 0.28 mmol, 1.0 equiv.).

Yield of crystals (81.6 mg, 37 %)

Of note **3.1_{Tb}** was not analyzed through SC-XRD as an extensive drying period removed one THF from the coordination sphere yielding a terbium dimer similar to **3.1_{dimer}**.

Synthesis of **3.1_{Er}**

Prepared according to the general procedure with ErI_3 (148.7 mg, 0.28 mmol, 1.0 equiv) and KCp^{ttt} (73.9 mg, 0.28 mmol, 1.0 equiv).

Yield of crystals (87.2 mg, 44 %)

General synthesis for **3.3_{Ln}** (Ln = Gd, Tb Er)

3.1_{Ln} (1 equiv.), KCnt (0.5 equiv.) and KC_8 (2 equiv.) were weighted into a vial. Toluene was added onto the solid mixture at room temperature and the reaction mixture was stirred for 1 h. The colored supernatant was filtered and the solvent was removed. The residual yellow-orange solid was washed with pentane and dried to give **3.3_{Ln}** as a microcrystalline product. Alternatively, XRD suitable crystals could be grown from recrystallization in hot toluene.

Synthesis of **3.3_{Gd}**

Prepared according to the general procedure with **3.1_{Gd}** (32.1 mg, 0.04 mmol, 1.0 equiv), KCnt (3.2 mg, 0.02 mmol, 0.5 equiv.) and KC_8 (11.3 mg, 0.08 mmol, 2 equiv.).

Yield of microcrystalline powder (2.1 mg, 10 %)

Synthesis of **3.3_{Tb}**

Prepared according to the general procedure with **3.1_{Tb}** (23.4 mg, 0.03 mmol, 1.0 equiv), KCnt (2.3 mg, 0.015 mmol, 0.5 equiv.) and KC_8 (8.7 mg, 0.06 mmol, 2 equiv.).

Yield of microcrystalline powder (4.5 mg, 30 %)

Synthesis of **3.3_{Er}**

Prepared according to the general procedure with **3.1_{Er}** (39.9 mg, 0.05 mmol, 1.0 equiv), KCnt (4.7 mg, 0.03 mmol, 0.6 equiv.) and KC_8 (14.9 mg, 0.11 mmol, 2 equiv.).

Yield of microcrystalline powder (3.8 mg, 13 %)

Synthesis of **3.4_{Er}**

3.1_{Er} (39.9 mg, 0.05 mmol, 1.0 equiv.), KCnt (4.7 mg, 0.03 mmol, 0.6 equiv.) and KC_8 (14.9 mg, 0.11 mmol, 2 equiv.) were weighted into a vial. Toluene was added onto the solid mixture at room temperature and the reaction mixture was stirred for 1 h. The colored supernatant was filtered and the solvent was removed. The residual solid was extracted with pentane. The resulting purple solution was filtered and concentrated. XRD suitable crystals could be grown from crystallization at low temperature (3.9 mg, 14%)

III. NMR characterization

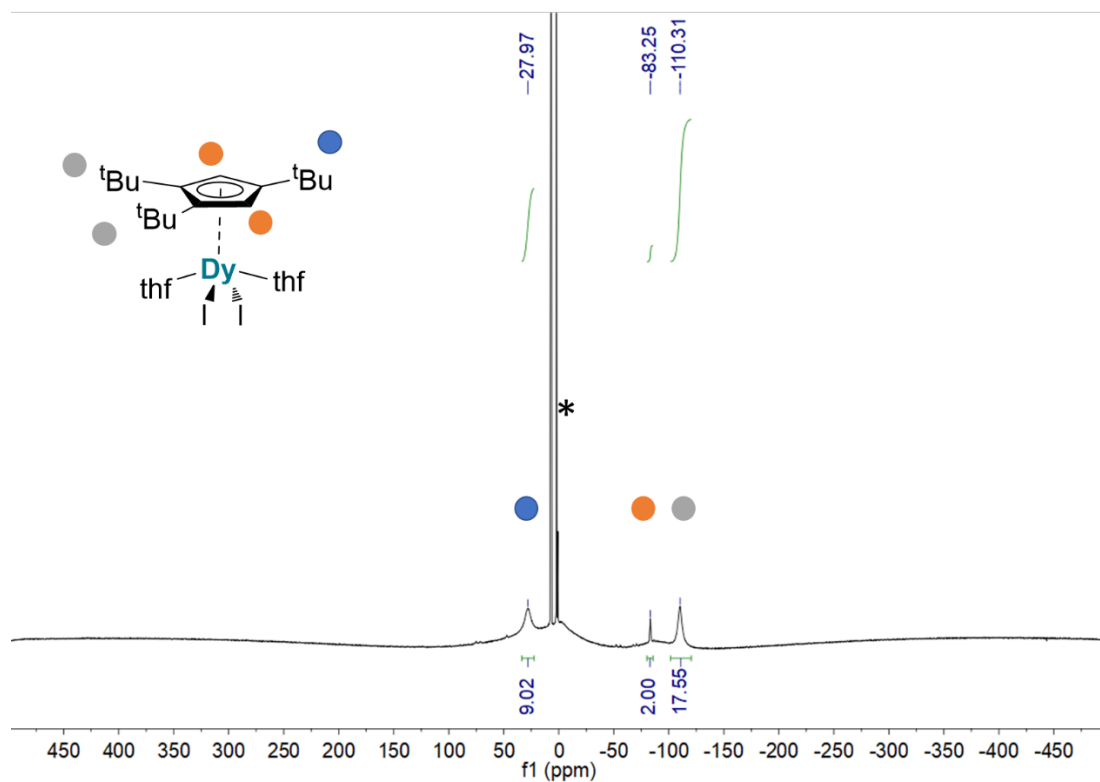


Figure S3. 1 ^1H NMR of **3.1** in toluene- d_8 measured at 293 K (* residual protio signal of the solvent)

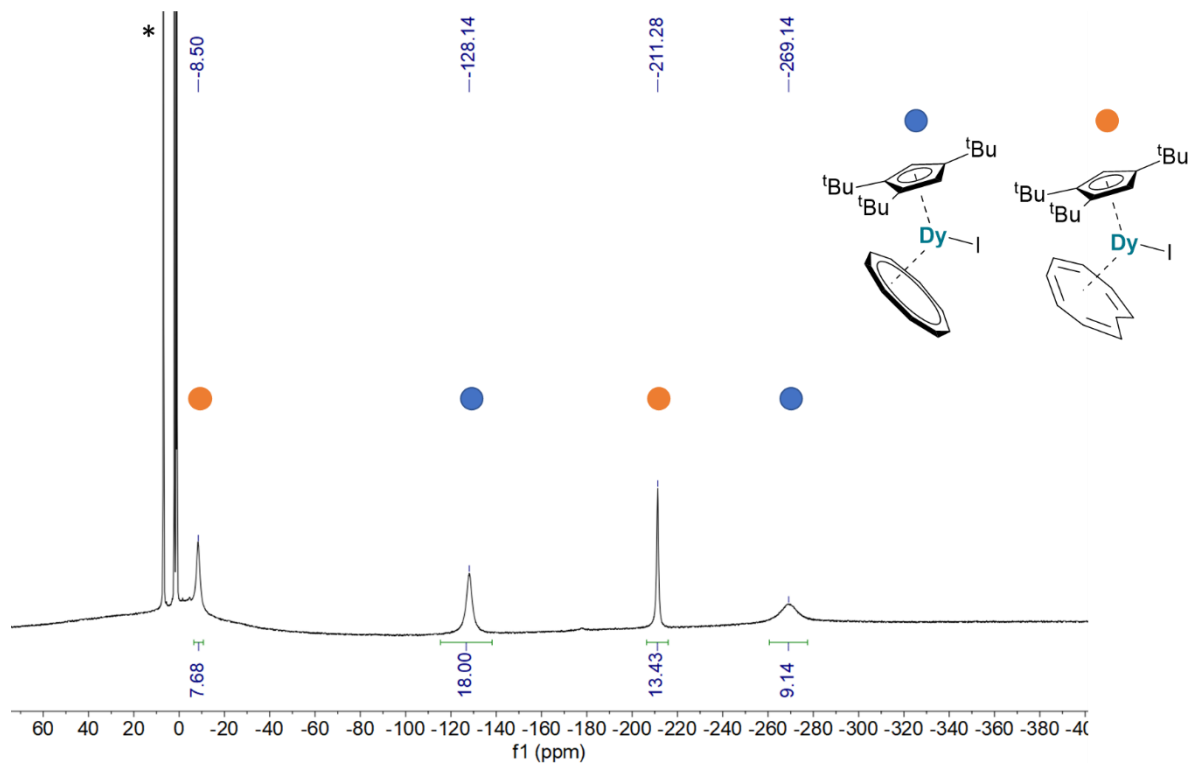


Figure S3. 2 ^1H NMR of **3.2** in toluene- d_8 measured at 293 K (* residual protio signal of the solvent)

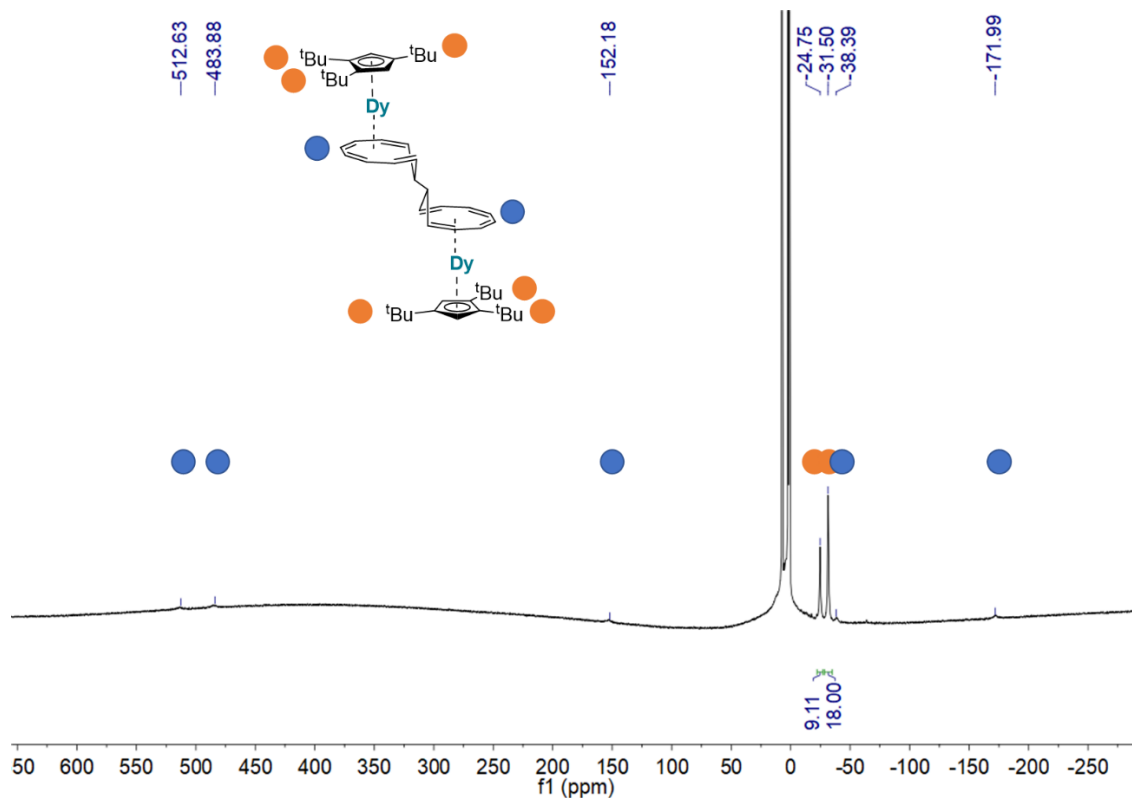


Figure S3. ^1H NMR of **3.3** in toluene- d_8 measured at 293 K (* residual protio signal of the solvent)

IV. XRD characterization

1. General methods

Single crystals of the complexes suitable for X-ray analysis were mounted on a Kapton loop using a Paratone N oil. Two diffractometers were used during this for the data acquisition, either a Bruker diffractometer equipped with an APEX II CCD detector and a graphite Mo- $K\alpha$ monochromator or a Stoe stadivari diffractometer with a Eiger2 detector and a Mo- $K\alpha$ microsource. All measurements were done at 150 K (unless otherwise stated) and a refinement method was used for solving the structure. The resolution of the solid-state structure was accomplished using the SHELXS-97 or SHELXT programs.^{6,7} The refinement was performed with the SHELXL program using the Olex2 software.^{7,8} All atoms – except hydrogens – were refined anisotropically.

2. Summary of crystal data

Compound	3.1	3.1 _{dimer}	3.2
Formula	C ₂₅ H ₄₅ DyI ₂ O ₂	C ₂₁ H ₃₇ DyI ₂ O	C _{28.5} H ₄₄ DyI
Crystal size (mm ³)	0.27 × 0.16 × 0.1	0.24 × 0.14 × 0.1	0.19 × 0.15 × 0.13
Crystal system	Monoclinic	Monoclinic	Monoclinic
Space group	C2/c	P2 ₁ /c	C2/c
Volume (Å ³)	5963.6(4)	2396.85(14)	5477.1(3)
a (Å)	36.3533(12)	9.8664(4)	29.2509(9)
b (Å)	9.4734(3)	14.0541(4)	9.1956(3)
c (Å)	17.4887(7)	17.3826(6)	20.8987(5)
α (deg)	90	90	90
β (deg)	98.050(3)	96.062(2)	103.006
γ (deg)	90	90	90
Z	8	4	8
Formula weight (g/mol)	793.91	721.80	676.03
Density (calcd) (g/cm ³)	1.768	2.000	1.640
Absorption coefficient (mm ⁻¹)	4.593	5.700	3.868
F(000)	3064.0	1720.0	2672.0
Temp (K)	150	150.01	150
Diffractometer	Stoe Stadivari	Bruker APEX-II CCD	Stoe Stadivari
Radiation	Mo Kα (λ = 0.71073)	Mo Kα (λ = 0.71073)	Mo Kα (λ = 0.71073)
2θ range for data collection (deg)	4.446 to 54.97	6.258 to 55.23	4.362 to 56.56
Absorption correction	Multi-scan	Multi-scan	Multi-scan
Total no. reflections	26396	29249	32753
Unique reflections [R _{int}]	6847 [R _{int} = 0.0308]	5570 [R _{int} = 0.0585]	6790 [R _{int} = 0.0369]
Final R indices [I > 2σ(I)]	R ₁ = 0.0234, wR ₂ = 0.0532	R ₁ = 0.0259, wR ₂ = 0.0512	R ₁ = 0.0265, wR ₂ = 0.0572
R indices (all data)	R ₁ = 0.0320, wR ₂ = 0.0545	R ₁ = 0.0355, wR ₂ = 0.0545	R ₁ = 0.0400, wR ₂ = 0.0591
Largest diff. peak and hole (e.Å ⁻³)	2.09/-0.64	1.03/-0.80	1.04/-0.85
Goof	0.978	1.031	0.947

Compound	3.3	3.4	3.1 _v
Formula	C ₂₆ H ₃₈ Dy ₂	C ₄₃ H ₆₇ Dy ₂ l	C ₂₅ H ₄₅ l ₂ O ₂ Y
Crystal size (mm ³)	0.14 × 0.13 × 0.1	0.17 × 0.11 × 0.08	0.25 × 0.10 × 0.05
Crystal system	Orthorhombic	Monoclinic	Triclinic
Space group	Pccn	P2 ₁ /c	P-1
Volume (Å ³)	4489.32(19)	4144.1(9)	1489.8(2)
a (Å)	20.1113(5)	18.311(3)	9.9202(8)
b (Å)	14.1633(3)	8.7211(8)	12.036(6)
c (Å)	15.7607(4)	27.591(4)	12.8684(10)
α (deg)	90	90	87.036(6)
β (deg)	90	109.855(10)	76.051(6)
γ (deg)	90	90	88.926(6)
Z	8	4	2
Formula weight (g/mol)	513.06	1035.86	720.32
Density (calcd) (g/cm ³)	1.518	1.660	1.606
Absorption coefficient (mm ⁻¹)	3.336	4.35	4.046
F(000)	2080.0	2040.0	712.0
Temp (K)	150	250	200
Diffractometer	Stoe Stadivari	Stoe Stadivari	Stoe Stadivari
Radiation	Mo Kα (λ = 0.71073)	Mo Kα (λ = 0.71073)	Mo Kα (λ = 0.71073)
2θ range for data collection (deg)	4.364 to 56.562	4.526 to 52.744	4.59 to 54.204
Absorption correction	Multi-scan	Multi-scan	Multi-scan
Total no. reflections	39955	46140	18977
Unique reflections [R _{int}]	5570 [R _{int} = 0.0409]	8466 [R _{int} = 0.0534]	8220 [R _{int} = 0.0511]
Final R indices [I > 2σ(I)]	R ₁ = 0.0286, wR ₂ = 0.0747	R ₁ = 0.0401, wR ₂ = 0.0934	R ₁ = 0.0590, wR ₂ = 0.1486
R indices (all data)	R ₁ = 0.0456, wR ₂ = 0.0772	R ₁ = 0.0707, wR ₂ = 0.1035	R ₁ = 0.0940, wR ₂ = 0.1571
Largest diff. peak and hole (e.Å ⁻³)	2.01/-0.52	1.66/-0.75	1.87/-1.07
GooF	0.985	0.993	1.071

Compound	3.1 _{Nd}	3.1 _{Gd}	3.1 _{Er}
Formula	C ₂₅ H ₄₅ I ₂ NdO ₂	C ₂₅ H ₄₅ I ₂ GdO ₂	C ₂₁ H ₃₇ ErI ₂ O
Crystal size (mm ³)	0.18 × 0.13 × 0.09	0.12 × 0.05 × 0.02	0.24 × 0.2 × 0.1
Crystal system	Triclinic	Orthorhombic	Monoclinic
Space group	P-1	Pbca	P2 ₁ /c
Volume (Å ³)	1514.03(19)	5862.8(4)	2492.79(19)
a (Å)	9.8973(8)	10.6536(4)	17.9985(6)
b (Å)	12.2558(8)	17.7932(6)	9.0959(4)
c (Å)	12.9006(9)	30.9280(12)	16.7692(8)
α (deg)	87.139(6)	90	90
β (deg)	75.637(6)	90	114.768(2)
γ (deg)	89.281(6)	90	90
Z	2	8	4
Formula weight (g/mol)	775.65	788.66	726.56
Density (calcd) (g/cm ³)	1.701	1.787	1.936
Absorption coefficient (mm ⁻¹)	3.770	4.386	5.850
F(000)	754.0	3048.0	1380.0
Temp (K)	200	150	149.99
Diffractometer	Stoe Stadivari	Stoe Stadivari	Bruker APEX-II CCD
Radiation	Mo Kα (λ = 0.71073)	Mo Kα (λ = 0.71073)	Mo Kα (λ = 0.71073)
2θ range for data collection (deg)	4.546 to 61.204	4.578 to 52.74	2.492 to 59.47
Absorption correction	Multi-scan	Multi-scan	Multi-scan
Total no. reflections	22301	40254	23336
Unique reflections [R _{int}]	8353 [R _{int} = 0.0233]	5996 [R _{int} = 0.0813]	7087 [R _{int} = 0.0450]
Final R indices [I > 2σ(I)]	R ₁ = 0.0219, wR ₂ = 0.0372	R ₁ = 0.0339, wR ₂ = 0.0586	R ₁ = 0.0289, wR ₂ = 0.0685
R indices (all data)	R ₁ = 0.0361, wR ₂ = 0.0380	R ₁ = 0.0718, wR ₂ = 0.0645	R ₁ = 0.0426, wR ₂ = 0.0839
Largest diff. peak and hole (e.Å ⁻³)	0.91/-0.64	1.51/-0.76	0.78/-1.03
Goof	0.854	0.883	1.058

Compound	3.1Tm	3.3Gd	3.3Tb
Formula	C ₂₁ H ₃₇ I ₂ OTm	C ₅₃ H ₇₆ Gd ₂	C ₅₃ H ₇₆ Tb ₂
Crystal size (mm ³)	0.19 × 0.08 × 0.05	0.18 × 0.15 × 0.13	0.16 × 0.15 × 0.09
Crystal system	Monoclinic	Orthorhombic	Orthorhombic
Space group	P2 ₁ /c	Pccn	Pccn
Volume (Å ³)	2500.50(9)	4465.8(3)	4452.4(4)
a (Å)	16.8122(4)	20.0527(9)	20.0500(13)
b (Å)	9.09210(10)	14.1362(5)	14.1116(6)
c (Å)	18.0261(4)	15.7542(7)	15.7364(7)
α (deg)	90	90	90
β (deg)	114.841(2)	90	90
γ (deg)	90	90	90
Z	4	4	4
Formula weight (g/mol)	728.23	1015.62	1018.96
Density (calcd) (g/cm ³)	1.934	1.511	1.520
Absorption coefficient (mm ⁻¹)	6.024	2.978	3.184
F(000)	1384.0	2064.0	2072.0
Temp (K)	150	150	150
diffractometer	Stoe Stadivari	Stoe Stadivari	Stoe Stadivari
Radiation	Mo Kα (λ = 0.71073)	Mo Kα (λ = 0.71073)	Mo Kα (λ = 0.71073)
2θ range for data collection (deg)	4.98 to 66.224	4.372 to 58.532	5.178 to 56.564
Absorption correction	Multi-scan	Multi-scan	Multi-scan
Total no. reflections	52834	48557	44939
Unique reflections [R _{int}]	7033 [R _{int} = 0.0329]	5763 [R _{int} = 0.0579]	5311 [R _{int} = 0.0482]
Final R indices [I > 2σ(I)]	R ₁ = 0.0242, wR ₂ = 0.0535	R ₁ = 0.0245, wR ₂ = 0.0494	R ₁ = 0.0332, wR ₂ = 0.0825
R indices (all data)	R ₁ = 0.0405, wR ₂ = 0.0558	R ₁ = 0.0435, wR ₂ = 0.0528	R ₁ = 0.0614, wR ₂ = 0.0931
Largest diff. peak and hole (e.Å ⁻³)	1.22/-0.78	0.73/-0.41	2.32/-0.76
Goof	0.963	0.944	1.111

3. Crystal structures and main distances

Structure of 3.1

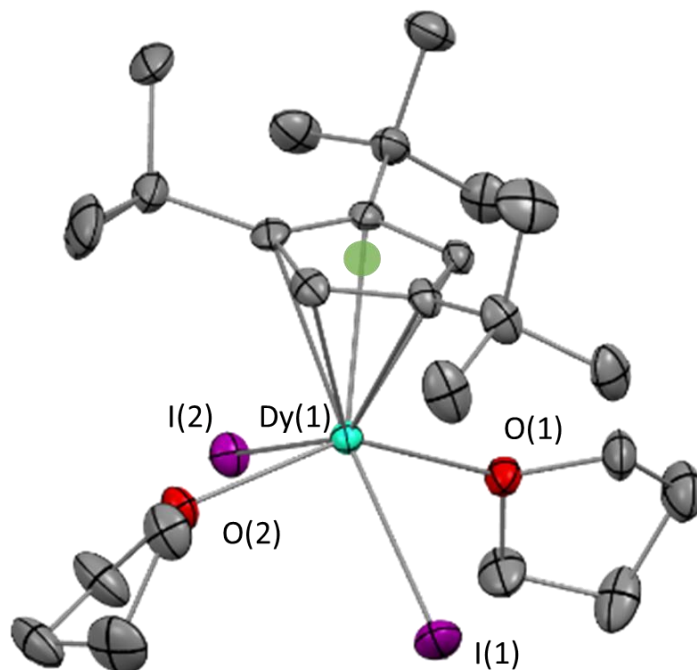


Figure S3. 4 Molecular structure of **3.1**, thermal ellipsoids are depicted at 50% probability level. Dysprosium atoms are in light green, carbon in grey, oxygen and iodine in red and purple respectively. Hydrogen atoms are omitted for clarity. The green spot represents the constructed centroid for the Cp^{ttt} ligand.

	Main distances in Å
Dy(1)—I(1)	3.0012(3)
Dy(1)—I(2)	2.9713(3)
Dy(1)—C (Cp ^{ttt})	2.629(3) – 2.709(3)
Dy—C (Cp ^{ttt}) avg	2.66(12)
Dy—Cent (Cp ^{ttt})	2.38
Dy(1)—O(1)	2.390(2)
Dy(1)—O(2)	2.389(2)

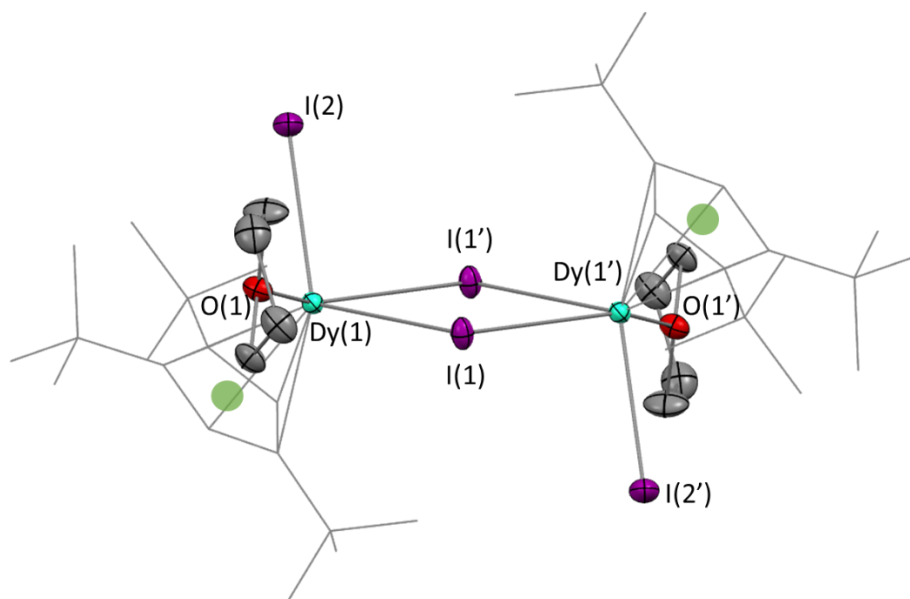
Structure of **3.1**_{dimer}

Figure S3. 5 Molecular structure of **3.1**_{dimer}, thermal ellipsoids are depicted at 50% probability level. Dysprosium atoms are in light green, carbon in grey, oxygen and iodine in red and purple respectively. Hydrogen atoms are omitted for clarity and Cp^{ttt} are represented in wireframe.

	Main distances in Å
Dy(1)—I(1)	3.0944(3)
Dy(1)—I(1')	3.1598(3)
Dy(1)—I(2)	2.9289
Dy(1)—O(1)	2.376(2)
Dy(1)—C(1)	2.614(3)
Dy(1)—C(2)	2.597(3)
Dy(1)—C(3)	2.672(3)
Dy(1)—C(4)	2.708(3)
Dy(1)—C(5)	2.630(3)
Dy(1)—C (Cp ^{ttt}) avg	2.64(5)
Dy(1)—Cent (Cp ^{ttt})	2.35

Structure of 3.2

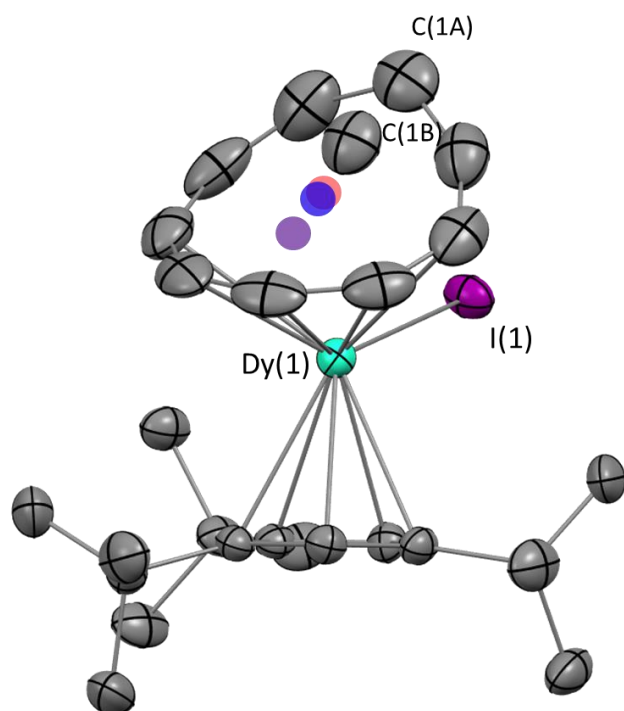


Figure S3. 6 Molecular structure of **3.2**, thermal ellipsoids are depicted at 50% probability level. Dysprosium atoms are in light green, carbon in grey and iodine in purple. Hydrogen atoms are omitted for clarity and the red, blue and purple spots represent the centroids for the Cnt-cis, the Cnt-trans and the Cnt in η^6 hapticity respectively.

	Main distances in Å
Dy(1)—I(1)	3.0117(4)
Dy(1)—C (Cp ^{ttt})	2.596(3) – 2.689(3)
Dy(1)—Cent (Cp ^{ttt})	2.35
Dy(1)—C (Cnt η^6 ligand)	2.906(4) – 2.652(4)
Dy(1)—C(1A)	3.610
Dy(1)—C(1B)	2.779
Dy(1)—Cent (Cnt- η^6)	2.01
Dy(1)—Cent (Cnt- η^9 -cis)	2.16
Dy(1)—Cent (Cnt- η^9 -trans)	2.11

Structure of 3.3

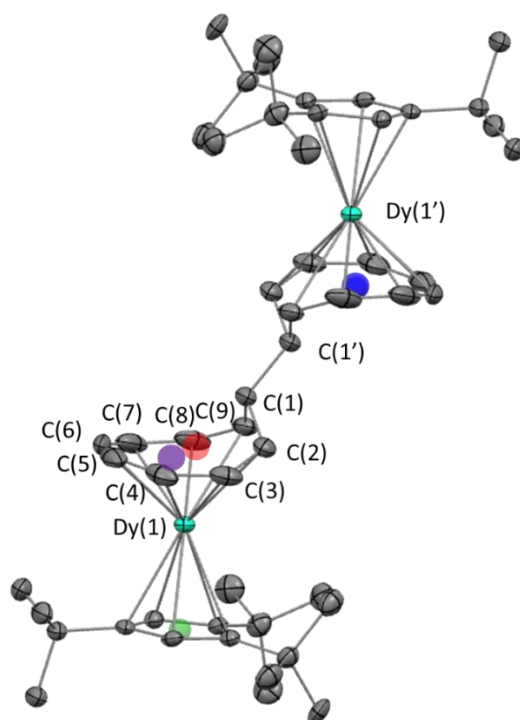


Figure S3. 7 Molecular structure of **3.3**, thermal ellipsoids are depicted at 50% probability level. Dysprosium atoms are in light green, and carbon in grey. Hydrogen atoms are omitted for clarity. Red, blue, purple and green spots represent the centroids for the η^9 Cnt, the η^8 Cnt, the η^6 Cnt and the η^5 Cp^{ttt} hapticity respectively.

	Main distances in Å
Dy(1)—C (Cp ^{ttt})	2.610(3) – 2.688(3)
Dy(1)—Cent (Cp ^{ttt})	2.35
Dy(1)—C(1) (Cnt)	3.134(3)
Dy(1)—C(2) (Cnt)	2.735(3)
Dy(1)—C(3) (Cnt)	2.545(3)
Dy(1)—C(4) (Cnt)	2.504(3)
Dy(1)—C(5) (Cnt)	2.536(4)
Dy(1)—C(6) (Cnt)	2.527(3)
Dy(1)—C(7) (Cnt)	2.488(5)
Dy(1)—C(8) (Cnt)	2.531(4)
Dy(1)—C(9) (Cnt)	2.727(3)
Dy(1)—Cent (Cnt- η^6)	1.66
Dy(1)—Cent (Cnt- η^8)	1.65
Dy(1)—Cent (Cnt- η^9)	1.78
C(1)—C(1')	1.538(5)

Structure of 3.4

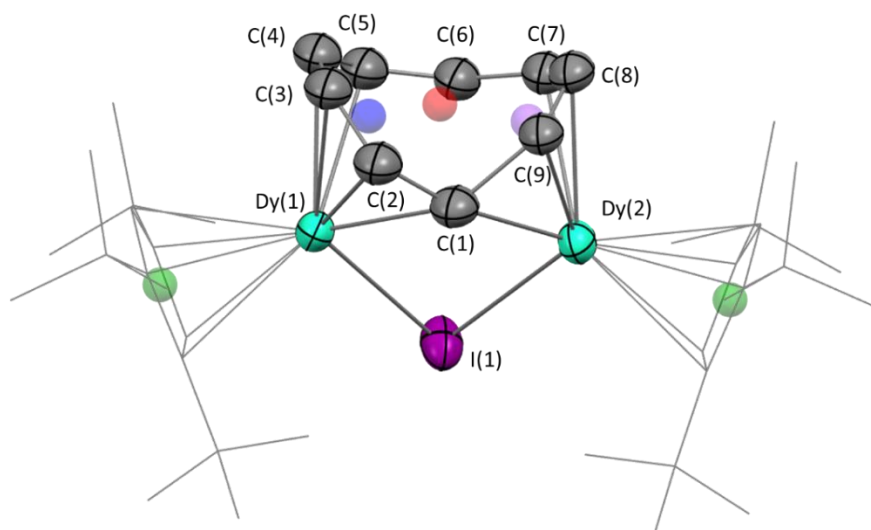


Figure S3. 8 Molecular structure of **3.4**, thermal ellipsoids are depicted at 50% probability level. Dysprosium atoms are in light green, carbon in grey and iodine in purple. Cp^{ttt} are represented in wireframe and hydrogen atoms are omitted for clarity. Red, blue, purple and green spots represent the centroids for the η^9 Cnt, the η^5 Cnt, the η^4 Cnt and the η^5 Cp^{ttt} hapticity respectively.

Main distances in Å		
Dy(1) — Dy(2)	3.757(1)	
	Dy(1)	Dy(2)
Dy(X)—I(1)	3.1144 (6)	3.0293 (5)
Dy(X)—C(1)	2.532 (7)	2.471 (7)
Dy(X)—C(2)	2.508 (11)	3.816 (10)
Dy(X)—C(3)	2.609 (10)	4.537 (10)
Dy(X)—C(4)	2.559 (11)	4.610 (10)
Dy(X)—C(5)	2.596 (11)	3.997 (10)
Dy(X)—C(6)	3.263 (10)	3.125 (10)
Dy(X)—C(7)	4.051 (10)	2.520 (10)
Dy(X)—C(8)	4.376 (10)	2.570 (10)
Dy(X)—C(9)	3.899 (10)	2.440 (12)
Dy(X)—Cent (Cnt- η^9)	2.61	2.87
Dy(X) —Cent (Cnt- η^5)	2.04	NA
Dy(X) —Cent (Cnt- η^4)	NA	2.09
Dy(X)—C (Cp ^{ttt})	2.650(6)	2.643(5)
Dy(X)—C (Cp ^{ttt})	2.643(6)	2.644(5)
Dy(X)—C (Cp ^{ttt})	2.624(6)	2.658(6)
Dy(X)—C (Cp ^{ttt})	2.695(5)	2.604(6)
Dy(X)—C (Cp ^{ttt})	2.656(5)	2.635(6)
Avg Dy(X)—C (Cp ^{ttt})	2.65(3)	2.64(2)
Dy(X)—Cent (Cp ^{ttt})	2.36	2.35

Bond distances are given for one of the disordered Cnt given the small relative differences between the two molecules.

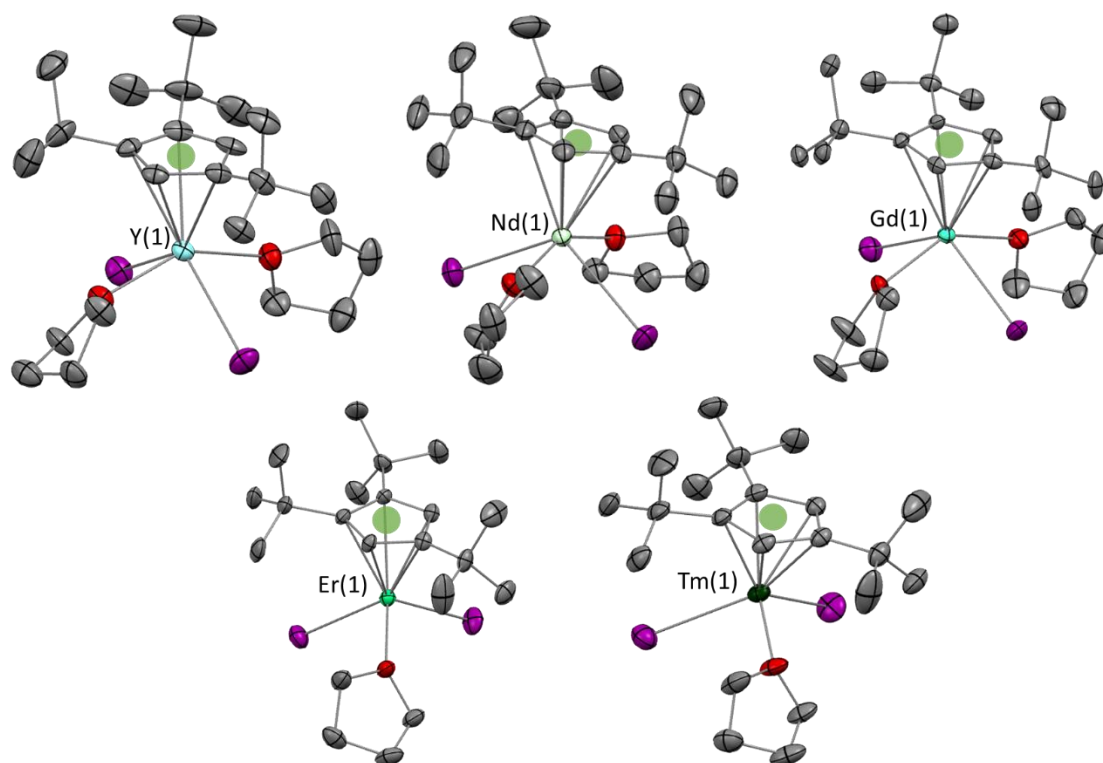
Structure of **3.1_{Ln}**

Figure S3. 9 Molecular structure of **3.1_{Ln}**, thermal ellipsoids are depicted at 50% probability level. Ln = Y, Nd, Gd, Er, Tm represented in light blue, light yellow, light green, green, dark green respectively. Additionally, carbon atoms are represented in grey, oxygen in red and iodine in purple and hydrogen have been omitted for clarity.

Main distances in Å	3.1_Y	3.1_{Nd}	3.1_{Gd}	3.1_{Er}	3.1_{Tm}
Ln(1)—I(1)	2.9735(10)	3.0603(3)	3.0008(4)	2.8900(4)	3.0883(3)
Ln(1)—I(2)	3.0112(11)	3.0831(3)	3.0194(5)	2.8793(5)	2.8393(2)
Ln(1)—C (Cp ^{ttt})	2.635(8) – 2.711	2.705(2) – 2.778(2)	2.737(5) – 2.648(5)	2.571(3) – 2.614(3)	2.416(3) – 2.600(3)
Ln—Cent (Cp ^{ttt})	2.37	2.46	2.41	2.29	2.16
Ln(1)—O(1)	2.378(6)	2.4671(14)	2.418(3)	2.263(3)	2.2090(19)
Ln(1)—O(2)	2.371(6)	2.4760(13)	2.443(3)	--	--

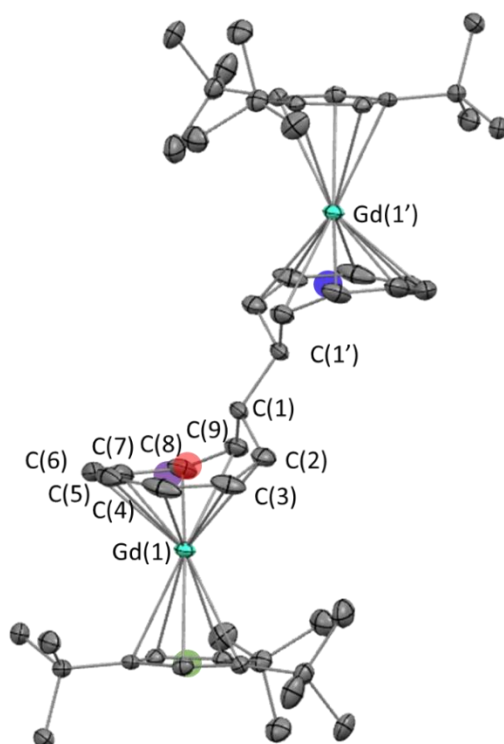
Structure of **3.3_{Gd}**

Figure S3. 10 Molecular structure of **3.3_{Gd}**, thermal ellipsoids are depicted at 50% probability level. Gadolinium atoms are in light green, and carbon in grey. Hydrogen atoms are omitted for clarity. Red, blue, purple and green spots represent the centroids for the η^9 Cnt, the η^8 Cnt, the η^6 Cnt and the η^5 Cp^{ttt} hapticity respectively.

Main distances in Å	
Gd(1)—C (Cp ^{ttt})	2.7134(17) – 2.644(2)
Gd(1)—Cent (Cp ^{ttt})	2.39
Gd(1)—C1 (Cnt)	3.164(2)
Gd(1)—C2 (Cnt)	2.758(2)
Gd(1)—C3 (Cnt)	2.571(2)
Gd(1)—C4 (Cnt)	2.524(2)
Gd(1)—C5 (Cnt)	2.555(2)
Gd(1)—C6 (Cnt)	2.555(2)
Gd(1)—C7 (Cnt)	2.521(2)
Gd(1)—C8 (Cnt)	2.569(2)
Gd(1)—C9 (Cnt)	2.754(2)
Gd(1)—Cent (Cnt- η^6)	1.74
Gd(1)—Cent (Cnt- η^8)	1.69
Gd(1)—Cent (Cnt- η^9)	1.82
C(1)—C(1')	1.523(4)

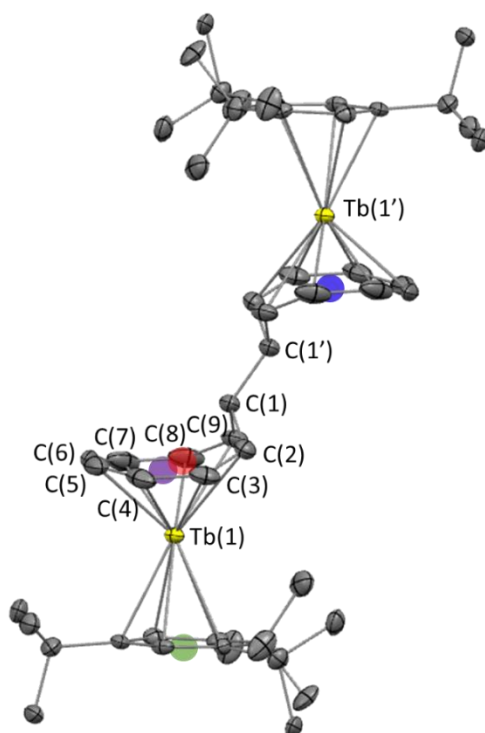
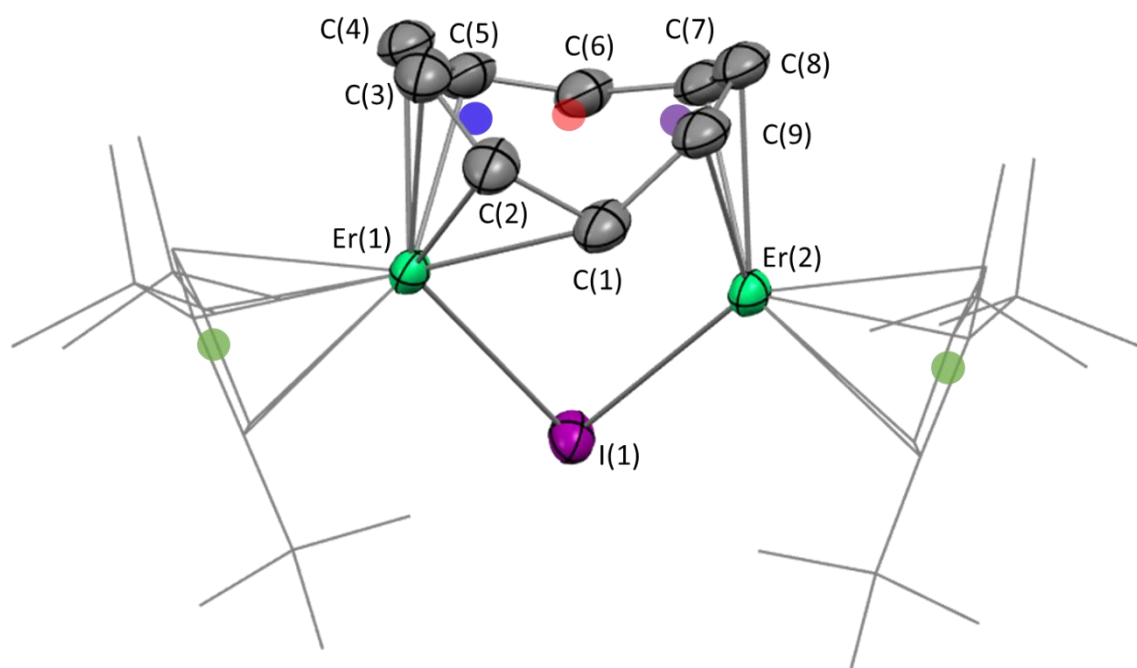
Structure of **3.3_{Tb}**

Figure S3. 11 Molecular structure of **3.3_{Tb}**, thermal ellipsoids are depicted at 50% probability level. Terbium atoms are in yellow, terbium atoms are in light green, and carbon in grey. Hydrogen atoms are omitted for clarity. Red, blue, purple and green spots represent the centroids for the η^9 Cnt, the η^8 Cnt, the η^6 Cnt and the η^5 Cp^{ttt} hapticity respectively.

	Main distances in Å
Tb(1)—C (Cp ^{ttt})	2.630(4) - 2.697(4)
Tb(1)—Cent (Cp ^{ttt})	2.37
Tb(1)—C(1) (Cnt)	3.146(4)
Tb(1)—C(2) (Cnt)	2.732(4)
Tb(1)—C(3) (Cnt)	2.548(4)
Tb(1)—C(4) (Cnt)	2.505(5)
Tb(1)—C(5) (Cnt)	2.532(4)
Tb(1)—C(6) (Cnt)	2.540(5)
Tb(1)—C(7) (Cnt)	2.507(5)
Tb(1)—C(8) (Cnt)	2.559(4)
Tb(1)—C(9) (Cnt)	2.740(4)
Tb(1)—Cent (Cnt- η^6)	1.72
Tb(1)—Cent (Cnt- η^8)	1.67
Tb(1)—Cent (Cnt- η^9)	1.794
C(1)—C(1')	1.514(8)

Structure of **3.4_{Er}**

Molecular structure of **3.4_{Er}**, thermal ellipsoids are depicted at 50% probability level. Erbium atoms are in green, carbon in grey and iodine in purple. Cp^{ttt} are represented in wireframe and hydrogen atoms are omitted for clarity. Red, blue, purple and green spots represent the centroids for the η^9 Cnt, the η^5 Cnt, the η^4 Cnt and the η^5 Cp^{ttt} hapticity respectively.

Main distances in Å		
	Er(1)	Er(2)
Er(1)—Er(2)	3.7216(10)	
Er(X)—I(1)	3.1157(11)	2.9628(11)
Er(X)—C(1)	2.758(14)	2.417(15)
Er(X)—C(2)	2.454(14)	3.84(1)
Er(X)—C(3)	2.547(15)	4.57(1)
Er(X)—C(4)	2.491(14)	4.64(2)
Er(X)—C(5)	2.531(14)	4.01(2)
Er(X)—C(6)	3.16(2)	3.15(2)
Er(X)—C(7)	3.95(1)	2.49(2)
Er(X)—C(8)	4.27(1)	2.544(14)
Er(X)—C(9)	3.80(1)	2.459(14)
Er(X)—Cent (Cnt- η^9)	2.52	2.88
Er(X)—Cent (Cnt- η^5)	1.98	NA
Er(X)—Cent (Cnt- η^4)	NA	2.08
Er(X)—C (Cp ^{ttt})	2.579(14)	2.571(12)
Er(X)—C (Cp ^{ttt})	2.592(14)	2.600(14)
Er(X)—C (Cp ^{ttt})	2.609(13)	2.601(13)
Er(X)—C (Cp ^{ttt})	2.618(14)	2.643(12)
Er(X)—C (Cp ^{ttt})	2.647(14)	2.648(12)
Er(X)—Cent (Cp ^{ttt})	2.31	2.32

V. Magnetic studies

1. General considerations

Magnetic measurements were obtained in a Quantum Design MPMS-XL SQUID magnetometer. An applied magnetic field of 2 kOe is used in the temperature range 2-20 K, and 10 kOe for temperatures above 20 K, for the $\chi_M T$ vs. T curves. To avoid reorientation and sample degradation the microcrystals are trapped and slightly pressed between quartz wool and sealed in quartz tubes.

2. Magnetization and magnetic susceptibility

Magnetization of **3.3**

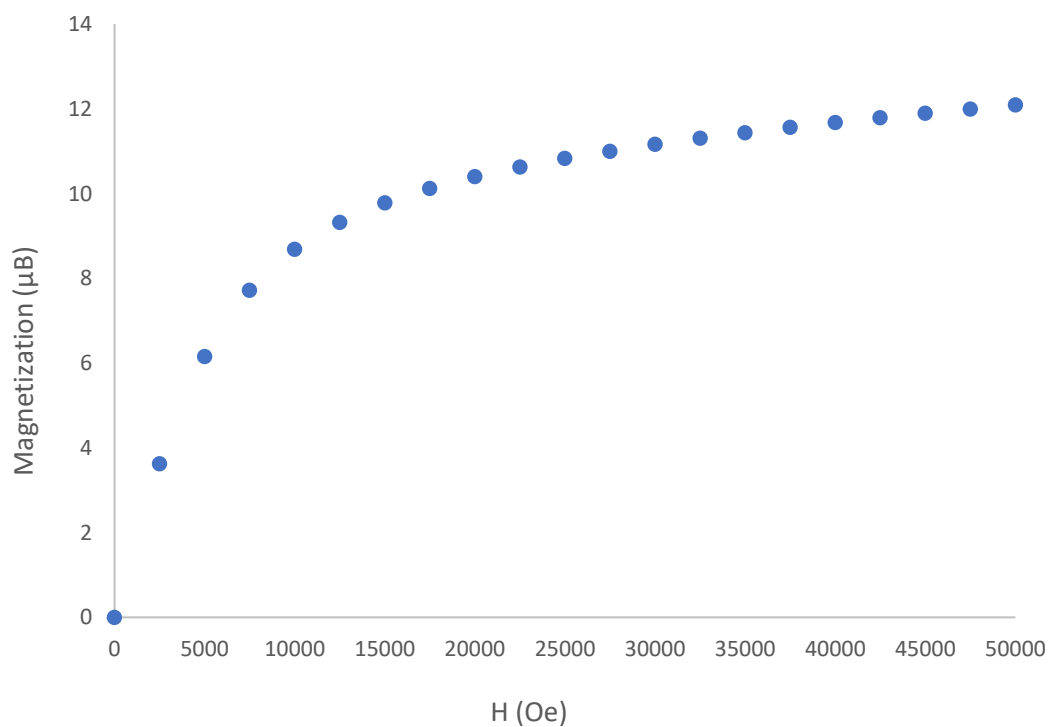


Figure S3. 12 Graphical representation of the magnetization of **3.3** at 2 K as a function of the external field.

Magnetization of **3.4**

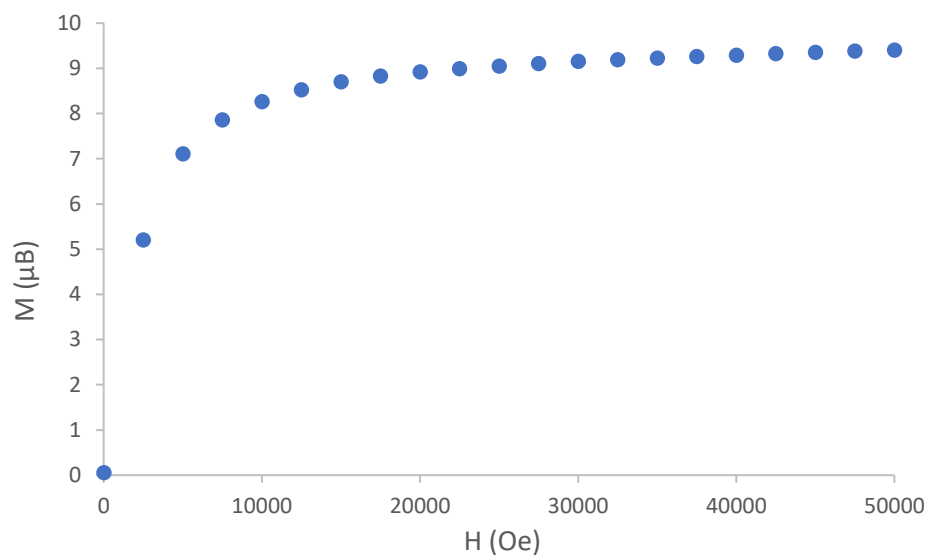


Figure S3. 13 Graphical representation of the magnetization of **3.4** at 2 K as a function of the external field.

Magnetic susceptibility of **3.3**

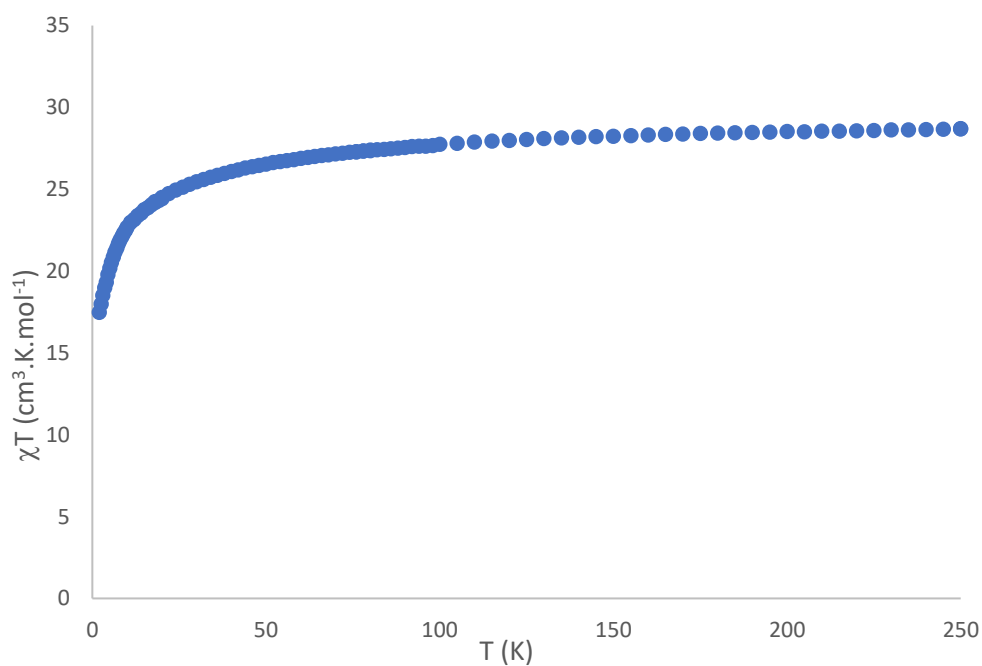


Figure S3. 14 Graphical representation of the product of the magnetic susceptibility by the temperature of **3.3** as a function of the temperature.

Magnetic susceptibility of **3.4**

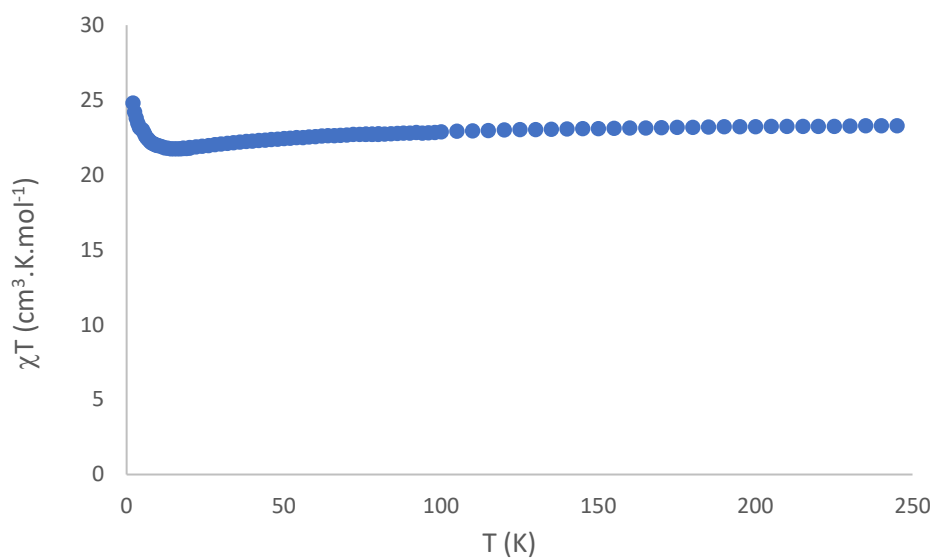


Figure S3. 15 Graphical representation of the product of the magnetic susceptibility by the temperature of **3.4** as a function of the temperature.

3. AC measurements

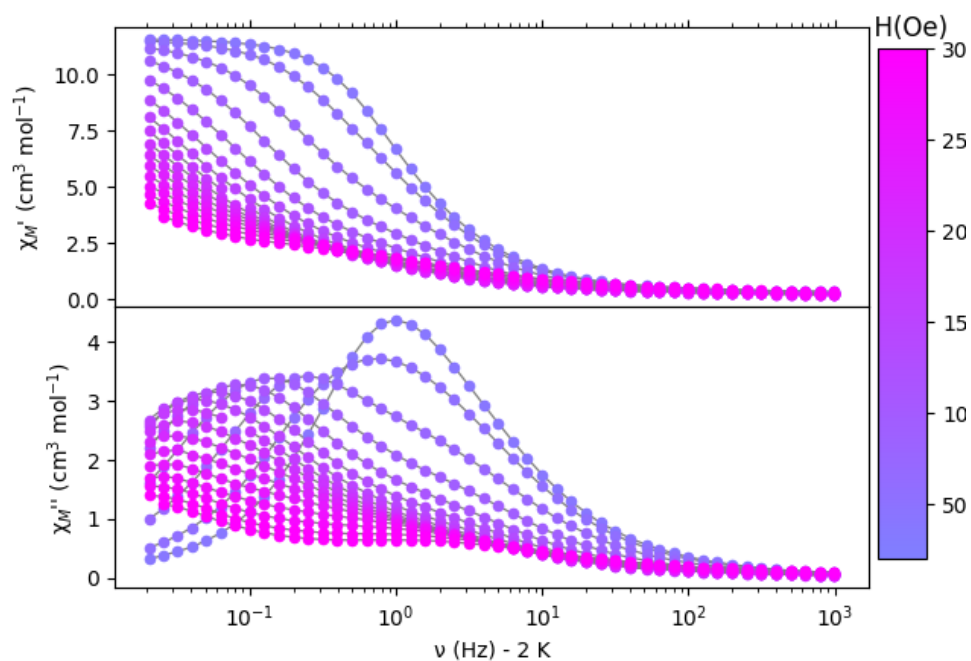


Figure S3. 16 Frequency dependences of both the in-phase, χ_M' and out-of-phase, χ_M'' components of the ac susceptibility of **3.4** at various external dc field at 2 K

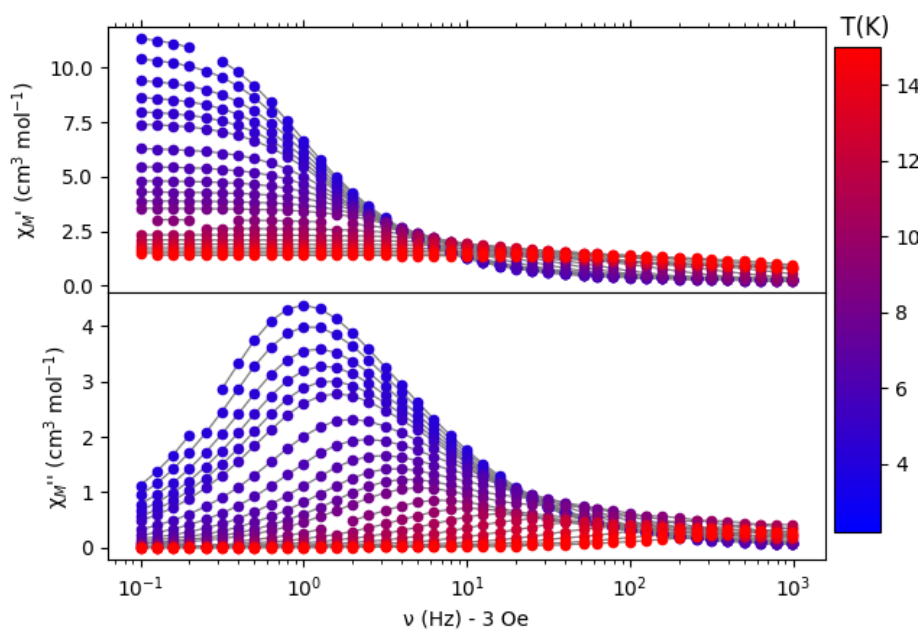


Figure S3. 17 Frequency dependences of both the in-phase, χ_M' and out-of-phase, χ_M'' components of the ac susceptibility of **3.4** at various temperature without external field.

VI. UV-visible spectroscopy

Spectra of **3.4** and **3.4_{Er}** were recorded in toluene in quartz cuvettes of width $l = 0.2$ cm adapted with a J. Young valve. Uncertainties were evaluated for the concentration to be $\Delta c = 0.0002$ mol.L⁻¹. For the absorption an uncertainty of $\Delta A = 0.01$ is considered.

Study of **3.4**

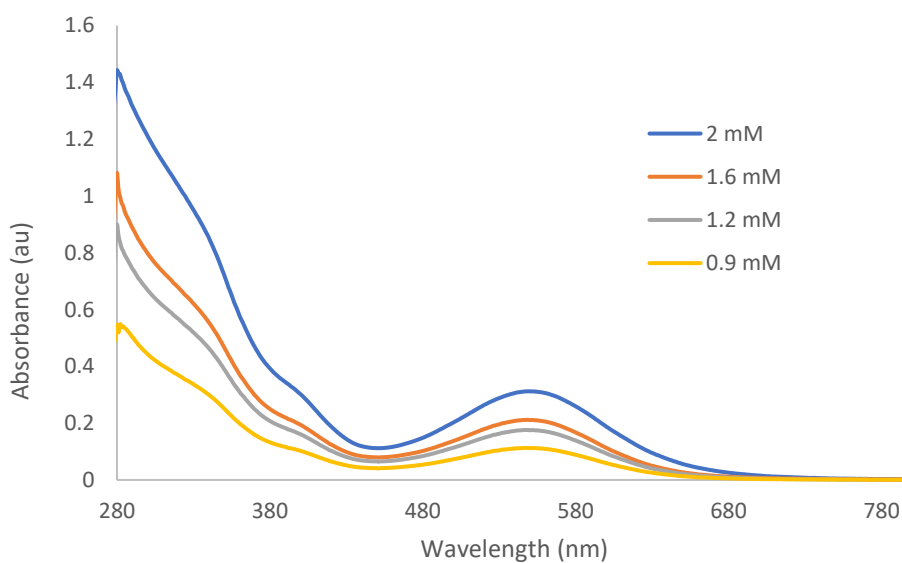


Figure S3. 18 UV-visible spectra of **3.4** in toluene.

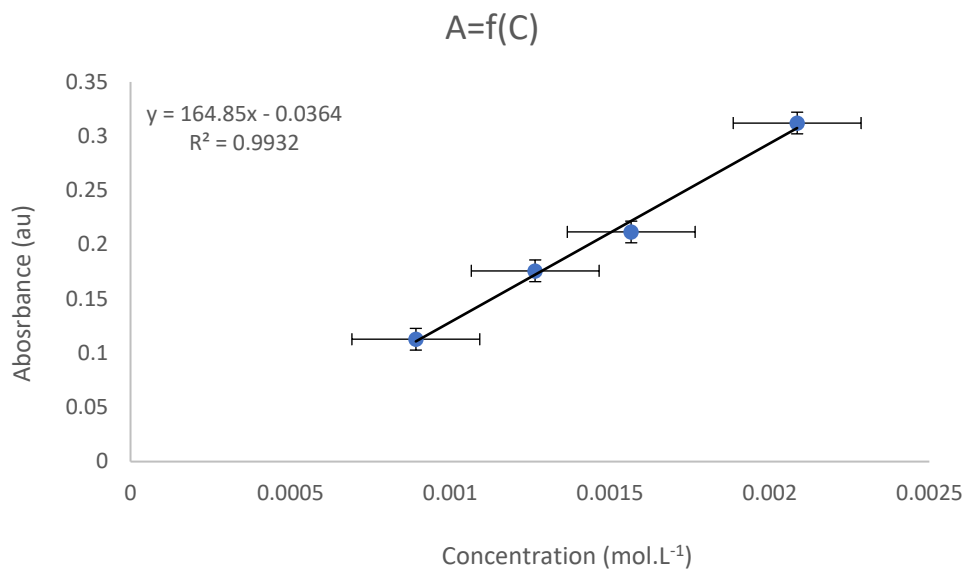


Figure S3. 19 Plot of absorbance VS concentration for 3.4 in toluene at $\lambda = 549$ nm.

Study of 3.4_{Er}

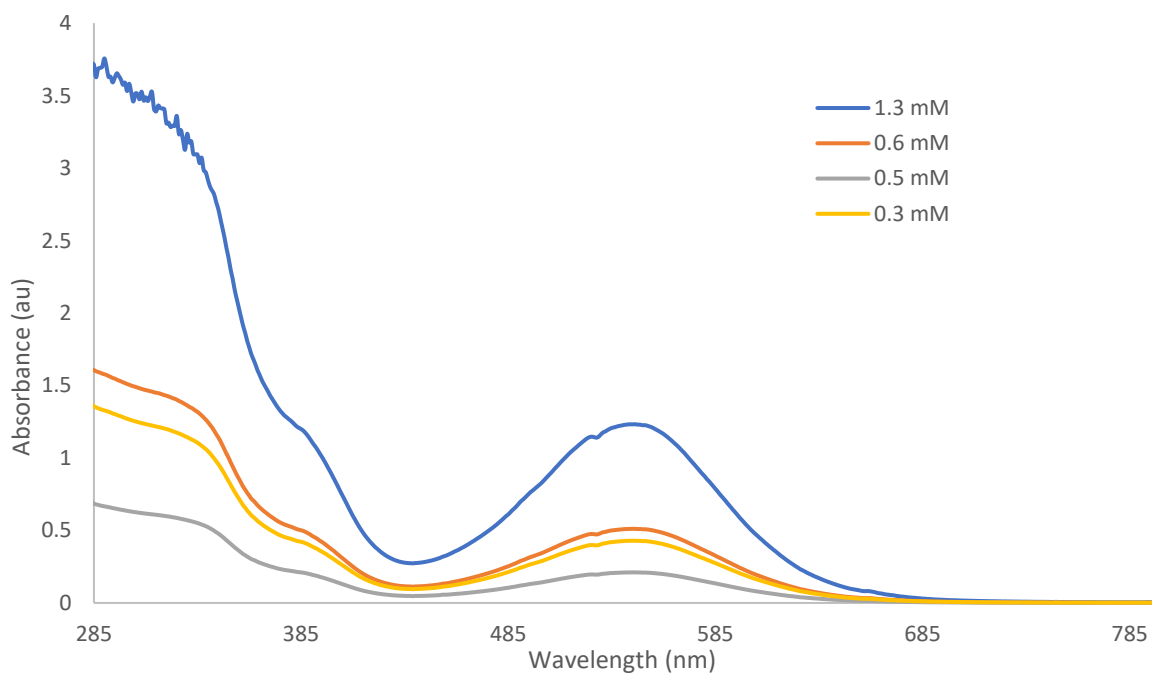


Figure S3. 20 UV-visible spectra of 3.4_{Er}.

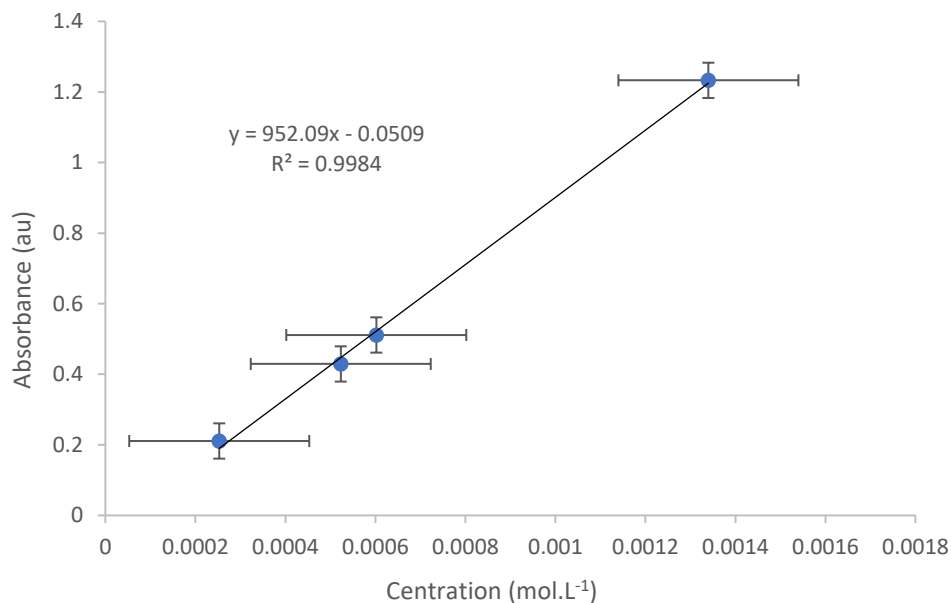


Figure S3. 21 Plot of absorbance VS concentration for 3.4_{Er} in toluene at $\lambda = 546$ nm.

VII. Computation studies

Computations were performed in collaboration with Léo La Droitte et Dr. Boris Le Guennic, the necessary information were presented in the manuscript. The general details of the computations are presented below.

The atomic positions were extracted from the X-ray diffraction crystal structures. Structure optimizations were performed using density functional theory (DFT) as implemented in the 2017 release of the Amsterdam Density Functional (ADF) package.^{9–11} The exchange-correlation was treated within the generalized gradient approximation (GGA) using the revPBE functional.^{12–14} The scalar relativistic (SR) effects were treated within the zeroth-order regular approximation (ZORA). All atoms were described using triple- ζ polarized all-electron Slater type basis (TZP). During the geometry optimization, only H positions are allowed to relax while all other positions are kept frozen

All wave function-based calculations were performed using the State-Averaged Complete Active Space Self-Consistent Field approach with Restricted-Active-Space-State-Interaction method (SA-CASSCF/RASSI-SO), as implemented in the OpenMolcas quantum-chemistry package.¹⁵ In this approach, the relativistic effects are treated in two steps on the basis of the Douglas–Kroll Hamiltonian.¹⁶ The scalar terms are included in the basis-set generation and are used to determine the CASSCF wave functions and energies.¹⁷ Spin-orbit coupling is then added within the RASSI-SO method, which mixes the calculated CASSCF wave functions.^{18,19} Spin-orbit (SO) integrals are calculated using the AMFI (atomic mean-field integrals)

approximation.²⁰ The resulting spin-orbit wave functions and energies are used to compute the magnetic properties and g-tensors of the ground state multiplet following the pseudospin $S = 1/2$ formalism, as implemented in the SINGLE_ANISO routine.²¹ Cholesky decomposition of the bielectronic integrals was employed to save disk space and to speed up the calculations.²²

References

- (1) Anatolii A. Fagin, M. N. B. **1999**, *5* (10), 2990–2992.
- (2) Evans, W. J.; Allen, N. T.; Ziller, J. W. *J. Am. Chem. Soc.* **2000**, *122* (47), 11749–11750.
- (3) Reiners, M.; Ehrlich, N.; D. Walter, M. *Inorganic Synthesis*; 2018; Vol. 18, pp 199–204.
- (4) Lalancette, J.-M.; Rollin, G.; Dumas, P. *Can. J. Chem.* **1972**, *50* (18), 3058–3062.
- (5) Bergbreiter, D. E.; Killough, J. M. *J. Am. Chem. Soc.* **1978**, *100* (7), 2126–2134.
- (6) Sheldrick, G. M. *Acta Crystallogr. A* **2008**, *64* (1), 112–122.
- (7) Sheldrick, G. M. *Acta Crystallogr. Sect. Found. Adv.* **2015**, *71* (1), 3–8.
- (8) Dolomanov, O. V.; Bourhis, L. J.; Gildea, R. J.; Howard, J. A. K.; Puschmann, H. *J. Appl. Crystallogr.* **2009**, *42* (2), 339–341.
- (9) Te Velde, G.; Bickelhaupt, F. M.; Baerends, E. J.; Fonseca Guerra, C.; Van Gisbergen, S. J. A.; Snijders, J. G.; Ziegler, T. *J. Comput. Chem.* **2001**, *22* (9), 931–967.
- (10) Fonseca Guerra, C.; Snijders, J. G.; Te Velde, G.; Baerends, E. J. *Theor. Chim. Acta* **1998**, *99* (6), 391–403.
- (11) ADF 2017, SCM Theoretical Chemistry, Vrije Universiteit, Amsterdam, The Netherlands <http://www.scm.com>.
- (12) Perdew, J. P.; Burke, K.; Ernzerhof, M. *Phys. Rev. Lett.* **1996**, *77* (18), 3865–3868.
- (13) Ernzerhof, M.; Scuseria, G. E. *J. Chem. Phys.* **1999**, *110*, 5029.
- (14) Lenthe, E. V.; Baerends, E. J. *J. Chem. Phys.* **1993**, *99*, 4597.
- (15) Fdez. Galván, I.; Vacher, M.; Alavi, A.; Angeli, C.; Aquilante, F.; Autschbach, J.; Bao, J. J.; Bokarev, S. I.; Bogdanov, N. A.; Carlson, R. K.; Chibotaru, L. F.; Creutzberg, J.; Dattani, N.; Delcey, M. G.; Dong, S. S.; Dreuw, A.; Freitag, L.; Frutos, L. M.; Gagliardi, L.; Gendron, F.; Giussani, A.; González, L.; Grell, G.; Guo, M.; Hoyer, C. E.; Johansson, M.; Keller, S.; Knecht, S.; Kovačević, G.; Källman, E.; Li Manni, G.; Lundberg, M.; Ma, Y.; Mai, S.; Malhado, J. P.; Malmqvist, P. Å.; Marquetand, P.; Mewes, S. A.; Norell, J.; Olivucci, M.; Oppel, M.; Phung, Q. M.; Pierloot, K.; Plasser, F.; Reiher, M.; Sand, A. M.; Schapiro, I.; Sharma, P.; Stein, C. J.; Sørensen, L. K.; Truhlar, D. G.; Ugandi, M.; Ungur, L.; Valentini, A.; Vancoillie, S.; Veryazov, V.; Weser, O.; Wesolowski, T. A.; Widmark, P.-O.; Wouters, S.; Zech, A.; Zobel, J. P.; Lindh, R. *J. Chem. Theory Comput.* **2019**, *15* (11), 5925–5964.
- (16) Hess, B. *Phys. Rev. A* **1986**, *33* (6), 3742–3748.
- (17) Roos, B. O.; Taylor, P. R.; Sigbahn, P. E. M. **1980**, *48* (2), 157–173.
- (18) Malmqvist, P. Å.; Roos, B. O.; Schimmelpfennig, B. *Chem. Phys. Lett.* **2002**, *357* (3–4), 230–240.
- (19) Malmqvist, P.-Å.; Roos, B. O. *Chem. Phys. Lett.* **1989**, *155* (2), 189–194.
- (20) Heß, B. A.; Marian, C. M.; Wahlgren, U.; Gropen, O. *Chem. Phys. Lett.* **1996**, *251* (5–6), 365–371.
- (21) Chibotaru, L. F.; Ungur, L. *J. Chem. Phys.* **2012**, *137* (6), 064112.
- (22) Ungur, L.; Van Den Heuvel, W.; Chibotaru, L. F. *New J. Chem.* **2009**, *33* (6), 1224.

Supplementary information for Chapter 4:

I. General information	279
II. Synthetic details	280
III. NMR characterization	284
IV. XRD characterization	292
V. UV-visible spectroscopy	315
VI. Isomerization reactions	320
References	324

I. General information

All air- and moisture-sensitive reactions were performed using standard Schlenk-line techniques under dry N₂ or Ar atmosphere or in argon-filled gloveboxes (MBraun). All glassware was dried at 140 °C for at least 12 h prior to use. All solvents (Et₂O, toluene, benzene, pentane, C₆D₆, tol-d₈, THF-d₈) were dried over sodium, degassed, and transferred under reduced pressure in a cold flask. Acetonitrile, deuterated acetonitrile and deuterated methylene chloride were dried over CaH₂, degassed, and transferred under reduced pressure in a cold flask. KC₈, K₂Cot, KCnt and were prepared according to literature procedures.¹⁻⁴ Precursors of the type LnCotI(thf)_n were synthesized according to published literature for Ln = Sm^{5,6} and adapted synthesis for Ln = Tb-Ho⁷. All other chemicals were obtained from commercial sources and used without further purification. ¹H NMR spectra were recorded in 5 mm tubes adapted with a J. Young valve on a Bruker Avance III-300 MHz spectrometer and chemical shifts are expressed relative to internal solvent references in ppm. UV-visible absorption spectra were recorded on a Cary60 spectrometer in quartz cuvettes adapted with a J. Young valve. Elemental analyses were obtained from Mikroanalytisches Labor Pascher (Remagen, Germany).

II. Synthetic details

General synthesis for 4.1_{Ln}

LnI₃ (1 equiv.) and K₂Cot (1.05 equiv.) were weighted in different vials and suspended in THF. The resulting mixtures were placed at low temperature for 20 min. The cold solution of K₂Cot was added dropwise on the stirring suspension of the lanthanide salt. The mixture was allowed to warm up and stir for 12 h at r.t.. The supernatant was then filtered, concentrated, and cooled to -40°C to yield LnCotI(thf)_n (n = 2, 3) as crystals suitable for XRD.

General synthesis for 4.2_{Ln}^{cis}

A mixture of LnCotI(thf)_n (n = 2, 3) (1.05 equiv.) and KCnt (1 equiv.) in toluene and acetonitrile (10:1) was allowed to stir at room temperature. After 12 h, the vessel was protected from light and the solvent were removed under reduced pressure. The reaction mixture was then suspended in toluene. The evaporation / suspension in toluene step was repeated once. The colored supernatant was then filtered and concentrated to yield LnCot(*cis*-Cnt). The desired compound can be obtained as microcrystalline powder through toluene extraction and evaporation. XRD suitable crystals were obtained by concentration of the toluene solution at -40°C.

Additional considerations: The light protection steps has been added to the general procedure after discovering the impact on the isomerization reaction. As such, the 4.2_{Ln}^{cis} compounds presented here after were obtained without it and characterized as purely *cis* through single crystal XRD. There is a possibility that the bulk micro-crystalline powder featured *trans* compounds which was not identified at the time.

General synthesis for 4.2_{Ln}^{trans}

All steps are protected from light. A mixture of LnCotI(thf)_n (n = 2, 3) (1 equiv.) and KCnt (1 equiv.) in toluene was protected from light with aluminum foil and allowed to stir. After 14 h, the supernatant was filtered, concentrated, and cooled to yield a mixture of isomers with a high ratio of LnCot(*trans*-Cnt). The desired compound can be obtained as microcrystalline powder through toluene extraction and slow evaporation of dryness. XRD suitable crystals were obtained by concentration of the toluene solution at -40 °C.

Synthesis of 4.1_{La}

Synthesized according to general procedure with LaI₃ (208.0 mg, 0.40 mmol, 1.0 equiv.) and K₂Cot (76.6 mg, 0.42 mmol, 1.05 equiv.).

4.1_{La} was obtained as yellowish crystals (179.8 mg, 0.31 mmol, 77 %)

¹H NMR (300 MHz, thf-*d*₃, 293 K): δ (ppm), 6.30 (s, 8H, Cot), *coordinated thf molecules are not visible*.

Synthesis of **4.1_{Ce}**

Synthesized according to general procedure with CeI₃ (123.8 mg, 0.24 mmol, 1.0 equiv.) and K₂Cot (45.5 mg, 0.25 mmol, 1.05 equiv.).

4.1_{Ce} was obtained as deep yellow crystals (100.0 mg, 0.17 mmol, 71 %)

¹H NMR (300 MHz, thf-*d*₈, 293 K): δ (ppm), 2.66 (s br, 8H, Cot), *coordinated thf molecules are not visible*.

Synthesis of **4.1_{Pr}**

Synthesized according to general procedure with PrI₃ (217.6 mg, 0.42 mmol, 1.0 equiv.) and K₂Cot (79.9 mg, 0.44 mmol, 1.05 equiv.).

4.1_{Pr} was obtained as yellow crystals (205.6 mg, 0.35 mmol, 84 %)

¹H NMR (300 MHz, thf-*d*₈, 293 K): δ (ppm), 8.04 (s, 8H, Cot), *coordinated thf molecules are not visible*.

Synthesis of **4.1_{Gd}**

Synthesized according to general procedure with GdI₃ (126.4mg, 0.24 mmol, 1.0 equiv.) and K₂Cot (45.0 mg, 0.25 mmol, 1.05 equiv.).

4.1_{Gd} was obtained as yellowish crystals (79.9 mg, 0.15 mmol, 63 %)

¹H NMR (300 MHz, thf-*d*₈, 293 K): δ (ppm), 95.11 (s br, 8H, Cot), *coordinated thf molecules are not visible*.

Synthesis **4.2_{La}^{cis}**

Synthesized according to general procedure with **4.1_{La}** (61.1 mg, 0.10 mmol, 1.0 equiv.) and KCnt (17.2 mg, 0.11 mmol, 1.05 equiv.)

4.2_{La}^{cis} was identified as small orange needles through single-crystal diffraction methods.

Yield: orange micro-crystalline powder (26.9 mg, 0.07 mmol, 71 %)

¹H NMR (300 MHz, dichloromethane-*d*₂, 293 K): δ (ppm), 7.53 (s, 9H, Cnt), 6.03 (s, 8H, Cot)

Synthesis **4.2_{Ce}^{cis}**

Synthesized according to general procedure with **4.1_{Ce}** (1.0 equiv.) and KCnt (1.05 equiv.)

4.2_{Ce}^{cis} was identified as small green needles through single-crystal diffraction methods.

¹H NMR (300 MHz, toluene-*d*₈, 293 K): δ (ppm), 6.22 (br s, 8H, Cot), 4.56 (br s, 9H, Cnt)

Synthesis **4.2_{Pr}^{cis}**

Synthesized according to general procedure with **4.1_{Pr}** (70.9 mg, 0.12 mmol, 1.0 equiv.) and KCnt (19.9 mg, 0.13 mmol, 1.05 equiv.)

4.2_{Pr}^{cis} was identified as small pale needles through single-crystal diffraction methods.

Yield: light brown micro-crystalline powder (25.6 mg, 0.071 mmol, 59 %)

Synthesis **4.2_{Nd}^{cis}**

Synthesized according to general procedure with **4.1_{Nd}** (72.1 mg, 0.12 mmol, 1.0 equiv.) and KCnt (20.4 mg, 0.13 mmol, 1.05 equiv.)

4.2_{Nd}^{cis} was identified as small green needles through single-crystal diffraction methods.

Yield: greenish micro-crystalline powder (24.0 mg, 0.065 mmol, 54 %)

¹H NMR (300 MHz, toluene-*d*₈, 293 K): δ (ppm), 1.43 (br s, 9H, Cnt), -13.70 (br s, 8H, Cot)

Synthesis **4.2_{Sm}^{cis}**

Synthesized according to general procedure with **4.1_{Sm}** (100 mg, 0.17 mmol, 1 equiv.) and KCnt (25 mg, 0.18 mmol, 1 equiv.)

4.2_{Sm}^{cis} was identified as small green needles through single-crystal diffraction methods.

Yield: green crystals (24 mg, 38 %)

¹H NMR (300 MHz, toluene-*d*₈, 293 K): δ (ppm) 16.47 (br s, 8H, Cot), 11.39 (s, 9H, Cnt)

Synthesis **4.2_{Gd}^{cis}**

Synthesized according to general procedure with **4.1_{Gd}** (79.9 mg, 0.15 mmol, 1.0 equiv) and KCnt (24.8 mg, 0.16 mmol, 1.05 equiv).

4.2_{Gd}^{cis} was identified as small orange needles through single-crystal diffraction methods.

¹H NMR (300 MHz, toluene-*d*₈, 293 K): δ (ppm), 97.88 (br s), 23.45 (br s)

Synthesis **4.2_{Tb}^{cis}**

Synthesized according to general procedure with **4.1_{Tb}** (154.4 mg, 0.29 mmol, 1.0 equiv.) and KCnt (46.9 mg, 0.30 mmol, 1.05 equiv.).

4.2_{Tb}^{cis} was identified as small orange needles through single-crystal diffraction methods.

Yield: yellow-orange micro-crystalline powder (32 mg, 0.084 mmol, 29 %)

¹H NMR (300 MHz, toluene-*d*₈, 293 K): δ (ppm) 246.25 (s, 8H, Cot), 101.59 (s, 9H, Cnt)

Synthesis **4.2_{La}^{trans/cis}**

Synthesized according to general procedure with **4.1_{La}** (64.7 mg, 0.11 mmol, 1.00 equiv.) and KCnt (18.7 mg, 0.12 mmol, 1.09 equiv.)

4.2_{La}^{trans/cis} was obtained as small orange crystalline needles (4.0 mg, 0.01 mmol, 10 % yield)

¹H NMR (300 MHz, dichloromethane-*d*₂, 293 K): δ (ppm) 7.52 (s, Cnt^{cis}), 7.50(s, Cnt^{trans}), 6.96 (m, Cnt^{trans}), 6.83(m, Cnt^{trans}), 6.12 (s, Cot-*trans*), 6.02(s, Cot-*cis*), -3.92 (t, Cnt^{trans}, J = 12 Hz)

Synthesis 4.2_{Ce}^{trans/cis}

Synthesized according to general procedure with 4.1_{Ce} (58.2 mg, 0.099 mmol, 1 equiv.) and KCnt (15.8 mg, 0.10 mmol, 1.01 equiv.)

4.2_{Ce}^{trans/cis} was obtained as small green crystalline needles (4.3 mg, 0.012 mmol, 12 % yield)

¹H NMR (300 MHz, dichloromethane-*d*₂, 293 K): δ (ppm) 25.68 (br s, Cnt^{trans}), 15.55 (br s, Cnt^{trans}), 6.75 (br s, Cnt^{cis}), 4.46 (br s, Cot-*Cis*), 3.36 (br s, Cot-*trans*), -16.23 (br s, Cnt^{trans}), -50.30 (br s, Cnt^{trans})

Synthesis 4.2_{Pr}^{trans/cis}

Synthesized according to general procedure with 4.1_{Pr} (65.5 mg, 0.11 mmol, 1 equiv.) and KCnt (18.9 mg, 0.12 mmol, 1.09 equiv.)

4.2_{Pr}^{trans/cis} was obtained as small orange crystalline needles (5.6 mg, 0.015 mmol, 14 % yield)

Synthesis 4.2_{Nd}^{trans/cis}

Synthesized according to general procedure with 4.1_{Nd} (62.2 mg, 0.105 mmol, 1 equiv.) and KCnt (17.2 mg, 0.109 mmol, 1.04 equiv.)

4.2_{Nd}^{trans/cis} was obtained as small orange crystalline needles (5.3 mg, 0.014 mmol, 14% yield)

¹H NMR (300 MHz, dichloromethane-*d*₂, 293 K): δ (ppm) 21.16 (br s, 2H, Cnt^{trans}), 7.19 (br s, 2H, Cnt^{trans}), -6.68 (br s, 2H, Cnt^{trans}), -13.84 (br s, 8H, Cot), -26.83 (br s, 2H, Cnt^{trans}) (*only the peaks from the trans can be observed*)

Synthesis 4.2_{Sm}^{trans/cis}

Synthesized according to general procedure with 4.1_{Sm} (52 mg, 0.09 mmol, 1 equiv.) and KCnt (14 mg, 0.17 mmol, 1 equiv.)

4.2_{Sm}^{trans/cis} was obtained as brownish crystalline needles (5.2 mg, 15 %)

¹H NMR (300 MHz, toluene-*d*₈, 293 K): δ (ppm) 16.41 (s, Cot-*cis*), 15.55 (s, Cot-*trans*), 14.97 (s, Cnt^{trans}), 14.53 (d, Cnt^{trans}, J = 15 Hz), 11.35 (s, Cnt^{cis}), 10.96 (s, Cnt^{trans}), 6.15 (s, Cnt^{trans}), -40.54 (s, Cnt^{trans})

Synthesis 4.2_{Tb}^{trans/cis}

Synthesized according to general procedure with 4.1_{Tb} (42.2 mg, 0.079 mmol, 1.00 equiv.) and KCnt (13.0 mg, 0.083 mmol, 1.05 equiv.)

4.2_{Tb}^{trans/cis} was obtained as small orange crystalline needles (8.0 mg, 0.021 mmol, 27 % yield)

¹H NMR (300 MHz, toluene-*d*₈, 293 K): δ (ppm), 404.98 (s, Cnt^{trans}), 247.60 (s, Cot-*cis*), 230.40 (s, Cot-*trans*), 203.94 (s, Cnt^{trans}), 165.17 (s, Cnt^{trans}), 103.20 (s, Cnt^{cis}), -163.06 (s, Cnt^{trans})

Synthesis 4.2_{Dy}^{trans/cis}

Synthesized according to general procedure with **4.1_{Dy}** (67.7 mg, 0.126 mmol, 1.00 equiv.) and KCnt (21.1 mg, 0.134 mmol, 1.06 equiv.)

4.2_{Dy}^{trans/cis} was obtained as small orange crystalline needles (4.5 mg, 9 %)

¹H NMR (300 MHz, dichloromethane-*d*₂, 293 K): δ (ppm), 158.33 (br s, Cnt^{trans}), 115.04 (br s, Cnt^{cis}), 99.55 (br s, Cnt^{trans}), 72.10 (br s, Cot), 44.47 (br s, Cnt^{trans}), -168.91 (br s, Cnt^{trans})

Synthesis 4.2_{Ho}^{trans/cis}

Synthesized according to general procedure with **4.1_{Ho}** (54.8 mg, 0.101 mmol, 1.00 equiv.) and KCnt (16.6 mg, 0.106 mmol, 1.05 equiv.)

4.2_{Ho}^{trans/cis} was obtained as small orange crystalline needles (5.7 mg, 15 %)

¹H NMR (300 MHz, dichloromethane-*d*₂, 293 K): δ (ppm) 198.17 (br s, Cnt^{trans}), 101.99 (br s, Cnt^{trans}), 87.22 (br s, Cnt^{cis}), 66.81 (br s, Cot-*trans*); 57.81 (br s, Cot-*cis*), 18.98 (br s, Cnt^{trans}), -124.84 (br s, Cnt^{trans})

III. NMR characterization

¹H NMR of **4.1_{Pr}**

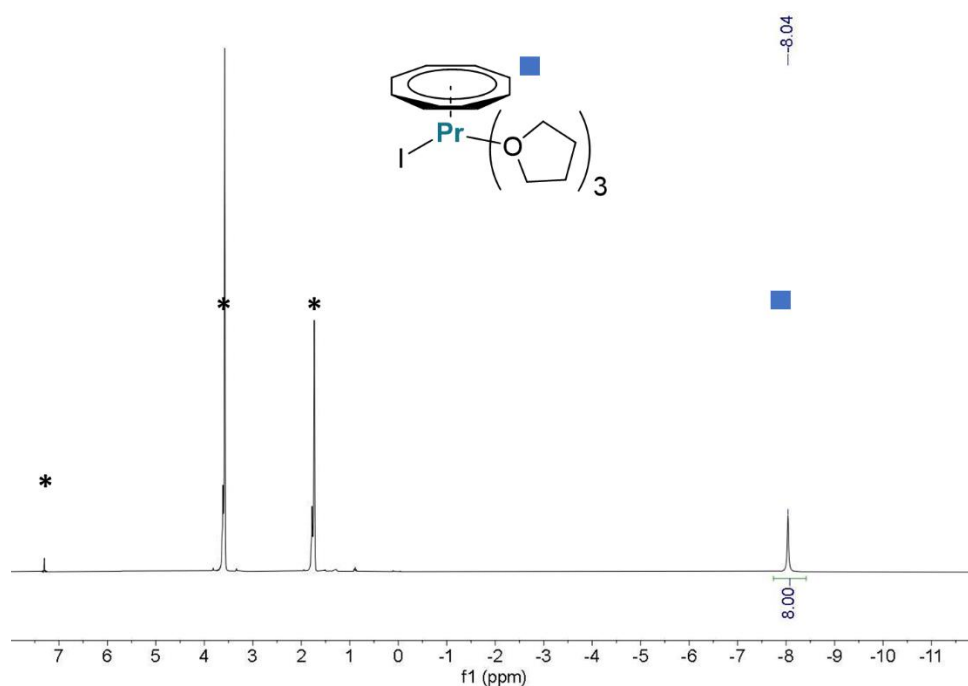


Figure S4. 1 ¹H NMR of **4.1_{Pr}** in THF-*d*₈ measured at 293 K (* residual protio signal of the solvent and benzene impurity)

^1H NMR of 4.2La^{cis}

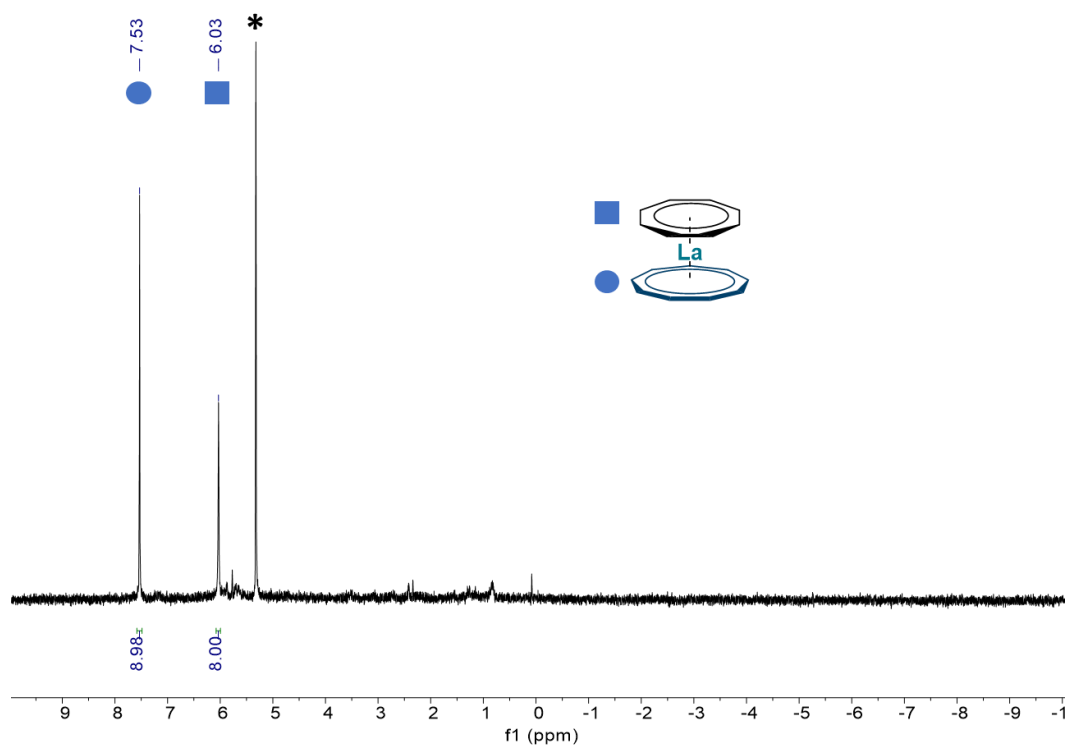


Figure S4. ^2H NMR of 4.2La^{cis} in dichloromethane- d_2 (* residual protio signal of the solvent and degradation product)

^1H NMR of $4.2\text{La}^{trans/cis}$

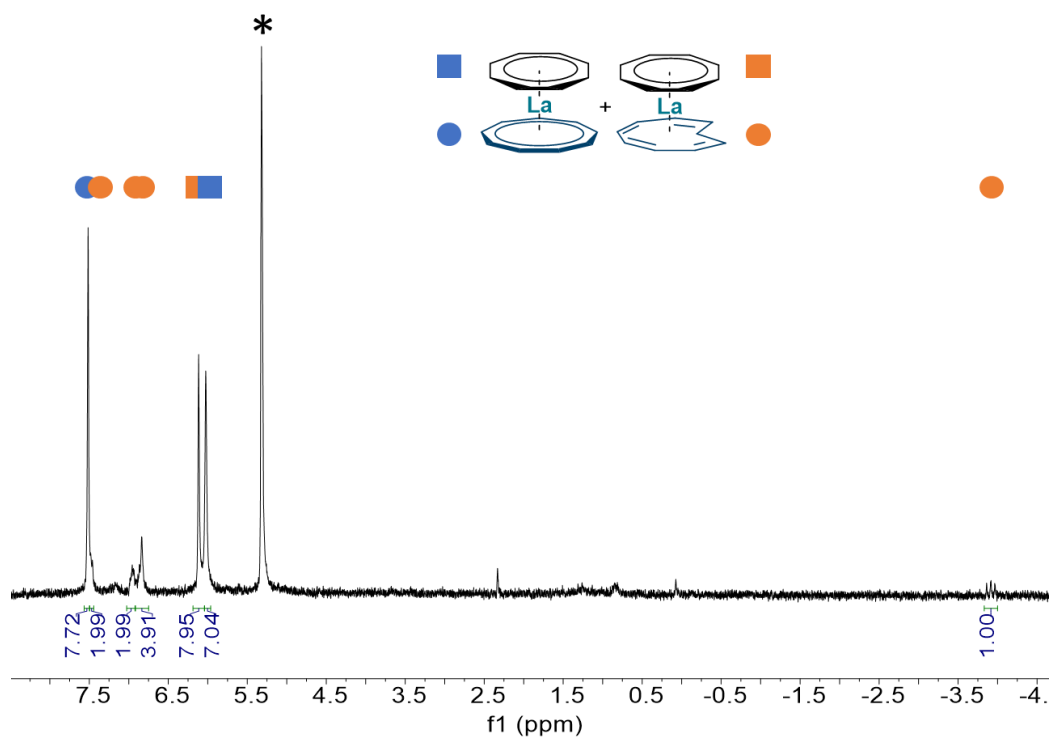


Figure S4. 3 ^1H NMR of $4.2\text{La}^{trans/cis}$ in dichloromethane- d_2 (* residual protio signal of the solvent and degradation product)

^1H NMR of $4.2_{\text{Ce}}^{\text{cis}}$

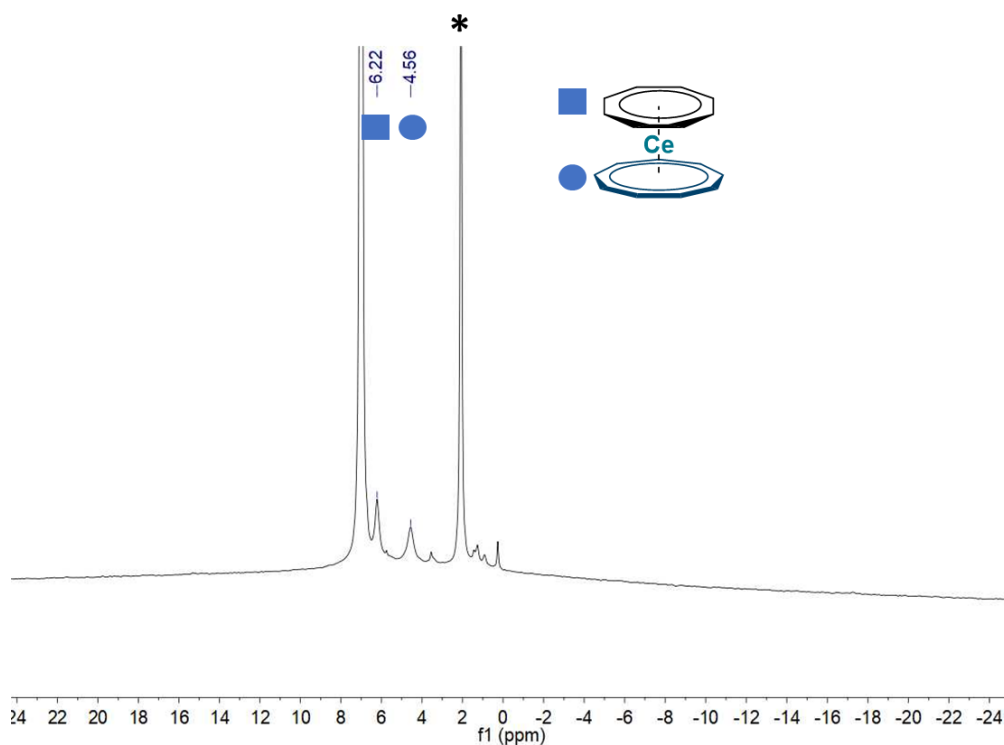


Figure S4. 4 ^1H NMR of $4.2_{\text{Ce}}^{\text{cis}}$ in dichloromethane- d_2 (* residual protio signal of the solvent and degradation product)

^1H NMR of $4.2_{\text{Ce}}^{\text{trans/cis}}$

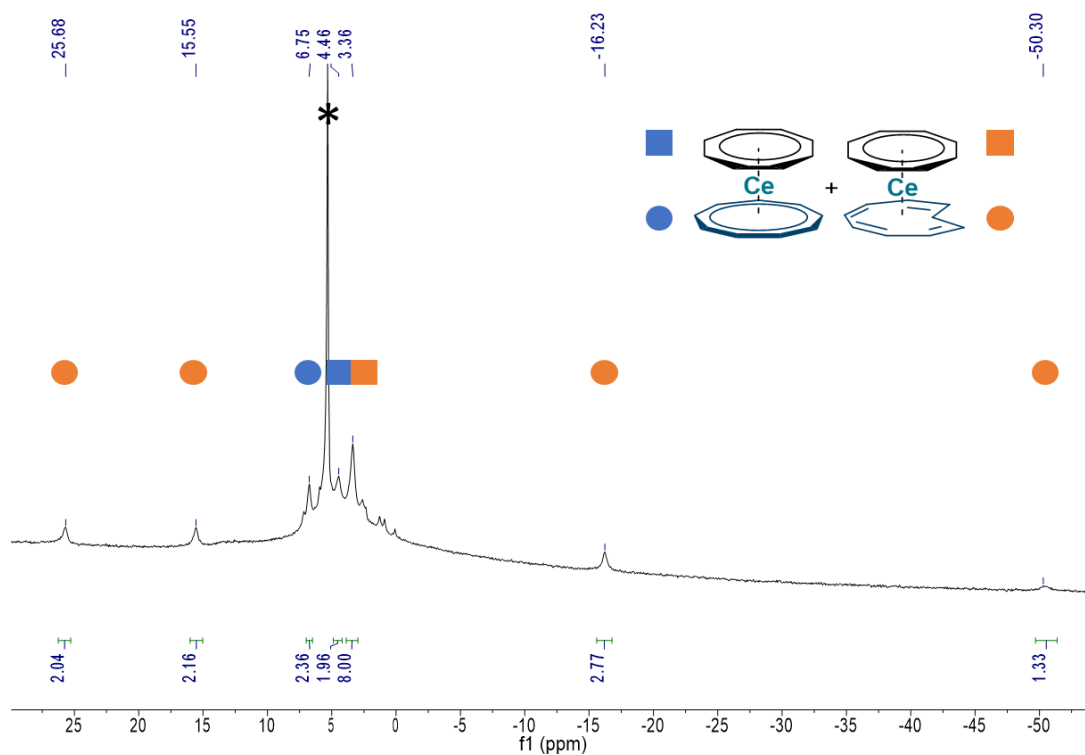


Figure S4. 5 ^1H NMR of $4.2_{\text{Ce}}^{\text{trans/cis}}$ in dichloromethane- d_2 (* residual protio signal of the solvent and degradation product)

^1H NMR of 4.2Nd^{cis}

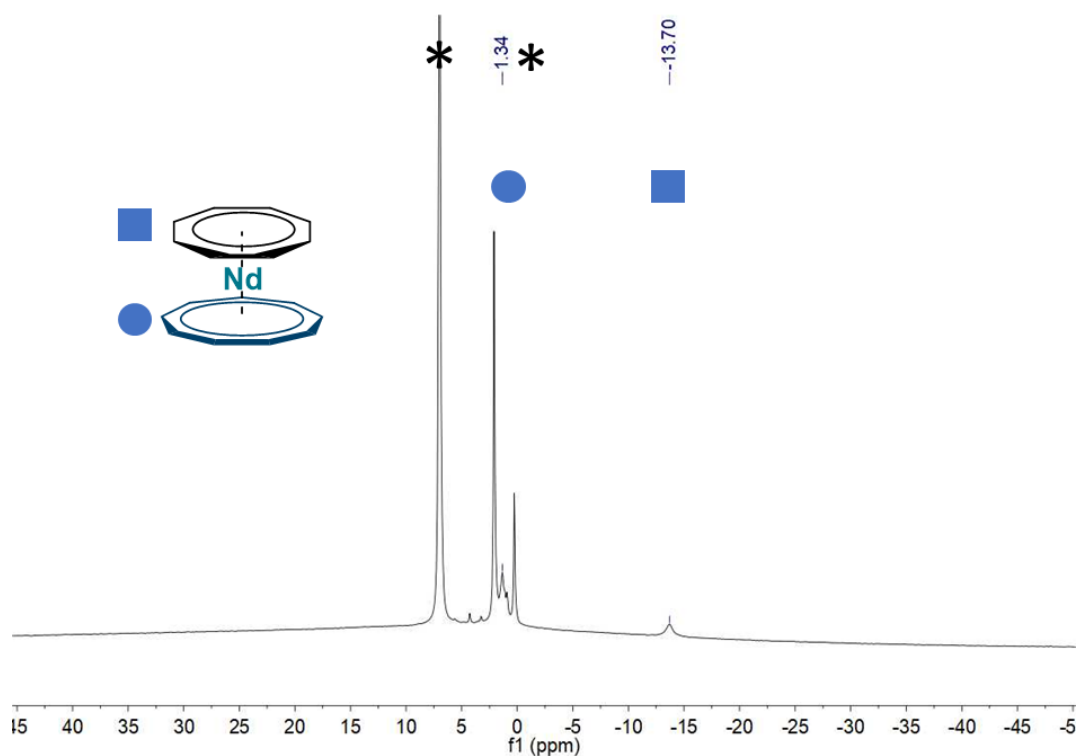


Figure S4. 6 ^1H NMR of 4.2Nd^{cis} in toluene-d_8 (* residual proton signal of the solvent and residual grease)

^1H NMR of $4.2\text{Nd}^{trans/cis}$

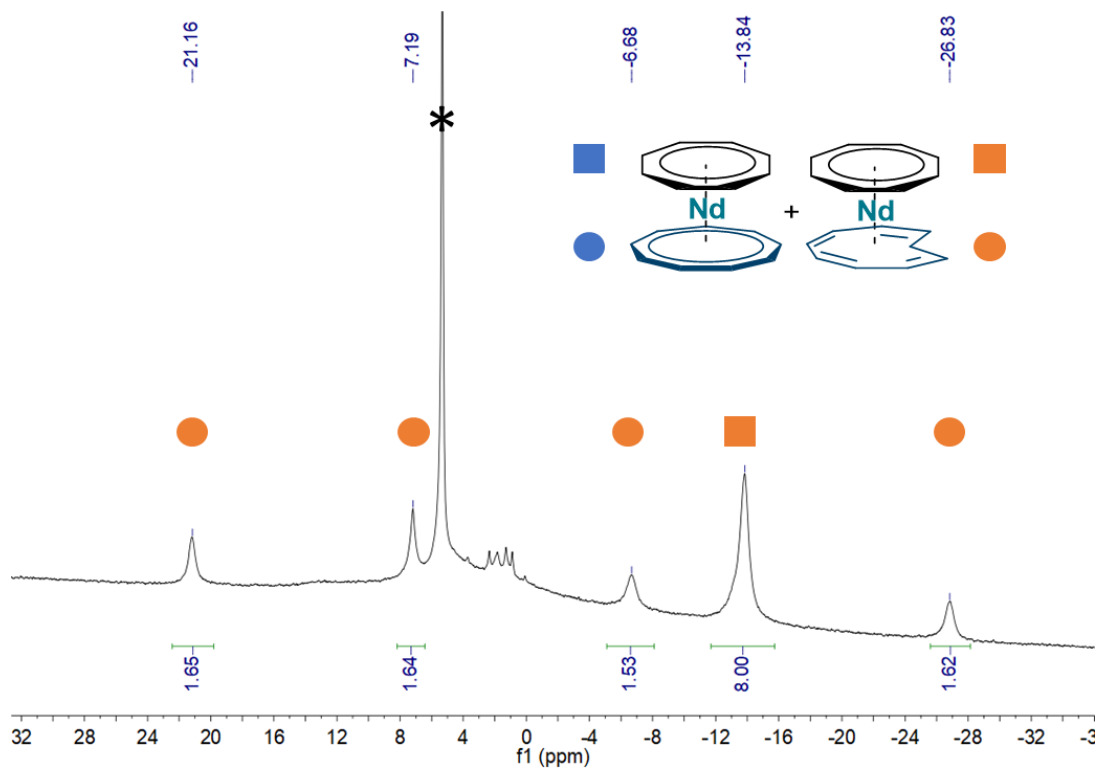


Figure S4. 7 ^1H NMR of $4.2\text{Nd}^{cis/trans}$ in $\text{dichloromethane-d}_2$ (* residual proton signal of the solvent, only the peaks from the trans analogue can be observed)

^1H NMR of $4.2_{\text{Sm}}^{\text{cis}}$

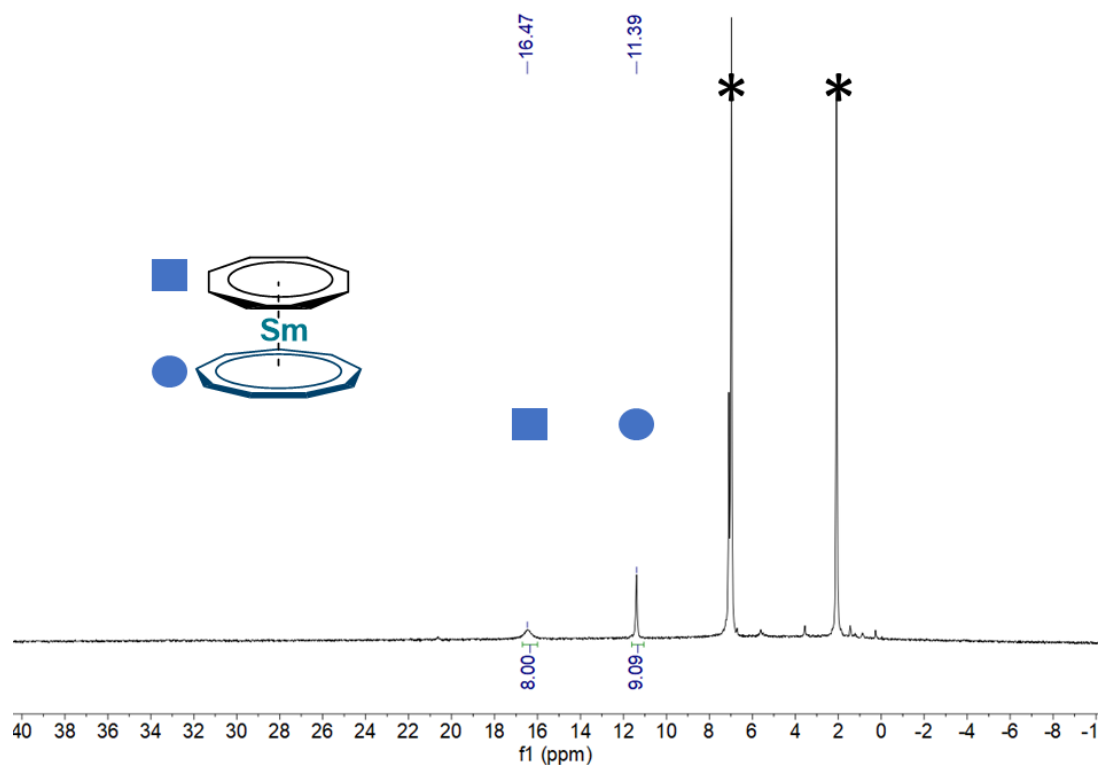


Figure S4. 8 ^1H NMR of $4.2_{\text{Sm}}^{\text{cis}}$ in toluene-d_8 (* residual protio signal of the solvent)

^1H NMR of $4.2_{\text{Sm}}^{\text{trans/cis}}$

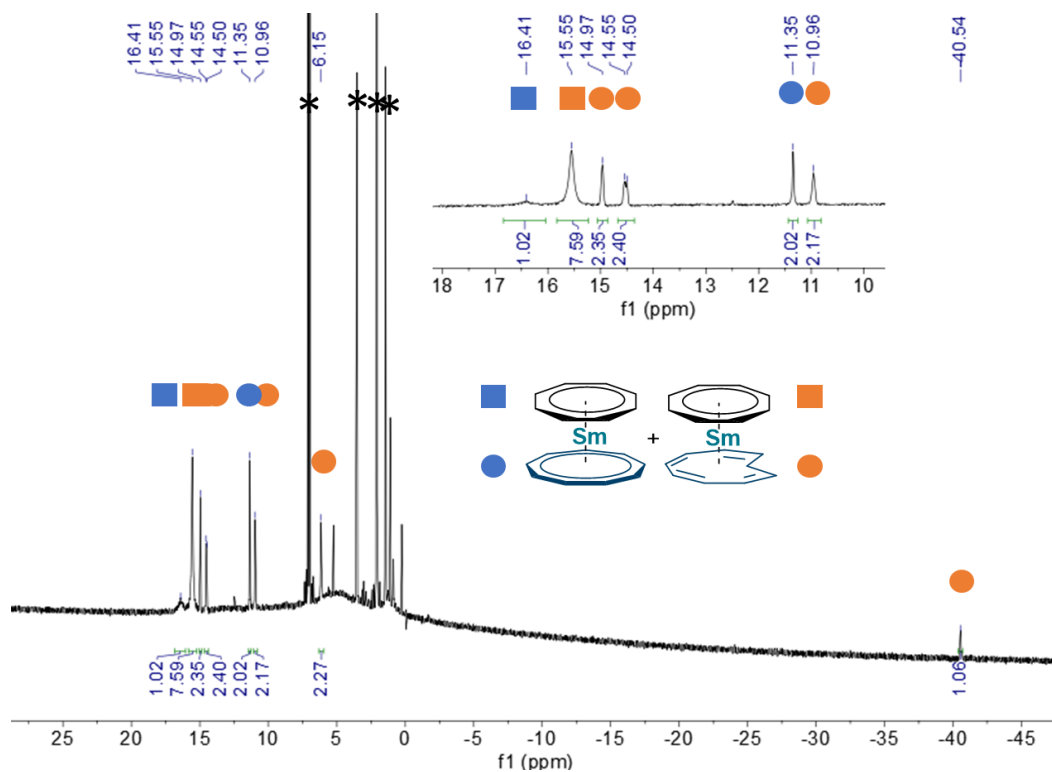


Figure S4. 9 ^1H NMR of $4.2_{\text{Sm}}^{\text{cis/trans}}$ in toluene-d_8 (* residual protio signal of the solvent)

^1H NMR of 2Gd^{cis}

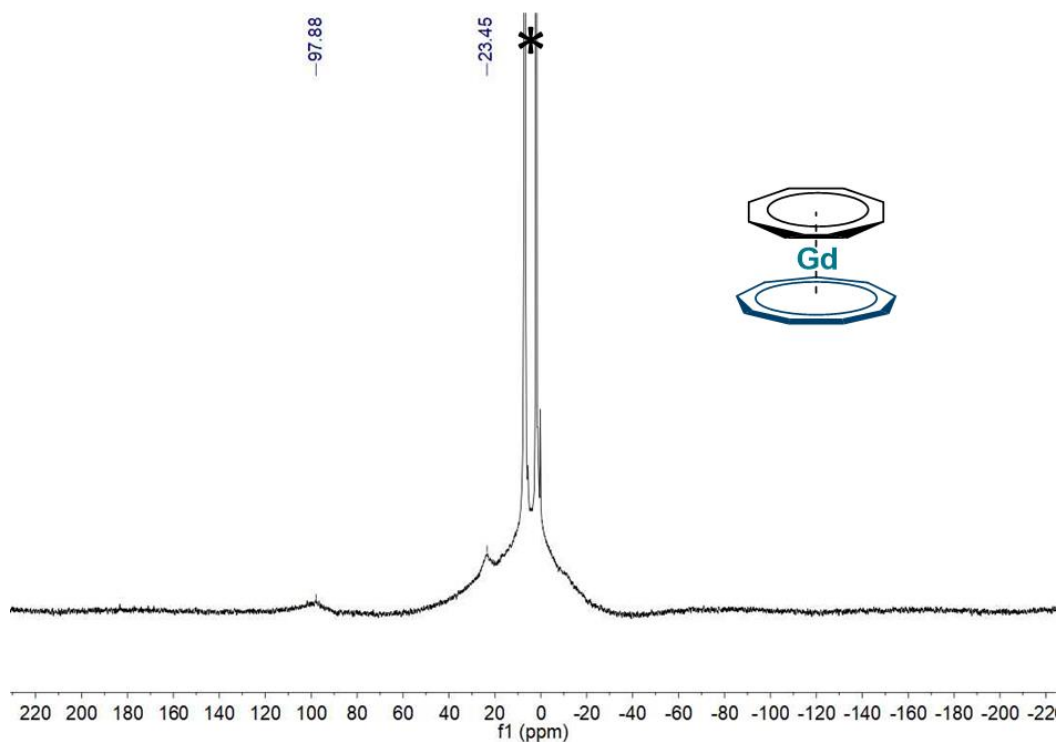


Figure S4. 10 ^1H NMR of 4.2Gd^{cis} in toluene-d_8 (* residual proton signal of the solvent)

^1H NMR of $4.2\text{Gd}^{trans/cis}$

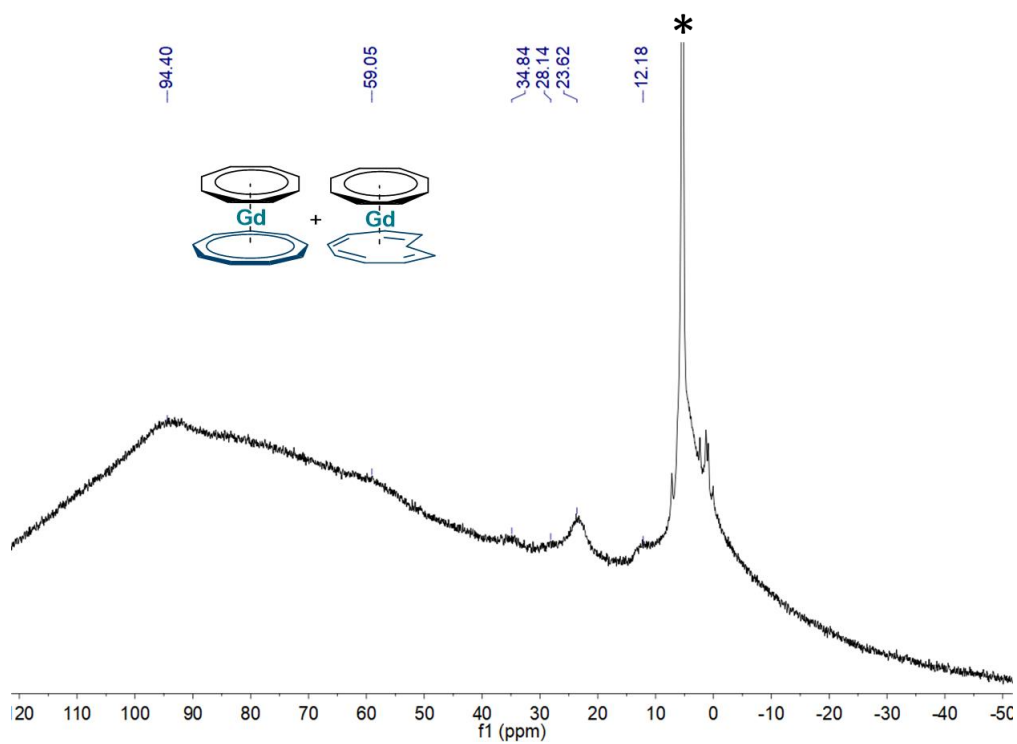


Figure S4. 11 ^1H NMR of $4.2\text{Gd}^{trans/cis}$ in $\text{dichloromethane-d}_2$ (* residual proton signal of the solvent)

^1H NMR of $4.2_{\text{Tb}}^{\text{cis}}$

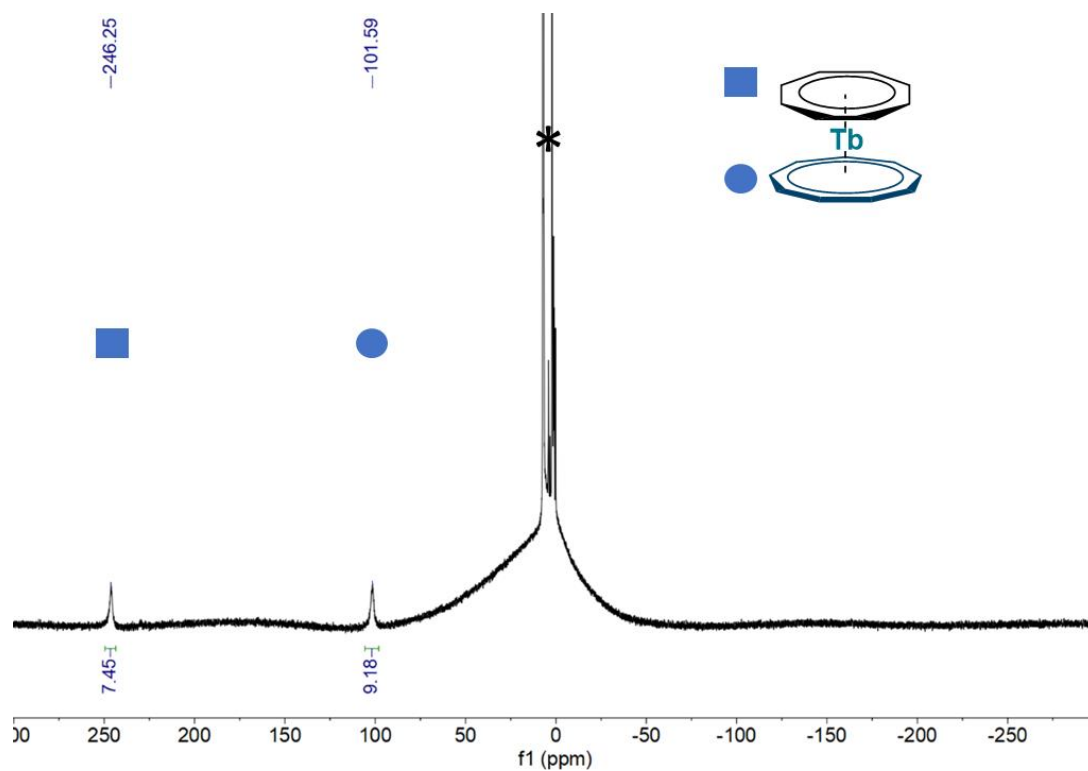


Figure S4. 12 ^1H NMR of $4.2_{\text{Tb}}^{\text{cis}}$ in toluene-d_8 (* residual protio signal of the solvent and degradation product)

^1H NMR of $4.2_{\text{Tb}}^{\text{trans/cis}}$

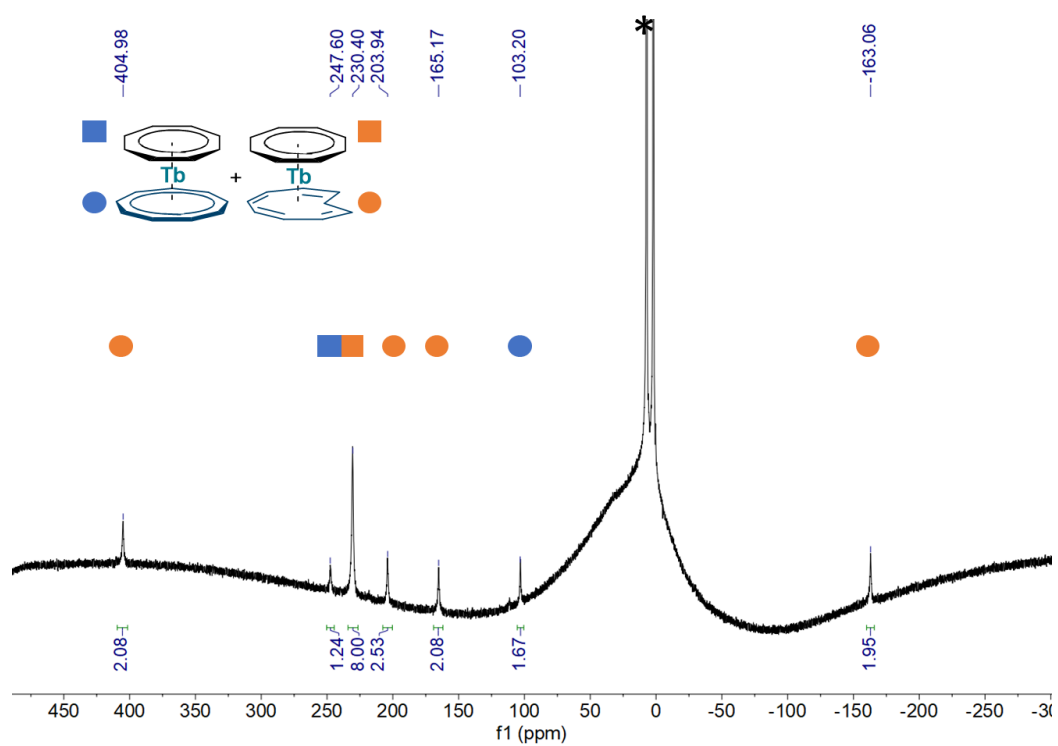


Figure S4. 13 ^1H NMR of $4.2_{\text{Tb}}^{\text{trans/cis}}$ in toluene-d_8 (* residual protio signal of the solvent and degradation product)

^1H NMR of $4.2_{\text{Dy}}^{\text{trans/cis}}$

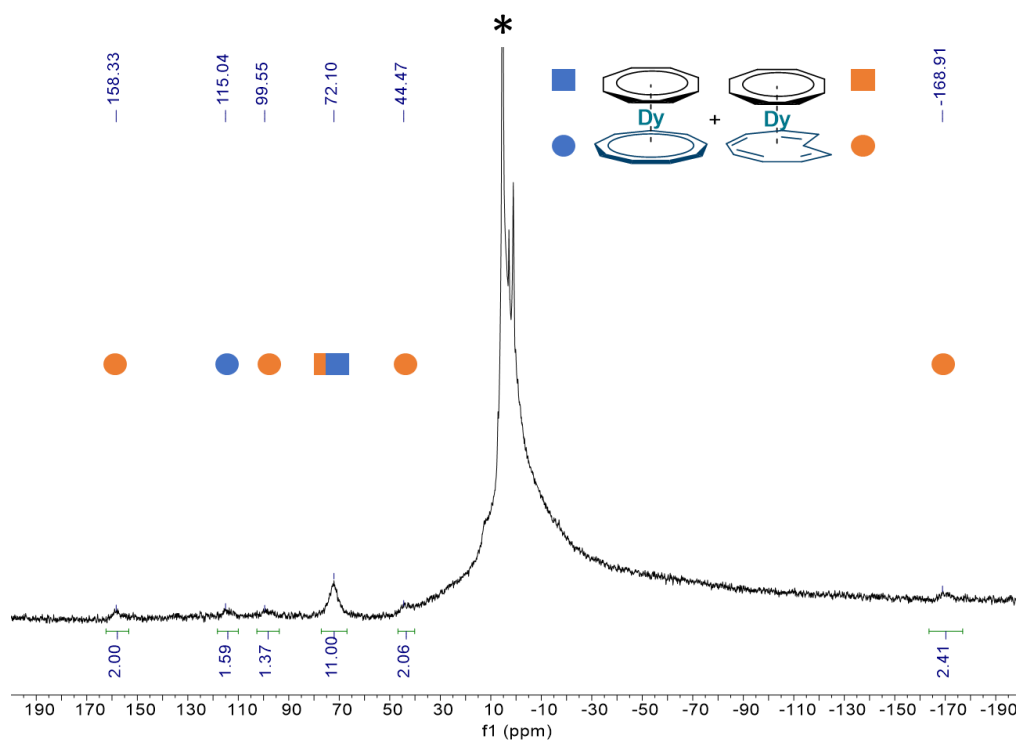


Figure S4. 14 ^1H NMR of $4.2_{\text{Dy}}^{\text{trans/cis}}$ in dichloromethane- d_2 (* residual protio signal of the solvent and degradation product)

^1H NMR of $4.2_{\text{Ho}}^{\text{trans/cis}}$

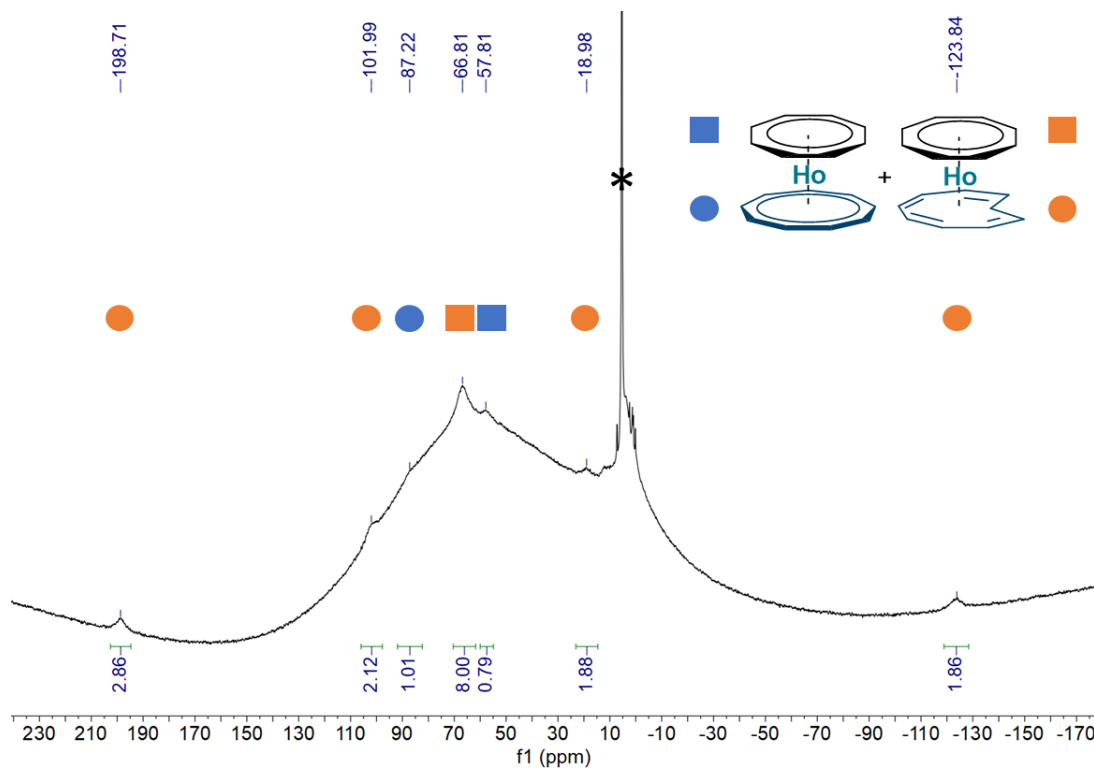


Figure S4. 15 ^1H NMR of $4.2_{\text{Ho}}^{\text{trans/cis}}$ in dichloromethane- d_2 (* residual protio signal of the solvent and degradation product)

IV. XRD characterization

1. General methods

Single crystals of the complexes suitable for X-ray analysis were mounted on a Kapton loop using a Paratone N oil. Two diffractometers were used during this for the data acquisition, either a Bruker diffractometer equipped with an APEX II CCD detector and a graphite Mo-K α monochromator or a Stoe stadivari diffractometer with a Eiger2 detector and a Mo-K α microsource. All measurements were done at 150 K (unless otherwise stated) and a refinement method was used for solving the structure. The resolution of the solid-state structure was accomplished using the SHELXS-97 or SHELXT programs.^{8,9} The refinement was performed with the SHELXL program using the Olex2 software.^{9,10} All atoms – except hydrogens – were refined anisotropically.

Atoms denoted C(X') refer to equivalent atoms constructed by the symmetry operation of the associated space group. For the Cnt ligand, the terme Cnt – 8C refers to the 8 atoms of the Cnt ligand excluding the isomerized atoms.

2. Summary of crystal data

Compound	4.1 _{Pr}	4.2 _{La} ^{cis}	4.2 _{Ce} ^{cis}
Formula	C ₂₀ H ₃₂ I ₃ O ₃ Pr	C ₁₇ H ₁₇ La	C ₁₇ H ₁₇ Ce
Crystal size (mm ³)	0.3 x 0.2 x 0.02	0.14 x 0.06 x 0.03	0.2x0.02x0.02
Crystal system	Orthorhombic	Orthorhombic	Orthorhombic
Space group	Pbca	Pnma	Pnma
Volume (Å ³)	4271.3(5)	1392.9(6)	1381.6(3)
a (Å)	12.9663(8)	12.187(3)	12.1258(14)
b (Å)	14.9636(9)	12.736(3)	12.7752(16)
c (Å)	22.0146(17)	8.974(2)	8.9190(10)
α (deg)	90	90	90
β (deg)	90	90	90
γ (deg)	90	90	90
Z	8	4	4
Formula weight (g/mol)	588.26	360.21	361.42
Density (calcd) (g/cm ³)	1.830	1.718	1.738
Absorption coefficient (mm ⁻¹)	3.742	3.046	3.273
F(000)	2304.0	704.0	708.0
Temp (K)	150.01	150.1	150
Diffractometer	Bruker APEX-II CCD	Bruker APEX-II CCD	Bruker APEX-II CCD
Radiation	MoKα (λ = 0.71073)	MoKα (λ = 0.71073)	MoKα (λ = 0.71073)
2θ range for data collection (deg)	4.55 to 71.672	5.554 to 54.958	5.57 to 56.544
Absorption correction	Multi-scan	Multi-scan	Multi-scan
Total no. reflections	47510	21648	27170
Unique reflections [R _{int}]	9992 [R _{int} = 0.0898]	1674 [R _{int} = 0.1354]	1786 [R _{int} = 0.0965]
Final R indices [I>2σ(I)]	R1 = 0.0398, wR2 = 0.0776	R ₁ = 0.0363, wR ₂ = 0.0785	R ₁ = 0.0267, wR ₂ = 0.0562
R indices (all data)	R1 = 0.0757, wR2 = 0.0930	R ₁ = 0.0879, wR ₂ = 0.0980	R ₁ = 0.0635, wR ₂ = 0.0676
Largest diff. peak and hole (e.Å ⁻³)	1.26/-1.52	0.72/-1.06	0.65/-0.76
Goof	1.011	1.011	1.009

Compound	4.2 _{Pr} ^{cis}	4.2 _{Nd} ^{cis}	4.2 _{Sm} ^{cis}
Formula	C ₁₇ H ₁₇ Pr	C ₁₇ H ₁₇ Nd	C ₁₇ H ₁₇ Sm
Crystal size (mm ³)	0.12x0.03x0.03	0.24x0.03x0.02	
Crystal system	Orthorhombic	Orthorhombic	Orthorhombic
Space group	Pnma	Pnma	Pnma
Volume (Å ³)	1365.3(8)	1368.1(14)	1356.78(15)
a (Å)	12.055(4)	12.0748(18)	11.9982(8)
b (Å)	12.777(5)	12.8129(19)	12.8760(8)
c (Å)	8.864(3)	8.8427(14)	8.7824(6)
α (deg)	90	90	90
β (deg)	90	90	90
γ (deg)	90	90	90
Z	4	4	4
Formula weight (g/mol)	362.21	365.54	371.65
Density (calcd) (g/cm ³)	1.762	1.775	1.819
Absorption coefficient (mm ⁻¹)	3.547	3.773	4.306
F(000)	712.0	716.0	724.0
Temp (K)	150.15	150.15	150.15
Diffractometer	Bruker APEX-II CCD	Bruker APEX-II CCD	Bruker APEX-II CCD
Radiation	MoKα (λ = 0.71073)	MoKα (λ = 0.71073)	MoKα (λ = 0.71073)
2θ range for data collection (deg)	5.594 to 51.992	5.598 to 59.346	5.614 to 71.262
Absorption correction	Multi-scan	Multi-scan	Multi-scan
Total no. reflections	7946	28912	107017
Unique reflections [R _{int}]	1404 [R _{int} = 0.1682]	1986 [R _{int} = 0.1464]	3242 [R _{int} = 0.1536]
Final R indices [I > 2σ(I)]	R ₁ = 0.0528, wR ₂ = 0.1097	R ₁ = 0.0389, wR ₂ = 0.0861	R ₁ = 0.0324, wR ₂ = 0.0679
R indices (all data)	R ₁ = 0.1319, wR ₂ = 0.1445	R ₁ = 0.1015, wR ₂ = 0.1087	R ₁ = 0.0631, wR ₂ = 0.0822
Largest diff. peak and hole (e.Å ⁻³)	1.25/-1.22	1.96/-1.07	1.50/-1.41
Goof	1.007	1.022	1.009

Compound	4.2 _{Gd} ^{cis}	4.2 _{Tb} ^{cis}	4.2 _{Ce} ^{trans/cis}
Formula	C ₁₇ H ₁₇ Gd	C ₁₇ H ₁₇ Tb	C ₁₇ H ₁₇ Ce
Crystal size (mm ³)	0.14x0.03x0.03	0.16x0.04x0.04	0.118 x 0.03 x 0.24
Crystal system	Orthorhombic	Orthorhombic	Orthorhombic
Space group	Pnma	Pnma	Pnma
Volume (Å ³)	1348.0(3)	1345.4(5)	1381.8(2)
a (Å)	11.965(15)	11.939(2)	12.0523(9)
b (Å)	12.9116(19)	12.952(3)	12.8172(12)
c (Å)	8.7283(10)	8.7005(17)	8.9448(10)
α (deg)	90	90	90
β (deg)	90	90	90
γ (deg)	90	90	90
Z	4	4	4
Formula weight (g/mol)	378.55	380.22	361.52
Density (calcd) (g/cm ³)	1.865	1.877	1.738
Absorption coefficient (mm ⁻¹)	4.898	5.234	3.273
F(000)	732.0	736.0	708.0
Temp (K)	150	149.99	150
Diffractometer	Bruker APEX-II CCD	Bruker APEX-II CCD	Stoe Stadivari
Radiation	MoKα (λ = 0.71073)	MoKα (λ = 0.71073)	MoKα (λ = 0.71073)
2θ range for data collection (deg)	5.634 to 54.954	5.64 to 58.256	5.554 to 61.224
Absorption correction	Multi-scan	Multi-scan	Multi-scan
Total no. reflections	8390	27069	12034
Unique reflections [R _{int}]	1618 [R _{int} = 0.1237]	1881 [R _{int} = 0.1360]	2056 [R _{int} = 0.0622]
Final R indices [I>2σ(I)]	R ₁ = 0.0486, wR ₂ = 0.0960	R = 0.0422, R w = 0.0986	R1 = 0.0328, wR2 = 0.0629
R indices (all data)	R ₁ = 0.1100, wR ₂ = 0.1171	R = 0.0762, R w = 0.1156	R1 = 0.0714, wR2 = 0.0688
Largest diff. peak and hole (e.Å ⁻³)	0.88/-1.18	2.00/-0.94	1.08/-0.71
Goof	0.997	1.025	0.917

Compound	4.2 _{Pr} ^{trans/cis}	4.2 _{Nd} ^{trans/cis}	4.2 _{Sm} ^{trans/cis}
Formula	C ₁₇ H ₁₇ Pr	C ₁₇ H ₁₇ Nd	C ₁₇ H ₁₇ Nd
Crystal size (mm ³)	0.083x0.049x0.032	0.2x0.04x0.02	0.47 x 0.287 x 0.07
Crystal system	Orthorhombic	Orthorhombic	Orthorhombic
Space group	Pnma	Pnma	Pnma
Volume (Å ³)	1369.48(16)	1370.2(5)	1355.13(14)
a (Å)	12.0063(7)	11.983(2)	11.8943(7)
b (Å)	12.8295(10)	12.877(3)	12.9414(6)
c (Å)	8.8907(6)	8.8927(17)	8.8036(6)
α (deg)	90	90	90
β (deg)	90	90	90
γ (deg)	90	90	90
Z	4	4	4
Formula weight (g/mol)	362.21	365.54	371.65
Density (calcd) (g/cm ³)	1.757	1.769	1.822
Absorption coefficient (mm ⁻¹)	3.536	3.762	4.311
F(000)	712.0	716.0	724.0
Temp (K)	150.01	149.99	150.01
Diffractometer	Stoe Stadivari	Bruker APEX-II CCD	Stoe Stadivari
Radiation	MoKα (λ = 0.71073)	MoKα (λ = 0.71073)	MoKα (λ = 0.71073)
2θ range for data collection (deg)	5.574 to 54.198	5.568 to 52.292	5.596 to 54.2
Absorption correction	Multi-scan	Multi-scan	Multi-scan
Total no. reflections	5122	15587	7609
Unique reflections [R _{int}]	1536 [R _{int} = 0.0542]	1435 [R _{int} = 0.1352]	1454 [R _{int} = 0.0533]
Final R indices [I>2σ(I)]	R ₁ = 0.0342, wR ₂ = 0.0608	R ₁ = 0.0396, wR ₂ = 0.0849	R ₁ = 0.0323, wR ₂ = 0.0697
R indices (all data)	R ₁ = 0.0771, wR ₂ = 0.0663	R ₁ = 0.0885, wR ₂ = 0.1043	R ₁ = 0.0561, wR ₂ = 0.0763
Largest diff. peak and hole (e.Å ⁻³)	0.97/-0.64	0.90/-1.89	0.93/-0.67
Goof	0.788	1.047	0.958

Compound	4.2 _{Gd} ^{trans/cis}	4.2 _{Tb} ^{trans/cis}	4.2 _{Dy} ^{trans/cis}
Formula	C ₁₇ H ₁₇ Gd	C ₁₇ H ₁₇ Tb	C ₁₇ H ₁₇ Dy
Crystal size (mm ³)	0.087x0.045x0.032	0.14x0.04x0.04	0.64x0.08x0.06
Crystal system	Orthorhombic	Orthorhombic	Orthorhombic
Space group	Pnma	Pnma	Pnma
Volume (Å ³)	1348.36(15)	1335.5(13)	1336.6(2)
a (Å)	11.8553(8)	11.781(6)	11.8081(12)
b (Å)	13.0113(8)	13.017(8)	13.057(10)
c (Å)	8.7412(6)	8.708(5)	8.6690(9)
α (deg)	90	90	90
β (deg)	90	90	90
γ (deg)	90	90	90
Z	4	4	4
Formula weight (g/mol)	378.55	380.22	383.80
Density (calcd) (g/cm ³)	1.865	1.891	1.907
Absorption coefficient (mm ⁻¹)	4.897	5.273	5.568
F(000)	732.0	736.0	710.0
Temp (K)	150.01	150.01	150.02
Diffractometer	Stoe Stadivari	Bruker APEX-II CCD	Bruker APEX-II CCD
Radiation	MoKα (λ = 0.71073)	MoKα (λ = 0.71073)	MoKα (λ = 0.71073)
2θ range for data collection (deg)	5.614 to 54.206	5.628 to 54.204	5.64 to 63.14
Absorption correction	Multi-scan	Multi-scan	Multi-scan
Total no. reflections	6971	17144	12046
Unique reflections [R _{int}]	1552 [R _{int} = 0.0699]	1539 [R _{int} = 0.1491]	2315 [R _{int} = 0.0701]
Final R indices [I>2σ(I)]	R ₁ = 0.0397, wR ₂ = 0.0866	R ₁ = 0.0447, wR ₂ = 0.1093	R ₁ = 0.0384, wR ₂ = 0.0776
R indices (all data)	R ₁ = 0.0643, wR ₂ = 0.0915	R ₁ = 0.0726, wR ₂ = 0.1274	R ₁ = 0.0550, wR ₂ = 0.0844
Largest diff. peak and hole (e.Å ⁻³)	1.38/-0.86	1.60/-2.27	1.52/-1.68
Goof	0.933	1.101	1.082

Compound	4.2 _{Ho} ^{trans/cis}
Formula	C ₁₇ H ₁₇ O
Crystal size (mm ³)	0.1x0.04x0.02
Crystal system	Orthorhombic
Space group	Pnma
Volume (Å ³)	1336.0(2)
a (Å)	11.7641(10)
b (Å)	13.1227(12)
c (Å)	8.6544(9)
α (deg)	90
β (deg)	90
γ (deg)	90
Z	4
Formula weight (g/mol)	386.23
Density (calcd) (g/cm ³)	1.920
Absorption coefficient (mm ⁻¹)	5.900
F(000)	744.0
Temp (K)	150.01
Diffractometer	Bruker APEX-II CCD
Radiation	MoKα (λ = 0.71073)
2θ range for data collection (deg)	5.638 to 52.042
Absorption correction	Multi-scan
Total no. reflections	18294
Unique reflections [R _{int}]	1376 [R _{int} = 0.1726]
Final R indices [I > 2σ(I)]	R ₁ = 0.0379, wR ₂ = 0.0640
R indices (all data)	R ₁ = 0.0615, wR ₂ = 0.0677
Largest diff. peak and hole (e.Å ⁻³)	1.10/-1.11
Goof	0.842

3. Crystal structures and main distances

Structure of 4.1Pr

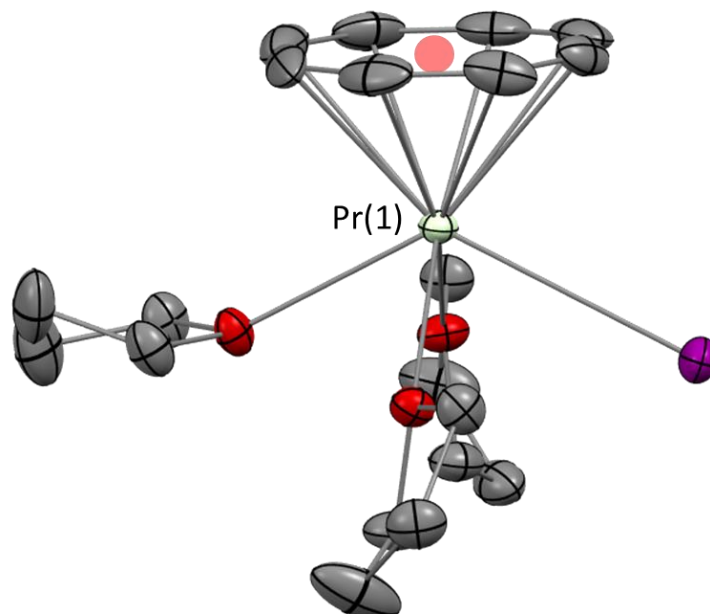


Figure S4. 16 Molecular structure of **4.1Pr**, thermal ellipsoids are depicted at 50% probability level. Praseodymium atoms are in light yellow, carbons in grey, oxygens and iodine in red and purple respectively. Hydrogen atoms and disorder of the Cot ligand are omitted for clarity.

Main distances in Å	
Pr(1)—I(1)	3.2647(3)
Pr(1)—C Cot	2.66(2) – 2.73(2)
Pr(1)—Cent (Cot)	1.97
Pr(1)—O(1)	2.537(2)
Pr(1)—O(2)	2.589(2)
Pr(1)—O(3)	2.524(4)

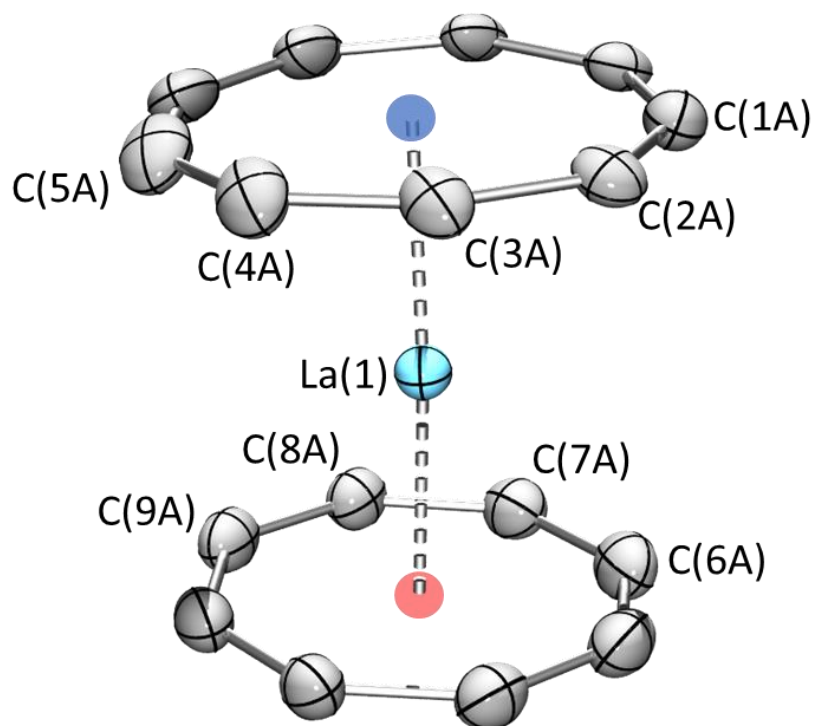
Structure of 4.2_{La}^{cis} 

Figure S4. 17 Molecular structure of 4.2_{La}^{cis} , thermal ellipsoids are depicted at 50% probability level. Lanthanum atoms are in light blue and carbon atoms in grey. Hydrogen atoms and disorder of the Cot and the Cnt ligand are omitted for clarity. The blue and red spots represent the constructed centroids for Cnt^{cis} and Cot respectively.

	Main distances in Å
La(1) – C(6A) (Cot)	2.699(11)
La(1) – C(7A) (Cot)	2.694(12)
La(1) – C(8A) (Cot)	2.700(13)
La(1) – C(9A) (Cot)	2.686(13)
La(1) – Cent (Cot)	1.98
La(1) – C(1A) (Cnt)	2.93(2)
La(1) – C(2A) (Cnt)	2.944(14)
La(1) – C(3A) (Cnt)	2.971(13)
La(1) – C(4A) (Cnt)	2.952(13)
La(1) – C(5A) (Cnt)	2.927(13)
La(1) – Cent (Cnt)	2.14
Plane (Cot) ^Plane (Cnt)	3.69 °
Cent (Cot) - La(1) – Cent (Cnt)	176.86 °

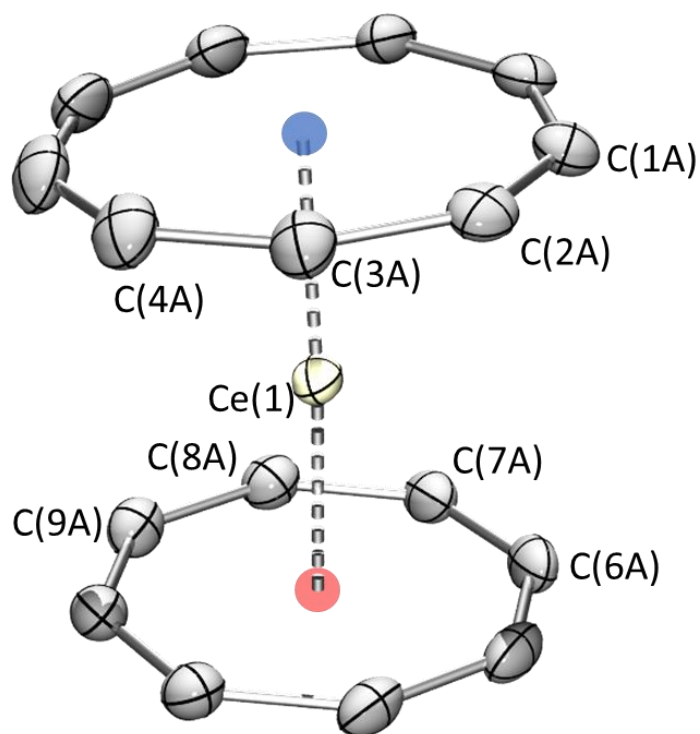
Structure of $4.2_{\text{Ce}^{\text{cis}}}$ 

Figure S4. 18 Molecular structure of $4.2_{\text{Ce}^{\text{cis}}}$, thermal ellipsoids are depicted at 50% probability level. Cerium atoms are in light yellow and carbon atoms in grey. Hydrogen atoms and disorder of the Cot and the Cnt ligand are omitted for clarity. The blue and red spots represent the constructed centroids for Cnt^{cis} and Cot respectively.

	Main distances in Å
Ce(1) – C(6A) (Cot)	2.689(7)
Ce(1) – C(7A) (Cot)	2.675(8)
Ce(1) – C(8A) (Cot)	2.684(8)
Ce(1) – C(9A) (Cot)	2.657(8)
Ce(1) – Cent (Cot)	1.95
Ce(1) – C(1A) (Cnt)	2.891(13)
Ce(1) – C(2A) (Cnt)	2.933(8)
Ce(1) – C(3A) (Cnt)	2.942(8)
Ce(1) – C(4A) (Cnt)	2.925(8)
Ce(1) – C(5A) (Cnt)	2.905(8)
Ce(1) – Cent (Cnt)	2.10
Plane (Cot) ^Plane (Cnt)	3.75 °
Cent (Cot) - Ce(1) – Cent (Cnt)	177.01 °

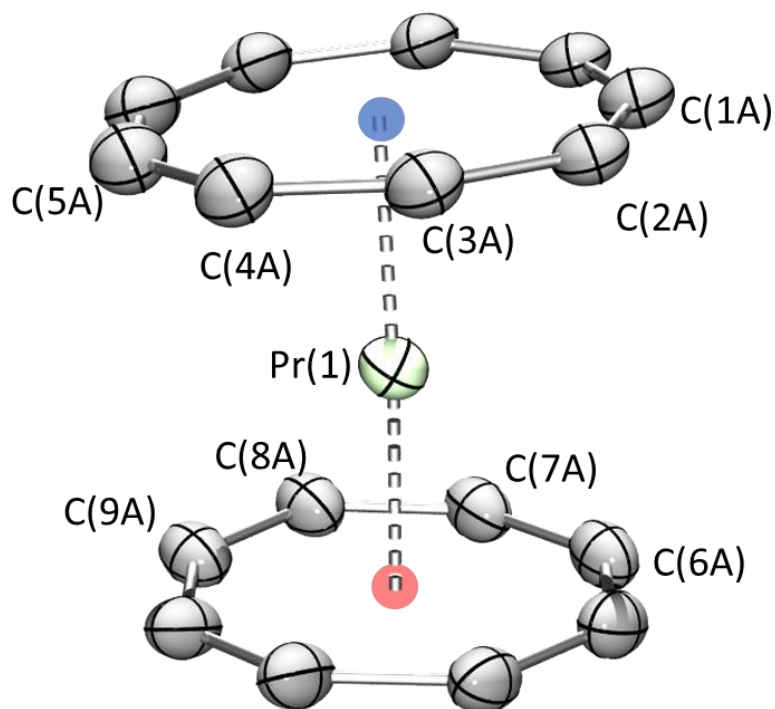
Structure of $4.2_{Pr^{cis}}$ 

Figure S4. 19 Molecular structure of $4.2_{Pr^{cis}}$, thermal ellipsoids are depicted at 50% probability level. Praseodymium atoms are in light green and carbon atoms in grey. Hydrogen atoms and disorder of the Cot and the Cnt ligand are omitted for clarity. The blue and red spots represent the constructed centroids for Cnt^{cis} and Cot respectively.

	Main distances in Å
Pr(1) – C(6A) (Cot)	2.67(2)
Pr(1) – C(7A) (Cot)	2.65(2)
Pr(1) – C(8A) (Cot)	2.64(2)
Pr(1) – C(9A) (Cot)	2.64(2)
Pr(1) – Cent (Cot)	1.91
Pr(1) – C(1A) (Cnt)	2.89(4)
Pr(1) – C(2A) (Cnt)	2.91(2)
Pr(1) – C(3A) (Cnt)	2.93(2)
Pr(1) – C(4A) (Cnt)	2.90(4)
Pr(1) – C(5A) (Cnt)	2.85(2)
Pr(1) – Cent (Cnt)	2.07
Plane (Cot) ^Plane (Cnt)	3.86 °
Cent (Cot) - Pr(1) – Cent (Cnt)	177.39 °

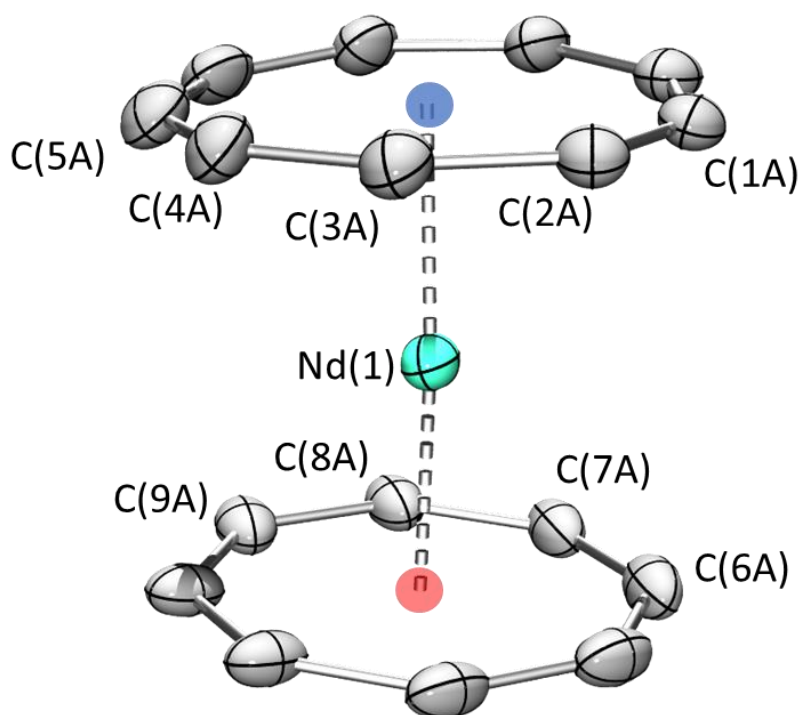
Structure of $4.2\text{Nd}^{\text{cis}}$ 

Figure S4. 20 Molecular structure of $4.2\text{Nd}^{\text{cis}}$, thermal ellipsoids are depicted at 50% probability level. Neodymium atoms are in green and carbon atoms in grey. Hydrogen atoms and disorder of the Cot and the Cnt ligand are omitted for clarity. The blue and red spots represent the constructed centroids for Cnt^{cis} and Cot respectively.

	Main distances in Å
Nd(1) – C(6A) (Cot)	2.66(1)
Nd(1) – C(7A) (Cot)	2.65(1)
Nd(1) – C(8A) (Cot)	2.64(1)
Nd(1) – C(9A) (Cot)	2.64(1)
Nd(1) – Cent (Cot)	1.90
Nd(1) – C(1A) (Cnt)	2.84(1)
Nd(1) – C(2A) (Cnt)	2.89(1)
Nd(1) – C(3A) (Cnt)	2.92(1)
Nd(1) – C(4A) (Cnt)	2.90(1)
Nd(1) – C(5A) (Cnt)	2.86(1)
Nd(1) – Cent (Cnt)	2.05
Plane (Cot) ^Plane (Cnt)	3.62 °
Cent (Cot) - Nd(1) – Cent (Cnt)	176.70 °

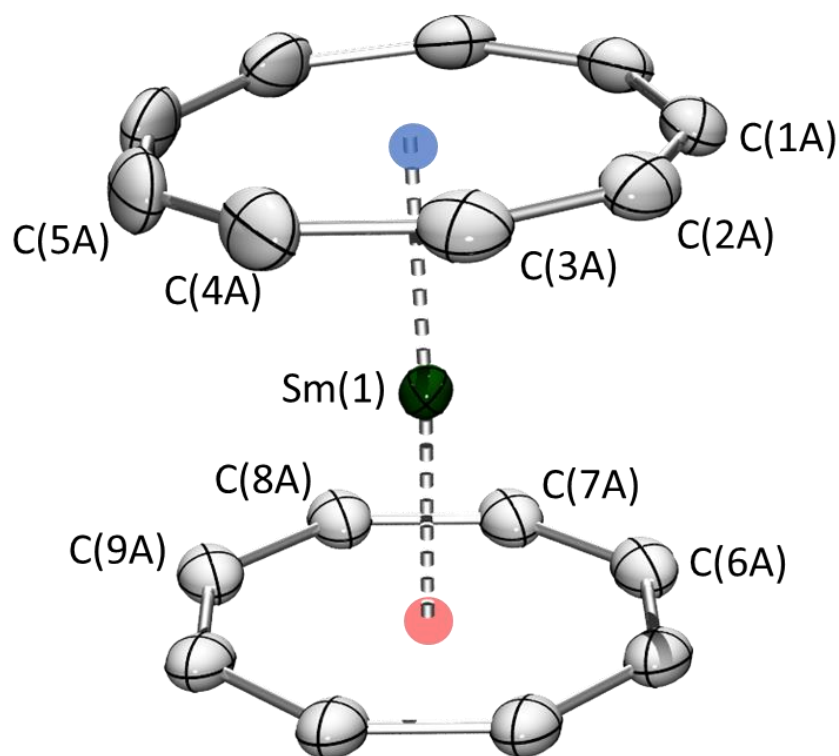
Structure of 4.2_{Sm}^{cis} 

Figure S4. 21 Molecular structure of 4.2_{Sm}^{cis} , thermal ellipsoids are depicted at 50% probability level. Samarium atoms are in dark green and carbon atoms in grey. Hydrogen atoms and disorder of the Cot and the Cnt ligand are omitted for clarity. The blue and red spots represent the constructed centroids for Cnt^{cis} and Cot respectively.

	Main distances in Å
Sm(1) – C(6A) (Cot)	2.624(6)
Sm(1) – C(7A) (Cot)	2.627(7)
Sm(1) – C(8A) (Cot)	2.629(7)
Sm(1) – C(9A) (Cot)	2.618(6)
Sm(1) – Cent (Cot)	1.87
Sm(1) – C(1A) (Cnt)	2.824(9)
Sm(1) – C(2A) (Cnt)	2.873(6)
Sm(1) – C(3A) (Cnt)	2.892(7)
Sm(1) – C(4A) (Cnt)	2.878(7)
Sm(1) – C(5A) (Cnt)	2.831(6)
Sm(1) – Cent (Cnt)	2.01
Plane (Cot) ^Plane (Cnt)	3.02 °
Cent (Cot) - Sm(1) – Cent (Cnt)	177.17 °

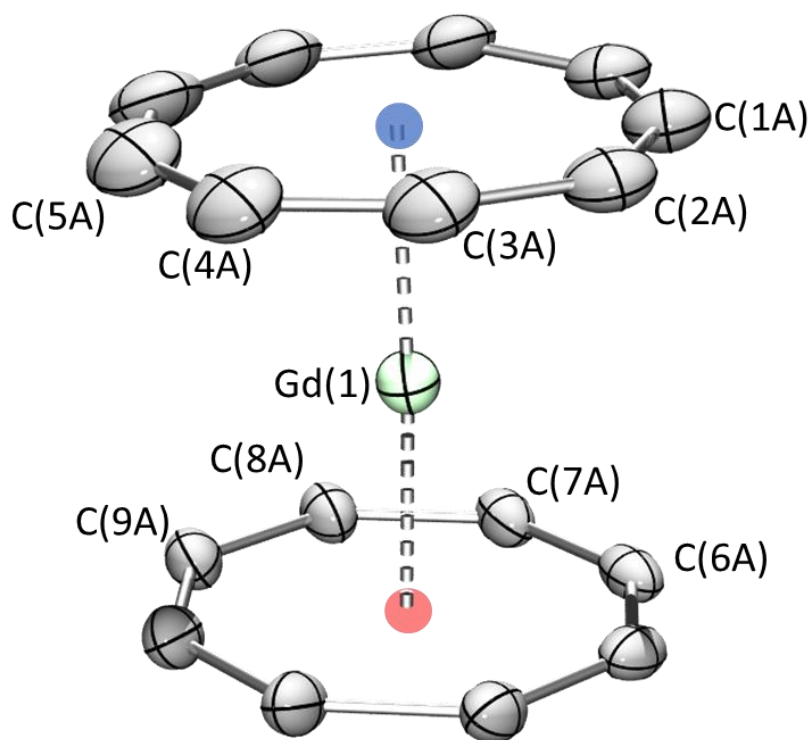
Structure of $4.2_{\text{Gd}^{\text{cis}}}$ 

Figure S4. 22 Molecular structure of $4.2_{\text{Gd}^{\text{cis}}}$, thermal ellipsoids are depicted at 50% probability level. Gadolinium atoms are in dark green and carbon atoms in grey. Hydrogen atoms and disorder of the Cot and the Cnt ligand are omitted for clarity. The blue and red spots represent the constructed centroids for Cnt^{cis} and Cot respectively.

Main distances in Å	
Gd(1) – C(6A) (Cot)	2.607(15)
Gd(1) – C(7A) (Cot)	2.630(17)
Gd(1) – C(8A) (Cot)	2.613(17)
Gd(1) – C(9A) (Cot)	2.586(15)
Gd(1) – Cent (Cot)	1.83
Gd(1) – C(1A) (Cnt)	2.77(3)
Gd(1) – C(2A) (Cnt)	2.817(18)
Gd(1) – C(3A) (Cnt)	2.873(19)
Gd(1) – C(4A) (Cnt)	2.861(19)
Gd(1) – C(5A) (Cnt)	2.801(17)
Gd(1) – Cent (Cnt)	2.00
Plane (Cot) ^Plane (Cnt)	2.53 °
Cent (Cot) - Gd(1) – Cent (Cnt)	177.34 °

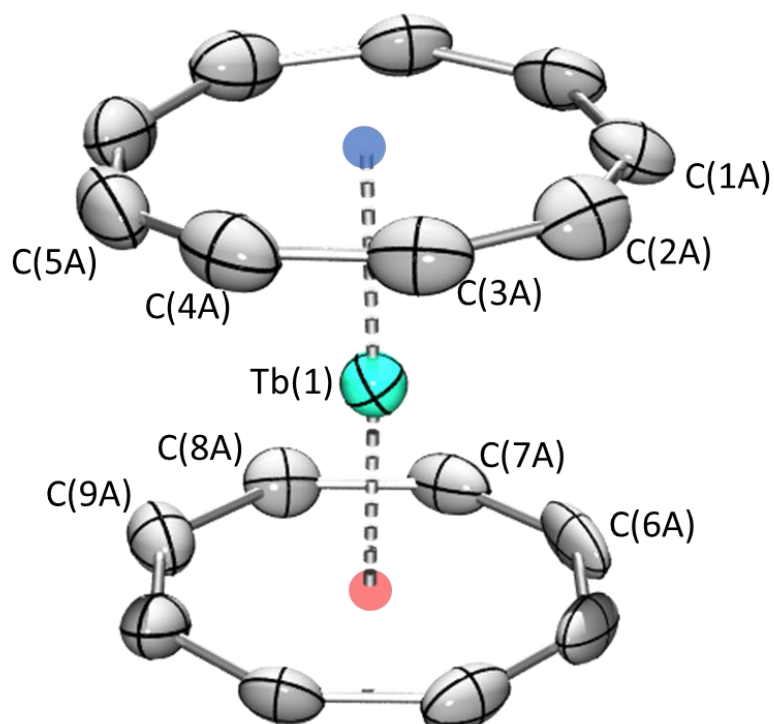
Structure of 4.2_{Tb}^{cis} 

Figure S4. 23 Molecular structure of 4.2_{Tb}^{cis} , thermal ellipsoids are depicted at 50% probability level. Terbium atoms are in dark green and carbon atoms in grey. Hydrogen atoms and disorder of the Cot and the Cnt ligand are omitted for clarity. The blue and red spots represent the constructed centroids for Cnt^{cis} and Cot respectively.

Main distances in Å	
Tb(1) – C(6A) (Cot)	2.573(14)
Tb(1) – C(7A) (Cot)	2.591(16)
Tb(1) – C(8A) (Cot)	2.586(14)
Tb(1) – C(9A) (Cot)	2.573(13)
Tb(1) – Cent (Cot)	1.80
Tb(1) – C(1A) (Cnt)	2.78(2)
Tb(1) – C(2A) (Cnt)	2.839(16)
Tb(1) – C(3A) (Cnt)	2.874(15)
Tb(1) – C(4A) (Cnt)	2.852(16)
Tb(1) – C(5A) (Cnt)	2.780(14)
Tb(1) – Cent (Cnt)	1.97
Plane (Cot) ^Plane (Cnt)	2.15 °
Cent (Cot) - Tb(1) – Cent (Cnt)	177.46 °

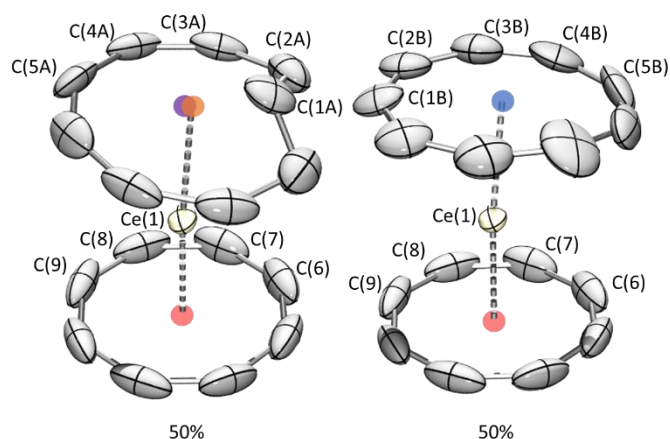
Structure of $4.2_{\text{Ce}}^{\text{trans/cis}}$ 

Figure S4. 24 Molecular structure of $4.2_{\text{Nd}}^{\text{trans/cis}}$, thermal ellipsoids are depicted at 50% probability level. Cerium atoms are in light green and carbon atoms in grey. The Cnt ring being disordered, the two partitions are represented side by side. Hydrogen atoms are omitted for clarity and the red, orange, purple and blue spots represent the centroids for the Cot, the $\text{Cnt}^{\text{trans}}$, the Cnt-8C and the Cnt^{cis} respectively.

	Main distances in Å
Ce(1) – C(6) (Cot)	2.640(4)
Ce(1) – C(7) (Cot)	2.657(4)
Ce(1) – C(8) (Cot)	2.656(4)
Ce(1) – C(9) (Cot)	2.664(4)
Ce(1) – Cent (Cot)	1.94
Ce(1) – C(1A) (Cnt)	2.750(12)
Ce(1) – C(1B) (Cnt)	2.84(2)
Ce(1) – C(2A) (Cnt)	2.878(15)
Ce(1) – C(2B) (Cnt)	2.88(2)
Ce(1) – C(3A) (Cnt)	2.900(15)
Ce(1) – C(3B) (Cnt)	2.89(2)
Ce(1) – C(4A) (Cnt)	2.887(15)
Ce(1) – C(4B) (Cnt)	2.90(2)
Ce(1) – C(5A) (Cnt)	2.857(15)
Ce(1) – C(5B) (Cnt)	2.94(2)
Ce(1) – Cent ($\text{Cnt}^{\text{trans}}$)	2.08
Ce(1) – Cent (Cnt^{cis})	2.14
Ce(1) – Cent (Cnt-8C)	2.04
Plane (Cot) ^Plane (Cnt^{cis})	5.53 °
Plane (Cot) ^Plane (Cnt-8C)	3.39 °
Cent (Cot) - Ce(1) – Cent ($\text{Cnt}^{\text{trans}}$)	176.27 °
Cent (Cot) - Ce(1) - Cent (Cnt^{cis})	176.41 °
Cent (Cot) - Ce(1) - Cent (Cnt-8C)	179.6 °
Plane (C(2)/C(1)/C(2')) ^Plane (Cnt^{cis})	5.53 °

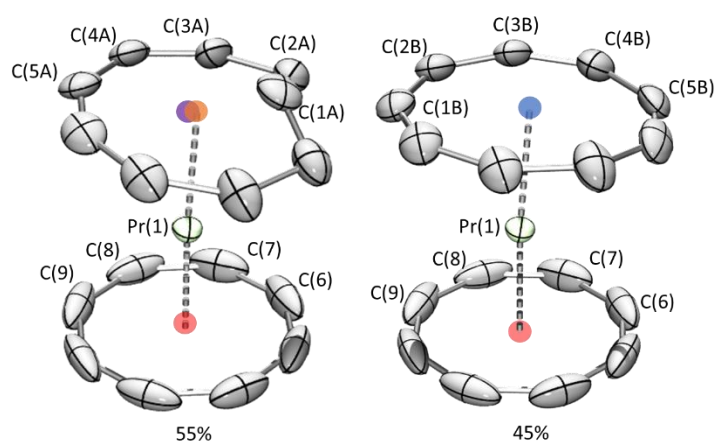
Structure of $4.2_{Pr}^{trans/cis}$ 

Figure S4. 25 Molecular structure of $4.2_{Nd}^{trans/cis}$, thermal ellipsoids are depicted at 50% probability level. Praseodymium atoms are in light green and carbon atoms in grey. The Cnt ring being disordered, the two partitions are represented side by side. Hydrogen atoms are omitted for clarity and the red, orange, purple and blue spots represent the centroids for the Cot, the Cnt^{trans} , the Cnt-8C and the Cnt^{cis} respectively.

	Main distances in Å
Pr(1) – C(6) (Cot)	2.637(5)
Pr(1) – C(7) (Cot)	2.631(6)
Pr(1) – C(8) (Cot)	2.639(6)
Pr(1) – C(9) (Cot)	2.637(5)
Pr(1) – Cent (Cot)	1.91
Pr(1) – C(1A) (Cnt)	2.749(15)
Pr(1) – C(1B) (Cnt)	2.84(2)
Pr(1) – C(2A) (Cnt)	2.87(2)
Pr(1) – C(2B) (Cnt)	2.87(2)
Pr(1) – C(3A) (Cnt)	2.87(2)
Pr(1) – C(3B) (Cnt)	2.88(2)
Pr(1) – C(4A) (Cnt)	2.88(2)
Pr(1) – C(4B) (Cnt)	2.89(2)
Pr(1) – C(5A) (Cnt)	2.815(16)
Pr(1) – C(5B) (Cnt)	2.90(2)
Pr(1) – Cent (Cnt^{trans})	2.09
Pr(1) – Cent (Cnt^{cis})	2.08
Pr(1) – Cent (Cnt-8C)	2.04
Plane (Cot) ^Plane (Cnt^{cis})	5.12°
Plane (Cot) ^Plane (Cnt-8C)	2.88°
Cent (Cot) - Pr(1) – Cent (Cnt^{trans})	176.76°
Cent (Cot) - Pr(1) - Cent (Cnt^{cis})	176.16°
Cent (Cot) - Pr(1) - Cent (Cnt-8C)	178.99°
Plane (C(2)/C(1)/C(2')) ^Plane (Cnt^{cis})	47.68°

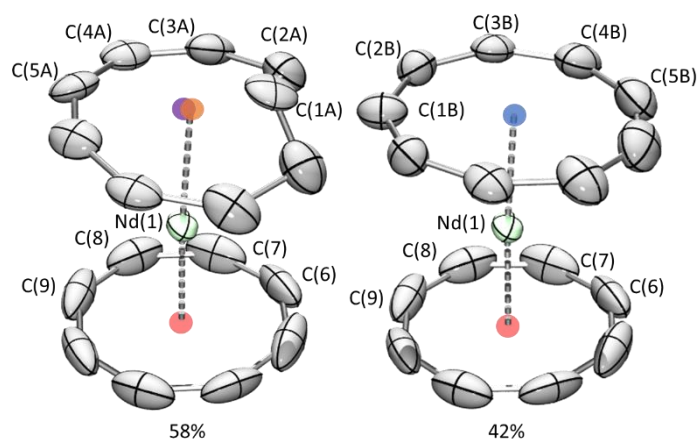
Structure of $4.2\text{Nd}^{\text{trans/cis}}$ 

Figure S4.26 Molecular structure of $4.2\text{Nd}^{\text{trans/cis}}$, thermal ellipsoids are depicted at 50% probability level. Neodymium atoms are in light green and carbon atoms in grey. The Cnt ring being disordered, the two partitions are represented side by side. Hydrogen atoms are omitted for clarity and the red, orange, purple and blue spots represent the centroids for the Cot, the $\text{Cnt}^{\text{trans}}$, the Cnt-8C and the Cnt^{cis} respectively.

Main distances in Å	
Nd(1) – C(6) (Cot)	2.619(8)
Nd(1) – C(7) (Cot)	2.614(9)
Nd(1) – C(8) (Cot)	2.641(9)
Nd(1) – C(9) (Cot)	2.629(9)
Nd(1) – Cent (Cot)	1.90
Nd(1) – C(1A) (Cnt)	2.79(2)
Nd(1) – C(1B) (Cnt)	2.84(2)
Nd(1) – C(2A) (Cnt)	2.89(2)
Nd(1) – C(2B) (Cnt)	2.88(2)
Nd(1) – C(3A) (Cnt)	2.91(2)
Nd(1) – C(3B) (Cnt)	2.91(2)
Nd(1) – C(4A) (Cnt)	2.85(2)
Nd(1) – C(4B) (Cnt)	2.89(2)
Nd(1) – C(5A) (Cnt)	2.81(2)
Nd(1) – C(5B) (Cnt)	2.86(2)
Nd(1) – Cent ($\text{Cnt}^{\text{trans}}$)	2.08
Nd(1) – Cent (Cnt^{cis})	2.06
Nd(1) – Cent (Cnt-8C)	2.03
Plane (Cot) ^Plane (Cnt^{cis})	4.44 °
Plane (Cot) ^Plane (Cnt-8C)	3.74 °
Cent (Cot) - Nd(1) – Cent ($\text{Cnt}^{\text{trans}}$)	177.00 °
Cent (Cot) - Nd(1) - Cent (Cnt^{cis})	176.8 °
Cent (Cot) - Nd(1) - Cent (Cnt-8C)	178.78 °
Plane (C(2)/C(1)/C(2')) ^Plane (Cnt^{cis})	50.15 °

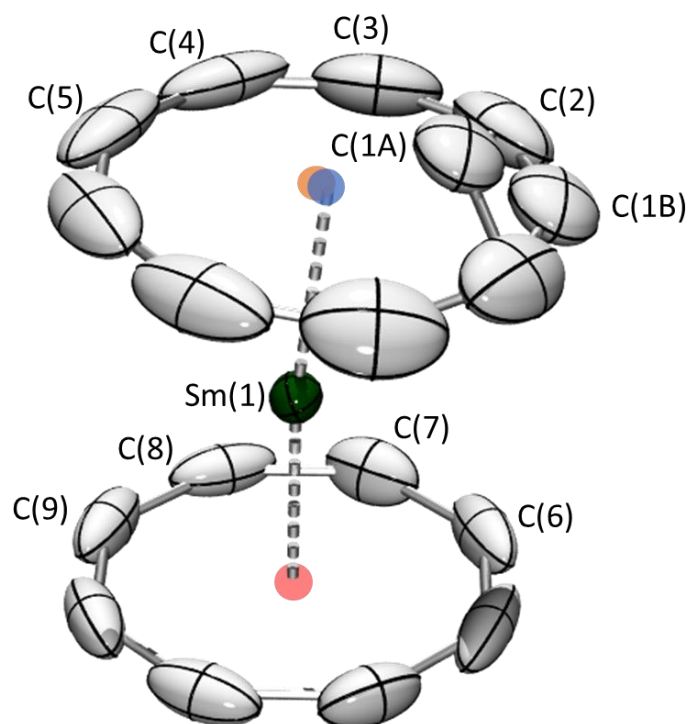
Structure of $4.2_{Sm}^{trans/cis}$ 

Figure S4. 27 Molecular structure of $4.2_{Sm}^{trans/cis}$, thermal ellipsoids are depicted at 50% probability level. Samarium atoms are in dark green and carbon atoms in grey. Hydrogen atoms are omitted for clarity and the red, orange and blue spots represent the centroids for the Cot, the Cnt^{trans} and the Cnt^{cis} respectively.

	Main distances in Å
Sm(1) – C(6) (Cot)	2.594(5)
Sm(1) – C(7) (Cot)	2.591(6)
Sm(1) – C(8) (Cot)	2.601(6)
Sm(1) – C(9) (Cot)	2.595(6)
Sm(1) – Cent (Cot)	1.85
Sm(1) – C(1A) (Cnt)	2.687(13)
Sm(1) – C(1B) (Cnt)	2.82(3)
Sm(1) – C(2) (Cnt)	2.857(9)
Sm(1) – C(3) (Cnt)	2.879(9)
Sm(1) – C(4) (Cnt)	2.834(9)
Sm(1) – C(5) (Cnt)	2.763(6)
Sm(1) – Cent (Cnt^{trans})	2.054
Sm(1) – Cent (Cnt^{cis})	2.01
Plane (Cot) ^Plane (Cnt^{cis})	3.54 °
Cent (Cot) - Sm(1) – Cent (Cnt^{trans})	175.96 °
Cent (Cot) - Sm(1) - Cent (Cnt^{cis})	173.37 °
Plane (C(2)/C(1)/C(2')) ^Plane (Cnt^{cis})	42.80 °

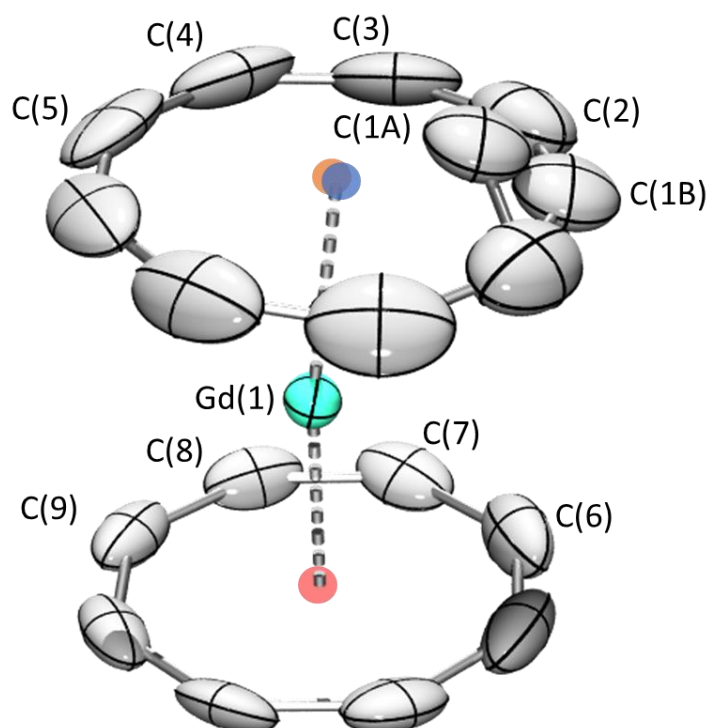
Structure of $4.2_{\text{Gd}}^{\text{trans/cis}}$ 

Figure S4. 28 Molecular structure of $4.2_{\text{Gd}}^{\text{trans/cis}}$, thermal ellipsoids are depicted at 50% probability level. Gadolinium atoms are in light green and carbon atoms in grey. Hydrogen atoms are omitted for clarity and the red, orange and blue spots represent the centroids for the Cot, the $\text{Cnt}^{\text{trans}}$ and the Cnt^{cis} respectively.

	Main distances in Å
Gd(1) – C(6) (Cot)	2.559(7)
Gd(1) – C(7) (Cot)	2.575(7)
Gd(1) – C(8) (Cot)	2.582(6)
Gd(1) – C(9) (Cot)	2.565(7)
Gd(1) – Cent (Cot)	1.82
Gd(1) – C(1A) (Cnt)	2.703(17)
Gd(1) – C(1B) (Cnt)	2.81(5)
Gd(1) – C(2) (Cnt)	2.853((10))
Gd(1) – C(3) (Cnt)	2.872(9)
Gd(1) – C(4) (Cnt)	2.828(10)
Gd(1) – C(5) (Cnt)	2.749(9)
Gd(1) – Cent (Cnt^{trans})	2.04
Gd(1) – Cent (Cnt^{cis})	2.003
Plane (Cot) ^Plane (Cnt ^{cis})	3.63 °
Cent (Cot) - Gd(1) – Cent (Cnt ^{trans})	175.04 °
Cent (Cot) - Gd(1) - Cent (Cnt ^{cis})	172.72 °
Plane (C(2)/C(1)/C(2')) ^Plane (Cnt ^{cis})	45.34 °

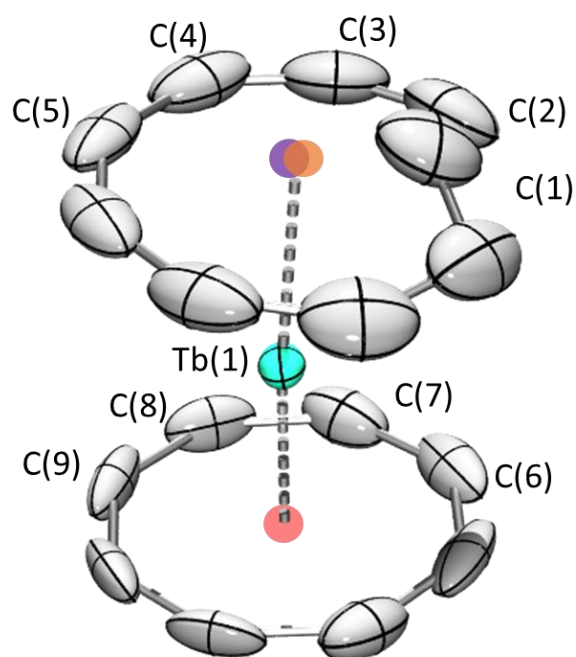
Structure of $4.2_{Tb}^{trans/cis}$ 

Figure S4. 29 Molecular structure of $4.2_{Tb}^{trans/cis}$, thermal ellipsoids are depicted at 50% probability level. Terbium atoms are in light green and carbon atoms in grey. Hydrogen atoms are omitted for clarity and the red, orange and purple spots represent the centroids for the Cot, the Cnt^{trans} and the Cnt-8C respectively.

	Main distances in Å
Tb(1) – C(6) (Cot)	2.537(9)
Tb(1) – C(7) (Cot)	2.563(11)
Tb(1) – C(8) (Cot)	2.566(9)
Tb(1) – C(9) (Cot)	2.540(9)
Tb(1) – Cent (Cot)	1.80
Tb(1) – C(1) (Cnt)	2.664(16)
Tb(1) – C(2) (Cnt)	2.837(12)
Tb(1) – C(3) (Cnt)	2.885(12)
Tb(1) – C(4) (Cnt)	2.828(12)
Tb(1) – C(5) (Cnt)	2.722(10)
Tb(1) – Cent (Cnt)	2.01
Tb(1) – Cent (Cnt –8C)	1.97
Plane (Cot) ^Plane (Cnt-8C)	3.94 °
Cent (Cot) - Tb(1) – Cent (Cnt)	175.74 °
Cent (Cot) - Tb(1)- Cent (Cnt-8C)	179.97 °
Plane (C(2)/C(1)/C(2')) ^Plane (Cnt-8C)	48.14 °

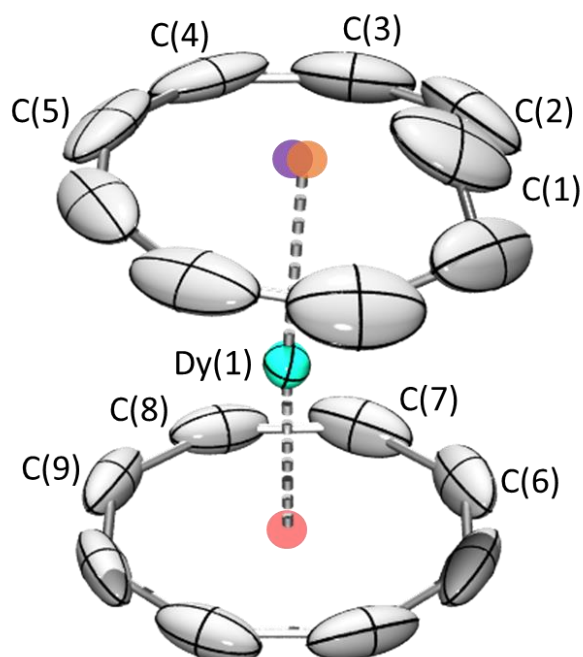
Structure of $4.2_{Dy}^{trans/cis}$ 

Figure S4. 30 Molecular structure of $4.2_{Dy}^{trans/cis}$, thermal ellipsoids are depicted at 50% probability level. Dysprosium atoms are in light green and carbon atoms in grey. Hydrogen atoms are omitted for clarity and the red, orange and purple spots represent the centroids for the Cot, the Cnt^{trans} and the $Cnt-8C$ respectively.

	Main distances in Å
Dy(1) – C(6) (Cot)	2.534(5)
Dy(1) – C(7) (Cot)	2.544(5)
Dy(1) – C(8) (Cot)	2.543(5)
Dy(1) – C(9) (Cot)	2.544(5)
Dy(1) – Cent (Cot)	1.78
Dy(1) – C(1) (Cnt)	2.660(9)
Dy(1) – C(2) (Cnt)	2.825(9)
Dy(1) – C(3) (Cnt)	2.858(9)
Dy(1) – C(4) (Cnt)	2.806(6)
Dy(1) – C(5) (Cnt)	2.720(6)
Dy(1) – Cent (Cnt)	1.99
Dy(1) – Cent (Cnt) –8C	1.96
Plane (Cot) ^Plane (Cnt-8C)	3.52 °
Cent (Cot) - Dy(1) – Cent (Cnt)	179.57 °
Cent (Cot) - Dy(1)- Cent (Cnt-8C)	175.75 °
Plane (C(2)/C(1)/C(2')) ^Plane (Cnt-8C)	52.63 °

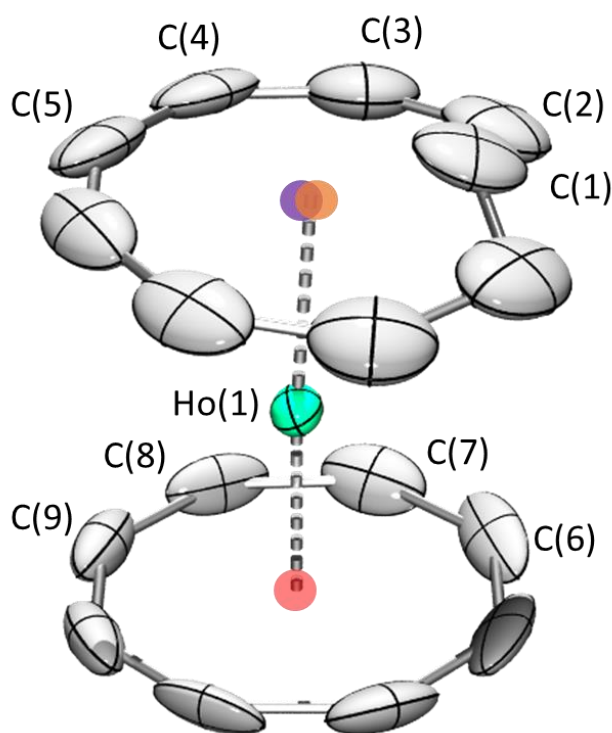
Structure of $4.2_{\text{Ho}}^{\text{trans/cis}}$ 

Figure S4. 31 Molecular structure of $4.2_{\text{Ho}}^{\text{trans/cis}}$, thermal ellipsoids are depicted at 50% probability level. Holmium atoms are in green and carbon atoms in grey. Hydrogen atoms are omitted for clarity and the red, orange and purple spots represent the centroids for the Cot, the $\text{Cnt}^{\text{trans}}$ and the Cnt-8C respectively.

Main distances in Å	
Ho(1) – C(6) (Cot)	2.518(7)
Ho(1) – C(7) (Cot)	2.529(8)
Ho(1) – C(8) (Cot)	2.524(7)
Ho(1) – C(9) (Cot)	2.534(6)
Ho(1) – Cent (Cot)	1.76
Ho(1) – C(1) (Cnt)	2.673(11)
Ho(1) – C(2) (Cnt)	2.819(9)
Ho(1) – C(3) (Cnt)	2.86(1)
Ho(1) – C(4) (Cnt)	2.805(8)
Ho(1) – C(5) (Cnt)	2.684(7)
Ho(1) – Cent (Cnt)	2.00
Ho(1) – Cent (Cnt) –8C	1.95
Plane (Cot) ^Plane (Cnt-8C)	3.36 °
Cent (Cot) - Ho(1) – Cent (Cnt)	176.73 °
Cent (Cot) - Ho(1) - Cent (Cnt-8C)	178.81 °
Plane (C(2)/C(1)/C(2')) ^Plane (Cnt-8C)	50.85 °

V. UV-visible spectroscopy

For the complexes, the presented spectra correspond to the signature of the crystals obtained through the synthesis according to general procedure for the obtention of $4.2_{Ln}^{trans/cis}$.

UV spectra of $KCn^{trans/cis}$

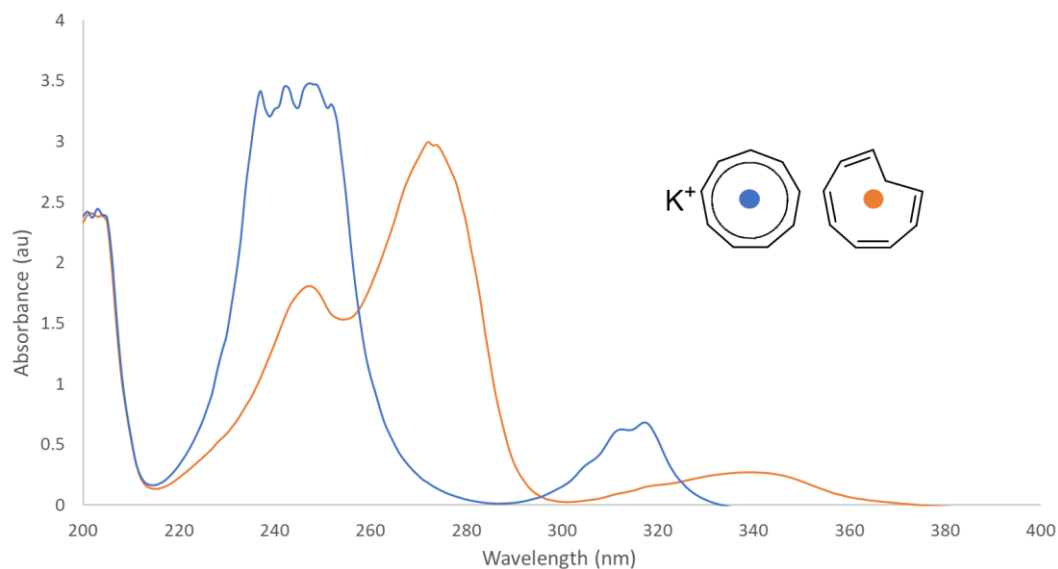


Figure S4. 32 UV-visible spectra of KCn in its most trans form (orange trace) and its pure cis form (blue trace).

UV-visible spectra of $4.2_{La}^{trans/cis}$

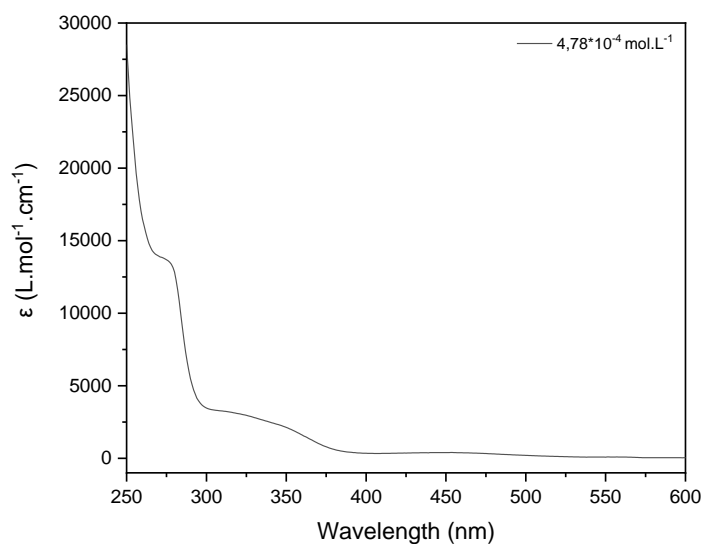


Figure S4. 33 UV-visible spectra of $4.2_{La}^{trans/cis}$.

UV-visible spectra of $4.2_{Ce}^{trans/cis}$

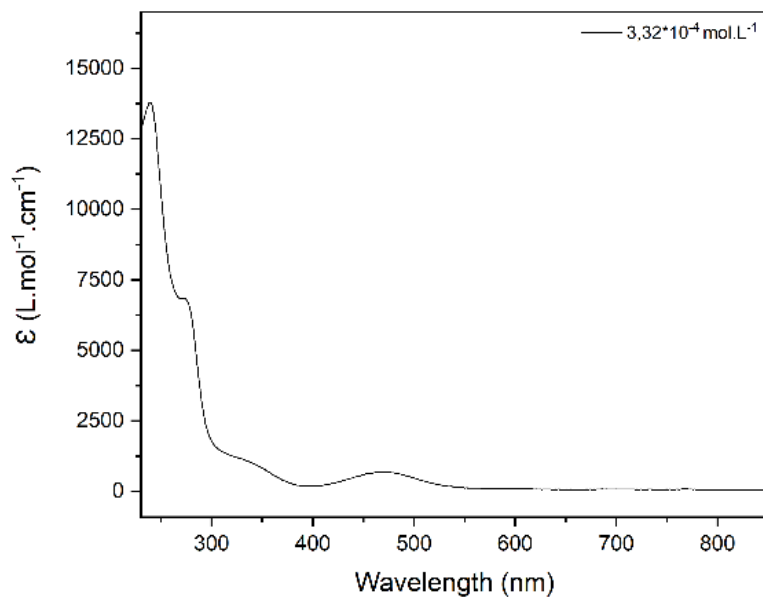


Figure S4. 34 UV-visible spectra of $4.2_{Ce}^{trans/cis}$.

UV-visible spectra of $4.2_{Pr}^{trans/cis}$

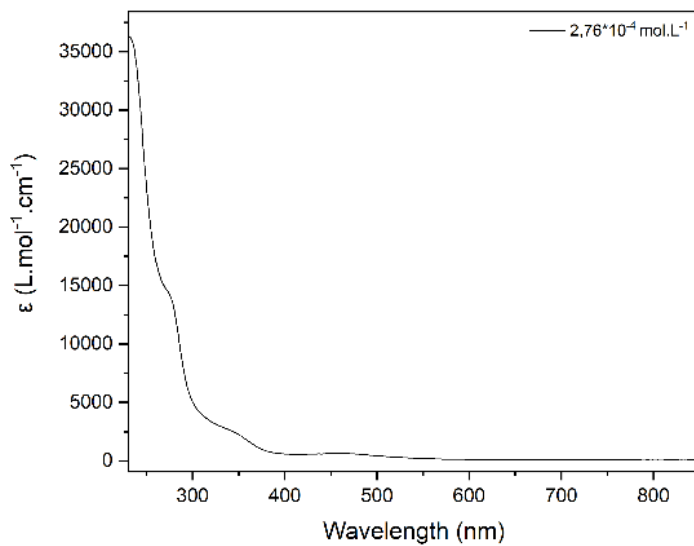


Figure S4. 35 UV-visible spectra of $4.2_{Pr}^{trans/cis}$.

UV-visible spectra of $4.2_{Nd}^{trans/cis}$

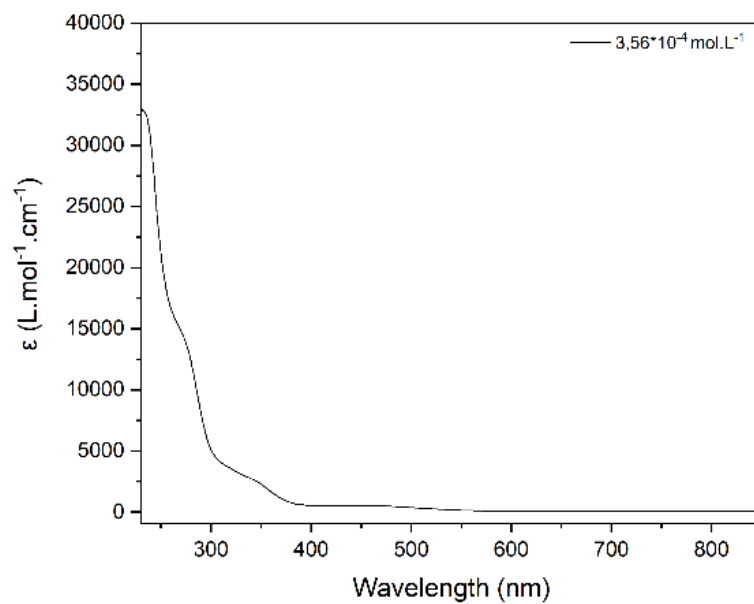


Figure S4. 36 UV-visible spectra of $4.2_{Nd}^{trans/cis}$.

UV-visible spectra of $4.2_{Sm}^{trans/cis}$

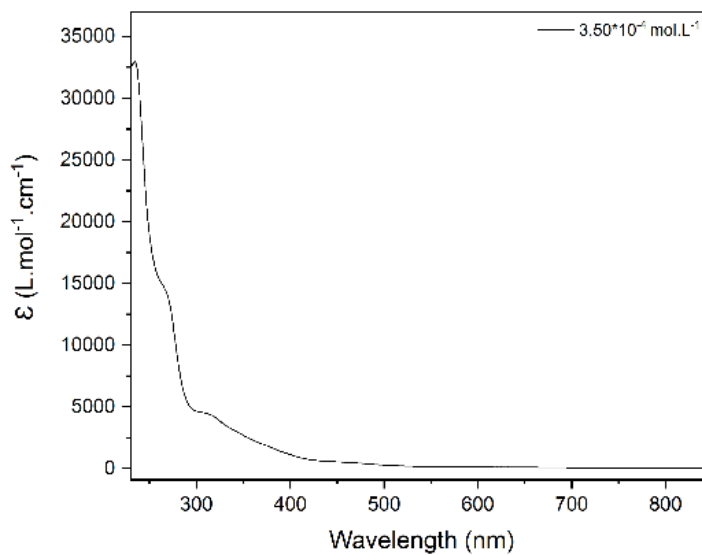


Figure S4. 37 UV-visible spectra of $4.2_{Sm}^{trans/cis}$.

UV-visible spectra of $4.2_{Gd}^{trans/cis}$

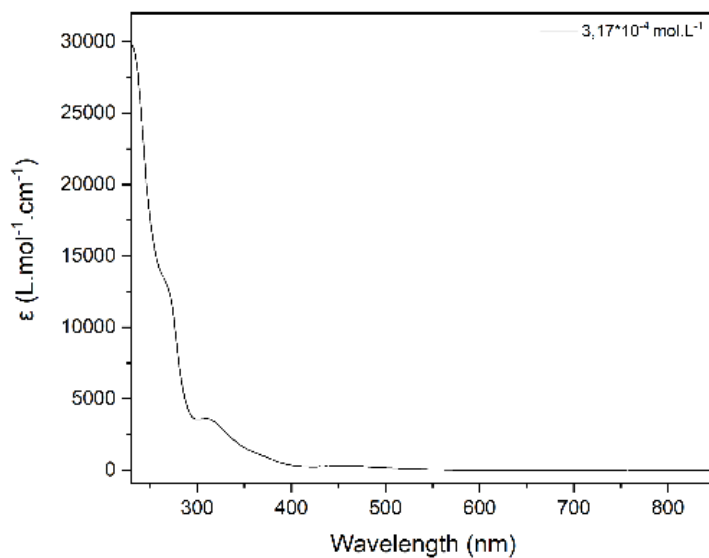


Figure S4. 38 UV-visible spectra of $4.2_{Gd}^{trans/cis}$.

UV-visible spectra of $4.2_{Tb}^{trans/cis}$

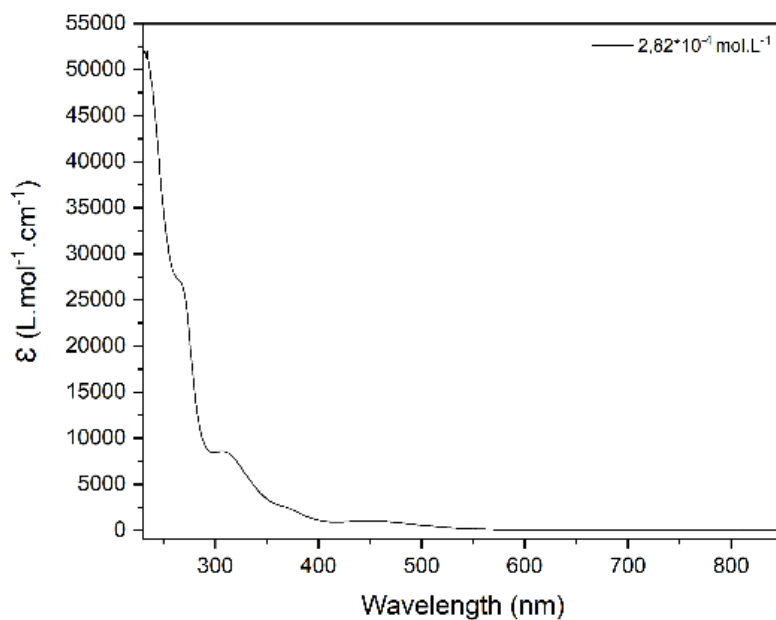


Figure S4. 39 UV-visible spectra of $4.2_{Tb}^{trans/cis}$.

UV-visible spectra of $4.2_{Dy}^{trans/cis}$

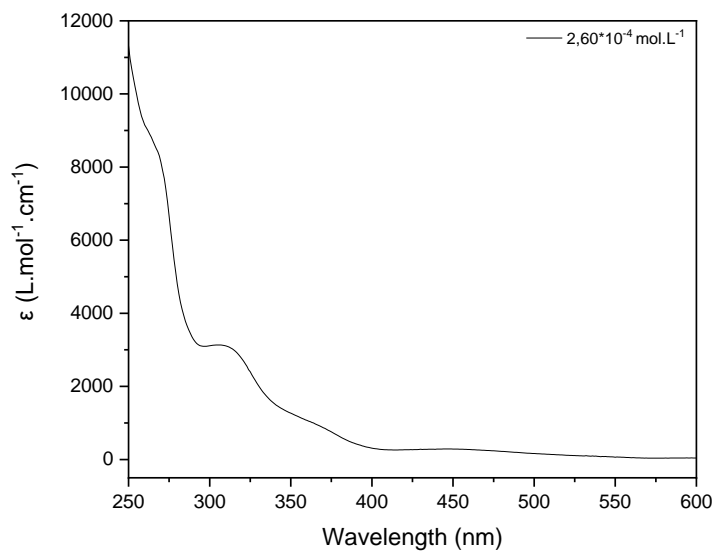


Figure S4. 40 UV-visible spectra of $4.2_{Dy}^{trans/cis}$.

UV-visible spectra of $4.2_{Ho}^{trans/cis}$

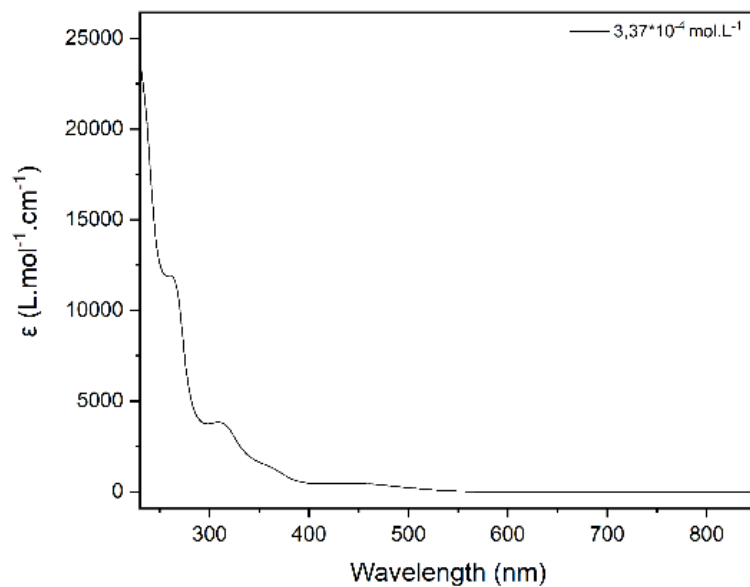
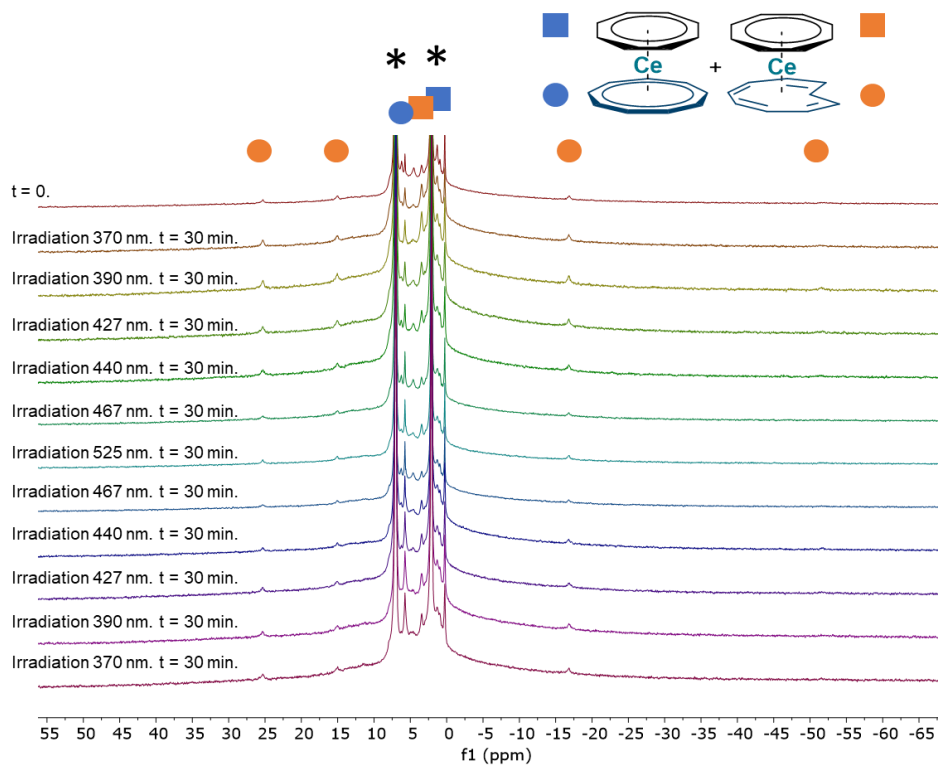


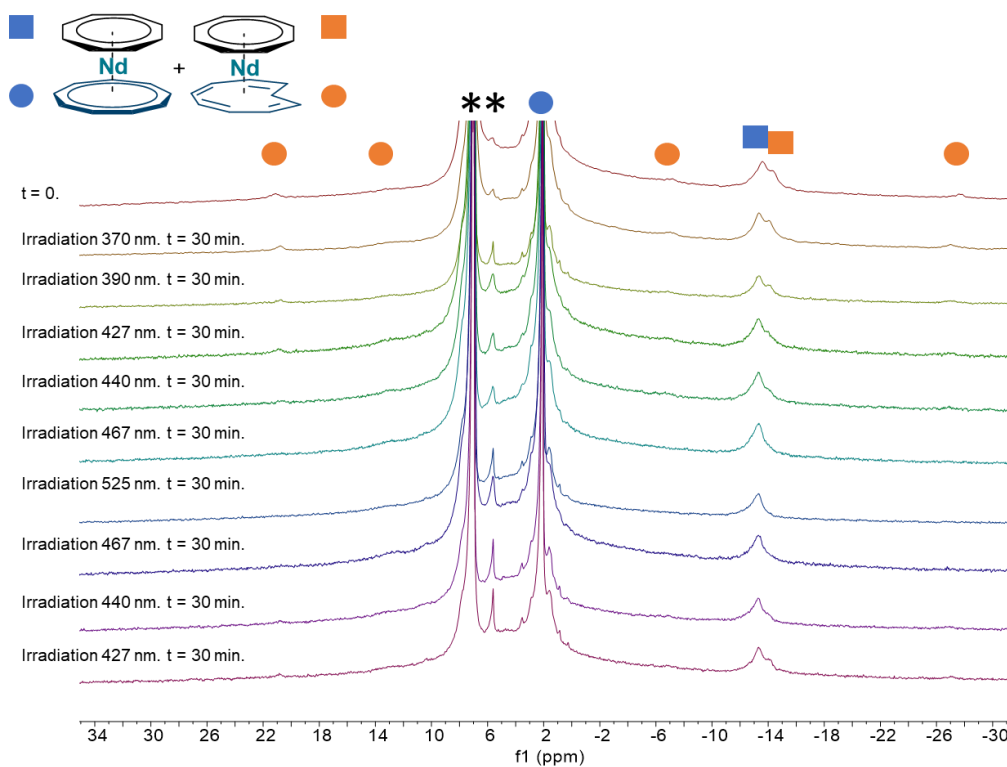
Figure S4. 41 UV-visible spectra of $4.2_{Ho}^{trans/cis}$.

VI. Isomerization reactions

Isomerization of $4.2_{\text{Ce}}^{\text{trans/cis}}$



Isomerization of $4.2_{\text{Nd}}^{\text{trans/cis}}$



Isomerization of $4.2_{Sm}^{trans/cis}$

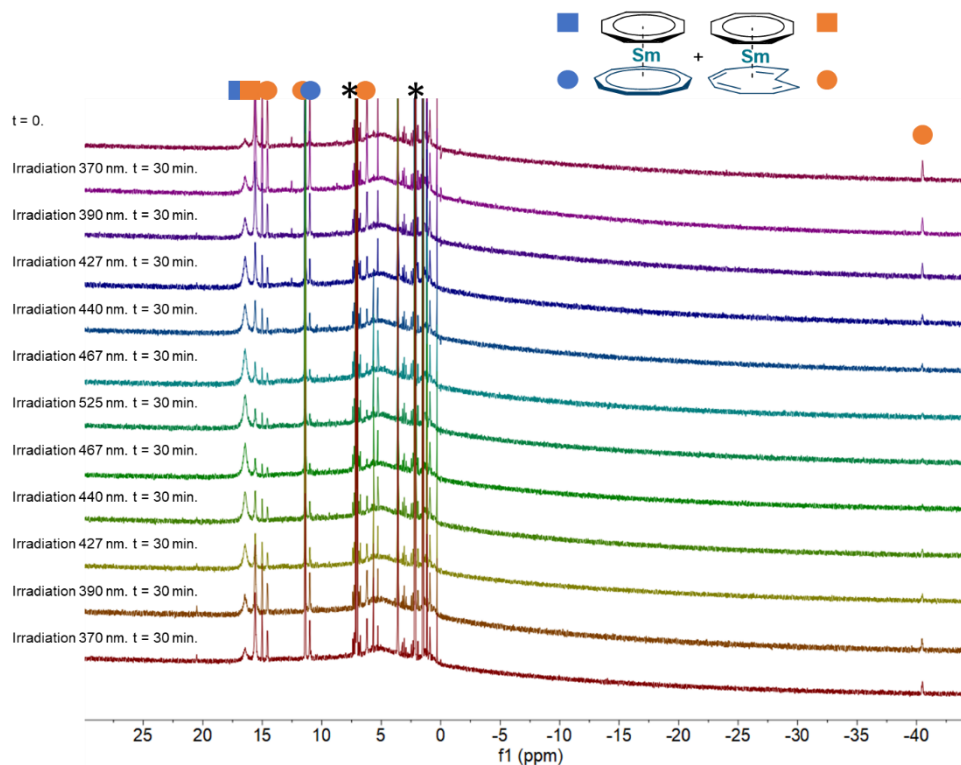


Figure S4. 44 ^1H NMR follow up of the irradiation of $4.2_{Sm}^{trans/cis}$ in toluene- d_8 (* residual protio signal of the solvent and degradation product).

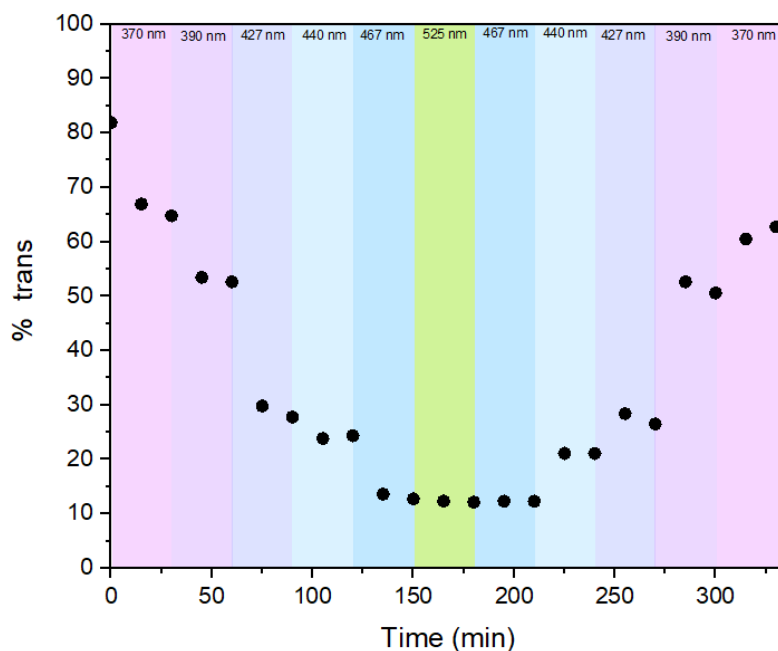


Figure S4. 45 Graphical representation of the $r^{trans/cis}$ after successive periods of irradiation.

Isomerization of $4.2_{Tb}^{trans/cis}$

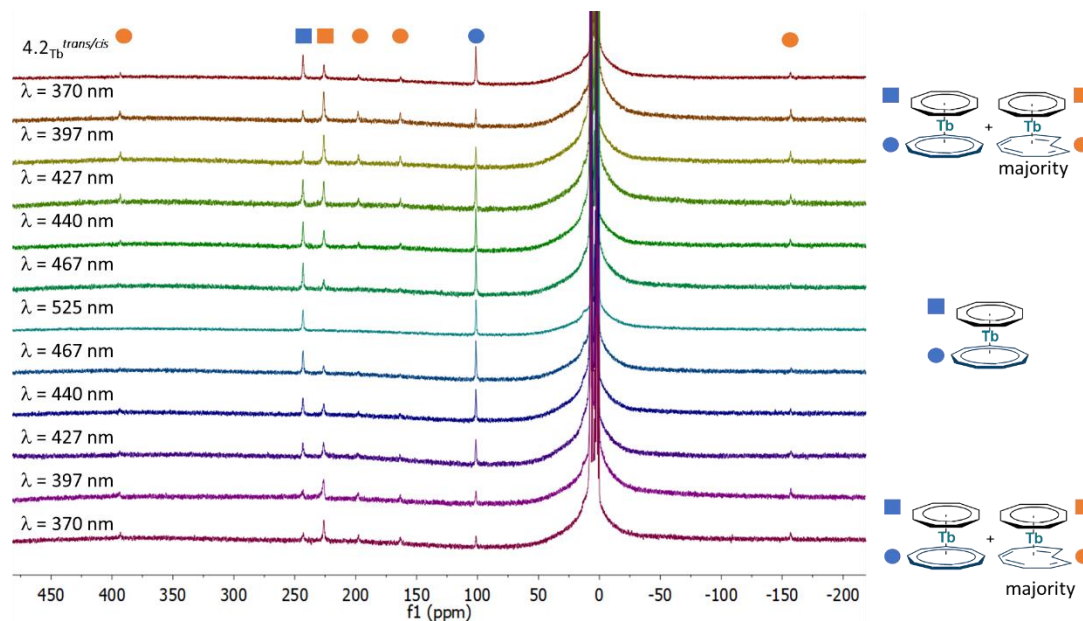


Figure S4. 46 ^1H NMR follow up of the irradiation of 4.2_{Tb} in toluene- d_8 (* residual protio signal of the solvent and degradation product).

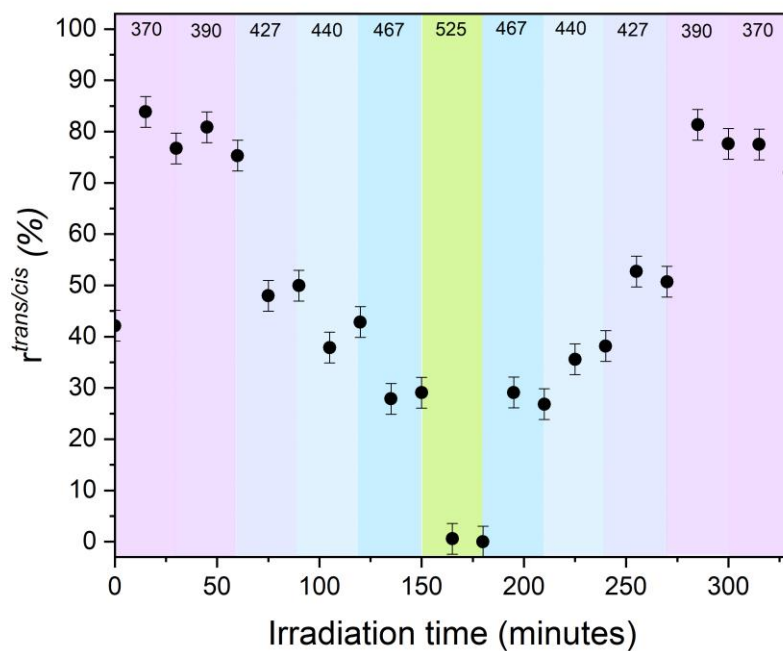


Figure S4. 47 Graphical representation of the $r^{trans/cis}$ after successive periods of irradiation.

Isomerization of $4.2_{Dy}^{trans/cis}$

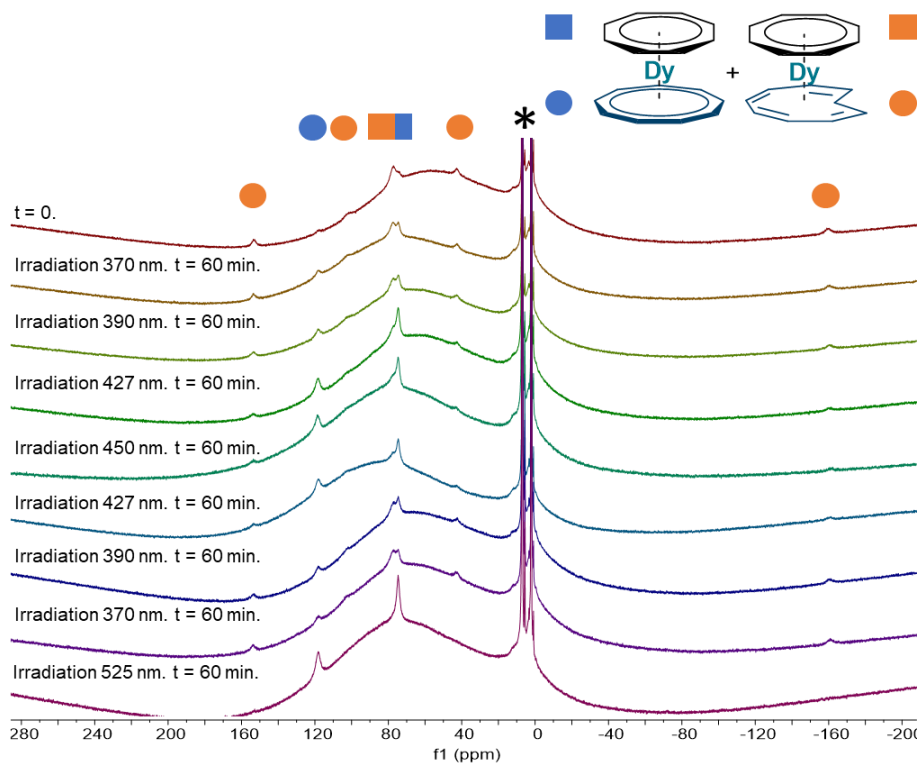


Figure S4. 48 1H NMR follow up of the irradiation of 4.2_{Ho} in toluene- d_8 (* residual protio signal of the solvent and degradation product).

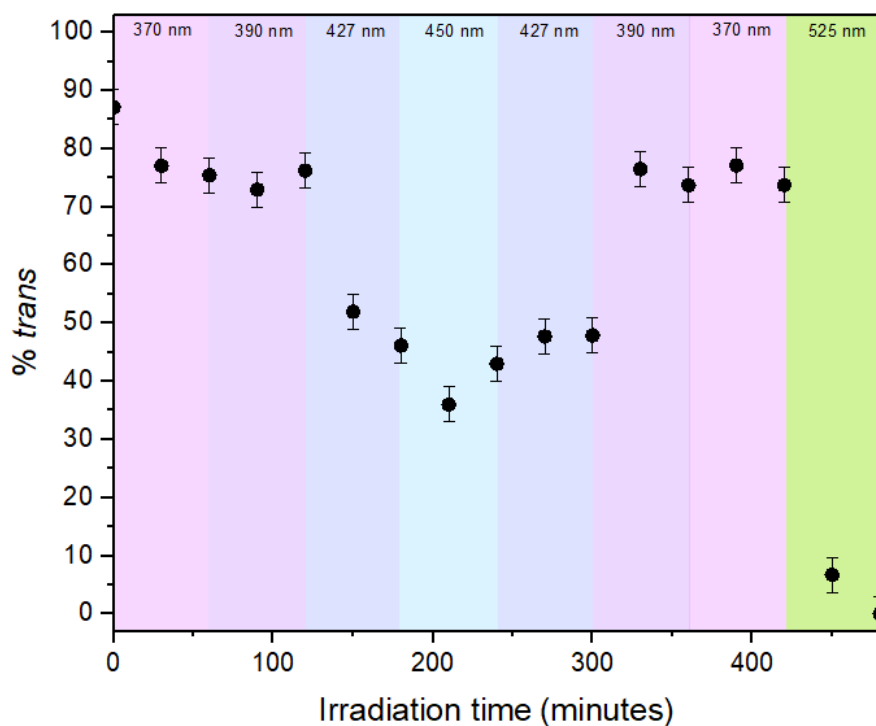


Figure S4. 49 Graphical representation of the $r^{trans/cis}$ after successive periods of irradiation.

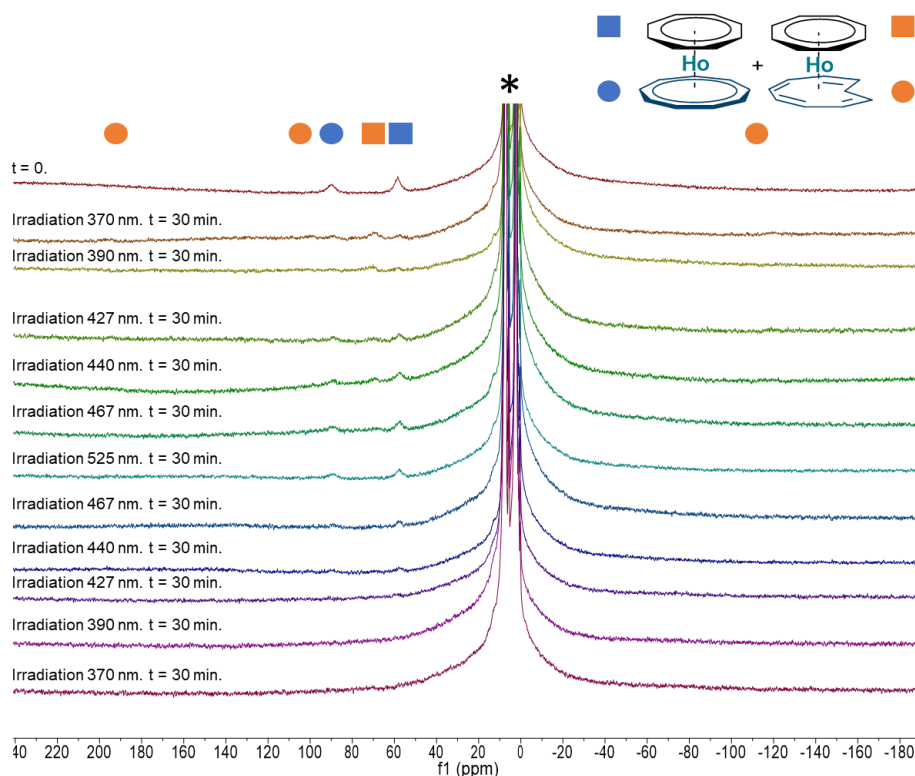
Isomerization of 4.2_{Ho} ^{trans/cis}

Figure S4. $50\text{ }^1\text{H}$ NMR follow up of the irradiation of 4.2_{Ho} in toluene- d_8 (* residual protio signal of the solvent and degradation product).

References

- (1) Lalancette, J.-M.; Rollin, G.; Dumas, P. *Can. J. Chem.* **1972**, *50* (18), 3058–3062.
- (2) Bergbreiter, D. E.; Killough, J. M. *J. Am. Chem. Soc.* **1978**, *100* (7), 2126–2134.
- (3) Katz, T. J. *J. Am. Chem. Soc.* **1960**, *82* (14), 3784–3785.
- (4) Xémard, M.; Zimmer, S.; Cordier, M.; Goudy, V.; Ricard, L.; Clavaguéra, C.; Nocton, G. *J. Am. Chem. Soc.* **2018**, *140* (43), 14433–14439.
- (5) Mashima, K.; Takaya, H. *Tetrahedron Lett.* **1989**, *30* (28), 3697–3700.
- (6) Mashima, K.; Nakayama, Y.; Nakamura, A.; Kanehisa, N.; Kai, Y.; Takaya, H. *J. Organomet. Chem.* **1994**, *473* (1–2), 85–91.
- (7) Tricoire, M.; Münzfeld, L.; Moutet, J.; Mahieu, N.; La Droitte, L.; Moreno-Pineda, E.; Gendron, F.; Hilgar, J. D.; Rinehart, J. D.; Ruben, M.; Le Guennic, B.; Cador, O.; Roesky, P. W.; Nocton, G. *Chem. – Eur. J.* **2021**.
- (8) Sheldrick, G. M. *Acta Crystallogr. A* **2008**, *64* (1), 112–122.
- (9) Sheldrick, G. M. *Acta Crystallogr. Sect. Found. Adv.* **2015**, *71* (1), 3–8.
- (10) Dolomanov, O. V.; Bourhis, L. J.; Gildea, R. J.; Howard, J. A. K.; Puschmann, H. *J. Appl. Crystallogr.* **2009**, *42* (2), 339–341.

Appendices

Résumé en Français	327
Published articles	329
Graphical Appendices	373
Abstract	378

Résumé de thèse

Ce travail de thèse s'intéresse à différents aspects de la chimie organométallique des lanthanides.

Dans un premier temps, l'utilisation de ligands aromatiques encombrés permettant la stabilisation des espèces divalentes de thulium a été appliquée à des réactions d'activation de petites molécules. Notamment, l'addition de CO₂ et de composés pyridines sur un dimer de thulium avec un fragment ethynediolate ont permis l'obtention d'une série de complexes. Les composés obtenus possédant de fortes colorations, une étude combinée de leurs structures moléculaires et de leurs spectres d'absorption UV-visible a été menée. Cela a révélé une corrélation entre l'angle formé par le dérivé pyridine avec le squelette carboné et le profil du spectre d'absorption, particulièrement des angles faibles mènent à des coefficients molaires d'absorption élevés. De plus, la donation électronique des substituents sur les dérivés de pyridine semble influencer sur le maximum d'absorption, les groupements donneurs paraissent favoriser un décalage des bandes d'absorption vers les hautes énergies. La rapidité des réactions mises en jeu avec les CO₂ a motivé une étude de réactivité avec d'autres petites molécules oxygénées.

La compréhension de la réactivité des lanthanides divalents développée dans la première partie a été utilisée dans une seconde étude, où un ligand plus large, le cyclononatétraenyl ligand, ou Cnt, a été étudié. Des réactions préliminaires avaient montré qu'il permettait la formation de complexes sandwichs linéaires et neutre avec les lanthanides moins réducteurs comme samarium, europium, thulium et ytterbium. Cependant, lors de sa réaction avec le diiodure de dysprosium, une nouvelle espèce a été observée. Celle-ci montre la formation d'une liaison carbonée entre deux unités de Cnt, procédant probablement par couplage radicalaire. Le dimère de dysprosium ainsi formé possède les caractéristiques d'un complexe contenant des dysprosiums trivalents. Il est donc probable que le centre métallique divalent ait transféré un électron vers le ligand lui conférant un caractère radicalaire qui permet ensuite le couplage. De légers changements dans les conditions de réactions et particulièrement un abaissement de la température (-35 °C), ont permis l'isolation d'un autre dimère où le Cnt réduit forme un pont entre les deux centres métalliques. L'analyse de la structure obtenue par diffraction des rayons X montre une certaine symétrie dans l'arrangement, ce qui est également supporté par les calculs menés sur cette molécule qui prévoient la délocalisation d'un électron sur les deux dysprosiums, leur conférant un degré d'oxydation de 2,5 chacun. En revanche, cette hypothèse est infirmée par la signature magnétique, elle-même plus compatible avec une faible interaction antiferromagnétique entre les deux métaux. D'autres caractérisations ont été effectuées mais il reste difficile de tirer une conclusion claire en raison de l'extrême sensibilité du complexe dimère.

Pour continuer d'explorer ces complexes, la synthèse a été modifiée pour utiliser des composés trivalents plus facile à manipuler. De plus, une stratégie hétéroleptique a été choisie, permettant l'isolation de composés dimériques très similaires. La structure obtenue pour l'un de ces dimères montre un motif Cnt ponté mais également une dissymétrie indiquant une potentielle différence électronique pour les deux dysprosiums. Cette valence mixte est aussi supportée par la présence d'une forte bande d'absorption dans le visible, typique de cette structure électronique. Grâce à l'utilisation des composés de départ trivalent, ces synthèses ont été étendu à d'autres lanthanides. Les structures obtenues montrent une grande similarité avec les complexes de dysprosium. La combinaison des études sur les divalents et trivalents a permis la réduction du nombre d'hypothèses expliquant le comportement des dimères pontés.

De plus, cela a permis de mettre en exergues les particularités du ligand Cnt notamment son caractère redox actif, sa flexibilité et sa présence comme deux isomères : *cis-cis,cis,trans* (*trans*) et *cis-cis,cis,cis* (*cis*). Afin de mieux comprendre leurs comportements, des études d'isomérisation, du ligand seul et dans un complexe hétéroleptique avec le ligand cyclooctatétraenyl, ont été menés. Ainsi, la forme *cis-cis,cis,trans* (*trans*) du ligand Cnt s'isomérisent sous irradiations, à des longueurs d'onde du proche UV et du visible (370 nm – 450 nm), aucune isomérisation n'est observée avec des longueurs d'ondes plus élevées. De plus, aucune retro-isomérisation de la forme *cis* vers la forme *trans* n'a été observée. La situation du complexe est très différente car le ratio *trans/cis* a pu être contrôlé par la nature du lanthanide ainsi que les longueurs d'ondes d'irradiation utilisées. Cela a permis de rationaliser le comportement d'isomérisation du ligand Cnt et permettra d'explorer la possibilité d'une réactivité associée.

Finalement, ce travail de thèse a permis d'étendre notre connaissance sur la réactivité des lanthanides divalents ainsi que notre compréhension du comportement du ligand Cnt.

Abstract: Over more than 50 years, intermediate valence states in lanthanide compounds have often resulted in unexpected or puzzling spectroscopic and magnetic properties. Such experimental singularities could not be rationalised until new theoretical models involving multiconfigurational electronic ground states were established. In this minireview, the different singularities that have been observed among

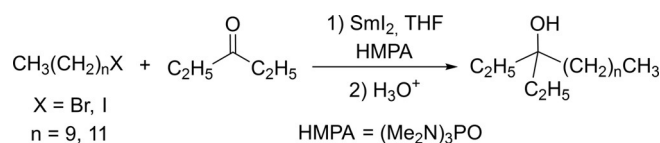
lanthanide complexes are highlighted, the models used to rationalise them are detailed and how such electronic effects may be adjusted depending on energy and symmetry considerations is considered. Understanding and tuning the ground-state multiconfigurational behaviour in lanthanide complexes may open new doors to modular and unusual reactivities.

1. Introduction

The chemistry of lanthanide compounds finds a significant number of direct applications especially because of their important and specific optical and magnetic behaviour.^[1–7] The industry of rare earth elements produces strong magnets for data storage or electrical devices, optics for health and technology and also many materials and molecular complexes for catalysis—including photocatalysis, polymerisation and reductive chemistry.^[7–9] The physical properties of these species are strongly correlated to high spin-orbit coupling, which is due to relativistic effects in these relatively heavy elements. Thus, the appropriate quantum number is J and the ligand field is significantly smaller than the spin-orbit coupling. Moreover, the weak screening of f-electrons leads to contraction of the ionic radius when the atomic number increases. Another important physical property of the f-orbitals is their core nature in the shell. As a consequence, the surrounding ligands often do not play a large role in the energy of those core f-orbitals; minimal spatial overlap occurs between the f-orbitals and the Lewis bases coordinated to the lanthanide ions.^[10] Finally, except for cerium and europium, the principal formal oxidation state of these elements is trivalent. These textbook properties have, however, been challenged in recent years, in particular as several groups have been able to synthesise divalent complexes for all the lanthanide series (except for the radioactive Pm) with adapted ligand environments,^[11–18] but also with the number of examples of high-valent molecular compounds increasing rapidly.^[19–23] The multiple occurrences of these unusual oxidation states ask the question as to whether the physical properties discussed above and the models used to understand them are still valid. If any unexpected properties appear

in those unusual oxidation state species, it would then indicate that some aspects of the metal–ligand bonding nature might have been underestimated. In low-valent species, the participation of the empty 5d-manifold is in question,^[18,24] as is the role of strongly donating ligands in high-valent species.^[23,25] This observation notably tends to indicate that the choice of the ligand should not be dictated only by the sterics but also by symmetry and energetic considerations, which is an important paradigm shift in lanthanide chemistry.

In low-valent chemistry, the question of a possible electronic contribution of the ligand to the reduction potential appeared with the important work of Flowers and co-workers on the role of hexamethylphosphoramide (HMPA) addition in reductive chemistry with divalent samarium (Scheme 1).^[26–27]





Scheme 1. Samarium Barbier reaction as described by Flowers and co-workers (adapted from Ref. [27]).

Procter, Maron and co-workers followed this by examining the role of water as solvent in these reactions.^[28] Aside from the study of organic transformations, in typical synthetic low-valent chemistry, the ligands were often chosen for solubility and stability reasons; the bulkier the ligand, the more stable the complex, even with non-classical divalent lanthanides.^[13] The use of elaborated ligands to stabilise low-valent lanthanides also generated important information on the influence of the ligand electronics in the reduction reactivity; if most samarium complexes do not reduce N_2 or CO , decamethyl samarocene is thought to do so,^[29,30] and is capable as well of reducing pyridine to form a C–C coupled dimeric complex whereas the same reactivity was not observed with a similar phospholyl ligand,^[31] presumably because of a redox potential modulation induced by the ligand. The ligand–metal pair thus takes importance and several electronic effects in the reduction reactivity have been noticed. For instance, a reversible C–C bond coupling was observed,^[32,33] the free enthalpy of which can be correlated to the redox potential of the reductive lanthanide fragment versus that of the ligand.

This proposition of an adapted energy for the ligand–lanthanide pair is extremely important because it is related to the

[a] M. Tricoire, N. Mahieu, Dr. T. Simler, Dr. G. Nocton
LCM, CNRS
Ecole polytechnique
Institut Polytechnique de Paris
Route de Saclay, 91128 Palaiseau, cedex (France)
E-mail: thomas.simler@polytechnique.edu
gregory.nocton@polytechnique.edu

 The ORCID identification number(s) for the author(s) of this article can be found under:
<https://doi.org/10.1002/chem.202004735>.

 © 2020 The Authors. Chemistry - A European Journal published by Wiley-VCH GmbH. This is an open access article under the terms of the Creative Commons Attribution Non-Commercial License, which permits use, distribution and reproduction in any medium, provided the original work is properly cited and is not used for commercial purposes.

theory of covalency in metal complexes.^[34] If an immediate relation with covalency is drawn in the case of a strong overlap between the ligand and the metal orbitals (nephelauxetic effect), the energy gap between them is often neglected. Given that the 4f electrons do not mix to a great extent with ligand orbitals of hard donors—such as oxygen, carbon and nitrogen—most lanthanide complexes are expected to present a purely ionic bonding with no covalency (Figure 1).^[35–37]

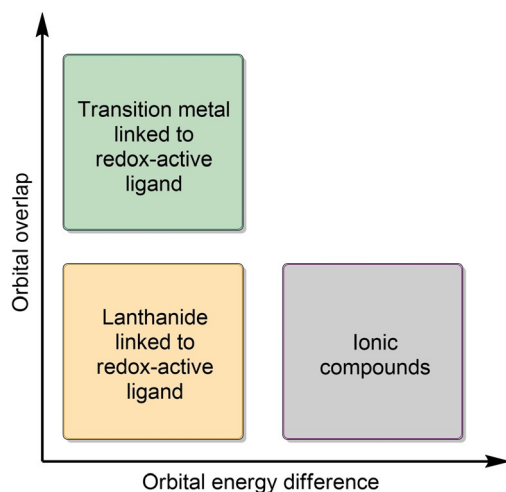


Figure 1. Orbital overlap versus orbital energy difference plot and the related compound categories (adapted from Ref. [38]).

However, when the ligand and the metal both possess similar energies, even with a very little overlap, the electron(s), statistically, have similar probabilities of being found on one or the other site. This situation leads to multiple possible configurations, in which the redox state of the metal is different: the metal and the ligand share electrons even with little overlap between the respective orbitals. This situation of multiple configurations is also known in transition-metal complexes when the orbitals are almost orthogonal, resulting in a small-to-zero overlap extent. Notably, the Wieghardt group and some of us have reported transition-metal complexes with multiple configurations, in which the corresponding redox states are different.^[39–46]

Thus, in lanthanide complexes, when the ligand orbitals and the lanthanide ion are of similar energy, these situations of multiple configurations with different redox states (of both the ligand and the metal ion) can occur, leading to a disturbance in their physical properties. The formal oxidation state is therefore not suitable anymore, as neither one nor the other value is appropriate. The valence is rather intermediate, as discussed in the field by the pioneers, Dolg, Fulde, Maron and Andersen.^[47–51] Indeed, the computation of multiple states of similar energy requires cautious choices of the methods used and, although density-based methods usually lead to fast analyses, in most cases, it solely points out delocalised density over the metal and ligand orbitals but does not reproduce nor explain the abnormal spectroscopic signatures that were observed. In this area, Field considered in the 1980s the computation of di-

atomic molecules of lanthanides for the better understanding of their non-trivial spectroscopic properties, especially arising from low-lying electronic states, and introduced the concept of “super-configurations”.^[52] At the time, if the key theoretical milestones of modern theoretical wave-function-based methodologies^[53,54] and DFT calculations^[55,56] were known, the large number of electrons in f-element complexes rendered the task

Maxime Tricoire did his studies at Ecole Normale Supérieure (ENS) in Paris. After getting his master's degree from Université Pierre et Marie Curie in Paris (now Sorbonne Université) in 2017, he joined Dr. G. Nocton's group at Ecole polytechnique in 2018 for his Ph.D. project involving lanthanides, redox-active ligands and transition metals.



Nolwenn Mahieu started her studies at the Ecole Normale Supérieure (ENS) Paris-Saclay in 2016. After a stay in Pr. E.J. Schelter's group at the university of Pennsylvania working on imido-thorium complexes, she graduated in 2020 with a master in molecular chemistry from ENS Paris-Saclay. She then joined Dr. G. Nocton's group at Ecole polytechnique for her Ph.D. studies on the synthesis of organolanthanide complexes.



Thomas Simler graduated in 2012 from the Ecole Normale Supérieure in Lyon. He received his Ph.D. in 2016 from the Université de Strasbourg working on functionalised NHC and pincer complexes with Dr. P. Braunstein and Dr. A.A. Danopoulos. He then joined the group of Prof. P.W. Roesky at the Karlsruhe Institute of Technology for a first postdoctoral stay supported by an Humboldt fellowship. Since 2019, he is working as postdoc in the group of Dr. G. Nocton at Ecole polytechnique.



Grégory Nocton was born in Reims, France in 1983. After a master of science at the Universities of Reims and Grenoble (2006), he obtained his Ph.D. in 2009 in Grenoble with Prof. Marinella Mazzanti, working on redox reactivity of uranium. He then joined UC Berkeley for two years working with Prof. R.A. Andersen and was appointed CNRS researcher in 2011 at Ecole polytechnique. He obtained the bronze medal of CNRS in 2016 and he is also associate professor at Ecole polytechnique since 2017.



rather difficult. Similarly, when multiconfigurational methods^[57,58] appeared, such as multiconfiguration Hartree–Fock/self-consistent field (MCHF/SCF), configuration interaction (CI) methods, many-body perturbation theory (MBPT) and coupled-clusters (CC),^[59–62] only a few studies were attempted with lanthanide complexes. It is only in the late 1980s that Fulde et al. developed the foundations of the proper understanding of the theoretical approach of such fluctuating systems,^[47,63] notably rationalising the formation of open-shell singlets and/or low-lying multiplet states by using the interaction between two partners (metal–metal or ligand–metal). This approach provided a possible explanation for several experimental observations based on the analogy with the Kondo singlet-state known in solid-state physics.^[64,65]

The present review gathers the historical basis that allowed the development of intermediate valence in lanthanide compounds over more than 50 years of spectroscopic singularities and many computational studies. It opens with a rational basis of the symmetry and energetic considerations that can lead to the prediction of these events and, importantly, describes how they may relate to the reactivity of the complexes (Figure 2). With the abundance of low- and high-valent lanthanide compounds isolated in the last few years, this topic is likely to receive broad and increasing attention.

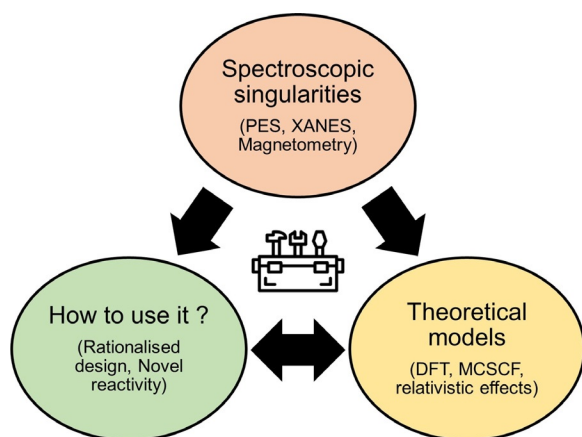
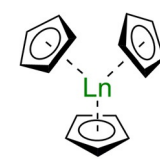


Figure 2. Intermediate valence and multiconfigurational ground states in lanthanide compounds: from spectroscopic singularities to the development of new theoretical models and the application in novel reactivity.

2. Spectroscopic Singularities

In the 1950s, Wilkinson and Birmingham reported the synthesis of a series of $[\text{LnCp}_3]$ ($\text{Cp} = \eta^5\text{-C}_5\text{H}_5$) complexes (Table 1).^[66–68] The latter were obtained as crystalline solids after sublimation under reduced pressure at high temperatures. The ionic nature of the new compounds was evidenced by their reactivity towards ferrous chloride (FeCl_2), resulting in an instantaneous ligand exchange reaction and quantitative formation of ferrocene, $[\text{FeCp}_2]$. Such an ionic nature would result from a dominant electrostatic interaction between the highly electropositive metal centres and the Cp rings with well-separated charges.^[69] The effective magnetic moments for the $[\text{LnCp}_3]$ com-

Table 1. General structure of the $[\text{LnCp}_3]$ complexes and magnetic data at room temperature (295–300 K) for selected compounds.



Ln	Electronic configuration of metal ion	Ground state of metal ion	Exptl. $\mu_{\text{eff}}^{[a]}$	Calcd. $\mu_{\text{eff}}^{[b]}$
Ce ^{III}	4f ¹	² F _{5/2}	2.46	2.54
Eu ^{III}	4f ⁶	⁷ F ₀	3.74 ^[c]	3.40–3.61 ^[e]
Yb ^{III}	4f ¹³	² F _{7/2}	4.00	4.54
Lu ^{III}	4f ¹⁴	¹ S ₀	diamagnetic	

[a] Values from Ref. [67], unless otherwise stated. [b] Theoretical values in the free-ion approximation. [c] Value from Ref. [71]. [d] Value for the mono-THF adduct, calculated with the data from Ref. [72]. [e] Non-magnetic ground state but presence of thermally populated magnetic excited states,^[73] estimated values at room temperature from Ref. [74].

plexes were determined experimentally. The overall values were in good agreement with the free-ion values, to the exception of one noticeable discrepancy: the reported magnetic moment of $[\text{YbCp}_3]$, $4.0 \mu_{\text{B}}$,^[67] differs from the expected value of $4.5 \mu_{\text{B}}$ for an Yb^{III} ion in a ²F_{7/2} ground state and is significantly lower than the experimental values for other typical Yb^{III} coordination compounds.^[70]

Following this seminal report, in-depth analysis of the electronic and magnetic properties of several $[\text{LnCp}_3]$ complexes or other lanthanide compounds have been carried out to evaluate and quantify covalency in such compounds, and revealed other spectroscopic singularities that are gathered in this sub-section.

2.1. YbCp₃

Gas-phase photoelectron spectra were recorded for a series of $[\text{LnCp}_3]$ ($\text{Ln} = \text{Ce}, \text{Pr}, \text{Nd}, \text{Sm}, \text{Yb}, \text{Lu}$) complexes using variable photon energy.^[75–79] Photoelectron (PE) spectroscopy has especially proved to be a valuable technique to assess the molecular electronic structure of lanthanide complexes and identify ion states resulting from 4f ionisation. In the case of a lanthanide complex featuring a 4fⁿ ground-state configuration, the spectrum obtained upon ionisation of a 4f valence electron gives information on the ground and excited states of the corresponding 4f^{n–1} cation.

The PE spectrum of $[\text{LuCp}_3]$ ^[80] can be readily interpreted: upon f-electron ionisation from the closed 4f¹⁴ shell of Lu³⁺, two bands were observed and assigned to the ²F_{7/2} and ²F_{5/2} ion states associated with the 4f¹³ configuration of Lu⁴⁺.^[77] In the case of $[\text{YbCp}_3]$, a more complex spectrum was obtained with signals arising from both the 4f¹² and 4f¹³ final-state configurations. An important question is whether the presence of both signals is the result of initial or final-state effects, that is, if the multiconfigurational character of the $[\text{YbCp}_3]^+$ cation ob-

tained upon ionisation does reflect (or not) that of the corresponding neutral $[\text{YbCp}_3]$ complex. The fact that ytterbium readily forms divalent complexes supports the idea of an initial-state effect, that is, contributions from both $\text{Yb}^{\text{III}} 4f^{13}$ and $\text{Yb}^{\text{II}} 4f^{14}$ configurations in the ground state of $[\text{YbCp}_3]$. More precisely, the mixed-configuration ground state corresponds to the superposition of a Lf^{13} configuration and a $\underline{\text{L}}f^{14}$ charge-transfer configuration involving electronic transfer from the Cp ring to the Yb^{3+} ion, where L represents a full ligand shell (the ligand molecular orbitals collectively) and $\underline{\text{L}}$ a hole in that shell.^[77] Careful analysis of the intensities of the bands associated with the two ion states allowed a determination of the relative contributions of the two configurations in the ground state.^[78] The $\text{Yb}^{\text{III}} \text{Lf}^{13}$ configuration was determined to account for 88% of the density in the ground state whereas the $\text{Yb}^{\text{II}} \underline{\text{L}}f^{14}$ charge-transfer configuration contributes 12%. Independent estimations of the relative weights of the two configurations were also obtained by thorough EPR investigations.^[78] Analysis of the ^{13}C hyperfine coupling, as determined by HYS-CORE (hyperfine sublevel correlation)^[81] pulsed EPR experiments, revealed an increase of $12.6 \pm 0.9\%$ in the spin density on the ^{13}C atoms of the Cp rings. In parallel, a decrease in the ^{171}Yb hyperfine coupling interaction was observed compared with a series of standard Yb^{3+} compounds, indicating a reduced spin density in the 4f shell of the ytterbium atom. The observed $\text{Yb} \rightarrow \text{Cp}$ spin transfer is linked to the $\text{Cp} \rightarrow \text{Yb}$ charge transfer associated with the $\underline{\text{L}}f^{14}$ configuration. Finally, the relative weights of the two configurations could also be estimated by analysis of the principal values of the g -tensor and the axial anisotropy, which is partially quenched owing to the charge-transfer configuration.^[78]

The presence of two configurations in the ground state of $[\text{YbCp}_3]$ is expected to have an influence on the magnetic susceptibility of the compound. Therefore, magnetic studies were performed in the solid state in the range 2–305 K.^[77] Above 20 K, a Curie behaviour was observed over the entire temperature range with an associated magnetic moment of $3.53 \mu_{\text{B}}$.^[77] This low magnetic moment compared with that of typical Yb^{III} complexes can be explained if the ground-state wavefunction includes a $\underline{\text{L}}f^{14}$ charge-transfer contribution, with a largely quenched orbital angular momentum. A slightly lower value for the magnetic moment ($3.33 \mu_{\text{B}}$) was derived from EPR measurements in frozen solution. The higher value obtained from solid-state magnetic measurements can be explained by a higher dielectric constant in the solid state, which stabilises the more polar Lf^{13} configuration and reduces the weight of the $\underline{\text{L}}f^{14}$ charge-transfer contribution in the solid state.^[78] As a result of the Curie behaviour, the magnetic moment showed almost no dependence on the temperature in the range 20–305 K, which can be explained by a negligible thermal population at 300 K of high-lying excited states (higher than 1000 cm^{-1}).^[77] Below 20 K, substantial departure from the Curie behaviour was observed, which may be interpreted as a structural phase change occurring at a temperature of 20 K.^[77] As a result of this phase change, the relative weights of the f^{13} and f^{14} configurations in the ground state are likely to be perturbed, leading to different magnetic properties.

Anomalous features were also observed in the electronic spectra of $[\text{YbCp}_3]$. Such spectra, in the solid state^[82] and in solution,^[83] had already been reported in 1967 and 1983, respectively, but remained largely uninterpreted until more recent work by Denning et al. in 2011.^[78] In the visible/near IR spectrum of $[\text{YbCp}_3]$, the f–f region is highly anomalous compared with that of conventional Yb^{3+} compounds, such as, for example, $[\text{Cp}^*_2\text{Yb}(\text{L})^+(\text{X})^-]$ (L = 1,10-phenanthroline (phen) or 2,2'-bipyridine (bipy)); X = I or PF_6^- ; see also below, section 2.7).^[84,85] Indeed, f–f transitions in lanthanide compounds (similarly to d–d transitions for transition-metal complexes) are parity forbidden on the basis of the selection rules. The intensities of the corresponding bands were found to be 20 to 50 times larger than those for typical Yb^{3+} compounds and vibronic structures associated with f–f transitions spanned a much larger energy range (ca. 2000 cm^{-1} compared with $597 \pm 185 \text{ cm}^{-1}$). Such anomalous features can be explained by charge-transfer transitions supporting a configuration interaction in the ground state.^[78]

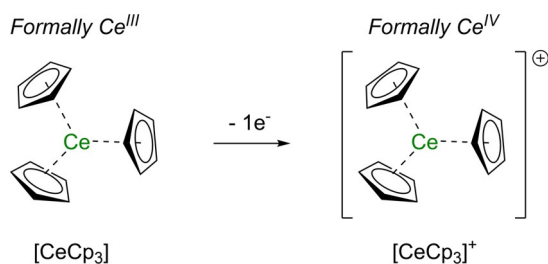
Although routine DFT calculations clearly indicated delocalisation of the spin density away from the Yb atom, they were not appropriate to evaluate the residual spin density on Yb. Using different DFT methods, large differences in the spin density values were obtained. Yet, such computational methods were still useful to give certain insights in the electronic structure, such as the relative orbital energies, and rationalise the experimental electronic and EPR spectra.^[78]

2.2. EuCp_3

The involvement of a $\text{Cp} \rightarrow \text{Ln}$ charge-transfer contribution similar to that in $[\text{YbCp}_3]$ is also expected in the more easily reduced Eu^{III} analogue. Indeed, the $\text{Ln}^{3+}/\text{Ln}^{2+}$ redox potentials versus NHE (NHE = normal hydrogen electrode) are -0.35 V and -1.15 V for Eu and Yb, respectively.^[86] In the case of europium compounds, ^{151}Eu Mössbauer spectroscopy is a useful technique to probe the electronic properties at the europium nucleus. The ^{151}Eu isomer shift strongly depends on the oxidation state of the europium ion whereas the quadrupole interaction gives information about the symmetry of the environment at the metal centre.^[87] In the ^{151}Eu Mössbauer spectrum of $[\text{EuCp}_3(\text{THF})]$, an unusual isomer shift lying between the typical values for Eu^{II} and Eu^{III} complexes was observed, together with a large negative quadrupole interaction, which is also unusual for europium organometallic compounds.^[88] To explain such features, a strong interaction between the Eu 4f orbitals and the three Cp ligands, resulting in the transfer of approximately 0.14 electrons from the ligand sphere to the metal, was suggested.^[88]

2.3. CeCp_3

Among $[\text{LnCp}_3]$ complexes, the cerium analogue was reported to be the most reactive towards oxidation by traces of air, which can be traced back to the easy oxidation of the Ce^{III} centre to Ce^{IV} (Scheme 2).^[66,67] The reported magnetic moment of $[\text{CeCp}_3]$ ($2.46 \mu_{\text{B}}$) at room temperature is consistent with



Scheme 2. Structures of the formally Ce^{III} complex [CeCp₃] and its related Ce^{IV} cation [CeCp₃]⁺.

that expected for an unperturbed Ce^{III} 4f¹ configuration with a ²F_{5/2} ground state (2.54 μ_B, Table 1).^[67] Insights into the electronic ground state of [CeCp₃] and in the optical transition energies of this 4f¹ complex were given by non-relativistic and relativistic DFT calculations.^[89] Analysis of the symmetry of the orbitals revealed that the C_{3v} ligand environment observed in [CeCp₃] is particularly adapted for f-block elements featuring valence f-orbitals, in contrast to transition metals that possess valence d-orbitals. Although the incorporation of relativity into the calculations only had minor effects on the largely ligand-based molecular orbitals (MOs), it did affect the energies of metal-localised atomic orbitals (AOs). Indeed, relativistic effects destabilise the f-orbitals, bringing the Ce 4f and 5d orbitals closer in energy, which has a direct influence on the electronic absorption spectrum. Although both non-relativistic and relativistic calculations predicted a 4f¹ ground-state configuration for [CeCp₃], the inclusion of relativity led to a 6d¹ ground state for the heavier actinide analogue [ThCp₃]. The calculated electronic absorption spectrum of [CeCp₃] revealed weak f→f transitions with a more intense low-lying f→d transition.^[89]

The electronic structures of the neutral complex and of its cationic form [CeCp₃]⁺ were further investigated by variable photon energy photoelectron (PE) spectroscopy in the gas phase.^[75] Upon ionisation of the single f-electron of [CeCp₃], a simple orbital model would predict only one possible ion state for the corresponding 4f⁰ [CeCp₃]⁺ cation, that is, only one photoelectron band in the PE spectrum. However, two bands separated by a large energy gap (3.2 eV) and associated with two different final states were observed.^[75] It should be noted that the occurrence of two signals associated with f-ionisation had already been reported in the photoemission spectra of solid inorganic Ce compounds.^[90–92] In the PE spectrum of [CeCp₃], the lower energy state associated with the first PE band corresponds to the ground state of the gas-phase [CeCp₃]⁺ cation. Its electronic structure was rationalised in terms of an interaction between two different electronic configurations.^[75] Further studies revealed that, although the ground state of [CeCp₃]⁺ does not possess a Ce-localised f-electron, it has significant f-density arising from population of natural orbitals (NOs) with f-character.^[76] The higher energy band in the PE spectrum also arises from f-ionisation and is associated with an excited state of [CeCp₃]⁺. This excited state features significant Ce5d population owing to intramolecular Cp→Ce5d charge transfer occurring upon f-ionisation. Insights into the electronic structure of the different states of [CeCp₃]⁺

was provided by ab initio calculations using the complete active space self-consistent field (CASSCF)^[93]/complete active-space second-order perturbation theory (CASPT2) approach.^[76] The CASPT2 methodology includes perturbations by additional corrections for dynamic correlation.^[94]

However, electronic configurations involving canonical CASSCF orbitals were found not to reliably describe the electronic structures of the ground and excited states of [CeCp₃]⁺. Indeed, the weights of these configurations were highly influenced by the number of states included in the state-averaged (SA) CASSCF calculation (see discussion below on cerocene). The NOs and their occupations (NOOs) are specific to each state and are more informative. They are computed from the reduced density matrix of each state and not from the state-averaged matrix, the latter being used to produce pseudo-NOs in CASSCF/CASPT2 calculations. The f-electron occupancy can then be derived from the NOOs and their f-coefficients for all the active space orbitals. A deviation >0.1 from an integer value for the NOOs ensures the presence of a multiconfigurational state. As a result, in the [CeCp₃]⁺ cation, several configurations were found to compose the wavefunction, resulting in an intermediate-valent ground state. The same conclusion was obtained for the excited states involved in the second PE band. Yet, as no NO is purely f-based in the electronic ground state of [CeCp₃]⁺, the latter does not possess any metal-localised 4f electron, which supports the description of this cation as formally Ce^{IV}. The significant f-density on the metal centre, similar to that in the formally Ce^{III} [CeCp₃], is due to population of delocalised NOs with f-character.^[76] This conclusion highlights the very core of the semantic issue arising in these kind of systems. How to qualify a Ln ion that shows properties from a different oxidation state than its formal one? The theoretical model supports intermediate valence as it uses multiconfigurational states to define the system but these states may bear no fundamental characteristics of one or the other oxidation state involved (i.e., no pure f-orbital localised electron in this case).

2.4. Cerocene and derivatives

Aside from the [LnCp₃] complexes, the electronic structure of cerocene, [Ce(Cot)₂] (Cot = η⁸-C₈H₈; Figure 3), has been the subject of a great deal of research from both experimental and theoretical points of view.

The successful synthesis of cerocene was first reported in 1976 by Cesca and co-workers, by reaction of [Ce(OⁱPr)₄] with [AlEt₃] in the presence of excess cyclooctatetraene (Cot).^[95] Cer-

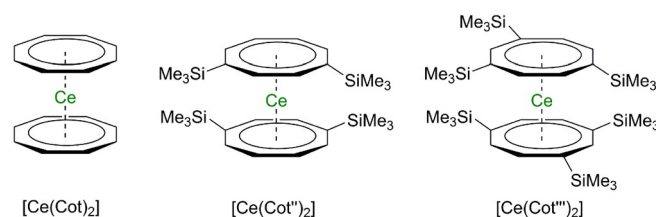


Figure 3. Structure of cerocene and its trimethylsilyl-substituted analogues.

ocene combines a strong reducing agent (the Cot^{2-} dianion) and a strong oxidising agent (a Ce^{4+} ion). Alternative and higher-purity syntheses of $[\text{Ce}(\text{Cot})_2]^{[96,97]}$ and of several substituted cerocenes have also been described.^[98,99] In such complexes, the distance between the ring centroid and the Ce metal centre is approximately 1.97 Å, which is approximately 0.10 Å shorter than the corresponding distance in the Ce^{III} $[\text{Ce}(\text{Cot})_2]$ diglyme salt.^[100] Such a shortening is consistent with the smaller ionic radius of the Ce^{4+} cation compared with that of the Ce^{3+} cation.^[101] In addition, electrochemical studies and the apparent diamagnetism of cerocene were further pointing to a formal Ce^{IV} complex.

In the gas-phase PE spectrum of $[\text{Ce}(\text{Cot})_2]$, no clear sign of f-electron ionisation was observed, also supporting a $4f^0$ configuration, that is, a +IV oxidation state for the metal centre, similarly to the situation encountered in the heavier 5f thorium analogue.^[102] In the UV/Vis spectrum, strong absorption bands in the visible region at 469 nm (ϵ ca. 8000) with a shoulder at 570 nm (ϵ ca. 1000) were assigned to ligand-to-metal charge-transfer transitions. The substituted cerocene $[\text{Ce}(\text{Cot}'')_2]$ ($\text{Cot}'' = 1^8\text{-}1,4\text{-}(\text{Me}_3\text{Si})_2\text{C}_8\text{H}_6$; Figure 3), first reported in 1994 by Edlmann and co-workers, was obtained by oxidation of the Ce^{III} complex $\text{Li}[\text{Ce}(\text{Cot}'')_2]$ with AgI, and isolated as a deep-purple oil.^[99] An alternative synthesis, consisting of the oxidation of $\text{Na}[\text{Ce}(\text{Cot}'')_2]$ with allyl bromide, was described by Streitwieser and co-workers and led to the same compound, $[\text{Ce}(\text{Cot}'')_2]$, isolated as a dark-brown semisolid material.^[96] The UV/Vis spectra of $[\text{Ce}(\text{Cot}'')_2]$ and of other substituted cerocenes ($[\text{Ce}(\text{C}_8\text{H}_7\text{R})_2]$ with $\text{R} = \text{Me}, n\text{Bu}, t\text{Bu}, t\text{BuO}$) were recorded and revealed a maximum absorption band in the region 470–494 nm.^[96,99] This band was first attributed to a ligand-to-metal charge-transfer transition occurring in formal Ce^{IV} complexes,^[96] similarly to the situation in cerocene.^[102] However, further spectroscopic studies on $[\text{Ce}(\text{Cot}'')_2]$ at variable temperatures reported by Amberger et al. were more consistent with a Ce^{III} formulation.^[103] In the luminescence spectrum at low temperature (90 K), two bands were observed with maxima at 14 250 and 17 900 cm^{-1} , which is typical for Ce^{III} complexes, as, for example, $[\text{Li}(\text{THF})_4][\text{Ce}(\text{Cot})_2]$. The separation between the two bands, 3650 cm^{-1} , is, however, bigger than that usually observed in Ce^{III} complexes (typically 1250–1400 cm^{-1}) and is in agreement with the energy separation predicted by calculations corresponding to a $\text{Ce}^{3+}[(\text{Cot})^{1.5-}]_2$ formulation (see below).^[47–49] The authors could nonetheless not totally exclude the possibility that some of the luminescence signals detected a low temperature may arise from Ce^{III} decomposition products under laser irradiation.^[103]

X-ray absorption near-edge structure (XANES) spectroscopy studies have been carried out to further investigate the oxidation state of Ce in cerocene and its substituted analogues.^[97,104–106] Through the exposure to high-energy X-rays, core electrons are excited into empty or singly occupied valence orbitals of the metal complex (Figure 4). XANES has been recognised as a useful tool to determine the oxidation state of an atom and has been used to evaluate the degree of f-orbital participation in the bonding of lanthanide and actinide compounds.^[107,108] The absorption is measured below and above a

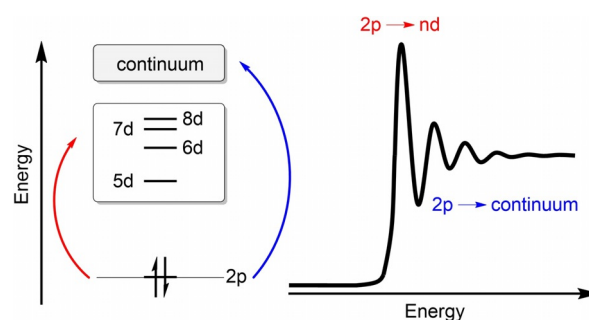


Figure 4. Schematic representation of L_3 -edge XANES transitions and their origin. Adapted from Ref. [24].

characteristic X-ray elemental edge. For example, for metal ions, K-, L-, or M-edge X-ray absorption spectroscopy (XAS) has been employed. Some reports focused on ligand K-edge XAS studies on the atoms directly bound to Ln centres to investigate metal/ligand orbital mixing and covalency in lanthanide compounds.^[23,106,109–111] These different XAS techniques differ by the energy of the transitions involved. Whereas lanthanide K-edge XAS involves high-energy excitations of metal 1s electrons to empty orbitals of p character, lanthanide L_3 -edge XANES studies probe transitions between Ln2p orbitals and unoccupied states of 5d character (i.e., transitions from a $2p^6 4f^n 5d^0$ to a $2p^5 4f^{n+1} 5d^1$ electronic state where n corresponds to the number of f-electrons in the ground state).^[24] The energies of the transitions are related to the ground-state $4f^n$ occupation and the effective nuclear charge on the lanthanide ion.

Recently, lanthanide $M_{5,4}$ -edge XAS studies, which involve transitions from core-level 3d electrons to empty 4f orbitals, that is, transitions from $3d^{10} 4f^n$ to $3d^9 4f^{n+1}$ configurations, have been employed to probe 4f valency in lanthanide ions.^[24,106,109,111] The energy at which the absorption edge occurs is linked to the metal oxidation state or f-occupancy in intermediate valence systems. In Ce^{III} complexes, the presence of only one initial state with a configuration $L2p^6 4f^1$ (L corresponding to the orbitals of the ligand) results in a single final state of $L2p^5 4f^1 5d^1$ configuration after L-edge XAS irradiation.

Formal Ce^{IV} compounds, and more generally Ln^{IV} compounds, usually feature a superposition of Lf^0 and Lf^1 (L is a ligand hole) configurations in their ground states. It is, for example, the case in CeO_2 , which is generally considered a strongly mixed-valent compound,^[111–115] although its electronic ground state is still controversial.^[116]

In the corresponding XAS spectra, the white line usually displays multiple peaks, typically in the shape of a white line doublet, owing to contributions of the different configurations in the final state. Quantitative analysis of the multiple features observed in the core-level X-ray photoemission (XPS) spectrum of CeO_2 led to similar conclusions, supporting a mixture of $L4f^0$ and $L4f^1$ configurations in the ground state.^[112] However, the physical origin and the interpretation of the white line doublet in Ln XAS measurements is still under debate and the XPS core final states are different from the XANES final states.^[113] The presence of contributions from both configurations could be the result of either a multiconfigurational ground-state (i.e., ini-

tial-state effects) or final-state effects.^[106,109,111] Final-state effects would support the presence of a single ground state leading to a doublet feature as the result of transitions to unoccupied 5d states split by the crystal field, or strong perturbation and relaxation effects around the core hole.^[23,113] However, most studies support initial-state effects. Analysis of the XANES data of the substituted cerocenes [Ce(Cot'')₂] and [Ce(Cot''')₂] (Cot''' = η⁸-1,3,6-(SiMe₃)₃C₈H₅; Figure 3) revealed K-edge shifts at energies similar to those observed in various Ce³⁺ model compounds, therefore supporting a Ce^{III} oxidation state.^[104] However, the edge energies were slightly shifted (about 4.5 eV) towards a higher oxidation state in comparison with the edge energies of the corresponding alkali metal Ce^{III} adducts. Therefore, XANES data support mixed-valence in substituted cerocenes. The lower electronic density compared with typical Ce^{III} compounds was interpreted as an admixture of Ce^{III} $\underline{L}4f^1$ and Ce^{IV} $L4f^0$ configurations in the ground state of cerocene, as predicted in earlier calculations by Dolg, Fulde and co-workers.^[47–49] Andersen and co-workers reported that, using Ce L₃-edge (rather than Ce K-edge) XAS, a well-defined white line doublet can be observed in formal Ce^{IV} compounds, which allows a more precise estimation of the cerium valence in these compounds.^[105] The high-resolution Ce L₃-edge XANES spectrum of [Ce(Cot)₂] was found to be more consistent with that of a Ce^{III} rather than Ce^{IV} compound, but still displayed some characteristic Ce^{IV} features.^[105] These data were in agreement with earlier Ce K-edge XANES data recorded by Edelstein and co-workers on the substituted cerocenes [Ce(Cot'')₂] and [Ce(Cot''')₂].^[104] By fitting the Ce L₃-edge XANES data, the relative contributions of the two configurations can be determined. The f-occupancy, n_f , is defined in Equation (1) where $A_{Ln^{3+}}$ is the intensity of the $\underline{L}2p^{5.4}f^{n+1}5d^1$ final-state contribution and $A_{Ln^{4+}}$ that of the $L2p^{5.4}f^05d^1$ contribution.

$$n_f = \frac{A_{Ln^{3+}}}{A_{Ln^{3+}} + A_{Ln^{4+}}} \quad (1)$$

For cerocene, the estimated value $n_f = 0.89 \pm 0.03$ supports the calculation predictions of Dolg and co-workers (Figure 5).^[49] No influence of the temperature on the n_f value was observed until 400 K, the temperature at which conversion of [Ce(Cot)₂] to [Ce₂(Cot)₃] begins to occur.^[97] The latter compound, in contrast to [Ce(Cot)₂], is clearly trivalent with $n_f = 1$.

Very recent studies focused on Ce M_{5,4}-edge and carbon K-edge XAS to investigate covalency in [Ce(Cot)₂].^[106] The Ce M_{5,4}-edge XAS data were compared with those obtained by L₃-edge XAS studies for other formally Ce^{IV} ([Ce(Cot)₂], CeO₂,

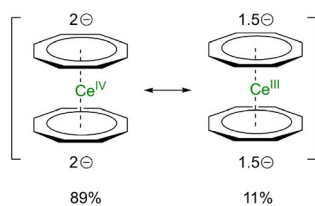


Figure 5. Ce^{IV} and Ce^{III} contributions in cerocene as determined by Andersen and co-workers.^[105]

CeCl₆²⁻) and Ce^{III} ([Ce(Cot)₂][Li(THF)₂] and CeCl₆³⁻) species.^[105,109,111] It should be noted that, compared with L₃-XANES, the intensity ratio between M_{5,4}-XANES final states are quite different and the deduction of ground-state intermediate valence requires a theoretical description of the final states. Although the Ce M_{5,4}-edge XAS spectrum for [Ce(Cot)₂] is more similar to that of formal Ce³⁺ compounds, successful fitting of the data was only possible when including both Ce^{IV} $L3d^{10}4f^0$ and Ce^{III} $\underline{L}3d^{10}4f^1$ initial-state configurations, and the corresponding $\underline{L}3d^94f^1$ and $\underline{L}3d^94f^2$ final-state configurations. A contribution of 51 % of the charge-transfer Ce^{III} configuration to the ground state was established, which is larger than that derived from Ce M_{5,4}-edge XAS data on other formally Ce^{IV} compounds, such as CeCl₆²⁻ (25 %)^[109] or CeO₂ (ca. 44 %).^[111] However, this Ce^{III} contribution to the ground state is much lower than that established by L₃-edge XANES spectroscopy (89 %).^[105]

SQUID magnetic studies revealed that high-purity [Ce(Cot)₂] displays temperature-independent paramagnetism (TIP) in the range 5–300 K, with the magnetic susceptibility χ being slightly positive and temperature independent, which rules out a diamagnetic molecule that would present $\chi_m < 0$.^[97,105] Neumann and Fulde suggested that cerocene may be considered as a molecular analogue of a Kondo singlet.^[47] The Kondo effect is a term derived from the physics of solid-state materials and arises when paramagnetic sites antiferromagnetically couple to conduction electrons, resulting in cancelation of the local magnetic moment.^[64–65,117] The term Kondo singlet means that an open-shell singlet is lying lower in energy than the open-shell triplet, as a result of a mixture of two configurations (in this case the Ce^{III} $\underline{L}f^1$ and Ce^{IV} Lf^0 configurations, with \underline{L} and L corresponding to (Cot^{1.5-})₂ and (Cot²⁻)₂, respectively). In Kondo systems, the triplet state becomes populated by increasing the temperature until the Kondo temperature at which the spins become uncorrelated. In this case, cerocene behaves as a Kondo singlet in the temperature range 5–300 K but decomposes to [Ce₂(Cot)₃] and free Cot before the triplet state begins to be populated.^[97]

Studies of other [Ln(Cot)₂]⁻ complexes by anion photoelectron spectroscopy revealed a pair of prominent peaks in the PE spectra of the middle-range lanthanide (Ln = Sm, Gd, Tb, Dy and Ho) complexes. In contrast, simpler features were observed for the lighter and heavier lanthanide analogues. These results were rationalised in terms of configuration interaction involving both Ln³⁺ and Ln⁴⁺ configurations after photodetachment of one electron.^[118]

As DFT calculations are not well-adapted for these particular systems, they do not properly describe the multiconfigurational character of [Ce(Cot)₂]. Yet, broken-symmetry DFT (B3LYP) calculations seemed to reproduce some aspects of the multiconfigurational character observed by CASSCF calculations and revealed an open-shell singlet ground state resulting from an admixture of singlet and triplet states.^[106] Concerning theoretical models, following the theoretical studies by Rösch and Streitwieser stating that cerocene is at the +IV oxidation state, similarly to uranocene and thorocene,^[119] Neumann and Fulde were the pioneers who opened cerocene's Pandora box in

which was concealed numerous questions about its oxidation state. With the rise of relativistic pseudo-potentials developed for f-elements in the beginning of the 1990s,^[120–123] a huge gap was filled, making possible the study of cerocene with complex MCSCF methods. This led to Dolg's works on the topic, validating the fact that cerocene's ground state had to be considered as intermediate valent with two 1A_g configurations (in D_{8h} symmetry), the open-shell singlet $Ce^{III} \underline{1}f^1$ (or $Ce^{3+}[(Cot)^{1.5-}]_2$) and the closed-shell singlet $Ce^{IV} Lf^0$ (or $Ce^{4+}[(Cot)^{2-}]_2$), which coexist with the Ce^{III}/Ce^{IV} ratio being approximately 83:17. This ratio can be noted $n_f=0.83$ to represent the effective number of f-electrons left on the Ce atom.^[48,49,124] This initial statement that the ground-state wavefunction of cerocene is multiconfigurational was later endorsed by Kerridge. However, suspicions about the Ce^{III} character being predominant led in 2009 to SA-CASSCF^[93] studies coupled with CASPT2^[94] calculations, which resulted in $Ce^{II}/Ce^{III}/Ce^{IV}$ contributions to the wavefunction being 9:23:60, respectively.^[125] One important notion highlighted in this paper is the difference between canonical CASSCF orbitals and natural orbitals. As stated earlier with the $[CeCp_3]$ study, canonical CASSCF MO coefficients are theoretically and numerically relevant but they are subject to large changes upon modulation of the number of states considered in the SA calculation. The more reliable NOs should be considered to evaluate n_f , resulting in a value of $n_f=0.9$ close to that obtained in Dolg's studies and in the experimental ones. Yet, the fact that the NOs remain largely localised on the π -ring system led to the conclusion that this f-density is mostly due to covalency between the Cot and the empty f-orbital on the Ce, which is contradictory with a Ce^{III} definition. A later update using quantum theory of atoms in molecules (QTAIM) topological analyses^[126] derived from CASSCF-CASPT2 level of theory studies confirmed the non-negligible covalency arising from electron sharing between the Cot ring and the Ce ion with a charge of approximately 2.9.^[127] This study enforced the conjecture in which the cerocene ground state is of mixed-valence and closer to the formal oxidation state +IV. The n_f value being close to 1 (0.95 in this study) mainly originates from Cot–Ce covalency and not from the Ce ion itself. The fact that the first excited state is, however, best defined as Ce^{III} from both CASSCF and QTAIM with a similar electronic structure is proposed as another reason why experimental measurements are in better agreement with a +III oxidation state. In 2014, Mooßen and Dolg answered these different statements by using the invariance of the CASSCF wavefunction by a unitary transformation in the orbital space.^[128] Indeed, given this property, by applying the transformation ($a' = a \cos \alpha + b \sin \alpha$) and ($b' = b \cos \alpha - a \sin \alpha$) to any set of starting a and b CASSCF orbitals, it is possible to create a new set of orbitals that will end up representing the very same wavefunction but with a different representation and different contributions (see Figure 6). By incrementing this, Mooßen and Dolg highlighted two extreme cases, on the one hand the purest π and 4f orbitals can be created with $\alpha=25^\circ$ leading to a' being approximately 95% pure π and b' approximately 100% pure 4f. The weights of the configurations to the wavefunction are then 80% for $a'^3b'^1$, 10% for a'^4 and 10% for $a'^2b'^2$, which therefore corre-

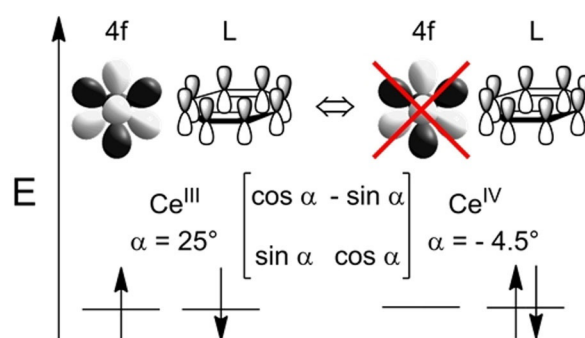


Figure 6. Representation of the two extreme cases of orbital rotation highlighted in Mooßen and Dolg's work of 2014.

sponds to a mostly Ce^{III} intermediate-valent state. On the other hand, the a'^4 configuration contribution is maximised (81%) with $\alpha=-4.5^\circ$, resulting in a' being composed of an 80:20 ratio of $\pi/4f$ orbitals and b' the inverse. As a result, a mostly Ce^{IV} model is obtained but with the resulting orbitals being of mixed character. With these two cases in mind and knowing that an infinite number of combinations may give intermediate results, there is no single best way to describe the formal oxidation state of cerocene. Moreover, all of these combinations are giving a relatively stable n_f close to 1, which concurs relatively well with the experimental value that remains the absolute reference.

These works enlighten us about why intermediate-valent species are so hard to qualify. Dolg stated in his conclusion that the choice between a +III (where a pure 4f electron is present) and a +IV (where the 4f electron density arises from π -4f covalency) oxidation state is "to a certain extent a matter of taste",^[128] which, for a pioneer of the field, is quite meaningful.

2.5. $[Ce(Pn)_2]$ substituted pentalene

Recently, magnetic and spectroscopic studies have focused on the related substituted pentalene analogues of $[Ce(Cot)_2]$, cerium bis(hexamethylpentalene) $[Ce(Pn^*)_2]$ ($Pn^* = \eta^8-Me_6C_8$) and bis(triisopropylsilyl)pentalene $[Ce(Pn'')_2]$ ($Pn'' = \eta^8-(1,4-iPr_3Si)_2C_8H_4$) (Figure 7).^[129,130] In both cases, sharp signals were observed in the 1H and ^{13}C NMR spectra in solution, suggesting diamagnetic molecules, but with several abnormal chemical shifts revealing some paramagnetic character. The unusual

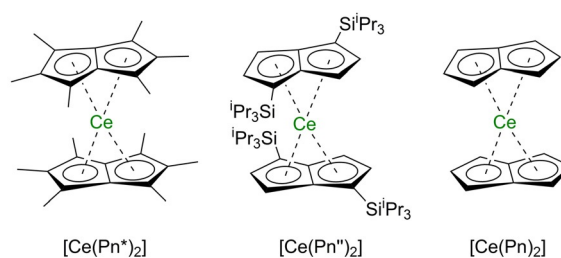


Figure 7. Structures of the different Ce pentalene complexes discussed in this section.

NMR chemical shifts were explained by a strongly “mixed-valent” system with $4f^1$ contributions to the ground state. No appreciable changes in the chemical shifts were observed by variable-temperature NMR studies, implying temperature-independent paramagnetism (TIP). Solid-state magnetic studies revealed a TIP paramagnetism ($(25.0 \pm 0.1) \times 10^{-4}$ and $(4.5 \pm 0.3) \times 10^{-4} \text{ emu mol}^{-1}$ for $[\text{Ce}(\text{Pn}^*)_2]$ and $[\text{Ce}(\text{Pn}^{\prime\prime})_2]$, respectively) larger than that reported for $[\text{Ce}(\text{Cot})_2]$ ($(1.4 \pm 0.2) \times 10^{-4} \text{ emu mol}^{-1}$),^[105] which was attributed to smaller HOMO–LUMO gaps in the pentalene complexes.^[129,130] In the UV/Vis spectra, intense absorption bands were detected at 530 nm ($\epsilon = 17000$) and 590 nm ($\epsilon = 5000$) for $[\text{Ce}(\text{Pn}^*)_2]$ and $[\text{Ce}(\text{Pn}^{\prime\prime})_2]$, respectively, and were assigned to charge-transfer transitions. The comparative feature in cerocene was observed at 469 nm ($\epsilon = 8000$).^[102]

For both $[\text{Ce}(\text{Pn}^*)_2]$ and $[\text{Ce}(\text{Pn}^{\prime\prime})_2]$ systems, XANES studies revealed intermediate-valent systems, with a formal valence close to Ce^{III} .^[129,130] In the case of $[\text{Ce}(\text{Pn}^*)_2]$, the f -occupancy was determined by fitting the variable-temperature Ce L_3 -edge XANES spectra. A value $n_f = 0.87 \pm 0.05$ close to that in $[\text{Ce}(\text{Cot})_2]$ ($n_f = 0.89 \pm 0.03$) was obtained over the whole temperature range (30–300 K).

DFT calculations were carried out on $[\text{Ce}(\text{Pn}^*)_2]$ and on the model $[\text{Ce}(\text{Pn})_2]$ complex.^[129,130] Although such calculations could not accurately reproduce the observed multiconfigurational ground state, they helped to identify trends in the electronic structure. Contributions from the $\text{Ce}^{\text{IV}} \text{L}^0$ and $\text{Ce}^{\text{III}} \text{L}^1$ configuration were suggested with, in the latter configuration, the f -electron antiferromagnetically coupled to a hole in the ligand shell (L) of the same symmetry. Similarly to what has been discussed in the case of cerocene, the *observed* oxidation state, as determined experimentally from XANES data, is closer to Ce^{III} ,^[129] whereas the *formal* oxidation state, derived from the redox potential and the apparent diamagnetism, might be better described as Ce^{IV} .^[130]

Further *ab initio* calculations were carried out independently by the groups of Kaltsoyannis and Dolg.^[131,132] Using the same methodology as described for the analysis of cerocene (see above),^[125] CASPT2 calculations were performed to determine the electronic ground state of $[\text{Ce}(\text{Pn})_2]$. A particularly large active space correlating 12 electrons in 16 orbitals was used, which allows for occupation of any of the twelve $4f$ and $5d$ levels. Although the symmetry of the ground state, 1A_1 , is in agreement with that obtained by DFT calculations, the multiconfigurational character of the ground state is not accurately described by single-configuration DFT calculations. Analysis of the NOOs derived from CASPT2 calculations led to a calculated f -occupancy $n_f = 0.78 \pm 0.04$ in good agreement with that obtained experimentally ($n_f = 0.87 \pm 0.05$).^[131] These calculations also reproduced the energy of the first band in the UV/Vis spectrum of $[\text{Ce}(\text{Pn}^*)_2]$ with a great accuracy.^[131]

Similarly to the calculations performed on cerocene,^[48,49] Dolg investigated the ground-state electronic structure of $[\text{Ce}(\text{Pn})_2]$ by using advanced CASSCF calculations.^[132] By means of a rotation of the CASSCF natural orbitals, leaving the wavefunction and total energy invariant, a dominant $4f^1\pi^1$ configuration based on nearly pure $\text{Ce}4f$ and ligand π orbitals was ob-

tained. This description is particularly adapted to illustrate the *observed* oxidation state determined experimentally.

These two substituted pentalene cerium complexes are further examples of self-contained Kondo effect in a single molecule.

2.6. Other formally tetravalent lanthanide complexes

Until very recently, no other lanthanide than cerium was reported as a molecular complex in the formal +IV oxidation state.^[23,25] Also, formal Ce^{IV} complexes are not restricted to organometallic complexes and other coordination compounds have been reported (Figure 8).

Mixed valence in cerium bis(phthalocyaninato)cerium $[\text{Ce}(\text{Pc})_2]$ (Figure 8) complexes has been established on the basis of IR and Ce3d XPS spectroscopic data. The cerium centre in these complexes is neither tri- nor tetravalent.^[133] Although similarities in the IR spectra of $[\text{Ce}(\text{Pc})_2]$ and of trivalent $[\text{Ln}(\text{Pc})_2]$ complexes supported a formal Ce^{III} view, careful analysis of the different absorption bands revealed discrepancies with other trivalent $[\text{Ln}(\text{Pc})_2]$ complexes. The absorption band at around 880 cm^{-1} was found to be especially sensitive to the ionic radius of the metal within the lanthanide series, and a linear correlation between the band energy and the metal ionic radius was established. The observed absorption band in $[\text{Ce}(\text{Pc})_2]$ suggested an ionic radius of approximately 1.01 Å for the Ce centre in $[\text{Ce}(\text{Pc})_2]$, which is intermediate between the ionic radii of Ce^{III} (1.14 Å) and Ce^{IV} (0.96 Å) ions in similar coordination environments. Ce3d XPS data further supported a cerium mixed-valent complex with contributions from the $[(\text{Ce}^{4+})(\text{Pc}^{2-})_2]$ and $[(\text{Ce}^{3+})(\text{Pc}^{\cdot-})(\text{Pc}^{2-})]$ configurations in the ground state.^[133] The valence of Ce in a series of tetrapyrrole double-decker complexes bearing (na)phthalocyaninato and porphyrinato ligands with different electronic properties has also been investigated.^[134] The UV/Vis absorption spectra of the substituted Ce phthalocyaninate complexes displayed two ligand absorption bands (the phthalocyanine Q-bands) at un-

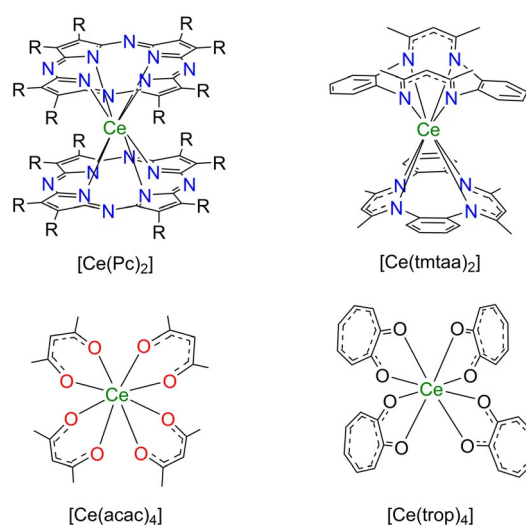


Figure 8. Structures of formal Ce^{IV} complexes bearing non-organometallic ligands.

expected wavelengths. Using a similar approach as above, the ionic radius of the Ce centre was estimated through a linear correlation between the energy of the electronic transition and the lanthanide ionic radius. From this study, the ionic radius of the cerium centre was found to be smaller than that expected for a Ce^{III} ion (1.143 Å) and close to that of Nd^{III} (1.109 Å), suggesting an intermediate valence between +III and +IV for the Ce centre.^[134] Further evidence was given by L₃-edge XANES analyses, which revealed two edge absorption peaks corresponding to the L4^f and L4^f contributions.

Magnetic susceptibility studies on [Ce(tmtaa)₂] (tmtaaH₂ corresponding to tetramethyldibenzotetraaza[14]annulene), cerium tetrakis(acetylacetonate) [Ce(acac)₄] and cerium tetrakis(tropolonate) [Ce(trop)₄] (Figure 8) as a function of temperature have shown that these formally 4f⁰ complexes exhibit temperature-independent paramagnetism (TIP) with low but positive values of χ for the metal centre (after subtraction of the ligand diamagnetic contribution).^[135–137] The small energy difference between the ground state (open-shell singlet) and the first excited state (open-shell triplet) was found to be responsible for the TIP behaviour. In an applied magnetic field, thermal mixing of the two states occurs with a relative population following the Boltzmann distribution, which results in a small net value of the magnetic moment μ_{eff} (in the range 0.1–0.7 μ_{B} at 300 K). The experimental results were therefore not consistent with diamagnetic cerium centres (associated with negative values of χ), which would arise from a single 4f⁰ Ce^{IV} ground-state configuration. Ce L₃-edge XAS studies and ab initio calculations based on multireference wavefunctions further confirmed a Ce^{III} 4f¹ and Ce^{IV} 4f⁰ multiconfigurational character in the ground states of these complexes. The calculations were performed by using CASSCF/CAS-SDCI methodologies starting with a relatively large active space (four electrons distributed over five orbitals) further reduced to two active electrons. Averaged orbitals of the f²L⁶, f¹L⁷ and f⁰L⁸ states were used in the calculations. Finally, the addition of configuration interaction calculations on top of the CASSCF was necessary to obtain satisfactory results. The combination of one cerium 4f electron and one ligand-based electron can lead to four possible electronic states (Figure 9).

The calculations supported an open-shell singlet ground state. The first excited state, an open-shell triplet, was found to be close in energy and only 40–75 cm⁻¹ higher in energy than the open-shell singlet ground state. In contrast, the 4f⁰ closed-shell singlet is much higher in energy (> 400 cm⁻¹), and so is the 4f² closed-shell singlet.

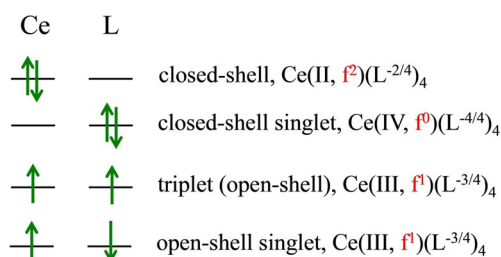


Figure 9. Different configurations considered. Adapted from Ref. [136].

Very recently, high-energy-resolution fluorescence detection X-ray absorption spectroscopy (HERFD-XAS) has been used to analyse a formal di-cerium(IV) phenolate complex and confirmed mixed valency with considerable 4f⁰ character.^[138] In addition, the multiconfigurational ground state of formal Ce^{IV} complexes stabilised by imidophosphorane ligands or imidophosphorane-functionalised guanidinate ligands has been established through Ce L₃-edge XANES studies.^[139–141] Notably, the imidophosphorane Ce^{IV} complexes exhibited the lowest reported relative proportion of Ce^{III} L₃ character ($n_f=0.38(2)$). However, some limits to the dominant two-peak model in the analysis of the L₃-edge XANES spectra of tetravalent lanthanides were presented.^[140]

In 2019, access to the first molecular formal Tb^{IV} complexes has been described in independent reports by the groups of La Pierre and Mazzanti by using imidophosphorane and bulky siloxide ligands, respectively (Figure 10).^[19,20] The use of bulky Ph₃SiO ligands further allowed, in 2020, the synthesis of the first molecular Pr^{IV} complex.^[22] The reduction potential associated with the Pr^{IV}/Pr^{III} couple (+3.4 V) is very close to that of the Tb^{IV}/Tb^{III} couple (+3.3 V), which supports that similar ligand environments and procedures might be used to access both Tb^{IV} and Pr^{IV} complexes.^[21,22]

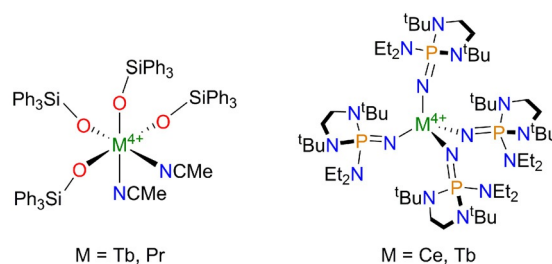


Figure 10. Recent ligand environments used for the stabilisation of formal tetravalent lanthanide compounds including Tb^{IV} and Pr^{IV} complexes.

The electronic structure of the imidophosphorane-stabilised Tb^{IV} complex was investigated by magnetic susceptibility, EPR and XANES studies.^[20] A multiconfigurational behaviour similar to that observed in TbO₂ was established by Tb L₃-edge XAS measurements. The characteristic double-peak structure was attributed to both Tb^{IV} and Tb^{III} configurations in the final state. The relative amount of the Tb^{III} L₃ character in the ground state has been evaluated to be 0.39(4), a value similar to that observed for TbO₂ (0.42(3)).^[111] These results indicate that ligand control of the multiconfigurational behaviour is of utmost importance to achieve stabilisation of formal Ln^{IV} complexes.

The multiconfigurational ground state established in these complexes shows that the mixed valency observed in formal Ln^{IV} compounds is not restricted to organometallic complexes but can be extended to other coordination compounds featuring electron-rich donor ligands.

2.7. [Cp*₂Yb(L)] adducts with L = N-heterocyclic redox-active ligands

The group of Andersen engaged in an in-depth study of the electronic structure and physical properties of ytterbocene adducts by using 2,2'-bipyridyl (bipy), 1,10-phenanthroline (phen) and other diazabutadiene (dad) ligands, which are known to be redox non-innocent or redox-active ligands (Figure 11).^[32,50,51,84,105,142–147] These compounds provide strong

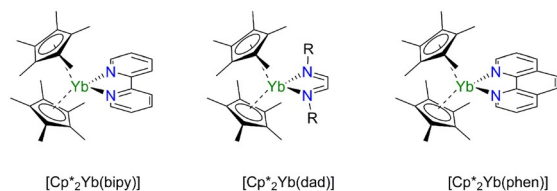


Figure 11. Structures of ytterbocene adducts with nitrogen-based redox-active ligands.

magnetic and spectroscopic evidence that both Yb^{II} f¹⁴ and Yb^{III} f¹³ configurations are represented in the ground state. In such complexes, depending on the ytterbocene substituents and on the nature of the ligand (bipy vs. phen), reduction of the redox-active ligand by the Yb^{II} centre may occur. The detailed analyses of the reasons allowing the transfer or not will be examined in section 3. In these complexes, the reduced nature of the bipyridyl ligand in [Cp*₂Yb(bipy)] can be qualitatively assessed by IR measurements where strong absorption bands in the regions 800–1000 cm⁻¹ and 1490–1575 cm⁻¹ are typical for a bipyridyl radical anion.^[84,142] In addition, analysis of the bond lengths within the bipyridyl ligand in the X-ray structures was indicative of the neutral or reduced character of the ligand and therefore of the ytterbium valence (for example, a variation in the C–C backbone distance of the bipy ligand from 1.49 (Yb^{II}) to 1.43 Å (Yb^{III}) was observed).^[50,84] The distance between the Yb and the centroid of the Cp* ligand was also suggested as an efficient probe of the ytterbium valence, with distances varying continuously from 2.74 (Yb^{II}) to 2.59 Å (Yb^{III}).^[51] Raman spectroscopy gave further evidence that the ligands in the [Cp*₂Yb(L)] (L = bipy, phen) adducts were reduced radical anions.^[85] Additionally, in the UV/Vis/near IR electronic absorption spectra of [Cp*₂Yb(L)] (L = bipy, phen), f–f transition bands typical of Yb^{III} compounds were detected but with some singularities.^[85] The intensities of the bands in the neutral complexes were 5–10 times greater than those in the corresponding oxidised cationic complexes, revealing unusually large oscillator strengths for f–f transitions. In the case of [Cp*₂Yb(phen)], the energies (ca. 11 000 cm⁻¹) and separations between adjacent f–f bands (ca. 510 and 780 cm⁻¹) were found significantly different from the values found in the cationic oxidised complex [Cp*₂Yb(phen)]⁺.^[85]

Magnetic studies on [Cp*₂Yb(L)] (L = bipy, phen) revealed that these complexes were not simple Yb^{II} f¹⁴ diamagnetic adducts. The magnetic moments at room temperature were lower than that expected for an Yb^{III} ion coordinated by a radi-

cal anionic ligand with non-interacting spins (4.5–5 μ_B). The low magnetic moment of the ground state can be explained by antiferromagnetic coupling between the Yb^{III} centre and the radical anion, and is consistent with the field dependence observed at low temperatures. The effective magnetic moment was also found to depend on the substituents on the cyclopentadienide rings (Cp*, Cp^{tt} (η⁵-1,3-tBu₂C₅H₃), Cp^{rr} (η⁵-1,3-(Me₃Si)₂C₅H₃)) and reflects the extent of electron transfer from the Yb^{II} centre to the N-heterocyclic ligand (see section 3).^[84] Although the 1/χ versus T plot of the phenanthroline adducts of Cp*₂Yb, Cp^{tt}₂Yb and (C₅Me₄H)₂Yb featured as expected a linear dependence, a nonlinear shape was observed for [Cp*₂Yb(bipy)] and [(C₅Me₄H)₂Yb(bipy)] with a maximum χ value at 380 K. Similarly, analysis of the ¹H NMR spectra of [Cp*₂Yb(bipy)] at variable temperatures revealed a nonlinear plot for δ versus 1/T, which cannot be explained by a Curie–Weiss behaviour.^[84] More generally, variable-temperature analysis of the ¹H NMR chemical shifts of ytterbocene adducts constitutes a useful tool to probe the magnetic behaviour, especially to reveal intermediate valence.^[143,144,146] Further investigation of the magnetic properties was carried out by using the sealed quartz tube technology, allowing a more precise determination of the magnetic moment for highly air-sensitive and weakly paramagnetic compounds, which feature low but non-zero values of μ.^[142] This is especially the case for [Cp^{tt}₂Yb(bipy)] and [Cp^{rr}₂Yb(bipy)], which were found to be weakly paramagnetic. Their 1/χ versus T plots were significantly curved but did not exhibit the unusual behaviour evidenced in [Cp*₂Yb(bipy)] and [(C₅Me₄H)₂Yb(bipy)]. To account for the unusual magnetic behaviour observed in bipyridine, phenanthroline and in a related 4'-cyanoterpyridyl adduct of ytterbocene, a thermally induced valence tautomeric equilibrium between paramagnetic 4f¹³–π*¹ and diamagnetic 4f¹⁴–π*⁰ forms was first suggested.^[84,85,148] However, the lack of temperature dependence of the ytterbium valence observed in XANES studies^[50,105,145] and variable-temperature electronic absorption spectra^[149] were not consistent with valence tautomerism. Moreover, the higher contribution of the Yb^{II} 4f¹⁴–π*⁰ configuration at low temperature was not consistent either with genuine redox-isomerism in a lanthanide complex. Indeed, valence tautomerism being an entropy-driven process, the isomeric form with the shorter metal–ligand bond lengths, that is, involving the more oxidised Yb^{III} ion, should be stabilised at lower temperatures.^[150,151]

For many ytterbocene adducts, temperature-independent paramagnetism (TIP) was observed at low temperatures, which can be interpreted as a van Vleck interaction between the ground-state singlet and the triplet configuration at some higher energy.^[50] The magnetic behaviour can be explained by a multiconfigurational singlet ground state, with contributions of both Yb^{II} f¹⁴ and Yb^{III} f¹³ configurations, which is lower in energy than the triplet configuration. When the temperature thermally allows the population of the triplet configuration, the susceptibility initially increases (out of the TIP regime) and then decreases, as in a conventional Curie–Weiss paramagnet.^[50]

In the case of methyl-substituted bipyridine and phenanthroline adducts of ytterbocene, unusual magnetic susceptibility data were observed and supported a temperature-dependent variation of the Yb valence.^[51,145,147] In several cases, the presence of inflection points was observed in the plots of χT versus T , which was rationalised by a multiconfigurational open-shell singlet ground state with low-lying excited states.^[51,146,152] Especially, different open-shell singlets were found below the triplet state and their thermal population with increasing temperatures accounts for the unusual temperature dependence of the magnetic data (see below). Ab initio calculations were first performed by using the model $[\text{Cp}_2\text{Yb}(\text{bipy})]$ compound,^[50] and further improved by using Cp^* (instead of Cp) fragments.^[51] Such calculations typically involve a first DFT geometry optimisation of the molecule using small core Relativistic Effective Core Potentials (RECP)^[120,121,123,153] followed by CASSCF calculations. After testing active spaces of different sizes and careful comparison of the results, the smallest active space giving the same qualitative results was used for the complete calculations.^[154] To obtain a better adequation between the calculations and the experimental results, a larger active space that included additional π^* configurations for the substituted bipyridine ligand was used in the computational model and a perturbative PT2 correction was added.^[51] The calculations revealed that the ground states and first excited states were dependent on the number and position of the methyl substituents.^[51,145,147] In addition, a correlation between the relative populations of the f^{13} and f^{14} configurations and the redox properties of the two fragments (ytterbocene and redox-active ligand) was established.^[145]

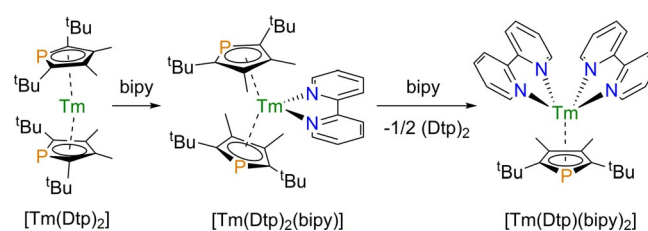
To support the magnetism studies, Yb L_3 -edge XANES data of $[\text{Cp}^*_2\text{Yb}(\text{bipy})]$ were recorded at different temperatures. The f-hole occupancy (n_f), which is directly linked to the ytterbium valence ($v=2+n_f$), was estimated to be 0.80 ± 0.03 for $[\text{Cp}^*_2\text{Yb}(\text{bipy})]$ without any change from 10 K up to decomposition at above approximately 400 K.^[105] Similar results were obtained for a series of 4,4'-disubstituted bipyridine and 1,4-diazabutadiene (dad) adducts of ytterbocene, which were found to feature between 83 and 95% of trivalent character with no significant change of the lanthanide valence with temperature (in the range 20–300 K).^[50] In methyl-substituted bipyridine adducts of ytterbocene, depending on the number and position of the methyl substituents, Yb L_3 -edge XANES data revealed different contributions of the Yb^{II} and Yb^{III} forms with temperature and therefore temperature-dependent variation of the Yb valence.^[51,145,147]

In addition, the coordination of unsubstituted imino-pyridine ligands to Cp^*_2Yb resulted in an electronic transfer reaction and formation of an Yb^{III} complex featuring a radical-anionic ligand.^[155] Variable-temperature magnetic measurements revealed a maximum at 170 K in the χ_M versus T data, consistent with a multiconfigurational ground state for the Yb ion. Ab initio calculations (CASSCF) using the same methodology as above, supported an open-shell singlet ground state constituted of 78% Yb^{III} and 22% Yb^{II} .

CASSCF and CASPT2 calculations were also carried out on the 1,4-diazabutadiene (dad) $[\text{Cp}^*_2\text{Yb}(\text{dad})]$ and $[\text{Ind}_2\text{Yb}(\text{dad})]$ ($\text{Ind} = \eta^5\text{-C}_9\text{H}_7$) complexes.^[156] Owing to the near degeneracy of the low-lying electronic states, DFT methods were again not appropriate to determine the correct electronic ground state of the system and explain its magnetic properties. Both ligands on the ytterbium centre, Cp^* and indenyl on the one hand, bipy and DAB on the other hand, were found to have an effect on the electronic ground-state configuration. Only one of the possible ligand combinations, corresponding to the diamagnetic $[\text{Ind}_2\text{Yb}(\text{bipy})]$ complex, could be properly studied by using a standard single-configuration DFT approach. Compared with ab initio calculations, DFT calculations are less computationally demanding and can be applied to the real molecules. In contrast, ab initio calculations are typically performed on reduced model systems. The latter should, however, be realistic enough to reproduce the electronic complexity and specificities of the experimental systems.

2.8. Other lanthanide complexes with redox-active ligands

Multiconfigurational ground states were also invoked to rationalise the unusual magnetic properties of bipyridine and bisphosphinine (phosphorus analogues of bipyridine) adducts of bis(phospholyl) thulium(II) ($[\text{Tm}(\text{Dtp})_2]$, see Scheme 3) but the precise electronic structures of the complexes have remained elusive to date.^[157]



Scheme 3. Synthesis and reactivity of a bipyridine adduct of $[\text{Tm}(\text{Dtp})_2]$.^[157]

Recently, the electronic structures of lanthanide tetrakisbipyridine complexes were investigated.^[158] Both magnetic susceptibility measurements and L_3 -edge XANES data on the Ce and Yb species were consistent with the metals being trivalent. CASSCF calculations were performed on the closed-shell La^{III} and Lu^{III} (f^0 and f^{14} configuration, respectively) complexes, as well as on the Ce^{III} and Yb^{III} derivatives featuring one f-electron (f^1) or one f-hole (f^{13}), respectively. The different multiconfigurational nature of the corresponding ground states helped understand the slight differences observed in their physical properties such as subtle bond length variations and magnetic susceptibility dependencies with temperature. For such systems, multireference calculations,^[57,58] as opposed to single reference DFT calculations, are often necessary to properly reproduce some of the physical properties such as temperature dependency of the magnetic susceptibility.

2.9. Concluding remarks on spectroscopic singularities

The systems presented above can be considered molecules in which the oxidation number is ambiguous and they are representatives of intermediate valence compounds using the term as defined by the physics community. The contribution of the ligand and metal charge transfer configuration will allow the formation of a state, in which the covalency, that is, the electronic delocalisation extent, is substantial. Clearly, in Yb, Eu, Tm and Ce compounds, the redox potential is adapted for these charge transfers with the ligand. It would mean that the energy match or mismatch between ligand and metal orbitals is at the origin of the situation the phenomenon; at least as much as the symmetry consideration for spatial overlap.

3. Energy and Symmetry Considerations

All these spectroscopic singularities, reinforced by adapted theoretical computations, clearly established that coordination compounds (or organometallics) of lanthanides can develop intermediate-valent states, that is, multiconfigurational energy states with configurations featuring different oxidation states. In these compounds, the relative ratio between their configurations varies and can be quantified from adapted experimental measurements and confirmed by adapted theoretical computations. An important point going forward is the rationalisation of this ratio from simple symmetric and energetic considerations.

The covalency represents the extent of the electronic delocalisation over both the metallic and ligand sites, as defined by Neidig and co-authors [Equation (2)].^[34] In this description, to allow a non-zero mixing coefficient, that is, covalency, two parameters are at play: the ligand and metal orbital overlap, and the energy difference between both fragments. In lanthanide compounds, little overlap is expected between these orbitals as f-orbitals are core orbitals. Nevertheless, according to Equation (2), the covalency can also be maximised when the energy gap is minimised. In this situation, the electronic density is statistically delocalised over both the ligand and metal radical, leading to an intermediate-valent charge at the lanthanide centre.

$$\sigma = \frac{\varphi_M + \lambda\varphi_L}{\sqrt{1 + 2\lambda S_{ML} + \lambda^2}} \quad \lambda = \frac{H_{ML}}{E_M^0 - E_L^0} \quad (2)$$

where σ is the mixing metal and ligand orbital from perturbation theory of the ionic limit, φ_M is the metal orbital and φ_L the ligand orbital, both characterised by the metal and ligand energies, E_M^0 and E_L^0 . S_{ML} is the orbital overlap, λ the mixing coefficient and H_{ML} the off-diagonal matrix element of the Hamiltonian. Note that in the Hückel theory, H_{ML} is proportional to S_{ML} .

For example, if [U(Cot)₂] and [Ce(Cot)₂] are compared,^[106] the former has greater metal–ligand overlap, whereas the latter has better metal–ligand energy matching, which results in so-called “degeneracy-driven covalency”,^[34] and participates in the bonding while simultaneously appearing localised.

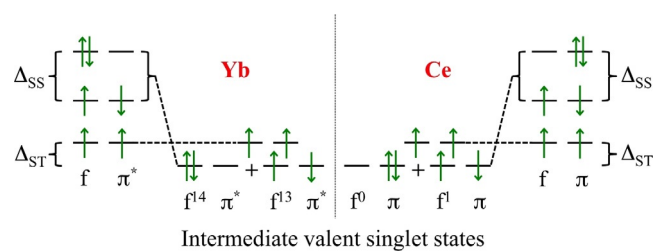


Figure 12. Qualitative energy level diagram showing the origin of the intermediate valence states for ytterbium and cerium complexes.

Overall, in Ce and Yb complexes, the description is simpler. They are empty—or full shell—in one configuration and singly occupied—or having only one hole—in the other. The energy diagram of both cases is shown in Figure 12.^[50] The mixing of the singlet configurations results in a multiconfigurational state of lower energy, in which the two configurations have different valency, leading to intermediate-valent states. It is clear from this energy scheme that the energy difference between the open-shell and closed-shell singlets, Δ_{SS} , and the energy gap singlet-triplet Δ_{ST} are going to govern the overall electronic structure.

As discussed above, a series of complexes with substituted bipyridine and diazabutadiene ligands with the Cp*₂Yb fragments has been synthesised in several articles from the Andersen group.^[51,145] The energy of the ligand fragment and that of the metal fragment, E_M and E_L , which is intimately related to Δ_{SS} , can be extrapolated from their respective redox potentials.^[50,145] As written in the previous paragraph, L₃-edge XANES data indicated an n_f value of 0.83 for [Cp*₂Yb(bipy)], that is, an intermediate-valent ground state composed of 83% Yb^{III} and 17% Yb^{II}. This ratio can evolve depending upon the substituents added to the bipy, which change the ligand redox potential. In other words, when substituents decrease the redox potential, the n_f value becomes lower and the valency closer to Yb^{II}. Likewise, when substituents increase the redox potential, the n_f gets closer to 1 and the net valency approaches that of Yb^{III}. This effect can be easily verified by synthesising the 3,3'-Me₂bipy adduct of Cp*₂Yb, which has a n_f value of 0.17(2) for a reduction potential of the ligand below −2.8 V (Figure 13).

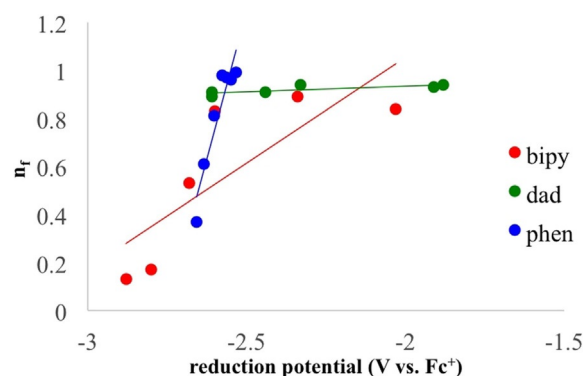


Figure 13. Plot of the redox potentials of the (substituted) bipy, phen and dad ligands taken from the literature^[50,145,159,160] versus the measured n_f for each series. Linear fitting is only to guide the eye.

This relatively low reduction potential is due to the steric hindrance of the two methyl groups, which are close to each other, inducing a NCCN torsion angle that lowers the reduction potential. As an additional note, when the reduction potential of the metallic fragment is increased, for example, when the Cp* ligand is replaced by the Cp ligand, the n_f also decreases; the n_f of [Cp*₂Yb(bipy)] is 0.83(2) whereas that of [Cp₂Yb(bipy)] is 0.30(1).

The problem became more complex after another series of substituted bipyridine ligands exhibited multiple intermediate valence singlet states below the triplet state. This situation is possible when several low-lying π^* orbitals of the ligand are close enough to accommodate spin density from the Cp*₂Yb fragment; each orbital then has a configuration with a given ratio (n_f). Figure 14 represents a typical situation. The different natures of the multiple intermediate-valent singlet states were identified thanks to the L₃-edge XANES data combined with the temperature-dependent magnetic data. As a result of the different ratio in each configuration, the overall n_f and thus the intermediate valency becomes temperature dependent. The corresponding thermodynamic parameters can be extracted by fitting the temperature-dependent n_f by using a Boltzmann distribution; these values can be then incorporated in the analysis of the magnetic data.

In the case of 4,5-diazafluorene, the magnetic data indicated three singlet states below the triplet, coming from three low-lying empty π^* orbitals (Figure 14).^[146]

However, if the energetic consideration described above helped to estimate the n_f ratio within one series of ligands, a quick look at Figure 13 also indicates that the correlation between the redox potential and the n_f cannot be generalised and remained true only within each ligand series, the bipy, the phen and the dad series. Additionally, this correlation remained also problematic in the case of the higher energy singlet states (below the triplet) of the substituted bipy ligands. This situation thus tended to indicate that the energy is not the single factor controlling the intermediate valency: the second impor-

tant parameter is the symmetry of the π orbital that accepts the electron. The correlation between redox potential and n_f value is valid only for orbitals of similar symmetry.

In this matter, the study of the phenanthroline series was of great importance as the ligand is known to possess two empty π orbitals of similar energy that have two very different symmetries.^[161] In C_{2v} symmetry, these two orbitals have b₁ and a₂ symmetry (Figure 15); b₁ is similar to the low-lying orbital of bipyridine and has much density located on the nitrogen atoms, which coordinate to the lanthanide metal centre; a₂, however, has very little density on the nitrogen atoms and a node at the 3,8-position of the phenanthroline. A molecular orbital diagram of the f-shell orbitals indicated that the singly occupied f-orbital possesses b₁ symmetry in C_{2v}.^[32,147]

Thus, as opposed to the bipy adduct, the phen adduct was analysed as a triplet, meaning that the symmetry orbital requirements must also be validated to stabilise the intermediate-valent singlet state. Interestingly, depending upon the substituents and their positions, the ground state can be different (triplet or intermediate valent). This means that the relative energy between the different symmetry orbitals can be modulated,^[161] which then leads to the modulation of the ground state as shown by the temperature-dependent magnetic data and L₃-edge XANES.^[32,145–147] An important example is the 3,8-phenanthroline adduct of ytterbocene. Indeed, as the a₂ orbital possesses a node at the 3,8-position, when a methyl replaces the hydrogen at these positions, the energy of the a₂ is not modified whereas that of the b₁ is slightly increased; the ground state is then similar to that of the phen analogue, which is triplet (Figure 16). Accordingly, donating substituents at the 5,6-positions increase the energy of the a₂ and slightly increase that of the b₁, leading to a situation in which both orbitals have similar energies; the singlet and triplet states have similar energies. Now, when substituents are at the 4,7-positions, the energies of both orbitals are increased but one should note that the coordination of the ytterbium fragment lowers the energy of the b₁ as much density is located in the nitrogen atoms. Thus, the b₁ becomes lower in energy and the ground state is the intermediate-valent singlet (Figure 16).

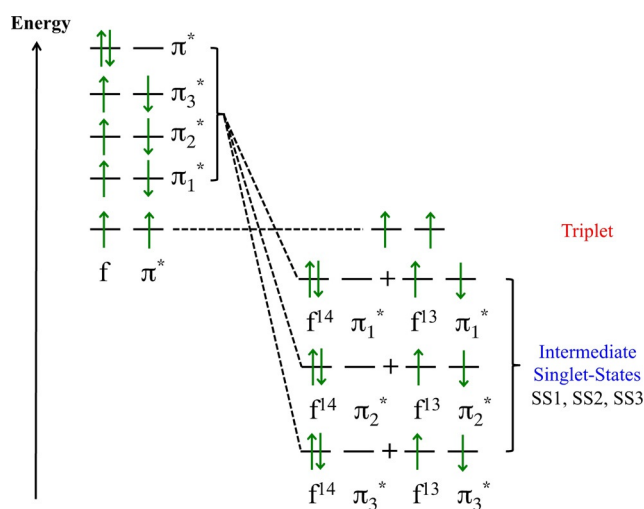


Figure 14. Energy scale with multiple π^* orbitals accepting electronic density and forming multiple intermediate-valent singlet states below the triplet.

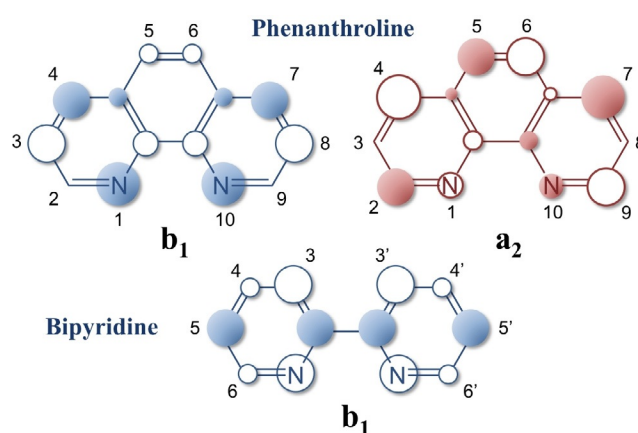


Figure 15. Representation of the π^* orbitals for bipy and phen and numbering positions.

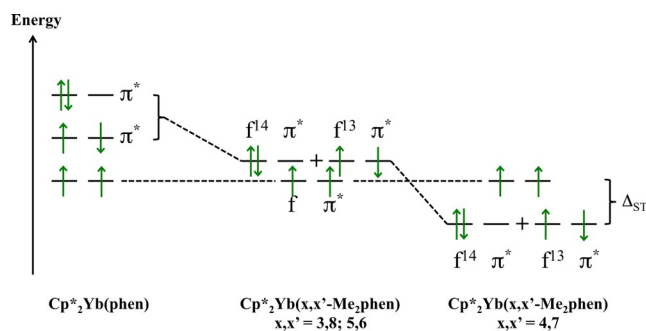
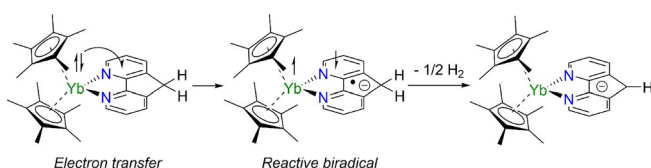


Figure 16. Qualitative MO diagrams showing the influence of the nitrogenated ligand on the electronic structure of the resulting complex.^[147]

As it has been noted early in the literature, intermediate valence state compounds are interesting molecular Kondo systems.^[47] This phenomenon can occur in nanometre-sized metallic particles and is explained by the presence of paramagnetic impurities, which break the continuous conduction band and creates localised conduction states.^[64,65] In the case of the Ce and Yb compounds discussed above, the f-moment is cancelled by coupling with extended conjugated π systems such as bipyridine, phenanthroline, but also Cot and tropolonate among others. Additionally, the formation of these intermediate-valent states also demonstrated that the exchange coupling of a radical spin with f-electrons can be rather large, compared with what is usually known in magnetic coupling involving f-elements. Using a model that combined the ligand-to-metal charge transfer energy (Hubbard model), it was possible to determine an exchange coupling value of -920 cm^{-1} for $[\text{Cp}^*_2\text{Yb}(\text{bipy})]$.^[162] This very large value also explains why the use of extended π systems is particularly relevant for the design of compounds with high magnetic coupling between lanthanides. The presence of a π -radical between lanthanide metal centres increases greatly the coupling between them and led notably to performing single molecules magnets.^[163–166]

4. Chemical Ramifications

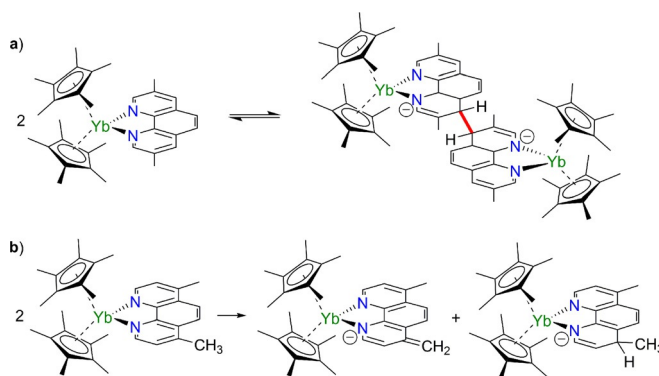
The symmetry of the orbitals became a crucial consideration when talking about reactivity as was demonstrated when the bipy was switched for other di-nitrogenated ligands such as diazafluorene and phenanthroline.^[32,146,147] The $[\text{Cp}^*_2\text{Yb}(4,5\text{-diazfluorene})]$ complex was shown by Nocton et al. to slowly release H_2 , leading to the corresponding $[\text{Cp}^*_2\text{Yb}(4,5\text{-diazfluorenyl})]$ complex (Scheme 4).^[146] Experimental and computational studies indicated that the electronic structure of the com-



Scheme 4. Elimination of H_2 from the 4,5-diazfluorene ligand triggered by the intermediate-valent behaviour.^[146]

pound was similar to that of bipyridine adducts of Cp^*_2Yb with an intermediate-valent ytterbium centre and two open-shell singlet states lying below the triplet state. Analysis of the π^* orbitals of the ligand revealed that the LUMO + 1 orbital of the fluorene was of b_1 symmetry in the C_{2v} space group and featured non-negligible spin density on the C9 carbon atom. The presence of unpaired spin density at this position helped to rationalise the observed reactivity. It is thought that the electronic structure of $[\text{Cp}^*_2\text{Yb}(4,5\text{-diazfluorene})]$, and the formation of a reactive biradical, is responsible for the C–H activation reaction.^[146] Importantly, the configuration interaction allowed the LUMO + 1 to be substantially populated at room temperature (see Figure 14, energy of SS1, SS2, SS3), the one orbital responsible for the observed reactivity. In contrast, the biradical adducts formed in the case of bipyridine adducts of ytterbocene was more stable and not involved in further chemical evolutions.

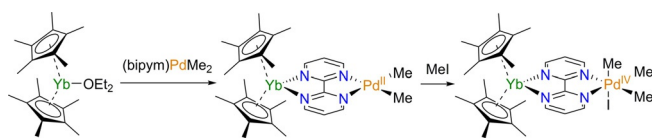
The influence of orbital symmetries on the reactivity was further evidenced in the $[\text{Cp}^*_2\text{Yb}(\text{phen})]$ complex and its methylated analogues.^[32,147] Experimental and computational results revealed a triplet ground state with a trivalent ytterbium centre, which contrasts with the open-shell singlet ground state of the bipyridine adducts. Such a different electronic structure has a direct influence on the reactivity of the complexes. Indeed, the $[\text{Cp}^*_2\text{Yb}(\text{phen})]$ complex, as well as the (3,8)- and (5,6)-di-methylated analogues, dimerised in solution with formation of a reversible C–C bond between the two phenanthroline moieties at the 4,4'-positions (Scheme 5). This unusual reactivity originates in the energy and symmetry of the ligand empty orbitals. In the phenanthroline complex, two π^* orbitals of different symmetry (b_1 and a_2 for the LUMO and LUMO + 1, respectively) are accessible but their respective interaction with either the half-filled 4f orbitals of b_1 symmetry or the empty 5d orbitals of a_2 symmetry results in different cases. As discussed above, on the one hand, if the b_1 orbital is lower in energy than the a_2 orbital, an open-shell singlet ground state is favoured, as is the case in the bipyridine adducts of Cp^*_2Yb . On the other hand, if the ligand a_2 and b_1 orbitals are close in energy, as is the case in the phenanthroline adducts, the final a_2 MO ends up lower in energy, resulting in



Scheme 5. Two different reactivities observed for two different phenanthroline derivatives (a) C4–C4' coupling, (b) C4-position-mediated intermolecular HAT.^[32,147]

stabilisation of the triplet ground state (Figure 16). As this result is based on the energy of the phenanthroline ligand orbitals, it can be tuned by the presence of methyl substituents affecting the b_1 - a_2 gap. The population of the a_2 orbital results in an increased spin density in the π system especially at the C4 and C7 positions. The radical character at these positions is responsible for the formation of a reversible C–C bond between the two phenanthroline units (Scheme 5).^[32] Nonetheless, when the phenanthroline is substituted at the 4,7-positions with methyl groups, a different configuration is observed, with a multiconfigurational open-shell singlet ground state.^[147] The altered electronic structure, similar to that observed in the bipyridine adducts, results in a different reactivity. In $[\text{Cp}^*_2\text{Yb}(4,7\text{-Me}_2\text{phen})]$, accumulation of electronic density at the C4 and C7 positions leads to an intermolecular hydrogen atom transfer (HAT) reaction between two complexes (Scheme 5), reminiscent of the H_2 elimination reactivity observed in the case of the diazafluorene complex.^[146,147]

Taking advantage of the particular and tuneable electronic structures of $[\text{Cp}^*_2\text{Yb}(\text{L})]$ systems, the influence of the ligand was further explored to modulate the chemical reactivity. The possibility of impacting the reactivity of another metal centre was explored through the formation of heterobimetallic complexes using bridging 2,2'-bipyrimidine (bipym) and 4,5,9,10-tetraazaphenanthrene (taphen) ligands instead of bipyridine and phenanthroline ligands. In 2017, the group of Nocton reported the syntheses and electronic structures of the Yb/Pd heterobimetallic complexes $[\text{Cp}^*_2\text{Yb}(\text{L})\text{PdMe}_2]$ ($\text{L} = \text{bipym}$ or taphen; Scheme 6).^[152] Depending on the nature of the ligand, different electronic structures were observed owing to different symmetries for the corresponding LUMOs. In the bipym system, similarly to bipyridine adducts of ytterbocene, the ground state is a multiconfigurational open-shell singlet with a low-lying triplet state populated at room temperature. In contrast, the taphen complex features a triplet ground state, in analogy with the ground-state structure of the phenanthroline adduct of Cp^*_2Yb . The influence of the different electronic structures on the reactivity was exemplified in the reactivity of the complexes towards MeI. In both cases, the addition of MeI triggered an oxidative addition step, resulting in the formation of a Pd^{IV} complex. Although the resulting Pd^{IV} complex rapidly evolved through a reductive elimination process in the taphen system, it presented a much higher stability in the case of the bipym ligand, allowing isolation and characterisation. The increased stability of the $[\text{Cp}^*_2\text{Yb}(\text{bipym})\text{PdMe}_2]$ complex is mainly due to the spin density mostly held by the N atoms in the b_1 orbital, which support the Pd centre. In the taphen analogue instead, the a_2 orbital is populated and features smaller coefficients on the N atoms. As a result, a lower spin density is



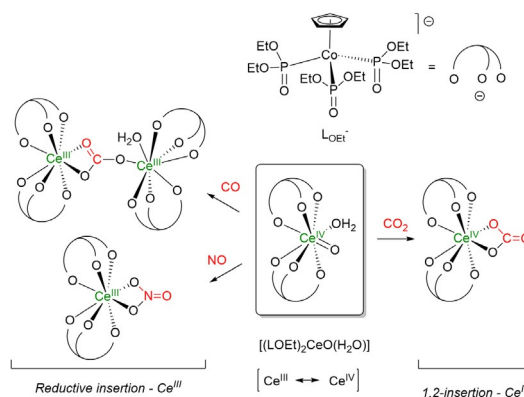
Scheme 6. Heterobimetallic Yb–Pd association leading to the stabilisation of a Pd^{IV} oxidation state.^[152]

present next to the Pd centre, which decreases the stability of the high oxidation state Pd^{IV} complex and triggers a fast reductive elimination step as expected for such Pd^{IV} species.^[152]

Another chemical ramification of the electronic structure of heterobimetallic complexes was reported with the same $\text{Cp}^*_2\text{Yb}(\text{bipym})$ backbone using a NiMe_2 fragment instead of PdMe_2 .^[167] Both the monometallic $[(\text{bipym})\text{NiMe}_2]$ and the heterobimetallic $[\text{Cp}^*_2\text{Yb}(\text{bipym})\text{NiMe}_2]$ complexes were found to react with CO, resulting in CO insertion reactions in the Ni–C bonds. Kinetic studies revealed that the intermediate-valent lanthanide-bipym fragment led to an increased stabilisation of the expected acyl intermediate through a process similar to that allowing the stabilisation of the Pd^{IV} complex discussed above.^[167] This result offers a new strategy to stabilise and study reactive metal intermediates for which isolation has remained elusive to date.

The influence of the multiconfigurational character of lanthanide complexes on the reactivity was further exemplified in the case of Ce^{IV} oxo complexes supported by the bulky Kläui oxygen tripodall metallo-ligand $[\text{CoCp}\{\text{P}(\text{O})(\text{OEt})_2\}_3]^-$ (LOEt^- , Scheme 7).^[168,169]

The multiconfigurational character of the $[(\text{LOEt})_2\text{CeO}(\text{H}_2\text{O})]$ complex was established by CASSCF calculations together with magnetic susceptibility measurements. The combined experimental and theoretical results revealed a multiconfigurational ground state composed of 74% of Ce^{IV} and 26% of Ce^{III} . The reactivity of the oxocerium(IV) complexes was evaluated towards small molecules such as CO, CO_2 , SO_2 and NO. Depending on the substrate, two different types of reactivity for the $\text{Ce}=\text{O}$ moiety were observed (Scheme 7). Although a classical 1,2-insertion reactivity was observed with CO_2 , which corresponds to the typical reactivity of Ce^{IV} f^0 complexes, the reaction with CO, SO_2 and NO resulted in an unusual reductive insertion reactivity. As a result, (bi)carbonate, hydrogensulfate and nitrate Ce^{III} complexes were isolated, respectively. Such a reductive insertion reactivity is thought to arise from the multiconfigurational nature of the ground state, the $\text{Ce}=\text{O}$ moiety featuring both some Ce^{IV} oxo and Ce^{III} oxyl character. The Ce^{III} oxyl character results in a radical-like reactivity by forming a singlet metal–ligand biradical similar to the situation in cerocene.^[169]



Scheme 7. Schematic representation of the reactivity of the oxocerium complex $[(\text{LOEt})_2\text{CeO}(\text{H}_2\text{O})]$.^[169]

6. Concluding Remarks

The minireview gathers the spectroscopic singularities that have been reported for lanthanide compounds. In these compounds, the net valency remains ambiguous because of possible redox events with the ligand, whether charge density is transferred from the ligand to the metal or from the metal to the ligand. In addition to physical chemistry reports containing XANES, PES and/or magnetic analysis, adapted theoretical analyses of these peculiar compounds have allowed the rationalisation of their original electronic nature: they are intermediate valent; the wavefunction of the ground and excited state is defined by multiple configurations, in which the valency is of different nature. These observations can be rationalised first from energetic considerations, as the result of the energy difference between both metallic and ligand fragments, and second from the symmetry of both fragments, which needs to be adapted to allow stabilisation of the energy with formation of an intermediate-valent energy state. This typical situation is predominant in lanthanide compounds, in which the spatial orbital overlap is small, whereas in transition metal ions or 5f complexes, the nephelauxetic effect allows the formation of molecular orbitals with delocalised electron density over both the metallic and ligand centres (so-called covalency). Both situations are, however, similar from the perspective of the Pauling electroneutrality principle. As well-established for transition metals and for 5f compounds, the strong electron correlation between a d- and/or f-parentage electron and the σ - and π -electron is then likely to influence the physical properties (relaxation, anisotropy, conductivity) but also the reactivity of these electrons: this review sheds light on several examples of this nature.

Acknowledgments

This work is part of a project that has received funding from the *European Research Council (ERC)* under *European Union's Horizon 2020 research and innovation program* under grant agreement No 716314. CNRS and Ecole polytechnique are thanked for funding.

Conflict of interest

The authors declare no conflict of interest.

Keywords: intermediate valence · lanthanides · organometallics · spectroscopy · theoretical computations

- [1] J.-C. G. Bünzli, C. Piguet, *Chem. Soc. Rev.* **2005**, *34*, 1048–1077.
- [2] S. Cotton in *Lanthanide and Actinide Chemistry*, Wiley, Chichester, **2006**, pp. 61–87.
- [3] E. G. Moore, A. P. S. Samuel, K. N. Raymond, *Acc. Chem. Res.* **2009**, *42*, 542–552.
- [4] D. N. Woodruff, R. E. P. Winpenny, R. A. Layfield, *Chem. Rev.* **2013**, *113*, 5110–5148.
- [5] J.-L. Liu, Y.-C. Chen, M.-L. Tong, *Chem. Soc. Rev.* **2018**, *47*, 2431–2453.

- [6] B. M. Day, F.-S. Guo, R. A. Layfield, *Acc. Chem. Res.* **2018**, *51*, 1880–1889.
- [7] R. Pöttgen, T. Jüstel, C. A. Strassert, *Rare Earth Chemistry*, De Gruyter, Berlin, **2020**, pp. 1–654.
- [8] J.-C. G. Bünzli in *Kirk-Othmer Encyclopedia of Chemical Technology*, **2013**, pp. 1–43.
- [9] D. A. Atwood, *The Rare Earth Elements: Fundamentals and Applications*, Wiley, Chichester, **2013**, pp. 1–654.
- [10] P. Pyykko, *Chem. Rev.* **1988**, *88*, 563–594.
- [11] M. N. Bochkarev, *Coord. Chem. Rev.* **2004**, *248*, 835–851.
- [12] P. B. Hitchcock, M. F. Lappert, L. Maron, A. V. Protchenko, *Angew. Chem. Int. Ed.* **2008**, *47*, 1488–1491; *Angew. Chem.* **2008**, *120*, 1510–1513.
- [13] F. Nief, *Dalton Trans.* **2010**, *39*, 6589–6598.
- [14] M. R. MacDonald, J. E. Bates, M. E. Fieser, J. W. Ziller, F. Furche, W. J. Evans, *J. Am. Chem. Soc.* **2012**, *134*, 8420–8423.
- [15] M. R. MacDonald, J. E. Bates, J. W. Ziller, F. Furche, W. J. Evans, *J. Am. Chem. Soc.* **2013**, *135*, 9857–9868.
- [16] M. E. Fieser, M. R. MacDonald, B. T. Krull, J. E. Bates, J. W. Ziller, F. Furche, W. J. Evans, *J. Am. Chem. Soc.* **2015**, *137*, 369–382.
- [17] C. M. Kotyk, M. E. Fieser, C. T. Palumbo, J. W. Ziller, L. E. Darago, J. R. Long, F. Furche, W. J. Evans, *Chem. Sci.* **2015**, *6*, 7267–7273.
- [18] W. J. Evans, *Organometallics* **2016**, *35*, 3088–3100.
- [19] C. T. Palumbo, I. Zivkovic, R. Scopelliti, M. Mazzanti, *J. Am. Chem. Soc.* **2019**, *141*, 9827–9831.
- [20] N. T. Rice, I. A. Popov, D. R. Russo, J. Bacsa, E. R. Batista, P. Yang, J. Telsler, H. S. La Pierre, *J. Am. Chem. Soc.* **2019**, *141*, 13222–13233.
- [21] A. R. Willauer, C. T. Palumbo, R. Scopelliti, I. Zivkovic, I. Douair, L. Maron, M. Mazzanti, *Angew. Chem. Int. Ed.* **2020**, *59*, 3549–3553; *Angew. Chem.* **2020**, *132*, 3577–3581.
- [22] A. R. Willauer, C. T. Palumbo, F. Fadaei-Tirani, I. Zivkovic, I. Douair, L. Maron, M. Mazzanti, *J. Am. Chem. Soc.* **2020**, *142*, 5538–5542.
- [23] T. P. Gomba, A. Ramanathan, N. T. Rice, H. S. La Pierre, *Dalton Trans.* **2020**, *49*, 15945–15987.
- [24] M. E. Fieser, M. G. Ferrier, J. Su, E. Batista, S. K. Cary, J. W. Engle, W. J. Evans, J. S. Lezama Pacheco, S. A. Kozimor, A. C. Olson, A. J. Ryan, B. W. Stein, G. L. Wagner, D. H. Woen, T. Vitova, P. Yang, *Chem. Sci.* **2017**, *8*, 6076–6091.
- [25] N. Li, W.-X. Zhang, *Chin. J. Chem.* **2020**, *38*, 1449–1450.
- [26] E. Prasad, B. W. Knettle, R. A. Flowers, *J. Am. Chem. Soc.* **2004**, *126*, 6891–6894.
- [27] K. A. Choquette, D. V. Sadasivam, R. A. Flowers, *J. Am. Chem. Soc.* **2010**, *132*, 17396–17398.
- [28] X. Zhao, L. Perrin, D. J. Procter, L. Maron, *Dalton Trans.* **2016**, *45*, 3706–3710.
- [29] W. J. Evans, J. W. Grate, L. A. Hughes, H. Zhang, J. L. Atwood, *J. Am. Chem. Soc.* **1985**, *107*, 3728–3730.
- [30] W. J. Evans, T. A. Ulibarri, J. W. Ziller, *J. Am. Chem. Soc.* **1988**, *110*, 6877–6879.
- [31] S. Labouille, F. Nief, X.-F. Le Goff, L. Maron, D. R. Kindra, H. L. Houghton, J. W. Ziller, W. J. Evans, *Organometallics* **2012**, *31*, 5196–5203.
- [32] G. Nocton, W. W. Lukens, C. H. Booth, S. S. Rozenel, S. A. Medling, L. Maron, R. A. Andersen, *J. Am. Chem. Soc.* **2014**, *136*, 8626–8641.
- [33] G. Nocton, L. Ricard, *Chem. Commun.* **2015**, *51*, 3578–3581.
- [34] M. L. Neidig, D. L. Clark, R. L. Martin, *Coord. Chem. Rev.* **2013**, *257*, 394–406.
- [35] D. G. Karraker, *J. Chem. Educ.* **1970**, *47*, 424.
- [36] K. N. Raymond, C. W. Eigenbrot, *Acc. Chem. Res.* **1980**, *13*, 276–283.
- [37] S. Cotton in *Lanthanide and Actinide Chemistry*, Wiley & Sons, Chichester, **2006**, pp. 35–60.
- [38] N. C. Tomson, M. R. Crimmin, T. Petrenko, L. E. Rosebrugh, S. Sproules, W. C. Boyd, R. G. Bergman, S. DeBeer, F. D. Toste, K. Wieghardt, *J. Am. Chem. Soc.* **2011**, *133*, 18785–18801.
- [39] K. Ray, T. Weyhermüller, F. Neese, K. Wieghardt, *Inorg. Chem.* **2005**, *44*, 5345–5360.
- [40] K. Ray, T. Petrenko, K. Wieghardt, F. Neese, *Dalton Trans.* **2007**, 1552–1566.
- [41] C. C. Scarborough, S. Sproules, T. Weyhermüller, S. DeBeer, K. Wieghardt, *Inorg. Chem.* **2011**, *50*, 12446–12462.
- [42] C. C. Scarborough, K. Wieghardt, *Inorg. Chem.* **2011**, *50*, 9773–9793.
- [43] N. C. Tomson, K. D. Williams, X. Dai, S. Sproules, S. DeBeer, T. H. Warren, K. Wieghardt, *Chem. Sci.* **2015**, *6*, 2474–2487.

- [44] J. England, E. Bill, T. Weyhermüller, F. Neese, M. Atanasov, K. Wieghardt, *Inorg. Chem.* **2015**, *54*, 12002–12018.
- [45] C. Wolff, A. Gottschlich, J. England, K. Wieghardt, W. Saak, D. Haase, R. Beckhaus, *Inorg. Chem.* **2015**, *54*, 4811–4820.
- [46] I. Mustieles Marín, T. Cheisson, R. Singh-Chauhan, C. Herrero, M. Cordier, C. Clavaguéra, G. Nocton, A. Auffrant, *Chem. Eur. J.* **2017**, *23*, 17940–17953.
- [47] C. S. Neumann, P. Fulde, *Z. Phys. B* **1989**, *74*, 277–278.
- [48] M. Dolg, P. Fulde, W. Kühle, C. S. Neumann, H. Stoll, *J. Chem. Phys.* **1991**, *94*, 3011–3017.
- [49] M. Dolg, P. Fulde, H. Stoll, H. Preuss, A. Chang, R. M. Pitzer, *Chem. Phys.* **1995**, *195*, 71–82.
- [50] C. H. Booth, M. D. Walter, D. Kazhdan, Y.-J. Hu, W. W. Lukens, E. D. Bauer, L. Maron, O. Eisenstein, R. A. Andersen, *J. Am. Chem. Soc.* **2009**, *131*, 6480–6491.
- [51] C. H. Booth, D. Kazhdan, E. L. Werkema, M. D. Walter, W. W. Lukens, E. D. Bauer, Y.-J. Hu, L. Maron, O. Eisenstein, M. Head-Gordon, R. A. Andersen, *J. Am. Chem. Soc.* **2010**, *132*, 17537–17549.
- [52] R. W. Field, *Ber. Bunsen-Ges.* **1982**, *86*, 771–779.
- [53] E. Schrödinger, *Ann. Phys.* **1926**, *384*, 361–376.
- [54] M. Born, R. Oppenheimer, *Ann. Phys.* **1927**, *389*, 457–484.
- [55] P. Hohenberg, W. Kohn, *Phys. Rev.* **1964**, *136*, B864–B871.
- [56] W. Kohn, L. J. Sham, *Phys. Rev.* **1965**, *140*, A1133–A1138.
- [57] P. G. Szalay, T. Müller, G. Gidofalvi, H. Lischka, R. Shepard, *Chem. Rev.* **2012**, *112*, 108–181.
- [58] J. W. Park, R. Al-Saadon, M. K. MacLeod, T. Shiozaki, B. Vlaisavljevich, *Chem. Rev.* **2020**, *120*, 5878–5909.
- [59] J. C. Slater, *Phys. Rev.* **1929**, *34*, 1293–1322.
- [60] E. U. Condon, *Phys. Rev.* **1930**, *36*, 1121–1133.
- [61] F. Coester, H. Kümmel, *Nucl. Phys.* **1960**, *17*, 477–485.
- [62] G. Das, A. C. Wahl, *J. Chem. Phys.* **1967**, *47*, 2934–2942.
- [63] P. Fulde, J. Keller, G. Zwignagl in *Solid State Physics, Vol. 41* (Eds.: H. Ehrenreich, D. Turnbull), Academic Press, Cambridge, MA, **1988**, pp. 1–150.
- [64] P. S. Riseborough, *Adv. Phys.* **2000**, *49*, 257–320.
- [65] A. Gilbert, N. S. Vidhyadhiraja, D. E. Logan, *J. Phys. Condens. Matter* **2007**, *19*, 106220.
- [66] G. Wilkinson, J. M. Birmingham, *J. Am. Chem. Soc.* **1954**, *76*, 6210.
- [67] J. M. Birmingham, G. Wilkinson, *J. Am. Chem. Soc.* **1956**, *78*, 42–44.
- [68] H. Schumann, J. A. Meese-Marktscheffel, L. Esser, *Chem. Rev.* **1995**, *95*, 865–986.
- [69] R. A. Andersen, J. M. Boncella, C. J. Burns, J. C. Green, D. Hohl, N. Rösch, *J. Chem. Soc. Chem. Commun.* **1986**, 405–407.
- [70] C. Benelli, D. Gatteschi, *Introduction to Molecular Magnetism: From Transition Metals to Lanthanides*, Wiley-VCH, Weinheim, **2015**, p. 71.
- [71] M. Tsutsui, T. Takino, D. Lorenz, *Z. Naturforsch.* **1966**, *21b*, 1–2.
- [72] S. Manastyrskij, M. Dubeck, *Inorg. Chem.* **1964**, *3*, 1647–1648.
- [73] O. Kahn, *Molecular Magnetism*, VCH, New York, N.Y., **1993**, pp. 31–52.
- [74] M. N. Bochkarev, L. N. Zakharov, G. S. Kalinina in *Organoderivatives of Rare Earth Elements*, Springer Netherlands, Dordrecht, **1995**, pp. 138–249.
- [75] M. Coreno, M. de Simone, J. C. Green, N. Kaltsoyannis, N. Narband, A. Sella, *Chem. Phys. Lett.* **2006**, *432*, 17–21.
- [76] R. Coates, M. Coreno, M. DeSimone, J. C. Green, N. Kaltsoyannis, A. Ker-ridge, N. Narband, A. Sella, *Dalton Trans.* **2009**, 5943–5953.
- [77] M. Coreno, M. de Simone, R. Coates, M. S. Denning, R. G. Denning, J. C. Green, C. Hunston, N. Kaltsoyannis, A. Sella, *Organometallics* **2010**, *29*, 4752–4755.
- [78] R. G. Denning, J. Harmer, J. C. Green, M. Irwin, *J. Am. Chem. Soc.* **2011**, *133*, 20644–20660.
- [79] M. Coreno, M. de Simone, J. C. Green, N. Kaltsoyannis, R. Coates, C. Hunston, N. Narband, A. Sella, *Dalton Trans.* **2014**, *43*, 5134–5141.
- [80] E. O. Fischer, H. Fischer, *J. Organomet. Chem.* **1965**, *3*, 181–187.
- [81] C. Calle, A. Srekanth, M. V. Fedin, J. Forrer, I. Garcia-Rubio, I. A. Gromov, D. Hinderberger, B. Kasumaj, P. Léger, B. Mancosu, G. Mitrikas, M. G. Santangelo, S. Stoll, A. Schweiger, R. Tschaggelar, J. Harmer, *Helv. Chim. Acta* **2006**, *89*, 2495–2521.
- [82] R. Pappalardo, C. K. Jørgensen, *J. Chem. Phys.* **1967**, *46*, 632–638.
- [83] C. J. Schlessener, A. B. Ellis, *Organometallics* **1983**, *2*, 529–534.
- [84] M. Schultz, J. M. Boncella, D. J. Berg, T. D. Tilley, R. A. Andersen, *Organometallics* **2002**, *21*, 460–472.
- [85] R. E. Da Re, C. J. Kuehl, M. G. Brown, R. C. Rocha, E. D. Bauer, K. D. John, D. E. Morris, A. P. Shreve, J. L. Sarrao, *Inorg. Chem.* **2003**, *42*, 5551–5559.
- [86] L. R. Morss, *Chem. Rev.* **1976**, *76*, 827–841.
- [87] F. Grandjean, G. J. Long in *Mössbauer Spectroscopy Applied to Inorganic Chemistry* (Eds.: G. J. Long, F. Grandjean), Springer US, Boston, **1989**, pp. 513–597.
- [88] G. Depaoli, U. Russo, G. Valle, F. Grandjean, A. F. Williams, G. J. Long, *J. Am. Chem. Soc.* **1994**, *116*, 5999–6000.
- [89] N. Kaltsoyannis, B. E. Bursten, *J. Organomet. Chem.* **1997**, *528*, 19–33.
- [90] Y. Baer, R. Hauger, C. Zürcher, M. Campagna, G. K. Wertheim, *Phys. Rev. B* **1978**, *18*, 4433–4439.
- [91] A. Franciosi, J. H. Weaver, N. Mårtensson, M. Croft, *Phys. Rev. B* **1981**, *24*, 3651–3654.
- [92] J. W. Allen, S. J. Oh, O. Gunnarsson, K. Schönhammer, M. B. Maple, M. S. Torikachvili, I. Lindau, *Adv. Phys.* **1986**, *35*, 275–316.
- [93] B. O. Roos, P. R. Taylor, P. E. M. Sigbahn, *Chem. Phys.* **1980**, *48*, 157–173.
- [94] K. Andersson, P.-Å. Malmqvist, B. O. Roos, A. J. Sadlej, K. Wolinski, *J. Phys. Chem.* **1990**, *94*, 5483–5488.
- [95] A. Greco, S. Cesca, W. Bertolini, *J. Organomet. Chem.* **1976**, *113*, 321–330.
- [96] A. Streitwieser, S. A. Kinsley, C. H. Jenson, J. T. Rigsbee, *Organometallics* **2004**, *23*, 5169–5175.
- [97] M. D. Walter, C. H. Booth, W. W. Lukens, R. A. Andersen, *Organometallics* **2009**, *28*, 698–707.
- [98] T. R. Bousie, D. C. Eisenberg, J. Rigsbee, A. Streitwieser, A. Zalkin, *Organometallics* **1991**, *10*, 1922–1928.
- [99] U. Kilimann, R. Herbst-Irmer, D. Stalke, F. T. Edelmann, *Angew. Chem. Int. Ed. Engl.* **1994**, *33*, 1618–1621; *Angew. Chem.* **1994**, *106*, 1684–1687.
- [100] K. O. Hodgson, K. N. Raymond, *Inorg. Chem.* **1972**, *11*, 3030–3035.
- [101] R. Shannon, *Acta Crystallogr. Sect. A* **1976**, *32*, 751–767.
- [102] A. Streitwieser, S. A. Kinsley, J. T. Rigsbee, I. L. Fragala, E. Ciliberto, *J. Am. Chem. Soc.* **1985**, *107*, 7786–7788.
- [103] H.-D. Amberger, H. Reddmann, F. T. Edelmann, *J. Organomet. Chem.* **2005**, *690*, 2238–2242.
- [104] N. M. Edelstein, P. G. Allen, J. J. Bucher, D. K. Shuh, C. D. Sofield, N. Kaltsoyannis, G. H. Maunder, M. R. Russo, A. Sella, *J. Am. Chem. Soc.* **1996**, *118*, 13115–13116.
- [105] C. H. Booth, M. D. Walter, M. Daniel, W. W. Lukens, R. A. Andersen, *Phys. Rev. Lett.* **2005**, *95*, 267202.
- [106] D. E. Smiles, E. R. Batista, C. H. Booth, D. L. Clark, J. M. Keith, S. A. Kozimor, R. L. Martin, S. G. Minasian, D. K. Shuh, S. C. E. Stieber, T. Tylicszak, *Chem. Sci.* **2020**, *11*, 2796–2809.
- [107] J. L. Sarrao, C. D. Immer, Z. Fisk, C. H. Booth, E. Figueroa, J. M. Lawrence, R. Modler, A. L. Cornelius, M. F. Hundley, G. H. Kwei, J. D. Thompson, F. Bridges, *Phys. Rev. B* **1999**, *59*, 6855–6866.
- [108] T. Vitova, K. O. Kvashnina, G. Nocton, G. Sukharina, M. A. Denecke, S. M. Butorin, M. Mazzanti, R. Caciuffo, A. Soldatov, T. Behrends, H. Geckeis, *Phys. Rev. B* **2010**, *82*, 235118.
- [109] M. W. Löble, J. M. Keith, A. B. Altman, S. C. E. Stieber, E. R. Batista, K. S. Boland, S. D. Conradson, D. L. Clark, J. Lezama Pacheco, S. A. Kozimor, R. L. Martin, S. G. Minasian, A. C. Olson, B. L. Scott, D. K. Shuh, T. Tylicszak, M. P. Wilkerson, R. A. Zehnder, *J. Am. Chem. Soc.* **2015**, *137*, 2506–2523.
- [110] A. B. Altman, J. I. Pacold, J. Wang, W. W. Lukens, S. G. Minasian, *Dalton Trans.* **2016**, *45*, 9948–9961.
- [111] S. G. Minasian, E. R. Batista, C. H. Booth, D. L. Clark, J. M. Keith, S. A. Kozimor, W. W. Lukens, R. L. Martin, D. K. Shuh, S. C. E. Stieber, T. Tylicszak, X.-d. Wen, *J. Am. Chem. Soc.* **2017**, *139*, 18052–18064.
- [112] A. Fujimori, *Phys. Rev. B* **1983**, *28*, 2281–2283.
- [113] A. Bianconi, A. Marcelli, H. Dexpert, R. Karnatak, A. Kotani, T. Jo, J. Petiau, *Phys. Rev. B* **1987**, *35*, 806–812.
- [114] A. Kotani, T. Jo, J. C. Parlebas, *Adv. Phys.* **1988**, *37*, 37–85.
- [115] G. Kaindl, G. Schmiester, E. V. Sampathkumaran, P. Wachter, *Phys. Rev. B* **1988**, *38*, 10174–10177.
- [116] M. V. Ganduglia-Pirovano, A. Hofmann, J. Sauer, *Surf. Sci. Rep.* **2007**, *62*, 219–270.
- [117] A. Kotani, H. Mizuta, T. Jo, J. C. Parlebas, *Solid State Commun.* **1985**, *53*, 805–810.

- [118] N. Hosoya, K. Yada, T. Masuda, E. Nakajo, S. Yabushita, A. Nakajima, *J. Phys. Chem. A* **2014**, *118*, 3051–3060.
- [119] N. Roesch, A. Streitwieser, *J. Am. Chem. Soc.* **1983**, *105*, 7237–7240.
- [120] M. Dolg, H. Stoll, *Theor. Chim. Acta* **1989**, *75*, 369–387.
- [121] M. Dolg, H. Stoll, H. Preuss, *J. Chem. Phys.* **1989**, *90*, 1730–1734.
- [122] W. Küchle, M. Dolg, H. Stoll, H. Preuss, *J. Chem. Phys.* **1994**, *100*, 7535–7542.
- [123] M. Dolg, X. Cao, *Chem. Rev.* **2012**, *112*, 403–480.
- [124] M. Dolg, P. Fulde, *Chem. Eur. J.* **1998**, *4*, 200–204.
- [125] A. Kerridge, R. Coates, N. Kaltsoyannis, *J. Phys. Chem. A* **2009**, *113*, 2896–2905.
- [126] R. F. W. Bader, *Atoms in Molecules: A Quantum Theory*, Clarendon Press, Oxford, **1994**, p. 438.
- [127] A. Kerridge, *Dalton Trans.* **2013**, *42*, 16428–16436.
- [128] O. Mooßen, M. Dolg, *Chem. Phys. Lett.* **2014**, *594*, 47–50.
- [129] A. Ashley, G. Balazs, A. Cowley, J. Green, C. H. Booth, D. O'Hare, *Chem. Commun.* **2007**, 1515–1517.
- [130] G. Balazs, F. G. N. Cloke, J. C. Green, R. M. Harker, A. Harrison, P. B. Hitchcock, C. N. Jardine, R. Walton, *Organometallics* **2007**, *26*, 3111–3119.
- [131] A. Kerridge, N. Kaltsoyannis, *C. R. Chimie* **2010**, *13*, 853–859.
- [132] M. Dolg, O. Mooßen, *J. Organomet. Chem.* **2015**, *794*, 17–22.
- [133] I. Hiroaki, S. Masahiko, *Chem. Lett.* **1992**, *21*, 147–150.
- [134] Y. Bian, J. Jiang, Y. Tao, M. T. M. Choi, R. Li, A. C. H. Ng, P. Zhu, N. Pan, X. Sun, D. P. Arnold, Z.-Y. Zhou, H.-W. Li, T. C. W. Mak, D. K. P. Ng, *J. Am. Chem. Soc.* **2003**, *125*, 12257–12267.
- [135] M. D. Walter, R. Fandos, R. A. Andersen, *New J. Chem.* **2006**, *30*, 1065–1070.
- [136] R. L. Halbach, G. Nocton, C. H. Booth, L. Maron, R. A. Andersen, *Inorg. Chem.* **2018**, *57*, 7290–7298.
- [137] R. L. Halbach, G. Nocton, C. H. Booth, L. Maron, R. A. Andersen, *Inorg. Chem.* **2018**, *57*, 8692.
- [138] P. L. Arnold, K. Wang, S. J. Gray, L. M. Moreau, C. H. Booth, M. Curcio, J. A. L. Wells, A. M. Z. Slawin, *Dalton Trans.* **2020**, *49*, 877–884.
- [139] N. T. Rice, J. Su, T. P. Gomba, D. R. Russo, J. Telsler, L. Palatinus, J. Bacsa, P. Yang, E. R. Batista, H. S. La Pierre, *Inorg. Chem.* **2019**, *58*, 5289–5304.
- [140] N. T. Rice, I. A. Popov, D. R. Russo, T. P. Gomba, A. Ramanathan, J. Bacsa, E. R. Batista, P. Yang, H. S. La Pierre, *Chem. Sci.* **2020**, *11*, 6149–6159.
- [141] L. M. Aguirre Quintana, N. Jiang, J. Bacsa, H. S. La Pierre, *Dalton Trans.* **2020**, *49*, 14908–14913.
- [142] M. D. Walter, M. Schultz, R. A. Andersen, *New J. Chem.* **2006**, *30*, 238–246.
- [143] M. D. Walter, D. J. Berg, R. A. Andersen, *Organometallics* **2006**, *25*, 3228–3237.
- [144] M. D. Walter, D. J. Berg, R. A. Andersen, *Organometallics* **2007**, *26*, 2296–2307.
- [145] G. Nocton, C. H. Booth, L. Maron, R. A. Andersen, *Organometallics* **2013**, *32*, 5305–5312.
- [146] G. Nocton, C. H. Booth, L. Maron, R. A. Andersen, *Organometallics* **2013**, *32*, 1150–1158.
- [147] G. Nocton, C. H. Booth, L. Maron, L. Ricard, R. A. Andersen, *Organometallics* **2014**, *33*, 6819–6829.
- [148] J. M. Veauthier, E. J. Schelter, C. J. Kuehl, A. E. Clark, B. L. Scott, D. E. Morris, R. L. Martin, J. D. Thompson, J. L. Kiplinger, K. D. John, *Inorg. Chem.* **2005**, *44*, 5911–5920.
- [149] C. N. Carlson, C. J. Kuehl, L. Ogallo, D. A. Shultz, J. D. Thompson, M. L. Kirk, R. L. Martin, K. D. John, D. E. Morris, *Organometallics* **2007**, *26*, 4234–4242.
- [150] I. L. Fedushkin, O. V. Maslova, E. V. Baranov, A. S. Shavyrin, *Inorg. Chem.* **2009**, *48*, 2355–2357.
- [151] I. L. Fedushkin, O. V. Maslova, A. G. Morozov, S. Dechert, S. Demeshko, F. Meyer, *Angew. Chem. Int. Ed.* **2012**, *51*, 10584–10587; *Angew. Chem.* **2012**, *124*, 10736–10739.
- [152] V. Goudy, A. Jaoul, M. Cordier, C. Clavaguéra, G. Nocton, *J. Am. Chem. Soc.* **2017**, *139*, 10633–10636.
- [153] M. Dolg, H. Stoll, H. Preuss, *Theor. Chim. Acta* **1993**, *85*, 441–450.
- [154] C. E. Kefalidis, L. Castro, A. Yahia, L. Perrin, L. Maron in *Computational Methods in Lanthanide and Actinide Chemistry* (Ed.: M. Dolg), **2015**, pp. 343–373.
- [155] A. A. Trifonov, T. V. Mahrova, L. Luconi, G. Giambastiani, D. M. Lyubov, A. V. Cherkasov, L. Sorace, E. Louyriac, L. Maron, K. A. Lyssenko, *Dalton Trans.* **2018**, *47*, 1566–1576.
- [156] N. A. G. Bandeira, C. Daniel, A. Trifonov, M. J. Calhorda, *Organometallics* **2012**, *31*, 4693–4700.
- [157] L. Jacquot, M. Xémard, C. Clavaguéra, G. Nocton, *Organometallics* **2014**, *33*, 4100–4106.
- [158] R. L. Halbach, G. Nocton, J. I. Amaro-Estrada, L. Maron, C. H. Booth, R. A. Andersen, *Inorg. Chem.* **2019**, *58*, 12083–12098.
- [159] C. V. Krishnan, C. Creutz, H. A. Schwarz, N. Sutin, *J. Am. Chem. Soc.* **1983**, *105*, 5617–5623.
- [160] H. Ferreira, M. M. Conradie, K. G. von Eschwege, J. Conradie, *Polyhedron* **2017**, *122*, 147–154.
- [161] A. Klein, W. Kaim, E. Waldhör, H.-D. Hausen, *J. Chem. Soc. Perkin Trans. 2* **1995**, 2121–2126.
- [162] W. W. Lukens, N. Magnani, C. H. Booth, *Inorg. Chem.* **2012**, *51*, 10105–10110.
- [163] J. D. Rinehart, M. Fang, W. J. Evans, J. R. Long, *Nat. Chem.* **2011**, *3*, 538–542.
- [164] J. D. Rinehart, M. Fang, W. J. Evans, J. R. Long, *J. Am. Chem. Soc.* **2011**, *133*, 14236–14239.
- [165] S. Demir, J. M. Zadrozny, M. Nippe, J. R. Long, *J. Am. Chem. Soc.* **2012**, *134*, 18546–18549.
- [166] C. A. Gould, L. E. Darago, M. I. Gonzalez, S. Demir, J. R. Long, *Angew. Chem. Int. Ed.* **2017**, *56*, 10103–10107; *Angew. Chem.* **2017**, *129*, 10237–10241.
- [167] D. Wang, J. Moutet, M. Tricoire, M. Cordier, G. Nocton, *Inorganics* **2019**, *7*, 58.
- [168] W.-H. Leung, Q.-F. Zhang, X.-Y. Yi, *Coord. Chem. Rev.* **2007**, *251*, 2266–2279.
- [169] L. Castro, Y.-M. So, C.-w. Cho, R. Lortz, K.-H. Wong, K. Wang, P. L. Arnold, K.-C. Au-Yeung, H. H.-Y. Sung, I. D. Williams, W.-H. Leung, L. Maron, *Chem. Eur. J.* **2019**, *25*, 10834–10839.

Manuscript received: October 27, 2020

Accepted manuscript online: December 19, 2020

Version of record online: February 25, 2021



Size-Controlled Hapticity Switching in [Ln(C₉H₉)(C₈H₈)] Sandwiches

Maxime Tricoire,^[a] Luca Münzfeld,^[b] Jules Moutet,^[a] Nolwenn Mahieu,^[a] Léo La Droitte,^[c] Eufemio Moreno-Pineda,^[d, e, f] Frédéric Gendron,^[c] Jeremy D. Hilgar,^[h] Jeffrey D. Rinehart,^[h] Mario Ruben,^[b, d, i, j] Boris Le Guennic,^[c] Olivier Cador,^[c] Peter W. Roesky,^{*,[b]} and Grégory Nocton^{*,[a]}

Abstract: Sandwich complexes of lanthanides have recently attracted a considerable amount of interest due to their applications as Single Molecule Magnet (SMM). Herein, a comprehensive series of heteroleptic lanthanide sandwich complexes ligated by the cyclononatetraenyl (Cnt) and the cyclooctatetraenyl (Cot) ligand [Ln(Cot)(Cnt)] (Ln=Tb, Dy, Er, Ho, Yb, and Lu) is reported. The coordination behavior of the

Cnt ligand has been investigated along the series and shows different coordination patterns in the solid-state depending on the size of the corresponding lanthanide ion without altering its overall anisotropy. Besides the characterization in the solid state by single-crystal X-ray diffraction and in solution by ¹H NMR, static magnetic studies and ab initio computational studies were performed.

Introduction

Many different applications of rare-earth-based compounds originate from their unique physical properties:^[1] strong spin-orbit coupling, large magnetization and core 4f-orbitals.^[2] The specific design of compounds adapted to specific applications is facilitated by the small orbital contributions of the ligand-field. This allows the prediction of fundamental physical properties with qualitative electrostatic models.^[3] These considerations have motivated a large number of fundamental structure/properties studies, especially for luminescent materials,^[4] MRI contrast agents^[5] and more recently for the design of high-performance Single Molecule-Magnets (SMMs).^[1a,6]

In this particular area, the gap from liquid helium (2 K) to liquid nitrogen (77 K) temperatures has recently been closed, and organometallic compounds of lanthanides have played a crucial role in this breakthrough.^[7] The possible geometries allowed by typical anionic cyclo-aromatic ligands used in organometallic chemistry, such as cyclopentadienyl (Cp),^[6] cyclooctatetraenyl (Cot)^[8] and cyclononatetraenyl (Cnt),^[9] led to unusual arrangements, which can be tuned by the bulk of their substituents. When a linear geometry with localized charge density in the axial position is necessary to get interesting magnetic properties, as in the case of oblate ions such as Dy, small Cp ligands with large bulk are used to provide the localized charge and enforce a nearly linear geometry.^[7a-c,10]

[a] M. Tricoire, Dr. J. Moutet, N. Mahieu, Prof. G. Nocton
Laboratoire de Chimie Moléculaire (LCM)
CNRS, Ecole polytechnique, Institut Polytechnique de Paris
Route de Saclay, 91120 Palaiseau (France)
E-mail: gregory.nocton@polytechnique.edu

[b] L. Münzfeld, Prof. Dr. M. Ruben, Prof. Dr. P. W. Roesky
Institute of Inorganic Chemistry
Karlsruhe Institute of Technology (KIT)
Engesserstraße 15, 76131, Karlsruhe (Germany)
E-mail: peter.roesky@kit.edu

[c] L. La Droitte, Dr. F. Gendron, Prof. Dr. B. Le Guennic, Prof. Dr. O. Cador
ISCR (Institut des Sciences Chimiques de Rennes)-UMR 6226
Université de Rennes, CNRS
35000 Rennes (France)

[d] Dr. E. Moreno-Pineda, Prof. Dr. M. Ruben
Institute of Nanotechnology (INT)
Karlsruhe Institute of Technology (KIT)
Hermann-von-Helmholtz-Platz 1, 76344, Eggenstein-Leopoldshafen (Germany)

[e] Dr. E. Moreno-Pineda
Depto. de Química-Física, Escuela de Química
Facultad de Ciencias Naturales, Exactas y Tecnología, Universidad de Panamá, Panamá

[f] Dr. E. Moreno-Pineda
Panamanian National System of Investigators (SNI, SENACYT), Panama

[h] J. D. Hilgar, Prof. Dr. J. D. Rinehart
Department of Chemistry and Biochemistry
University of California-San Diego
La Jolla, CA (United-States)

[i] Prof. Dr. M. Ruben
Centre Européen de Science Quantique (CESQ), Institut de Science et d'Ingénierie Supramoléculaires (ISIS)
Université de Strasbourg
8, Allée Gaspard Monge, F-67000 Strasbourg (France)

[j] Prof. Dr. M. Ruben
Institute of Quantum Materials and Technology (IQMT)
Karlsruhe Institute of Technology (KIT)
Hermann-von-Helmholtz-Platz 1, 76344, Eggenstein-Leopoldshafen (Germany)

Supporting information for this article is available on the WWW under <https://doi.org/10.1002/chem.202101599>

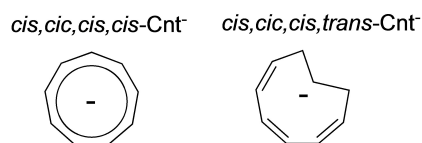
© 2021 The Authors. Chemistry - A European Journal published by Wiley-VCH GmbH. This is an open access article under the terms of the Creative Commons Attribution License, which permits use, distribution and reproduction in any medium, provided the original work is properly cited.

With prolate ions, such as Er, large ligands, such as the Cot dianion and the Cnt anion, are better suited to enhance equatorial ligand field contributions in sandwiched compounds.^[8b,11]

However, some of these specificities can be antagonistic, making the rational design of such compounds difficult resulting in a narrow edge, at which all the desired properties are maximized. Typically, a bulk increase of the Cp ligand favors linearity while driving away the point charge of the ligand from the metal ion.^[7c,12] It is thus extremely important to rationalize the dynamic coordination properties of these aromatic ligands in order to be able to control the metal-ligand pair anisotropy.^[11c] Additionally, because magnetism and luminescent applications often require solid-state measurements, the understanding of how packing forces influence the inner coordination as well as the exact arrangement of the closest neighbors in the crystal lattice is important. Recent studies led by some of us have underlined the importance of the orientation of the anisotropy axes in a series of binuclear Er(Cot) fragments^[11d] as well as the second sphere environment in divalent [Tm(Cot)₂]²⁻ compounds, when designing performing SMMs.^[11e]

Among others, the cyclononatetraenyl ligand (Cnt) is a promising ligand for the rational design of SMMs: it allows the formation of perfectly linear homoleptic sandwiches with divalent lanthanides and exhibits labile coordination dynamics in coordinating solvents,^[9a] contrary to Cot and Cp ligands. In this work, the bis-Cnt [Ln(Cnt)₂] divalent complexes of Ln=Sm, Eu, Tm and Yb have been obtained in good yields through the use of a mixture of two isomers of the Cnt potassium salt: the *cis-cis-cis-cis* and the *cis-cis-cis-trans* forms (Scheme 1). A step further was the use of this mono-anionic ligand in combination with the dianionic Cot ligand to form neutral sandwiches with linear geometry.^[13] In this series, the geometry is particularly well adapted for maximizing the anisotropy of the erbium complex and, indeed, the latter was reported to present interesting SMM properties, confirming the adapted Er-Cnt/Cot pair anisotropy. Yet, the specific coordination of the Cnt ligand in various environments, with various bulk, and different lanthanide size remains to be studied to enlarge the scope of Cnt compounds with promising applications.

In the present work, a series of heteroleptic sandwich complexes, [Ln(Cot)(Cnt)], is presented with Ln=Tb, Dy, Ho, Er, Tm, Lu with a focus on their structural aspects, both in the solid-state and in solution. This work reinforces the versatility of the Cnt ligand as a useful candidate for the design of specific geometries needed in organolanthanide chemistry for a given application including magnetism.

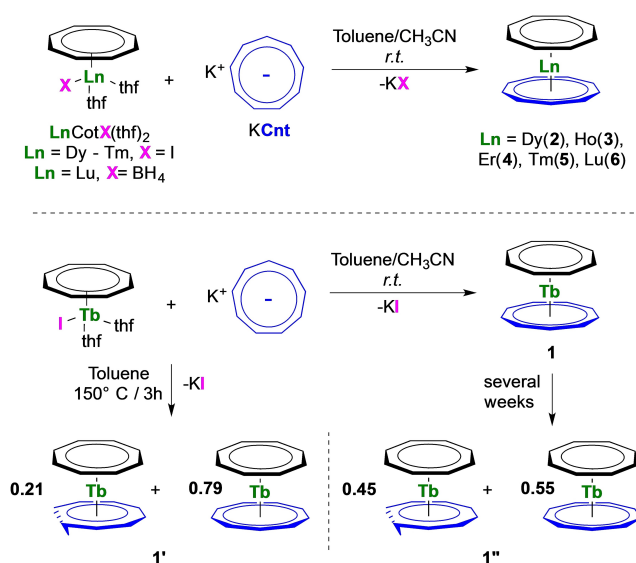


Scheme 1. Isomers of the Cnt ligand

Results and Discussion

Synthesis

The heteroleptic trivalent late lanthanide sandwich complexes [Ln(Cot)(Cnt)] (Ln=Tb (1), Dy (2), Ho (3), Er (4), Yb (5), Lu (6)) were synthesized from a toluene/acetonitrile mixture of KCnt and the corresponding [Ln(Cot)I(thf)₂] complexes (Ln=Tb, Dy,^[13] Ho, Er,^[11c,13] Tm) at room temperature (Scheme 2). Due to the facile reduction of Yb³⁺ in the presence of the Cot ligand, the Yb compound is not accessible.^[14] [Ln(Cot)I(thf)₂] were prepared from K₂Cot and lanthanide tris-iodides in thf,^[11c] a faster alternative compared to the elegant procedure proposed by Mashima et al. for the earlier lanthanides.^[15] The Lu complex is best prepared from the borohydride [Lu(BH₄)₃(thf)₃] precursor^[16] to afford either the monomeric [Lu(Cot)(BH₄)(thf)₂] or the dimeric [Lu(Cot)(BH₄)(thf)₂]₂ complex as original compounds depending on the crystallization conditions, similar to the procedure of Ephritikhine for the synthesis of the Nd analogues.^[17] The three new crystal structures with Ln=Tb, Ho and Lu are discussed in the Supporting Information. The Tm structure was reported by Schumann et al. but was made from direct reaction of TmI₂ with free Cot.^[18] In the case of Tb, Dy, Ho, Er, and Tm, the potassium salt of the Cnt ligand (both all-*cis* and *cis-cis-cis-trans* isomers can be used)^[9a,19] is best dissolved in acetonitrile before use. After 12 h of stirring, the suspensions turned to pale-colored solutions with a gradual color change along the lanthanide series (pale yellow for Tb, yellow for Dy,^[13] pale orange for Ho, orange for Er,^[13] salmon orange for Tm). The reaction time of 12 h is necessary to complete the isomerization when the more soluble *cis-cis-cis-trans* isomer is used. Synthesis of the lutetium complex [Lu(Cot)(Cnt)] (6) was best performed by heating KCnt and [Lu(Cot)(BH₄)(thf)₂] in toluene under reflux for 16 h. Another important step is the removal of all the volatiles and thorough drying of the resulting solid. Several steps of drying and re-suspension in toluene are necessary to



Scheme 2. Synthesis of 1–6.

ensure complete de-coordination of the acetonitrile (or remaining thf molecule in the case of lutetium). If this step is not complete, an acetonitrile adduct of $[\text{Ln}(\text{Cot})(\text{Cnt})]$ may be isolated, in which the Cnt ligand binds in lower hapticity than η^9 . A crystal structure of such a dysprosium complex has been obtained with partial coordination of acetonitrile. The structure is discussed in the Supporting Information (Figure S19–S20). Once the coordinated solvent has been removed, extraction in a large amount of toluene followed by filtration, concentration and cooling (-40°C) allows the crystallization of the title compounds (1–6) as crystals suitable for X-ray diffraction. The erbium and dysprosium complexes, 2 and 4, respectively, were already recently published using a different procedure and analyzed by multiple approaches. The η^9 -Cnt coordination remained an open question because of a crystallographic disorder.^[13] For the Tb complex (1), several different crystals (crystallized at room temperature and grown over a week) of red color have been analyzed to reveal a mixture of the *cis-cis-cis-cis* and of the *cis-cis-cis-trans* Cnt ligand in a 79:21 ratio (1'). The structure is discussed in Supporting Information. However, when the terbium complex was prepared by an alternative method from hot toluene, the crystallized structure was similar to that of 1' with a ratio of *cis-cis-cis-cis*:*cis-cis-cis-trans* ligand of 55:45 (1''). Upon heating, all compounds degraded at higher temperature.

Solution analysis

Compounds 1–6 have been analyzed by ^1H NMR spectroscopy. Except for the Lu compound (6), which is diamagnetic, 1–5 are highly paramagnetic but signals have been obtained for all compounds (Figure 1, Supporting Information, Figure S1–S14). The broad signals obtained for the Er (4) and Tm (5) complexes did not allow distinguishing the Cnt from the Cot ligand on the basis of their relative integrations. The signals appear at -5.01 , -128.7 ppm and -23.2 and -235.8 ppm, for 4 and 5, respectively, at room temperature. For 1–3 and 6, ^1H NMR spectra feature two similar signals with chemical shifts of 245.9, 118.7, 90.5 and 5.83 ppm for the Cot, respectively, and of 101.5, 72.9, 59.2, and 6.54 ppm for the Cnt, respectively. In 1–3, the shapes of the f-electron density in the lanthanide ions are oblate, while in 4–5, they are prolate.^[3b] The modification in the anisotropy orientation between 3 and 4 is well reflected by the sign change of their chemical shifts for both ligands. Variable temperature ^1H NMR was performed for 6 but no fluxional behavior^[20] for both ligands was observed in the range from $+80$ to -80°C .

The crystallization of different terbium complexes, 1, 1', and 1'' with a different configuration for the Cnt ligand was intriguing to us. The free Cnt⁻ ligand indeed possesses two different isomers, easily quantified by ^1H NMR spectroscopy: the *cis-cis-cis-cis* ligand gives rise to one singlet in agreement with D_{9h} symmetry while the *cis-cis-cis-trans* one features 5 signals in agreement with C_{2v} symmetry.^[21] In a previous work, the use of a soluble mixture of these two isomers leads to multiple $\text{Ln}(\text{Cnt})_2$ sandwich isomers, which were also easily identified by

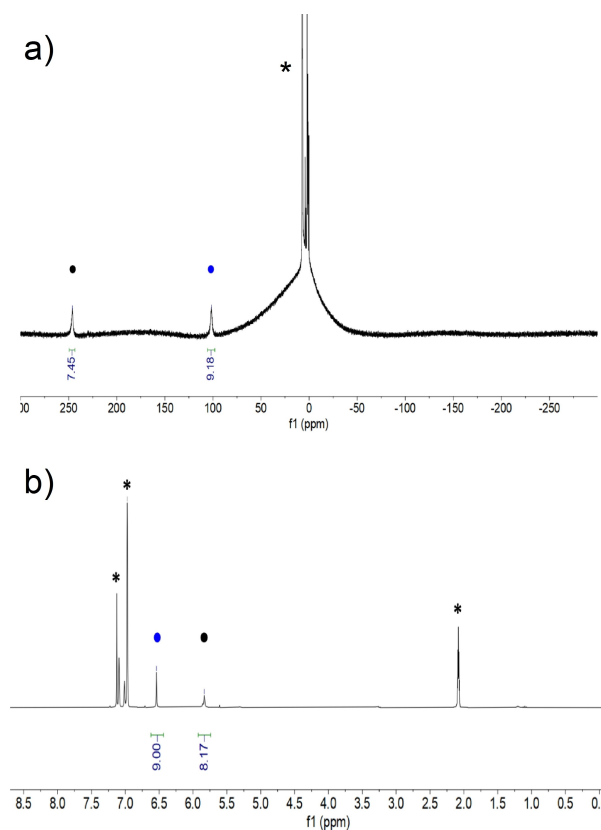
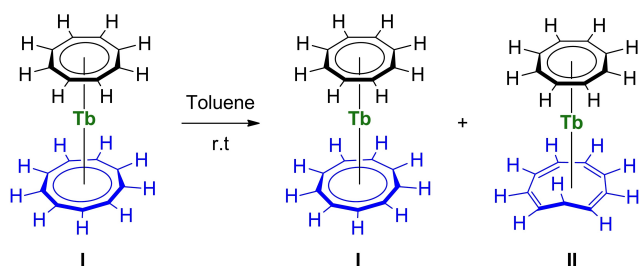


Figure 1. ^1H NMR of 1 (a) and 6 (b) at 293 K in toluene- d_8 . Blue mark (●) is for the signals of the Cnt ligand and the black mark (●) for the Cot ligand. * residual protio signal of the solvent.

^1H NMR spectroscopy.^[9a] Additionally, Boche et al. gathered, in a comprehensive series of three articles, useful information on the Cnt ligand synthesis, as well as its topomerization and isomerization.^[19,22] These studies unveil several questions on the real nature of the isomerization process when assisted by metal complexes. An interesting connection to this is that 1'' in which one ligand is partially isomerized in the *cis-cis-cis-trans* form, is obtained in a relatively high-temperature synthesis (150°C for 3 h) from the *cis-cis-cis-cis* ligand, supposedly thermodynamically more stable. In contrast, 1 only contains the *cis-cis-cis-cis* ligand and is prepared under milder conditions (room temperature synthesis). Thus, in order to probe a possible temperature effect on the isomerization of the ligand in the Tb complex, a solution of 1 in toluene- d_8 was let stand for several days at room temperature. The resulting ^1H NMR spectra of this experiment are shown in Figure S14. A new set of 6 signals increases with time at δ 404.0, 230.1, 203.6, 196.2, 165.1 and -169.5 ppm while the two initial signals of 1 (Scheme 3, I) were still present. The estimated ratio based on integration, 2:8:2:2:1:2, needs to be considered cautiously because of the highly paramagnetic nature of the complex. Yet, it is in full agreement with the formation of a $[\text{Tb}(\text{Cot})(\text{Cnt})]$ isomer in which the Cnt ligand is in the *cis-cis-cis-trans* configuration (Scheme 3, II). Indeed, the isomerized Cnt ligand in 1' and 1'' gives rise to 5 distinct proton resonances, as also observed in



Scheme 3. Isomerization of I to II in solution.

the free cis-cis-cis-trans Cnt ligand,^[9a] while the Cot signal remains a singlet integrating for 8 protons. The ratio between the isomers I and II is ca. 66:34 after three days and stabilizes over time to approximately 60:40 after 20 days, remarkably close to the ratio found in the solid state structure of 1'' (55:45), while 1', which was obtained from a slow evolution of 1 at room temperature features a higher I:II ratio of 79:21.

This unexpected situation again connects to Boche's findings and shows that the nature of the coordinated metal greatly affects the inter-conversion between topologic isomers of the Cnt ligand. Although this isomerization has only been observed so far in case of the Tb complex 1, a thorough investigation of the Cnt isomerization within the [Ln(Cot)(Cnt)] series (which is outside the scope of this article) would still be necessary to understand whether it is related to size effects or other physical properties.

X-ray solid-state crystal structure

The crystal structures are isomorphous from Dy to Lu (2–6) and were solved in $P2_1/n$ irrespective of the data collection temperatures (Figure 2). There is a positional disorder in both ligands, the first one featuring eight carbon atoms (Cot), the second one nine carbon atoms (Cnt). Within this space group, the presence

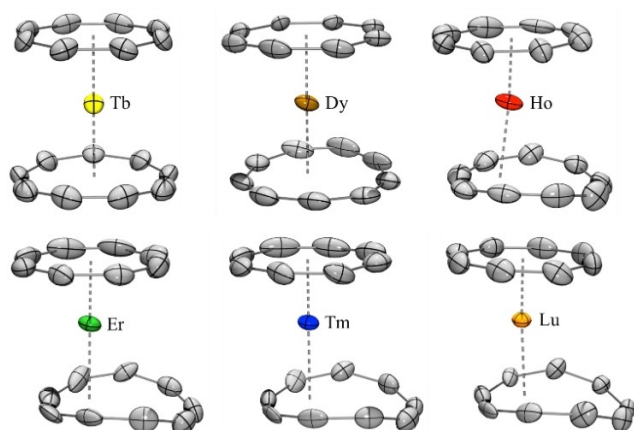


Figure 2. ORTEP of 1–6. Thermal ellipsoids are depicted at 50% probability level. Hydrogen atoms and the disorder are omitted for clarity (see main text for the discussion of the coordination mode).

of these specificities creates a situation in which the final solution has two rings embedded in each other with occupancy of 0.5 on each atom (See Figure S25a). Additionally, for the complexes 2–6, the lanthanide ion is not placed at a special position (i.e. sitting on a symmetry element) but lies close to an inversion center, also with occupancy of 0.5. As a result, the lanthanide ion is not centered with the ligands but is slightly moved away, which seems to point out a possible lower coordination mode (hapticity) of one of the ligands. This situation also drastically complicates the resolution when one wants to separate the ligands from one another since the symmetry generation by the $P2_1/n$ space group creates two more rings embedded with each other along with an additional lanthanide atom close to the inversion center (See Figure S25b). However, because of the symmetry rules, only two variants exist and it is not possible to mix the two different configurations.

Thus, from a crystallographic point of view, two solutions are possible; viz. a lower hapticity either for the Cot or for the Cnt ligand (See Figure S25d, e). However, it seems that the deviation from planarity observed in the 9-membered ring is in better agreement with a perturbed coordination mode for the Cnt ligand rather than for the Cot ligand. Additionally, the Ln–Ctr (Ctr, centroid) distance with both rings must respect the increased negative charge of Cot^{2-} with respect to Cnt^- and longer Ln–Cnt distances are therefore expected.^[13] If the η^9 -Cnt coordination mode was preferred, both the Ln–Ctr distances and the coordination mode of Cot are unrealistic from a chemical point of view for the lutetium compound (6) (See Supporting Information). Lowering the symmetry to the $P1$ symmetry group (See Figure S26) increases the size of the asymmetric unit but does not allow to better define the disorder; it is still necessary to assume either longer Ln–Ctr distances for the Cnt- or for the Cot- ligand. When solving the data, it is also necessary to allow positional freedom to the carbon atoms except for the aromaticity restraint on the C–C distances on both rings in order to avoid scrambling of the carbon atoms between the two ligands moieties upon refinement. If the ring having eight carbon atoms (Cot) ends up relatively planar, in agreement with most Cot ligands coordinated to lanthanide ions in the literature, the one with nine carbon atoms (Cnt) shows a strong deviation from planarity with a curvature at the extremity, which tends to be indicative of a different coordination mode. In 2–6, a closer look to the Ln–C set of distances within the eight values of the eight-membered ring (See Table 1) shows a relatively close set of distances in the range 2.44(2)–2.50(2) Å in 6, 2.43(3)–2.54(3) Å in 5, 2.45(2)–2.55(3) Å in 4, 2.46(2)–2.65(2) Å in 3, and 2.52(2)–2.64(2) Å in 2. In contrast, the variation in the nine membered Cnt ring is much more pronounced (Table 1) with $\eta(\text{Ln–C}(\text{Cnt})_{\text{max}}\text{–LnC}(\text{Cnt})_{\text{min}})$ values of 1.426 Å in Lu (6) (2.50(2) to 3.930(9) Å), 1.228 Å in Tm (5) (2.54(3) to 3.769(8) Å), 1.213 Å in Er (4) (2.55(3) to 3.763(15) Å), 0.906 Å in Ho (3) (2.56(2) to 3.47(2) Å), and 0.284 Å in Dy (2) (2.66(2) to 2.96(2) Å).

The space group of the Tb complex (1) is modified from $P2_1/n$ to $Pnma$ with the removal of the inversion center on the lanthanide atom, which was confirmed by the analysis of the precession images. An additional symmetry plane that contains

Table 1. Main metric parameters for 1–6 at 150 K. [a] Only the carbon atoms formally η^1 -coordinated are considered in the average calculation.

	Tb (1, η^9)	Dy (2, η^8)	Ho (3, η^6)	Er (4, η^6)	Tm (5, η^6)	Lu (6, η^6)
Ln–C(Cnt)	2.775(7)	2.68(2)	2.56(2)	2.55(3)	2.54(3)	2.50(2)
	2.775(7)	2.72(2)	2.61(2)	2.59(3)	2.57(2)	2.54(2)
	2.79(1)	2.74(2)	2.62(2)	2.61(3)	2.64(2)	2.6(2)
	2.82(3)	2.74(2)	2.72(2)	2.69(3)	2.73(2)	2.68(2)
	2.83(1)	2.79(2)	2.82(2)	2.88(0)	2.875(13)	2.943(12)
	2.84(2)	2.86(2)	3.02(3)	3.10(2)	3.11(2)	3.14(2)
	2.85(3)	2.86(2)	3.212(14)	3.443(13)	3.449(9)	3.59(10)
	2.85(1)	2.95(2)	3.37(2)	3.60(0)	3.594(12)	3.719(13)
	2.86(2)	2.96(2)	3.47(2)	3.76(2)	3.769(8)	3.930(9)
	$\eta(\text{Ln–C(Cnt)}_{\text{max}}\text{–LnC(Cnt)}_{\text{min}})$	0.094	0.284	0.906	1.213	1.228
Ln–C(η -Cnt) ^[a] ave	2.82(3)	2.79(9)	2.73(17)	2.74(21)	2.74(21)	2.73(26)
C(η -Cnt)-Ln–C(η -Cnt) ^[a]	177.4	172.0	169.6	174.7	173.8	174.2
Ln–C(Cnt) ave	2.82(3)	2.81(10)	2.93(33)	3.02(44)	3.03(44)	3.07(55)
Ln–C(Cot) range	2.57(3)–2.63(2)	2.52(2)–2.64(2)	2.46(2)–2.65(2)	2.45(2)–2.55(3)	2.43(3)–2.54(3)	2.44(2)–2.50(2)
Ln–C(Cot) ave	2.58(2)	2.58(4)	2.55(7)	2.50(4)	2.48(3)	2.46(1)
Ln–C(η -all) ^[a] ave	2.71	2.69	2.63	2.60	2.59	2.58

the centroids of both the Cot and Cnt ligands and the Tb metal center is present. The latter thus separates both ligands in two symmetrical sections. The differentiation in the space group between the late lanthanide ions (2–6) and the Tb one (1) could be explained by a hapticity switching of the Cnt ligand in the case of larger lanthanide ions, imposing a different symmetry than that observed in 1. Consequently, the structure visually appears to be in better agreement with a formal η^9 -coordination mode. A lower variation in the Ln–C(Cnt) distance range ($\eta(\text{Ln–C(Cnt)}_{\text{max}}\text{–LnC(Cnt)}_{\text{min}}) = 0.094 \text{ \AA}$) (See Table 1) is observed. The deformation of the Cnt ligand is minimal.

Several metric parameters help to visualize and quantify the structural modifications (curved vs. planar) and the hapticity modulation of the Cnt ligand in 1–6. First, three main planes were constructed; the plane defined by the Cot ligand (in grey, Figure 3), the mean plane made by the six Cnt carbon atoms that are the closest to the lanthanide ion (in color) and the one set up by three remaining Cnt carbon atoms (in color), which are located further away from the lanthanide ion. The angle between the two Cnt planes decreases from the Lu to the Tb complexes in agreement with a stronger deviation from planarity with smaller lanthanide ions. At low-temperature, the angle is decreasing gradually from 34.2° in Lu (6) to 4.80° in Tb (1), with intermediate values of 31.3° , 29.7° , 23.7° , and 12.4° in

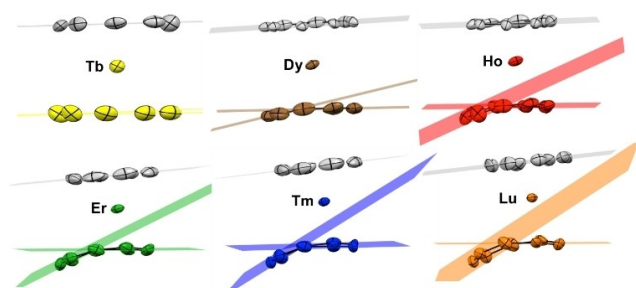


Figure 3. Plane constructions in 1–6. The grey plane is constructed with the eight carbon atoms of the Cot ligand. The colored planes are constructed with the six closest carbon atoms and the three remaining carbons of the Cnt ligand, respectively (see main text for limits of this construction)

Tm (5), Er (4), Ho (3) and Dy (2), respectively (Table S8). At room temperature, the decrease is weaker from 25.3° to 14.8° from 6 to 2. Complex 5 has also been recorded at 100 K, 150 K, 200 K, and 250 K with no clear break in the metric parameters.

The plane angle difference between the low- and room-temperature X-ray structures is also significant. This set of angular parameters intends to show how the curvature of the Cnt ligand gradually evolves from Tb to Lu in agreement with the lanthanide contraction of the ionic radius.^[23]

The plane angle difference between the low- and room-temperature X-ray structures is also significant. This set of angular parameters intends to show how the curvature of the Cnt ligand gradually evolves from Tb to Lu in agreement with the lanthanide contraction of the ionic radius.^[23]

A second set of useful metric parameters corresponds to the distances and angles from the metal ion to the constructed centroids of both ligands (See Table S8). While the centroid of the Cot ligand is always defined by its eight carbon atoms, three different centroids were constructed for the Cnt ligand: the first with the eight carbon atoms of the Cot ligand and the three others with i) the six atoms closest to the lanthanide ion (Ctr6), ii) the eight atoms closest (Ctr8) and iii) the nine atoms of the Cnt ligand (Ctr9). The Ln–Cot(Ctr) distances (at 150 K) vary from 1.804 Å (1), 1.772 Å (2), 1.735 Å (3), 1.701 Å (4), 1.681 Å (5), to 1.653 Å (6). The overall trend in the distances follows the lanthanide contraction. It is rather informative to compare these distances with those in the mono-Cot iodide or borohydride analogues $[\text{Ln}(\text{Cot})\text{I}(\text{S})_2]$ ($\text{S} = \text{thf}$, pyridine or CH_3CN) of 1.814 (Tb), 1.80(1) (Dy), 1.78 (Ho), 1.763(12) (Er),^[11c] 1.750(5) Å (Tm)^[18] and $[\text{Lu}(\text{Cot})(\text{BH}_4)(\text{thf})_2]$ of 1.724 Å. Within this series, for Ln = Dy, Ho, Er, Tm, and Lu, the Ln–Cot(Ctr) distances are shorter than those reported for 2–6 while they are similar in 1.

The Ln–Cnt distances are somewhat informative to distinguish three potential coordination modes (See Figure 4): at low-temperature, for the late lanthanides (Ho to Lu), the shortest Ln–Cnt distances are that with Ctr6. In contrast, for Dy and Tb, the shortest Ln–Cnt distances are obtained with Ctr8 and Ctr9, respectively. Similarly, within all the series, the Cot(Ctr)–Ln–Cnt (Ctr) angles are also the largest using the same aforementioned

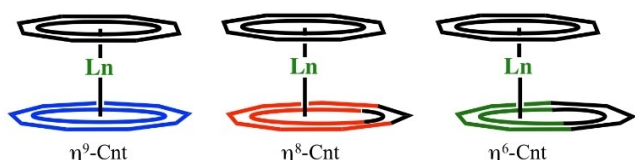


Figure 4. Representation of the different limit coordination modes of the Cnt ligand.

Cnt centroids (See Table S8). This set of data would best describe the hapticity of the Cnt ligand as formal η^6 for Ho (3) to Lu (6), while the hapticity would be best described as formal η^8 for Dy (2) and η^9 for Tb (1). Interestingly, at higher temperature, the picture is slightly different and the coordination mode of the Cnt in Ho (3) would be best described as formal η^8 . The hapticity of the Cnt in the Er (4), Tm (5) and Lu (6) complexes would remain best described as η^6 at room temperature. Thus, the average Ln–C distances on all formally η -coordinated carbon atoms were calculated for 1–6 and are reported in Table 1. A smooth variation with the lanthanide ion size is reported from 2.71 Å for [Tb(Cot)(Cnt)] (1) complex to 2.58 Å for [Lu(Cot)(Cnt)] (6).

Additionally, it is possible to consider the sum of the van der Waals radii as additional information on the nature of the interaction, i.e. distance metrics that are larger than the sum of the van der Waals radii are not expected to size any interaction.^[24] The range of these van der Waals radii for Tb–Lu is 1.80 to 1.72 Å and that of aromatic C atom is 1.70 Å. Thus the maximum distance is 3.42 Å for 6 (Lu) and 3.47 Å for 1 (Tb). In these considerations 4–6 are η^6 , 3 is η^8 and 1,2 are η^9 . However, these analyses should be taken cautiously because these metrics present the limit forms of coordination (η^6 and η^9) but the real hapticity is probably best found in between these limit forms, as found in solution (See ¹H NMR). Moreover, from a strict crystallographic point of view, the opposite construction, i.e. η^9 -coordination of the Cnt and lower coordination mode of the Cot ligand, remains valid.

Magnetic measurements

The solid-state magnetic data for compounds 1–3 and 5 are reported in Figure 5. The room temperature $\chi_{\text{M}}T$ values are equal to 11.34, 14.12, 13.2 and 6.8 cm³K mol⁻¹ for compounds 1–3 and 5 respectively. These values are in fairly good agreement with the calculated Curie constants for the ground state multiplets ⁷F₆ (Tb(III), 1, 11.82 cm³K mol⁻¹, $g_J=3/2$), ⁶H_{15/2} (Dy(III), 2, 14.17 cm³K mol⁻¹, $g_J=4/3$), ⁵I₈ (Ho(III), 3, 14.07 cm³K mol⁻¹, $g_J=5/4$) and ³H₆ (Tm(III), 5, 7.15 cm³K mol⁻¹, $g_J=7/6$). On cooling, $\chi_{\text{M}}T$'s decrease monotonically down to 2 K: 2.52 cm³K mol⁻¹ for 1, 7.2 cm³K mol⁻¹ for 2, 5.1 cm³K mol⁻¹ for 3 and 5.9 cm³K mol⁻¹ for 5. These values reflect the signature of the effect of the crystal field splitting that lifts the degeneracy of the ground state multiplets. The magnetization curves at 2 K are given in the Supporting Information (Figure S15). None of these compounds show slowing down of the relaxation of the

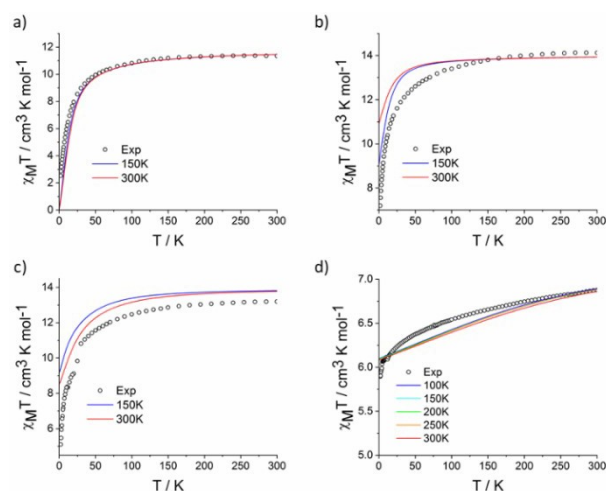


Figure 5. Temperature dependent $\chi_{\text{M}}T$ values for compounds 1 (a), 2 (b), 3 (c) and 5 (d) in dots with the calculated curves from structures at various temperatures.

magnetic moment in the absence of external dc field, which means that they do not behave as Single-Molecule Magnets (SMM) in zero field as opposed to the reported Er complex, 4.^[13]

Computational studies

Theoretical computations at the SA-CASSCF/RASSI-SO level have been performed for 1–5 based on the X-ray crystal structures at the different temperatures at which the X-ray data have been obtained (See Supporting Information for computational details). This series of computations can be compared to those done on the basis of the DFT optimized structure of [Er(Cot)(Cnt)] that lead to a perfectly linear structure.^[13] Ground and excited state wave functions for 1–5 along with the corresponding energy gaps are shown in Tables S30–S34.

Terbium is next to the isotropic gadolinium and is oblate. Tb is a non-Kramers ion, and thus, the crystal field allows the formation of non-degenerated m_J states. In the geometry imposed by the two large aromatic ligands, the linear geometry does not favor axial anisotropy, which shall allow mixing the m_J states and/or accounting for $m_J=0$ ground state. The theoretical treatment needs to take into account this singularity and is then rendered more difficult. Thus, the ground calculated state is then the $m_J=0$ state and just above the $m_J=\pm 1$ state, which is not in good agreement with the low temperature data for the above-mentioned considerations.

However, the $2J+1$ states split on 873 cm⁻¹ and give a reasonable agreement with the experimental data (Figure 5) at higher temperatures.

Following the trend described above, the oblate Dy and Ho ions have similar mixed configurations with principally $m_J=\pm 15/2$ (65%) and $\pm 11/2$ (13%) for 2 and principally $m_J=\pm 8$ (65%) and ± 6 (14%) for 3, both at 150 K. The m_J composition evolves at 300 K to be $m_J=\pm 15/2$ (83%) and $\pm 11/2$ (12%) for 2 and $m_J=\pm 8$ (56%), ± 6 (13%), and ± 7 (12%) for 3, explaining the

different calculated low temperature magnetic susceptibility data observed (Figure S26 and S27). In **2**, six energy states are found within 109 cm^{-1} , while in **3**, the overall splitting is only 397 cm^{-1} with 5 states within 136 cm^{-1} . The modification of the energy state composition and splitting when different structures are used (X-ray, 150 K, 300 K) is not greatly modulated, and thus the overall calculated magnetic temperature dependent curves is comparable with that of the experiments (Figure 5). These computations rationalize very well the magnetic behavior of **2** and **3**, showing no SMM behavior, as expected from the electrostatic model. Additionally, as expected for oblate ions with large aromatic ligands, the anisotropy orientation is not following the axial symmetry (Figure 6).

For the prolate ions, erbium and thulium, large aromatic ligands are usually well adapted for maximizing the anisotropy compared to the three ions discussed above; they disfavor the mixing of the m_j states and maximize anisotropy. Accordingly, the ground state is pure $m_j = \pm 15/2$ for the erbium complex (**4**), while it is pure $m_j = \pm 6$ for the thulium complex (**5**). For **4**, the first excited state of $m_j = \pm 13/2$ (98%) and the second excited state, which is principally a mixed configuration of $m_j = \pm 1/2$ (68.2%) and $m_j = \pm 3/2$ (19.9%) are located at 170 and 251 cm^{-1} , respectively. In **4**, the relative energy of the m_j crystal field states varies very little depending upon the structure (160 and 255 cm^{-1}) chosen for the computations (X-ray, 150 K, 300 K). However, as expected from the higher symmetry of the structure obtained from DFT optimization, the nature of the energy states differs in the fact that they are pure in symmetric structure but mixed with more realistic solid-states structures. However, despite this, the computed variable temperature magnetic susceptibility curve is very similar to that reported experimentally in previous work.^[13] In **4**, the anisotropy is typically perpendicular to the aromatic sandwich ligands in agreement with the high symmetry of the complexes. In the case of the X-ray structures, the anisotropy is not perfectly perpendicular to the Cot plane but crosses the two ligands in the approximate position of the η^8 -centroid of the Cot ligands and the η^6 -centroid of the Cnt ligand (Figure 3). In turn, this does not impact the magnetic properties and the magnetic barrier of 251 cm^{-1} measured in previous work. According to the computations, the barrier is therefore of good agreement with a thermally accessed QTM via the second excited state.

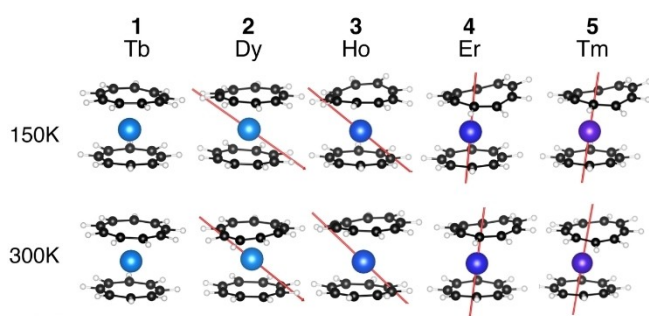


Figure 6. Computed structures of **1–5** at 150 and 300 K and ground-state anisotropy axis (not represented for Tb due to planar anisotropy).

In **5**, the computations indicate a ground state with pure $m_j = \pm 6$, in agreement with the experimental low temperature $\chi_{\text{M}}T$ value. The first excited state is found 431 cm^{-1} above and is pure $m_j = \pm 5$. The large gap between the ground and first excited state contrasts with the experimental curve shape that increases relatively fast between 2 and 50 K, which would agree with a Boltzmann population of lower excited energy states. The overall splitting is 770 cm^{-1} .

Conclusion

In conclusion, we report the synthesis and characterization of a series of heteroleptic late trivalent lanthanide complexes from Tb to Lu with the dianionic Cot and the monoanionic Cnt ligand. The terbium complex adopts a linear structure in which both ligands are aligned and their hapticity is η^8 for the Cot and η^9 for the Cnt ligand. However, the latter was shown to partially isomerize over time. This yields a structure, in which one of the carbon atoms of the Cnt moves inside the ring, giving a *cis-cis-trans* motif and modifying the overall hapticity of the ligand from nine to eight. The isomerization process has been tracked by ^1H NMR spectroscopy and X-ray crystallography. From Dy to Lu, the complexes are highly disordered, which makes the analysis more difficult. The solid-state bond metrics show that the Cnt ligand curves with several carbon atoms being moved away from the metal center. The data follow well the ionic contraction of the lanthanide with the Lu complex being the most distorted one. In solution, in the 183–273 K temperature range, the ligand signal is single and remains flexible as observed by ^1H NMR spectroscopy. The temperature-dependent magnetic data show that the presence of large aromatic ligand suits the prolate ions Er and Tm particularly well. However, only the Er analogue was shown to exhibit SMM behavior.³² The *ab initio* wavefunction-based computations insist on the role of the ligand geometry on the nature of the ground state and indicate that the deviation of the linearity of the Cnt ligand does not affect the anisotropy in the prolate ions significantly, while this modulates the composition and the ratio of the mixed m_j states of the non-adapted oblate ions. Together, the data strongly indicate that the coordination versatility of the Cnt ligand might be a great tool for the modulation of the physical properties of lanthanide complexes.

Experimental Section

General considerations: All reactions were performed using standard Schlenk-line techniques or in an argon filled glovebox (MBraun). All glassware was dried at 140°C for at least 12 h prior to use. THF, DME, toluene and toluene- d_8 were dried over sodium, degassed and transferred under reduced pressure in a cold flask. TmI_3 , ErI_3 , HoI_3 , DyI_3 and TbI_3 were purchased from Sigma Aldrich and used without further purification. NMR spectra were recorded in 5 mm tubes adapted with a J. Young valve on Bruker 300 MHz Avance III spectrometers. Chemical shifts are expressed relative to TMS in ppm. Infrared (IR) spectra were recorded at room temperature under argon on a Thermo Scientific Nicolet iS5 spectrometer equipped with the iD7 ATR-Diamond unit. Magnetic measurements

were obtained in a Quantum Design MPMS-XL SQUID magnetometer. An applied magnetic field of 2 kOe is used in the temperature range 2–20 K, and 10 kOe for temperatures above 20 K, for the $\chi_M T$ vs. T curves. To avoid reorientation and sample degradation the microcrystals are trapped and slightly pressed between quartz wool and sealed in quartz tubes or were fixated with dried and degassed eicosane in flame sealed quartz tubes.

Crystal-structure analysis: Deposition Numbers 2073511 (for [Tb(Cot)(thf)₂]), 2073512 (for [Ho(Cot)I(thf)₂]), 2073513 (for [Lu(Cot)(BH₄)(THF)]₂), 2073514 (for 1 at 150 K), 2073515 (for 1 at 300 K), 2073516 (for 2 at 150 K), 2073517 (for 2 at 300 K), 2073518 (for 3 at 150 K), 2073519 (for 3 at 300 K), 2073520 (for 4 at 150 K), 2073521 (for 4 at 300 K), 2073522 (for 5 at 150 K), 2073523 (for 5 at 300 K), 2073524 (for 6 at 150 K), 2073525 (for 6 at 300 K), 2073526 (for 1' at 150 K), 2073527 (for 1'' at 150 K), 2073528 (for 5 at 100 K), 2073529 (for 5 at 200 K), 2073530 (for 5 at 250 K), 2073531 (for 2b at 150 K) contain the supplementary crystallographic data for this paper. These data are provided free of charge by the joint Cambridge Crystallographic Data Centre and Fachinformationszentrum Karlsruhe Access Structures service.

Syntheses

[Er(Cot)I(thf)]: The complex was synthesized as previously described.^[11c] A similar procedure was used for the other late lanthanides. [Lu(BH₄)₃(thf)₃] was synthesized using the procedure reported for the Nd analogue.^[17]

[Tb(Cot)I(thf)]: A cold thf solution (-40 °C) of K₂Cot (4 mL, 117 mg, 0.64 mmol, 1 equiv) was added to a stirred cold (-40 °C) thf suspension of Tbl₃ (3 mL, 346 mg, 0.64 mmol, 1 equiv). The mixture was allowed to warm to room temperature (r.t.) and was stirred for 16 h. The resultant light yellow suspension was filtered through a frit and the filtrate dried under reduced pressure. The solids were suspended in 5 mL thf and heated to 60 °C forming a deep yellow solution. Diethyl ether was layered on the top and the solution was stored at -40 °C. Yellow needles of the desired compound formed slowly (181 mg, 53%). ¹H NMR (300 MHz, thf-d₈, 293 K): δ (ppm), 194.92 (s br, 8H), *coordinated thf molecules are not visible*. IR (ATR): ν^- = 2970 (br m), 2889 (m), 1859 (w), 1753 (w), 1616 (w), 1556 (w), 1444 (br m), 1343 (w), 1309 (w), 1245 (w), 1180 (w), 1011 (vs), 895 (s), 860 (vs), 775 (m), 749 (m), 708 (vs), 667 (s), 573 (m) cm⁻¹. Anal. Calcd. for C₁₆H₂₄O₂Tb (534.19): C, 35.97; H, 4.53; Found: C, 35.77; H, 4.56.

[Dy(Cot)I(thf)]: A cold thf solution (-40 °C) of K₂Cot (5 mL, 138 mg, 0.76 mmol, 1 equiv) was added to a stirred cold (-40 °C) thf suspension of DyI₃ (10 mL, 411 mg, 0.76 mmol, 1 equiv). The mixture was allowed to warm to r.t. and was stirred for 16 h. The resultant light yellow suspension was filtered through a frit and the filtrate dried under reduced pressure. The solids were suspended in 8 mL thf and heated to 60 °C forming a deep yellow solution. Diethyl ether was layered on the top and the solution was stored at -40 °C. Yellow needles of desired compound formed slowly (265 mg, 63%). ¹H NMR (300 MHz, thf-d₈, 293 K): δ (ppm), 88.66 (s br, 8H), *coordinated thf molecules are not visible*. IR (ATR): ν^- = 2951 (br m), 2889 (m), 1858 (w), 1752 (w), 1614 (w), 1554 (w), 1453 (br m), 1343 (w); 1309 (w), 1256 (w), 1178 (w), 1010 (vs), 895 (s), 860 (vs), 750 (m), 705 (vs), 670 (s), 575 (m) cm⁻¹. Anal. Calcd. for C_{15.4}H_{19.2}O₂Dy (537.77): C, 33.03; H, 3.91; Found: C, 32.94; H, 4.07. The number of thf was decreased upon drying.

[Ho(Cot)I(thf)]: A cold thf solution (-40 °C) of K₂Cot (5 mL, 223 mg, 1.22 mmol, 1 equiv) was added to a stirred cold (-40 °C) thf suspension of Hol₃ (668 mg, 1.22 mmol, 1 equiv). The mixture was allowed to warm to r.t. and was stirred for 16 h. The resultant light yellow suspension was filtered through a frit and the filtrate dried

under reduced pressure. The solids were suspended in 7 mL thf and heated to 60 °C forming a deep yellow solution. Diethyl ether was layered on the top and the solution was stored at -40 °C. Yellow needles of desired compound formed slowly (583 mg, 88%). ¹H NMR (300 MHz, thf-d₈, 293 K): δ (ppm), 70.88 (s br, 8H), *coordinated thf molecules are not visible*. IR (ATR): ν^- = 2969 (br m), 2888 (m), 1852 (w), 1747 (w), 1601 (w), 1441 (br m), 1343 (w), 1212 (br w), 1008 (vs), 856 (vs), 750 (m), 704 (vs), 645 (s) cm⁻¹. Anal. Calcd. for C₁₆H₂₄O₂Ho (540.20): C, 35.57; H, 4.48; Found: C, 35.63; H, 4.53.

[Tm(Cot)I(thf)]: A cold solution (-40 °C) of K₂Cot (3 mL, 32 mg, 0.17 mmol, 1 equiv) was added to a stirred cold (-40 °C) thf suspension of Tml₃ (5 mL, 95 mg, 0.17 mmol, 1 equiv). The mixture was allowed to warm to r.t. and was stirred for 16 h. The resultant light yellow suspension was filtered through a frit and the filtrate dried under reduced pressure. The solids were suspended in 7 mL thf and heated to 60 °C forming a deep yellow solution. Diethyl ether was layered on the top and the solution was stored at -40 °C. Yellow needles of desired compound formed slowly (54 mg, 57%). The ¹H NMR (300 MHz, thf-d₈, 293 K) remained silent. The compound was previously published by Fedushkin et al.^[18]

[Lu(Cot)(BH₄)(thf)]: A cold solution (-40 °C) of K₂Cot (61 mg, 0.33 mmol, 1 equiv) was added to a stirred cold (-40 °C) thf solution of [Lu(BH₄)₃(thf)₃] (145 mg, 0.33 mmol, 1 equiv). The mixture was allowed to warm to r.t. and was stirred for 16 h. The resultant light yellow suspension was filtered through a teflon syringe filter. The filtrate was concentrated under reduced pressure until incipient crystallization and stored at -40 °C to afford the title compound as light yellow crystals (117 mg, 0.27 mmol, 81%). Recrystallization from toluene led to the decoordination of one thf molecule and formation of [(Cot)Lu(BH₄)(thf)₂] as colorless crystals suitable for X-ray diffraction studies. ¹H NMR (300 MHz, thf-d₈, 293 K): δ (ppm), 6.31 (s, 8H, Cot), 3.68–3.59 (m, ca. 4H, OCH₂ coordinated thf), 1.84–1.74 (m, ca. 4H, OCH₂CH₂ coordinated thf), 0.04 (1:1:1:1 quartet ¹J_{BH} = 83.0 Hz, 4H, BH₄). ¹³C^[25] NMR (75 MHz, thf-d₈, 293 K): δ (ppm), 92.6 (Cot), 68.0 (OCH₂ coordinated thf), 26.1 (OCH₂CH₂ coordinated thf). IR (ATR): ν^- = 3021 (w), 2989 (w), 2930 (br m), 2889 (m), 2426 (m), 2272 (s), 2239 (s), 2164 (m), 2040 (w), 1855 (w), 1746 (w), 1610 (w), 1494 (w), 1453 (m), 1316 (br m), 1245 (m), 1213 (w), 1092 (s), 1012 (vs), 898 (s), 877 (vs), 752 (m), 706 (vs) cm⁻¹. No satisfactory EA was obtained.

[Tb(Cot)(Cnt)] (1'): A brown acetonitrile solution of KCnt (2 mL, 42 mg, 0.27 mmol, 1.1 equiv) was added at r.t. to a toluene suspension of [Tb(Cot)I(thf)₂] (10 mL, 149 mg, 0.25 mmol, 1 equiv). The resulting suspension was left to stir at r.t. for 12 h and was then dried under reduced pressure. The pale-yellow residue was suspended in toluene (5 mL). After 1 h of stirring, the volatiles were removed under reduced pressure and the residue was further dried for 5 h at r.t. and extracted in several crops with large amounts of toluene. The pale-yellow solution was filtered and cooled at -40 °C yielding X-ray suitable pale yellow needles of 1' (32 mg, 29%). ¹H NMR (300 MHz, toluene-d₈, 293 K): δ (ppm), 246.3 (s, 8H, Cot), 101.6 (s, 9H, Cnt). The ¹H NMR evolves with time and crystals of 1' can be obtained after few days. IR (ATR): ν^- = 3006 (m) 2920 (s), 2851 (s), 1935 (w), 1853 (w), 1746 (w), 1602 (w), 1551 (w), 1493 (w), 1457 (m), 1375 (w), 1313 (w), 1018 (w), 892 (vs), 846 (w), 772 (m), 747 (s), 704 (vs), 654 (vs) cm⁻¹. Anal. Calcd. for C₁₇H₁₇Tb.0.2 Toluene (398.67): C, 55.43; H, 4.70; Found: C, 55.35; H, 5.03.

[Tb(Cot)(Cnt)] (1''): Toluene (20 mL) was condensed to a mixture of KCnt (30.0 mg, 0.192 mmol, 1 equiv), and [Tb(Cot)I(thf)₂] (103 mg, 0.193 mmol; 1.01 eq) at -78 °C. The resulting suspension was heated to 150 °C for three hours and immediately passed through a syringe PTFE-filter, while still hot. Upon slowly cooling the orange filtrate to r.t., single crystals of 1'' suitable for X-ray diffraction were obtained. Subsequent decantation of the mother liquor and drying

in vacuo yielded **1'** as orange crystalline solid (30.0 mg, 34%). Raman (solid state, sealed ampule): $\tilde{\nu}$ [cm^{-1}]=3044 (vw), 3008 (vw), 1515 (vw), 1495 (vw), 750 (s), 660(s), 366 (vw), 280 (w), 239 (s).

[Dy(Cot)(Cnt)] (2): A brown acetonitrile solution of KCnt (2 mL, 47 mg, 0.30 mmol, 1.1 equiv) was added at r.t. to a toluene suspension of [Dy(Cot)(thf)₂] (10 mL, 146 mg, 0.27 mmol, 1 equiv). The resulting suspension was left to stir at r.t. for 12 h and was then dried under reduced pressure. The yellow residue was suspended in toluene (5 mL). After 1 h of stirring, the volatiles were removed under reduced pressure and the residue was further dried for 5 h at r.t. and extracted in several crops with large amounts of toluene. The yellow solution was filtered and cooled at -40°C yielding X-ray suitable yellow needles of **2** (62.5 mg, 60%). ¹H NMR (300 MHz, toluene-d₈, 293 K): δ (ppm), 118.7 (s, 8H, Cot), 72.90 (s, 9H, Cnt). IR (ATR): $\tilde{\nu}$ = 3005 (br m), 2917 (m), 1970 (w), 1851 (w), 1744 (w), 1601 (w), 1456 (m), 1373 (w), 1313 (w), 1018 (w), 892 (vs), 848 (w), 773 (m), 748 (s), 706 (vs), 654 (vs), 507 (w) cm^{-1} . Anal. Calcd. for C₁₇H₁₇Dy (383.82): C, 53.20; H, 4.46; Found: C, 53.14; H, 4.48.

[Ho(Cot)(Cnt)] (3): A brown acetonitrile solution of KCnt (2 mL, 60 mg, 0.39 mmol, 1.05 equiv) was added at r.t. to a toluene suspension of [Ho(Cot)(thf)₂] (15 mL, 189 mg, 0.35 mmol, 1 equiv). The resulting suspension was left to stir at r.t. for 12 h and was then dried under reduced pressure. The pale-orange residue was suspended in toluene (5 mL). After 1 h of stirring, the volatiles were removed under reduced pressure and the residue was further dried for 5 h at r.t. and extracted in several crops with large amounts of toluene. The pale-orange solution was filtered and cooled at -40°C yielding X-ray suitable pale-orange needles of **3** (77.8 mg, 67%). ¹H NMR (300 MHz, toluene-d₈, 293 K): δ (ppm), 90.45 (s, 8H, Cot), 59.17 (s, 9H, Cnt). IR (ATR): $\tilde{\nu}$ = 3003 (br m), 2920 (m), 1969 (w), 1852 (w), 1745 (w), 1602 (w), 1455 (w), 1374 (w), 1313 (w), 1016 (m), 892 (s), 850 (w), 776 (m), 748 (m), 704 (vs), 656 (vs), 506 (m) cm^{-1} . Anal. Calcd. for C₁₇H₁₇Ho (386.25): C, 52.86; H, 4.44; Found: C, 52.34; H, 4.53.

[Er(Cot)(Cnt)] (4): A brown acetonitrile solution of KCnt (2 mL, 65 mg, 0.42 mmol, 1.05 equiv) was added at r.t. to a toluene suspension of [Er(Cot)(thf)₂] (15 mL, 215 mg, 0.40 mmol, 1 equiv). The resulting suspension was left to stir at r.t. for 12 h and was then dried under reduced pressure. The orange residue was suspended in toluene (5 mL). After 1 h of stirring, the volatiles were removed under reduced pressure and the residue was further dried for 5 h at r.t. and extracted in several crops with large amounts of toluene. The orange solution was filtered and cooled at -40°C yielding X-ray suitable orange needles of **4** (73.6 mg, 63%). ¹H NMR (300 MHz, toluene-d₈, 293 K): δ (ppm), -5.01 (br s), -128.7 (br s). IR (ATR): $\tilde{\nu}$ = 3030 (br m), 2959 (s), 2921 (m), 2851 (m), 1966 (w), 1854 (w), 1748 (w), 1604 (br w), 1451 (w), 1376 (w), 1313 (w), 1259 (s), 1087 (s), 1014 (s), 892 (s), 797 (s), 748 (m), 702 (vs), 657 (vs), 505 (m) cm^{-1} . Anal. Calcd. for C₁₇H₁₇Er (388.58): C, 52.55; H, 4.41; Found: C, 52.80; H, 5.04.

[Tm(Cot)(Cnt)] (5): A brown acetonitrile solution of KCnt (2 mL, 65 mg, 0.42 mmol, 1.05 equiv) was added at r.t. to a toluene suspension of [Tm(Cot)(thf)₂] (15 mL, 217 mg, 0.40 mmol, 1 equiv). The resulting suspension was left to stir at r.t. for 12 h and was then dried under reduced pressure. The salmon-orange residue was suspended in toluene (5 mL). After 1 h of stirring, the volatiles were removed under reduced pressure and the residue was further dried for 5 h at r.t. and extracted in several crops with large amounts of toluene. The salmon-orange solution was filtered and cooled at -40°C yielding X-ray suitable salmon-orange needles of **5** (74.6 mg, 48%). ¹H NMR (300 MHz, toluene-d₈, 293 K): δ (ppm), -23.21 (br s), -235.8 (br s). IR (ATR): $\tilde{\nu}$ = 2998 (br m), 2920 (m), 2852 (m), 1965 (w), 1856 (w), 1753 (w), 1451 (w), 1314 (w), 1259 (w), 1016 (m), 893 (s), 781 (s), 749 (m), 703 (vs), 658 (vs), 505 (m) cm^{-1} .

Anal. Calcd. for C₁₇H₁₇Tm (390.25): C, 52.32; H, 4.39; Found: C, 52.80; H, 4.64.

[Lu(Cot)(Cnt)] (6): A mixture of [Lu(Cot)(BH₄)(thf)₂] (146 mg, 0.33 mmol) and KCnt (52 mg, 0.33 mmol) in toluene (15 mL) was heated at 110°C for 16 h and was then dried under reduced pressure for 2 h. The light yellow residue was extracted with hot toluene. The yellow filtrate was stored at -40°C yielding yellow needles of **6** suitable for X-ray diffraction studies (44 mg, 0.11 mmol, 34%). ¹H NMR (300 MHz, toluene-d₈, 293 K): δ (ppm), 6.54 (s, 9H, Cnt), 5.83 (s, 8H, Cot). ¹³C[25] NMR (75 MHz, toluene-d₈, 293 K): δ (ppm), 107.8 (Cnt), 93.5 (Cot). IR (ATR): $\tilde{\nu}$ = 2992 (br m), 1963 (w), 1857 (w), 1748 (w), 1604 (w), 1490 (w), 1447 (w), 1375 (w), 1313 (w), 1158 (w), 1018 (w), 892 (vs), 780 (m), 750 (m), 704 (vs), 662 (vs), 502 (w) cm^{-1} . Anal. Calcd. for C₁₇H₁₇Lu (396.29): C, 51.52; H, 4.32; Found: C, 51.16; H, 4.34.

Acknowledgements

Dr. Louis Ricard is gratefully thanked for his very important insights in the crystal structure analysis. Parts of this work have received funding from the ERC under grant agreement No 716314 and from an ANR (French National Research Agency) granted collaborative project (ANR-19-CE07-0019-1). CNRS and Ecole polytechnique are thanked for financial support. N.M. thanks ENS Paris-Saclay. B.L.G., F.G. and L.L.D. thank the French GENCI/IDRIS-CINES centers for high-performance computing resources. Open access funding enabled and organized by Projekt DEAL.

Conflict of Interest

The authors declare no conflict of interest.

Keywords: cyclononatetraenyl · lanthanides · organometallics · magnetism · single molecule magnets

- [1] a) J.-L. Liu, Y.-C. Chen, M.-L. Tong, *Chem. Soc. Rev.* **2018**, *47*, 2431–2453; b) J.-C. G. Bünzli, C. Piguet, *Chem. Soc. Rev.* **2005**, *34*, 1048–1077; c) D. N. Woodruff, R. E. P. Winpenny, R. A. Layfield, *Chem. Rev.* **2013**, *113*, 5110–5148.
- [2] S. Cotton in *Lanthanide and Actinide Chemistry*, Wiley, **2006**, pp. 9–22.
- [3] a) S. V. Eliseeva, J.-C. G. Bunzli, *Vol. 7* (Eds.: P. Hänninen, H. Härmä), Springer Series on Fluorescence, **2010**; b) J. D. Rinehart, J. R. Long, *Chem. Sci.* **2011**, *2*, 2078–2085.
- [4] a) E. G. Moore, A. P. S. Samuel, K. N. Raymond, *Acc. Chem. Res.* **2009**, *42*, 542–552; b) F. Pointillart, B. le Guennic, O. Cador, O. Maury, L. Ouahab, *Acc. Chem. Res.* **2015**, *48*, 2834–2842; c) J. Kido, Y. Okamoto, *Chem. Rev.* **2002**, *102*, 2357–2368.
- [5] a) P. Caravan, J. J. Ellison, T. J. McMurphy, R. B. Lauffer, *Chem. Rev.* **1999**, *99*, 2293–2352; b) M. Bottrill, L. Kwok, N. J. Long, *Chem. Soc. Rev.* **2006**, *35*, 557–571; c) T. J. Clough, L. Jiang, K.-L. Wong, N. J. Long, *Nat. Commun.* **2019**, *10*, 1420.
- [6] B. M. Day, F.-S. Guo, R. A. Layfield, *Acc. Chem. Res.* **2018**, *51*, 1880–1889.
- [7] a) F.-S. Guo, B. M. Day, Y.-C. Chen, M.-L. Tong, A. Mansikkamäki, R. A. Layfield, *Science* **2018**; b) C. A. P. Goodwin, F. Ortu, D. Reta, N. F. Chilton, D. P. Mills, *Nature* **2017**, *548*, 439; c) K. R. McClain, C. A. Gould, K. Chakarawet, S. Teat, T. J. Groshens, J. R. Long, B. G. Harvey, *Chem. Sci.* **2019**; d) A. Chiesa, F. Cugini, R. Hussain, E. Macaluso, G. Allodi, E. Garlatti, M. Giansiracusa, C. A. P. Goodwin, F. Ortu, D. Reta, J. M. Skelton, T. Guidi, P. Santini, M. Solzi, R. De Renzi, D. P. Mills, N. F. Chilton, S. Carretta, *Phys. Rev. B* **2020**, *101*, 174402; e) N. Ishikawa, M. Sugita, T.

- Ishikawa, S.-y. Koshihara, Y. Kaizu, *J. Am. Chem. Soc.* **2003**, *125*, 8694–8695.
- [8] a) W. J. Evans, M. A. Johnston, R. D. Clark, J. W. Ziller, *J. Chem. Soc. Dalton Trans.* **2000**, 1609–1612; b) J. J. Le Roy, I. Korobkov, M. Murugesu, *Chem. Commun.* **2014**, *50*, 1602–1604; c) K. L. M. Harriman, I. Korobkov, M. Murugesu, *Organometallics* **2017**, *36*, 4515–4518.
- [9] a) M. Xémard, S. Zimmer, M. Cordier, V. Goudy, L. Ricard, C. Clavaguéra, G. Nocton, *J. Am. Chem. Soc.* **2018**, *140*, 14433–14439; b) M. D. Walter, G. Wolmershäuser, H. Sitzmann, *J. Am. Chem. Soc.* **2005**, *127*, 17494–17503.
- [10] C. A. Gould, K. R. McClain, J. M. Yu, T. J. Groshens, F. Furche, B. G. Harvey, J. R. Long, *J. Am. Chem. Soc.* **2019**, *141*, 12967–12973.
- [11] a) K. R. Meihaus, J. R. Long, *J. Am. Chem. Soc.* **2013**, *135*, 17952–17957; b) Y.-S. Meng, Y.-S. Qiao, Y.-Q. Zhang, S.-D. Jiang, Z.-S. Meng, B.-W. Wang, Z.-M. Wang, S. Gao, *Chem. Eur. J.* **2016**, *22*, 4704–4708; c) J. D. Hilgar, M. G. Bernbeck, B. S. Flores, J. D. Rinehart, *Chem. Sci.* **2018**, *9*, 7204–7209; d) J. D. Hilgar, M. G. Bernbeck, J. D. Rinehart, *J. Am. Chem. Soc.* **2019**, *141*, 1913–1917; e) J. Moutet, J. Schleinitz, L. La Droitte, M. Tricoire, F. Pointillart, F. Gendron, T. Simler, C. Clavaguéra, B. Le Guennic, O. Cador, G. Nocton, *Angew. Chem. Int. Ed.* **2021**, *60*, 6042–6046; *Angew. Chem.* **2021**, *133*, 6107–6111.
- [12] a) G. B. Deacon, C. M. Forsyth, F. Jaroschik, P. C. Junk, D. L. Kay, T. Maschmeyer, A. F. Masters, J. Wang, L. D. Field, *Organometallics* **2008**, *27*, 4772–4778; b) C. Ruspic, J. R. Moss, M. Schürmann, S. Harder, *Angew. Chem. Int. Ed.* **2008**, *47*, 2121–2126; *Angew. Chem.* **2008**, *120*, 2151–2156.
- [13] L. Münzfeld, C. Schoo, S. Bestgen, E. Moreno-Pineda, R. Köppe, M. Ruben, P. W. Roesky, *Nat. Commun.* **2019**, *10*, 3135.
- [14] A. Edelmann, C. G. Hrib, S. Blaurock, F. T. Edelmann, *J. Organomet. Chem.* **2010**, *695*, 2732–2737.
- [15] K. Mashima, Y. Nakayama, A. Nakamura, N. Kanehisa, Y. Kai, H. Takaya, *J. Organomet. Chem.* **1994**, *473*, 85–91.
- [16] a) U. Mirsaidov, I. B. Shaimuradov, M. Khikmatov, *Zh. Neorg. Khim.* **1986**, *31*, 1321–1323; b) M. Ephritikhine, *Chem. Rev.* **1997**, *97*, 2193–2242; c) A. Momin, F. Bonnet, M. Visseaux, L. Maron, J. Takats, M. J. Ferguson, X.-F. Le Goff, F. Nief, *Chem. Commun.* **2011**, *47*, 12203–12205.
- [17] a) S. M. Cendrowski-Guillaume, M. Nierlich, M. Lance, M. Ephritikhine, *Organometallics* **1998**, *17*, 786–788; b) S. M. Cendrowski-Guillaume, G. Le Gland, M. Nierlich, M. Ephritikhine, *Organometallics* **2000**, *19*, 5654–5660.
- [18] I. L. Fedushkin, M. N. Bochkarev, S. Dechert, H. Schumann, *Chem. Eur. J.* **2001**, *7*, 3558–3563.
- [19] B. Gernot, B. Andreas, *Chem. Ber.* **1978**, *111*, 2850–2858.
- [20] F. A. Cotton, *Acc. Chem. Res.* **1968**, *1*, 257–265.
- [21] a) G. Boche, D. Martens, W. Danzer, *Angew. Chem. Int. Ed. Eng.* **1969**, *8*, 984–984; b) G. Boche, H. Weber, D. Martens, A. Bieberbach, *Chem. Ber.* **1978**, *111*, 2480–2496.
- [22] G. Boche, H. Weber, A. Bieberbach, *Chem. Ber.* **1978**, *111*, 2833–2849.
- [23] R. Shannon, *Acta Crystallogr. A* **1976**, *32*, 751–767.
- [24] A. Wells, F. in *Structural Inorganic Chemistry*, 5th ed., Oxford university press, Oxford, **2012**.
- [25] C. Apostolidis, G. B. Deacon, E. Dornberger, F. T. Edelmann, B. Kanellakopulos, P. MacKinnon, D. Stalke, *Chem. Commun.* **1997**, 1047–1048.

Manuscript received: May 5, 2021

Accepted manuscript online: July 1, 2021

Version of record online: August 21, 2021

Cite this: *Chem. Sci.*, 2023, 14, 443

All publication charges for this article have been paid for by the Royal Society of Chemistry

Received 29th October 2022
Accepted 29th November 2022

DOI: 10.1039/d2sc05976b

rsc.li/chemical-science

Back to the future of organolanthanide chemistry†

Nolwenn Mahieu,^{ID} Jakub Piątkowski,^{ID} Thomas Simler^{ID}*
and Grégory Nocton^{ID}*

At the dawn of the development of structural organometallic chemistry, soon after the discovery of ferrocene, the description of the LnCp₃ complexes, featuring large and mostly trivalent lanthanide ions, was rather original and sparked curiosity. Yet, the interest in these new architectures rapidly dwindled due to the electrostatic nature of the bonding between π -aromatic ligands and 4f-elements. Almost 70 years later, it is interesting to focus on how the discipline has evolved in various directions with the reports of multiple catalytic reactivities, remarkable potential in small molecule activation, and the development of rich redox chemistry. Aside from chemical reactivity, a better understanding of their singular electronic nature – not precisely as simplistic as anticipated – has been crucial for developing tailored compounds with adapted magnetic anisotropy or high fluorescence properties that have witnessed significant popularity in recent years. Future developments shall greatly benefit from the detailed reactivity, structural and physical chemistry studies, particularly in photochemistry, electro- or photoelectrocatalysis of inert small molecules, and manipulating the spins' coherence in quantum technology.

LCM, CNRS, Ecole Polytechnique, Institut Polytechnique de Paris, Route de Saclay, 91120 Palaiseau, France. E-mail: gregory.nocton@polytechnique.edu; thomas.simler@polytechnique.edu

† This perspective is dedicated to Prof. Peter Junk on the occasion of his 60th birthday.

Introduction

During the winter of 1951, reading the journal *Nature* surprised many chemists.¹ A new type of iron compound had been discovered (Fig. 1), and, with this discovery, a fantastic scientific adventure began. This story would culminate (but not end) with



Nolwenn Mahieu started her studies at the Ecole Normale Supérieure (ENS) Paris-Saclay in 2016. After a stay in Pr. Eric J. Schelter's group at the university of Pennsylvania working on imido–thorium complexes, she graduated in 2020 with a master in molecular chemistry from ENS Paris-Saclay. She then joined Dr G. Nocton's group at Ecole polytechnique for her PhD studies on the synthesis of organolanthanide complexes.



Jakub Piątkowski was born in 1997 in Działdowo, Poland. In 2019, he received his B.S. degree in general chemistry from the University of Warsaw (Warsaw, Poland), under the supervision of Prof. Karol Grela, working on ruthenium-based olefin metathesis catalysts. After getting his M.S. degree in organic synthesis from the same alma mater within Grela's Group in 2021, he moved to France and

joined Greg Nocton's Group at Ecole polytechnique (Palaiseau, France), where he carried out research on lanthanide complexes with large aromatic ligands and heterobimetallic species involving lanthanides and transition metals. After a short experience in Nocton's Group, he moved to the industrial sector, holding a position of medical chemist at CelonPharma (Warsaw, Poland), where he is currently conducting research in the development of new innovative pharmaceutical products.



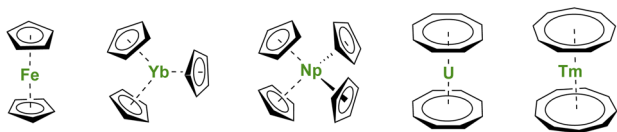


Fig. 1 Molecular structures of ferrocene, $\text{Yb}(\text{Cp})_3$, $\text{Np}(\text{Cp})_4$, uranocene, and thulocene with unsubstituted C_nH_n aromatic ligands.

a Nobel Prize in 1973 for organometallic sandwich compounds. As several witnesses remember, the new structure at that time brought many questions related to the effects of π -coordination on the symmetry and physical properties of the complexes.^{2–4} A new field, similar to coordination chemistry, opened but with carbon-based ligands. The genesis of the metallocene success story lies in the chemical properties of the cyclopentadienyl (Cp) ligand, a small cyclic and mono-anionic ligand featuring 6π -electron Hückel aromaticity. Besides, this ligand framework is easy to modify and relatively robust.

Soon after the first report of unusual sandwich structures with the Cp ligand, several research groups became motivated to investigate its coordination behavior towards most metals of the periodic table, including, already at a very early stage, lanthanide ions.^{5–7} However, the result was not surprising, and several conclusions were drawn: (a) lanthanide ions are mostly trivalent with significantly larger ionic radii than most transition metal ions, and three Cp ligands easily fit around the metal center; (b) the metal–ligand bonding is principally ionic as demonstrated by the easy Cp ligand exchange from $\text{Ln}(\text{Cp})_3$ to iron halide to form ferrocene.⁵ The known divalent lanthanide analogs, $\text{Ln}(\text{Cp})_2$,^{8,9} are forming polymeric assemblies in the solid state to accommodate empty coordination sites with ligand electronic density, but these weak interactions can be broken by solvation.^{10–12} In all cases, the Cp ligands remain bent due to the bonding and respective sizes of the ligand and metal ion, as well as attractive dispersion or van der Waals interactions.^{13–15} The lanthanide series was completed with few

of the actinides with similar findings,¹⁶ although the tetravalent states of Np or U allowed the wrapping of up to four Cp ligands around the metal centers (Fig. 1).^{17–20} In the original articles by Wilkinson, the magnetic moments of several $\text{Ln}(\text{Cp})_3$ complexes were measured at room temperature, and no significant deviations from the expected values were reported, except for the ytterbium complex $\text{Yb}(\text{Cp})_3$ (Fig. 1) exhibiting an unexpectedly low room temperature moment.⁶ This particular feature has been later explained by Denning *et al.*²¹ and relates to an unusual intermediate valent electronic structure for these, in appearance only, simple molecules.²²

The size mismatch between the small cyclopentadienyl ligand and the large metallic f-elements has been easily corrected by increasing the size of the aromatic ligand used, either by substituting the hydrogens with bulkier groups^{23,24} or using larger aromatic rings.^{25,26} Both methods proved very efficient in accessing sandwich compounds of various charges and oxidation states with f-elements.

First, the use of large ligands such as the C_8H_8 ring, the dianionic cyclooctatetraenyl ligand (Cot), with uranium led to the formation of uranocene, $\text{U}(\text{Cot})_2$, a linear sandwich with a +4 metal oxidation state (Fig. 1). In the report from 1968, Streitwieser stated that the ligand size was nicely adapted to the f-orbitals, a situation similar to that found in between iron and Cp ligands.²⁷ Lanthanide complexes supported by Cot ligands have been synthesized, but because of their predominant +3 oxidation state, the complexes are not neutral but anionic.^{28,29} The only exception to date is cerocene, $\text{Ce}(\text{Cot})_2$, the only neutral +4 complex of this family.^{30,31} The oxidation state in cerocene is also considered as intermediate valent,^{22,32,33} yet the overall complex remains neutral. The size of the aromatic ligand can be further increased to the C_9H_9 ring, corresponding to the monoanionic cyclononatetraenyl ligand (Cnt), which can be used with divalent Sm, Eu, Tm (Fig. 1) and Yb to form linear neutral sandwiches of 4f elements. Although the synthesis of the Cnt ligand was already reported in 1963,^{34,35} the first lanthanidocene $\text{Ln}(\text{Cnt})_2$ complexes were published in 2017 and



Thomas Simler graduated from the Ecole Normale Supérieure in Lyon. He received his PhD in 2016 from the University of Strasbourg working on functionalised NHC and pincer complexes with Dr Pierre Braunstein and Dr Andreas A. Danopoulos. He then joined the group of Prof. Peter W. Roesky (KIT Karlsruhe) as an Alexander von Humboldt postdoctoral fellow and the group of Prof.

Grégory Nocton at Ecole polytechnique for a second postdoctoral stay. In 2022, he was appointed CNRS researcher at Ecole polytechnique and focuses on the reactivity of low-valent lanthanide complexes for small molecule activation.



Grégory Nocton was born in Reims, France in 1983. After a master of science at the Universities of Reims and Grenoble (2006), he obtained his PhD in 2009 in Grenoble with Prof. Marinella Mazzanti, working on the redox reactivity of uranium. He then joined UC Berkeley working with Prof. Richard A. Andersen and was appointed CNRS researcher in 2011 at Ecole polytechnique. He

received the bronze medal from the CNRS (2016) and the Junior Prize of the Coordination Chemistry Division (French Chemical Society, 2021). He is Associate Professor at Ecole Polytechnique since 2017 and Vice-President of the chemistry department (2022).



2018,^{36,37} *i.e.* 50 years after the first report of uranocene. Note that the flexibility of the Cnt ligand also allows the formation of $\text{Ln}(\text{Cnt})_3$ complexes (*vide infra*).³⁸

The neutral 4f-element sandwich complexes with unsubstituted aromatic ligands often suffer from poor solubility in organic solvents, which hinders both their characterization and the study of their reactivity. As such, derivatives of the versatile Cp and Cot ligands were used and constitute most of the sandwich complexes made in this area.^{23,25}

Once the novelty of those arrangements wore off, the structural properties were primarily designed for the reactivity of the complexes. One key example is the development of the pentamethylcyclopentadienyl ligand (Cp^*) and the corresponding Sm^{II} and Yb^{II} complexes as base-free or solvate adduct versions. Their vibrant chemistry prompted a generation of chemists to navigate through their stoichiometric reductive reactivity and catalytic properties, including in polymerization reactions.

The $\text{Ln}(\text{Cp}^*)_2$ complexes are bent sandwich compounds, which adducts of THF or diethyl ether were reported in the early 1980s (Fig. 2).^{39,40} The reduction potential of the Sm^{II} compound is lower than that of the Yb^{II} analog. It allows the reduction of CO ,⁴¹ CO_2 ,⁴² and even the non-polar and inert dinitrogen molecule: one N_2 molecule can be reduced twice from two $\text{Sm}(\text{Cp}^*)_2$ fragments.⁴³ The ytterbium complex is less reductive, yet it can easily reduce N-heteroaromatic fragments, such as bipyridine derivatives. The $(\text{Cp}^*)_2\text{Yb}(\text{bipy})$ complex was made originally in the early 1980s but only published in 2002.⁴⁴ Indeed, during those years, its electronic structure remained difficult to rationalize until L_{III} -edge XANES measurements and CASSCF computations pointed towards intermediate valent states.^{45–48} Other examples of N-heteroaromatic cycles followed,^{48–52} contributing to straightening the rationalization of the single electron transfer in ytterbium complexes.²²

The reactivity of divalent organolanthanides extends to catalytic reactions, such as in ethylene polymerization,^{53,54} while the trivalent alkyl complex $(\text{Cp}^*)_2\text{LuMe}$ (Fig. 2) reacts with methane,^{55,56} showing the vast scope of possible reactivity with one ligand set.

Larger substituents on the Cp ligands are also useful to stabilize kinetically “non-classical divalent lanthanides”⁵⁷ as sandwich complexes of Tm (Fig. 3),^{58,59} Dy,⁶⁰ and Nd,⁶¹ which still retain high reactivity for potential applications in the activation of small and inert molecules.^{61,62} Additionally, Lappert showed that using bulky substituents on the Cp rings from the original $\text{Ln}(\text{Cp})_3$ complexes allowed more straightforward reduction to form divalent lanthanide ions.^{63,64} This strategy has

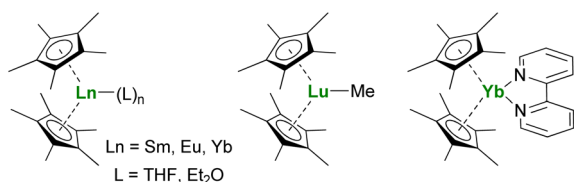


Fig. 2 Molecular structures of $\text{Ln}(\text{Cp}^*)_2$ adducts, $(\text{Cp}^*)_2\text{LuMe}$, and $(\text{Cp}^*)_2\text{Yb}(\text{bipy})$.

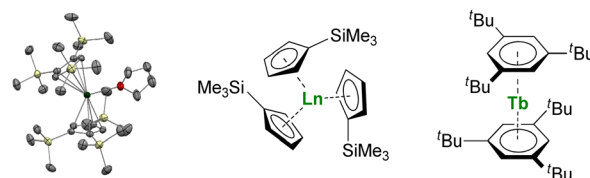


Fig. 3 ORTEP plot of $\text{Tm}(\text{Cp}')_2(\text{thf})$ (Tm atom is in green, carbon in grey, silicon in yellow, and hydrogen are removed for clarity) and molecular structures of $\text{Ln}(\text{Cp}')_3$ and $\text{Tb}(\text{Bz}^{\text{ttt}})_2$.

been more recently extended to almost all the lanthanide ions, even the most difficult to reduce, using multiple bulky Cp-derived ligands such as $\eta^5\text{-C}_5\text{H}_4(\text{SiMe}_3)$ (Cp') (Fig. 3), and showing the role of the ligand in the control of the redox properties of the lanthanide ion.^{65,66} Upon reduction, if the classical divalent lanthanide ions adopt a $4f^{n+1}$ configuration, in the other 4f-ions, the extra electron is promoted to the d-shell, opening a vast area of new applications for the redox chemistry of organolanthanides.

When the steric pressure induced by the ligands around the metal center reaches a certain level, the bulky ligands may enable an electron transfer to provide reductive chemistry, described as “sterically induced reduction”.^{67–69} A possible electronic contribution to these spontaneous reductions was also considered in the report of the $\text{Ln}(\text{Cnt})_3$ complexes. The corresponding synthesis was impossible for Sm or Yb but could be performed for the Tm and Y analogs.³⁸ The original structures of tris-Cp arrangements made in 1954 found new horizons in the most recent studies.

Alongside reactivity studies, the fast development of molecules behaving as permanent magnets below a given temperature (Single Molecule Magnets, SMMs) became attractive.⁷⁰ Rinehart and Long highlighted the relation between the ground m_j state of a given lanthanide metal ion and the coordination surroundings.⁷¹ Following this foundational perspective, the structural chemistry of 4f-organometallic sandwiches started to evolve for the formation of linear complexes with small and bulky Cp-based ligands,^{72–75} or large-size aromatic ligands,⁷⁶ digging up the classic uranocene-like structures and building up the size of the Cp substituents' bulk from previous examples.^{58,77,78}

Another great field evolution instance is the report of sandwich compounds supported by the neutral six-electron aromatic tris-tert-butylbenzene (Bz^{ttt}) ligands. Using the metal vapor technique, Cloke was able to synthesize a few so-called zero valent neutral compounds (Fig. 3).^{79–82} Yet, the spectroscopic oxidation state and magnetic properties remain to be fully explored (*vide infra*) and may re-open the case of C_6 rings with lanthanides.

The structural chemistry of organolanthanide complexes moved forward and back multiple times following the timely active area of applications, but the molecules resisted time. It is likely that a few abandoned molecules of the past will serve as figureheads for future developments. Synthetic innovation and rigorous methods thus remain the critical contribution. Along



this perspective, we will attempt to focus on several possible horizons for organolanthanides.

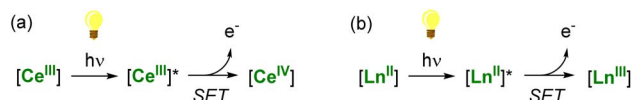
Reactivity and catalysis

Light-promoted redox reactions

Photoinduced transformations, which encompass photoredox catalysis, are becoming increasingly popular methods to promote chemical transformations by taking advantage of light irradiation to alter the redox properties of compounds. This area of chemistry has long been governed by using photosensitizers based on rare and precious transition metals such as Ru and Ir.^{83,84} For sustainable chemistry, the development of earth-abundant and cheaper photocatalysts is a significant objective.⁸⁵ Lanthanide-based photosensitizers can be considered promising candidates based on their unique optical properties and higher abundance in the Earth's crust compared to platinum group metals. It is worth noting that Ce, the most readily available lanthanide, features an abundance similar to that of the 3d metals Cu, Ni, and Zn. In contrast, the rarest lanthanides, Tm and Lu, are still more abundant than Ru and Ir.⁸⁶

Upon light excitation, photosensitizers can behave as either potent reductants or oxidants, activating organic substrates through single electron transfer (SET) events, resulting in the formation of reactive radical intermediates. As a result of their partly filled 4f shell, most trivalent lanthanide ions absorb electromagnetic radiation in the visible region of the spectrum through parity-forbidden electronic transitions within the 4f shell. In addition to f–f transitions, electric-dipole allowed $4f^7 5d^0 \rightarrow 4f^7-1 5d^1$ transitions are also accessible but usually occur at much higher energies, typically in the UV region.⁸⁷ The application of lanthanide complexes in light-promoted transformations, especially reduction reactions, strongly relies on such $4f \rightarrow 5d$ transitions. Upon photoirradiation, the 5d excited state features a stronger reducing character, *i.e.* a more negative redox potential than the ground state, potentially allowing the reduction of challenging substrates typically not reduced under standard conditions without light irradiation.⁸⁸ Although 4f orbitals are strongly shielded and remain largely unperturbed by the surrounding donor ligands, the 5d orbitals are sensitive to the ligand environment. Thus, the energies of the $4f \rightarrow 5d$ transitions can be tuned depending on the nature and geometry of the surrounding ligands.⁸⁹ In this context, organometallic ligands are exciting candidates as they usually enforce rigid and well-defined geometric coordination environments, potentially allowing tuning of the photophysical properties.

A thermodynamically stable trivalent oxidation state characterizes all lanthanide ions. Only a few can easily shuttle between two oxidation states depending on their position in the lanthanide series and electronic configuration. The $\text{Ln}^{\text{IV}}/\text{Ln}^{\text{III}}$ couple is easily accessible for Ce, while the divalent oxidation state can be readily obtained in the case of Sm, Eu, and Yb complexes. These specific ions (Ce^{III} , Sm^{II} , Eu^{II} , and Yb^{II}) are excellent candidates for photoinduced reduction reactions and applications in (photo)catalysis through light-promoted amplification of their reducing properties (Scheme 1).

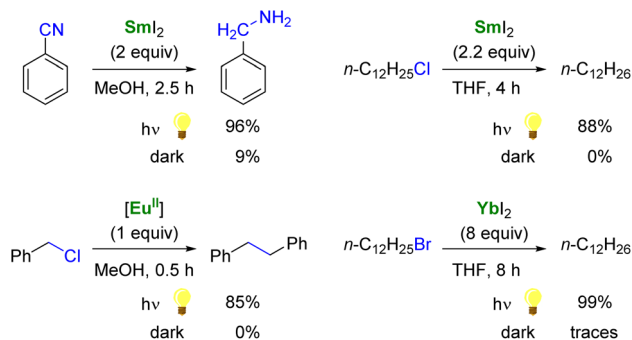


Scheme 1 Light-promoted single-electron reduction reactions by trivalent (a) or divalent lanthanides (b).

As a result of its $4f^1$ electronic configuration, the Ce^{III} ion gives rise to a broad $4f^1 \rightarrow 4f^0 5d^1$ transition in the near-UV/visible region and at the lowest energy compared to the other trivalent lanthanide ions. The energy of this transition involving 5d orbitals can be tuned by adjustment of the ligand environment.⁹⁰ After photoexcitation, the redox-active Ce^{3+} ion acts as a highly reducing metalloradical that may participate in single-electron transfer (SET) reactions. The group of Schelter has primarily investigated the use of Ce^{III} complexes as photosensitizers for light-induced reductive transformations of organic compounds,⁹⁰ including challenging substrates such as benzyl or aryl chlorides.^{91–93} The hexachloroacetate(III) anion, $[\text{Ce}^{\text{III}}\text{Cl}_6]^{3-}$, was especially found to be a potent photosensitizer with an estimated excited-state reduction potential of -3.45 V vs. Fc^+/Fc (ferrocenium/ferrocene couple).⁹²

To design efficient Ce^{III} photosensitizers, the relaxation of the excited state through nonradiative decay processes, such as ligand vibrational modes, should be minimized so that a maximum energy from light can be converted into chemical transformations.⁹⁴ One strategy is to use rigid ligands and control C–H oscillators from proximity to the metal cation to minimize vibrational relaxation of the excited state. To this extent, developing new organocerium(III) complexes may be interesting. The recent development of the Tb^{IV} and Pr^{IV} chemistry may also have an increasing interest in light of the $\text{Ce}^{\text{IV}}/\text{Ce}^{\text{III}}$ photochemistry.^{95–100} However, organometallic Tb or Pr complexes in the +4 oxidation state have not yet been reported.

As single-electron reductants, divalent lanthanides, especially Sm^{II} ,^{101,102} have been extensively studied for their applications in organic chemistry.^{103–105} Compared to trivalent Ln ions, divalent lanthanides present $4f^7 5d^0 \rightarrow 4f^7-1 5d^1$ transitions at lower energies, typically in the UV to IR region.¹⁰⁶ Photoexcitation to promote the $4f \rightarrow 5d$ transition has been



Scheme 2 Examples of enhanced reductive reactivity of Ln^{II} ($\text{Ln} = \text{Sm}, \text{Eu}, \text{Yb}$) species upon photoirradiation.^{108,110–113}



reported to enhance the rate of several reduction reactions mediated by divalent lanthanide species (Scheme 2).⁸⁸ For example, the photoexcitation of SmI_2 was found to lead to a more potent SET reductant, capable of reducing substrates such as organic chlorides and nitriles typically not affected by SmI_2 without light irradiation.^{107–110} Similarly, although YbI_2 is a weaker SET reagent with a redox potential *vs.* NHE of -1.15 V, photoirradiation in the near UV (300–400 nm) led to a more potent reductant with a reducing power similar to that of SmI_2 in THF (-1.55 V).^{111,112} With a half-filled $4f^7$ ground-state electronic configuration, Eu^{II} ions are remarkably stable towards oxidation and show only a weak reducing character (-0.35 V *vs.* NHE). Recently, the group of Allen has demonstrated that a Eu^{II} complex supported by an azacryptand macrocyclic ligand (see below) could reduce organic chlorides upon photoexcitation in the visible region and exhibited an estimated reduction potential of -2.8 V *vs.* NHE, much more negative than that of SmI_2 .¹¹³

As discussed above, the organometallic chemistry of Yb^{II} and Sm^{II} complexes has been dominated by the $\text{Ln}(\text{Cp}^*)_2(\text{L})_n$ ($\text{L} = \text{THF}, \text{Et}_2\text{O}; n = 0-2$) complexes typically used for SET reactions. Although the group of Watson already reported in 1990 that the rate of C–F activation on fluorinated olefins and aromatics by $\text{Ln}(\text{Cp}^*)_2(\text{OEt}_2)$ ($\text{Ln} = \text{Yb}, \text{Eu}$) complexes could be enhanced upon visible-light irradiation,¹¹⁴ similar applications involving organolanthanide(II) complexes have remained relatively unexplored. The interesting photophysical properties of Eu^{II} complexes¹¹⁵ have led to the recent synthesis and study of divalent organoeuropium complexes with tunable luminescence properties depending on the ligand environment (Fig. 4).^{36,77,116–122} With the recent introduction of novel organometallic architectures as supporting ligands, such as large ring ligands,^{25,36,37} further development in this field is likely to be expected. The development of ligand structures inducing long luminescence lifetimes is highly desirable for light-promoted photoredox reactions to maximize the probability of an electron transfer from the organolanthanide complex to the substrate.

For application in organic transformations, new organometallic reducing agents based on Eu^{II} , Sm^{II} , and Yb^{II} may offer alternatives to “non-classical divalent lanthanide” species, such as TmI_2 , DyI_2 and NdI_2 , which feature stronger reducing properties but are more challenging to synthesize and handle.^{57,123}

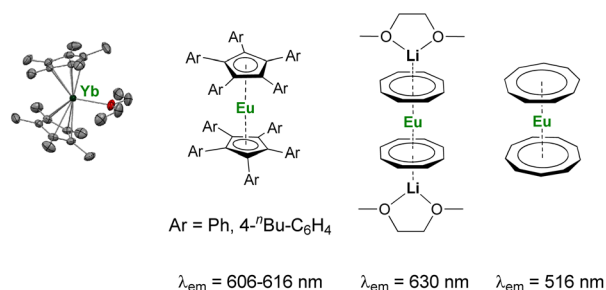


Fig. 4 Example of organometallic divalent lanthanide complexes with potential applications in photoinduced reduction reactions.^{36,40,116,117,119,120}

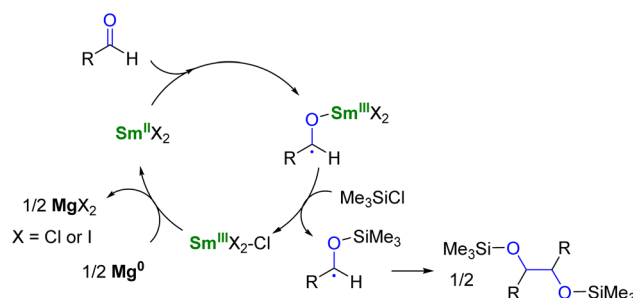
The primary focus in the organometallic chemistry of reductive divalent lanthanides is prone to go back to the early years (before 2000) when Eu^{II} , Sm^{II} , and Yb^{II} were the major representatives. Detailed studies of the ligand effects on the $4f \rightarrow 5d$ transitions may lead to photoredox catalysts with greater tunability and negative electrochemical potentials. The remaining challenge in using divalent lanthanide complexes for photoredox catalysis is the reduction of the oxidized trivalent complexes back to their divalent states. A challenge is also the sensitivity toward air and moisture of organolanthanide complexes.

Application in (photo)electrocatalysis

To use lanthanide complexes as SET reductants in catalytic transformations, different strategies can be used to regenerate the active, reducing species (Ce^{III} , Sm^{II} , Eu^{II} , or Yb^{II}).

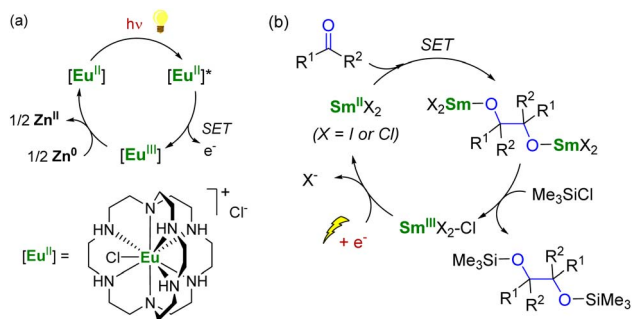
In the field of divalent lanthanides, only very scarce examples have been reported, mainly focusing on the recycling of SmI_2 when used in catalytic amounts.¹²⁴ Three different strategies have been described to reduce the Sm^{III} species back into Sm^{II} . The most common strategy corresponds to a chemical approach involving the addition of a sacrificial reductant. For example, elemental magnesium,^{125–129} mischmetal (a low-cost alloy of the light lanthanides)^{130,131} or Zn/Hg amalgam¹³² have been used for this purpose (Scheme 3). Typically, a silyl-based electrophilic reagent (Me_3SiCl , Me_3SiOTf) is added to trap the anionic organic product and favor its decoordination from the oxophilic metal center. This strategy involving an external reductant has been successfully applied in the first catalytic visible-light-promoted reductive coupling of benzyl chloride by a Eu^{II} complex coordinated by an azacryptand macrocyclic ligand (Scheme 4).¹¹³ In this reaction, Zn^0 powder is used as a sacrificial reducing agent to reduce the Eu^{III} complex formed after the SET step into its divalent Eu^{II} analog.

Although the chemical reduction approach is powerful, developing alternative methods that avoid using terminal reductants in stoichiometric quantities would be desirable. In this context, the group of Mellah has investigated electrochemical methods to reduce Sm^{III} species back into Sm^{II} at the surface of an electrode (Scheme 4). The corresponding system has been applied in carbon–carbon coupling reactions such as pinacol formation and Barbier-type reactions,¹³³ in the



Scheme 3 SmI_2 -catalyzed pinacol coupling reaction in the presence of Mg^0 as co-reductant.¹²⁵

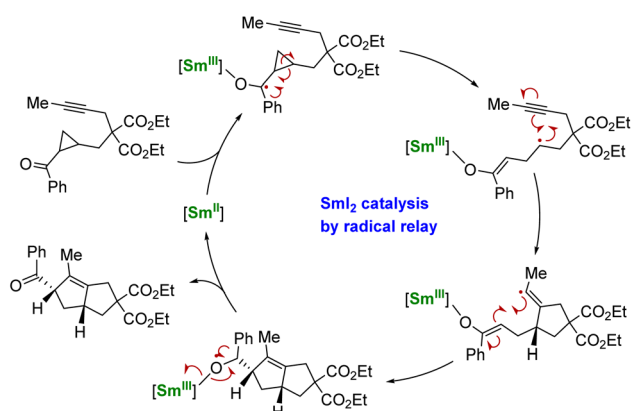




Scheme 4 (a) (Photo)catalytic cycle with a Eu^{II} complex (a)¹¹³ and electrochemical approach for the recycling of Sm^{II} species (b).¹³³

reduction of nitrobenzenes into azobenzenes,¹³⁴ in the carboxylation of benzyl halides with CO_2 ,¹³⁵ and reductive alkoxylation of phthalimides into isoindolinone derivatives (using 10–20 mol% of Sm^{II} species).¹³⁶ The best results were obtained using a Sm metal electrode, which, acting as a cathode, is not consumed during electrolysis. Other more conventional cathode materials such as platinum, carbon, nickel, lead, or stainless steel did not lead to the successful regeneration of the Sm^{II} active species. The extension of the electrochemical strategy to the recycling of divalent organometallic complexes, such as those depicted in Fig. 4, may be very promising for developing new electrocatalytic transformations with organo-lanthanide complexes.

Using another strategy, the group of Procter demonstrated that a radical relay approach could allow the use of SmI_2 in catalytic amounts for organic transformations.^{137,138} In this strategy, no external reducing agent is necessary as the Sm^{II} species is regenerated through back electron transfer from a negatively charged organic intermediate (Scheme 5). However, this method requires the particular design of phenone substrates compatible with radical relay cyclization cascades and is, therefore, currently limited to very specific molecules. Despite its elegance, this strategy shows a heavy dependence on the nature of the substrate and the relative stability of the ketyl



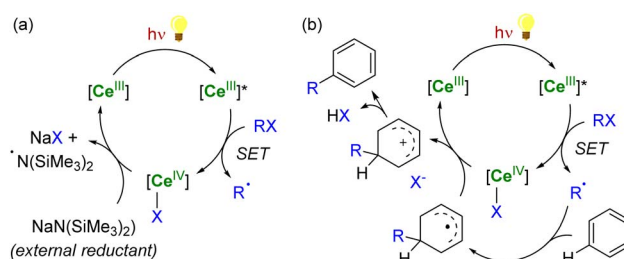
Scheme 5 Schematic catalytic cycle of the Sm^{II} -induced electron transfer followed by cyclization and back electron transfer.¹³⁷

radical intermediates: tuning the ligand may be a key to developing this peculiar chemistry.¹³⁸

Indeed, similar back electron transfer reactions between a radical anion intermediate and a Sm^{III} metal center have been observed in several instances in organosamarium complexes but highly depend on the reaction conditions and nature of the substrates. For example, the reduction of diphenylacetylene,¹³⁹ conjugated alkenes,^{140,141} and polycyclic aromatic hydrocarbons¹⁴² by $\text{Sm}(\text{Cp}^*)_2(\text{thf})$ was found to be reversible depending on the solvent used. While the different substrates are reduced in hydrocarbon solvents, leading to the formation of dinuclear Sm^{III} complexes, these reactions can be reversed by adding THF, resulting in the regeneration of samarocene and the corresponding free alkyne/alkene. Similar observations involving Yb^{II} or Sm^{II} organometallic complexes have also been reported using different redox-active ligands.^{51,143,144}

In the case of Ce^{IV} species obtained upon SET reductions induced by photoexcited Ce^{III} complexes, the regeneration of the latter can also be achieved by different strategies. External reductants have been used to recycle the photoactive Ce^{III} species, which allowed the use of a catalytic amount of cerium photosensitizer. For example, $\text{MN}(\text{SiMe}_3)_2$ ($\text{M} = \text{Na}, \text{K}$) has been used as a sacrificial reductant that effectively reduces the $\text{Ce}^{\text{IV}}\text{-Cl}$ products to Ce^{III} products through the formation of an aminyl $\text{N}(\text{SiMe}_3)_2$ radical (Scheme 6a).^{91,94} The presence of an external reductant, such as Ce or Zn metal powder, was sometimes necessary to quench the aminyl radical and prevent the formation of by-products.⁹¹ Depending on the nature of the substrate, the organic radical generated after the SET reduction step may also be oxidized by the Ce^{IV} complex, which provides a way to regenerate the photoactive Ce^{III} complexes for applications in catalytic transformations (Scheme 6b).⁹⁴

Another strategy for regenerating Ln^{III} photosensitizers, which has been especially developed over the last decade, corresponds to the photoreduction of the corresponding Ln^{IV} complexes with the concomitant formation of organic radicals. This strategy may be used for lanthanide compounds featuring a relatively stable +IV oxidation state, such as Ce^{IV} and Tb^{IV} species, with $4f^0$ and $4f^7$ electron configurations, respectively. These oxidizing ions display low-energy metal-to-ligand charge transfer (LMCT) absorptions, typically in the near UV and visible region. The corresponding excited states are usually not emissive but reactive.⁸⁷ Upon irradiation, Ce^{IV} complexes



Scheme 6 Schematic (photo)catalytic cycle involving the $\text{Ce}^{\text{III/IV}}$ couple with (a) or without (b) the use of an external sacrificial reductant.^{91,94}



undergo LMCT transitions which promote homolysis of the metal–ligand bond, leading to the photoreduction of the lanthanide center together with the generation of reactive ligand-centered radicals (Scheme 7). It should also be mentioned that this photochemical strategy had already been reported more than 30 years ago for recycling Ln^{II} ($\text{Ln} = \text{Sm}, \text{Eu}, \text{Yb}$) species for catalytic applications,^{145–147} but has only recently seen a renaissance in Ce chemistry.^{90,148,149}

Using this procedure, reactive heteroatom-centered radical species such as carboxyl,¹⁵⁰ alkoxy¹⁵¹ and chlorine^{92,152} radicals can be formed and used to activate other substrates under mild conditions. This strategy has recently been employed by Zuo and Schelter in several photocatalytic transformations induced by soluble cerium complexes and relying on the +IV/+III redox couple of the cerium center.^{90,148,149} For example, cerium photoredox catalysis has been applied in photocatalytic dehydrogenation of amines, C–C bond cleavage and functionalization of alcohols,^{153–157} C–H activation of alkanes^{152,158,159} and functionalization of aryl substrates.⁹³ Although commercially available Ce^{III} salts (chlorides or triflates) are typically used in these photocatalytic reactions, the development of new stable Ln^{IV} complexes may be attractive for photocatalytic applications and to control the homolysis of the Ln^{IV} –ligand bonds.

In organometallic chemistry, synthesizing organocerium(IV) complexes is challenging, which can be traced back to the strong oxidizing character of the Ce^{IV} ion and the reducing properties of carbon-based anionic ligands.¹⁶⁰ Therefore, only limited examples of organometallic cerium(IV) complexes have been reported in the literature, and the development of an organometallic scaffold allowing the stabilization of Ce^{IV} species is highly desirable. To date, organometallic Ce^{IV} complexes have been mostly limited to metallocene structures with examples of Ce^{IV} complexes bearing monoanionic cyclopentadienyl (Cp) ligands,^{161–167} dianionic cyclooctatetraenyl rings,^{30,31,168,169} and substituted pentalene dianionic ligands^{170,171} (Fig. 5). Improvement of the kinetic stability of Ce^{IV} organometallic complexes, especially by tuning the steric properties of the ligands, may be a direction of future work to go toward catalysis by organocerium complexes.

Single-ion magnets and quantum technologies

Single-molecule magnets (SMMs) and f-elements. A single-molecule magnet is a molecule that can behave as a magnet

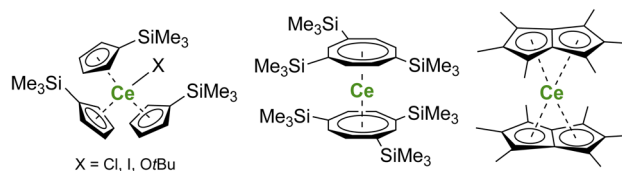
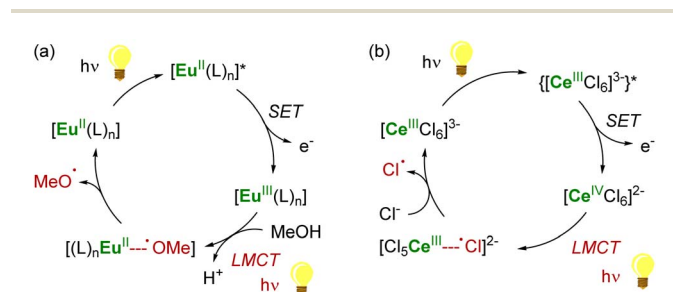


Fig. 5 Examples of Ce^{IV} metallocene complexes.

below a given temperature, allowing a coercive field, which is a typical property of bulk magnetic materials. The first representative of this family was discovered in 1993 and corresponded to a molecular manganese cluster.¹⁷² Initially, the chosen strategy was to increase the spin state of the molecule, playing with strong metal–metal magnetic interactions to increase the barrier rapidly. Those studies showed that the overall barrier to spin reversal was far from the only important criterion.¹⁷³ For this reason, lanthanide ions which had been ignored mainly because of their poor metal–metal magnetic communication, were placed back under the spotlight. Indeed, 4f-elements have strong magnetization thanks to the unquenched orbital moment. Due to the spin–orbit coupling, the good quantum number is J , and m_J values can reach $\pm 15/2$ with a strong anisotropy under a magnetic field.¹⁷⁴

This point was demonstrated in 2003 by Ishikawa *et al.* with a single-metal ion complex of Tb bis-phthalocyanine $\text{Tb}(\text{Pc})_2^-$ (Fig. 6),^{70,175} which presented a remanent field under zero applied magnetic field. This critical study also underlined that the relaxation paths were multiple and that the surrounding of the central metal ion was crucial for maximizing the anisotropy and preventing the under-barrier relaxation sources from excited m_J states. The single-ion-magnet property was extended to 5f-ions with the neutral diphenyl bis(pyrazolyl borate) complex $\text{U}(\text{Ph}_2\text{BPz}_2)_3$.^{176,177} However, a key challenge remained: to maximize the metal–metal magnetic exchange in f-elements combining anisotropy and high ground m_J value. This strategy particularly advanced by using bridging radical ligands, such as N_2^{3-} (Fig. 6), for which the strong magnetic exchange with f-elements provides strong metal–metal alignment and, inevitably, single-magnet properties.^{178–180} This powerful strategy is currently still used for the design of f-element single-molecule



Scheme 7 LMCT-induced homolysis in $\text{Eu}^{\text{III}}/\text{Eu}^{\text{II}}$ (a)^{146,149} and $\text{Ce}^{\text{IV}}/\text{Ce}^{\text{III}}$ (photo)catalysis (b).⁹⁰

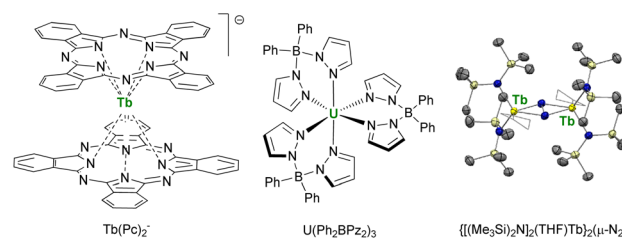


Fig. 6 Molecular structures of $\text{Tb}(\text{Pc})_2^-$,⁷⁰ $\text{U}(\text{Ph}_2\text{BPz}_2)_3$,^{176,177} and ORTEP plot of $\{[(\text{Me}_3\text{Si})_2\text{N}]_2(\text{THF})\text{Tb}\}_2(\mu\text{-N}_2)^-$,¹⁸⁰ (terbium atoms are in yellow, nitrogen atoms in blue, silicon atoms in pale yellow, carbon atoms in grey, hydrogen atoms are not represented, and coordinated thf molecules are represented in wireframe).



magnets, particularly with organometallic fragments (*vide infra*).¹⁸¹

These early studies strongly emphasized two points: the control of the ground m_J value is critical for maximizing the anisotropy. In contrast, the nature and energy of the excited m_J states are critical for controlling the relaxation paths. From these starting points, Rinehart and Long elaborated a comprehensive description of the relationship between the coordination environment of the 4f-elements and the relative energies of the m_J states using a simple electrostatic model.⁷¹ This article was followed by a series of similar important notions,¹⁸² which moved the field to the rational design of SMMs. From then on, the unique structural arrangements accessible using organometallic complexes started to play a more significant role.

Single-ion magnet design. The prediction model shows three categories of lanthanide ions: the isotropic ions (Gd^{III} , Eu^{II}), the oblate-shaped ions, and the prolate ions.⁷¹ The first category is not interesting for the design of SMMs; the second requires a localized axial field to favor an isolated maximal m_J state value while equatorial fields are most desirable for the third category. More precisely, each ion fits best with one specific structural arrangement. If one focuses on the largest m_J ground state, the dysprosium(III) ion requires a strongly localized axial field. In contrast, the erbium(III) ion requires typical sandwich π -coordination, in which the overall charge surrounds the metal ion.¹⁸²

A short review of the compounds known from the organo-lanthanide chemistry that would have an approaching adapted structure established that the $(Cp^{tBu})_2Dy(X)$ ($X = Br, I, BH_4$) complexes made in 2007 by Nief and co-workers (Fig. 7),⁶⁰ and the Er^{III} representative of the $K[Ln(Cot)_2]$ family, pioneered by Streitwieser,²⁹ would meet most criteria. In the latter, the chelation of the potassium ion led to the isolated $Er(Cot)_2^-$ anion (Fig. 7) that was reported with record SMMs properties at the time.¹⁸³ The formation of heteroleptic neutral π -sandwich complexes was also investigated and led to good SMMs properties,^{184,185} particularly with the large monoanionic Cnt ligand.^{186,187} The Cot-Er pair is highly relevant as an excellent example of the perfect adequation between the metal and the ligand coordination for maximal anisotropy: this is referred to as ligand-metal pair anisotropy.^{188,189} The concept has been extended to divalent thulium, an ion with prolate-shaped density. However, the SMM properties of the corresponding complex (Fig. 7) remain very modest due to the decrease of the ground m_J states to $\pm 7/2$.⁷⁶

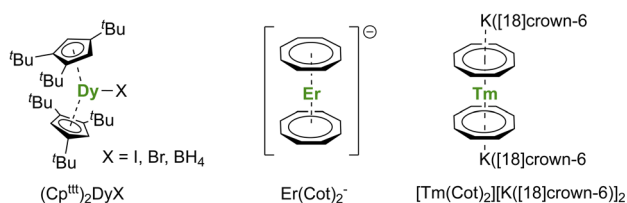


Fig. 7 Molecular structures of $(Cp^{tBu})_2Dy(\mu-I)K([18]crown-6)$,⁶⁰ $Er(Cot)_2^-$,¹⁸³ and $[Tm(Cot)_2][K([18]crown-6)]_2$.⁷⁶

For the $Dy(III)$ case, building on the previous observations that steric bulk on the Cp substituents could provide linearity to the corresponding sandwich complexes,^{77,120,190} the Cp^{tBu} was found a suitable ligand that enforces axial ligand field. However, a problem remained owing to the presence of the halide counteranion coordinated in the equatorial sphere, even upon reduction.⁶⁰ The key solution consisted of using $[H(SiEt_3)_2]^+[B(C_6F_5)_4]^-$ as a halide abstraction reagent, leading to the separated $[Dy(Cp^{tBu})_2]^+[B(C_6F_5)_4]^-$ ion-pair (Fig. 8).^{72,73} The SMM properties of this molecule hammered the previous record with a 60 K blocking temperature and a $1541(11) \text{ cm}^{-1}$ energy barrier. A few months later, this landmark was increased to 80 K, *i.e.* above the liquid nitrogen temperature, by increasing the bulk of the ligand with the use of the Cp^{iPr5} ligand (Fig. 8),⁷⁴ a ligand previously used for the formation of $Ln(Cp^{iPr5})_2$ ($Ln = Sm, Eu, Yb$).^{77,191,192} The modulation of the Cp substituents leads to variations in the complexes' geometry, directly impacting the magnetic properties. Additionally, the strategy was extended to non-classical divalent lanthanide complexes featuring a linear geometry (Fig. 8), which is remarkable, considering the larger size of the Ln^{II} ions.¹⁹³ However, reducing the lanthanide ions does not necessarily fill the f-shell, resulting in complications in the magnetic analysis because of 5d and 6s contributions.

In addition, a few lanthanide complexes bearing aromatic rings with sizes other than C_5 or C_8 also showed interesting SMM properties.¹⁹⁴ One intriguing question remains in the case of the $Ln(Bz^{tBu})_2$ family of complexes (Fig. 3) reported by Cloke and co-workers, since the ligand is intermediate between a large ring and a strongly localized aromatic anion.^{79–82} In these compounds, the electron count and charge on the ligand will depend on the actual oxidation state of the lanthanide ion.

Radical bridge for strong metal-metal enhancement

After the description of radical-induced metal alignment with reduced dinitrogen radicals, a series of compounds was reported with the objective of increasing the energetic barrier. For such a purpose, the target of choice corresponds to soluble and versatile lanthanide fragments associated with redox-active bridging ligands. For example, the N_2^{3-} bridging ligand can be easily replaced by another π -accepting ligand such as N-aromatic heterocycles. The known $\{(Cp^*)_2Ln\}_2(\mu\text{-bipym})$ (bipym = bipyrimidine) complex was an obvious choice because of the symmetrical and bridging nature of the ligand,¹⁹⁵ which would compare well with the terminal bipyridine ligand.^{46,47} However, this complex, obtained upon reaction of two

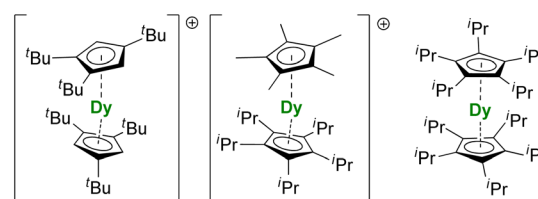


Fig. 8 Molecular structures $[Dy(Cp^{tBu})_2]^+$,^{72,73} $[Dy(Cp^*)(Cp^{iPr5})_2]^+$,⁷⁴ and $Dy(Cp^{iPr5})_2$.¹⁹³



equivalents of divalent lanthanide precursor with free bipym, features a doubly reduced dianion bridge. Therefore, no radical is present on the ligand, which renders the corresponding complex of limited interest in terms of magnetic exchange. The more appealing radical bridged $\{[(\text{Cp}^*)_2\text{Ln}]_2(\mu\text{-bipym})\}^+$ cations (Fig. 9) could be obtained by first coordination of bipym to cationic $\{(\text{Cp}^*)_2\text{Ln}\}^+$ fragments, followed by single-electron reduction. As a result, both lanthanide ions are trivalent, and the bipym is in a radical mono-anionic form.¹⁹⁶ These compounds exhibit SMM behavior, with barriers essentially smaller than those in the N_2^{3-} -radical-bridged analogs,^{179,180} but can be compared to the values obtained in complexes with larger ligands such as the 2,3,5,6-tetra(2-pyridyl)pyrazine (tppz)¹⁹⁷ or in related trimetallic arrangements using the μ_3 -hexaazatrinaphthylene (HAN)¹⁹⁸ ligand (Fig. 9). The great advantage of such systems is that both the organometallic fragment and the bridging ligand can be easily and independently tuned: the influence of the coordination sphere around the lanthanide ion,¹⁹⁹ as well as that of the bridging ligand electronic properties, through the use of electron-donating and withdrawing substituents, could be evaluated.²⁰⁰ The two conclusions of this remarkable series of works by Demir and Long are that the best SMMs should possess maximal magnetic exchange while retaining as much as possible an axial field. The ligand's size and electronics (nature of the bonding) are both critical in this matter.

An ideal way to embrace both conditions would be to have one single electron placed between two lanthanide ions, each possessing a strong and highly localized axial field. This strategy was recently addressed by Long and coworkers, who designed the $\{\text{Cp}^{\text{ipr5}}\text{Ln}\}_2(\mu\text{-I})_2$ dimeric structures in which the Cp^{ipr5} ligands are each capping one lanthanide ion. The rest of the metal coordination sphere was completed by iodide ligands.²⁰¹ The single electron that would favor the magnetic exchange was placed by simply reducing one metal center to afford a mixed-valent organometallic complex, $\{\text{Cp}^{\text{ipr5}}\text{Ln}\}_2(\mu\text{-I})_3$, in which both metal ions can magnetically communicate. When the extra electron is placed in the f-shell, the coupling is not strong; however, when it is placed in the d-shell, the coupling is maximum, and the Hund's rules are verified. As a result, all metallic spins align, leading to a giant coercive field and ultrahard magnetism at high temperatures (60 K).²⁰¹

Beyond these remarkable results, there are a few take-home points: the blocking temperature and effective barrier can reach very high values so that feasible quantum applications may be considered in the future. The ligand design is a crucial

parameter to find adapted metal–ligand anisotropy, and it seems that π -coordinating ligands are particularly well-suited for designing high-performance SMMs and providing the correct geometry. These characteristics rely on how the relaxation paths are selected, an essential key for designing future quantum devices.

Relaxation paths analysis

As mentioned above, the thermally activated barrier, corresponding to the Orbach model, is not satisfactory as a sole criterion for describing the SMM properties.²⁰² This is mainly due to possible under-the-barrier magnetic relaxation paths *via* Raman (spin phonon) and quantum tunneling, which need to be unraveled. It is essential to rationalize how these processes can be avoided using an appropriate molecular design.²⁰³

Several approaches were proposed, such as using rigid ligands to increase the energy of the phonons and avoid them from meeting with the energies of the m_J excited states.^{202,204} A second approach, which is appealing, consists in preventing resonance phonon transitions from the magnetic energy window. For this purpose, it is necessary to relate the structural features to the energetic ladder, which has been attempted on several occasions and is an important current objective in the theoretical chemistry community.²⁰⁵ As such, in the dysprosium series, the reasons for recording SMM behavior can be understood by two distinct phenomena. First, the near linear arrangement of the ligands allows maximal splitting of the energy states. In their article, Chilton *et al.* argued that the larger crystal field splitting is the primary driver of the slower relaxation rate for $[\text{Dy}(\text{Cp}^*)(\text{Cp}^{\text{ipr5}})]^+$ compared to $[\text{Dy}(\text{Cp}^{\text{tnt}})_2]^+$.²⁰⁵ Then, the first complex also has the advantage of possessing electronic states that are off-resonance with vibronic states. The investigation of such an interplay between the structural features and the electronic structure is of great importance for bringing the rational design of SMM even further. Combining theory and luminescence spectroscopy could be instrumental in rationalizing a potential correlation.^{206,207}

Additionally, the development of heterocyclic ligands such as phospholyl or new aminoborolide ligands could bring new data to enable broader comprehension of the magnetic relaxation pathways.^{208–210}

Quantum devices

A very promising application of the structure–physical property relationship made over the most recent years lies in the development of quantum devices. Molecular qubits are increasingly cited as potential tools for tailoring quantum algorithms²¹¹ since they are highly tunable and would be easily excited by external physical stimuli, such as microwaves or light.²¹² Organometallic compounds have recently been highlighted as potent molecules to pursue in this direction.²¹³

Aromi and Sessoli proposed lanthanide coordination compounds in this direction,^{214–216} and the report of the electronic relaxation of $\text{Lu}(\text{Cp}^*)_3^-$ (Fig. 10) further increased the interest.^{217,218} Indeed, the sizeable hyperfine coupling constant,

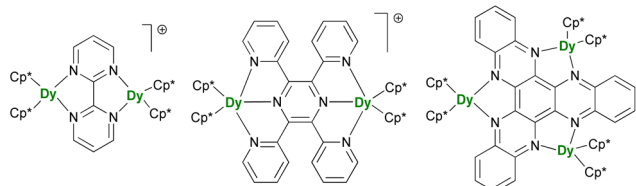


Fig. 9 Molecular structures of $\{[(\text{Cp}^*)_2\text{Dy}]_2(\mu\text{-bipym})\}^+$,¹⁹⁶ $\{[(\text{Cp}^*)_2\text{Dy}]_2(\mu\text{-tppz})\}^+$,¹⁹⁷ and $(\text{Cp}^*)_6\text{Dy}_3(\mu_3\text{-HAN})$.¹⁹⁸



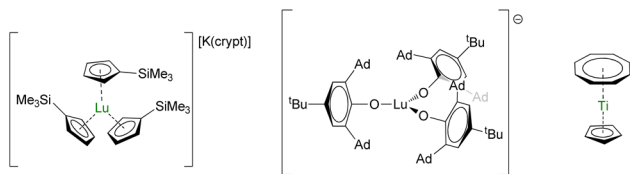


Fig. 10 Molecular structures of [Lu(Cp')₃][K(crypt)],²¹⁷ Lu(OAr*)₃⁻,²¹⁸ and (Cp)Ti(Cot).²¹³

$A_{\text{ISO}} = 428.5$ G, can be associated with a significant *s*-character to the magnetic orbital carrying the spin. In turn, spin-orbit coupling is minimized and spin-lattice relaxation is reduced in systems with $J > 1/2$. Maximizing A_{ISO} is this key, which can be done by modifying the ligand set around the metal center. With this in mind, high-field EPR measurements were performed on the bulky tris(aryloxide) Lu(OAr*)₃⁻ (OAr* = 2,6-Ad₂-4^tBu-C₆H₂O, Ad is for adamantyl, Fig. 10), which displayed a massive A_{ISO} value of 3467 MHz, similar to that in a Bi^{II} radical,²¹⁹ with giant clock transition.²¹⁸ The control of the bonding is primordial for manipulating the electronic properties and systematic structure/properties correlations will be necessary for the design of future molecules or reinvestigating ghosts from the past.

Materials, such as Er³⁺:CaWO₄ and Yb³⁺:YSO (YSO = yttrium orthosilicate, Y₂SiO₅),^{220,221} have shown interesting coherence properties, and the molecular extension to these molecules shall bring much information to the field. The use of carbon-based ligands, which possess 99% ¹²C ($I = 0$) and only 1% ¹³C ($I = 1/2$) and are relatively easy to deuterate at specific positions, should bring valuable information. In contrast, access to multimetallic compounds with close-but-different ligand fields would be appealing. These requirements are reminiscent of the lanthanide multiple-decker chemistry developed with large aromatic ligands such as Cot and its substituted analogs.^{25,222} Monometallic sandwich compounds have already shown promising results, as in the case of titanium for example, which also demonstrated that the presence of protons could not be as critical as anticipated with such ligands (Fig. 10).²¹³ The use of multiple oxidation states, such as in divalent thulium, a simple f¹³ ($I = 1/2$) ion which ground m_j state and hyperfine coupling constants can be easily tuned,^{223,224} is also a future topic of interest while the population of the 5d-shell (often hybridized with the 6s-orbital) in non-classical divalent lanthanides will provide many future research directions.^{76,225}

Conclusions

What started as a search for peculiar geometry promptly developed into a vast array of original chemistry, from single electron reductants to polymerization catalysts. The interplay between the aromatic ligand and the lanthanide center was better understood through these different applications. This allowed, in turn, a rational tuning of the ligand to harness the intrinsic magnetic and electronic properties of the metallic center, leading to the recent breakthrough in these fields. Given the constant back-and-forth shuttle between old structures and

new outlooks, highlighted in this perspective, a modern look at classic lanthanide organometallic compounds from the past will likely lead to a bright future.

Author contributions

GN designed the structure of the perspective. All authors contributed to the writing of the article.

Conflicts of interest

There are no conflicts to declare.

Acknowledgements

This project has received funding from the European Research Council (ERC) under the European Union's Horizon H2020 research program (grant agreement no. 716314) and from ANR (French National Research Agency) under project number ANR-19-CE07-0019-1. CNRS and Ecole Polytechnique are thanked for funding.

References

- 1 T. J. Kealy and P. L. Pauson, *Nature*, 1951, **168**, 1039–1040.
- 2 P. Laszlo and R. Hoffmann, *Angew. Chem., Int. Ed.*, 2000, **39**, 123–124.
- 3 H. Werner, *Angew. Chem., Int. Ed.*, 2012, **51**, 6052–6058.
- 4 J. Okuda, *Eur. J. Inorg. Chem.*, 2017, **2017**, 217–219.
- 5 G. Wilkinson and J. M. Birmingham, *J. Am. Chem. Soc.*, 1954, **76**, 6210.
- 6 J. M. Birmingham and G. Wilkinson, *J. Am. Chem. Soc.*, 1956, **78**, 42–44.
- 7 P. Štěpnička, *Dalton Trans.*, 2022, **51**, 8085–8102.
- 8 E. O. Fischer and H. Fischer, *Angew. Chem., Int. Ed. Engl.*, 1964, **3**, 132–133.
- 9 E. O. Fischer and H. Fischer, *J. Organomet. Chem.*, 1965, **3**, 181–187.
- 10 G. Deacon, A. Koplick and T. Tuong, *Aust. J. Chem.*, 1984, **37**, 517–525.
- 11 C. Apostolidis, G. B. Deacon, E. Dornberger, F. T. Edelmann, B. Kanellakopoulos, P. MacKinnon and D. Stalke, *Chem. Commun.*, 1997, 1047–1048.
- 12 M. Schultz, C. J. Burns, D. J. Schwartz and R. A. Andersen, *Organometallics*, 2000, **19**, 781–789.
- 13 R. A. Andersen, J. M. Boncella, C. J. Burns, J. C. Green, D. Hohl and N. Rösch, *J. Chem. Soc., Chem. Commun.*, 1986, 405–407.
- 14 L. Perrin, L. Maron, O. Eisenstein, D. J. Schwartz, C. J. Burns and R. A. Andersen, *Organometallics*, 2003, **22**, 5447–5453.
- 15 S. Labouille, C. Clavaguéra and F. Nief, *Organometallics*, 2013, **32**, 1265–1271.
- 16 D. Seyferth, *Organometallics*, 2004, **23**, 3562–3583.
- 17 E. O. Fischer and Y. Hristidu, *Z. Naturforsch., B*, 1962, **17**, 275–276.
- 18 F. Baumgärtner, E. O. Fischer, B. Kanellakopoulos and P. Laubereau, *Angew. Chem., Int. Ed. Engl.*, 1968, **7**, 634.



- 19 J. H. Burns, *J. Am. Chem. Soc.*, 1973, **95**, 3815–3817.
- 20 M. S. Dutkiewicz, C. Apostolidis, O. Walter and P. L. Arnold, *Chem. Sci.*, 2017, **8**, 2553–2561.
- 21 R. G. Denning, J. Harmer, J. C. Green and M. Irwin, *J. Am. Chem. Soc.*, 2011, **133**, 20644–20660.
- 22 M. Tricoire, N. Mahieu, T. Simler and G. Nocton, *Chem.–Eur. J.*, 2021, **27**, 6860–6879.
- 23 F. Benner, F. Delano, E. R. Pugliese and S. Demir, in *Comprehensive Organometallic Chemistry IV*, ed. G. Parkin, K. Meyer and D. O'hare, Elsevier, Oxford, 2022, pp. 98–184.
- 24 A. J. Gremillion and J. R. Walensky, in *Comprehensive Organometallic Chemistry IV*, ed. G. Parkin, K. Meyer and D. O'hare, Elsevier, Oxford, 2022, pp. 185–247.
- 25 O. Stetsiuk, V. Cemortan, T. Simler and G. Nocton, in *Comprehensive Organometallic Chemistry IV*, ed. G. Parkin, K. Meyer and D. O'hare, Elsevier, Oxford, 2022, pp. 550–581.
- 26 O. Walter, in *Comprehensive Organometallic Chemistry IV*, ed. G. Parkin, K. Meyer and D. O'hare, Elsevier, Oxford, 2022, pp. 582–606.
- 27 A. Streitwieser and U. Mueller-Westerhoff, *J. Am. Chem. Soc.*, 1968, **90**, 7364.
- 28 F. Mares, K. Hodgson and A. Streitwieser, *J. Organomet. Chem.*, 1970, **24**, C68–C70.
- 29 K. O. Hodgson, F. Mares, D. F. Starks and A. Streitwieser, *J. Am. Chem. Soc.*, 1973, **95**, 8650–8658.
- 30 A. Greco, S. Cesca and W. Bertolini, *J. Organomet. Chem.*, 1976, **113**, 321–330.
- 31 M. D. Walter, C. H. Booth, W. W. Lukens and R. A. Andersen, *Organometallics*, 2009, **28**, 698–707.
- 32 N. M. Edelstein, P. G. Allen, J. J. Bucher, D. K. Shuh, C. D. Sofield, N. Kaltsoyannis, G. H. Maunder, M. R. Russo and A. Sella, *J. Am. Chem. Soc.*, 1996, **118**, 13115–13116.
- 33 O. Moofen and M. Dolg, *Chem. Phys. Lett.*, 2014, **594**, 47–50.
- 34 T. J. Katz and P. J. Garratt, *J. Am. Chem. Soc.*, 1963, **85**, 2852–2853.
- 35 T. J. Katz and P. J. Garratt, *J. Am. Chem. Soc.*, 1964, **86**, 5194–5202.
- 36 K. Kawasaki, R. Sugiyama, T. Tsuji, T. Iwasa, H. Tsunoyama, Y. Mizuhata, N. Tokitoh and A. Nakajima, *Chem. Commun.*, 2017, **53**, 6557–6560.
- 37 M. Xémard, S. Zimmer, M. Cordier, V. Goudy, L. Ricard, C. Clavaguéra and G. Nocton, *J. Am. Chem. Soc.*, 2018, **140**, 14433–14439.
- 38 O. Stetsiuk, L. La Droitte, V. Goudy, B. Le Guennic, O. Cador and G. Nocton, *Organometallics*, 2022, **41**, 133–140.
- 39 T. D. Tilley, R. A. Andersen, B. Spencer, H. Ruben, A. Zalkin and D. H. Templeton, *Inorg. Chem.*, 1980, **19**, 2999–3003.
- 40 W. J. Evans, I. Bloom, W. E. Hunter and J. L. Atwood, *J. Am. Chem. Soc.*, 1981, **103**, 6507–6508.
- 41 W. J. Evans, J. W. Grate, L. A. Hughes, H. Zhang and J. L. Atwood, *J. Am. Chem. Soc.*, 1985, **107**, 3728–3730.
- 42 W. J. Evans, C. A. Seibel and J. W. Ziller, *Inorg. Chem.*, 1998, **37**, 770–776.
- 43 W. J. Evans, T. A. Ulibarri and J. W. Ziller, *J. Am. Chem. Soc.*, 1988, **110**, 6877–6879.
- 44 M. Schultz, J. M. Boncella, D. J. Berg, T. D. Tilley and R. A. Andersen, *Organometallics*, 2002, **21**, 460–472.
- 45 C. H. Booth, M. D. Walter, M. Daniel, W. W. Lukens and R. A. Andersen, *Phys. Rev. Lett.*, 2005, **95**, 267202.
- 46 C. H. Booth, M. D. Walter, D. Kazhdan, Y.-J. Hu, W. W. Lukens, E. D. Bauer, L. Maron, O. Eisenstein and R. A. Andersen, *J. Am. Chem. Soc.*, 2009, **131**, 6480–6491.
- 47 C. H. Booth, D. Kazhdan, E. L. Werkema, M. D. Walter, W. W. Lukens, E. D. Bauer, Y.-J. Hu, L. Maron, O. Eisenstein, M. Head-Gordon and R. A. Andersen, *J. Am. Chem. Soc.*, 2010, **132**, 17537–17549.
- 48 G. Nocton, C. H. Booth, L. Maron and R. A. Andersen, *Organometallics*, 2013, **32**, 5305–5312.
- 49 M. D. Walter, M. Schultz and R. A. Andersen, *New J. Chem.*, 2006, **30**, 238–246.
- 50 M. D. Walter, D. J. Berg and R. A. Andersen, *Organometallics*, 2006, **25**, 3228–3237.
- 51 G. Nocton, C. H. Booth, L. Maron and R. A. Andersen, *Organometallics*, 2013, **32**, 1150–1158.
- 52 G. Nocton, W. W. Lukens, C. H. Booth, S. S. Rozenel, S. A. Medling, L. Maron and R. A. Andersen, *J. Am. Chem. Soc.*, 2014, **136**, 8626–8641.
- 53 Z. Hou and Y. Wakatsuki, *Coord. Chem. Rev.*, 2002, **231**, 1–22.
- 54 F. Allouche, K. W. Chan, A. Fedorov, R. A. Andersen and C. Copéret, *Angew. Chem., Int. Ed.*, 2018, **57**, 3431–3434.
- 55 P. L. Watson, *J. Am. Chem. Soc.*, 1983, **105**, 6491–6493.
- 56 P. L. Watson and G. W. Parshall, *Acc. Chem. Res.*, 1985, **18**, 51–56.
- 57 F. Nief, *Dalton Trans.*, 2010, **39**, 6589–6598.
- 58 F. Jaroschik, F. Nief and L. Ricard, *Chem. Commun.*, 2006, 426–428.
- 59 F. Jaroschik, F. Nief, X.-F. Le Goff and L. Ricard, *Organometallics*, 2007, **26**, 3552–3558.
- 60 F. Jaroschik, F. Nief, X.-F. Le Goff and L. Ricard, *Organometallics*, 2007, **26**, 1123–1125.
- 61 F. Jaroschik, A. Momin, F. Nief, X.-F. Le Goff, G. B. Deacon and P. C. Junk, *Angew. Chem., Int. Ed.*, 2009, **48**, 1117–1121.
- 62 T. Simler, K. N. McCabe, L. Maron and G. Nocton, *Chem. Sci.*, 2022, **13**, 7449–7461.
- 63 M. C. Cassani, D. J. Duncalf and M. F. Lappert, *J. Am. Chem. Soc.*, 1998, **120**, 12958–12959.
- 64 P. B. Hitchcock, M. F. Lappert, L. Maron and A. V. Protchenko, *Angew. Chem., Int. Ed.*, 2008, **47**, 1488–1491.
- 65 W. J. Evans, *Organometallics*, 2016, **35**, 3088–3100.
- 66 J. C. Wedal and W. J. Evans, *J. Am. Chem. Soc.*, 2021, **143**, 18354–18367.
- 67 W. J. Evans, *J. Organomet. Chem.*, 2002, **647**, 2–11.
- 68 W. J. Evans, *J. Alloys Compd.*, 2009, **488**, 493–510.
- 69 C. Ruspic, J. R. Moss, M. Schürmann and S. Harder, *Angew. Chem., Int. Ed.*, 2008, **47**, 2121–2126.
- 70 N. Ishikawa, M. Sugita, T. Ishikawa, S.-y. Koshihara and Y. Kaizu, *J. Am. Chem. Soc.*, 2003, **125**, 8694–8695.
- 71 J. D. Rinehart and J. R. Long, *Chem. Sci.*, 2011, **2**, 2078–2085.
- 72 C. A. P. Goodwin, F. Ortu, D. Reta, N. F. Chilton and D. P. Mills, *Nature*, 2017, **548**, 439–442.



- 73 F.-S. Guo, B. M. Day, Y.-C. Chen, M.-L. Tong, A. Mansikkamäki and R. A. Layfield, *Angew. Chem., Int. Ed.*, 2017, **56**, 11445–11449.
- 74 F.-S. Guo, B. M. Day, Y.-C. Chen, M.-L. Tong, A. Mansikkamäki and R. A. Layfield, *Science*, 2018, **362**, 1400–1403.
- 75 B. M. Day, F.-S. Guo and R. A. Layfield, *Acc. Chem. Res.*, 2018, **51**, 1880–1889.
- 76 J. Moutet, J. Schleinitz, L. La Droitte, M. Tricoire, F. Pointillart, F. Gendron, T. Simler, C. Clavaguéra, B. Le Guennic, O. Cadour and G. Nocton, *Angew. Chem., Int. Ed.*, 2021, **60**, 6042–6046.
- 77 H. Sitzmann, T. Dezember, O. Schmitt, F. Weber, G. Wolmershäuser and M. Ruck, *Z. Anorg. Allg. Chem.*, 2000, **626**, 2241–2244.
- 78 F. Nief, B. T. de Borms, L. Ricard and D. Carmichael, *Eur. J. Inorg. Chem.*, 2005, 637–643.
- 79 J. G. Brennan, F. G. N. Cloke, A. A. Sameh and A. Zalkin, *J. Chem. Soc., Chem. Commun.*, 1987, 1668–1669.
- 80 D. M. Anderson, F. G. N. Cloke, P. A. Cox, N. Edelstein, J. C. Green, T. Pang, A. A. Sameh and G. Shalimoff, *J. Chem. Soc., Chem. Commun.*, 1989, 53–55.
- 81 F. G. N. Cloke, *Chem. Soc. Rev.*, 1993, **22**, 17–24.
- 82 P. L. Arnold, M. A. Petrukhina, V. E. Bochenkov, T. I. Shabatina, V. V. Zagorskii, G. B. Sergeev and F. G. N. Cloke, *J. Organomet. Chem.*, 2003, **688**, 49–55.
- 83 J. M. R. Narayanam and C. R. J. Stephenson, *Chem. Soc. Rev.*, 2011, **40**, 102–113.
- 84 C. K. Prier, D. A. Rankic and D. W. C. MacMillan, *Chem. Rev.*, 2013, **113**, 5322–5363.
- 85 C. B. Larsen and O. S. Wenger, *Chem.–Eur. J.*, 2018, **24**, 2039–2058.
- 86 S. Cotton, in *Lanthanide and Actinide Chemistry*, John Wiley & Sons, Ltd., Chichester (U.K.), 2006, pp. 9–22.
- 87 A. Vogler and H. Kunkely, *Inorg. Chim. Acta*, 2006, **359**, 4130–4138.
- 88 R. Barraza and M. J. Allen, *Molecules*, 2020, **25**, 3892.
- 89 S. Cotton, in *Lanthanide and Actinide Chemistry*, John Wiley & Sons, Ltd., Chichester (U.K.), 2006, pp. 61–87.
- 90 Y. Qiao and E. J. Schelter, *Acc. Chem. Res.*, 2018, **51**, 2926–2936.
- 91 H. Yin, P. J. Carroll, J. M. Anna and E. J. Schelter, *J. Am. Chem. Soc.*, 2015, **137**, 9234–9237.
- 92 H. Yin, Y. Jin, J. E. Hertzog, K. C. Mullane, P. J. Carroll, B. C. Manor, J. M. Anna and E. J. Schelter, *J. Am. Chem. Soc.*, 2016, **138**, 16266–16273.
- 93 Y. Qiao, Q. Yang and E. J. Schelter, *Angew. Chem., Int. Ed.*, 2018, **57**, 10999–11003.
- 94 H. Yin, P. J. Carroll, B. C. Manor, J. M. Anna and E. J. Schelter, *J. Am. Chem. Soc.*, 2016, **138**, 5984–5993.
- 95 N. T. Rice, I. A. Popov, D. R. Russo, J. Bacsá, E. R. Batista, P. Yang, J. Telser and H. S. La Pierre, *J. Am. Chem. Soc.*, 2019, **141**, 13222–13233.
- 96 C. T. Palumbo, I. Zivkovic, R. Scopelliti and M. Mazzanti, *J. Am. Chem. Soc.*, 2019, **141**, 9827–9831.
- 97 A. R. Willauer, C. T. Palumbo, R. Scopelliti, I. Zivkovic, I. Douair, L. Maron and M. Mazzanti, *Angew. Chem., Int. Ed.*, 2020, **59**, 3549–3553.
- 98 A. R. Willauer, C. T. Palumbo, F. Fadaei-Tirani, I. Zivkovic, I. Douair, L. Maron and M. Mazzanti, *J. Am. Chem. Soc.*, 2020, **142**, 5538–5542.
- 99 A. R. Willauer, I. Douair, A.-S. Chauvin, F. Fadaei-Tirani, J.-C. G. Bünzli, L. Maron and M. Mazzanti, *Chem. Sci.*, 2022, **13**, 681–691.
- 100 T. P. Gomba, A. Ramanathan, N. T. Rice and H. S. La Pierre, *Dalton Trans.*, 2020, **49**, 15945–15987.
- 101 P. Girard, J. L. Namy and H. B. Kagan, *J. Am. Chem. Soc.*, 1980, **102**, 2693–2698.
- 102 H. B. Kagan, *Inorg. Chim. Acta*, 1987, **140**, 3–6.
- 103 H. B. Kagan, *Tetrahedron*, 2003, **59**, 10351–10372.
- 104 K. C. Nicolaou, S. P. Ellery and J. S. Chen, *Angew. Chem., Int. Ed.*, 2009, **48**, 7140–7165.
- 105 M. Szostak, N. J. Fazakerley, D. Parmar and D. J. Procter, *Chem. Rev.*, 2014, **114**, 5959–6039.
- 106 M. Suta and C. Wickleder, *J. Lumin.*, 2019, **210**, 210–238.
- 107 W. G. Skene, J. C. Scaiano and F. L. Cozens, *J. Org. Chem.*, 1996, **61**, 7918–7921.
- 108 A. Ogawa, Y. Sumino, T. Nanke, S. Ohya, N. Sonoda and T. Hirao, *J. Am. Chem. Soc.*, 1997, **119**, 2745–2746.
- 109 E. Prasad, B. W. Knettle and R. A. Flowers II, *Chem.–Eur. J.*, 2005, **11**, 3105–3112.
- 110 C. N. Rao and S. Hoz, *J. Org. Chem.*, 2012, **77**, 4029–4034.
- 111 A. Ogawa, S. Ohya, Y. Sumino, N. Sonoda and T. Hirao, *Tetrahedron Lett.*, 1997, **38**, 9017–9018.
- 112 Y. Sumino, N. Harato, Y. Tomisaka and A. Ogawa, *Tetrahedron*, 2003, **59**, 10499–10508.
- 113 T. C. Jenks, M. D. Bailey, J. L. Hovey, S. Fernando, G. Basnayake, M. E. Cross, W. Li and M. J. Allen, *Chem. Sci.*, 2018, **9**, 1273–1278.
- 114 P. L. Watson, T. H. Tulip and I. Williams, *Organometallics*, 1990, **9**, 1999–2009.
- 115 J. Garcia and M. J. Allen, *Eur. J. Inorg. Chem.*, 2012, **2012**, 4550–4563.
- 116 A. C. Thomas and A. B. Ellis, *Organometallics*, 1985, **4**, 2223–2225.
- 117 S. Harder, D. Naglav, C. Ruspici, C. Wickleder, M. Adlung, W. Hermes, M. Eul, R. Pöttgen, D. B. Rego, F. Poineau, K. R. Czerwinski, R. H. Herber and I. Nowik, *Chem.–Eur. J.*, 2013, **19**, 12272–12280.
- 118 T. Tsuji, N. Hosoya, S. Fukazawa, R. Sugiyama, T. Iwasa, H. Tsunoyama, H. Hamaki, N. Tokitoh and A. Nakajima, *J. Phys. Chem. C*, 2014, **118**, 5896–5907.
- 119 T. Tsuji, S. Fukazawa, R. Sugiyama, K. Kawasaki, T. Iwasa, H. Tsunoyama, N. Tokitoh and A. Nakajima, *Chem. Phys. Lett.*, 2014, **595–596**, 144–150.
- 120 R. P. Kelly, T. D. M. Bell, R. P. Cox, D. P. Daniels, G. B. Deacon, F. Jaroschik, P. C. Junk, X. F. Le Goff, G. Lemercier, A. Martinez, J. Wang and D. Werner, *Organometallics*, 2015, **34**, 5624–5636.
- 121 T. Simler, T. J. Feuerstein, R. Yadav, M. T. Gamer and P. W. Roesky, *Chem. Commun.*, 2019, **55**, 222–225.



- 122 H. Ramanantoanina, L. Merzoud, J. T. Muya, H. Chermette and C. Daul, *J. Phys. Chem. A*, 2020, **124**, 152–164.
- 123 M. Szostak and D. J. Procter, *Angew. Chem., Int. Ed.*, 2012, **51**, 9238–9256.
- 124 S. Maity, *Eur. J. Org. Chem.*, 2021, **2021**, 5312–5319.
- 125 R. Nomura, T. Matsuno and T. Endo, *J. Am. Chem. Soc.*, 1996, **118**, 11666–11667.
- 126 H. C. Aspinall, N. Greeves and C. Valla, *Org. Lett.*, 2005, **7**, 1919–1922.
- 127 T. Ueda, N. Kanomata and H. Machida, *Org. Lett.*, 2005, **7**, 2365–2368.
- 128 F. Orsini and E. M. Lucci, *Tetrahedron Lett.*, 2005, **46**, 1909–1911.
- 129 S. Maity and R. A. Flowers, *J. Am. Chem. Soc.*, 2019, **141**, 3207–3216.
- 130 F. Hélicon and J.-L. Namy, *J. Org. Chem.*, 1999, **64**, 2944–2946.
- 131 M.-I. Lannou, F. Hélicon and J.-L. Namy, *Tetrahedron*, 2003, **59**, 10551–10565.
- 132 E. J. Corey and G. Z. Zheng, *Tetrahedron Lett.*, 1997, **38**, 2045–2048.
- 133 L. Sun, K. Sahloul and M. Mellah, *ACS Catal.*, 2013, **3**, 2568–2573.
- 134 Y.-F. Zhang and M. Mellah, *ACS Catal.*, 2017, **7**, 8480–8486.
- 135 S. Bazzi, E. Schulz and M. Mellah, *Org. Lett.*, 2019, **21**, 10033–10037.
- 136 Y.-F. Zhang and M. Mellah, *Org. Chem. Front.*, 2022, **9**, 1308–1314.
- 137 H.-M. Huang, J. J. W. McDouall and D. J. Procter, *Nat. Catal.*, 2019, **2**, 211–218.
- 138 S. Agasti, N. A. Beattie, J. J. W. McDouall and D. J. Procter, *J. Am. Chem. Soc.*, 2021, **143**, 3655–3661.
- 139 W. J. Evans, I. Bloom, W. E. Hunter and J. L. Atwood, *J. Am. Chem. Soc.*, 1983, **105**, 1401–1403.
- 140 W. J. Evans, T. A. Ulibarri and J. W. Ziller, *J. Am. Chem. Soc.*, 1990, **112**, 219–223.
- 141 W. J. Evans, D. G. Giarikos, C. B. Robledo, V. S. Leong and J. W. Ziller, *Organometallics*, 2001, **20**, 5648–5652.
- 142 W. J. Evans, S. L. Gonzales and J. W. Ziller, *J. Am. Chem. Soc.*, 1994, **116**, 2600–2608.
- 143 A. A. Trifonov, Y. A. Kurskii, M. N. Bochkarev, S. Muehle, S. Dechert and H. Schumann, *Russ. Chem. Bull.*, 2003, **52**, 601–606.
- 144 J. Wang, R. I. J. Amos, A. S. P. Frey, M. G. Gardiner, M. L. Cole and P. C. Junk, *Organometallics*, 2005, **24**, 2259–2261.
- 145 A. Ishida, S. Toki and S. Takamuku, *Chem. Lett.*, 1985, **14**, 893–896.
- 146 A. Ishida, S. Toki and S. Takamuku, *J. Chem. Soc., Chem. Commun.*, 1985, 1481–1483.
- 147 T. Kondo, M. Akazome and Y. Watanabe, *J. Chem. Soc., Chem. Commun.*, 1991, 757–758.
- 148 H. Tsurugi and K. Mashima, *J. Am. Chem. Soc.*, 2021, **143**, 7879–7890.
- 149 A. Prieto and F. Jaroschik, *Curr. Org. Chem.*, 2022, **26**, 6–41.
- 150 R. A. Sheldon and J. K. Kochi, *J. Am. Chem. Soc.*, 1968, **90**, 6688–6698.
- 151 L. Chang, Q. An, L. Duan, K. Feng and Z. Zuo, *Chem. Rev.*, 2022, **122**, 2429–2486.
- 152 Q. Yang, Y.-H. Wang, Y. Qiao, M. Gau, P. J. Carroll, P. J. Walsh and E. J. Schelter, *Science*, 2021, **372**, 847–852.
- 153 J.-J. Guo, A. Hu, Y. Chen, J. Sun, H. Tang and Z. Zuo, *Angew. Chem., Int. Ed.*, 2016, **55**, 15319–15322.
- 154 A. Hu, Y. Chen, J.-J. Guo, N. Yu, Q. An and Z. Zuo, *J. Am. Chem. Soc.*, 2018, **140**, 13580–13585.
- 155 A. Hu, J.-J. Guo, H. Pan, H. Tang, Z. Gao and Z. Zuo, *J. Am. Chem. Soc.*, 2018, **140**, 1612–1616.
- 156 J. Schwarz and B. König, *Chem. Commun.*, 2019, **55**, 486–488.
- 157 K. Zhang, L. Chang, Q. An, X. Wang and Z. Zuo, *J. Am. Chem. Soc.*, 2019, **141**, 10556–10564.
- 158 A. Hu, J.-J. Guo, H. Pan and Z. Zuo, *Science*, 2018, **361**, 668–672.
- 159 Q. An, Z. Wang, Y. Chen, X. Wang, K. Zhang, H. Pan, W. Liu and Z. Zuo, *J. Am. Chem. Soc.*, 2020, **142**, 6216–6226.
- 160 R. Anwander, M. Dolg and F. T. Edelman, *Chem. Soc. Rev.*, 2017, **46**, 6697–6709.
- 161 A. Gulino, M. Casarin, V. P. Conticello, J. G. Gaudiello, H. Mauermann, I. Fragala and T. J. Marks, *Organometallics*, 1988, **7**, 2360–2364.
- 162 W. J. Evans, T. J. Deming and J. W. Ziller, *Organometallics*, 1989, **8**, 1581–1583.
- 163 P. Dröse, A. R. Crozier, S. Lashkari, J. Gottfriedsen, S. Blaurock, C. G. Hrib, C. Maichle-Mössmer, C. Schädle, R. Anwander and F. T. Edelman, *J. Am. Chem. Soc.*, 2010, **132**, 14046–14047.
- 164 A. D. Sutton, D. L. Clark, B. L. Scott and J. C. Gordon, *Inorganics*, 2015, **3**, 589–596.
- 165 D. Schneider, N. Harmgarth, F. T. Edelman and R. Anwander, *Chem.–Eur. J.*, 2017, **23**, 12243–12252.
- 166 L. Hirneise, C. Maichle-Mössmer and R. Anwander, *Inorg. Chem.*, 2021, **60**, 18211–18224.
- 167 L. Hirneise, J. Langmann, G. Zitzer, L. Ude, C. Maichle-Mössmer, W. Scherer, B. Speiser and R. Anwander, *Organometallics*, 2021, **40**, 1786–1800.
- 168 T. R. Boussie, D. C. Eisenberg, J. Rigsbee, A. Streitwieser and A. Zalkin, *Organometallics*, 1991, **10**, 1922–1928.
- 169 U. Kilimann, R. Herbst-Irmer, D. Stalke and F. T. Edelman, *Angew. Chem., Int. Ed. Engl.*, 1994, **33**, 1618–1621.
- 170 A. Ashley, G. Balazs, A. Cowley, J. Green, C. H. Booth and D. O'Hare, *Chem. Commun.*, 2007, 1515–1517.
- 171 G. Balazs, F. G. N. Cloke, J. C. Green, R. M. Harker, A. Harrison, P. B. Hitchcock, C. N. Jardine and R. Walton, *Organometallics*, 2007, **26**, 3111–3119.
- 172 R. Sessoli, D. Gatteschi, A. Caneschi and M. A. Novak, *Nature*, 1993, **365**, 141–143.
- 173 A. M. Ako, I. J. Hewitt, V. Mereacre, R. Clérac, W. Wernsdorfer, C. E. Anson and A. K. Powell, *Angew. Chem., Int. Ed.*, 2006, **45**, 4926–4929.
- 174 O. Kahn, *Molecular Magnetism*, VCH, New York, N.Y., 1993.
- 175 N. Ishikawa, M. Sugita, T. Okubo, N. Tanaka, T. Iino and Y. Kaizu, *Inorg. Chem.*, 2003, **42**, 2440–2446.



- 176 L. Maria, M. Paula Campello, Â. Domingos, I. Santos and R. Andersen, *J. Chem. Soc., Dalton Trans.*, 1999, 2015–2020.
- 177 J. D. Rinehart and J. R. Long, *J. Am. Chem. Soc.*, 2009, **131**, 12558–12559.
- 178 W. W. Lukens, N. Magnani and C. H. Booth, *Inorg. Chem.*, 2012, **51**, 10105–10110.
- 179 J. D. Rinehart, M. Fang, W. J. Evans and J. R. Long, *Nat. Chem.*, 2011, **3**, 538–542.
- 180 J. D. Rinehart, M. Fang, W. J. Evans and J. R. Long, *J. Am. Chem. Soc.*, 2011, **133**, 14236–14239.
- 181 D. N. Woodruff, R. E. P. Winpenny and R. A. Layfield, *Chem. Rev.*, 2013, **113**, 5110–5148.
- 182 J.-L. Liu, Y.-C. Chen and M.-L. Tong, *Chem. Soc. Rev.*, 2018, **47**, 2431–2453.
- 183 K. R. Meihaus and J. R. Long, *J. Am. Chem. Soc.*, 2013, **135**, 17952–17957.
- 184 S.-D. Jiang, B.-W. Wang, H.-L. Sun, Z.-M. Wang and S. Gao, *J. Am. Chem. Soc.*, 2011, **133**, 4730–4733.
- 185 M. D. Korzyński, M. Bernhardt, V. Romankov, J. Dreiser, G. Matmon, F. Pointillart, B. Le Guennic, O. Cador and C. Copéret, *Chem. Sci.*, 2022, **13**, 10574–10580.
- 186 L. Münzfeld, C. Schoo, S. Bestgen, E. Moreno-Pineda, R. Köppe, M. Ruben and P. W. Roesky, *Nat. Commun.*, 2019, **10**, 3135.
- 187 M. Tricoire, L. Münzfeld, J. Moutet, N. Mahieu, L. La Droitte, E. Moreno-Pineda, F. Gendron, J. D. Hilgar, J. D. Rinehart, M. Ruben, B. Le Guennic, O. Cador, P. W. Roesky and G. Nocton, *Chem.–Eur. J.*, 2021, **27**, 13558–13567.
- 188 J. D. Hilgar, M. G. Bernbeck, B. S. Flores and J. D. Rinehart, *Chem. Sci.*, 2018, **9**, 7204–7209.
- 189 J. D. Hilgar, M. G. Bernbeck and J. D. Rinehart, *J. Am. Chem. Soc.*, 2019, **141**, 1913–1917.
- 190 G. Nocton and L. Ricard, *Dalton Trans.*, 2014, **43**, 4380–4387.
- 191 M. D. Walter, G. Wolmershäuser and H. Sitzmann, *J. Am. Chem. Soc.*, 2005, **127**, 17494–17503.
- 192 S. Lauk and A. Schäfer, *Eur. J. Inorg. Chem.*, 2021, **2021**, 5026–5036.
- 193 C. A. Gould, K. R. McClain, J. M. Yu, T. J. Groshens, F. Furche, B. G. Harvey and J. R. Long, *J. Am. Chem. Soc.*, 2019, **141**, 12967–12973.
- 194 K. L. M. Harriman, J. J. Le Roy, L. Ungur, R. J. Holmberg, I. Korobkov and M. Murugesu, *Chem. Sci.*, 2017, **8**, 231–240.
- 195 D. J. Berg, J. M. Boncella and R. A. Andersen, *Organometallics*, 2002, **21**, 4622–4631.
- 196 S. Demir, J. M. Zadrozny, M. Nippe and J. R. Long, *J. Am. Chem. Soc.*, 2012, **134**, 18546–18549.
- 197 S. Demir, M. Nippe, M. I. Gonzalez and J. R. Long, *Chem. Sci.*, 2014, **5**, 4701–4711.
- 198 C. A. Gould, L. E. Darago, M. I. Gonzalez, S. Demir and J. R. Long, *Angew. Chem., Int. Ed.*, 2017, **56**, 10103–10107.
- 199 S. Demir, M. I. Gonzalez, L. E. Darago, W. J. Evans and J. R. Long, *Nat. Commun.*, 2017, **8**, 2144.
- 200 C. A. Gould, E. Mu, V. Vieru, L. E. Darago, K. Chakarawet, M. I. Gonzalez, S. Demir and J. R. Long, *J. Am. Chem. Soc.*, 2020, **142**, 21197–21209.
- 201 C. A. Gould, K. R. McClain, D. Reta, J. G. C. Kragoskow, D. A. Marchiori, E. Lachman, E.-S. Choi, J. G. Analytis, R. D. Britt, N. F. Chilton, B. G. Harvey and J. R. Long, *Science*, 2022, **375**, 198–202.
- 202 K. S. Pedersen, J. Dreiser, H. Weihe, R. Sibille, H. V. Johannesen, M. A. Sørensen, B. E. Nielsen, M. Sigrist, H. Mutka, S. Rols, J. Bendix and S. Piligkos, *Inorg. Chem.*, 2015, **54**, 7600–7606.
- 203 L. Escalera-Moreno, J. J. Baldoví, A. Gaita-Ariño and E. Coronado, *Chem. Sci.*, 2018, **9**, 3265–3275.
- 204 A. Lunghi, F. Totti, R. Sessoli and S. Sanvito, *Nat. Commun.*, 2017, **8**, 14620.
- 205 D. Reta, J. G. C. Kragoskow and N. F. Chilton, *J. Am. Chem. Soc.*, 2021, **143**, 5943–5950.
- 206 H.-D. Amberger, H. Reddmann and F. T. Edelmann, *J. Organomet. Chem.*, 2005, **690**, 2238–2242.
- 207 F. Guégan, J. Jung, B. Le Guennic, F. Riobé, O. Maury, B. Gillon, J.-F. Jacquot, Y. Guyot, C. Morell and D. Luneau, *Inorg. Chem. Front.*, 2019, **6**, 3152–3157.
- 208 P. Evans, D. Reta, G. F. S. Whitehead, N. F. Chilton and D. P. Mills, *J. Am. Chem. Soc.*, 2019, **141**, 19935–19940.
- 209 D. P. Mills and P. Evans, *Chem.–Eur. J.*, 2021, **27**, 6645–6665.
- 210 J. C. Vanjak, B. O. Wilkins, V. Vieru, N. S. Bhuvanesh, J. H. Reibenspies, C. D. Martin, L. F. Chibotaru and M. Nippe, *J. Am. Chem. Soc.*, 2022, **144**, 17743–17747.
- 211 A. Gaita-Ariño, F. Luis, S. Hill and E. Coronado, *Nat. Chem.*, 2019, **11**, 301–309.
- 212 S. L. Bayliss, D. W. Laorenza, P. J. Mintun, B. D. Kovos, D. E. Freedman and D. D. Awschalom, *Science*, 2020, **370**, 1309–1312.
- 213 L. C. de Camargo, M. Briganti, F. S. Santana, D. Stingham, R. R. Ribeiro, G. G. Nunes, J. F. Soares, E. Salvadori, M. Chiesa, S. Benci, R. Torre, L. Sorace, F. Totti and R. Sessoli, *Angew. Chem., Int. Ed.*, 2021, **60**, 2588–2593.
- 214 D. Aguilà, L. A. Barrios, V. Velasco, O. Roubeau, A. Repollés, P. J. Alonso, J. Sesé, S. J. Teat, F. Luis and G. Aromí, *J. Am. Chem. Soc.*, 2014, **136**, 14215–14222.
- 215 G. Aromí, F. Luis and O. Roubeau, in *Lanthanides and Actinides in Molecular Magnetism*, 2015, pp. 185–222.
- 216 M. Atzori and R. Sessoli, *J. Am. Chem. Soc.*, 2019, **141**, 11339–11352.
- 217 M. R. MacDonald, J. E. Bates, J. W. Ziller, F. Furche and W. J. Evans, *J. Am. Chem. Soc.*, 2013, **135**, 9857–9868.
- 218 K. Kundu, J. R. K. White, S. A. Moehring, J. M. Yu, J. W. Ziller, F. Furche, W. J. Evans and S. Hill, *Nat. Chem.*, 2022, **14**, 392–397.
- 219 R. J. Schwamm, J. R. Harmer, M. Lein, C. M. Fitchett, S. Granville and M. P. Coles, *Angew. Chem., Int. Ed.*, 2015, **54**, 10630–10633.
- 220 H.-J. Lim, S. Welinski, A. Ferrier, P. Goldner and J. J. L. Morton, *Phys. Rev. B*, 2018, **97**, 064409.
- 221 M. Le Dantec, M. Rančić, S. Lin, E. Billaud, V. Ranjan, D. Flanigan, S. Bertaina, T. Chanelière, P. Goldner, A. Erb, R. B. Liu, D. Estève, D. Vion, E. Flurin and P. Bertet, *Sci. Adv.*, 2021, **7**, eabj9786.
- 222 L. Münzfeld, A. Hauser, P. Hädinger, F. Weigend and P. W. Roesky, *Angew. Chem., Int. Ed.*, 2021, **60**, 24493–24499.



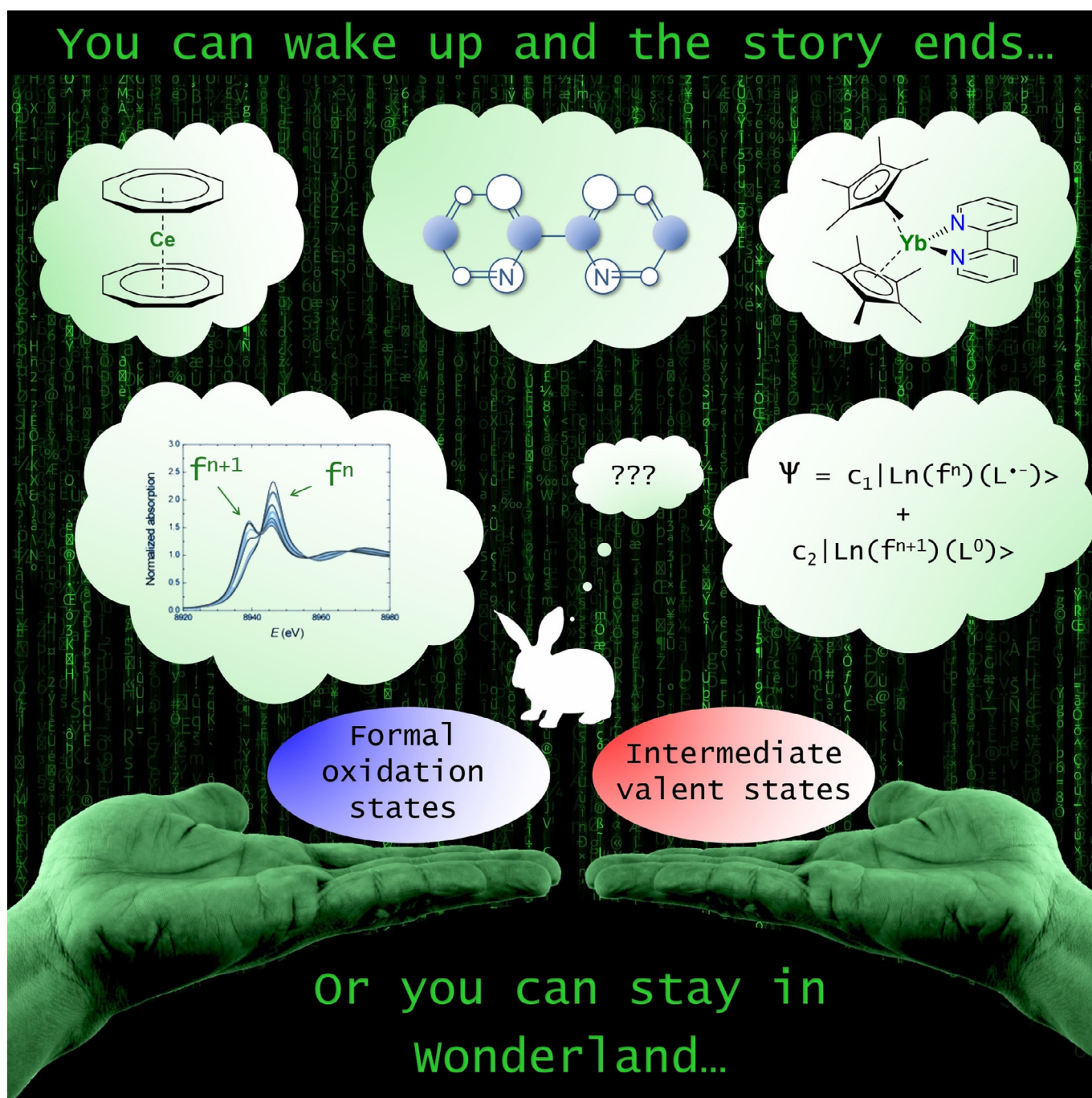
- 223 C. A. P. Goodwin, N. F. Chilton, G. F. Vettese, E. Moreno Pineda, I. F. Crowe, J. W. Ziller, R. E. P. Winpenny, W. J. Evans and D. P. Mills, *Inorg. Chem.*, 2016, **55**, 10057–10067.
- 224 M. Xémard, M. Cordier, F. Molton, C. Duboc, B. Le Guennic, O. Maury, O. Cador and G. Nocton, *Inorg. Chem.*, 2019, **58**, 2872–2880.
- 225 A.-M. Ariciu, D. H. Woen, D. N. Huh, L. E. Nodaraki, A. K. Kostopoulos, C. A. P. Goodwin, N. F. Chilton, E. J. L. McInnes, R. E. P. Winpenny, W. J. Evans and F. Tuna, *Nat. Commun.*, 2019, **10**, 3330.



Lanthanide Complexes

Intermediate Valence States in Lanthanide Compounds

Maxime Tricoire, Nolwenn Mahieu, Thomas Simler,* and Grégory Nocton*[a]

In memory of Prof. Richard A. Andersen

ORGANOMETALLICS

JANUARY 24, 2022 VOLUME 41 • ISSUE 2

pubs.acs.org/organometallics



ACS Publications
Most Trusted. Most Cited. Most Read.

www.acs.org

Chemistry A European Journal



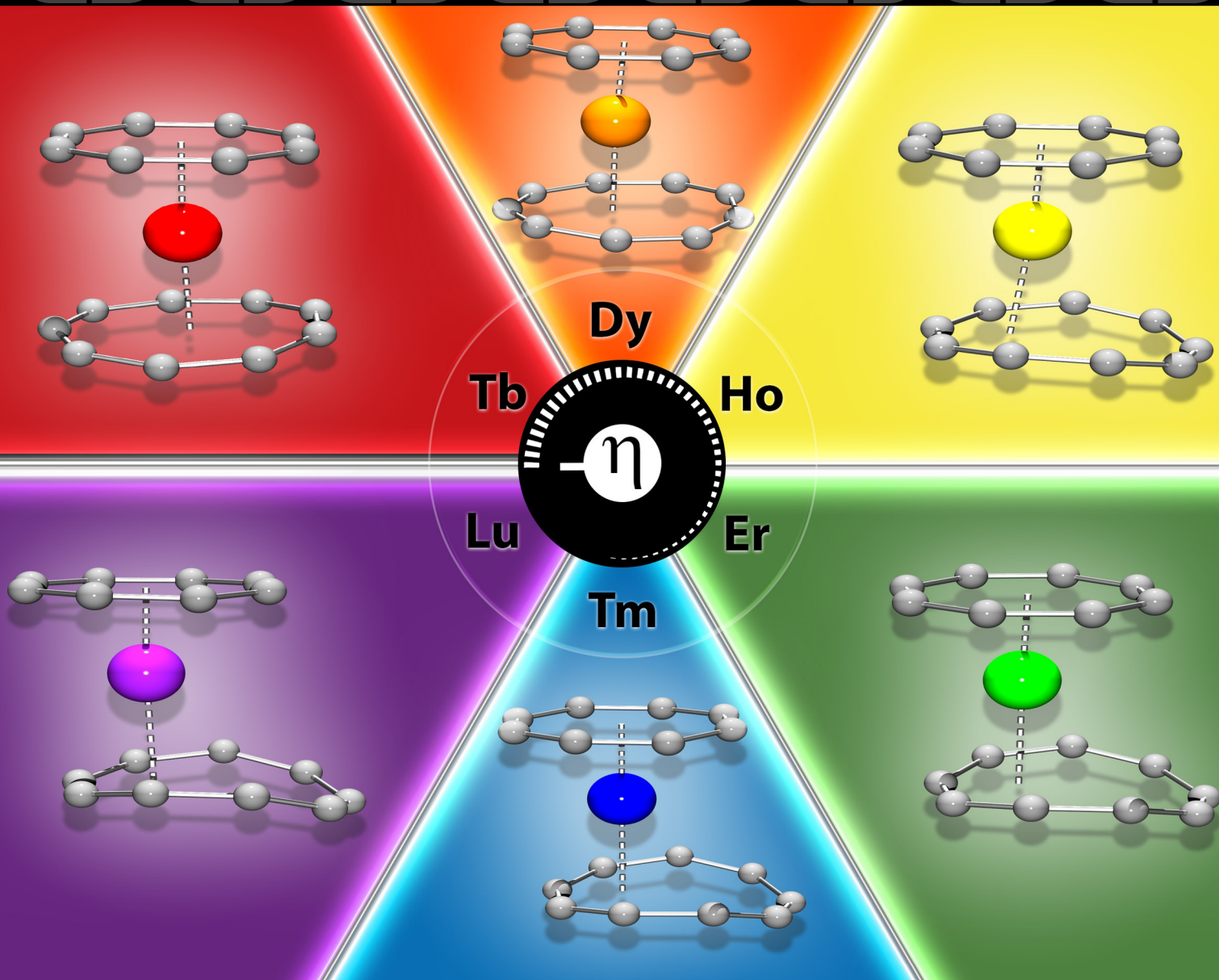
Chemistry
Europe

European Chemical
Societies Publishing

Cover Feature:

P. W. Roesky, G. Nocton et al.

Size-Controlled Hapticity Switching in $[\text{Ln}(\text{C}_9\text{H}_9)(\text{C}_8\text{H}_8)]$ Sandwiches



Chemical Science

Volume 14
Number 3
21 January 2023
Pages 397–724

rsc.li/chemical-science



ISSN 2041-6539

Titre : Synthèse, chimie redox et étude de la structure électronique de complexes de lanthanides avec des ligands aromatiques de tailles différentes

Mots clés : Lanthanides, Structure électronique, Synthèse, Ligand Cyclononatétraényl

Résumé : Ce travail de thèse s'intéresse à différents aspects de la chimie organo-métalliques des lanthanides. Des complexes de thulium divalents ont été utilisés pour l'activation de petites molécules telles que le CO et le CO₂. Ces complexes ont été étudiés par divers moyens spectroscopiques. Les connaissances acquises sur les composés de thulium, ont été utilisés pour investiguer les réactions de réduction du ligand cyclononatetraenyl par des composés de dysprosium divalent. Cette étude a permis l'obtention et la caractérisation de deux complexes dimériques. Dans un premier cas, le centre dysprosium semble avoir favorisé un transfert électronique vers le ligand, créant un radical qui a ensuite formé une liaison carbone-carbone par couplage radicalaire. Le second cas est plus complexe et malgré les différentes techniques utilisées, le degré d'oxydation des métaux est complexe à déterminer. Pour obtenir des informations supplémentaires sur la nature de ces Cnt réduits, cette chimie a donc été étendue à des composés trivalents hétéroleptiques. Ces nouveaux complexes ont permis de préciser les hypothèses issues de la première étude. Finalement, la capacité de ce ligand à s'isomériser a été étudiée. Notamment l'influence de la lumière sur ce phénomène dans le sel de ligand et dans une série de complexes a été rationalisée. Ainsi, ce travail a permis d'étendre la compréhension de la réactivité des lanthanides divalents ainsi que du comportement du ligand Cnt.

Title : Synthesis, redox chemistry, and electronic structure investigation of lanthanide complexes with aromatic ligands of various sizes and bulkiness

Keywords : Lanthanide ions, Electronic Structure, Synthesis, Cyclononatetraenyl ligand

Abstract : This work has investigated organolanthanide complexes to better understand their reactivity and electronic structure. First divalent thulium complexes have been used in small molecule activation with CO and CO₂. The new species were characterized through various spectroscopic methods. The knowledge of divalent lanthanide reactivity was then harnessed to investigate the reduction of the Cnt ligand with divalent dysprosium compounds. Two different dimers resulting from this reaction have been studied. First, in one case, the dysprosium center seems to have reduced the Cnt ligand creating a radical which then reacted to form a new C—C bond. The second reactivity has been more difficult to rationalize. Despite the use of several characterization methods, the oxidation state of the metallic centers remain uncertain. As such, an heteroleptic approach has been chosen to gather additional information. The combination of trivalent starting materials and a bulky ligand led to the synthesis of new organometallic complexes yielding complementary information on the nature of the reduced Cnt moieties. Finally, the isomerisation of the Cnt unit has been studied both for the ligand salt and in a series of sandwich-type compounds. In particular, the influence of light irradiation on the phenomenon has been rationalized. To conclude, this work deepened our understanding of divalent lanthanide reactivity and of the behavior of the Cnt ligand.